

# Spectroscopy of Polymer Nanocomposites

# Spectroscopy of Polymer Nanocomposites

Edited by

**Sabu Thomas**

*International and Inter University Centre for Nanoscience  
and Nanotechnology, School of Chemical Sciences,  
Mahatma Gandhi University, Kottayam, Kerala, India*

**Didier Rouxel**

*Institut Jean Lamour, CNRS, Université de Lorraine,  
Vandoeuvre-lès-Nancy, France*

**Deepalekshmi Ponnamma**

*Center for Advanced Materials, Qatar University, Doha, Qatar*



ELSEVIER

AMSTERDAM • BOSTON • HEIDELBERG • LONDON  
NEW YORK • OXFORD • PARIS • SAN DIEGO  
SAN FRANCISCO • SINGAPORE • SYDNEY • TOKYO

William Andrew is an imprint of Elsevier



William Andrew is an imprint of Elsevier  
The Boulevard, Langford Lane, Kidlington, Oxford, OX5 1GB, UK  
50 Hampshire Street, 5th Floor, Cambridge, MA 02139, USA

Copyright © 2016 Elsevier Inc. All rights reserved.

No part of this publication may be reproduced or transmitted in any form or by any means, electronic or mechanical, including photocopying, recording, or any information storage and retrieval system, without permission in writing from the publisher. Details on how to seek permission, further information about the Publisher's permissions policies and our arrangements with organizations such as the Copyright Clearance Center and the Copyright Licensing Agency, can be found at our website: [www.elsevier.com/permissions](http://www.elsevier.com/permissions).

This book and the individual contributions contained in it are protected under copyright by the Publisher (other than as may be noted herein).

#### Notices

Knowledge and best practice in this field are constantly changing. As new research and experience broaden our understanding, changes in research methods, professional practices, or medical treatment may become necessary.

Practitioners and researchers must always rely on their own experience and knowledge in evaluating and using any information, methods, compounds, or experiments described herein. In using such information or methods they should be mindful of their own safety and the safety of others, including parties for whom they have a professional responsibility.

To the fullest extent of the law, neither the Publisher nor the authors, contributors, or editors, assume any liability for any injury and/or damage to persons or property as a matter of products liability, negligence or otherwise, or from any use or operation of any methods, products, instructions, or ideas contained in the material herein.

ISBN: 978-0-323-40183-8

#### British Library Cataloguing-in-Publication Data

A catalogue record for this book is available from the British Library.

#### Library of Congress Cataloguing-in-Publication Data

A catalog record for this book is available from the Library of Congress.

For Information on all William Andrew publications  
visit our website at <https://www.elsevier.com/>



*Publisher:* Matthew Deans  
*Acquisition Editor:* Simon Holt  
*Editorial Project Manager:* Peter Gane  
*Production Project Manager:* Julie-Ann Stansfield  
*Designer:* Greg Harris

Typeset by MPS Limited, Chennai, India

# List of Contributors

**Abdulsalam Abdulkadir**

Department of Chemistry and Biochemistry, Lamar University, Beaumont, TX, United States

**Mariam Ali SA Al-Maadeed**

Center for Advanced Materials, Qatar University, Doha, Qatar; Materials Science and Technology Program, Qatar University, Doha, Qatar

**John-John Cabibihan**

Department of Mechanical and Industrial Engineering, Qatar University, Doha, Qatar

**Mihai Chirtoc**

GRESPI, Multiscale Thermophysics Lab, Université de Reims Champagne Ardenne URCA, Reims, France

**P. Fakhri**

Department of Physics, Bu Ali Sina University, Hamedan, Iran

**Yves Fort**

Université de Lorraine, SRSMC, UMR 7565, Vandoeuvre-lès-Nancy, France; CNRS, SRSMC, UMR 7565, Vandoeuvre-lès-Nancy, France

**Rohit Ranganathan Gaddam**

Polymers and Functional Materials Division, CSIR-Indian Institute of Chemical Technology, Hyderabad, India

**Zhanhu Guo**

Department of Chemical and Biomolecular Engineering, University of Tennessee, Knoxville, TN, United States

**Qingliang He**

Dan F. Smith Department of Chemical Engineering, Lamar University, Beaumont, TX, United States

**Nicolas Horny**

GRESPI, Multiscale Thermophysics Lab, Université de Reims Champagne Ardenne URCA, Reims, France

**B. Jaleh**

Department of Physics, Bu Ali Sina University, Hamedan, Iran

**Suresh Kattimuttathu I**

Polymers & Functional Materials Division, CSIR-Indian Institute of Chemical Technology, Hyderabad, India

**V.I. Krinichnyi**

Institute of Problems of Chemical Physics, Chernogolovka, Russian Federation

**Emmanuel Lamouroux**

Université de Lorraine, SRSMC, UMR 7565, Vandoeuvre-lès-Nancy, France;  
CNRS, SRSMC, UMR 7565, Vandoeuvre-lès-Nancy, France

**A.T. Mane**

Functional Materials Research Laboratory, School of Physical Sciences,  
Solapur University, Solapur, Maharashtra, India

**Mary Mutz**

University of Tennessee, Knoxville, TN, United States

**Ramanuj Narayan**

Polymers and Functional Materials Division, CSIR-Indian Institute of Chemical  
Technology, Hyderabad, India

**Van Son Nguyen**

Institut Jean Lamour, CNRS, Université de Lorraine, Vandoeuvre-lès-Nancy, France

**Rajender Nutenki**

Polymers & Functional Materials Division, CSIR-Indian Institute of Chemical  
Technology, Hyderabad, India

**Yukihiro Ozaki**

Department of Chemistry, School of Science and Technology, Kwansei Gakuin  
University, Sanda, Hyogo, Japan

**V.B. Patil**

Functional Materials Research Laboratory, School of Physical Sciences,  
Solapur University, Solapur, Maharashtra, India

**Deepalekshmi Ponnamma**

Center for Advanced Materials, Qatar University, Doha, Qatar

**KVSN Raju**

Polymers and Functional Materials Division, CSIR-Indian Institute of Chemical  
Technology, Hyderabad, India

**Didier Rouxel**

Institut Jean Lamour, CNRS, Université de Lorraine, Vandoeuvre-lès-Nancy,  
France

**Kishor Kumar Sadasivuni**

Center for Advanced Materials, Qatar University, Doha, Qatar

**Tanusree Sarker**

Department of Chemistry and Biochemistry, Lamar University, Beaumont, TX,  
United States

**Harumi Sato**

Graduate School of Human Development and Environment, Kobe University,  
Kobe, Japan

**Thomas P. Schuman**

Chemistry Department, Missouri University of Science and Technology  
(formerly the University of Missouri-Rolla), Rolla, MO, United States

**Sasidhar Siddabattuni**

Department of Chemistry, Sri Sathya Sai Institute of Higher Learning,  
Anantapur, Andhra Pradesh, India

**Ismail Tavman**

Mechanical Engineering Department, Dokuz Eylul University,  
Tinaztepe-Buca/Izmir, Turkey

**Camille Thevenot**

Institut Jean Lamour, CNRS, Université de Lorraine, Vandoeuvre-lès-Nancy,  
France

**Sabu Thomas**

International and Inter University Centre for Nanoscience and Nanotechnology,  
School of Chemical Sciences, Mahatma Gandhi University, Kottayam,  
Kerala, India

**Alpaslan Turgut**

Mechanical Engineering Department, Dokuz Eylul University,  
Tinaztepe-Buca/Izmir, Turkey

**Sridevi Venkatachalam**

Department of Chemistry, Lady Doak College, Madurai, Tamil Nadu, India

**Abhilash Venkateshaiah**

Polymers & Functional Materials Division, CSIR-Indian Institute of Chemical  
Technology, Hyderabad, India

**Brice Vincent**

Institut Jean Lamour, CNRS, Université de Lorraine, Vandoeuvre-lès-Nancy,  
France

**Suying Wei**

Department of Chemistry and Biochemistry, Lamar University, Beaumont, TX,  
United States; Dan F. Smith Department of Chemical Engineering, Lamar  
University, Beaumont, TX, United States

**Xinlei Yan**

Department of Chemistry, School of Science and Technology, Kwansei Gakuin  
University, Sanda, Hyogo, Japan

# Preface

Recent years have witnessed the steep growth of polymer-based industries; particularly those related to nanotechnology. Various fillers of nanodimensions impart abnormal properties when incorporated into polymers. For instance, the insulating polymers turn conducting, flexible elastomer chains become rigid, brittle materials become tougher, and so on. This substantiates the significance of nanoscience in the polymer industry and explains how various molecular properties can be tailored to achieve ultimately superior performance.

However, quality measurement of the materials synthesized has much more significance as far as determining the usefulness of a particular material is concerned. In this regard, spectroscopy has the utmost importance because it investigates both structural and functional features of materials. This book is written as a unique source by which the reader should understand the importance of all kinds of spectroscopic techniques in the field of polymer nanocomposites. It contains two parts; the first being Chapters 1–3, which give information about the significance of spectroscopic techniques in characterizing the nanocomposites, the meaning, definition, and types of nanocomposites, and the thermodynamics within the polymer nanocomposite systems. This part is particularly aimed at beginners in the field of material science, through which all basics of spectroscopy and the mode of characterization of polymer-based materials by this technique must be well understood.

The second part contains the remaining 12 chapters, each of which tells about particular spectroscopic techniques. The very common methods, such as infrared (IR) spectroscopy, ultraviolet (UV) spectroscopy, nuclear magnetic resonance (NMR) spectroscopy, Raman, and x-ray photoelectron spectroscopy are discussed in detail, with the basic mechanisms and proper examples from polymer science and nanotechnology. Some other techniques, such as Brillouin spectroscopy (BS), dielectric spectroscopy, photothermal, and Mossbauer spectroscopy, are also incorporated so that the whole book has become an encyclopedia in the area of polymer nanocomposite spectroscopy.

The authors were selected according to their expertise in specific techniques, and all of them deserve special thanks in making the contribution valuable.

**Sabu Thomas**  
**Didier Rouxel**  
**Deepalekshmi Ponnamma**

# Spectroscopy—introducing the advantages and application areas in polymer nanocomposites

# 1

Deepalekshmi Ponnamma<sup>1</sup>, Didier Rouxel<sup>2</sup> and Sabu Thomas<sup>3</sup>

<sup>1</sup>*Center for Advanced Materials, Qatar University, Doha, Qatar*

<sup>2</sup>*Institut Jean Lamour, CNRS, Université de Lorraine, Vandoeuvre-lès-Nancy, France*

<sup>3</sup>*International and Inter University Centre for Nanoscience and Nanotechnology, School of Chemical Sciences, Mahatma Gandhi University, Kottayam, Kerala, India*

## 1.1 INTRODUCTION

Polymer nanocomposites are remarkable in many applications of technology and industry. These include packaging materials for the food and agricultural industry to highly resistant energy storage materials for space explorations. The nanocomposites are often made by dispersing the matrix polymer with one or more fillers in nanodimensions. Sometimes instead of one polymer a blend is used. Depending on the size of the fillers and aspect ratio, the characteristic properties of the resulting composite and their applications vary. For example, high aspect ratio fillers provide large specific surface area and thus a higher level of interactions between the filler and the polymer [1]. This leads to enhanced mechanical strength and is thus applicable in those materials where high modulus and stiffness are required. If conducting fillers like expanded graphite, graphene, carbon nanotubes (CNTs), etc. are used to fill insulating polymer matrices, composites of good conductivity, dielectric properties, sensing capacity, etc., can be made. In short, the final application depends on the nature and dimension of the filler, its concentration, polymer type, modes of preparation, filler dispersion in the matrix, and filler-polymer compatibility [1,2].

Proper characterization facilities are the most significant tools which make the prepared nanocomposite samples applicable in technology. Out of the large number of analyses, spectroscopy is best for characterizing polymers and fillers, as well as nanocomposites. In general, spectroscopy measures the behavior of a material in the presence of electromagnetic radiations. Based on the electromagnetic spectra, the spectroscopic techniques also include many types. For instance

the radio frequency radiation acts as the basis of nuclear magnetic resonance (NMR) spectroscopy, infrared (IR) radiation for IR spectroscopy, gamma radiation for Mossbauer spectroscopy, etc. Since the spectral techniques differ in the mode of operation and the radiation used, their applications also differ in the case of polymer nanocomposites. While some of the spectral techniques analyze the extent of modification of fillers and their interactions with the matrix polymer, some other techniques address the characteristic properties of the final nanocomposites. This chapter gives an outline of different spectroscopic methods and their uses in the field of polymer nanotechnology. This will help beginners to get an idea of general spectroscopy before proceeding to the subsequent chapters, which deal with each spectral technique in depth.

---

## 1.2 POLYMER NANOCOMPOSITES

### 1.2.1 A LARGE RANGE OF APPLICATIONS AND A LARGE MARKET

Composite materials are of growing interest and offer a large range of applications in fields as varied as mechanics, electronics, and optics. They are nowadays used in all areas of industry. They increasingly replace or supplement various material ranges, especially in the field of plastics. They can combine the polymer processing and the properties generally associated with inorganic materials. They can be custom made, depending on the intended application, by the addition of particles (crystalline or not) having the targeted properties to a polymer simply used as a matrix, or presenting its optical, electrical, and/or mechanical properties. The particles can be of different types and in various forms. Mention may be made for the most common: particles or carbon fibers [3,4], clays [5], ceramics [6], metal particles [7], or polymers [8]. The properties of the resulting composites, however, are often difficult to model and predictive calculations are most often the result of empirical laws.

The market growth of nanocomposites is very important since the market was 1.91 billion dollars in 2011 and projections are expected to be 5.91 billion in 2018 [9]. One of the primary reasons that stimulate the development of nanocomposites lies in the tremendous increase in the interaction surface between the two (or more) components of these materials. This requires reducing dimensions of the compound considered as the “load.” This is one reason why the load is often characterized in terms of surface area. This growth of the contact surface induces a predominance of the physical effects of the interfaces. This leads the bulk composite material to exhibit new properties or behaviors. In addition there is often the creation of a new phase of the material, called “interphase,” on the border of the two components. This interphase can be several micrometers thick around loads which, owing to their volume fraction and their dimension, can make it the main phase of the composite.

### 1.2.2 BRINGING NEW PROPERTIES TO POLYMERS: APPLICATIONS OF NANOCOMPOSITES IN PLASTICS

In particular, nanostructured polymers and nanocomposites are one of the main roads of the future in plastics. Nanoclays, CNTs and nanofibers, metal and oxide nanoparticles, and organosilicon nanocompounds are already used on industrial scales for many applications. The presence of these nanofillers allows for reinforcing the strength of the polymer, but also improving its fire resistance, reducing its permeability to fluids, improving its surface properties (friction and wear), or making it conductive. Therefore the use of these nanofillers extends the standard polymer matrices performance but also their range of applications. For example, low temperature resistance and low impact strength are obstacles to the use of poly lactic acid for high-value packaging. These brakes may be waived by the incorporation of nanofillers which can be used to maintain the transparency of the biopolymer.

The addition of nanoparticles can improve or modify the performances of polymers, however, this requires mastering the dispersion of the nanofillers in the matrix and the interactions between the various components. This technological barrier, that remains industrially major, is now well identified and the subject of many research projects between academic and industrial partners. The incorporation of nanocrystals with specific properties can also permit the development of engineering polymers that can be incorporated into high-tech devices, sensors, or actuators. To develop a new generation of active polymer materials with physical coupling between electrical, mechanical, and optical functions is essential to future developments of innovative sensors and integrated optoelectronic devices. The nanocomposite approach had, in this context, the main objective to explore other technologies than those based on bulk crystals or ceramics, which are often costly in terms of development and shaping. The insertion of nanofillers is also motivated by the desire to maintain the transparency of the polymer, but also to influence sometimes major surface effects on the physical properties of the final material. In summary, the most important and obvious effects that can be expected from the incorporation of fillers in the polymer matrix are:

- Improving the mechanical reinforcement [10–19]. This constitutes the largest share of the market for polymer matrix composites. A major “defect” of the polymers is their low resistance to mechanical stress. The addition of hard nanoparticles will, therefore, not only help to improve stress resistance, but will also give polymers resistance properties that are variable depending on the frequency of shocks (e.g., soft matter at high frequency, useful to cash a shock, and on the contrary hard at low frequencies, to impart stiffness). Mechanical reinforcement also involves improving its wear resistance.
- The increase in thermal barrier effects or dissemination of chemical elements. The industry widely uses polymers as coatings, in particular for their ease of shaping and their good electrical and chemical resistance. The addition of

nanoparticles in organic matrices can greatly improve the properties and, for example, extend their lifetime [20–22]. We find the use of these barrier properties in the hydrogen cell [14], thermal barrier, [23] and limitation (delay) of the flame propagation [24,25].

- The change of the dielectric properties [26–32] for electrical insulation or electronic (i.e., condenser). Note that these properties can be varied, depending on the frequency of use and the type of fillers used.
- The addition of optical properties [33]. It is known that polymers often have poor linear or nonlinear optical properties: the use of hybrid nanocomposites circumvents this problem and gives polymers optical barrier properties [34].

Finally, and this list is not exhaustive, the organic matrix nanocomposites are excellent candidates for biotechnological and biomedical applications, for antimicrobial functions [35] as well as for the realization by bioengineering of bone substitutes [36] or dental substitutes [37]. In this area, nanocomposite materials potentially allow the development of artificial tissues [38].

### 1.2.3 FABRICATION AND THE CHALLENGES EXISTING IN THE FIELD

There are various methods to fabricate polymer nanocomposites; the major techniques involve solution mixing, melt compounding, and *in-situ* polymerization. The last synthetic route uses the monomers wherein the particles must first be stabilized, for example by a film of amphiphilic molecules or a modified monomer that has a chemical group reactive with respect to the surface of nanofillers [1,2]. Further polymerization may lead to the production of transparent nanocomposites because of the low agglomeration of the nanoparticles. This monomer approach is also well suited to an *in-situ* synthesis of the nanoparticles by coprecipitation, as the microemulsions mixture composed of nanoscale water droplets (containing the reagents) and stabilized by a surfactant film in methyl methacrylate, for example, allows for the production of dispersed particles, thus overcoming the problem of the loss of the initial powders.

Freeze drying, latex compounding, mill mixing, etc., are also practiced depending upon the nature of polymers and nanofillers, and the properties of the intended final composite. Electrospinning is another sample-preparing method employed very recently for making fibrous and porous nanocomposite membranes. Such materials are mostly used for tissue engineering. Despite the large number of fabrication methods used for synthesizing nanocomposites, there are still some issues to be resolved to attain the highest performance for the obtained materials [2].

A high quality of dispersion is the most important requirement considering the different methods of preparing nanocomposites. All fabrication methods are based on a dispersion of nanoparticles in the liquid phase. An implementation in the molten thermoplastic is very appropriate since it consists of disperse particles in a polymer melt which then perform extrusion. The dispersion of the particles is improved, however, after functionalization of the nanofillers with organic

molecules, whose chemical nature is compatible with the polymer, is completed. This method is, for example, widely used for integrating nanoclays in polyolefins. The identification of a suitable common solvent to disperse both the nanofillers and the polymer is rather competing. Polymer solubility and dispersibility of the nanoparticles in the solvent is critical to obtain a homogeneous material. Achieving good polymer filler interfacial compatibility is another important requirement to be fulfilled during the nanocomposite synthesis [1].

---

## 1.3 NANOCOMPOSITE SPECTROSCOPY

### 1.3.1 WHAT CAN SPECTROSCOPY DO?

Characterizing the bonding conditions and identification of components have a lot to do with microscopic spectroscopy. The progress in this field during the recent years is rather amazing, especially the development of fluorescent markers below the diffraction limit, microscope point spread function by structured illumination, and *in-vivo* measurements. Since engineering materials are the pillars on which technology stands and their performance ultimately depends on their microstructures, understanding the behavior of such materials at microlevels is essential. Various spectroscopic analyses such as IR, scanning electron microscopy, extended X-ray absorption fine structure, X-ray absorption spectroscopy, photoluminescence, ultraviolet (UV), Raman, Confocal Raman, fluorescence, X-ray photoelectron spectroscopy (XPS), Auger electron spectroscopy (AES), etc. are used for this purpose. The IR spectrum is applicable in pharmaceuticals, foods, and environmental science, and is used to detect *in vivo* analysis of pathological tissue, thus helping in the rapid and accurate diagnosis of diseases. The potential applications of all these techniques can be summarized to solid state structural simulations, mechanical, optical, and electrical properties of engineering materials, and quantum-chemical calculations of the electronic structure [39].

### 1.3.2 VARIOUS SPECTRAL TECHNIQUES AND THE ADVANTAGES

In general, a spectrum can be either absorption or emission. In the former case, a beam of light is monitored before and after passing through the sample. Absorption happens when the energy of the photons matches the energy difference between two states of the material which is found from the change in the wavelength of light [40,41].

#### i. *Fluorescence Spectroscopy*

Higher energy photons are used to excite the sample and the emitted lower energy photons are checked for the fluorescence spectra. This is used for confocal microscopy, fluorescence resonance energy transfer, and fluorescence lifetime imaging in biochemical and medical fields.

ii. *X-ray Spectroscopy*

X-rays of sufficient frequency are allowed to interact with a substance in which ionization of atoms result. When the electrons of outer shells jump to the inner vacancies, emission of energy takes place either as radiation (fluorescence) or some less-bound electrons will be removed (Auger effect). The frequency/wavelength variation is a specific characteristic of the atom and the chemical bonding within. Since the crystalline materials scatter X-rays at certain angles, the interplanar distance of crystal atoms can be calculated by knowing the wavelength of X-ray used. Though particular wavelength of X-radiations are used for this measurement instead of the whole X-ray region, it is not considered a typical spectroscopy. Instead, this is known as *X-ray diffraction (XRD) studies* and will be discussed in detail in subsequent chapters.

iii. *Atomic Emission Spectroscopy*

A higher-temperature flame excites the atoms in the sample and thus emits light. The emission intensity is monitored during the wavelength of radiation using a high-resolution polychromator and allows for the detection of multiple elements in one run. Single elements can also be analyzed by setting the measurements at a specific wavelength.

iv. *Atomic Absorption Spectroscopy*

Here a preburner nebulizer, along with a low flame, is used to atomize the sample and flame at various wavelengths to excite the sample atoms. The amount of analyte in the sample depends on the amount of light absorbed after going through the flame. Usually a graphite furnace of greater sensitivity is used for atomization and this provides good selectivity and longer pathlength.

v. *Atomic Fluorescence Spectroscopy*

In this method, the flame atomizes the sample, light of a specific wavelength from a lamp excites the analyte atoms, and the intensity of fluorescing light emitted from the sample is measured for quantifying the analyte. However, this is not a common method.

vi. *Plasma Emission Spectroscopy*

There are different methods in plasma emission spectroscopy depending on the type of radiation input. These include direct-current plasma, glow discharge-optical emission spectrometry, inductively coupled plasma-atomic emission spectrometry, laser-induced breakdown spectroscopy, also called laser-induced plasma spectrometry, and microwave-induced plasma techniques. In all cases a plasma support gas and Argon are common and samples are deposited on one electrode (or the sample itself is used as the electrode in the case of conducting material).

vii. *Spark or Arc (Emission) Spectroscopy*

The main criterion for this method is that all samples should be conducting. Nonconducting materials are made conducting by grinding them with graphite powder. This qualitative analysis detects the emitted light of

various wavelengths from analyte atoms while heating the sample using an electric arc or spark.

Though all kinds of flame spectroscopic methods allows detection of elements in very low concentration ranges (even in parts per billion), the consumption of fuel (i.e., acetylene or hydrogen) and oxidant (i.e., oxygen, air, or nitrous oxide), the requirement of light detectors, etc., are considered as some minor drawbacks.

**viii.** *UV-visible Spectroscopy*

Almost all atoms are capable of absorbing the high-energy photons of UV light and cause electron excitation. This spectrum characterizes proteins, amino acids, DNA, etc., and usually the ratio of 260/280-nm absorbance marks the relative purity of a solution. For visible regions, the vaporized substrates interact with the light, which can cause both absorption and emission. Often the visible absorption is combined with UV absorption under UV/Vis spectroscopy.

**ix.** *Vibrational Spectroscopy*

Both IR and Raman come under this category. In the IR spectroscopic method, the different types of interatomic bond vibrations existing in organic molecules, polymers, composites, etc. are investigated. As the near-IR radiation (near the visible range) can penetrate samples well, large samples are often checked at this range. It is very important in applications like rapid grain analysis, medical diagnosis, biotechnology, genomics analysis, interactomics research, inline textile monitoring, food analysis, chemical imaging/hyperspectral imaging, plastics, textiles, insect detection, and forensic and crime detection.

In Raman spectroscopy, the inelastic scattering of light is used to analyze vibrational and rotational modes of molecules. The recent method of CARS possesses high sensitivity and is used for *in vivo* spectroscopy and imaging.

**x.** *NMR Spectroscopy*

The structure of a compound is determined from the different electronic local environments of various atoms from their corresponding magnetic properties.

This is a very important method in chemistry to derive molecular structure.

**xi.** *Mössbauer Spectroscopy*

The properties of specific isotope nuclei in different atomic environments are investigated in this method by analyzing the resonant absorption characteristics using gamma-rays.

Other than these specific methods mentioned, a lot of other spectroscopic techniques exist in material characterization. Acoustic spectroscopy, cavity ring down spectroscopy, circular dichroism spectroscopy, deep-level transient spectroscopy, dielectric spectroscopy, thermal IR spectroscopy, dual polarization interferometry, Hadron spectroscopy, inelastic electron tunneling spectroscopy, inelastic neutron scattering, laser spectroscopy, neutron spin echo spectroscopy, photoacoustic, photo-thermal Raman optical activity, Terahertz, time-resolved spectroscopy, electron spin resonance (ESR), and mass spectroscopy (MS) are some examples.

### 1.3.3 SPECTRAL APPLICATIONS IN POLYMERS AND ITS NANOCOMPOSITES

The spectroscopic methods have a big role in characterizing the polymers and their nanocomposites. This section discusses the importance of various methods discussed so far in investigating the composite properties. Multilayered polymer composites are very much utilized in industries and their microscopic construction and unique properties are mostly addressed using Raman and Fourier transform infrared (FT-IR) micro-spectroscopy. Both of these vibrational spectral methods provide information on molecular structures, chemical environment, orientations, and conformations of polymer chains. FT-IR and Raman mapping and imaging differ in their spatial resolution and are considered as complementary methods [42].

FT-IR detects the change in the characteristic absorption patterns of a material and analyzes its composition or contamination. The near IR spectrum can be used to investigate the quality relevant parameters in polymers such as OH-number, acid or amine value, density, viscosity, degree of cross-linking, stabilizer, monomer content, as well as the role of chain scission in the mechanical degradation of polymers in a polymer nanocomposite [42]. Chemometric treatments and two-dimensional correlation spectroscopy also provide information on the reactive polymer-filler interaction sites and the interfaces. In nanocomposites, the influence of the average polymer phase dimensions on the filler loading along with the polymer chain deformation are understood from the IR absorption bands. The spatial resolution of up to approximately 100 nm for the fiber composite was reported using atomic force microscopy-IR spectroscopy with top-side illumination of the sample [43]. Diffuse reflectance FT-IR spectroscopy is a nondestructive method and can be obtained directly from the surface of composite materials with little or no sample preparation. This is useful in exploring the composition, curing, degradation, etc., of the matrix, surface contamination, and the degree of crystallinity of composites [44]. Finally FT-IR provides greater signal-to-noise ratio and digitized data with greater sensitivity.

Raman spectroscopy has the advantage of saving time when compared with other conventional methods. It is used to identify the property of fillers like CNTs, their functionalization as well as orientation. The Raman band shifts reveals mechanical deformation of CNTs, polymer-CNT interactions, phase transitions of the polymer, stress state, as well as the Young's modulus of the CNTs for the particular CNT composites [45]. The polarized micro-Raman spectroscopy is another recent technique which can explain the molecular orientation of composites. Micro-Raman analysis at the composite surface correlated the extent of surface-oriented relaxation and processing conditions for the polypropylene-oriented polymer composites [46].

NMR is an effective tool to study polymers, their end-groups, branching, functionalization, and various properties. The  $^1\text{H}$  NMR spectroscopy is simple, reproducible, and convenient for testing the polymer samples [47,48]. This method is reliable compared to gas permeation chromatography and mass spectroscopy, especially in detecting polymer molecular weight. Solid state NMR can analyze

insoluble polymers, high temperature NMR can analyze molten polymers, and high resolution magic angle spinning NMR can be used for swollen or semi-rigid polymers. Solid state C-13 NMR explained the chemical bonding and surface interactions of a series of organosilane coupling agents on the silica surface. The chemical shifts and line widths also indicated the effects on steric hindrance of the hydrocarbon chains of the coupling agent, and other silane-surface interactions [49].  $^{13}\text{C}$  spin-lattice relaxation times in the rotating frame of reference were also reported to study the graphite-filled epoxy composites [50].

The geometric and electronic structures and dynamics of paramagnetic molecules both in solution and solid state are obtained from electron paramagnetic resonance (EPR) spectroscopy. EPR also gives mechanism and kinetics of radical reactions and structural properties of transition metal complexes [51]. The spin labeling and spin trapping EPR techniques address issues such as membrane fluidity, oxidative stress, and antioxidant properties. The ESR spectrum of a spin probe is similar to EPR and it observes the hindrance of polymer segmental mobility in the presence of nanofiller and motional heterogeneity [52].

The UV-visible absorption spectrum of polyester-carbon black composites during 226–235-nm wavelengths exhibited its optical properties in terms of its absorption coefficient ( $\alpha$ ), dielectric constant, and energy gap [53]. For the polystyrene doped with copper powder samples, the UV-visible technique also demonstrated the transparency, the dispersion regions, refractive index, and optical band gap [54]. With copper (Cu) concentration, the refractive index increased while the energy gaps decreased. The analysis of multiwalled carbon nanotubes/polydimethylsiloxane composite in both specular and diffused models also revealed a linear increase in absorption coefficient and decrease in transmittance with the increasing CNTs [55]. Such films have promising applications in optical limiters against laser pulses. The photoluminescence of intensity and average decay time of carbon dots (C-dots) were monitored using fluorescent spectroscopy in the case of polyethylenimine-branched functionalized C-dots and observed that it is dependent on the C-dots crystallinity [56]. The intensity of the nanoparticles increased under excitation at 370 nm due to energy transfer to C-dots as there was a good spectral overlap between the C-dots emission spectra and the nanoparticles absorption spectra. An energy transfer efficiency up to 89% was observed depending upon the sample processing.

The dynamic measurements of nanoscale properties are done with dielectric spectroscopy which determines the electric strength, complex dielectric constant components, and dielectric loss factor for various electric field frequencies and at different temperatures [57]. In nanocomposites the dielectric properties are greatly determined by the filler content especially at lower frequencies. Both alternating current and direct current dielectric spectroscopies monitor the phase separation process, interactions between the separated phases, the effect of filler permittivity, filler purity (and conductivity), volume fraction, surface treatment, and processing conditions. XRD analyzes solid-state structural information for crystalline, semi-crystalline, amorphous polymeric, and composite materials [58].

This particular technique is very useful for deriving a number of information on polymer crystallinity, crystalline microstructure and orientation of polymers, lattice parameters, phase quantification, nanoscale analysis, dynamic studies, characteristics at various temperatures, and noncrystalline periodicity and size. Related to this method, XPS investigates surface modification of natural and synthetic polymers, carbon nanofillers, elemental chemical composition of a surface, and the bonding states of those elements and is applied in the analysis of tuned catalysts, engineered polymer coatings, and nanoelectronic heterostructures [59]. High-resolution Brillouin spectroscopy (HRBS) of TiO<sub>2</sub> filled ethylene–vinyl alcohol copolymer showed its dependence with concentration indicating the inclusion of TiO<sub>2</sub> nanoparticles inducing abnormal refractive index behavior for the nanocomposites at the applied laser wavelength [60]. Thus HRBS also stands out in its particular application in polymer nanocomposites.

To study the structure and composition of polymers, molecular weight distribution and bulk and surface properties, MS is yet another tool. This sensitive method is useful to identify minor polymer impurities and any by-product of polymerization. The main advantage of this method is that there is no need of any prior sample treatment or extensive separation [61]. Matrix assisted laser desorption ionization and electrospray ionization are the two types of MS in which the former technique analyzes polymers of narrow polydispersity with high precision and speed and the latter, high mass molecules that are easy to form multiply-charged gas phase ions and low molecular weight oligomers [62]. Mossbauer spectroscopy is used for exploring the structure of magnetostrictive metal/polymer composites for instance iron and gallium (Fe Ga)-filled polyurethane [63]. From the Mössbauer spectra based on single-domain magnetic particles, the spatial particle inhomogeneity, magnetic anisotropy, and interparticle interaction can be analyzed.

---

## 1.4 CONCLUSION

Spectroscopy is a very significant tool for deriving the polymer nanocomposite structure and their functional properties. Various types of spectroscopic techniques are explained here, along with specific advantages of the methods. Most importantly, the application of each method in investigating the nanocomposite behavior is well explained.

---

## REFERENCES

- [1] Ponnamma D, Sadasivuni KK, Grohens Y, Guo Q, Thomas S. Carbon nanotubes based elastomer composites—an approach towards multifunctional materials. 2014. <http://dx.doi.org/10.1039/C4TC01037J>.
- [2] Sadasivuni KK, Ponnamma D, Thomas S, Grohens Y. Evolution from graphite to graphene elastomer composites. *Prog Polym Sci* 2014;39:749–80.

- [3] Thostenson ET. Nanocomposites in context. *Composites Sci Technol* 2005;65:491–516.
- [4] Bokobza L. Multiwall carbon nanotube elastomeric composites: a review. *Polymer* 2007;48(17):4907–20.
- [5] Ray S, Okamoto M. Polymer/layered silicate nanocomposites: a review from preparation to processing. *Prog Polym Sci* 2003;28:1539–641.
- [6] Tjong SC. Structural and mechanical properties of polymer nanocomposites. *Mater Sci Eng R: Rep* 2006;53(3–4):73–197.
- [7] Horiuchi S, Nakao Y. Polymer/metal nanocomposites: assembly of metal nanoparticles in polymer films and their applications. *Curr Nanosci* 2007;3(3):206–14.
- [8] Yu L, Dean K, Li L. Polymer blends and composites from renewable resources. *Prog Polym Sci (Oxford)* 2006;31(6):576–602.
- [9] Nanocomposites (carbon nanotubes, polymer metal fiber, nanofibers, graphene, nanoplatelet and others) market for automotive, aviation, electronics, energy, construction, healthcare, plastics, military, consumer goods and other applications—global industry analysis, size, share, growth, trends and forecast, 2012–2018. 08/17/2013. Transparency Market Research.
- [10] Hsiao K-T, Alms J, Advani SG. Use of epoxy/multiwalled carbon nanotubes as adhesives to join graphite fibre reinforced polymer composites. *Nanotechnology* 2003;14(7):791–3.
- [11] Skákalová V, Dettlaff-Weglikowska U, Roth S. Electrical and mechanical properties of nanocomposites of single wall carbon nanotubes with PMMA. *Synth Met* 2005;152(1–3):349–52.
- [12] Friedrich K, Zhang Z, Scharb AK. Effects of various fillers on the sliding wear of polymer composites. *Composites Sci Technol* 2005;65(15–16 SPEC. ISS.):2329–43.
- [13] Pu Z, Mark JE, Jethmalani JM, Ford WT. Effects of dispersion and aggregation of silica in the reinforcement of poly(methyl acrylate) elastomers. *Chem Mater* 1997;9(11):2442–7.
- [14] Vivekchand SRC, Ramamurty U, Rao CNR. Mechanical properties of inorganic nanowire reinforced polymer-matrix composites. *Nanotechnology* 2006;17(11):S344–50.
- [15] Wang Q, Xue J, Shen W, Xue Q. The effect of nanometer SiC filler on the tribological behavior of PEEK. *Wear* 1997;209(1–2):316–21.
- [16] Wang Q, Xue Q, Liu W, Chen J. Effect of nanometer SiC filler on the tribological behavior of PEEK under distilled water lubrication. *J Appl Polym Sci* 2000;78(3):609–14.
- [17] Wetzel B, Hauptert F, Zhang MQ. Epoxy nanocomposites with high mechanical and tribological performance. *Composites Sci Technol* 2003;63(14):2055–67.
- [18] Iglesias P, Bermudez MD, Moscoso W, Rao BC, Shankar MR, Chandrasekar S. Friction and wear of nanostructured metals created by large strain extrusion machining. *Wear* 2007;263(1–6 SPEC. ISS.):636–42.
- [19] Ji QL, Zhang MQ, Wetzel RB, Friedrich K. Friction and wear of epoxy composites containing surface modified SiC nanoparticles. *Tribology Lett* 2005;20(2):115–23.
- [20] Choudalakis G, Gotsis AD. Permeability of polymer/clay nanocomposites: a review. *Eur Polym J* 2009;45:967–84.
- [21] Yeh JM, Chang KC. Polymer/layered silicate nanocomposite anticorrosive coatings. *J Ind Eng Chem* 2008;14(3):275–91.

- [22] Li X, Xu D, Zhang G, Wang Z, Zhao C, Na H. Influence of casting conditions on the properties of sulfonated poly(ether ether ketone ketone)/ phosphotungstic acid composite proton exchange membranes. *J Appl Polym Sci* 2007;103(6):4020–6.
- [23] Berghaus JO, Legoux JG, Moreau C, Tarasi F, Chráska T. Mechanical and thermal transport properties of suspension thermal-sprayed alumina-zirconia composite coatings. *J Therm Spray Technol* 2008;17(1):91–104.
- [24] Zhu J, Morgan AB, Lamelas FJ, Wilkie CA. Fire properties of polystyrene-clay nanocomposites. *Chem Mater* 2001;13:3774–80.
- [25] Chigwada G, Wilkie CA. Synergy between conventional phosphorus fire retardants and organically-modified clays can lead to fire retardancy of styrenics. *Polym Degrad Stab* 2003;81:551–7.
- [26] Ramajo L, Reboredo M, Castro M. Dielectric response and relaxation phenomena in composites of epoxy resin with BaTiO<sub>3</sub> particles. *Composites: Part A* 2005;36:1267–74.
- [27] Gross S, Camozzo D, Di Noto V, Armelao L, Tondello E. PMMA: a key macromolecular component for dielectric low-j hybrid inorganic–organic polymer films. *Eur Polym J* 2007;43:673–6969.
- [28] Dang ZM, Fan LZ, Shen Y, Nan CW. Dielectric behavior of novel three-phase MWNTs/BaTiO<sub>3</sub>/PVDF composites. *Mater Sci Eng B* 2003;103:140–4.
- [29] Capsal JF, Dantras E, Dandurand J, Lacabanne C. Electroactive influence of ferroelectricnanofillers on polyamide11 matrix properties. *J Non-Crystalline Solids* 2007;353:4437–42.
- [30] Kuo DH, Chang CC, Su TY, Wang WK, Lin BY. Dielectric Behaviors of multidoped BaTiO<sub>3</sub> epoxy composites. *J Eur Ceramics Soc* 2001;21:1171–7.
- [31] Dang ZM, Wang HY, Zhang YH, Qi JQ. Morphology and dielectric property of homogenous BaTiO<sub>3</sub>/PVDF nanocomposites prepared via the natural adsorption action of nanosized BaTiO<sub>3</sub>. *Macromol Rapid Commun* 2005;26:1185–9.
- [32] Dang ZM, Wang L, Ying Y, Zang Q, Lei QQ. Giant dielectric permittivities in functionalized carbon-nanotube/electroactive-polymer nanocomposites. *Adv Mater* 2007;19(6):1572–7.
- [33] Beecroft LL, Ober CK. Nanocomposites materials for optical applications. *Ober Chem Mater* 1997;9:6.
- [34] Xiong M, Gu G, You B, Wu L. Preparation and characterization of poly(styrene butylacrylate) latex/nano-ZnO nanocomposites. *J Appl Polym Sci* 2003;90:1923–31.
- [35] Hung HS, Hsu SH. Biological performances of poly(ether)urethane-silver nanocomposites. *Nanotechnology* 2007;18:47.
- [36] Hule RA, Pochan DJ. Polymer nanocomposites for biomedical applications. *MRS Bull* 2007;32:354–8.
- [37] Moszner N, Salz U. New developments of polymeric dental composites. *Prog Polym Sci* 2001;26(4):535–76.
- [38] Shahinpoor M, Bar-Cohen Y, Simpson JO, Smith J. Ionic polymer-metal composites (IPMCs) as biomimetic sensors, actuators and artificial muscles—a review. *Smart Mater Struct* 1998;7(6):R15–30.
- [39] Silva SM, Braga CR, Fook MV, Raposo CM, Carvalho LH, Canedo EL. Application of infrared spectroscopy to analysis of chitosan/clay nanocomposites. *Infrared spectroscopy-materials science, engineering and technology*. Croatia: InTech; 2012. p. 43–62.

- [40] Scheinmann F, editor. An introduction to spectroscopic methods for the identification of organic compounds: mass spectrometry, ultraviolet spectroscopy, electron spin resonance spectroscopy, nuclear magnetic resonance spectroscopy (recent developments), use of various spectral methods together, and documentation of molecular spectra, vol. 2. New York: Elsevier Ltd.; 2013.
- [41] Kumirska J, Czerwicka M, Kaczyński Z, Bychowska A, Brzozowski K, Thöming J, et al. Application of spectroscopic methods for structural analysis of chitin and chitosan. *Marine Drugs* 2010;8(5):1567–636.
- [42] Chang MC, Tanaka J. FT-IR study for hydroxyapatite/collagen nanocomposite cross-linked by glutaraldehyde. *Biomaterials* 2002;23(24):4811–18.
- [43] Kjoller K, Prater CB. Nanoscale infrared spectroscopy of polymer composites. *Am Lab* 2014.
- [44] Nuopponen MH, Birch GM, Sykes RJ, Lee SJ, Stewart D. Estimation of wood density and chemical composition by means of diffuse reflectance mid-infrared Fourier transform (DRIFT-MIR) spectroscopy. *J Agric Food Chem* 2006;54(1):34–40.
- [45] Yang K, Gu M, Guo Y, Pan X, Mu G. Effects of carbon nanotube functionalization on the mechanical and thermal properties of epoxy composites. *Carbon* 2009;47(7):1723–37.
- [46] Voyiatzis GA, Andrikopoulos KS. Fast monitoring of the molecular orientation in drawn polymers using micro-Raman spectroscopy. *Appl Spectrosc* 2002;56(4):528–35.
- [47] Postma A, Davis TP, Donovan AR, Li G, Moad G, Mulder R, et al. A simple method for determining protic end-groups of synthetic polymers by  $^1\text{H}$  NMR spectroscopy. *Polymer* 2006;47(6):1899–911.
- [48] Ponnamma D, Sadasivuni KK, Thomas S. NMR studies of natural rubber composites from macro- to nanoscales—a review. *Natural rubber materials: volume 2: composites and nanocomposites*. 2014. ISBN: 978-1-84973-631-2, <http://dx.doi.org/10.1039/9781849737654-00683>.
- [49] Joseph R, Zhang S, Ford WT. Structure and dynamics of a colloidal silica-poly (methyl methacrylate) composite by  $^{13}\text{C}$  and  $^{29}\text{Si}$  MAS NMR spectroscopy. *Macromolecules* 1996;29(4):1305–12.
- [50] Zaper AM, Cholli A, Koenig JL. Applications of solid-state magic angle NMR spectroscopy to fiber reinforced composites. *Molecular characterization of composite interfaces*. Berlin, Heidelberg: Springer; 1985.
- [51] Hinderberger D. EPR spectroscopy in polymer science. *EPR spectroscopy*. Berlin, Heidelberg: Springer; 2012.
- [52] John J, Klepac D, Petković Didović M, Raju KVS, Pius A, Andreis M, et al. Relaxations and chain dynamics of sequential full interpenetrating polymer networks based on natural rubber and poly (methyl methacrylate). *Polym Int* 2014;63(8):1427–38.
- [53] Al-Mosawi Ali I, Al-Maamori Mohammad H, AL-Mayalee Khalidah H. Spectroscopic studies of polyester—carbon black composites. *Res J Mater Sci* 2013;2320:6055 ISSN
- [54] Sharma PK, Kumar M, Pandey AC. Green luminescent ZnO:  $\text{Cu}^{2+}$  nanoparticles for their applications in white-light generation from UV LEDs. *J Nanoparticle Res* 2011;13(4):1629–37.
- [55] Khosla A, Gray BL. Preparation, characterization and micromolding of multi-walled carbon nanotube polydimethylsiloxane conducting nanocomposite polymer. *Mater Lett* 2009;63(13):1203–6.

- [56] Dong Y, Wang R, Li G, Chen C, Chi Y, Chen G. Polyamine-functionalized carbon quantum dots as fluorescent probes for selective and sensitive detection of copper ions. *Anal Chem* 2012;84(14):6220–4.
- [57] Fumagalli L, Ferrari G, Sampietro M, Gomila G. Quantitative nanoscale dielectric microscopy of single-layer supported biomembranes. *Nano Lett* 2009;9(4):1604–8.
- [58] Krishnamoorti R, Vaia RA, Giannelis EP. Structure and dynamics of polymer-layered silicate nanocomposites. *Chem Mater* 1996;8(8):1728–34.
- [59] Yang X, Tu Y, Li L, Shang S, Tao XM. Well-dispersed chitosan/graphene oxide nanocomposites. *ACS Appl Mater Interfaces* 2010;2(6):1707–13.
- [60] Riobóo RJ, De Andrés A, Kubacka A, Fernández-García M, Cerrada ML, Serrano C. Influence of nanoparticles on elastic and optical properties of a polymeric matrix: hypersonic studies on ethylene–vinyl alcohol copolymer–titania nanocomposites. *Eur Polym J* 2010;46(3):397–403.
- [61] Montaudo G, Lattimer RP, editors. *Mass spectrometry of polymers*. Boca Raton, Florida: CRC Press LLC; 2001.
- [62] Pandey JK, Reddy KR, Kumar AP, Singh RP. An overview on the degradability of polymer nanocomposites. *Polym Degrad Stab* 2005;88(2):234–50.
- [63] Zholudev SI, Kiseleva TY. Mössbauer study of new functional metal/polymer nanocomposites with spatially oriented FeGa particles. *Hyperfine Interact* 2014;226(1–3):375–82.

# An overview of nanocomposite nanofillers and their functionalization

# 2

Emmanuel Lamouroux<sup>1,2</sup> and Yves Fort<sup>1,2</sup>

<sup>1</sup>Université de Lorraine, SRSMC, UMR 7565, Vandoeuvre-lès-Nancy, France

<sup>2</sup>CNRS, SRSMC, UMR 7565, Vandoeuvre-lès-Nancy, France

## 2.1 INTRODUCTION

For decades, the development of polymer composites has been one of the most important areas in materials sciences. When a filler (the entity used to produce, reinforce, or to add to the properties of a polymer) is used at the nanometric scale—that is, at least one dimension is between 1 and 100 nm—it is called a nanofiller and the composites become nanocomposites. In other words, nanocomposites are considered as one family of nanomaterials, where a nano-object is dispersed into a matrix or a phase. A standardization committee, ISO TC229 “Nanotechnologies,” started in 2005 in the context of a joint group with IEC 113 “Nanotechnology Standardization for Electrical and Electronic Products and Systems,” defined terminology and nomenclature in a set of documents for the definition of nano-objects (ISO/TS27687 (2008), ISO/TS11360 (2010), ISO/TS88004 (2011)). Following these recommendations, the included nano-object in a nanocomposite must have one, two, or three dimensions less than 100 nm. In this new generation of materials, the properties imparted by the nanofillers are various: mechanical reinforcement, electrical conduction, optical or thermal properties, etc. These properties can be adjusted by modifying the chemical composition, shape, size, and surface chemical functions and/or physical properties of nanofillers. To incorporate nanofillers (generally at rates ranging from 1% to 10% of the total mass) into polymeric matrices, different strategies have been developed. Among them, there are: mixing nanoparticles and polymers at moderate temperature; adding nanofiller precursors into the polymerization reaction medium; polymerization of monomers in the presence of nanoparticles; and polymerization of monomers in the presence of functionalized nanoparticles. The last approach allows efficient grafting of nanoparticles to monomers during the polymerization step and better incorporation into nanocomposites.

In this chapter, we focus our attention on three types of nanofillers: (i) three-dimensional ones, like spherical nanoparticles or fullerenes, (ii) two-dimensional ones, like carbon nanotubes (CNTs), and (iii) one-dimensional ones, like graphene. After a presentation of these nano-objects' structures, properties, and preparation, their functionalization and dispersion are examined.

---

## 2.2 OVERVIEW OF NANOFILLERS

The choice of nanomaterials to prepare nanocomposites strongly depends on the application concerned. For example, the application might require special structural characteristics such as being tubular or spherical, or even optical or electrical properties. Hence, in this section, structure, properties, and preparation of inorganic nanoparticles including fullerene  $C_{60}$ , CNTs, graphene, and clays are briefly discussed.

### 2.2.1 INORGANIC NANOPARTICLES: METALS AND METALLOIDS

#### 2.2.1.1 *Nanoparticle structures*

An easy way to mentally picture an inorganic nanoparticle in comparison with the corresponding bulk material is to consider a cube made of metal, with edges measuring 1 cm, a volume of  $1 \text{ cm}^3$ , and a surface area of  $6 \text{ cm}^2$ . If this cube is divided into equivalent 10-nm nanocubes ( $10 \times 10^{-7} \text{ cm}$ ), the corresponding surface area becomes equal to  $600 \text{ m}^2$  ( $600 \times 10^4 \text{ cm}^2$ ). By further division of these 10-nm nanocubes into 2.5-nm nanocubes, a surface of  $1500 \text{ m}^2$  ( $1500 \times 10^4 \text{ cm}^2$ ) is reached. More concretely, imagine that the (nano) cubes consist of many spheres representing atoms. Let us consider the case of iron atoms. As a consequence of its volume, a 1-cm cube consists of  $5 \times 10^{24}$  iron atoms, corresponding to  $10^{-5}\%$  of surface atoms in proportion to core atoms. For 10 and 2.5-nm nanocubes, this ratio becomes 10% and 60%, respectively. Hence, this high proportion of surface atoms induces a high specific surface area leading to specific properties at nanoscale—such as surface plasmon resonance or quantum dot phenomena [1].

Any system tends to minimize its total free energy, which gives it higher stability. As nanoparticles exhibit high proportions of surface atoms, these systems have to minimize their surface free energy. The lowest surface free energy is conferred to the sphere, as because it has the lowest surface area compared with other simple shapes. Hence, atomic arrangement tends towards spherical symmetry to minimize its free energy. Moreover, as far as atomic arrangements are concerned, faces of different Miller indices, which possess different free energies, have to be considered. As more compact faces usually have lower free energies, faceted

**Table 2.1** Total Number of Atoms According to Number of Layers and Type of Structure

Number of Layers (K)	1	2	3	4	5
Octahedron	1	6	19	44	85
Cuboctahedron with triangle faces	1	13	55	147	309
Cuboctahedron with hexagonal faces	1	38	201	586	1289
Icosahedron	1	13	55	147	309
Decahedron	1	2	23	54	105
Truncated decahedron	1	13	55	147	309

structures have lower free energies than spherical ones. Consequently, for periodic arrangement construction, Wulff's theorem is applied:

$$\frac{\sigma_i}{h_i} = \text{Constant}$$

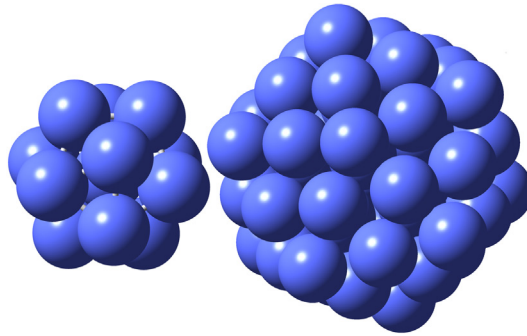
where  $\sigma_i$  is the surface-free energy of the surface under consideration and  $h_i$  corresponds to the distance between the central atom of the structure and surface  $i$ . Based on this theorem, different Wulff polyhedra can be constructed for periodic structures, such as hexagonal close packed (hcp) and face-centered cubic (fcc) ones. As truncated surfaces present more or less significant surface free energies, the exact structure depends on the surface free energies of the specific facets of the material. And since the construction of such polyhedral nanocrystals is based on a central atom around which whole layers of atoms are added successively, it will induce a series of magic numbers corresponding to the full number of atoms constituting the nanocrystals (Table 2.1).

The octahedral structure obtained from an fcc structure, presenting eight triangle faces (111) of low free energy, can serve as a starting point for cuboctahedral structure construction. A cuboctahedron has six square faces (100) and either eight triangular faces or eight hexagonal ones (111). Also, twinned cuboctahedra can be obtained from an hcp structure. The simplest cuboctahedron consists of 1 central atom and its 12 nearest close neighbors.

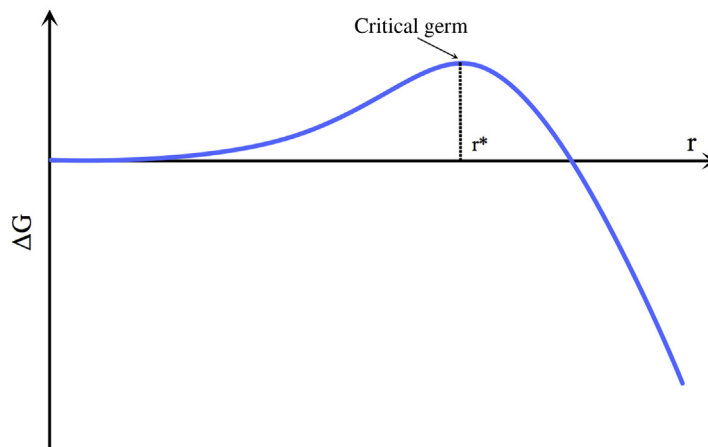
Besides periodic atomic arrangements, some nanoparticles—especially those with small sizes—adopt nonperiodic ones, leading to noncompact structures. Among them, there are icosahedra, which have a density of 0.688 and are very stable with small sizes—due to the sphericity of the structure and the density of its faces (Figure 2.1), decahedra, and truncated decahedra [2,3]. These structures have a  $C_5$  symmetry axis. It is worth underlining that nanocrystal stability strongly depends on chemical composition and environment.

### 2.2.1.2 Nucleation and growth

Starting from a metallic precursor—such as a metal target for the physical vapor desposition (PVD) process or metal salts or complexes for colloidal

**FIGURE 2.1**

Schematic representation of icosahedra consisting of 13 cobalt atoms (left) and 55 cobalt atoms (right).

**FIGURE 2.2**

Evolution of free energy versus germ radius.

processes—activation, metal ions, or atoms condense to reach equilibrium in system free energy. As soon as metal supersaturation in the precursor is reached, a critical germ forms (Figure 2.2) [4,5]. At this point the system has two possibilities to minimize its free energy: (i) to dissolve the critical germ, or (ii) to grow by either adding an atom to the critical germ or by coalescence with another critical germ, usually with both growth processes occurring at the same time.

As any system, germs/nanoparticles want to minimize their free energy, and in order to do that they will continue to grow until they form bulk materials. Thus, to obtain individual nanoparticles, it is necessary to stabilize their surfaces to stop growth and to avoid the aggregation process.

In the colloidal approach, three methods are widely used:

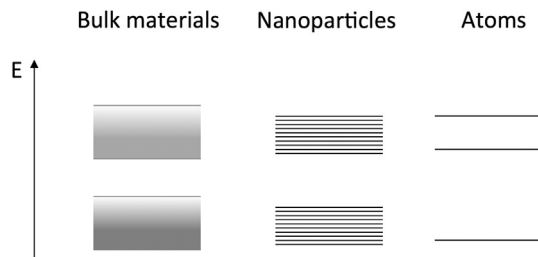
1. electrostatic repulsion stabilization, which consists in adding ionic species that form a double layer around nanoparticles. Thus, electrostatic stabilization is ensured by Coulombian repulsion between the double layers of two different nanoparticles.
2. steric hindrance stabilization is obtained by adsorbing molecules or macromolecules (i.e., ligands or polymers) onto the surface of nanoparticles. Thus, coalescence of nanoparticles coated by (macro) molecules is avoided by steric hindrance between these coatings.
3. stabilization by surfactant use implies both electrostatic interaction and steric hindrance. A surfactant is a molecule consisting of one polar head and an organic chain—usually ionic and alkyl ones, respectively. So, the ionic part interacts with the nanoparticles' surface while the alkyl chain acts as an anti-coalescence agent as a result of steric hindrance.

Furthermore, nanoparticles exhibit different face orientations—as discussed previously—mainly (111) and (100). The different chemicals used for nanoparticle stabilization have various affinities for these orientations. The stabilization of certain orientations in a specific way will induce the growth of nanoparticles with anisotropic forms. A good example is the anisotropic shaping of gold nanoparticle growth by a seeding process [6–8]. In this approach, nucleation and growth processes are separated. A first step consists in synthesizing small gold nanoparticles, which will be used as seeds in the second step. Then, these seeds are allowed to grow by feeding them gold atoms, but in presence of a soft reducing agent and specific stabilizers to control the nanoparticles' shape. For example, the use of cetyl trimethylammonium bromide (CTAB) as a stabilizer allows the growth of nanorods as a consequence of bromide anion adsorption onto (100) faces.

### **2.2.1.3 Physicochemical properties**

As nanomaterials have a higher specific surface area than the corresponding bulk material, their chemical reactivity will be influenced and can exhibit unusual catalytic properties. Moreover, the atomic arrangements of nanoparticles differ from those of bulk materials. The presence of vertices, edges, and faces in nanoparticle structures leads to electronic frustrations. Therefore, the electronic structure of nanoparticles contrasts with that of molecules or corresponding bulk material. The electronic structure of atoms and molecules consists of discrete energy levels, whereas that of bulk material exhibits energy bands—valence bands, and conduction bands which exist in semiconductors and conductors. As for nanoparticles' electronic structure, there is a dramatic change in the bands' structures; the continuity of states is replaced with a set of discrete energy levels. Hence, the electronic structure of nanoparticles is a hybrid between molecular and bulk ones (Figure 2.3) [9].

As a consequence of this particular electronic structure, nanoparticles possess interesting optical and magnetic properties. For example, a semiconductor's band

**FIGURE 2.3**

Schematic electronic structures of bulk materials, nanoparticles, and atoms.

gap increases as nanoparticle size decreases. Moreover, discrete energy levels and energy level separation are also dependent on the nanoparticles' size. Also, the energy needed for electron transition to an excited state will be affected. Such modifications are visible from changes in color—which can be evidenced by absorption spectra comparison—according to the size of the nanoparticles. Furthermore, a surface plasmon resonance phenomenon resulting from the interaction between an electromagnetic wave and the electrons of the conduction bands appears in metallic nanoparticles of sizes ranging from 10 to 100 nm. The electrons present at the surface oscillate, inducing charge separation on the nanoparticle surface. Thus, large electric fields are created near the nanoparticle surface.

Additionally, below a critical size depending on the nanomaterial, the magnetic moment of each atom constituting the nanoparticle will interact with the moments of the other atoms. Moreover, below this critical size, the nanoparticles will be magnetically monodomain—having a net magnetic moment. Thus, it is easier for them to exhibit ferromagnetic behaviors. In some cases, bulk materials which are not magnetic can acquire a net magnetic moment below a certain nanoparticle size. For instance, rhodium nanoparticles exhibit ferromagnetic properties below 1–1.5 nm [10].

#### **2.2.1.4 Nanoparticle preparation**

The properties of nanoparticles depend on both their composition and their morphology. As the first factor can be controlled mainly by the choice of chemicals for their preparation, many research efforts are made with regard to the size and disparity control of nanoparticles.

There are two main ways to prepare nanoparticles, one from gaseous phase to solid and another one from liquid phase to solid. In the gas to solid approach, metallic and metal oxide nanoparticles can be prepared using chemical vapor deposition or PLD (i.e., arc discharge, laser vaporization, etc.) processes. Gaseous phase to solid processes—for example, the Aerosil process developed by Degussa in 1942—are widely used for large-scale preparation of different nanostructured oxides such as  $\text{Al}_2\text{O}_3$  and  $\text{SiO}_2$ . However, these processes usually lead to the formation of aggregated (i.e., strongly bonded) nanoparticles. For metallic

nanoparticles, these techniques allow the formation of naked nanoparticles mainly used for properties study that are not appropriate for large-scale synthesis of individual nanoparticles [11].

The second approach, from liquid to solid, is widely used to prepare controlled-morphology nanoparticles. Its advantage lies in the great variety of chemicals that can be used as precursors. Nucleation, growth, and nanoparticle stabilization phenomena play an important role in all processes using this approach. Hence, difficulties lie in the control of each step of processes. To reach this goal, it is necessary to experiment with process parameters such as reaction temperature, chemical concentrations, partial pressure, reaction time, etc.

#### 2.2.1.4.1 Metallic nanoparticles

Metallic nanoparticles can easily be prepared from metal salts or organometallic complexes. These types of precursors are activated either via reduction or decomposition processes.

**2.2.1.4.1.1 Metal salt reduction.** Different kinds of reducing agents can be used, such as sodium borohydride ( $\text{NaBH}_4$ ), hydrated hydrazine ( $\text{N}_2\text{H}_4 \cdot 2\text{H}_2\text{O}$ ), or tri-sodium citrate dihydrate ( $\text{Na}_3\text{C}_6\text{H}_5\text{O}_7$ ), to reduce metallic cations ( $\text{M}^{n+}$ ) by dissolution of the metal salt in an aqueous solvent,  $[\text{M}^{n+} + n e^- \rightarrow \text{M}^0]$  coupled with oxidation of the reducing agent,  $[\text{Red} - n e^- \rightarrow \text{Red}^{n-}]$ . This approach is well-illustrated by two methods, which are still widely used for colloidal gold preparation: the Turkevich [12] and Brust–Shriffin [13] methods.

In Turkevich synthesis, an  $\text{HAuCl}_4 \cdot 2\text{H}_2\text{O}$  aqueous solution is boiled and then, tri-sodium citrate is quickly added to the solution. After a few minutes, a wine-red color, characteristic of gold colloid suspension, appears. The gold nanoparticles, which are spherically shaped, are characterized by a mean size of 20 nm. The  $\text{HAuCl}_4 \cdot 2\text{H}_2\text{O}$  to tri-sodium citrate ratio modification allows the formation of spherical nanoparticles with a mean size ranging from 15 to 150 nm. Nanoparticles larger than 20 nm are, however, poly-dispersed. A common way to prepare small gold nanoparticles is to use thiol molecules as a stabilizer (Brust method) [14]. As  $\text{AuCl}_4^-$  and thiol molecules form stable complexes, a strong reducing agent such as sodium borohydride has to be used. Thus,  $\text{HAuCl}_4 \cdot 2\text{H}_2\text{O}$  reduction by  $\text{NaBH}_4$  in the presence of thiophenol allows for the formation of gold nanoparticles with a size below 2 nm (Figure 2.4). This type of approach has been successfully used for the preparation of nanoparticles of different metals; among them iron, cobalt, nickel, copper, silver, and gold [15].

Metal salt reduction is also performed in non-aqueous solvents. For example, a tri-alkali-metal borohydride reducing agent (alkali = Li, Na, or K), in an organic solvent such as tetrahydrofuran (THF), toluene, or diethyl ether allows the preparation of a wide range of transitional metals of the d-block with a mean size ranging from 1 to 5 nm [17]. An interesting method is the polyol one, which consists in using a polyol as both a reducing agent and solvent in the reduction of metal salts. For example,  $\text{RuCl}_3$ , in presence of dodecanethiol in different polyols yields mono-dispersed ruthenium nanoparticles ranging from 1 to 5 nm [18].

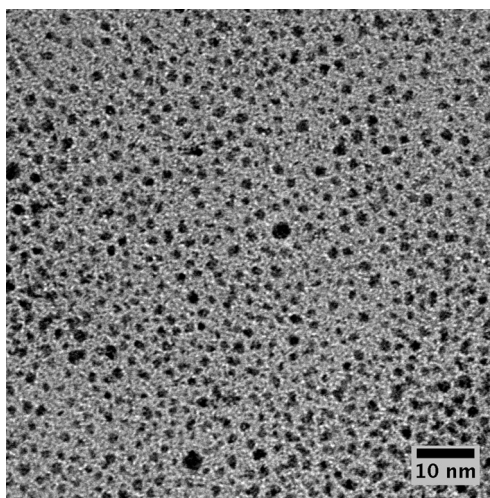


**FIGURE 2.4**

Gold nanoparticles obtained by  $\text{NaBH}_4$  reduction of  $\text{HAuCl}_4 \cdot 2\text{H}_2\text{O}$  in the presence of thiophenol using the procedure described in [16].

**2.2.1.4.1.2 Organometallic complex reduction/decomposition.** If an organometallic complex is zero-valent, nanoparticle preparation consists in a simple complex decomposition in the presence of stabilizer, usually in organic solutions. This is the case for carbonyl complexes, such as  $[\text{Fe}(\text{CO})_5]$  and  $[\text{Co}_2(\text{CO})_8]$  [19,20], which serve as precursors for iron and cobalt nanoparticle preparation. For example, Hess et al. described a series of stabilized colloidal metallic cobalt particles obtained from  $[\text{Co}_2(\text{CO})_8]$  as a metallic precursor and different polymers (e.g., methyl methacrylate-ethyl acrylate-vinylpyrrolidone, polycycloprene, etc.) in toluene, chlorobenzene, or dimethylformamide (DMF) [20]. The resulting cobalt nanoparticles have a uniform size in the 1–100 nm range.

However, if the metallic center is in an oxidized state, a reduction reaction will be required. This can be achieved either by the polyol process or by using another reducing agent or even another organometallic complex. The advantage of using  $\text{H}_2$  or  $\text{CO}$  as a reducing agent coupled with an appropriate organometallic complex is the possibility to prepare nanoparticles at a moderate temperature and even below room temperature, to obtain a “clean” nanoparticle surface. With  $\text{CO}$  as a reducing agent, some carbon impurities can however be found in the final product [21]. Precursors of choice for such an approach are coordination complexes, which release inert molecules (such as alkanes in the case of olefinic complexes) that will not bond with nanoparticle surfaces during the reduction step [22].

Finally, metallic nanoparticles can also be obtained using electrochemical processes or microwave- and sonication-assisted processes. Moreover, all of these

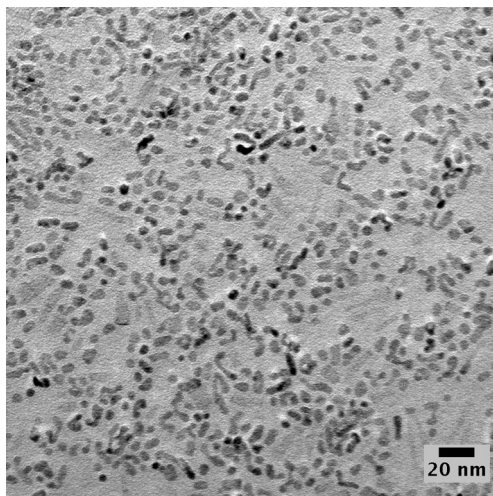


**FIGURE 2.5**

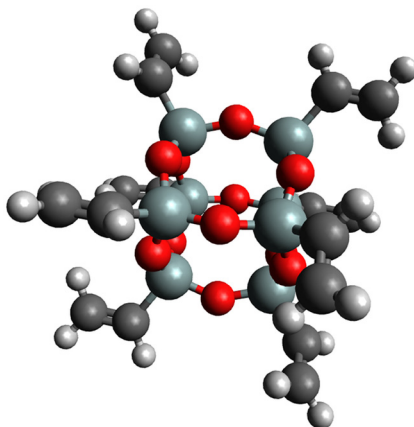
TEM micrograph of ZnO prepared by adding lithium amide to zinc chloride, hexadecylamine, and palmitic acid in THF at room temperature (E. Lamouroux, unpublished results).

methods can be combined with previous ones in order to facilitate precursor reduction and/or activation.

#### 2.2.1.4.2 Metal oxide nanoparticles

Oxide nanoparticles can easily be obtained by metallic nanoparticle preparation methods followed by an oxidation step. Other methods are available, such as precipitation of the oxo-hydroxide form of the metal precursor (e.g., chloride or nitrate) in water as a result of the presence of a base. Following this approach, it is difficult to regulate nanoparticle size; moreover, in case of mixed oxides, chemical homogeneity of the sample is also difficult to control. These difficulties can be circumvented by the addition of surfactants or the use of sonochemical activation. For example, by adding a base to a solution of zinc chloride in the presence of hexadecylamine and palmitic acid in THF at room temperature, a colloidal suspension of ZnO nanoparticles around 2–5 nm in size can be obtained (Figure 2.5).

The sol–gel process involves the hydrolysis of precursors, usually alkoxides—such as tetraethyl orthosilicate (TEOS) for SiO<sub>2</sub> synthesis—yielding corresponding oxo-hydroxides. Then, the polycondensation process can occur, giving off water molecules, and leads to the formation of three-dimensional networks of metal hydroxide. Then a step of calcination leads to oxide formation. For the formation of nanoparticles, this process is performed in the presence of surfactants to control nanoparticle size as well as morphology. For example, the Stober

**FIGURE 2.6**

Schematic of octavinyl-POSS structure (O: red, H: white, Si: light bluish-gray, and C: dark gray).

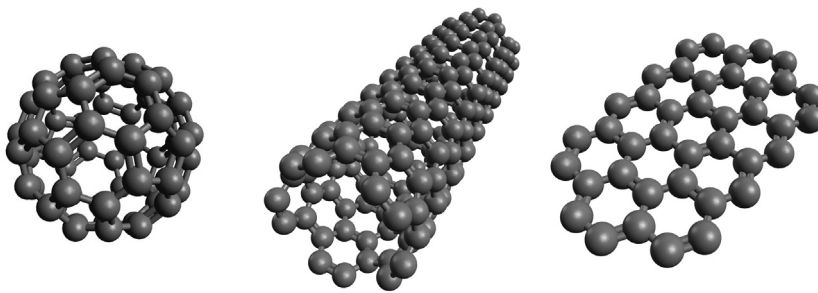
process allows the synthesis of mono-dispersed silica nanoparticles. This process involves hydrolysis and condensation reactions in an alcoholic solution in presence of ammonia as a catalyst. The increase in silica precursor or ammonia concentrations leads to the increase in silica nanoparticle size.

Polyhedral oligomeric silsesquioxane (POSS) is an inorganic-organic hybrid consisting of a cage of silica with at least one organic substituent or OH group in each corner of the structure (Figure 2.6). Thus, it is an intermediate between silica ( $\text{SiO}_2$ ) and silicones ( $\text{R}_2\text{SiO}$ ). These materials are prepared using the sol-gel process, usually starting from trichlorosilane or trialkoxysilane [23]. Hybrid Plastics Inc., located in the US [24], sells different kinds of POSS, including octavinyl-POSS, octaphenyl-POSS, and trisilanolphenyl-POSS. The presence of organic moieties allows users to take advantage of the compounds' organic reactivity for further chemical modifications for specific applications such as reactions with oxide surfaces or with polymers for nanocomposite formation [25,26].

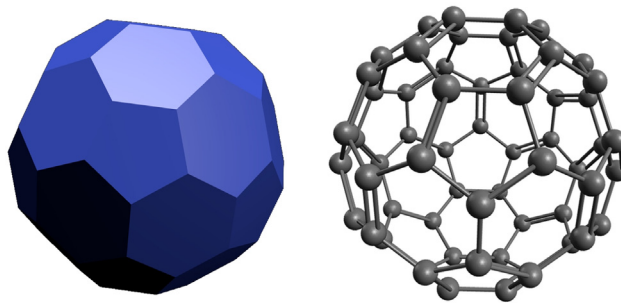
## 2.2.2 CARBON-BASED NANO-OBJECTS: FULLERENES, GRAPHENE, AND CARBON NANOTUBES

### 2.2.2.1 Structural considerations

As a result of its valency, carbon is capable of forming many allotropes such as diamond, amorphous carbon, graphite (consisting of many graphene sheets), fullerenes, and CNTs. Among them, graphene, fullerenes, and CNTs—which are constituted of  $\text{sp}^2$  hybridized carbon atoms (Figure 2.7)—are frequently used as nanofillers.

**FIGURE 2.7**

Schemes of a fullerene (left), an SWCNT (middle), and graphene (right).

**FIGURE 2.8**

Representation of an Archimedean solid, the truncated icosahedron (left), and the fullerene  $C_{60}$  (right).

Graphene is a one-dimensional atomic-scale honeycomb lattice made of  $sp^2$  hybridized carbon atoms. It can be considered as a building block for different carbon materials including fullerenes, nanotubes, and graphite.

Fullerenes, also known as bucky-balls, are three-dimensional materials. To obtain such types of structures, it is necessary to use 12 pentagonal rings and  $m$  hexagonal rings (with  $m = (n - 20)/2$  where  $n$  is the total number of carbon atoms in the considered fullerene). As pentagon rings have to be isolated from each other by hexagon rings to avoid instability of the structure—due to fused pentagon rings—the smallest fullerene is the  $C_{60}$  molecule. Moreover, the  $C_{60}$  structure corresponds to an Archimedean solid (Figure 2.8): the truncated icosahedron, which possesses 32 faces (12 pentagons and 20 hexagons), 90 edges, 60 vertices, and belongs to the  $I_h$  point group. The  $C_{60}$  molecule is obtained by placing carbon atoms at the vertex of the truncated icosahedron.

CNTs are two-dimensional carbon materials and their structures are derivative from the  $C_{60}$  molecule structure. They are of nanometric diameter and their aspect ratio (length/diameter ratio) can exceed 1000 [27]. Two types of CNTs, which differ

by the number of walls, can be distinguished: single-walled CNTs (SWCNTs) and multiwalled CNTs (MWCNTs). SWCNTs can be conceptualized as a graphene layer rolled up into a seamless cylinder, which is closed at its ends by two hemi-fullerenes—which have six pentagon rings. The rolling up of a graphene sheet implies a decrease in the length of the carbon–carbon bonds: 0.125 nm for SWCNTs and 0.141 nm for graphite [28], which induces a modification of the  $\pi$  electron cloud coupled to a rehybridization of p-orbitals [29]. As they have a high surface energy, they tend to be arranged in bundles more than individual CNTs.

Furthermore, a sheet of graphene can be rolled up in different ways, which leads to different structures of SWCNTs. Indeed, their structure is determined by a vector  $\vec{R}$ , expressed in the graphene sheet basis ( $\vec{a}_1, \vec{a}_2$ ), and an angle of helicity  $\theta$  ranging from  $0^\circ$  to  $30^\circ$  due to the symmetry of the hexagonal net. The helicity vector is defined as follows:

$$\vec{R} = n \times \vec{a}_1 + m \times \vec{a}_2$$

where  $n$  and  $m$  are integers, while the angle  $\theta$  is defined by the helicity vector and the armchair line, which divides hexagon rings into two equal parts (Figure 2.9). There are three possible ways of rolling up a graphene sheet: (i) SWCNTs for which  $n = m$  and  $\theta = 0$ , which are called armchair SWCNTs, (ii) those for which the helicity vector is  $(n, 0)$  and  $\theta = 30^\circ$ , which are called zig-zag SWCNTs, and (iii) other SWCNTs characterized by a couple  $(n, m)$ , which are named chiral SWCNTs.

MWCNTs consist of two or more concentric tubes of graphene arranged around a central hollow core. Double-walled CNTs (DWCNTs) could however constitute a third type of CNTs due to their similarity with SWCNTs concerning

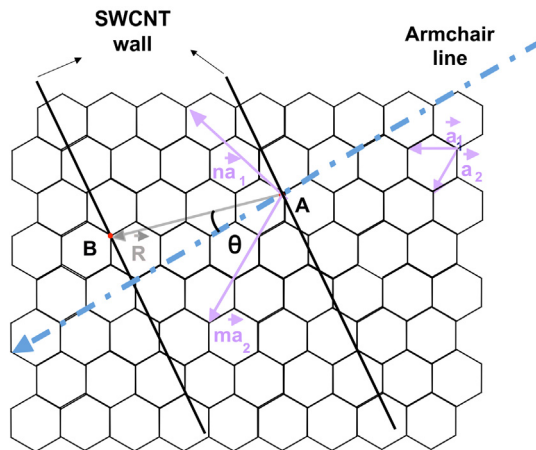


FIGURE 2.9

Vectorial representation of SWCNT construction.

their morphology and properties. It is worth underlining that in comparison to SWCNTs, DWCNTs have better resistance to chemicals [30]. For MWCNTs, the interlayer distance ( $\approx 0.34$  nm) is greater than that between graphene layers in graphite (0.33 nm) [31]. The effect of the curvature of the tube and the interactions of van der Waals type between the layers reduce this distance.

### 2.2.2.2 Properties of carbon-based nanomaterials

CNTs and graphene have good thermal stabilities over 600 °C and good thermal conductivities yielding 3500, 3000, and 2000–4000 W m<sup>-1</sup> K<sup>-1</sup> for SWCNTs, MWCNTs, and graphene, respectively [32,33]. But theoretical modelizations pointed out that the upper limits of thermal conductivity for SWCNTs and MWCNTs are 6600 and 7000 W m<sup>-1</sup> K<sup>-1</sup>, respectively. In addition, CNTs and graphene exhibit high electron mobility of about 10<sup>4</sup>–10<sup>5</sup> cm<sup>2</sup> V<sup>-1</sup> s<sup>-1</sup>.

These materials also have interesting mechanical properties. For example, Young's moduli are as high as that of diamond. Mechanical properties, however, depend on sample quality and homogeneity, especially for CNT samples. Thus, Young's modulus values range from 0.60 to 1.25 TPa and from 0.27 to 1.80 TPa for SWCNTs and MWCNTs, respectively—they reach 1.01 TPa for graphene. Hence, CNTs and graphene are widely used in nanocomposite preparation to enhance mechanical properties. It is worth underlining that graphene has a more beneficial effect on nanocomposites, Young's modulus, and tensile strength, than graphite or CNTs.

### 2.2.2.3 Preparation methods

State of the art carbon nanomaterial preparation includes numerous processes and new approaches are continuously explored. In this section, an overview of the most established preparation methods is given—more details can be found in several devoted review articles.

#### 2.2.2.3.1 Fullerene and CNTs

**2.2.2.3.1.1 Laser ablation.** This technique was first developed for the preparation of metallic clusters [34]. Smalley's group adapted it for the synthesis of fullerenes and CNTs [35]. In 1985, it allowed for the discovery of the C<sub>60</sub> fullerene [36]. The principle of this method consists in inducing ablation of a graphite target by a laser beam. Then the evaporated carbon atoms condense to form fullerenes. This technique made possible the preparation of CNTs from a catalyst-doped graphite electrode [37]. CNT yields and morphologies can be improved by process parameter optimization [38,39]. Also, using a pulsed laser, SWCNT quality can be enhanced [40]. But this process modification also induces the formation of amorphous carbon and encapsulated catalyst nanoparticles.

This technique is expensive and therefore not suitable for industrial production, but it remains a technique of choice for SWCNT production devoted to fundamental studies. Figure 2.10 gives an example of a laser ablation reactor used for CNT production.

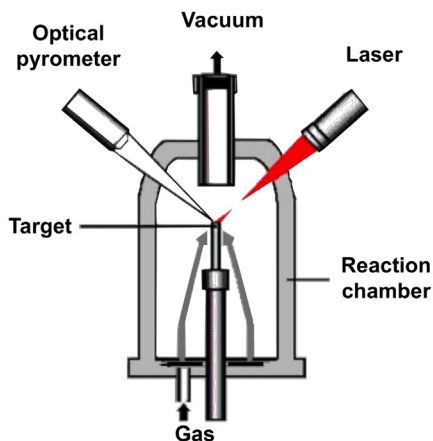


FIGURE 2.10

Schematic of a laser ablation setup.

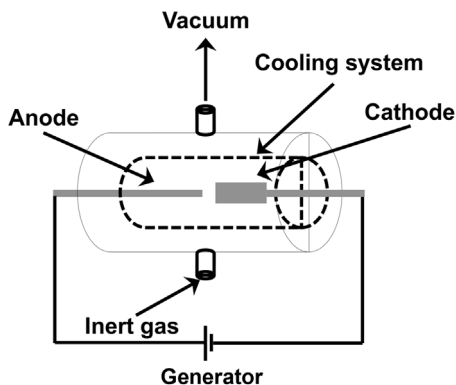
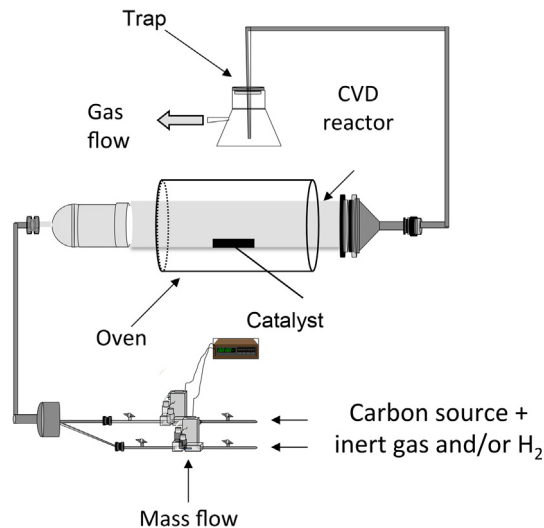


FIGURE 2.11

Schematic of an arc discharge setup.

**2.2.2.3.1.2 Arc discharge.** This method was initially used for fullerene synthesis [41] and also allows the preparation of CNTs [42]. Figure 2.11 shows a setup for CNT production by an arc discharge process. It consists of two graphite electrodes placed in a chamber under vacuum. Applying an electrical field between them leads to the ignition of an arc, which consumes the anode, forming a plasma ( $T \approx 3000\text{--}4000\text{ }^\circ\text{C}$ ). This anode vaporization, in a gaseous atmosphere—usually made of a mixture of  $\text{H}_2/\text{Ar}$ —at a controlled pressure, allows carbonaceous product condensation at the cathode surface. For this process, yield and selectivity mainly depend on the electrodes' positions and catalyst and atmosphere compositions.



**FIGURE 2.12**

Schematic of C-CVD setup.

Catalyst modifications, for example, when replacing iron [43] or cobalt [44] with nickel–cobalt [45] or nickel–yttrium [46], or when adding elemental sulfur [47], enhance selectivity in SWNCT production.

Even if this method, coupled with its setup, seems to be easily accessible and hence attractive for CNT synthesis on a large scale, the simultaneous formation of different types of carbeneous products makes several post-synthetic purification steps necessary.

**2.2.2.3.1.3 Catalyzed chemical vapor deposition.** This method traditionally used for carbon fibers and filamentous products was adapted to the preparation of CNTs (Figure 2.12) [48]. The catalyzed CVD (C-CVD) process is performed at moderate temperature ( $T < 1200$  °C) and easily allows production scale-up, which makes it the technique of choice for industrialization.

One specific strength of this process is that it can be adjusted in several manners leading to various CVD-based methods. Among them there are thermochemical CVD, alcohol catalytic CVD, plasma enhanced CVD, laser assisted thermal CVD, high pressure CO conversion (HiPco), and aerosol assisted CVD [49]. CVD can be considered as a chemical process in which a carbon source in a vapor phase—such as hydrocarbons or carbon monoxide—decomposes at the surface of the catalyst particles, which are mainly made of iron, cobalt, or nickel.

During a CVD reaction, catalyst nanoparticles—which can be supported or unsupported—are saturated in carbon. When the carbon supersaturation limit is reached, carbon grows off the catalyst nanoparticle and forms a CNT structure. One of the critical aspects of C-CVD CNT production remains the preparation

and composition monitoring of the catalyst [49]. Instead of preparing the catalyst before the C-CVD reaction, it can be formed *in situ* by direct injection of metal-based precursors in a heated flow of carbon source in the reactor—one example is the HiPco process consisting of a coordination complex  $[\text{Fe}(\text{CO})_5]$  in a CO flow at 800–1200 °C (1–10 atm CO) [50]. Preparing the catalyst *in situ* allows good control of CNT morphologies coupled with a high yield as a result of process parameter optimization.

**2.2.2.3.1.4 Miscellaneous preparation techniques.** In addition to the above mentioned preparation routes, there are many various other approaches used or under development. For example, the synthetic route to fullerene production by flash vacuum pyrolysis is under development [51], while CNTs can be produced by ball-milling processes, flame synthesis, and even silicon carbide decomposition.

#### 2.2.2.3.2 Graphene

As graphene is the building block for graphite, the earliest method—which seems the simplest—consists in direct extraction of graphene sheets from bulk graphite. Different techniques have been explored for cleavage and exfoliation of graphene from graphite, such as micromechanical cleavage, liquid phase mechanical exfoliation, and also chemical cleavage [52]. Mechanical exfoliation gives the highest quality of graphene—this process is also known as the Scotch® tape method. Samples obtained this way allowed K.S. Novoselov et al. to study the electronic properties of a single sheet of graphene [53]. Another well-established technique is surfactant assisted graphene exfoliation, which belongs to liquid phase approaches. The chemical cleavage approach to obtain a graphene layer is mainly based on graphite intercalation compounds. During the intercalation process, the distance between two graphene sheets is increased and hence, their separation is made easier [54,55]. Another chemical approach starts from graphite oxide, which is usually prepared by mixing graphite with an acidic medium [56]. As the starting material is graphite oxide, a two-step process is necessary to obtain graphene sheets: (i) exfoliation of graphite oxide, and (ii) reduction of individual graphite oxide sheets to provide graphene ones (see Section 2.5).

In addition to the approaches starting from bulk graphite, other routes using different precursors have been explored. Among them, there are the epitaxial growth of graphene by thermal decomposition of SiC ( $T > 1000$  °C), C-CVD using flat copper or nickel surfaces as catalysts most of the time and also chemical preparation by a bottom-up synthesis via a polymerization process (Figure 2.13) [52,57].

### 2.2.3 CLAYS

Clay minerals (natural and synthetic) are a large class of inorganic layered silicate structures, also known as phyllosilicates. These inorganic structures are characterized by their layered structure with one dimension in the nanoscale range. Also, they exhibit different properties such as ease of modification (either exchange, adsorption, or grafting), plasticity, and hardening on drying or firing [58].

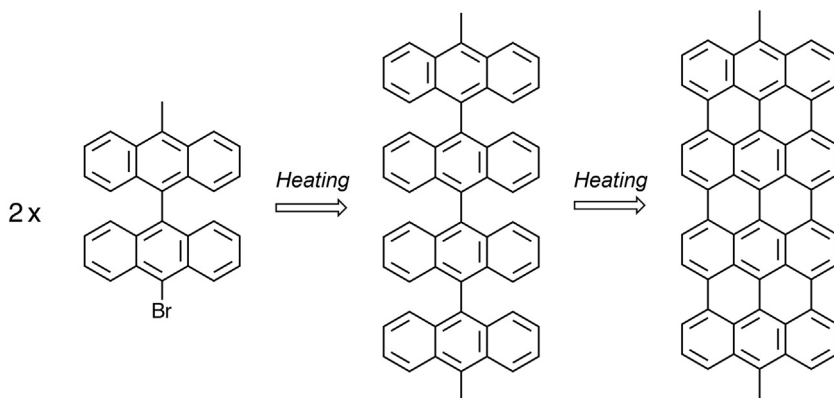


**FIGURE 2.13**

Scheme of a bottom-up approach from aromatic precursors adapted from [52].

### 2.2.3.1 Clay structures

Clay minerals consist of two basic building blocks: silicate tetrahedron [ $\text{Si}_2\text{O}_5^{2-}$ ] and aluminum octahedral [ $\text{Al}(\text{OH})_6^{3-}$ ] species. In general, clays adopt layered structures composed of silicate tetrahedron sheets and sheets of aluminum (III) or magnesium (II) surrounded by eight oxygen atoms. These two kinds of sheets are fused together by shared oxygen atoms. The unshared ones are present in hydroxyl form. Clays are divided into three subfamilies: Kaolinite, Illite (mica-clays), and Smectite.

Kaolinite [ $\text{Al}_2\text{Si}_2\text{O}_5(\text{OH})_4$ ] is composed of layers consisting of one tetrahedral silicate sheet fused to one octahedral aluminate sheet by oxygen atoms. This type of structure is named clay (1:1). In this case, the thickness of the layers is around 0.7 nm [58]. Another common clay structure is the (2:1) structure, in which two tetrahedral sheets are separated by one octahedral sheet. The corresponding layer thickness is around 0.94 nm [59]. The structure can be either electrostatically neutral or charged, due to silicon or aluminum cation substitution. Concerning charged clay (2:1), there are two possibilities. The first one is the substitution of tetravalent cations by trivalent ones. For example, an  $\text{Si}^{4+}$  cation can be substituted by an  $\text{Al}^{3+}$  cation, resulting in a negatively charged layer. Thus, to counterbalance this negative charge, small cations, such as  $\text{K}^+$ , are present between layers, but without forming an interlayer space allowing swelling or exfoliation processes. Illite clays adopt this kind of structure of general formula  $[(\text{K}, \text{H})\text{Al}_2(\text{Si}, \text{Al})_4\text{O}_{10}(\text{OH})_2 \cdot x\text{H}_2\text{O}]$ , where  $x$  represents the number of water molecules. The second possibility is the substitution of trivalent  $\text{Al}^{3+}$  cations by bivalent ones such as  $\text{Mg}^{2+}$ ,  $\text{Fe}^{2+}$ , or  $\text{Zn}^{2+}$ , leading to the smectite clay group—general formula  $[(\text{Ca}, \text{Na}, \text{H})(\text{Al}, \text{Mg}, \text{Fe}, \text{Zn})_2(\text{Si}, \text{Al})_4\text{O}_{10}(\text{OH})_2 \cdot x\text{H}_2\text{O}]$ , where  $x$  represents the amount of water. In this case, the negative charges are counterbalanced by the presence of interlayer cations, for example,  $\text{Na}^+$  or  $\text{Ca}^{2+}$ . However, as their

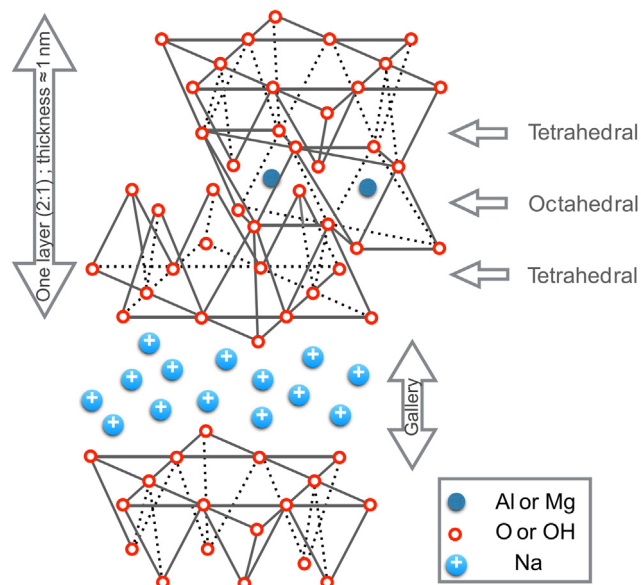


**FIGURE 2.14**

Schematic representation of Montmorillonite structure ( $[M_x(Al_{4-x}Mg_x)Si_8O_{20}(OH)_4]$ ; Si atoms omitted for more clarity).

repartition is not homogenous between layers, a gap is induced between them, called interlayer or gallery. It is worth underlining that smectites are the most commonly used clays for polymer-nanocomposite preparation. Montmorillonite (Figure 2.14), which possesses a gallery thickness of 0.28–1.45 nm—depending on water content—and a Young’s modulus of 178–265 GPa [60], is a naturally occurring clay largely used for nanocomposite preparation and thus a representative example of clay nanofillers.

### 2.2.3.2 Clay modifications

Due to interactions between a clay’s layers, it is not easy—even sometimes impossible—to prepare clay nanocomposites by physical mixing of clay nanoplates and polymers. Moreover, as a clay’s surface is hydrophilic (i.e., presence of cations) and a polymer’s surface is often hydrophobic, it is necessary to modify the surface of the clay with a hydrophobic agent for the clay to become more compatible with polymers.

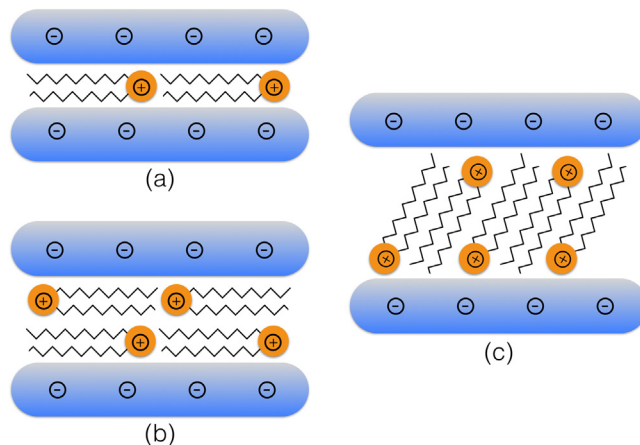
This modification results in the preparation of organoclays. To achieve this goal, cations located in a clay’s galleries, such as  $Na^+$  and  $Ca^{2+}$ , are exchanged with alkyl onium cations—for example, alkylammonium or alkylphosphonium. This cation exchange results in an increase of interlayer space.

A typical cation exchange using alkylammonium is conducted as follows. An ammonium precursor is prepared by reaction between a solution of alkylamine and concentrated hydrochloric acid in water. This solution is poured into a suspension of sodium montmorillonite in hot water. After several minutes of stirring, a white precipitate is isolated, washed, and dried. By using stearyl ammonium as alkyl ammonium, the interlayer spacing of the clay increases from 1.2 to 2.2 nm—determined by X-ray diffraction analysis [61]. In addition to interlayer space increase, the alkyl chain can be functionalized in order to improve its compatibility with polymer chains or to participate in or initiate the polymerization reaction. Using this approach, Toyota successfully prepared a polypropylene-clay hybrid by incorporation of end group modified polypropylene into stearyl ammonium modified montmorillonite.

It is worth noting that a low density of surface charges implies weak interactions between a clay's layers, and thus higher efficiency in nanocomposite formation. Hence, the efficiency of cation exchange will control the quality of nanocomposites.

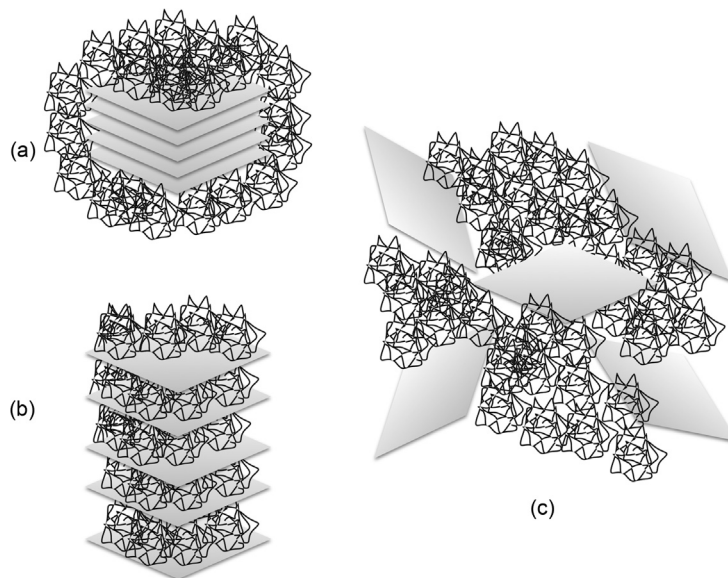
As surface properties depend on clay structure, different layered alkyl oxonium structures can be obtained such as mono-, bi-, tri-, or even paraffin-layer structures (Figure 2.15). All of these adopted structures will lead to increased gallery space. The length and size of the organic tail of alkyl onium cations coupled with the charge density of the clay's surface govern interlayer spacing (i.e., the higher the charge density of the clay, the larger the interlayer space).

When clays are used for nanocomposite preparation, three configurations have to be considered (Figure 2.16). The clays have layered structures, so a nanocomposite's structure is intimately linked to the degree of layer interaction. If this degree is relatively high, a segregated structure, which consists of a few layers of



**FIGURE 2.15**

Examples of alkyl chain structures, (a) lateral monolayer, (b) lateral bilayer, and (c) paraffin-type structure.

**FIGURE 2.16**

Clay nanocomposites configurations, (a) segregated structure, (b) intercalated structure, and (c) exfoliated structure.

clay stacked together and surrounded by polymer, is obtained. This configuration appears when polymer molecules are unable to intercalate within clay layers. An intermediate degree of interaction leads to intercalated structures, corresponding to a well-ordered hybrid-multilayer morphology. Lastly, a low degree of interaction allows insertion of polymer chains within each gallery, leading to clay layer separation. Thus, individual layers are dispersed within the polymer matrix creating an exfoliated structure.

Hence, as far as clay minerals are concerned, it is critical to control their inter-layer spacing to facilitate polymer intercalation, but also to enhance clay gallery and polymer compatibility. These two parameters are regulated by cation exchange using modified alkylonium.

---

### 2.3 INORGANIC NANOPARTICLES INCLUDING CLAYS: CHEMICAL AND PHYSICAL MODIFICATIONS FOR THEIR INCLUSION AS FILLER IN NANOCOMPOSITES

Significant scientific and technological interest has focused on nanoparticles (including nanocomposites) over the past three decades. Classically, nanofillers

can be divided into two groups, inorganic and organic. The dominant species used are inorganic fillers (including carbon ones, such as CNTs or graphene, discussed in the next section of this chapter). Hollow microspheres and porous fillers are only suitable for special applications due to their high cost of production and processing. They are not considered in this section. The use of inorganic nanoparticles in a polymer matrix can provide high-performance novel materials that find applications in many industrial fields. This section describes polymer/inorganic nanocomposites (PINCs), which were recently reviewed by Li et al. [62]

As nanotechnologies have developed, inorganic nanostructured materials exhibiting important cooperative physical phenomena (such as superparamagnetism or ferromagnetism, size-dependent band-gap, electron and phonon transport, absorbing or emitting properties, etc.) have been designed, discovered, or prepared. However, they suffer from high manufacturing costs as well as drawbacks in shaping and processing [63]. In contrast, polymers are flexible lightweight materials and can be produced and processed at a low cost. For example, thin films can be produced by various techniques such as deep-coating, spin-coating, film-casting, as well as printing. Thus, polymeric matrices containing small amounts of PINCs can advantageously replace nanostructured materials, since both the properties of inorganic nanoparticles and polymer can be combined and often enhanced. To obtain the desired mechanical, thermal, and chemical stability properties, nanosized inorganic nanoparticles (typically in the range of 1–100 nm) have to be uniformly dispersed in and, if possible, fixed to the polymer matrix. In fact, inorganic nanoparticles, also termed *nanofillers* or *nanoinclusions*, can be viewed as “additives” that can enhance or modify polymer performance [64–66].

The first example of a nanofiller was probably found in the polymer-Au nanocomposite (a gold salt reduced in the presence of arabic gum) described by Lüdorsdorff in 1833, which can be compared to the Lycurgus cup, a well-known glass cup from antiquity whose ruby color is due to gold nanoparticles. In the same way, other metals such as silver (Ag), copper (Cu), mercury (Hg), platinum (Pt), palladium (Pd), and rhodium (Rh) were also used with other natural polymers [67]. In the 1990s, polymer-clay nanocomposites appeared, with interesting mechanical and thermal properties that can be used in the car industry [68]. More recently, taking advantage of the development of nanostructured materials, new nanofillers including metals and metal alloys (e.g., Au, Ag, Cu, Ge, Pt, Fe, and CoPt), semiconductors (e.g., ZnO, CdS, PbS, CdSe, and CdTe), clay minerals (e.g., CaCO<sub>3</sub>, montmorillonite, smectite, vermiculite, and hectorite), other oxides (e.g., TiO<sub>2</sub>, SiO<sub>2</sub>, and ferric oxides), and carbon-based materials (e.g., CNT, graphite, graphene, and carbon nanofibers (see next section)) were developed for magnetic, catalytic, electrochemical, electrical, and bioimaging or therapeutic applications. The polymer matrices can be industrial plastics [e.g., nylons, polyimide, and polypropylene (PP)], conducting polymers [e.g., polypyrrole, polyaniline (PANI) and polyvinylidene fluoride (PVDF)], as well as transparent polymers [e.g., polystyrene (PS) and polymethyl methacrylate (PMMA)].

Recent research and related papers in the field of flexible composites revealed that the major key challenge is the regulation of the dispersion of the nanofillers, including nanoparticles, in the polymeric hosts. Indeed, nanoscale particles tend to aggregate, inducing the cancelling out of any benefits associated with the nanometric dimension [69]. Thus, physical or chemical synthetic strategies for obtaining high homogeneity are needed. Physical methods include solvent processing, melt-processing, polymer melt intercalation, while chemical methods are generally *in situ* processes [70]. It is worth noting that the latter often imply a previous surface modification step.

### 2.3.1 PHYSICAL METHODS OF INCLUSION

Physical methods for nanoparticle inclusion are based on liquid dispersion of the filler. Depending on the nature of the continuous phase, two main techniques can be used: melt processing and film casting (Figure 2.17).

In the film casting approach, hydrophobic nanoparticles are dissolved in a polymer solution. Nanocomposite thin films or composite sheets are then prepared by spin coating of the nanoparticle-polymer solution. The evaporation of the solvent takes place during the coating process, or by subsequent treatment in an oven [71]. This method appears somewhat limited for large-scale production.

In the melt process, nanofillers (typically clays, oxides, and CNTs) are dispersed into a polymer melt and nanocomposites are obtained by extrusion [72,73]. This route allows the production of large quantities of material and is

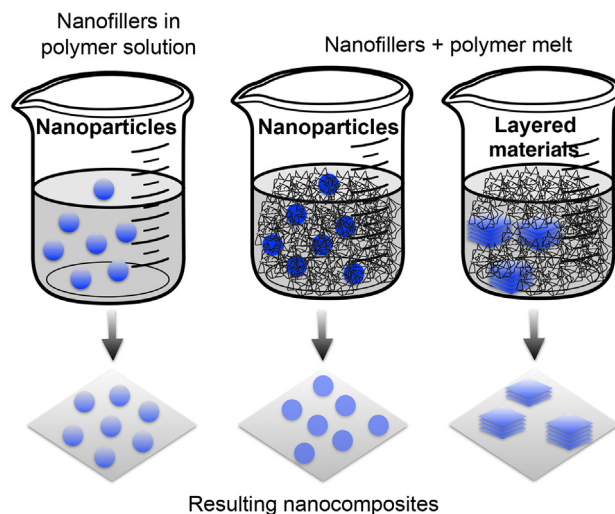


FIGURE 2.17

Melt processing and film casting techniques.

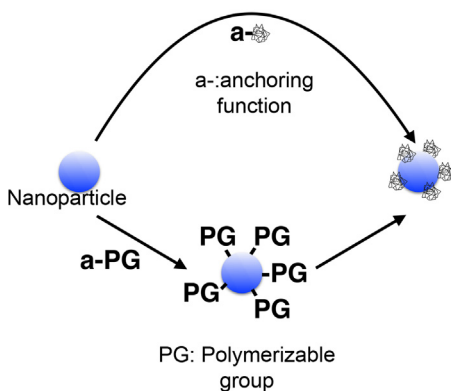
economically viable. Without regard to their efficiency, these physical methods suffer from some drawbacks due to the uncontrolled agglomeration of the nanoparticles during direct mixing and melt processing. Nanofiller agglomeration can be overcome by the use of chemically modified fillers: that is, organophilic surface modified clays [74], polylactide organically modified layered silicate [75], surface-treated ZnO nanoparticles [71]. Alternatively, chemical methods such as *in situ* polymerization and *in situ* nanoparticle formation methods were developed as substitutes for physical ones.

### 2.3.2 *IN SITU* POLYMERIZATION WITH PRE-FORMED NANOPARTICLES

The preparation of nanocomposites via *in situ* polymerization techniques requires a dispersion step of inorganic nanoparticles into the monomer solution prior to the polymerization process. However, due to antagonist interactions, inorganic particles tend to phase separate, agglomerate, or sediment from the organic polymer. In order to ensure a good link or favorable interactions at the interface, specific groups have to be anchored onto their surfaces. This produces efficient stabilization of the nanoparticle dispersions and consequently a decrease in agglomeration phenomena. Emulsion polymerization was utilized for the fabrication of clay nanocomposites intercalated with PMMA or hydrophobic styrene [76,77]. In these methods, well-dispersed particles with a narrow size distribution are needed. In order to reach this goal, amphiphilic molecules (also called surfactants) such as long-chain carboxylic acids, alcohols, thiols, or amines can be adsorbed or chemisorbed onto the nanoparticle surface. The first effect of surfactant addition is easier isolation from the preparation medium without formation of insoluble aggregates because the obtained hydrophobic interface lowers the specific surface free energy of the inorganic particles [78–81]. The high dispersion of the nanoparticles in the monomeric solution allows their efficient embedding in the polymer during the polymerization. Obviously, the used surfactants do not directly participate in the polymerization process [82]. A number of examples of confinement or surrounding have been described, for example: (i) iron oxide prepared in the presence of oleic acid or oleyl amine groups [83,84], (ii) metallic (Au, Ag) and semiconducting nanoparticles (CdS, CdSe) surrounded by thiols or carboxylic acids [78–81], calcium carbonate nanoparticles covered in acrylic and stearic acid [85,86], or silica nanoparticles coated with -3-(trimethoxysilyl)propyl groups [87].

### 2.3.3 GRAFTING-TO OR GRAFTING-FROM METHODS OF INCLUSION

The nanoparticle surface can also be decorated with polymerizable groups (for surface modification, see next section). Polymerizations initiated at the nanofiller




---

**FIGURE 2.18**

Grafting-from and grafting-to processes.

surface (grafting from) and tethering processes (grafting-to) have proven to be very useful for homogenous nanocomposite synthesis (Figure 2.18) [88].

In the latter, the required functionalities can be embedded in the design of the polymer chain that will bind to, or strongly interact with, the nanoparticle surface. Note that functions present at the surface of nanoparticles (e.g., hydroxyl, silanol, or thiol groups) are sufficient to allow the grafting-to process. The anionic form of these organic moieties can also be used. By the reaction of these anchoring groups with functional sites at the nanoparticle surface, the polymer can be grafted onto the inorganic particle.

Nanoparticle surfaces can also be modified by adsorption or covalent linkage of monomers, which will be the starting point of polymer growth. Some examples can be given: (i) polymerizable group of maleic acid adsorbed on alumina [89]; (ii) ZnS functionalized by *N,N*-dimethylacrylamid [90]; ZnO embedded in poly (butanediolmonoacrylate) [91]. In most cases, photopolymerization is used to furnish the nanocomposites.

Atom transfer radical polymerization (ATRP) appears to be promising strategy for controlling the surface reactivity. For example, Yang et al. prepared a cross-linked PbS nanoparticle/polymer composite using this method. The described protocol combines the ATRP technique and a gas/solid reaction. Lead dimethacrylate polymer films (PLDMA) were then directly grown from surface-modified substrates. Then, PbS nanoparticles were generated *in situ* by exposing the PLDMA films to H<sub>2</sub>S gas [92].

On the other hand, nanocomposites can also be produced with grafting from techniques after prior functionalization of nanoparticle surfaces with initiating groups. In this case, the polymerization starts from the nanoparticle surface. A large variety of initiating groups can be used, leading to anionic, cationic, or free radical polymerization [82]. This type of surface modification is of particular

importance in the area of polymer-clay nanocomposites. Indeed, the highly polar-ionic surface of clay minerals is incompatible with most polymers, such as PS, polyethylene, or PP. To improve the compatibility between two constituents of the composite, the clay surfaces have to be modified with organic molecules. This results in an improvement of the dispersability of the clay in the polymer matrix. Chen and Evans proposed a method for *in situ* polymerization in the presence of clay materials in which the initiator is linked to the surface via ionic interactions. An efficient delamination of the layered silicate was thus obtained during the formation of the polymer [70].

Cationic initiators are known to form strong ionic interactions with negatively charged surfaces, as found on many oxide particles since most of the oxide particles have a wide range of pH values where they exhibit a net negative surface charge. Butyl butacrylate was grafted from TiO<sub>2</sub> particle surfaces by using 2,2'-azo-bis(2-amidinopropane) dihydrochloride (AIBA) as an initiator for *in situ* polymerization [93].

Layer by layer (LbL) deposition of nanoparticles and polymers can also be used for the formation of highly homogenous thin films including inorganic nanoparticles. An interesting approach described by Kotov et al., is the formation of ultrastrong and stiff layered nanocomposites [94]. The process is based on sequential adsorption of nanometer-thick layers of polyvinyl alcohol (PVA) and negatively charged clay montmorillonite by immersing a glass substrate in dilute solutions of components. Cross-linking of resulting layers was subsequently obtained by treatment with glutaraldehyde [95].

Finally, electron irradiation was reported to be an effective and attractive method to modify the surfaces of inorganic materials. The electron irradiation technique was successfully employed by Wang et al. to prepare PINCs consisting of TiO<sub>2</sub> (anatase/rutile) or  $\gamma$ -Al<sub>2</sub>O<sub>3</sub> nanoparticles and PMMA. It was suggested by the authors that the active species initiating the grafting polymerization might form on the nanoparticle surface because of electron irradiation [96].

### 2.3.4 *IN SITU* NANOPARTICLE AND/OR POLYMER FORMATION FOR NANOCOMPOSITE SYNTHESIS

Chemical methods based on the *in situ* sol-gel polymerization method allow single-step synthesis of polymer/inorganic nanocomposites in the presence of polymer or monomer [88,97,98]. This method makes it possible to manipulate the organic/inorganic interfacial interactions and thus overcomes the classical problem of nanoparticle agglomeration [97,99]. The synthesis of nanoparticles containing composites through the hydrolysis or reduction of metal salts in the presence of a polymer has been extensively studied. Alkaline hydrolysis or simple hydrolysis processes are largely described for Fe, Ti, Al, Si, Zn, and V nanooxides from corresponding salts or complexes [100–105]. Reactions can also be conducted in the presence of surfactants to ensure high dispersion, especially if

the oxides are preformed. The method appears particularly useful for thin film production as shown by Andrews et al. [73].

An interesting way of producing nanoparticle-containing composites in a single-step synthesis is the use of a microemulsion (oil in water) system in which the monomer is used as an oil phase, forming a completely polymerizable matrix [106]. Several inorganic nanoparticle systems have also been synthesized via an inverse microemulsion (water in oil) process [107,108]. For example, a CdS-polyacrylamide nanocomposite was prepared by  $\gamma$ -irradiation in a water in oil microemulsion [109].

Finally, a number of studies have recently reported on the preparation of nanocomposites combining polymer and inorganic UV-absorbers (especially the most promising, ZnO and TiO<sub>2</sub>) by directly incorporating preformed ZnO or TiO<sub>2</sub> fillers into a polymer matrix, mainly by physical methods [110–113]. In these chemical methods, *in situ* polymerization makes it easier to achieve a homogeneous dispersion of nanoparticles in the polymer matrix.

---

## 2.4 CARBON NANOTUBES AS FILLERS IN NANOCOMPOSITES: THE DISPERSION CHALLENGE

The high cost of producing CNTs compared with other fillers (e.g., clays, graphite, carbon black, or carbon fiber) seems to limit their potential use as filler in nanocomposites. In addition, only poor interfacial interactions between filler and polymer host may be expected because the carbon atoms on CNT walls are chemically stable due to the aromatic nature of the bond. The surrounding polymer can then only interact through weak van der Waals forces, unable to provide an efficient load transfer across the CNT/matrix interface. In addition, the CNTs are generally supplied in the form of entangled bundles or ropes, resulting in inherent difficulties in dispersion and/or alignment in a polymer host. There are also some catalyst residuals, bucky onions, spheroidal fullerenes, amorphous carbon, polyhedron graphite nano-particles, and other forms of impurities in freshly grown CNTs that require purification before use.

However, the unique geometric shapes of CNTs (small nanometric diameter with high aspect ratio (> 1000 corresponding to a very large surface area) compared with other fillers leads one to expect synergistic effects with the host matrix and consequently interesting specific properties. The introduction of CNTs in nanocomposites is thus a challenge worth examining and which requires good dispersion and/or disentangling of the charge in the polymer matrix for its utilization in nanoscale device applications.

As a consequence of their structures (e.g., the bundles formation), it is very difficult to properly disperse CNTs in a solvent by simple stirring, especially in a polar medium. Thus, there are two approaches to solving the problem: (i) the dispersion of crude CNTs by physical methods classically used in materials sciences,

and (ii) the modification of the CNTs by chemicals. The latter can be envisaged with or without modification of the surface of CNTs, by covalent functionalization and by noncovalent interactions, respectively. The major principles of these approaches along with the corresponding advantages and disadvantages are summarized in this section.

### 2.4.1 PHYSICAL METHODS OF DISPERSION OF CNTs

The research literature has reported on numerous physical techniques developed for nude (non-functionalized) CNTs dispersion in a polymer matrix: calendaring [114,115], ball milling [116], the stir technique [117], extrusion [118], and the most popular, ultrasonication [119]. Examples of dispersion were given, but the mechanism and principles were not fully described in these studies. The principles, as well as the advantages and limits of these different techniques, were extensively reviewed by Kim et al. [32]. Polymers, pre-formed polymers as well as monomers can generally be used with post-treatment (i.e., polymerization, post-polymerization, reticulation) to ensure nanocomposite formation. Most recent studies are often based on the use of a combination of the aforementioned techniques, such as ultrasonication/ball milling in addition to covalent amino functionalization [120] or ultrasonication/extrusion [121].

The result obtained is strongly dependent on the nature and the state of the polymer matrices (i.e., solid or liquid, thermoplastic, or thermoset), the nature of the filler (i.e., SWCNTs, DWCNTs, or MWCNTs) or its initial state of aggregation (i.e., bundle or agglomerate sizes, level of entangling), and the envisioned filler content. The reproducibility of the process is also concerned. In addition, some techniques, such as (ultra)sonication or ball milling, induce damage to or defects in CNTs. Raman spectroscopy confirmed that ultrasonication of CNTs for a long time resulted in a significant increase in the intensity of the D band (representing disordered  $sp^3$  carbon in CNTs), suggesting the generation of defects on the CNTs' surfaces [122]. In extreme cases, the graphene layers of CNTs are completely destroyed and the nanotubes are converted into amorphous carbon nanofibers [123]. A careful study of experimental conditions is thus necessary. Finally, it should be underlined that whatever the physical method used, the dispersion rarely conducts to CNT dispersion in an individual manner, a condition which needs to be fulfilled in order to totally benefit from the specific properties of the filler (e.g., aspect ratio, high surface area, mechanical, electrical, conductivity, or optical properties).

### 2.4.2 CHEMICAL METHODS OF DISPERSION OF CNTs

As physical methods of dispersion suffer from some drawbacks, especially the absence of individualization and in terms of reproducibility or processability, significant efforts have been directed towards developing methods to modify surface properties of CNTs. It appears that the chemical functionalization is an effective

way to prevent nanotube aggregation and helps to better disperse and stabilize the CNTs within a polymer matrix.

Two approaches have been extensively described for this significant challenge: (i) a covalent one consisting in a chemical functionalization, and (ii) a noncovalent one based on interactions between active molecules and the CNTs' carbon atoms. In both cases, it can be expected that an adequate functionalization will change the environment, which becomes more conducive to dispersion. Additionally, the introduction of some functionalities on the surface of CNTs allows noncovalent interactions or covalent links (including grafting copolymerization) to ensure good adhesion between the filler and the surrounding polymer chains. There are several comprehensive review papers that describe the chemistry of functionalized CNTs and the reaction mechanisms between the CNTs and functional groups [124–127].

#### **2.4.2.1 Chemical functionalization or surface modification of CNTs**

CNTs are more reactive than flat graphene sheets (as described in the following section), since they have an enhanced tendency to covalently attach to chemical species [128]. Direct covalent functionalization takes place when  $sp^2$  hybridization changes into  $sp^3$  and a simultaneous loss of  $\pi$ -conjugation system on the graphene layer occurs. Note that such transformations modify electronic and transport properties of the concerned CNTs [129]. This approach conducts to the introduction of chemical groups at the termini or at the sidewalls of CNTs. The attachment of polar or ionic groups changes the nature of CNTs from hydrophobic to hydrophilic, favoring dispersion and interactions with the matrix host. All the described methods are also generally considered as activating treatments because they allow subsequent covalent binding in nanocomposites. Indeed, in many polymer/CNT nanocomposites, the final step in processing is the covalent binding of functionalized CNTs with polymer molecules. Two main techniques have been reported for the covalent grafting of polymers to nanotubes, “grafting to” and “grafting from,” which were reviewed by Tsubokawa, among others [130].

#### **2.4.2.2 Defect functionalization of CNTs**

Defect functionalization is an efficient method for covalent functionalization of CNTs, especially SWCNTs. This process takes advantage of chemical transformation of defect sites on CNTs (e.g., open ends, holes in the sidewalls, irregularities in the hexagonal graphene framework on the sidewalls or at end caps). Oxygenated sites can also be considered as defects. Such oxygenated defects appear during oxidative purification of CNTs. Oxidation of CNTs at high temperature in the presence of air conducts to the opening of the end caps, which shows that their tips are more reactive than their sidewalls [131–133]. Defects can be easily created on the sidewalls as well as at the termini of CNTs by an oxidative process with strong acids such as  $HNO_3$  [134,135],  $H_2SO_4$ , or a mixture of these [136,137], as well as with strong oxidants such as  $KMnO_4$  [138] or  $H_2O_2$  [139].

These procedures are generally accompanied by additive “cutting” processes providing disentangling, opening and active site formation on raw CNTs. Obviously, it is necessary to control and to adjust the reaction conditions to obtain very short SWCNTs with lengths of 100–300 nm. For example, Liu et al. obtained 150 nm in length CNTs by treatment of a crude sample by a 3:1 mixture of concentrated  $\text{H}_2\text{SO}_4/\text{HNO}_3$  [140]. Using the same procedure, Shafer et al. evidenced an electrostatic stabilized dispersion of CNTs in water with an average length of 1.1  $\mu\text{m}$ . The various short and open-ended CNTs can be subsequently treated with a 4:1 mixture of concentrated  $\text{H}_2\text{SO}_4$  and 30%  $\text{H}_2\text{O}_2$  to complete functionalization by carboxylic acid ( $-\text{COOH}$ ) or hydroxyl ( $-\text{OH}$ ) groups on the surface and at the end of CNTs.

Mawhinney et al. studied surface defect site density on SWCNTs by measuring the evolution of  $\text{CO}_2$  (g) and  $\text{CO}$  (g) when heating to 1273 K [141]. The results indicated that about 5% of the carbon atoms in the SWCNTs were located in defective sites. The acid base titration method was used to determine that the percentage of acidic sites of purified SWCNTs was about 1–3% [142]. It is concluded that the defective sites created at the CNT surfaces by this method are extremely sparse. In addition, they are very close to the graphitic surface and thus cannot really promote good dispersion in the polymer/CNT composites. An additional derivatization of hydroxyl or carboxyl groups is then carried out to improve chemical density around the CNTs. Thus, carboxylic acid functions are generally converted into acylchloride by reaction with thionyl chloride. Esters or amides can subsequently be obtained by reaction of carboxyl functions with alcohols [143–145] or amines [146,147] respectively. Functionalized CNTs are more soluble in organic solvents than raw CNTs (because the hydrophobic nature of CNTs is changed to hydrophilic due to the attachment of polar groups). Interestingly, most of the SWCNT bundles exfoliate as both individual nanotubes and small bundles of 2–5 nanotubes [127], if the reaction of acid chloride groups with amines is given four days at an elevated temperature.

In addition, hydroxyl functions can be converted into hydroxymethyl groups by reaction with formaldehyde. Hydroxymethyl groups allow further free radical graft polymerizations in the presence of cerium salts [148]. Other oxidative conditions such as ozone [149] or reactive plasma [150] can be used. For example, Mawhinney et al. reported that carboxylic acids, anhydrides, and esters could be introduced to CNTs by ozonization [151]. In addition, Chen et al. described how acetaldehyde and ethylenediamine vapors were plasma polymerized on the surface of CNTs, thereby introducing active aldehyde ( $-\text{CHO}$ ) and amino ( $-\text{NH}_2$ ) groups [152]. Vinyl groups ( $-\text{CH}=\text{CH}_2$ ) can be obtained by reaction of carboxylic acid ( $-\text{COOH}$ ) or hydroxyl ( $-\text{OH}$ ) with an isocyanate derivative [153,154].

To add to the rich chemistry of these functional groups, they also permit other transformations, such as silanation [155], polymer grafting [156], thiolation [140], alkylation or arylation [157], and even some biomolecules [158–163].

Chemically functionalized CNTs can produce strong interfacial bonds with many polymers, allowing CNT-based nanocomposites to possess highly interesting

mechanical and functional properties. In addition, reactive groups useful for copolymerization can be introduced. For example, Eitan et al. described the linking of di-glycidyl ether of bisphenol-A-based epoxide resin [143]. The epoxide function enables better interaction between the polymer matrix chains of the composite and the surfaces of the nanotubes. In the same way, thiocarboxylic and dithiocarboxylic esters groups can participate in cross-linking processes [164].

### 2.4.2.3 Other methods of sidewall and termini functionalization of CNTs

Chemical functionalization is based on the covalent linkage of functional entities onto the carbon scaffold of CNTs either at the termini of the tubes or at their sidewalls. Direct covalent sidewall functionalization is associated with a change of hybridization from  $sp^2$  to  $sp^3$  and a simultaneous loss of  $\pi$ -conjugation system on the graphene layer. This process can be achieved by reaction with some molecules of high chemical reactivity, such as fluorine [165,166]. SWCNTs were fluorinated at their sidewalls by passing elemental fluorine at different temperatures up to 325 °C [167]. The fluorination occurs at the sidewalls of CNTs and the process is reversible using anhydrous hydrazine, which can remove the fluorine. Fluorinated SWCNTs exhibited improved solubility in isopropanol (and generally alcohols) or in dimethyl formamide by ultrasonication [168].

The fluorination process alters some physical properties (i.e., electrical conductivity, optical properties, and solubility) but improves chemical reactivity. Fluorinated CNTs have C–F bonds that are weaker than those in alkyl fluorides [169] and thus provide substitution sites for additional functionalization by reaction with strong nucleophiles such as Grignard reagents or alkyllithium compounds [170], as well as with alkoxides, hydrazine and diamines, peroxides, etc. [166,171,172]. Note that a direct route to polymer reinforcement via the preparation of polymer-functionalized nanotubes using an organometallic approach was also reported [173]. In this way, CNTs were first lithiated by *n*-butyl lithium, and then covalently attached to a chlorinated polypropylene via a coupling reaction.

Besides fluorination of sidewalls, other techniques such as nucleophilic addition of carbenes [171], carbenes [174], nitrenes [175–177], cycloadditions [178], azomethine ylide [179,180], carbene and nitrene addition [174], chlorination, bromination [181], and hydrogenation [182] have also been successfully employed in recent years. All these methods can be regarded as the derivatives of sidewall functionalization and have been reviewed.

Recent interest has been devoted to “click” chemistry, a term coined for the Cu (I)-catalyzed Huisgen [3 + 2] dipolar cycloaddition reaction (reaction between terminal alkynes and azides resulting in the formation of 1,2,3-triazoles) [183]. It appears to be an efficient reaction for materials synthesis and modification, and for self-assembly of nanomaterials. The first application was reported by Adronov et al. in 2005 [184]. The CNTs were first decorated with alkynes via Pschorr-type arylation with *p*-aminophenyl propargylether and then coupled with well-defined azide-terminated polystyrene (PS) using a Cu (I) catalyst. Currently, click chemistry is an ideal modular and a popular methodology for the introduction of a wide

variety of complex molecules onto the surface of CNTs [185,186]. Cho et al. focused on the covalent attachment of bioactive molecules with SWCNTs using click chemistry [185]. In this approach, alkyne-functionalized SWCNTs react with chiral azides derived from amino acids in presence of Cu(I). The method has been extended to the attachment of bioactive molecules like peptides or polysaccharides. The wide range of attached molecules possible highlights the importance of click chemistry and certainly opens the new vista of CNT-based nanomaterials.

Extensively described radical processes [187–189], as well as diazonium uses [190], allow efficient successful functionalizations with various organic moieties. These functionalizing methods, which allow solubilization of CNTs, have been reviewed by Bahr and Tour [191]. Finally, chemical functionalization of nanotubes can also be accomplished through irradiation with electrons or ions. Electron irradiation of CNTs causes their collapse in an anisotropic manner from the expulsion of atoms in the nanotube walls [192,193]. On the other hand ion deposition can induce crosslinks between nanotubes in the bundle and between shells in MWCNTs, which could lead to efficient load transfer among the tube layers [194,195].

In summary, although covalent functionalization increases the solubility and processability of CNTs and also allows the introduction of useful functional groups and (bio) molecules onto the CNT surface, these methods' drawback lies in that alteration of the structural properties of CNTs takes place. The formation of defects results in severe degradation in mechanical, thermal, or electrical properties of CNTs by disruption of  $\pi$ -electron system in nanotubes. Therefore, many efforts have been put forward to develop methods that cause less damage to the CNT structure.

### 2.4.3 PHYSICAL FUNCTIONALIZATION (OR PHYSICAL BLENDING) OF CNTs

Noncovalent functionalization of nanotubes is of particular interest because it does not compromise the physical properties of CNTs, but can improve solubility and/or processability. As reviewed by the Cho and Li teams, preparation methods include solution mixing, microemulsion, sol–gel chemistry, electroactive interaction, dialysis, and in some cases, sonication [196].

Of course, solvent solution mixing appears to be the simplest method and is widely used for processing CNT/polymer nanocomposites in which CNTs and polymers (PMMA, PVA, PS) are mixed with a suitable solvent which evaporates in controlled conditions after forming nanocomposite films on the surface of the substrate. Due to the hydrophobic nature of CNTs produced in strongly associated bundles, the influence of a polar solvent remains weak if individualization is concerned. Thus, the dispersion process was done by physical (noncovalent) functionalization involving surfactants [197–199], biomacromolecules [200–204], or wrapping with polymers [205,206]. The main advantage of these approaches is

that the structure of the CNTs remains intact. Interestingly, they also serve as nondestructive purification methods since nanotubes can be transferred to the aqueous phase in the presence of surfactants [207,208]. In this case, the nanotubes are surrounded by the hydrophobic components of the corresponding micelles. The interaction becomes stronger when the hydrophobic part of the amphiphilic molecules contains an aromatic group to ensure efficient  $\pi$ - $\pi$  stacking with CNTs [209].

The process of dispersion is strongly dependent on the nature and the concentration of surfactants. For example, Rastogi et al. reported an efficient dispersion of MWCNTs with Triton X-100 characterized either by UV-vis spectroscopy and transmission electron microscopy (TEM) [210]. The classical sodium dodecyl sulfate (SDS) exhibited low dispersing properties. Note that the dispersion can easily be monitored by UV-vis spectroscopy [211] (absorbance characterized at 500 nm;  $\epsilon_{500} = 28.6 \text{ cm}^2 \text{ mg}^{-1}$ ) because only individual CNTs absorb in the UV-vis region while bundled ones are inactive in the same region [212,213]. Temperature stability of the surfactant is another important factor that affects the quality of CNT dispersion.

Besides surfactants, another approach has been described in the literature. It consists in wrapping macromolecules or biomolecules helically around the CNTs, by forming van der Waals bonds between planar groups and CNT walls,  $\pi$ - $\pi$  interactions, electrostatic attraction, surfactants, etc. Suspension of CNTs takes place in the presence of various polymers and leads to the wrapping of CNTs [214–216].

---

## 2.5 GRAPHENE AS FILLER IN NANOCOMPOSITES: THE BEHAVIOR OF GRAPHENE LAYERS

In his review in *Nature* [217], Kotov wrote, “When carbon fibers just won’t do, but nanotubes are too expensive, where can a cost-conscious materials scientist go to find a practical conductive composite? The answer could lie with graphene sheets.” Obviously, the intrinsic properties of graphene (i.e., it is the thinnest material in the universe, has a high thermal conductivity, exceptional mechanical properties, and is an excellent electronic transporter) have generated enormous interest in its possible use in numerous devices. If one considers that a CNT is a rolled-up graphene sheet and on the other hand, that graphene is densely packed in a honeycomb crystal lattice, the question is: does graphene have the same chemistry as bundles of CNTs? The answer is no and, in addition, graphene can be considered as a better nanofiller, especially in view of its thermal and electrical properties. Of course, the structure and consequently the properties of graphene-reinforced nanocomposites depend on the distribution of the graphene layers in the polymer matrix, as well as interfacial bonding between the graphene layers and the polymer matrix. Pristine graphene is incompatible with organic polymers

and thus does not form homogenous composites. This is deleterious because the unique properties of graphene are only associated with individual sheets. Exfoliation of graphene sheets is rarely described as such. However, in 2008, Luo et al. described a mild, one-step electrochemical approach for the preparation of ionic-liquid-functionalized graphite sheets with the assistance of an ionic liquid and water. These ionic-liquid-treated graphite sheets can be exfoliated into functionalized graphene nanosheets that can not only be individualized and homogeneously distributed into polar aprotic solvents, but also do not need to be further deoxidized [218]. Müllen describes a more recent example in which graphene is produced with high yield ( $> 85\%$ ,  $\leq 3$  layers), large lateral size (up to  $44 \mu\text{m}$ ), low oxidation degree (a C/O ratio of 17.2), and a remarkable hole mobility of  $310 \text{ cm}^2 \text{ V}^{-1} \text{ s}^{-1}$  [219].

In contrast, graphene oxide (GO) has attracted considerable attention as a nanofiller because GO sheets can bear numerous hydroxyl, epoxide, diol, ketone, and carboxyl functional groups that can alter the van der Waals interactions significantly and make them more compatible with organic polymers [220–225]. GO sheets are also dispersible in water because additional carbonyl and carboxyl groups are located at the edges of the sheets, which makes graphene oxide sheets strongly hydrophilic [226,227]. It is noteworthy that chemical reduction of GO can allow the regeneration of the graphitic network of  $\text{sp}^2$  bonds [228,229].

### 2.5.1 SURFACE MODIFICATION OF GRAPHENE

As mentioned previously, pristine graphene materials are unsuitable for intercalation. Consequently, researchers have devoted their efforts to GO, which appears to be a substrate of choice. Its synthesis was firstly described by Hummers (KOH oxidation-exfoliation) [230]. Also, treatment with  $\text{KMnO}_4$  and  $\text{H}_2\text{SO}_4$ , or  $\text{KClO}_3$ , and  $\text{HNO}_3$  allows GO preparation, as recently reviewed by Ruoff et al. [56,231]. Note that the obtained level of oxidation is high (more than that observed for CNTs, see above) since the C:O ratio is close to 2:1. Numerous organic approaches can then be used to exfoliate GO sheets under stable dispersion, to functionalize them and *in fine* to recover a graphene structure (similar to that of the initial pristine graphene) after dispersion or functionalization. Mechanically assisted (sonication and/or stirring) exfoliation in water or in a polar solvent produces colloidal suspensions [232]. Rapid heating or microwave irradiation can also be employed. As efficient as they are, these techniques often cause some damage to GO sheets [55,233].

Therefore, a chemical route is generally preferred. The Wallace [234] and Ruoff groups [235], have independently developed an exfoliation process in which hydrophilic GO is dispersed in water (under sonication) and treated with potassium hydroxide (KOH) and an ammonia solution. The formation of a large negative charge results, allowing stable dispersion of the GO sheets in the form of KOH oxidized graphene (KMG). Individual sheets of graphene are then

recovered by reduction with hydrazine (also called Wallace's approach) under the form hKMG (hydrazine-reduced KOH-modified graphene). The homogenous solution obtained is stable for more than four months, however the formation of aggregates has been observed, conducting to the formation of precipitates that cannot be redispersed even under ultrasonic activation. In fact, it appears that the procedure initially proposed by Ruoff [236], hydrazine-induced reduction in the presence of poly(sodium 4-styrenesulfonate), produces better results. Indeed, the amphiphilic polymer efficiently maintains the dispersion/individualization of exfoliated sheets of hKMG for subsequent applications. Other derived methods have been described, with anionic stabilizer such as 7,7,8,8-tetracyanoquinodimethane (TCNQ) anions, [237] an alkaline solution of pyrene butyric acid (PBA), [238] or sulfonated polyaniline (SPANI) [239]. The graphene sheets are then usable for nanocomposite preparation by simple mixing.

### 2.5.2 COVALENT FUNCTIONALIZATION OF GRAPHENE AND GRAPHENE OXIDE SHEETS

Besides reduction processes, a variety of other transformations have been developed, taking advantage of oxygenated functional groups of GO in order to prepare organo-modified graphene oxide/graphene [56,231]. The chemical functionalization of graphene is a particularly attractive target because it can improve the solubility and processability as well as enhance the interactions with organic polymers. In addition, it allows tuning of the hydrophilic character of graphene oxide sheets.

In order to use carboxylic acid groups on graphene oxide to anchor other molecules, the carboxylic acid groups generally have to be classically activated by thionyl chloride ( $\text{SOCl}_2$ ) or carbodiimides. Numerous examples reveal that subsequent addition of nucleophilic species, such as amino or alcohol substituent included in complex molecules, produces covalently attached functional groups or molecules [240–242]. An interesting application for the preparation of biomedical devices is the anchoring of biomolecules containing amino- or hydroxylated groups. For example, Xu et al. modified the surface of graphene via the covalent attachment of a porphyrin ring [243], while Bourlinos et al. introduced aminoacids on the GO surfaces [224]. Polymer wrapping can also be obtained after esterification of GO sheets using an hydroxylated polymer such as poly(vinyl alcohol) [241]. It is also possible to take advantage of the reactivity of epoxide groups that can be opened by nucleophiles [244]. Shan et al. used this reaction to produce water-soluble polylysine modified graphene.

Also of great interest is functionalization by isocyanates, which produce carbamates by reaction with all surface hydroxylated groups (hydroxyl or carboxyl). Isocyanate-modified graphene oxide readily forms a stable colloidal dispersion in all polar aprotic solvents (DMF, NMP, DMSO, and HMPA) [245]. Building blocks of GO sheets crosslinked to form lamellar porous structures can be

obtained by reaction of diisocyanate derivatives with oxygenated groups on both sides of the sheets [246].

As mentioned above for CNTs, aryldiazonium salts readily react in a radical process with  $sp^2$  graphene sheets, allowing the efficient grafting of hydrophobic or hydrophilic aryl groups [247]. The grafting of aryl groups was confirmed by FT-IR spectroscopy. It must be mentioned that soluble graphene layers bearing alkyl or aryl chains have been prepared by reacting graphite fluoride with alkyl or aryl lithium reagents [248]. Arylation can also be obtained by direct photochemical (laser illumination) reaction between graphene and benzoyl peroxide [249].

In spite of indisputable advantages, covalent functionalization of GO platelets can adversely affect the electrical conductivity of the platelets, as these functionalizations disrupt (or retain the disruption already present in) the  $sp^2$ -hybridized network required for good electron/hole conduction. Thus, noncovalent functionalization of graphene could be of interest.

### 2.5.3 INDIVIDUALIZATION BY $\pi-\pi$ INTERACTIONS

An alternative to covalent bonding is the use of  $\pi-\pi$  stacking interactions usually occurring between two relatively nonpolar aromatic rings that have overlapping p-orbitals.  $\pi-\pi$  stacking interactions are strong and comparable to covalent attachment. As a result, pyrene moieties have been successfully attached to aromatic macromolecules such as graphene oxide [250,251], while small aromatic molecules have been grafted to graphene sheets [238].

More recently, Davis et al. described an interesting method of graphene functionalization via  $\pi-\pi$  stacking [252]. They prepared a thermosensitive graphene-polymer composite by attaching poly(*N*-isopropylacrylamide) (PNIPAAm) to the basal plane of graphene sheets via  $\pi-\pi$  stacking. Aqueous solutions of the graphene-polymer composite were stable (below 24 °C) and thermosensitive. It could be expected that this methodology may be used with any polymer and should allow the retention of graphene's electrical properties. This synthetic approach could be a potent method to produce carefully designed graphene-polymer composites for electronic applications.

### 2.5.4 PREPARATION METHODS OF POLYMER/GRAPHENE NANOCOMPOSITES

Many parameters can influence the formation of polymer/graphene nanocomposites, such as pressure drop in nanogalleries, miscibility between polymer and graphite or graphene, electrostatic interactions, coordination, etc. Also many parameters have to be controlled, such as polarity, molecular weight, hydrophobicity, reactive groups, etc. The literature shows that three main strategies exist for incorporating the polymer at the core of the host layered materials.

The first one is the *in situ* intercalative polymerization method in which graphene or modified graphene is swollen within the liquid monomer before the initiation of polymerization, either by heat or radiation. A variety of polymer nanocomposites have been prepared using this procedure.

The second method is the solution intercalation procedure. It is based on a solvent system in which the polymer or pre-polymer is solubilized and graphene or modified graphene layers are dissolved or swollen. The suitable solvent (i.e., water, acetone, chloroform, tetrahydrofuran, dimethylsulfoxide, dimethylformamide, toluene, etc.) depends on the weak forces that hold the layers together. After adsorption of the polymer onto the exfoliated sheets and evaporation of the solvent, the sheets reassemble, sandwiching the polymer, to form the nanocomposite. This strategy can be employed to synthesize nanocomposites based on epoxy, polyethylene, polyvinylalcohol, or polyvinylchloride, for example.

The third procedure, which does not use solvent, consists in the intercalation of graphite or (modified) graphene by mixing it with the polymer matrix in a molten state. This melt mixing process is of course usable for preparing thermoplastic nanocomposites.

Some examples of various composites are given in several studies [253–263] and in recent review papers by Park et al. [264] and Ruoff et al. [265].

---

## 2.6 CONCLUSION

Nanocomposites are composed of nanofillers embedded in a polymer matrix. It appears that the specific structure of nanofillers dictates the intended applications for nanocomposites. The nanofillers' shapes, properties, and surface chemistry should thus be tuned either by modifying their preparation protocols or post-preparation treatments. To ensure an appropriate dispersion state, special attention has to be paid to the preparation, the modification and above all to the techniques used for inclusion in the polymer matrix. Hence, the remaining challenge is that individual nanofillers have to be carefully selected and functionalized according to the polymer's expected application.

---

## REFERENCES

- [1] Bréchnignac C, Houdy P, Lahmani M. European materials research society. Nanomaterials and nanochemistry. Berlin; New York, NY: Springer; 2007.
- [2] Mackay AL. A dense non-crystallographic packing of equal spheres. *Acta Crystallogr* 1962;15:916–18.
- [3] Doye JPK, Wales DJ. Structural consequences of the range of the interatomic potential A menagerie of clusters. *J Chem Soc Faraday Trans* 1997;93:4233–43.
- [4] Walton AG. Formation and properties of precipitates (chemical analysis, vol. 23). Interscience; 1967.

- [5] Zettlemoyer AC, editor. *Nucleation*. New York: Dekker; 1969.
- [6] Xia Y, Xiong Y, Lim B, Skrabalak SE. Shape-controlled synthesis of metal nanocrystals: simple chemistry meets complex physics? *Angew Chem Int Ed* 2009;48:60–103.
- [7] Jana NR, Gearheart L, Murphy CJ. Wet chemical synthesis of high aspect ratio cylindrical gold nanorods. *J Phys Chem B* 2001;105:4065–7.
- [8] Murphy CJ, Thompson LB, Chernak DJ, Yang JA, Sivapalan ST, Boulos SP, et al. Gold nanorod crystal growth: from seed-mediated synthesis to nanoscale sculpting. *Curr Opin Colloid Interface Sci* 2011;16:128–34.
- [9] Dupas C, Houdy P, Lahmani M. *Nanoscience*. Berlin, Heidelberg: Springer Berlin Heidelberg; 2007.
- [10] Cox AJ, Louderback JG, Apsel SE, Bloomfield LA. Magnetism in 4 *d*-transition metal clusters. *Phys Rev B* 1994;49:12295–8.
- [11] Billas IML, Chatelain A, de Heer WA. Magnetism from the atom to the bulk in iron, cobalt, and nickel clusters. *Science* 1994;265:1682–4.
- [12] Turkevich J, Stevenson PC, Hillier J. A study of the nucleation and growth processes in the synthesis of colloidal gold. *Discuss Faraday Soc* 1951;11:55.
- [13] Brust M, Walker M, Bethell D, Schiffrin DJ, Whyman R. Synthesis of thiol-derivatised gold nanoparticles in a two-phase liquid? Liquid system. *J Chem Soc Chem Commun* 1994:801.
- [14] Zhao P, Li N, Astruc D. State of the art in gold nanoparticle synthesis. *Coord Chem Rev* 2013;257:638–65.
- [15] Cushing BL, Kolesnichenko VL, O'Connor CJ. Recent advances in the liquid-phase syntheses of inorganic nanoparticles. *Chem Rev* 2004;104:3893–946.
- [16] Brust M, Fink J, Bethell D, Schiffrin DJ, Kiely C. Synthesis and reactions of functionalised gold nanoparticles. *J Chem Soc Chem Commun* 1995:1655.
- [17] Bönnemann H, Brijoux W, Jousset T. The preparation of finely divided metal and alloy powders. *Angew Chem Int Ed Engl* 1990;29:273–5.
- [18] Viau G, Brayner R, Poul L, Chakroun N, Lacaze E, Fiévet-Vincent F, et al. Ruthenium nanoparticles: size, shape, and self-assemblies. *Chem Mater* 2003;15:486–94.
- [19] Smith TW, Wychick D. Colloidal iron dispersions prepared via the polymer-catalyzed decomposition of iron pentacarbonyl. *J Phys Chem* 1980;84:1621–9.
- [20] Hess PH, Parker PH. Polymers for stabilization of colloidal cobalt particles. *J Appl Polym Sci* 1966;10:1915–27.
- [21] Meffre A, Mehdaoui B, Kelsen V, Fazzini PF, Carrey J, Lachaize S, et al. A simple chemical route toward monodisperse iron carbide nanoparticles displaying tunable magnetic and unprecedented hyperthermia properties. *Nano Lett* 2012;12:4722–8.
- [22] Chaudret B, Philippot K. Organometallic nanoparticles of metals or metal oxides. *Oil Gas Sci Technol—Rev IFP* 2007;62:799–817.
- [23] Cordes DB, Lickiss PD, Rataboul F. Recent developments in the chemistry of cubic polyhedral oligosilsesquioxanes. *Chem Rev* 2010;110:2081–173.
- [24] Hybrid Plastics®, <<http://www.hybridplastics.com/>>; [accessed 07.06.15].
- [25] Roberts JJP, Vuong KT, Murray RW. Synthesis and electrochemistry of 6 nm ferrocenated Indium–Tin oxide nanoparticles. *Langmuir* 2013;29:474–9.
- [26] Kuo S-W, Chang F-C. POSS related polymer nanocomposites. *Prog Polym Sci* 2011;36:1649–96.
- [27] Zhu H, Jiang B, Xu C, Wu D. Long super-bundles of single-walled carbon nanotubes. *Chem Commun* 2002:1858–9.

- [28] Sun CQ, Bai HL, Tay BK, Li S, Jiang EY. Dimension, strength, and chemical and thermal stability of a single C – C bond in carbon nanotubes. *J Phys Chem B* 2003;107:7544–6.
- [29] Nunzi F, Mercuri F, Sgamellotti A, Re N. The coordination chemistry of carbon nanotubes: a density functional study through a cluster model approach. *J Phys Chem B* 2002;106:10622–33.
- [30] Kim YA, Yang K-S, Muramatsu H, Hayashi T, Endo M, Terrones M, et al. Double-walled carbon nanotubes: synthesis, structural characterization, and application. *Carbon Lett* 2014;15:77–88.
- [31] Ge M, Sattler K. Vapor-Condensation generation and STM analysis of fullerene tubes. *Science* 1993;260:515–18.
- [32] Ma P-C, Siddiqui NA, Marom G, Kim J-K. Dispersion and functionalization of carbon nanotubes for polymer-based nanocomposites: a review. *Compos Part Appl Sci Manuf* 2010;41:1345–67.
- [33] Bhushan B, Luo D, Schrickler SR, Sigmund W, Zauscher S. *Handbook of nanomaterials properties*. Berlin, Heidelberg: Springer Berlin Heidelberg; 2014.
- [34] Morales AM. A laser ablation method for the synthesis of crystalline semiconductor nanowires. *Science* 1998;279:208–11.
- [35] Thess A, Lee R, Nikolaev P, Dai H, Petit P, Robert J, et al. Crystalline ropes of metallic carbon nanotubes. *Science* 1996;273:483–7.
- [36] Kroto HW, Heath JR, O'Brien SC, Curl RF, Smalley RE. C60: buckminsterfullerene. *Nature* 1985;318:162–3.
- [37] Yudasaka M, Zhang M, Iijima S. Porous target enhances production of single-wall carbon nanotubes by laser ablation. *Chem Phys Lett* 2000;323:549–53.
- [38] Arepalli S. Laser ablation process for single-walled carbon nanotube production. *J Nanosci Nanotechnol* 2004;4:317–25.
- [39] Jost O, Gorbunov A, Liu X, Pompe W, Fink J. Single-walled carbon nanotube diameter. *J Nanosci Nanotechnol* 2004;4:433–40.
- [40] Shimada T, Sugai T, Ohno Y, Kishimoto S, Mizutani T, Yoshida H, et al. Double-wall carbon nanotube field-effect transistors: ambipolar transport characteristics. *Appl Phys Lett* 2004;84:2412.
- [41] Krätschmer W, Lamb LD, Fostiropoulos K, Huffman DR. Solid C60: a new form of carbon. *Nature* 1990;347:354–8.
- [42] Iijima S. Helical microtubules of graphitic carbon. *Nature* 1991;354:56–8.
- [43] Iijima S, Ichihashi T. Single-shell carbon nanotubes of 1-nm diameter. *Nature* 1993;363:603–5.
- [44] Bethune DS, Kiang CH, de Vries MS, Gorman G, Savoy R, Vazquez J, et al. Cobalt-catalysed growth of carbon nanotubes with single-atomic-layer walls. *Nature* 1993;363:605–7.
- [45] Yudasaka M, Kasuya Y, Kokai F, Takahashi K, Takizawa M, Bandow S, et al. Causes of different catalytic activities of metals in formation of single-wall carbon nanotubes. *Appl Phys Mater Sci Process* 2002;74:377–85.
- [46] Journet C, Maser WK, Bernier P, Loiseau A, de la Chapelle ML, Lefrant S, et al. Large-scale production of single-walled carbon nanotubes by the electric-arc technique. *Nature* 1997;388:756–8.
- [47] Liu C, Cong H, Li F, Tan P, Cheng H, Lu K, et al. Semi-continuous synthesis of single-walled carbon nanotubes by a hydrogen arc discharge method. *Carbon* 1999;37:1865–8.

- [48] Baker RTK, Harris MA. The formation of filamentous carbon. In: Walker Jr. PL, Throrer PA, editors. *Chemistry and physics of carbon*, vol. 14. New York, NY: Marcel Dekker; 1978. p. 83–164.
- [49] Lamouroux E, Serp P, Kalck P. Catalytic routes towards single wall carbon nanotubes. *Catal Rev* 2007;49:341–405.
- [50] Nikolaev P. Gas-phase production of single-walled carbon nanotubes from carbon monoxide: a review of the HiPco process. *J Nanosci Nanotechnol* 2004;35:307–16.
- [51] Mojica M, Alonso JA, Méndez F. Synthesis of fullerenes: synthesis of fullerenes. *J Phys Org Chem* 2013;26:526–39.
- [52] Whitener KE, Sheehan PE. Graphene synthesis. *Diam Relat Mater* 2014;46:25–34.
- [53] Novoselov KS. Electric field effect in atomically thin carbon films. *Science* 2004;306:666–9.
- [54] Vallés C, Drummond C, Saadaoui H, Furtado CA, He M, Roubeau O, et al. Solutions of negatively charged graphene sheets and ribbons. *J Am Chem Soc* 2008;130:15802–4.
- [55] Park S, Ruoff RS. Chemical methods for the production of graphenes. *Nat Nanotechnol* 2009;4:217–24.
- [56] Dreyer DR, Park S, Bielawski CW, Ruoff RS. The chemistry of graphene oxide. *Chem Soc Rev* 2010;39:228–40.
- [57] Kataria S, Wagner S, Ruhkopf J, Gahoi A, Pandey H, Bornemann R, et al. Chemical vapor deposited graphene: from synthesis to applications: chemical vapor deposited graphene. *Phys Status Solidi A* 2014;211:2439–49.
- [58] Bergaya F, Lagaly G. Chapter 1 general introduction: clays, clay minerals, and clay science. *Dev. Clay Sci*. Elsevier; 2006. p. 1–18.
- [59] Ray SS. *Clay-containing polymer nanocomposites from fundamentals to real applications*. Amsterdam; Boston, MA: Elsevier; 2013.
- [60] Chen B, Evans JRG. Elastic moduli of clay platelets. *Scr Mater* 2006;54:1581–5.
- [61] Kawasumi M, Hasegawa N, Kato M, Usuki A, Okada A. Preparation and mechanical properties of polypropylene – clay hybrids. *Macromolecules* 1997;30:6333–8.
- [62] Li S, Meng Lin M, Toprak MS, Kim DK, Muhammed M. Nanocomposites of polymer and inorganic nanoparticles for optical and magnetic applications. *Nano Rev* 2010;1:5214.
- [63] Althues H, Henle J, Kaskel S. Functional inorganic nanofillers for transparent polymers. *Chem Soc Rev* 2007;36:1454.
- [64] Ramanathan T, Stankovich S, Dikin DA, Liu H, Shen H, Nguyen ST, et al. Graphitic nanofillers in PMMA nanocomposites—an investigation of particle size and dispersion and their influence on nanocomposite properties. *J Polym Sci Part B Polym Phys* 2007;45:2097–112.
- [65] Ramanathan AT, Stankovich S, Dikin DA, Liu H, Shen H, Nguyen ST, et al. Erratum: graphitic nanofillers in PMMA nanocomposites—an investigation of particle size and dispersion and their influence on nanocomposite properties. *J Polym Sci Part B Polym Phys* 2012;50 589–589
- [66] Vaisman L, Wachtel E, Wagner HD, Marom G. Polymer-nanoinclusion interactions in carbon nanotube based polyacrylonitrile extruded and electrospun fibers. *Polymer* 2007;48:6843–54.
- [67] Caseri W. Inorganic nanoparticles as optically effective additives for polymers. *Chem Eng Commun* 2008;196:549–72.

- [68] Okada A, Usuki A. Twenty years of polymer-clay nanocomposites. *Macromol Mater Eng* 2006;291:1449–76.
- [69] Balazs AC, Emrick T, Russell TP. Nanoparticle polymer composites: where two small worlds meet. *Science* 2006;314:1107–10.
- [70] Chen B, Evans JRG. Preferential intercalation in polymer-clay nanocomposites. *J Phys Chem B* 2004;108:14986–90.
- [71] Zhao H, Li RKY. A study on the photo-degradation of zinc oxide (ZnO) filled polypropylene nanocomposites. *Polymer* 2006;47:3207–17.
- [72] Chae DW, Kim BC. Characterization on polystyrene/zinc oxide nanocomposites prepared from solution mixing. *Polym Adv Technol* 2005;16:846–50.
- [73] Saravanamuttu K, Du XM, Najafi SI, Andrews MP. Photoinduced structural relaxation and densification in sol-gel-derived nanocomposite thin films: implications for integrated optics device fabrication. *Can J Chem* 1998;76:1717–29.
- [74] Hao C, Zhao Y, He A, Zhang X, Wang D, Ma Q, et al. Investigation on the melt spinning fibers of PP/organoclay nanocomposites prepared by *in-situ* polymerization. *J Appl Polym Sci* 2009;116:1384–91.
- [75] Sinha Ray S, Yamada K, Okamoto M, Ueda K. Polylactide-layered silicate nanocomposite: a novel biodegradable material. *Nano Lett* 2002;2:1093–6.
- [76] Lee DC, Jang LW. Preparation and characterization of PMMA-clay hybrid composite by emulsion polymerization. *J Appl Polym Sci* 1996;61:1117–22.
- [77] Kim TH, Jang LW, Lee DC, Choi HJ, Jhon MS. Synthesis and rheology of intercalated Polystyrene/Na<sup>+</sup>-montmorillonite nanocomposites. *Macromol Rapid Commun* 2002;23:191–5.
- [78] Dirix Y, Bastiaansen C, Caseri W, Smith P. Preparation, structure and properties of uniaxially oriented polyethylene-silver nanocomposites. *J Mater Sci* 1999;34:3859–66.
- [79] Dirix Y, Darribère C, Heffels W, Bastiaansen C, Caseri W, Smith P. Optically anisotropic polyethylene-gold nanocomposites. *Appl Opt* 1999;38:6581.
- [80] Park J, An K, Hwang Y, Park J-G, Noh H-J, Kim J-Y, et al. Ultra-large-scale syntheses of monodisperse nanocrystals. *Nat Mater* 2004;3:891–5.
- [81] Veinot JGC, Galloro J, Pugliese L, Pestrin R, Pietro WJ. Surface functionalization of cadmium sulfide quantum-confined nanoclusters. 5. Evidence of facile surface-core electronic communication in the photodecomposition mechanism of functionalized quantum dots<sup>†</sup>. *Chem Mater* 1999;11:642–8.
- [82] Bourgeat-Lami E. Organic-inorganic nanostructured colloids. *J Nanosci Nanotechnol* 2002;2:1–24.
- [83] Li S, Qin J, Fornara A, Toprak M, Muhammed M, Kim DK. Synthesis and magnetic properties of bulk transparent PMMA/Fe-oxide nanocomposites. *Nanotechnology* 2009;20:185607.
- [84] Park J, Lee E, Hwang N-M, Kang M, Kim SC, Hwang Y, et al. One-nanometer-scale size-controlled synthesis of monodisperse magnetic iron oxide nanoparticles. *Angew Chem* 2005;117:2932–7.
- [85] Avella M, Errico ME, Martuscelli E. Novel PMMA/CaCO<sub>3</sub> nanocomposites abrasion resistant prepared by an *in situ* polymerization process. *Nano Lett* 2001;1:213–17.
- [86] Avella M, Errico ME, Martelli S, Martuscelli E. Preparation methodologies of polymer matrix nanocomposites. *Appl Organomet Chem* 2001;15:435–9.
- [87] Sunkara HB, Jethmalani JM, Ford WT. Solidification of colloidal crystals of silica. In: Mark JE, Lee CY-C, Bianconi PA, editors. *Hybrid Org.-Inorg. Compos.* Washington, DC: American Chemical Society; 1995. p. 181–91.

- [88] Kickelbick G. Concepts for the incorporation of inorganic building blocks into organic polymers on a nanoscale. *Prog Polym Sci* 2003;28:83–114.
- [89] Mao Y, Fung BM. Formation and characterization of anchored polymer coatings on alumina. *Chem Mater* 1998;10:509–17.
- [90] Lü C, Cheng Y, Liu Y, Liu F, Yang B. A facile route to ZnS–polymer nanocomposite optical materials with high nanophase content via  $\gamma$ -ray irradiation initiated bulk polymerization. *Adv Mater* 2006;18:1188–92.
- [91] Althues H, Simon P, Philipp F, Kaskel S. Integration of zinc oxide nanoparticles into transparent poly(butanediolmonoacrylate) via photopolymerisation. *J Nanosci Nanotechnol* 2006;6:409–13.
- [92] Wang J-Y, Chen W, Liu A-H, Lu G, Zhang G, Zhang J-H, et al. Controlled fabrication of cross-linked nanoparticles/polymer composite thin films through the combined use of surface-initiated atom transfer radical polymerization and gas/solid reaction. *J Am Chem Soc* 2002;124:13358–9.
- [93] Wu M, Lv N, Lei L, Qi D, Lin H. Electrostatic absorption of azo initiator onto TiO<sub>2</sub> particles and *in situ* anchoring polymerization of butyl acrylate from modified TiO<sub>2</sub>. *Acta Polym Sin* 2009;009:445–50.
- [94] Podsiadlo P, Kaushik AK, Arruda EM, Waas AM, Shim BS, Xu J, et al. Ultrastrong and stiff layered polymer nanocomposites. *Science* 2007;318:80–3.
- [95] Sarkar MD, Deb P. Synthesis and characterization of hybrid nanocomposites comprising poly(vinyl alcohol) and colloidal silica. *Adv Polym Technol* 2008;27:152–62.
- [96] Wang ZG, Zu XT, Xiang X, Lian J, Wang LM. Preparation and characterization of polymer/inorganic nanoparticle composites through electron irradiation. *J Mater Sci* 2006;41:1973–8.
- [97] Hench LL, West JK. The sol–gel process. *Chem Rev* 1990;90:33–72.
- [98] Wen J, Wilkes GL. Organic/inorganic hybrid network materials by the sol–gel approach. *Chem Mater* 1996;8:1667–81.
- [99] Schottner G. Hybrid sol–gel-derived polymers: applications of multifunctional materials. *Chem Mater* 2001;13:3422–35.
- [100] Bian L, Bao L, Wang J, Lei J. *In situ* preparation of monodispersed Ag/polyaniline/Fe<sub>3</sub>O<sub>4</sub> nanoparticles via heterogeneous nucleation. *Nanoscale Res Lett* 2013;8:309.
- [101] Deng J, He C, Peng Y, Wang J, Long X, Li P, et al. Magnetic and conductive Fe<sub>3</sub>O<sub>4</sub>–polyaniline nanoparticles with core–shell structure. *Synth Met* 2003;139:295–301.
- [102] Li S, Toprak MS, Jo YS, Dobson J, Kim DK, Muhammed M. Bulk synthesis of transparent and homogeneous polymeric hybrid materials with ZnO quantum dots and PMMA. *Adv Mater* 2007;19:4347–52.
- [103] Wan M, Li J. Synthesis and electrical-magnetic properties of polyaniline composites. *J Polym Sci Part Polym Chem* 1998;36:2799–805.
- [104] Yuwono AH, Liu B, Xue J, Wang J, Elim HI, Ji W, et al. Controlling the crystallinity and nonlinear optical properties of transparent TiO<sub>2</sub>? PMMA nanohybrids. *J Mater Chem* 2004;14:2978.
- [105] Zhang Y, Zhu C, Kan J. Synthesis and characterization of ferromagnetic polyaniline with conductivity in an applied magnetic field. *J Appl Polym Sci* 2008;109:3024–9.
- [106] López-Quintela MA. Synthesis of nanomaterials in microemulsions: formation mechanisms and growth control. *Curr Opin Colloid Interface Sci* 2003;8:137–44.

- [107] Palkovits R, Althues H, Ruplecker A, Tesche B, Dreier A, Holle U, et al. Polymerization of W/O microemulsions for the preparation of transparent SiO<sub>2</sub>/PMMA nanocomposites. *Langmuir* 2005;21:6048–53.
- [108] Uskoković V, Drofenik M. Synthesis of materials within reverse micelles. *Surf Rev Lett* 2005;12:239–77.
- [109] Ni Y, Ge X, Liu H, Zhang Z, Ye Q. *In situ* synthesis and characterization of spherical CdS/polyacrylamide nanocomposites by gamma-irradiation in W/O microemulsions. *Chem Lett* 2001:924–5.
- [110] Khrenov V, Klapper M, Koch M, Müllen K. Surface functionalized ZnO particles designed for the use in transparent nanocomposites. *Macromol Chem Phys* 2005;206:95–101.
- [111] Sun D, Miyatake N, Sue H-J. Transparent PMMA/ZnO nanocomposite films based on colloidal ZnO quantum dots. *Nanotechnology* 2007;18:215606.
- [112] Xiong M, Gu G, You B, Wu L. Preparation and characterization of poly(styrene butylacrylate) latex/nano-ZnO nanocomposites. *J Appl Polym Sci* 2003;90:1923–31.
- [113] Zheng J, Siegel RW, Toney CG. Polymer crystalline structure and morphology changes in nylon-6/ZnO nanocomposites. *J Polym Sci Part B Polym Phys* 2003;41:1033–50.
- [114] Gojny FH, Wichmann MHG, Köpke U, Fiedler B, Schulte K. Carbon nanotube-reinforced epoxy-composites: enhanced stiffness and fracture toughness at low nanotube content. *Compos Sci Technol* 2004;64:2363–71.
- [115] Thostenson ET, Chou T-W. Processing-structure-multi-functional property relationship in carbon nanotube/epoxy composites. *Carbon* 2006;44:3022–9.
- [116] Ma PC, Tang BZ, Kim J-K. Conversion of semiconducting behavior of carbon nanotubes using ball milling. *Chem Phys Lett* 2008;458:166–9.
- [117] Sandler J, Shaffer MS, Prasse T, Bauhofer W, Schulte K, Windle A. Development of a dispersion process for carbon nanotubes in an epoxy matrix and the resulting electrical properties. *Polymer* 1999;40:5967–71.
- [118] Villmow T, Pötschke P, Pegel S, Häußler L, Kretzschmar B. Influence of twin-screw extrusion conditions on the dispersion of multi-walled carbon nanotubes in a poly(lactic acid) matrix. *Polymer* 2008;49:3500–9.
- [119] Chen SJ, Zou B, Collins F, Zhao XL, Majumber M, Duan WH. Predicting the influence of ultrasonication energy on the reinforcing efficiency of carbon nanotubes. *Carbon* 2014;77:1–10.
- [120] Ma PC, Wang SQ, Kim J-K, Tang BZ. *In-situ* amino functionalization of carbon nanotubes using ball milling. *J Nanosci Nanotechnol* 2009;9:749–53.
- [121] Isayev AI, Kumar R, Lewis TM. Ultrasound assisted twin screw extrusion of polymer–nanocomposites containing carbon nanotubes. *Polymer* 2009;50:250–60.
- [122] Lu KL, Lago RM, Chen YK, Green MLH, Harris PJF, Tsang SC. Mechanical damage of carbon nanotubes by ultrasound. *Carbon* 1996;34:814–16.
- [123] Mukhopadhyay K, Dwivedi CD, Mathur GN. Conversion of carbon nanotubes to carbon nanofibers by sonication. *Carbon* 2002;40:1373–6.
- [124] Balasubramanian K, Burghard M. Chemically functionalized carbon nanotubes. *Small* 2005;1:180–92.
- [125] Hirsch A. Functionalization of single-walled carbon nanotubes. *Angew Chem Int Ed* 2002;41:1853.

- [126] Tasis D, Tagmatarchis N, Bianco A, Prato M. Chemistry of carbon nanotubes. *Chem Rev* 2006;106:1105–36.
- [127] Xie X, Mai Y, Zhou X. Dispersion and alignment of carbon nanotubes in polymer matrix: a review. *Mater Sci Eng R Rep* 2005;49:89–112.
- [128] Niyogi S, Hamon MA, Hu H, Zhao B, Bhowmik P, Sen R, et al. Chemistry of single-walled carbon nanotubes. *Acc Chem Res* 2002;35:1105–13.
- [129] Park H, Zhao J, Lu JP. Effects of sidewall functionalization on conducting properties of single wall carbon nanotubes. *Nano Lett* 2006;6:916–19.
- [130] Tsubokawa N. Preparation and properties of polymer-grafted carbon nanotubes and nanofibers. *Polym J* 2005;37:637–55.
- [131] Ebbesen TW, Ajayan PM, Hiura H, Tanigaki K. Purification of nanotubes. *Nature* 1994;367:519–519.
- [132] Hiura H, Ebbesen TW, Tanigaki K. Opening and purification of carbon nanotubes in high yields. *Adv Mater* 1995;7:275–6.
- [133] Nalwa HS. *Handbook of nanostructured materials and nanotechnology*. San Diego, CA: Academic Press; 2000.
- [134] Cañete-Rosales P, Ortega V, Álvarez-Lueje A, Bollo S, González M, Ansón A, et al. Influence of size and oxidative treatments of multi-walled carbon nanotubes on their electrocatalytic properties. *Electrochimica Acta* 2012;62:163–71.
- [135] Tchoul MN, Ford WT, Lolli G, Resasco DE, Arepalli S. Effect of mild nitric acid oxidation on dispersability, size, and structure of single-walled carbon nanotubes. *Chem Mater* 2007;19:5765–72.
- [136] Esumi K, Ishigami M, Nakajima A, Sawada K, Honda H. Chemical treatment of carbon nanotubes. *Carbon* 1996;34:279–81.
- [137] Hussain S, Jha P, Chouksey A, Raman R, Islam SS, Islam T, et al. Spectroscopic investigation of modified single wall carbon nanotube (SWCNT). *J Mod Phys* 2011;02:538–43.
- [138] Yu R, Chen L, Liu Q, Lin J, Tan K-L, Ng SC, et al. Platinum deposition on carbon nanotubes via chemical modification. *Chem Mater* 1998;10:718–22.
- [139] Feng Y, Zhang H, Hou Y, McNicholas TP, Yuan D, Yang S, et al. Room temperature purification of few-walled carbon nanotubes with high yield. *ACS Nano* 2008;2:1634–8.
- [140] Liu J, Rinzler AG, Dai H, Hafner JH, Bradley RK, Boul PJ, et al. Fullerene pipes. *Sci Wash C* 1998;280:1253–6.
- [141] Mawhinney DB, Naumenko V, Kuznetsova A, Yates JT, Liu J, Smalley RE. Surface defect site density on single walled carbon nanotubes by titration. *Chem Phys Lett* 2000;324:213–16.
- [142] Hu H, Bhowmik P, Zhao B, Hamon M, Itkis M, Haddon R. Determination of the acidic sites of purified single-walled carbon nanotubes by acid–base titration. *Chem Phys Lett* 2001;345:25–8.
- [143] Eitan A, Jiang K, Dukes D, Andrews R, Schadler LS. Surface modification of multi-walled carbon nanotubes: toward the tailoring of the interface in polymer composites. *Chem Mater* 2003;15:3198–201.
- [144] Hamon MA, Hui H, Bhowmik P, Itkis HME, Haddon RC. Ester-functionalized soluble single-walled carbon nanotubes. *Appl Phys Mater Sci Process* 2002;74:333–8.

- [145] Sen R, Zhao B, Perea D, Itkis ME, Hu H, Love J, et al. Preparation of single-walled carbon nanotube reinforced polystyrene and polyurethane nanofibers and membranes by electrospinning. *Nano Lett* 2004;4:459–64.
- [146] Chen J, Hamon MA, Hu H, Chen Y, Rao AM, Eklund PC, et al. Solution properties of single-walled carbon nanotubes. *Sci Wash C* 1998;282:95–8.
- [147] Hamon MA, Chen J, Hu H, Chen Y, Itkis ME, Rao AM, et al. Dissolution of single-walled carbon nanotubes. *Adv Mater* 1999;11:834–40.
- [148] Sun D, Zhou Z, Chen G-X, Li Q. Regulated dielectric loss of polymer composites from coating carbon nanotubes with a cross-linked silsesquioxane shell through free-radical polymerization. *ACS Appl Mater Interfaces* 2014;6:18635–43.
- [149] Sham M-L, Kim J-K. Surface functionalities of multi-wall carbon nanotubes after UV/Ozone and TETA treatments. *Carbon* 2006;44:768–77.
- [150] Ávila-Orta CA, Cruz-Delgado VJ, Neira-Velázquez MG, Hernández-Hernández E, Méndez-Padilla MG, Medellín-Rodríguez FJ. Surface modification of carbon nanotubes with ethylene glycol plasma. *Carbon* 2009;47:1916–21.
- [151] Mawhinney DB, Naumenko V, Kuznetsova A, Yates JT, Liu J, Smalley RE. Infrared spectral evidence for the etching of carbon nanotubes: ozone oxidation at 298 K. *J Am Chem Soc* 2000;122:2383–4.
- [152] Chen Q, Dai L, Gao M, Huang S, Mau A. Plasma activation of carbon nanotubes for chemical modification. *J Phys Chem B* 2001;105:618–22.
- [153] Kang X, Ma W, Zhang H-L, Xu Z-G, Guo Y, Xiong Y. Vinyl-carbon nanotubes for composite polymer materials. *J Appl Polym Sci* 2008;110:1915–20.
- [154] Ha JU, Kim M, Lee J, Choe S, Cheong IW, Shim SE. A novel synthesis of polymer brush on multiwall carbon nanotubes bearing terminal monomeric unit. *J Polym Sci Part Polym Chem* 2006;44:6394–401.
- [155] Ma PC, Kim J-K, Tang BZ. Functionalization of carbon nanotubes using a silane coupling agent. *Carbon* 2006;44:3232–8.
- [156] Liu P. Modifications of carbon nanotubes with polymers. *Eur Polym J* 2005;41:2693–703.
- [157] Stephenson JJ, Sadana AK, Higginbotham AL, Tour JM. Highly functionalized and soluble multiwalled carbon nanotubes by reductive alkylation and arylation: the billups reaction. *Chem Mater* 2006;18:4658–61.
- [158] Daniel S, Rao TP, Rao KS, Rani SU, Naidu GRK, Lee H-Y, et al. A review of DNA functionalized/grafted carbon nanotubes and their characterization. *Sens Actuators B Chem* 2007;122:672–82.
- [159] Chakrabarti M, Kiseleva R, Vertegel A, Ray SK. Carbon nanomaterials for drug delivery and cancer therapy. *J Nanosci Nanotechnol* 2015;15:5501–11.
- [160] Wang H, Xiang Z, Hu C-F, Pastorin G, Fang W, Lee C. Microneedle array integrated with CNT nanofilters for controlled and selective drug delivery. *J Microelectromechanical Syst* 2014;23:1036–44.
- [161] Mallick K, Strydom AM. Biophilic carbon nanotubes. *Colloids Surf B Biointerfaces* 2013;105:310–18.
- [162] Chen B-D, Yang C-L, Yang J-S, Wang M-S, Ma X-G. Dynamic mechanism of HIV replication inhibitor peptide encapsulated into carbon nanotubes. *Curr Appl Phys* 2013;13:1001–7.
- [163] Jacobs CB, Peairs MJ, Venton BJ. Review: carbon nanotube based electrochemical sensors for biomolecules. *Anal Chim Acta* 2010;662:105–27.

- [164] Vasiliev I, Curran SA. Cross linking of thiolated carbon nanotubes: an *ab initio* study. *J Appl Phys* 2007;102:024317.
- [165] Lee J-M, Kim SJ, Kim JW, Kang PH, Nho YC, Lee Y-S. A high resolution XPS study of sidewall functionalized MWCNTs by fluorination. *J Ind Eng Chem* 2009;15:66–71.
- [166] Khabashesku VN, Billups WE, Margrave JL. Fluorination of single-wall carbon nanotubes and subsequent derivatization reactions. *Acc Chem Res* 2002;35:1087–95.
- [167] Mickelson ET, Huffman CB, Rinzler AG, Smalley RE, Hauge RH, Margrave JL. Fluorination of single-wall carbon nanotubes. *Chem Phys Lett* 1998;296:188–94.
- [168] Mickelson ET, Chiang IW, Zimmerman JL, Boul PJ, Lozano J, Liu J, et al. Solvation of fluorinated single-wall carbon nanotubes in alcohol solvents. *J Phys Chem B* 1999;103:4318–22.
- [169] Kelly KF, Chiang IW, Mickelson ET, Hauge RH, Margrave JL, Wang X, et al. Insight into the mechanism of sidewall functionalization of single-walled nanotubes: an STM study. *Chem Phys Lett* 1999;313:445–50.
- [170] Boul P, Liu J, Mickelson E, Huffman C, Ericson L, Chiang I, et al. Reversible sidewall functionalization of buckytubes. *Chem Phys Lett* 1999;310:367–72.
- [171] Holzinger M, Vostrowsky O, Hirsch A, Hennrich F, Kappes M, Weiss R, et al. Sidewall functionalization of carbon nanotubes this work was supported by the European Union under the 5th framework research training network 1999, HPRNT 1999-00011 FUNCARS. *Angew Chem Int Ed* 2001;40:4002.
- [172] Stevens JL, Huang AY, Peng H, Chiang IW, Khabashesku VN, Margrave JL. Sidewall amino-functionalization of single-walled carbon nanotubes through fluorination and subsequent reactions with terminal diamines. *Nano Lett* 2003;3:331–6.
- [173] Blake R, Gun'ko YK, Coleman J, Cadek M, Fonseca A, Nagy JB, et al. A generic organometallic approach toward ultra-strong carbon nanotube polymer composites. *J Am Chem Soc* 2004;126:10226–7.
- [174] Hu H, Zhao B, Hamon MA, Kamaras K, Itkis ME, Haddon RC. Sidewall functionalization of single-walled carbon nanotubes by addition of dichlorocarbene. *J Am Chem Soc* 2003;125:14893–900.
- [175] Chen Y, Haddon RC, Fang S, Rao AM, Eklund PC, Lee WH, et al. Chemical attachment of organic functional groups to single-walled carbon nanotube material. *J Mater Res* 1998;13:2423–31.
- [176] Bahr JL, Mickelson ET, Bronikowski MJ, Smalley RE, Tour JM. Dissolution of small diameter single-wall carbon nanotubes in organic solvents?. *Chem Commun* 2001:193–4.
- [177] Holzinger M, Abraham J, Whelan P, Graupner R, Ley L, Hennrich F, et al. Functionalization of single-walled carbon nanotubes with (R-)Oxycarbonyl nitrenes. *J Am Chem Soc* 2003;125:8566–80.
- [178] Holzinger M, Steinmetz J, Samaille D, Glerup M, Paillet M, Bernier P, et al. [2 + 1] cycloaddition for cross-linking SWCNTs. *Carbon* 2004;42:941–7.
- [179] Vázquez E, Prato M. Functionalization of carbon nanotubes for applications in materials science and nanomedicine. *Pure Appl Chem* 2010;82:853–61.
- [180] Ménard-Moyon C, Izard N, Doris E, Mioskowski C. Separation of semiconducting from metallic carbon nanotubes by selective functionalization with azomethine ylides. *J Am Chem Soc* 2006;128:6552–3.

- [181] Unger E, Graham A, Kreupl F, Liebau M, Hoenlein W. Electrochemical functionalization of multi-walled carbon nanotubes for solvation and purification. *Curr Appl Phys* 2002;2:107–11.
- [182] Kim KS, Bae DJ, Kim JR, Park KA, Lim SC, Kim J-J, et al. Modification of electronic structures of a carbon nanotube by hydrogen functionalization. *Adv Mater* 2002;14:1818–21.
- [183] Huisgen R. 1,3-Dipolar cycloaddition—introduction, survey, mechanism. In: Padwa A, editor. *1,3-Dipolar Cycloaddition Chemistry*. New York, NY: Wiley; 1984. p. 1–176.
- [184] Li H, Cheng F, Duft AM, Adronov A. Functionalization of single-walled carbon nanotubes with well-defined polystyrene by “click” coupling. *J Am Chem Soc* 2005;127:14518–24.
- [185] Kumar I, Rana S, Rode CV, Cho JW. Functionalization of single-walled carbon nanotubes with azides derived from amino acids using click chemistry. *J Nanosci Nanotechnol* 2008;8:3351–6.
- [186] Campidelli S, Ballesteros B, Filoramo A, Díaz DD, de la Torre G, Torres T, et al. Facile decoration of functionalized single-wall carbon nanotubes with phthalocyanines via “click chemistry”. *J Am Chem Soc* 2008;130:11503–9.
- [187] Bahr JL, Yang J, Kosynkin DV, Bronikowski MJ, Smalley RE, Tour JM. Functionalization of carbon nanotubes by electrochemical reduction of aryl diazonium salts: a bucky paper electrode. *J Am Chem Soc* 2001;123:6536–42.
- [188] Liu J, Zubiri MR i, Vigolo B, Dossot M, Fort Y, Ehrhardt J-J, et al. Efficient microwave-assisted radical functionalization of single-wall carbon nanotubes. *Carbon* 2007;45:885–91.
- [189] Liu J, Zubiri MRI, Dossot M, Vigolo B, Hauge RH, Fort Y, et al. Sidewall functionalization of single-wall carbon nanotubes (SWNTs) through aryl free radical addition. *Chem Phys Lett* 2006;430:93–6.
- [190] Bahr JL, Tour JM. Highly functionalized carbon nanotubes using *in situ* generated diazonium compounds. *Chem Mater* 2001;13:3823–4.
- [191] Bahr JL, Tour JM. Covalent chemistry of single-wall carbon nanotubes. *J Mater Chem* 2002;12:1952–8.
- [192] Yurekli K, Mitchell CA, Krishnamoorti R. Small-angle neutron scattering from surfactant-assisted aqueous dispersions of carbon nanotubes. *J Am Chem Soc* 2004;126:9902–3.
- [193] Crespi VH, Chopra NG, Cohen ML, Zettl A, Radmilović V. Site-selective radiation damage of collapsed carbon nanotubes. *Appl Phys Lett* 1998;73:2435.
- [194] Hu Y, Jang I, Sinnott S. Modification of carbon nanotube-polystyrene matrix composites through polyatomic-ion beam deposition: predictions from molecular dynamics simulations. *Model Charact Nanostructured Mater* 2003;63:1663–9.
- [195] Ni B, Andrews R, Jacques D, Qian D, Wijesundara MBI, Choi Y, et al. A combined computational and experimental study of ion-beam modification of carbon nanotube bundles. *J Phys Chem B* 2001;105:12719–25.
- [196] Sahoo NG, Rana S, Cho JW, Li L, Chan SH. Polymer nanocomposites based on functionalized carbon nanotubes. *Prog Polym Sci* 2010;35:837–67.
- [197] Doe C, Choi S-M, Kline SR, Jang H-S, Kim T-H. Charged rod-like nanoparticles assisting single-walled carbon nanotube dispersion in water. *Adv Funct Mater* 2008;18:2685–91.

- [198] Shin J-Y, Premkumar T, Geckeler KE. Dispersion of single-walled carbon nanotubes by using surfactants: are the type and concentration important?. *Chem—Eur J* 2008;14:6044–8.
- [199] Park I, Park M, Kim J, Lee H, Lee MS. Multiwalled carbon nanotubes functionalized with PS via emulsion polymerization. *Macromol Res* 2007;15:498–505.
- [200] Guo Z, Sadler PJ, Tsang SC. Immobilization and visualization of DNA and proteins on carbon nanotubes. *Adv Mater* 1998;10:701–3.
- [201] Barone PW, Strano MS. Reversible control of carbon nanotube aggregation for a glucose affinity sensor. *Angew Chem* 2006;118:8318–21.
- [202] Numata M, Sugikawa K, Kaneko K, Shinkai S. Creation of hierarchical carbon nanotube assemblies through alternative packing of complementary semi-artificial  $\beta$ -1,3-Glucan/Carbon nanotube composites. *Chem—Eur J* 2008;14:2398–404.
- [203] Yan LY, Poon YF, Chan-Park MB, Chen Y, Zhang Q. Individually dispersing single-walled carbon nanotubes with novel neutral pH water-soluble chitosan derivatives. *J Phys Chem C* 2008;112:7579–87.
- [204] Das D, Das PK. Superior activity of structurally deprived enzyme–carbon nanotube hybrids in cationic reverse micelles. *Langmuir* 2009;25:4421–8.
- [205] Rouse JH. Polymer-assisted dispersion of single-walled carbon nanotubes in alcohols and applicability toward carbon nanotube/sol–gel composite formation. *Langmuir* 2005;21:1055–61.
- [206] Yuan WZ, Sun JZ, Dong Y, Häussler M, Yang F, Xu HP, et al. Wrapping carbon nanotubes in pyrene-containing poly(phenylacetylene) chains: solubility, stability, light emission, and surface photovoltaic properties. *Macromolecules* 2006;39:8011–20.
- [207] Bandow S, Rao AM, Williams KA, Thess A, Smalley RE, Eklund PC. Purification of single-wall carbon nanotubes by microfiltration. *J Phys Chem B* 1997;101:8839–42.
- [208] Duesberg GS, Burghard M, Muster J, Philipp G. Separation of carbon nanotubes by size exclusion chromatography. *Chem Commun* 1998:435–6.
- [209] Chen RJ, Zhang Y, Wang D, Dai H. Noncovalent sidewall functionalization of single-walled carbon nanotubes for protein immobilization. *J Am Chem Soc* 2001;123:3838–9.
- [210] Rastogi R, Kaushal R, Tripathi SK, Sharma AL, Kaur I, Bharadwaj LM. Comparative study of carbon nanotube dispersion using surfactants. *J Colloid Interface Sci* 2008;328:421–8.
- [211] Ikeda A, Hamano T, Hayashi K, Kikuchi J. Water-solubilization of nucleotides-coated single-walled carbon nanotubes using a high-speed vibration milling technique. *Org Lett* 2006;8:1153–6.
- [212] Yu J, Grossiord N, Koning CE, Loos J. Controlling the dispersion of multi-wall carbon nanotubes in aqueous surfactant solution. *Carbon* 2007;45:618–23.
- [213] Lauret J-S, Voisin C, Cassabois G, Delalande C, Roussignol P, Jost O, et al. Ultrafast carrier dynamics in single-wall carbon nanotubes. *Phys Rev Lett* 2003.
- [214] Steuerman DW, Star A, Narizzano R, Choi H, Ries RS, Nicolini C, et al. Interactions between conjugated polymers and single-walled carbon nanotubes. *J Phys Chem B* 2002;106:3124–30.
- [215] Hsiao A-E, Tsai S-Y, Hsu M-W, Chang S-J. Decoration of multi-walled carbon nanotubes by polymer wrapping and its application in MWCNT/polyethylene composites. *Nanoscale Res Lett* 2012;7:240.

- [216] Li L-J, Nicholas RJ, Chen C-Y, Darton RC, Baker SC. Comparative study of photoluminescence of single-walled carbon nanotubes wrapped with sodium dodecyl sulfate, surfactin and polyvinylpyrrolidone. *Nanotechnology* 2005;16: S202–5.
- [217] Kotov NA. Materials science: carbon sheet solutions. *Nature* 2006;442:254–5.
- [218] Liu N, Luo F, Wu H, Liu Y, Zhang C, Chen J. One-step ionic-liquid-assisted electrochemical synthesis of ionic-liquid-functionalized graphene sheets directly from graphite. *Adv Funct Mater* 2008;18:1518–25.
- [219] Parvez K, Wu Z-S, Li R, Liu X, Graf R, Feng X, et al. Exfoliation of graphite into graphene in aqueous solutions of inorganic salts. *J Am Chem Soc* 2014;136:6083–91.
- [220] Dikin DA, Stankovich S, Zimney EJ, Piner RD, Dommett GHB, Evmenenko G, et al. Preparation and characterization of graphene oxide paper. *Nature* 2007;448:457–60.
- [221] Vickery JL, Patil AJ, Mann S. Fabrication of graphene-polymer nanocomposites with higher-order three-dimensional architectures. *Adv Mater* 2009;21:2180–4.
- [222] McAllister MJ, Li J-L, Adamson DH, Schniepp HC, Abdala AA, Liu J, et al. Single sheet functionalized graphene by oxidation and thermal expansion of graphite. *Chem Mater* 2007;19:4396–404.
- [223] Kuilla T, Bhadra S, Yao D, Kim NH, Bose S, Lee JH. Recent advances in graphene based polymer composites. *Prog Polym Sci* 2010;35:1350–75.
- [224] Bourlinos AB, Gournis D, Petridis D, Szabó T, Szeri A, Dékány I. Graphite oxide: chemical reduction to graphite and surface modification with primary aliphatic amines and amino acids. *Langmuir* 2003;19:6050–5.
- [225] Stankovich S, Dikin DA, Piner RD, Kohlhaas KA, Kleinhammes A, Jia Y, et al. Synthesis of graphene-based nanosheets via chemical reduction of exfoliated graphite oxide. *Carbon* 2007;45:1558–65.
- [226] Nethravathi C, Rajamathi JT, Ravishankar N, Shivakumara C, Rajamathi M. Graphite oxide-intercalated anionic clay and its decomposition to graphene–inorganic material nanocomposites. *Langmuir* 2008;24:8240–4.
- [227] Szabó T, Szeri A, Dékány I. Composite graphitic nanolayers prepared by self-assembly between finely dispersed graphite oxide and a cationic polymer. *Carbon* 2005;43:87–94.
- [228] Stankovich S, Dikin DA, Dommett GHB, Kohlhaas KM, Zimney EJ, Stach EA, et al. Graphene-based composite materials. *Nature* 2006;442:282–6.
- [229] Wei T, Luo G, Fan Z, Zheng C, Yan J, Yao C, et al. Preparation of graphene nanosheet/polymer composites using *in situ* reduction–extractive dispersion. *Carbon* 2009;47:2296–9.
- [230] Hummers WS, Offeman RE. Preparation of graphitic oxide. *J Am Chem Soc* 1958;80:1339.
- [231] Eigler S, Hirsch A. Chemistry with graphene and graphene oxide—challenges for synthetic chemists. *Angew Chem Int Ed* 2014;53:7720–38.
- [232] Gómez-Navarro C, Weitz RT, Bittner AM, Scolari M, Mews A, Burghard M, et al. Electronic transport properties of individual chemically reduced graphene oxide sheets. *Nano Lett* 2007;7:3499–503.
- [233] Park S, Ruoff RS. Chemical methods for the production of graphenes. *Nat Nanotechnol* 2010;5:309.

- [234] Li D, Müller MB, Gilje S, Kaner RB, Wallace GG. Processable aqueous dispersions of graphene nanosheets. *Nat Nanotechnol* 2008;3:101–5.
- [235] Park S, An J, Piner RD, Jung I, Yang D, Velamakanni A, et al. Aqueous suspension and characterization of chemically modified graphene sheets. *Chem Mater* 2008;20:6592–4.
- [236] Stankovich S, Piner RD, Chen X, Wu N, Nguyen ST, Ruoff RS. Stable aqueous dispersions of graphitic nanoplatelets via the reduction of exfoliated graphite oxide in the presence of poly(sodium 4-styrenesulfonate). *J Mater Chem* 2006;16:155–8.
- [237] Hao R, Qian W, Zhang L, Hou Y. Aqueous dispersions of TCNQ-anion-stabilized graphene sheets. *Chem Commun* 2008:6576–8.
- [238] Xu Y, Bai H, Lu G, Li C, Shi G. Flexible graphene films via the filtration of water-soluble noncovalent functionalized graphene sheets. *J Am Chem Soc* 2008;130:5856–7.
- [239] Bai H, Xu Y, Zhao L, Li C, Shi G. Non-covalent functionalization of graphene sheets by sulfonated polyaniline. *Chem Commun* 2009:1667.
- [240] Niyogi S, Bekyarova E, Itkis ME, McWilliams JL, Hamon MA, Haddon RC. Solution properties of graphite and graphene. *J Am Chem Soc* 2006;128:7720–1.
- [241] Salavagione HJ, Gómez MA, Martínez G. Polymeric modification of graphene through esterification of graphite oxide and poly(vinyl alcohol). *Macromolecules* 2009;42:6331–4.
- [242] Liu Z-B, Xu Y-F, Zhang X-Y, Zhang X-L, Chen Y-S, Tian J-G. Porphyrin and fullerene covalently functionalized graphene hybrid materials with large nonlinear optical properties. *J Phys Chem B* 2009;113:9681–6.
- [243] Xu Y, Liu Z, Zhang X, Wang Y, Tian J, Huang Y, et al. A graphene hybrid material covalently functionalized with porphyrin: synthesis and optical limiting property. *Adv Mater* 2009;21:1275–9.
- [244] Shan C, Yang H, Han D, Zhang Q, Ivaska A, Niu L. Water-soluble graphene covalently functionalized by biocompatible poly-L-lysine. *Langmuir* 2009;25:12030–3.
- [245] Stankovich S, Piner RD, Nguyen ST, Ruoff RS. Synthesis and exfoliation of isocyanate-treated graphene oxide nanoplatelets. *Carbon* 2006;44:3342–7.
- [246] Zhang D-D, Zu S-Z, Han B-H. Inorganic–organic hybrid porous materials based on graphite oxide sheets. *Carbon* 2009;47:2993–3000.
- [247] Bekyarova E, Itkis ME, Ramesh P, Berger C, Sprinkle M, de Heer WA, et al. Chemical modification of epitaxial graphene: spontaneous grafting of aryl groups. *J Am Chem Soc* 2009;131:1336–7.
- [248] Worsley KA, Ramesh P, Mandal SK, Niyogi S, Itkis ME, Haddon RC. Soluble graphene derived from graphite fluoride. *Chem Phys Lett* 2007;445:51–6.
- [249] Liu H, Ryu S, Chen Z, Steigerwald ML, Nuckolls C, Brus LE. Photochemical reactivity of graphene. *J Am Chem Soc* 2009;131:17099–101.
- [250] Liu Z, Robinson JT, Sun X, Dai H. PEGylated nanographene oxide for delivery of water-insoluble cancer drugs. *J Am Chem Soc* 2008;130:10876–7.
- [251] Yang X, Zhang X, Liu Z, Ma Y, Huang Y, Chen Y. High-efficiency loading and controlled release of doxorubicin hydrochloride on graphene oxide. *J Phys Chem C* 2008;112:17554–8.
- [252] Liu J, Yang W, Tao L, Li D, Boyer C, Davis TP. Thermosensitive graphene nanocomposites formed using pyrene-terminal polymers made by RAFT polymerization. *J Polym Sci Part Polym Chem* 2010;48:425–33.

- [253] Hu H, Wang X, Wang J, Wan L, Liu F, Zheng H, et al. Preparation and properties of graphene nanosheets–polystyrene nanocomposites via *in situ* emulsion polymerization. *Chem Phys Lett* 2010;484:247–53.
- [254] Yu Y-H, Lin Y-Y, Lin C-H, Chan C-C, Huang Y-C. High-performance polystyrene/graphene-based nanocomposites with excellent anti-corrosion properties. *Polym Chem* 2014;5:535–50.
- [255] Kim H, Kobayashi S, AbdurRahim MA, Zhang MJ, Khusainova A, Hillmyer MA, et al. Graphene/polyethylene nanocomposites: effect of polyethylene functionalization and blending methods. *Polymer* 2011;52:1837–46.
- [256] Bhattacharyya A. Graphene reinforced ultra high molecular weight polyethylene with improved tensile strength and creep resistance properties. *Express Polym Lett* 2013;8:74–84.
- [257] Galpaya D, Wang M, George G, Motta N, Waclawik E, Yan C. Preparation of graphene oxide/epoxy nanocomposites with significantly improved mechanical properties. *J Appl Phys* 2014;116:053518.
- [258] Liang J, Wang Y, Huang Y, Ma Y, Liu Z, Cai J, et al. Electromagnetic interference shielding of graphene/epoxy composites. *Carbon* 2009;47:922–5.
- [259] Pham VH, Dang TT, Hur SH, Kim EJ, Chung JS. Highly conductive poly(methyl methacrylate) (PMMA)-reduced graphene oxide composite prepared by self-assembly of PMMA latex and graphene oxide through electrostatic interaction. *ACS Appl Mater Interfaces* 2012;4:2630–6.
- [260] Ye L, Meng X-Y, Ji X, Li Z-M, Tang J-H. Synthesis and characterization of expandable graphite–poly(methyl methacrylate) composite particles and their application to flame retardation of rigid polyurethane foams. *Polym Degrad Stab* 2009;94:971–9.
- [261] Zhang M, Yuan W, Yao B, Li C, Shi G. Solution-processed PEDOT: PSS/Graphene composites as the electrocatalyst for oxygen reduction reaction. *ACS Appl Mater Interfaces* 2014;6:3587–93.
- [262] Luong ND, Hippi U, Korhonen JT, Soininen AJ, Ruokolainen J, Johansson L-S, et al. Enhanced mechanical and electrical properties of polyimide film by graphene sheets via *in situ* polymerization. *Polymer* 2011;52:5237–42.
- [263] Zhao C, Xing L, Xiang J, Cui L, Jiao J, Sai H, et al. Formation of uniform reduced graphene oxide films on modified PET substrates using drop-casting method. *Particuology* 2014;17:66–73.
- [264] Mittal G, Dhand V, Rhee KY, Park S-J, Lee WR. A review on carbon nanotubes and graphene as fillers in reinforced polymer nanocomposites. *J Ind Eng Chem* 2015;21:11–25.
- [265] Potts JR, Dreyer DR, Bielawski CW, Ruoff RS. Graphene-based polymer nanocomposites. *Polymer* 2011;52:5–25.

# Thermodynamics, phase segregation, polymer morphology, and interface/interphases in polymer nanocomposites

**Mary Mutz**

*University of Tennessee, Knoxville, TN, United States*

## 3.1 INTRODUCTION

The production of stronger, lightweight, and more cost-effective products is a particular area of interest for polymer science and is a predominant driving force for nanotechnology research [1–4]. Blends of polymers and nanoparticles offer a range of materials with tailored properties, and the resulting properties of the composite are a combination of both the nanoparticles and polymer matrix. Single-walled carbon nanotubes (SWCNTs), for instance, incorporated into a polymer matrix have been shown to improve the mechanical, electrical, and thermal properties of the material while maintaining the flexibility and light weight inherent to the plastic [1–6]. The wide commercial availability of plastics and nanoparticles makes it highly desirable to develop nanocomposite materials with reinforced properties for tailored end uses [6].

An important attribute of nanosized fillers is their exceptionally high surface to volume ratio, which provides a high amount of surface area for interaction with polymer chains [5–9]. With traditional fillers, there is less surface area per unit volume for interactions, and a significant amount of filler is required to improve the mechanical properties of the polymer [7]. The ratio of interfacial area per particle volume for nanosized fillers is up to four orders of magnitude more than that of conventional filler materials such as glass fiber [8–10]. The increased surface area allows more interactions between nanoparticle and polymer, reinforcing the mechanical properties of polymer materials with low loadings, affecting glass transition temperature, degree of thermoset cure, tensile strength, polymer chain mobility, and conformation [9,10]. For example, in nylon-6 filled with 5 wt% 50-nm silica nanoparticles, improvements of tensile

strength by 15%, strain to failure by 150%, Young's modulus by 23%, and impact strength of 78% can be attained [11]. Similarly, the Toyota Motor Company incorporated 4.2 wt% nanoclay into nylon-6 and doubled both the elastic modulus and tensile strength, allowing the material to be used under the hood of a car [4]. The small amount of nanoparticles necessary to achieve desirable properties is also environmentally friendly with less waste and material consumption. As an example, in order to improve the electrical conductivity using traditional fillers, 15 wt% Cu-powder or 35 wt% Al-powder must be added to epoxy; in contrast, based on predicted percolation limits of SWCNTs, only 0.1–0.2 wt% loadings should be required [12]. Due to the minimal filler loadings, the final product is also much more lightweight than traditionally filled composites [12].

In recent years, carbon and boron containing nanoparticles, such as SWCNTs and boron nitride nanotubes (BNNTs), have garnered attention since these particles have unique properties, including electrical conductivity and neutron capture, which can be imparted to the final product [12–17]. These particles have also been shown to improve the mechanical properties of polymeric materials by as much as 10% with very low loadings, <1.0 wt% [13,16]. Machado et al. blended 0.75 wt% SWCNTs into isotactic polypropylene and observed the modulus increase from 0.85 GPa to 1.19 GPa [17]. The strength of the material also increased 5 MPa. Similarly, with the addition of only 1 wt% BNNTs to poly methyl methacrylate (PMMA), a 19% increase in elastic modulus is observed [14]. A dramatic increase in thermal conductivity was also observed for PMMA composites containing 10 wt% BNNT, with a nearly threefold increase [14]. Potential applications include solar panels and lightweight materials with improved mechanical strength for military equipment. The ability of boron to shield neutrons is also of interest for nuclear and medicinal applications [14,15,18,19]. Ultra lightweight and reinforced bikes have already been developed using carbon nanotubes (CNTs) as nanofillers and are currently available in the marketplace [20]. In fact, the 2006 Tour de France was won riding a bike with a frame that weighed only 2.2 pounds, because it was fabricated from a composite reinforced with CNTs [20].

It is important to realize, however, that poorly dispersed nanoparticles may actually degrade the properties of the nanocomposite. For example, polystyrene (PS) nanocomposites prepared with the incorporation of BNNTs showed a decrease in elastic modulus when chloroform was used as the dispersant because chloroform was a poor solvent for the system [18]. Improvements in elastic modulus were achieved when dimethylformamide (DMF) was used instead, since the solvent was better able to disperse the nanotubes [18]. In another system with PMMA containing <0.5 wt% multiwalled CNTs (MWCNTs), only modest improvements in elastic modulus and tensile strength were observed [21]. The lack of improvement was attributed to poor adhesion between the PMMA and MWCNTs and the formation of MWCNT bundles. Such examples are numerous, exemplifying the fact that improving dispersion greatly affects product availability [21].

In the past, several methods were developed to improve the interactions between the polymer matrix and nanoparticles. These efforts include coating CNTs and fullerenes with a dispersant or grafting polymers to the sidewalls through chemical functionalization to improve dispersions [10,22–26]. Taking advantage of  $\pi$ – $\pi$  interactions between polymer chains and nanoparticles has also been attempted. For example, poly(vinyl pyrrolidone), poly(styrene sulfonate) and their derivatives have been shown to wrap SWCNTs, rendering the tubes soluble in organic solvents [27–30]. Success in dispersing nanoparticles has been obtained with these techniques; yet, several drawbacks to these methods exist. Processing is time consuming, expensive to realize on an industrial scale, and the added materials are difficult to remove once the nanoparticles are embedded inside the polymer matrix. Also, the introduction of a third component and the modification of sidewalls affect the properties of the pristine nanoparticles, such as their electrical and thermal conductive properties and should be avoided [22].

A few key issues remain, therefore, to rationally design and expand the technological applications of new nanocomposite materials. The thermodynamic behavior of nanoparticles and polymers in solution is not well understood, and optimizing processing protocols requires an understanding of this solubility behavior [4,5,14]. If the particles are not finely dispersed during processing, aggregates of the nanoparticles will form in the composites and adequate stress transfer will not be realized in the final product. Similarly, the percolation threshold of the composite will increase, limiting the improvement of electrical conductivity, since well dispersed particles are necessary in order to create three-dimensional networks that provide conductive pathways throughout the composite [4,5,14]. Also, the effect of the presence of nanoparticles on polymer chains in the melt state, which results in phase segregation and the formation of interphases is not well understood. With an improved knowledge base, nanocomposites can be fabricated to realize targeted properties that are required for specific end uses. This chapter attempts to summarize research focusing on the analysis of polymer interfaces and phase segregation and to summarize advances for nanocomposite behavior in solution.

---

## 3.2 THERMODYNAMIC SOLUTION BEHAVIOR OF NANOPARTICLE SYSTEMS

Common methods to fabricate polymer nanocomposites include spin casting or solution casting. These techniques involve mixing nanoparticles with a polymer in solution, the solvents then evaporate or the nanocomposite is precipitated out of solution using a nonsolvent [32]. In order to take advantage of both the polymer and nanoparticles unique characteristics and material properties, the system must be homogenous and well dispersed. However, nanoparticles have proven difficult to disperse in solvents, due to their strong intermolecular forces and a

strong tendency of the particles to agglomerate. SWCNTs, for example, clump together in solution due to strong Van der Waals forces. These forces must be overcome in order to thermodynamically dissolve the particles. Use of suitable solvents can dramatically improve the dispersions of the nanoparticle during processing and lead to improved dispersion and interaction in the resultant nanocomposite, which in turn provides targeted mechanical properties in the final composite material, such as increased tensile strength and elastic modulus [18]. However, there is a lack of a clearly defined protocol that quantifies the solubility behavior of nanoparticles in solutions and in polymers. Such a protocol, which defines the thermodynamic solution behavior, will enable the definition of a range of solvents that are able to disperse both nanoparticles and polymers during processing. This is especially important for boron-containing nanoparticles, such as BNNTs, and carboranes, since there is currently little information available regarding the solubility parameters of these materials. Carboranes, for instance, have potential medicinal applications as cancer treatment devices, and knowledge of the Hildebrand solubility parameter,  $\delta$ , will aid in the selection of nontoxic solvents and polymer matrices capable of producing fine dispersions of the particles for nanocomposites used *in vivo* [1–6,18,19,31–49].  $\delta$  is defined and tabulated for many solvents and polymers and this information is easily obtained in any polymer handbook. With  $\delta$  defined for nanoparticles as well, tailored nanocomposite systems may be designed.

For this discussion, an understanding of the thermodynamic solution behavior is necessary. The miscibility of two components is controlled by the free energy of mixing, which is quantified in Eqn (3.1) below, where  $\Delta H_m$  is the enthalpy of mixing,  $\Delta S_m$  is the entropy of mixing, and  $T$  is the temperature in Kelvin [36]. The interactions between components of a mixture are quantified with  $\Delta H_m$ , while the entropy change resulting from the change in disorder upon mixing is  $\Delta S$ . It is important to note that a negative free energy of mixing ( $\Delta G_m < 0$ ) results in mixing of the two components, and the discussion that follows is relevant for both the dissolution of nanoparticles in a polymer matrix itself or in a solvent, since the underlying physics is governed by this same equation:

$$\Delta G_m = \Delta H_m - T\Delta S_m \quad (3.1)$$

During the mixing process, a combination of entropy and enthalpy determines the structure of the final mixture and the dispersion of the solute in solution [36]. For the discussion of polymer chains that are long and disordered, the addition of nanoparticles does not produce a significant increase in  $\Delta S_m$ , and fine tuning the intermolecular interactions in the mixing process becomes the important factor in order to produce a negative free energy of mixing.

Chemical functionalization and chain wrapping are two methods used in the past to render nanoparticles more thermodynamically miscible in both polymers and solutions. As previously discussed, problems arise with these methods because the introduction of a third component and the modification of the side-walls effects the properties of the nanoparticles [22]. Therefore, identifying

solvents that interact favorably with nanoparticles is highly desirable, since attractive intermolecular interactions between solvent molecules and the solute creates a favorable enthalpic interaction and potentially leads to a negative free energy of mixing. Some success, for instance, has been achieved with aromatic and pyrrolidone solvents that appear to interact via  $\pi-\pi$  interactions with the sidewalls of SWCNTs and fullerenes to disperse the particles [32,33].

In order to identify and expand the range of solvents capable of dispersing both carbon based and boron-containing nanoparticles, the Flory Huggins Solution Theory can be used to define the solubility behavior. With this theory, the enthalpy of mixing is calculated by accounting for the interaction energies between neighboring molecules or polymer segments in a statistical approach that also relates the enthalpy and entropy of mixing to the free energy of mixing and molecular properties (i.e., interaction between the molecules) [36]. This is accomplished with Eqn (3.2), where  $\phi$  is the volume fraction of the solute,  $M$  is the molecular weight, and  $\chi$  is the solute-solvent interaction parameter that describes the enthalpic interaction between the components [36].

$$\underbrace{(\Delta G_{\text{mix}}/RT) = (\phi_A/M_A)\ln \phi_A}_{\text{Entropic}} + \underbrace{(\phi_B/M_B)\ln \phi_B}_{\text{Enthalpic}} + \chi_{AB}\phi_A\phi_B \quad (3.2)$$

Immiscible systems tend to have a  $\chi > 0.5$  that results from a positive  $\Delta H_m$ , which contributes to  $\Delta G > 0$  [36,49]. This is often due to repulsive interactions between components in the mixture that are significantly larger than the change in entropy for the system. Therefore, in order for miscibility to be achieved,  $\chi$  must be either small or negative [36,49].

In order to define  $\chi$ , static light scattering is one approach often carried out to determine the thermodynamics of a solution. The second virial coefficient,  $A_2$ , is readily obtained from light scattering, which is directly related to  $\chi$  in Eqn (3.3), where,  $V_s$  is the solvent molar volume and  $\rho$  is the density of the solute [36,49].

$$\chi = 1/2 - A_2 V_s \rho^2 \quad (3.3)$$

Finally, the interaction parameter of the nanoparticle with a range of solvents provides a route to determine the Hildebrand solubility parameter,  $\delta$ , of the nanoparticle.  $\delta$  provides a numerical estimate of the degree of interaction between materials and is a good indicator of solubility, since materials with similar values of  $\delta$  are likely to be miscible [37]. Many solvents have tabulated  $\delta$  values and a range of good solvents for a particle can be predicted based on this value, since “like dissolves like.” Equation (3.4) from Flory Huggins Solution Theory illustrates this concept, where  $\Delta H_m$  is the enthalpy of mixing,  $V$  is the solvent molar volume,  $\delta$  is the solubility parameter, and  $\phi$  is the volume fraction of components A and B [37]. In order for  $\Delta G_m < 0$ , the difference in the solubility parameters of the solute and solvent must be small, and therefore dissolution will occur.

$$\Delta H_m/V = (\delta_A - \delta_B)^2 \phi_A \phi_B \quad (3.4)$$

This relationship can be expanded in order to produce an equation for a straight line, which is useful for determining an unknown value of  $\delta$  for nanoparticles when performing laboratory experiments. Since  $\chi$  is also related to the difference in solubility parameters of the solvent and solute, another formula can be written (Eqn (3.5)), where  $V$  is solvent molar volume,  $\delta_A$  is the solubility parameter of component A, and  $\delta_B$  is the solubility parameter of component B.

$$\chi = V[(\delta_A - \delta_B)^2/RT] \quad (3.5)$$

This above relationship was actually taken from a combination of the Flory theory with the Hildebrand–Scatchard solution theory. Rearranging, the expression becomes Eqn (3.6): where  $\delta_A$  is the Hildebrand solubility parameter of the solvent, and  $\delta_B$  represents the Hildebrand solubility parameter of the nanoparticle or polymer under study [13,27–30]:

$$(\delta_A^2/RT - \chi/V_A) = (2\delta_B/RT)\delta_A - (\delta_B^2/RT) \quad (3.6)$$

This equation may be used when measuring  $\chi$  in multiple solvents with static light scattering. A plot of  $\delta_A^2/RT - \chi/V_A$  as a function of  $\delta_A$  produces a straight line, with the slope of the line =  $2\delta_B/RT$ , from which the unknown solubility parameter,  $\delta_B$ , can be determined [27–30].

It is important to keep in mind that predicting solvents based on  $\delta$  is made with the absence of specific interactions, especially H-bonding [37]. Additionally, effects of morphology, volume changes upon mixing, and cross-linking are not considered in this approach. Nonetheless, the solubility of small molecules and polymers is often successfully predicted with this relationship. For large particles, such as SWCNTs,  $\delta$  is not always an accurate predictor, since additional intermolecular forces are often at play, and it is challenging to determine the solubility behavior of these larger nanoparticles [38,39].

Besides light scattering, UV-Vis spectroscopy has been the method of choice for quantifying the thermodynamic behavior of solutions since it is a more straightforward method with little sample preparation time [31,40–42]. With this approach, the solubility limits of a solute are first established in a series of solvents, and a graph of solubility limit as a function of the solvent's  $\delta$  is plotted. The Hildebrand solubility parameter of the nanoparticle is then obtained from the maxima of the resulting graph where the solubility limit has the highest value [42–46]. CNTs, graphene, and polyherdraloligomeric silsesquioxanes (POSS) have all been studied in this manner using this technique [42–46]. Similarly, high pressure liquid chromatography (HPLC) may also be used to determine the concentrations of centrifuged samples with the establishment of a baseline in much the same manner [33,47]. For example, in a study by Hernandez et al., the dispersibility of graphene was measured in 40 solvents using UV-Vis spectroscopy [47]. Cyclopentanone, 1,3-dimethyl-2-imidazolidone, and *N*-ethyl-2-pyrrolidone showed the best dispersions, with 8.5, 5.2, and 4.0  $\mu\text{g mL}^{-1}$  solubilities, respectively. The solubility limits are graphed as a function of the solvent's  $\delta$ , showing that good solvents for graphene have  $\delta \sim 23 \text{ MPa}^{1/2}$ . Cyclopentanone, which had the highest solubility limit has a  $\delta$  in good agreement, 21.3  $\text{MPa}^{1/2}$ .

Acetylpyrrolidone, butyl alcohol, and cyclohexanol were suggested as good solvents based on this work. A similar study by Rouff et al. used HPLC to study graphene in 47 different solvents, where a  $\delta$  of  $\sim 20.45 \text{ MPa}^{1/2}$  was determined for graphene, which corresponds well to the findings from Hernandez's study [47]. Both UV-Vis spectroscopy and HPLC offer straightforward approaches for assessing solubility, but in recent years light scattering has proven important since additional information may be obtained from the measurements, leading to a more in-depth understanding of the interactions of solvents and nanoparticles in solution.

### 3.2.1 STATIC LIGHT SCATTERING

It is necessary to examine static light scattering more carefully. This technique is considered to be an important route for determining the thermodynamic solution behavior of polymers and nanoparticles, since  $\chi$  can be more directly determined with the measurements; moreover, information about the nanocomposite systems can also be obtained including the shape and size of particles in solution.

With static light scattering, the intensity of scattered light is measured at a variety of scattering angles, which can be analyzed to determine the average molecular weight ( $M_w$ ) of a scattering polymer chain [36,49,50]. This technique is used in polymer chemistry to determine the  $M_w$  of polymers or proteins. The root mean square radius of gyration ( $R_g$ ) of the scattering particle can also be determined [36,49,50], while measuring the scattering intensity for various concentrations, the second virial coefficient  $A_2$ , is obtained.

Light scattering is a powerful tool that is used to characterize a range of particle sizes. For example, Cabannes verified Avogadro's number by measuring the light intensity scattered by argon gas, and the molecular weight of large complex sugar molecules was determined by Debye et al. using light scattering [33]. It is also possible to quantify the ability of a solvent to finely disperse solutes. If the  $M_w$  or radius of a particle is known, for instance, then the  $M_w$  and  $R_g$  obtained from light scattering will quantify the aggregation behavior of the particles in solution [43].

### 3.2.2 STATIC LIGHT SCATTERING: THEORY

Light scattering is caused by fluctuations in the refractive index of a medium. Debye is credited with relating the fluctuations of the refractive index in liquids with the molecular weights of solutes, including polymers. Mathematical relationships were established, where the fluctuation of refractive index is ascribed to the presence of the polymer molecules themselves. The Eqn (3.7) below describes this relationship, which relates the osmotic pressure of a polymer solution to the light scattering intensity, where  $\Pi$  is the osmotic pressure,  $c$  is the concentration,  $R_0$  is the Rayleigh ratio, and  $H$  is the optical constant [36,49,50].

$$Hc/R_0 = 1/RT(\delta\Pi/\delta c) \text{ at constant temperature} \quad (3.7)$$

H is determined experimentally, and is a constant for a particular polymer-solvent system. This constant depends on the refractive index increment of the solution and the wavelength of the laser [36,49,50].  $R_0$  is defined with Eqn (3.8), where  $I_0$  is the scattered light intensity,  $\theta$  is the angle,  $V_s$  is the scattered volume,  $w$  is the distance from the source to the detector, and  $I_0$  is the intensity of the incident light. H is defined with Eqn (3.9), where  $n$  is the refractive index at wavelength  $\lambda$  and  $dn/dc$  is the refractive index increment.

$$R_0 = I_0 w^2 / I_0 V_s \quad (3.8)$$

$$H = 2\Pi^2 n^2 (dn/dc)^2 / N_A \lambda^4 \quad (3.9)$$

Equation (3.10) relates the scattered light intensity to the solution and solute characteristics [36,49,50]. This is a key relationship for light scattering, and the equation produces a straight line which is helpful for interpreting experimental results. Several derivations of this equation exists which may be used to graph Zimm plots, which will be detailed further.

$$Hc/R_0 - R_{\text{solvent}} = 1/M_w P_0 + 2A_2 c \quad (3.10)$$

In this equation,  $c$  is solution concentration and  $A_2$  is the second virial coefficient.  $A_2$  is a thermodynamic property that quantifies the interaction strength between the solute and solvent. When  $A_2 > 0$  the interactions between the solute and solvent are favorable and the system is soluble. In contrast, when  $A_2 < 0$  aggregation or precipitation occurs.

Information regarding the shape of particles is also determined from Eqn (3.10), where  $P_0$  is the particle form factor, which is dependent on scattering angle. Therefore, the angular variation in the scattering intensity provides a measure of the size of the structures under investigation [36,49,50].

For this discussion, it is important to define the term “radius of gyration,”  $R_g$ .  $R_g$  is the mean square average distance of the segments that make up the scattering particle from the center of gravity, where  $N$  is the number of scattering segments and  $r_i$  is the distance of segment  $i$  from the particles center of gravity in Eqn (3.11) [36,49,50].

$$R_g = (1/N) \sum_{i=1}^N r_i^2 \quad (3.11)$$

For a random polymer coil,  $R_g$  is related to the end-to-end distance,  $r$ , of a polymer chain by.

$$R_g^2 = r^2 / 6 \quad (3.12)$$

An analytical expression of  $P_0$  for a polymer chain is given in Eqns (3.13 and 3.14), where  $r$  is the end-to-end distance of a polymer chain and  $ks = (4 \Pi/\lambda) \sin(\theta/2)$  [36].

$$P_0 = 2/x^2 [e^{-x} - (1-x)] \quad (3.13)$$

$$x = [(ks)^2 r^2] / 6 \quad (3.14)$$

For a polymer coil, the above equations can be combined to yield:

$$P_{\theta} = 2/R_g^4/ks^4 \{R_g^2 ks^2 - [1 - \exp(-R_g^2 ks^2)]\} \quad (3.15)$$

Analytical functions have also been derived for the form factor of rods and spheres [36,49,50], as given by Eqns (3.16 and 3.17), where  $D$  is the diameter of a sphere and  $L$  is the length of a rod.

$$\text{Sphere } P_{\theta} = [3/x^3(\sin x - x \cos x)]^2 x = ksD/2 \quad (3.16)$$

$$\text{Rod } P_{\theta} = 1/x \int_0^{2x} (\sin w/w) dw - (\sin x/x)^2 x = ksL/2 \quad (3.17)$$

For a typical light scattering experiment, several concentrations and several scattering angles are measured, and the resulting data is plotted using two key equations in order to produce a Zimm plot, Eqns (3.18 and 3.19). Using these equations the subsequent straight lines are extrapolated to zero scattering angle and zero concentration, [36].

$$(Hc/R_{\theta})_{\theta=0} = 1/M_w + 2A_2c + \dots \quad (3.18)$$

$$(Hc/R_{\theta})_{c=0} = 1/M_w [1 + 1/3(4\pi/\lambda)^2 R_g^2 \sin^2 \theta/2 + \dots] \quad (3.19)$$

With this information,  $M_w$ ,  $R_g$ , and  $A_2$ , are thus determined from the  $y$ -intercept and slopes of the lines of the resulting Zimm plot following data collection with static light scattering.

Complexities arise for large or very small particles that make it difficult to quantify their size, but the Zimm plot remains a valuable tool for quantifying the behavior of particle-solvent systems. It is important to note, as the scattering angle approaches zero,  $P_{\theta}$  becomes independent of particle shape, and the calculation of the second virial coefficient, which quantifies the solute-solvent interaction, is also independent of  $P_{\theta}$ .

Additionally, the  $R_g$  obtained from a Zimm plot offers a means of qualitatively discussing the size and shape of the particles and their agglomeration behavior in solution, if prior knowledge regarding the  $M_w$  and shape of an individual particle is already established. It is important to keep in mind for subsequent discussions, however, that anisotropic and large particles have additional complex scattering that affects the precise value of the measured  $M_w$  [33,51,52].

Prior to a light scattering experiment, calibration is performed using a strong, known scatterer [33,34,36,49–53]. Typically toluene is used for calibration, since its Rayleigh Ratio is well established. Calibration determines the laser intensity, quantum efficiency of the detectors, and the full scattering volume and solid angles of the detectors. Additionally, if more than one angle is collected, it is important that all of the angles respond in the same way. Detectors will often have slightly different gains and detect different geometrical scattering volumes. Normalization is necessary to correct this. Measurement of pure solvent is established first, followed by the addition of an isotropic scatterer, typically a dilute

concentration of low  $M_w$  PS with a known Rayleigh ratio. The detector gain is then normalized by establishing the value of the gain detected at the  $90^\circ$  angle detector and correcting for differences in gain at the other angles.

### 3.2.3 LITERATURE REVIEW: THERMODYNAMIC SOLUTION BEHAVIOR OF NANOPARTICLE SYSTEMS AS DEFINED WITH STATIC LIGHT SCATTERING AND REFRACTOMETRY

Key research in this area was carried out by Bergin et al. who attempted to use static light scattering to quantify the solubility of CNTs [33,34]. Difficulties arise when using this approach to define the solubility of nanoparticles, since the refractive index increment,  $dn/dc$ , is often not known for nanoparticle solutions.  $dn/dc$  is a necessary parameter for static light scattering measurements, since the optical constant,  $H$ , is the ratio of refractive index increment to the wavelength of light [33,34]. The basic light scattering Eqn (3.20) that relates the scattered light intensity to the solution characteristics is presented below, where  $R$  is the Rayleigh ratio, and is dependent on the intensity of scattered light,  $P_\theta$  is the form factor of the scattering particle,  $M_w$  is the molecular weight of the scattering particle,  $c$  is solution concentration, and  $H$  is the optical constant [33,34].

$$Hc/R_\theta - R_{\text{solvent}} = 1/M_w P_\theta + 2A_2c \quad (3.20)$$

$dn/dc$  is often difficult to obtain since nanoparticles do not easily dissolve in common solvents, and most modern instrumentation requires the injection of the sample with constant solvent flow through. SWCNTs, for instance, clog the tubing due to their aggregation behavior, making measurements impossible.

Bergin et al. attempted to circumvent this issue by testing several polymer solvent systems with known  $M_w$  and  $A_2$  in order to estimate the instrument constants for their scattering setup [33,34]. In their experimental procedure, the instrument constant,  $H$ , is determined by rearranging Eqn (1.20). In the rearranged equation, Eqn (3.21),  $C$  is the concentration of the solute,  $S$  and  $S_0$  are the scattering intensities of the solution and pure solvent measured at  $90^\circ$ , and  $H'$  and  $H''$  are new instrument constants [33,34].

$$C/S - S_0 = (A_2/H')C + (1/M_w H'') \quad (3.21)$$

In this procedure, the scattering from multiple polymer solutions is measured and a graph of  $C/S - S_0$  is plotted as a function of concentration. The instrument constants are then estimated from the slope and intercept of the resultant lines [33,34]. The solubility behavior of SWCNTs in pyrrolidone solvents was studied using these optical constants by measuring the scattering at  $90^\circ$  and using Eqn (3.21) to calculate  $A_2$ . For SWCNTs in *N*-methyl pyrrolidone (NMP), a positive second virial coefficient was found,  $1.78 \text{ E}10^{-3} \text{ m}^3 \cdot \text{mol} \cdot \text{kg}^{-1}$ , and  $\chi$  was  $-0.074$ , which indicates that NMP is a thermodynamically favorable solvent. The authors also estimated the enthalpy of mixing,  $\Delta H_{\text{mix}}$ , from their estimated  $\chi$

values using Eqn (3.22) [33,34] where  $V_{\text{mix}}$  is the volume of mixing,  $R$  is the ideal gas constant,  $T$  is temperature, and  $\phi$  is the volume fraction of the nanoparticles.

$$\Delta H_{\text{mix}}/V_{\text{mix}} = \chi(RT/V_s) \phi(1 - \phi) \quad (3.22)$$

The estimated enthalpy of mixing is  $-720 \text{ KJ mol}^{-1}$  and was presented as further evidence of an energetically favorable mixing process. This approach was promising, since many nanoparticles, such as boron-containing particles, also have unknown  $dn/dc$  and have a tendency to clump in solution.

Researchers at the University of Tennessee took this one step further, however and determined the refractive index increment ( $dn/dc$ ) of nanoparticle solutions and the density of the nanoparticles [54,55]. In the past, these measurements were not possible to obtain because nanoparticles in solution tend to clog the instrument tubing on modern flow through refractometers. In order to solve this issue, an older-model Brice Phoenix refractometer, which does not require solvent flow-through, was used to measure the  $dn/dc$  of a range of nanoparticles in solutions including SWCNTs and boron cage compounds for the first time.

With  $dn/dc$  defined, the calculation of  $\chi$  was more accurate. The density of the nanoparticles is also difficult to obtain and necessary for these measurements. Previous methods for density determination include atomic force microscopy (AFM) or scanning electron microscopy (SEM) on spun-cast solutions to estimate the number of particles and bundle sizes. These methods had questionable accuracy because they employed simple counting methods with higher human errors inherent to the methods. [33,34]. The researchers in this study also used a specialized pycnometer capable of determining the density of fine-grain powders, enabling a more accurate final calculation of the solubility parameters [55].

As a self-consistent check, the researchers from the University of Tennessee also carried out UV-Vis analysis on all of the nanoparticle systems and also photographed the solutions in high resolution to check for visible aggregation. For all of the nanoparticle solutions studied, the scattering data collected was consistent with the UV-Vis solubility limits and physical observations; higher  $\chi$  values corresponded to lower solubility limits as determined from UV-Vis spectroscopy and observed particle settling. Additionally, smaller  $R_g$  values corresponded to better dispersion as determined from the scattering data. Finally, Eqn (1.6) was used to determine a list of possible good solvents for the nanoparticles based on calculated  $\delta$  values. This was a comprehensive study, and most importantly, good agreement was indicated between  $\delta$  and  $\chi$  for all of the systems tested, including SWCNT, graphene, and PS nanoparticle systems.

It is important to include a brief discussion of the importance of the  $R_g$  determined from light scattering.  $R_g$  provides additional information regarding solubility behavior, since this factor may be used to quantify aggregation behavior of particle solutions [56]. For example, in the past researchers used  $R_g$  to decipher the thermodynamic behavior of PS nanocomposites prepared in toluene with 10 wt% polyhedral oligomeric silsesquioxane (POSS), studied with static light

scattering. Octaisobutyl POSS (Oib-POSS) and trisilanophenyl POSS (Tsp-POSS), both with small radii  $< \sim 1$  nm were analyzed with light scattering [27]. The  $R_g$  reported from the light scattering measurements was larger for the Oib-POSS-PS nanocomposite relative to the unmodified PS. The authors interpreted these findings to indicate that aggregation was occurring in this system. In contrast, the  $R_g$  of the Tsp-POSS blend was smaller than the unmodified PS. Supporting additional evidence collected with electron microscopy indicated that Tsp-POSS had greater solubility in PS, and the smaller radius was the result of enhanced interactions of the TSP-POSS molecules with the PS chains [27]. This is but one example of the important information obtained with light scattering when compared with the more straightforward UV-Vis analysis.

Taken all together, research into the thermodynamic solution behavior of nanoparticle systems has evolved from UV-Vis and HPLC studies to include a comprehensive investigation of static light scattering, refractometry, and pycnometry. Several key parameters are defined with these techniques including the Hildebrand solubility parameters and  $R_g$ , which can be used to select suitable solvents for nanoparticle and polymer dissolution. Recent research indicates that all of these techniques show good agreement with one another. UV-Vis measurements correlate well to static light scattering data, as well as optical images captured to qualitatively measure the aggregation behavior in solution. As research progresses in this field, more and more data will become easily obtainable, tabulated, and ready for materials scientists and engineers to develop the next cutting edge nanocomposite material.

---

### 3.3 PHASE SEGREGATION AND INTERPHASES OF POLYMER NANOCOMPOSITES

While an understanding of methods to control the structure of a polymer nanocomposite is important, the impact of a nanoparticle's presence on the dynamics of the surrounding polymer chains is equally important. Once a nanocomposite material is formed, its resulting properties are dependent on the structure and dynamics of the polymer. Additionally, the composition of the resulting structure of the polymer mixture near the air surface often differs from the bulk composition, which has important implications for the product end use and may significantly affect surface sensitive properties such as biocompatibility, friction, lubrication, flammability, and adhesion [57–60].

Previous research has indicated that the size of a nanoparticle affects the segregation and diffusion behavior of polymer chains in the melt, offering a route to manipulate dispersion based on introduced particle size. PS-*b*-ethylene propylene (PS-PEP) diblock copolymers were prepared with 3.5 nm gold nanoparticles and 21.5 silica nanoparticles [8]. Upon annealing, the large silica particles were found embedded at the center of the PEP domains, while the small gold nanoparticles

went to the interface of the PEP-PS. The effect of chain branching and particle shape, such as SWCNT cylinders or boron nitride sheets, on the resulting segregation and diffusion behavior of polymer chains has been investigated but the behavior in more complex systems remain unclear.

This knowledge is relevant for designing materials with controlled dispersions. By understanding the entropic and enthalpic forces that guide the structural development in the melt, products with particles at specified interfaces or dispersed throughout the matrix can be realized. For example, a balance of these forces will maintain a homogenous dispersion of nanoparticles for use as electrically conductive plastics, or embedded porphyrin with lower surface energy than the polymer matrix may segregate to the air interface to kill bacteria and sterilize equipment. Tailored dispersions also have applications as block copolymer nanocomposites for nonlinear optics, sensors, or separation purposes [8,59,60].

### 3.3.1 SEGREGATION AND DIFFUSION OF POLYMER CHAINS

The properties of the final nanocomposite depend on how the presence of the nanoparticles influences the dynamics of the polymer matrix. For surface sensitive properties, the structure of the surface, which often differs from the bulk composition, becomes very important [57]. This knowledge has implications for the development of products as lubricants and antibacterial coatings [57,58].

Surface segregation occurs when polymer films are annealed above their glass transition temperature, and the polymer chains are in the melt state. The thermodynamic affinity of one component to the surfaces and the affinity of the polymer components to each other impact the segregation process and may result in the redistribution of the components near the air and substrate surfaces [60–73].

One aspect of particular importance is the migration of lower-surface energy components in a mixture to the air surface, which lowers the enthalpy and the free energy of the system [74–77]. Blends that contain strongly hydrophobic components, such as fluorinated polymers, will undergo segregation of the hydrophobic components to the air surface [77]. A study by Yang demonstrates this point with miscible blends of PMMA and poly (vinylidene fluoride) (PVDF) showing significant enrichment of PVDF at the air surface upon annealing [78].

When enthalpic interactions are not very strong, however, entropic forces may dominate [74–77]. Polymer chains typically take on a random coil conformation, and the presence of a surface constrains the coils, reducing the number of configurations possible for the polymer chains at the interface. Polymer chain ends will segregate to an interface to relieve this entropically unfavorable situation [78–84]. This finding was observed by Steiner et al. who varied the ethylene content in random ethylene-ethyl ethylene copolymers, and found that the more branched polymers segregated to the air surface [79].

Segregation to the solid substrate in a thin film is also impacted by the interaction energy between the solid substrate and the polymer. This interaction is short-ranged, occurring within only a few Angstroms, and the mobility of the chains is

affected mainly by the connectivity of the molecules and their molecular interactions with one another, rather than the interaction with the solid substrate itself [80,83]. When enthalpy dominates the selective surface segregation in a thin film, the higher surface energy components may be displaced to the solid substrate as lower energy components migrate to the air surface.

### 3.3.2 THE IMPORTANCE OF NEUTRON REFLECTIVITY IN INTERPHASE AND PHASE SEGREGATION STUDIES

Many times it is necessary to use depth-profiling techniques to determine the interfacial morphology or diffusion profiles of polymer samples. Such experimental techniques, which have been used in the past to study diffusion and segregation processes of polymers, include attenuated total reflection infrared spectroscopy, elastic recoil detection, forward recoil spectroscopy, neutron reflectivity, and nuclear reaction analysis. Neutron reflectivity (NR) has several advantages over other depth-profiling techniques, including its nondestructive behavior, increased resolution, and the ability to accurately construct interfacial profiles [78–84]. Radiation damage is negligible to the samples since the neutrons interact with the nuclei of the atoms and not the electrons. Most noteworthy is the high contrast between the neutron scattering lengths of hydrogen and deuterium:  $-0.374 \text{e}^{-12} \text{cm}$  versus  $0.6674 \text{e}^{-12} \text{cm}$  for hydrogen and deuterium, respectively. Due to the small wavelength and the high contrast between deuterium and hydrogen, NR is capable of subnanometer resolution [78–84]. Specific regions and interfaces can also be labeled with deuterium, and buried polymer interfaces can be explored. The accurate modeling of the width of the interface and the interfacial profile of the interdiffusing polymers is thus possible.

In order to take advantage of neutron reflectivity, systems must be carefully designed for the analysis. Deuterated polymers are of particular importance to this discussion, since they possess a lower surface energy than their protonated counterparts, which is the result of a smaller polarizability of the carbon–deuterium (C–D) bond relative to the carbon–hydrogen (C–H) bond and allow for high contrast between deuterated and nondeuterated materials [81]. Many studies of polymer diffusion and segregation behavior take advantage of the lower surface energy of deuterated polymers. These studies often use deuterated PS (dPS) as a tracer in order to follow the chain motion of annealed thin films, realizing that dPS will inevitably segregate to the air surface in a carefully planned experiment. NR is often used to monitor the segregation behavior by modeling scattering length density profiles (SLD profiles) and dPS concentration profiles from the collected reflectivity data [78–87]. The models allow the calculation of the excess dPS at the surface and the width of the interface upon annealing, providing insight into the thermodynamic driving force to selectively segregate dPS to the surface [78–87].

As further evidence, Monte Carlo simulations have also shown that dPS will segregate to the air surface in dPS/protonated PS (pPS) blends, as long as the pPS

chains have greater chain lengths, because a difference in surface energies at the surface of a thin film is the driving force for this segregation [78–87]. Kumar and Russell studied a series of deuterated and protonated polymers, and in all cases, as the molecular weight of the protonated species is lowered, the entropic driving force to sequester the shorter protonated chain dominates the enthalpic contribution, which results in selective segregation of the protonated polymer to the surface [75].

A study by Hong and Boerio, also illustrates this point [81]. Blends of equivalent molecular weight dPS and pPS were prepared, and it was found that the deuterated polymer enriched the surface upon annealing [81]. However, complicating the matter, when the pPS molecular weight was lowered, it was found to enrich the air surface instead. It is important to understand the energetic and entropic effects that contribute to the surface segregation in the system, and when the pPS chains were short in comparison to dPS, entropy is the driving force for the segregation of pPS to the air surface [81]. The authors confirmed this phenomenon by preparing a blend of 70 K pPS and 1950 K dPS, which was annealed at 200 °C for 24 hours. No surface segregation occurred in this blend, signifying that the chain length effect equaled the isotopic effect, and the surface free energy difference between the polymers was zero [81].

These experimental results demonstrate the utility of dPS as a tracer in equivalent molecular weight dPS/pPS blends, and also demonstrate that the morphology of a composite is controlled by manipulating the balance of enthalpic and entropic forces present in the system. In recent years, much research has focused on combining polymers with nanoparticles in order to improve the function and properties of the polymer matrix [82–87]. The addition of nanoparticles to a polymer matrix provides a new challenge for understanding segregation behavior, since additional molecular interactions are introduced into the system and chain motion becomes complex near surfaces and interfaces.

### 3.3.3 LITERATURE REVIEW OF NEUTRON REFLECTIVITY STUDIES

Understanding the enthalpic and entropic forces governing the surface segregation of polymer chains in the presence of nanofillers is relevant for achieving finely-tuned materials for specific applications that do not undergo segregation with applied heat, or have embedded components that segregate to specific interfaces upon annealing.

Studying these types of systems is not straightforward, and much information in the literature shows seemingly conflicting results. Several publications demonstrate the complexity of nanoparticle systems, which are summarized in this chapter. Krishnan et al. studied the surface segregation behavior of the components in two nanocomposite systems: a linear PS matrix that contains crosslinked PS nanoparticles and a system containing cadmium nanoparticles [82]. The PS nanoparticles ranged in size from 41 to 1500 kDa with  $R_g$  from 2.5 to 9.0 nm, while the cadmium particles had a radius of 2.4 nm and MW of 34.3 kDa. This publication

expanded on the work of Barnes et al., who discovered that the introduction of fullerene nanoparticles to polymer thin films inhibited dewetting of PS on native silicon oxide substrates [74]. Neutron reflectivity was used to investigate the depth profiles at different annealing times. The results indicate that the PS nanoparticles segregated to the silicon substrate upon annealing, and that higher molecular weight nanoparticles strongly enhanced the wetting behavior of the polystyrene thin films. The authors interpret this response as the result of an entropic gain by the linear PS chains when they moved from the solid substrate and pushed the nanoparticles down [74]. However, the cadmium particles had an opposite effect, minimizing the dewetting behavior and segregating to the air interface. In this system, the authors attributed this response to an entropically driven surface segregation process. [74].

In contrast, blends of PMMA and a branched random copolymer of PMMA and methoxy poly (ethylene glycol) monomethacrylate were prepared on silicon, annealed above the glass transition temperature, and the depth profiles were investigated using NR [87]. The branched copolymer in this work has a higher surface energy, and was expected to segregate to the silicon substrate upon annealing; instead, however, it segregated to the air surface. The entropic effect of chain branching dominates the surface segregation process in this system, where the chain ends localized at the air surface with annealing, which reduces the overall free energy of the system [85,86].

The reptation model, first proposed by de Gennes and Edwards, may be used to understand these results and how size and shape of introduced polymers and nanoparticles can result in the segregation and formation of interphases. This model describes the diffusion of polymer chains between miscible entangled linear polymers and can also be used to describe the process of interdiffusion [35,36,88–91]. For polymer bilayers annealed above their glass transition temperature, polymer-polymer interdiffusion is predicted to proceed in two stages. The first stage occurs during the period that is less than the time it takes for a polymer to diffuse a distance equal to its  $R_g$ , the reptation time. This stage is dominated by segmental motion. However, at longer annealing times (i.e., those longer than the reptation time), center of mass diffusion prevails, and the polymer chains cross the interface [35,36,88–91]. The addition of nanoparticles affects this reptation behavior, and in some cases, slows the diffusion of the polymer chains across the interface [35,36,88–91]. A significant paper by Mu et al. explains the research findings in conjunction with the Reptation model and diffusion. Mu reports that the diffusion of the dPS chains is slowed with the introduction of SWCNTs when compared to an unmodified bilayer system [92–97]. Fick's second law of diffusion was used to fit the data and calculate diffusion coefficients for each of the bilayers studied. [35,36,88–91].

Interestingly, Mu also reported that a minimum in diffusion coefficient occurred as the SWCNT concentration was increased, and with the addition of a high enough SWCNT concentration, the diffusion coefficient recovered to the pure PS value. Shorter dPS chains resulted in a deeper minimum in diffusion coefficient.

The lowest  $M_w$  dPS studied was  $75,000 \text{ g mol}^{-1}$ , and the minimum in diffusion coefficient occurred at 0.4 vol% SWCNT loading. The diffusion coefficient recovered to the pure PS value with the addition of 4.0 wt% SWCNTs [92,93].

The team modeled this behavior by simulating center-of-mass diffusion of the polymer chain about a three-dimensional cylinder. Anisotropic diffusion occurs near the SWCNT surface, in which PS diffuses more slowly in the direction perpendicular to a SWCNT relative to that which occurs in the parallel direction. The dPS diffusion decreased at low concentrations due to the anisotropy surrounding the SWCNTs, while at higher SWCNT concentrations, the nanotubes form a percolating network, which allows the dPS tracer to diffuse parallel to the tube and recover the pure PS diffusion coefficient [92,93]. The three-dimensional cylinder model used to fit the data and describe the dynamics of dPS in this work suggests that the cylinder shape of the introduced particles affects the diffusion of the surrounding polymer chains, with a minimum in diffusion coefficient observed at low loadings.

Another study by researchers at the University of Tennessee also correlated well with Mutz et al.'s findings [98]. Experimental data indicated that the presence of nanoparticles slowed diffusion of polymer chains in all cases at loadings of  $<0.1 \text{ wt}\%$ , which was similar to the findings of Mu et al. Large nanoparticles, such as graphene and CNTs, slowed this diffusion the most, and segregated to the silicon surface due to higher surface energy. In contrast, soft nanoparticles, made from highly branched polystyrene molecules with many chain ends were entropically driven to the air surface, resulting in a decrease in the free energy of the system.

Since segregation, diffusion, and mixing in thin polymer films are more complex with the introduction of nanoparticles, it is important to understand polymer dynamics for the development of new materials. The interdiffusion and segregation of thin polymer films in the presence of nanoparticles of various sizes and shapes has many practical applications, such as improving dewetting or end uses, such as packaging and barriers. Improving dewetting behavior is important for producing stable polymer films that do not rupture [94]. Work by Sharma et al. for instance, has shown the arrestment of dewetting when the interactions between the polymer matrix and particle filler is strong, as is the case of PS/PMMA bilayers prepared on silicon with introduced Si nanoparticles [94]. The authors conclude that the Si nanoparticles "pin" the polymer chains at the interface, since AFM images show the distribution of the nanoparticles at the boundary. In contrast, carbon black introduced into PS/PMMA thin films increased the rate of dewetting because unfavorable interactions between the polymer and particles led to phase separation and the repulsive interactions further destabilized the thin film [94].

Thin films for uses as barriers are another potential application [95,96]. Nanoparticle fillers are desirable for this purpose, since low loadings lead to the reinforcement of the material while maintaining the optical transparency, which is especially desirable for the beverage-liquor industry to produce clear plastic

bottles to replace conventional glass that are capable of protecting against oxidation, reduce breakage, and decrease the weight of the material (i.e., reduce shipping costs) [97]. The resulting diffusive properties of the material strongly depend on the morphology [99–101]. For instance, nanoparticles segregated at the interface decrease permeability of the plastic, and developing PS and polyolefin bottles that can extend the shelf life of beer for more than six months by preventing its oxidation is an important area of material design [102–104].

Research is ongoing in this area, and clearly, a more complete understanding of the impact of nanoparticle size, shape, and composition on the surface segregation in polymer nanocomposites is needed. This chapter has attempted to summarize the results achieved in the field using neutron reflectivity as the mode of choice for studying interphase and phase behavior.

---

## ACKNOWLEDGMENTS

Some of the research highlighted in this chapter was performed at the University of Tennessee under the advisement of Dr. Mark Dadmun, Dr. Charles Feigerle, Dr. Jimmy Mays, and Dr. Zawodzinski. Research support was provided by the Department of Energy, Office of Basic Sciences and Division of Materials Sciences and Engineering.

---

## REFERENCES

- [1] Binnig G, Rohrer H. Scanning tunneling microscopy. *IBM J Res Dev* 1986;30:4.
- [2] Kroto HW, Heath JR, O'Brien SC, Curl RF, Smalley RE. C60: buckminsterfullerene. *Nature* 1985;318(6042):162–3.
- [3] Qian L, Hinestroza JP. Application of nanotechnology for high performance textiles. *J Text Apparel Technol Manage* 2004;4:1–7.
- [4] Hussain F, Hojjati M, Okamoto M, Gorga RE. Review article: polymer-matrix nanocomposites, processing, manufacturing, and application: an overview. *J Composite Mater* 2006;40:1511–75.
- [5] Tanaka T, Kozako M, Fuse N, Ohki Y. Proposal of a multi-core model for polymer nanocomposite dielectrics. *IEEE Trans Dielectrics Electr Insulation* 2005;12:669–81.
- [6] Lem K, Curran SA, Sund SE, Gabriel MK. *Encyclopedia of chemical processing*. VCH publishers, New York; 2007.
- [7] Garcos JM, Moll DJ, Bicerano J, Fibiger R, McLeod DG. Polymeric nanocomposites for automotive applications. *Adv Mater* 2000;12:1835–9.
- [8] Bockstaller MR, Michiewicz RA, Thomas EL. Block copolymer nanocomposites: perspectives for tailored functional materials. *Adv Mater* 2005;17:1331–50.
- [9] Joly S, Garnaud G, Ollitrault R, Bokobza L. Organically modified layered silicates as reinforcing fillers for natural rubber. *Chem Mater* 2002;14:4202–8.
- [10] Balazas AC, Emrick T, Russell TP. Nanoparticle polymer composites: where two small worlds meet. *Science* 2006;214:1107–10.

- [11] Ou Y, Yang F, Yu Z. A new conception on the toughness of nylon... via *in situ* polymerization. *J Polym Sci Part B* 1998;36:789–95.
- [12] Hilding J, Grulke EA, Zhang ZG, Lockwood F. Dispersion of carbon nanotubes in liquids. *J Dispers Sci Technol* 2003;24:1–41.
- [13] Coleman JN, Khan U, Blau WJ, Gun'ko YK. Small but strong: a review of the mechanical properties of carbon nanotube-polymer composites. *Carbon* 2006;44:1624–52.
- [14] Zhi CY, Bando Y, Tang CC, Huang Q, Golberg D. Boron nitride nanotubes: functionalization and composites. *J Mater Chem* 2008;18:3900–8.
- [15] Golberg D, Bando Y, Tang C, Zhi C. Boron nitride nanotubes. *Adv Mater* 2007;19:2413–32.
- [16] Harris PJ. Carbon nanotube science: synthesis property and application. New York, NY: Cambridge University Press; 2009.
- [17] Machado MAL, Valentini L, Biagiotti J, Kenny JM. Thermal and mechanical properties of single-walled carbon nanotubes–polypropylene composites prepared by melt processing. *Carbon* 2005;43:1499–505.
- [18] Zhi Y, Bando C, Tang S, Honda H, Kerwahara J. Boron nitride nanotubes/polystyrene composites. *J Mater Res* 2006;21:2794–800.
- [19] Parrott MC, Marchington EB, Valliant JF, Adronov A. Synthesis and properties of carborane-functionalized aliphatic polyester dendrimers. *J Am Chem Soc* 2005;127:12081–7.
- [20] Artan R, Tepe A. The initial values method for buckling of nonlocal bars with application in nanotechnology. *Eur J Mech* 2006;3:469–77.
- [21] Gorga RE, Cohen RE. Toughness enhancements in poly (methyl methacrylate) by addition of oriented multiwall carbon nanotubes. *J Polym Sci: Part B* 2004;42:2690–702.
- [22] Furtado CA, Jim UJ, Gutierrez HR, Pan L, Dickey EC, Eklund PC. Debundling and dissolution of single-walled carbon nanotubes in amide solvents. *J Am Chem Soc* 2004;126:6095–105.
- [23] Rasheed A, Dadmun MD, Ivanov I, Britt PF, Geohegan DB. Improving dispersion of single walled carbon nanotubes in a polymer matrix using specific interactions. *Chem Mater* 2006;18:3513–22.
- [24] Zhu J, Kim J, Peng H, Margrave JL, Khabashesku VN, Barrera EV. Improving the dispersion and integration of single-walled carbon nanotubes in epoxy composites through functionalization. *Nano Lett* 2003;3:1107–13.
- [25] Rahmatpour A, Kaffashi B, Maghami S. Preparation and rheological properties of functionalized multiwalled carbon nanotube/waterborne polyurethane nanocomposites. *J Macromol Sci* 2011;50:1834–46.
- [26] Ajayan PM, Schadler LS, Giannaris C, Rubio A. Single-walled carbon nanotube–polymer composites: strength and weakness. *Adv Mater* 2000;12:750–3.
- [27] Misra R, Alidedeoglu AH, Jarett WL, Morgan SE. Molecular miscibility and chain dynamics in POSS/polystyrene blends: control of POSS preferential dispersion states. *Polymer* 2009;50:2906–18.
- [28] O'Connell MJ, Boul PJ, Smalley RE. Reversible water-solubilization of single-walled carbon nanotubes by polymer wrapping. *Chem Phys Lett* 2001;342:265–71.
- [29] Star A, Stoddart JF. Preparation and properties of polymer-wrapped single-walled carbon nanotubes. *Angew Chem Int Ed* 2001;40:1721–5.

- [30] Dalton AB, McCartry B, Coleman JN, Panhuis M, Carroll DL, Byrne HJ. *Mater Res Soc Sym Proc* 2001;675 w.4.5.1
- [31] Rouff RS, Tse DS, Malhotra R, Lorents DC. Solubility of fullerene (C60) in a variety of solvents. *J Phys Chem* 1993;97(13):3379–83.
- [32] Hiemenz PC, Lodge TP. *Polymer chemistry*. 2nd ed. Boca Raton, FL: CRC Press; 2007.
- [33] Bergin SD, Nicolosi V, Streich PV, Giordani S, Sun Z, Windle AH, et al. Towards solutions of single walled carbon nanotubes in common solvents. *Adv Mater* 2008;20:1876–81.
- [34] Bergin SD, Sun Z, Strich P, Hamilton J, Coleman JN. New solvents for nanotubes: approaching the dispersibility of surfactants. *J Phys Chem* 2010;114:231–7.
- [35] Mejlbro L. The complete solution of Fick's second law of diffusion with time-dependent diffusion coefficient and surface concentration: durability of concrete in saline environment. Sweden: Cementa AB, Danderyd; 1996.
- [36] Rubinstein M, Colby RH. *Polymer physics*. New York, NY: Oxford University Press; 2003.
- [37] Miller-Chou BA, Koenig JL. A review of polymer dissolution. *Prog Polym Sci* 2003;28:1223–70.
- [38] Cheng Q, Debnath S, Gregan E, Byrne HJ. Effects of chlorinated aromatic solvents on the dispersion of HiPco SWNTs. *Physica Stat Sol B* 2008;245:1947–50.
- [39] Cheng Q, Debnath S, Gregan E, Byrne HJ. Ultrasound-assisted SWNTs dispersion: effects of sonication parameters and solvent properties. *J Phys Chem C* 2010;114:8821–7.
- [40] King JW. University of Wisconsin Technology Publication. 1995; 28:190.
- [41] DiPaola-Baranyi G, Guillet JE. Estimation of solubility parameters for poly(vinyl acetate) by inverse gas chromatography. *J Chromatogr* 1978;166:349.
- [42] Kadish KM, Ruoff RS. *Fullerenes chemistry physics and technology*. New York, NY: Wiley Interscience; 2000.
- [43] Sivaraman N, Dhamodaran R, Kaliappan I, Srinivasan TG, Vasudeva Rao PR, Mathews CK. Solubility of C60 in organic solvents. *J Org Chem* 1992;57:6077–9.
- [44] Chen J, Hamon MA, Hu H, Chen Y, Rao AM, Eklund PC, et al. Solution properties of single-walled carbon nanotubes. *Science* 1998;282:95–8.
- [45] Bahr JL, Mickelson ET, Bronikowski MJ, Smalley RE, Tour JM. Dissolution of small diameter single-wall carbon nanotubes in organic solvents?. *Chem Comm* 2001:193–4.
- [46] Landi BJ, Ruf HJ, Worman JJ, Raffaele RP. Effects of alkyl amide solvents on the dispersion of single-wall carbon nanotubes. *J Phys Chem* 2004;108:17089–95.
- [47] Hernandez Y, Lotya M, Rickard D, Bergin SD, Coleman JN. Measurement of multi-component solubility parameters for graphene facilitates solvent discovery. *Langmuir* 2010;26:3208–13.
- [48] Sperling LH. *Introduction to physical polymer science*. New York, NY: John Wiley & Sons; 2006.
- [49] Frato KE. *Characterization of an unknown polymer using static and dynamic light scattering*. Wooster, OH: College of Wooster; 2003.
- [50] Bender M. A single exposure photographic method for depolarization factor measurements. *J Chem Educ* 1952;15:18.

- [51] Debye P. Molecular-weight determination by light scattering. *J Phys Colloid Chem* 1947;51:18–32.
- [52] Giacomelli MG, Chalut KJ, Ostrander JH, Wax A. Review of the application of T-matrix calculations for determining the structure of cell nuclei with angle-resolved light scattering measurements. *IEEE J Selected Topics Quantum Electron* 2010;16:900–8.
- [53] Scharlt W. Light scattering from polymer solutions and nanoparticle dispersions. New York, NY: Springer Berlin Heidelberg; 2007.
- [54] Mutz M, Eastwood E, Dadmun MD. Quantifying the solubility of boron nitride nanotubes and sheets with static light scattering and refractometry. *J Phys Chem C* 2013;25:13230–8.
- [55] Mutz M, Eastwood E, Lee MW, Dadmun MD. Quantifying the thermodynamic interactions of polyhedral boranes in solution to guide nanocomposite fabrication. *J Nanoparticle Res* 2012;14:1–12.
- [56] Huglin MB. Light scattering from polymer solutions. New York, NY: Academic Press; 1989.
- [57] Garbassi F, Morra M, Occhiello E. Polymer surfaces: from physics to technology. New York, NY: John Wiley & Sons; 2002.
- [58] Fakhraai Z, Forrest JA. Measuring the surface dynamics of glassy polymers. *Sci I* 2008;319:600–4.
- [59] Bockstaller MR, Lapetnikov Y. Size-selective organization of enthalpic compatibilized nanocrystals in ternary block copolymer/particle mixtures. *J Am Chem Soc* 2003;125:5276–7.
- [60] Spontak RJ. Selectivity-and size-induced segregation of molecular and nanoscale species in microphase-ordered triblock copolymers. *Nano Lett* 2006;6:2115–20.
- [61] Genzer J, Composto RJ. Effect of molecular weight on the interfacial excess, tension, and width in a homopolymer/binary polymer blend system. *Macromolecules* 1998;31:870–8.
- [62] Chee KK. You have full text access to this content. Molecular weight dependence of surface tension of polystyrene as studied by the corresponding states principle. *J Appl Polym Sci* 1998;70:697–703.
- [63] Gaines GL, Le Grand DG. The surface-tension of some deuterated hydrocarbons. *Colloids Surfaces* 1994;82:299–300.
- [64] Sauer BB, Dee GT. Molecular-weight dependence of surface-tension of linear perfluorinated alkane melts including high-molecular-weight poly(tetrafluoroethylenes). *Macromolecules* 1994;27:6112–16.
- [65] Lipatov YS. Encyclopedia of surface and colloid science. Kiev, Ukraine: Institute of Macromolecular Chemistry National Academy of Sciences; 2002.
- [66] Hong PP, Boerio FJ, Smith SD. Surface segregation in blends of polystyrene and deuterated polystyrene. *Macromolecules* 1993;26:1460–4.
- [67] Affrossman S, Hartshorne M, Kiff T, Pethrick RA, Richards RW. Surface segregation in blends of hydrogenous polystyrene and perfluorohexane end-capped deuterated polystyrene, studied by SSIMS and XPS. *Macromolecules* 1994;27:1588–91.
- [68] Schaub TF, Kellogg GJ, Mayes AM. Surface modification via chain end segregation in polymer blends. *Macromolecules* 1996;29:3982–90.
- [69] Kwei TK, Frisch HL. Interaction parameter in polymer mixtures. *Am Chem Soc*, 11. 1978. p. 1267–71.

- [70] Strzhemechny Y, Shapolvalov V, Zhou KG, Schwarz SA, Sokolov J, Rafailovich MH. Depth and time dependence of polystyrene chain diffusion near the polystyrene/silicon interface. *Mater Res Soc* 1999;543:151.
- [71] Jones RAL, Kramer EJ. Surface enrichment in an isotopic polymer blend. *Phys Rev Lett* 1989;62:280–3.
- [72] Composto RJ, Stein RS, Kramer EJ, Jones AJ, Mansour A, Karim A, et al. Surface enrichment in polymer blends—a neutron reflection test. *Phys B* 1989;156-157:434.
- [73] Geoghegan G, Boue R, Menelle A, Abels F, Russ T, Ermer H, et al. Surface segregation from polystyrene networks. *J Phys: Condensed Matter* 2000;12:5129–42.
- [74] Barnes KA, Karim A, Douglas JF, Nakatani AI, Gruell H, Amis EJ. Suppression of dewetting in nanoparticle-filled polymer films. *Macromolecules* 2000;33:4177–85.
- [75] Kumar SK, Russell TP. Behavior of isotopic, binary polymer blends in the vicinity of neutral surfaces: the effects of chain-length disparity. *Macromolecules* 1991;24:3816–20.
- [76] Kerle T, Lin Z, Kim HC, Russell TP. Mobility of polymers at the air/polymer interface. *Macromolecules* 2001;34:3484–92.
- [77] Stamm M, Sommer JU. Polymer–nanoparticle films: entropy and enthalpy at play. *Nat Mater* 2007;6:260–1.
- [78] Yang T, Rogers CE. *AIChE Symp. Ser* 1990;11:272.
- [79] Steiner I, Klein J, Eiser E, Budkowski A, Fetters LJ. Complete wetting from polymer mixtures. *Science* 1992;258:5085.
- [80] Lin EK, Kolb R, Satija SK, Wu W. Reduced polymer mobility near the polymer solid interface as measured by neutron reflectivity. *Macromolecules* 1999;32:3753–7.
- [81] Hong PP, Boerio FJ. Effect of annealing time, film thickness, and molecular weight on surface enrichment in blends of polystyrene and deuterated polystyrene. *Macromolecules* 1994;27:596–605.
- [82] Krishnan RS, Mackay ME, Duxbury PM, Hawker CJ, Asokan S, Wong MS, et al. Improved polymer thin-film wetting behavior through nanoparticle segregation to interfaces. *J Phys Condensed Matter* 2007;19:356003.
- [83] Vaia RA, Ishii H, Giannelis EP. Synthesis and properties of two-dimensional nanostructures by direct intercalation of polymer melts in layered silicates. *Chem Mater* 1993;5(12):1694–6.
- [84] He G, Pan Q. Synthesis of polystyrene and polystyrene/poly(methyl methacrylate) nanoparticles. *Macromol Rapid Commun* 2004;25:1545–8.
- [85] Jong WHD, Borm PJA. Drug delivery and nanoparticles: applications and hazards. *Int J Nanomedicine* 2008;3:133.
- [86] Quintanilla J. Microstructure and properties of random heterogeneous materials: a review of theoretical results. *Polym Eng Sci* 1990;35:559–85.
- [87] Petty MC. *Molecular electronics: from principles to practice*. New York, NY: John Wiley; 2007.
- [88] Karim A, Felcher GP. Interdiffusion of polymers at short times. *Macromolecules* 1994;27:6973–9.
- [89] Green PF, Palmstrom CJ, Mayer JW, Kramer EJ. Marker displacement measurements of polymer-polymer interdiffusion. *Macromolecules* 1985;18:501–7.
- [90] Green PF, Mills PJ, Palmstrom CJ, Mayer JW, Kramer EJ. Limits of reptation in polymer melts. *Phys Rev Lett* 1984;53:2145–8.

- [91] Bucknall DG, Butler SA, Higgins JS. Real-time measurement of polymer diffusion coefficients using neutron reflection. *Macromolecules* 1999;32:5453–6.
- [92] Mu M, Clarke N, Composto RJ, Winey KI. Polymer diffusion exhibits a minimum with increasing single-walled carbon nanotube concentration. *Macromolecules* 2009;42:7091–7.
- [93] Mu M, Composto RJ, Clarke N, Winey KI. Minimum in diffusion coefficient with increasing MWCNT concentration requires tracer molecules to be larger than nanotubes. *Macromolecules* 2009;42:8365–9.
- [94] Sharma S, Rafailovich MH, Peiffer D, Sokolov J. Control of dewetting dynamics by adding nanoparticle fillers. *Nano Lett* 2001;10:511–14.
- [95] Yethiraj A. Entropic and enthalpic surface segregation from blends of branched and linear polymers. *Phys Rev Lett* 1995;74:2018–21.
- [96] Tanaka K, Taura A, Ge S, Takahara A, Kajiyama T. Molecular weight dependence of surface dynamic viscoelastic properties for the monodisperse polystyrene film. *Macromolecules* 1996;29:3040–2.
- [97] Lange J, Wyser Y. Recent innovations in barrier technologies for plastic packaging—a review. *Packaging Technol Sci* 2003;16:149–58.
- [98] Mutz M, Holley DW, Mays JW, Dadmun MD. Impact of nanoparticle size and shape on selective surface segregation in polymer nanocomposites. *Polymer* 2012;53:5087–96.
- [99] Kaelble DH. Spin casting of polymer films. *J Appl Polym Sci* 1965;9:1209–12.
- [100] Kulkarni PP, Jafvert CT. Solubility of C60 in solvent mixtures. *Environ Sci Technol* 2008;42:845–51.
- [101] Barton AFM. Handbook of polymer-liquid interaction parameters and solubility parameters. Boca Raton, FL: CRC Press; 1990.
- [102] Sierra AQ, Mora AVD. Size-shape determination of nonspherical particles in suspension by means of full and depolarized static light scattering. *Appl Opt* 1995;34:6256–62.
- [103] Tamari S. Optimum design of the constant-volume gas pycnometer for determining the volume of solid particles. *Meas Sci Technol* 2004;15:549–58.
- [104] Siracusa V. Food packaging permeability behaviour—a report. *Int J Polym Sci* 2012; Article ID 302029, <http://dx.doi.org/10.1155/2012/302029>.

## 4

Raman and tip-enhanced  
Raman scattering  
spectroscopy studies of  
polymer nanocomposites

Xinlei Yan<sup>1</sup>, Harumi Sato<sup>2</sup> and Yukihiro Ozaki<sup>1</sup>

<sup>1</sup>Department of Chemistry, School of Science and Technology, Kwansai Gakuin University, Sanda, Hyogo, Japan <sup>2</sup>Graduate School of Human Development and Environment, Kobe University, Kobe, Japan

## 4.1 INTRODUCTION

Raman spectroscopy has been used to investigate carbon nanotubes (CNTs), graphene, and related nanomaterials. These materials yield very intense Raman bands, and thus, this technique can effectively explore the structure and properties of CNTs and graphenes, such as their degree of purity, defects, electronic structures, and structural modifications [1–3]. The assignments of Raman bands of CNTs and graphenes have been well established [4–6]. A series of bands observed in the 350–120 cm<sup>-1</sup> region of Raman spectra of CNTs have been assigned to the radial breathing mode (RBM), which indicates the length and the diameter of single-walled CNTs (SWCNTs). All carbon materials show a Raman band at approximately 1580 cm<sup>-1</sup> assigned to G band. The G band often splits into two components, G<sup>+</sup> and G<sup>-</sup> bands. In the case of SWCNTs the G<sup>+</sup> band located at approximately 1590 cm<sup>-1</sup> is attributed to a vibration of carbon atoms along the nanotube axis and is sensitive to a charge transfer from dopant additions to SWCNTs. The G<sup>-</sup> band at around 1570 cm<sup>-1</sup> arises from a vibration of carbon atoms along the circumferential direction of SWCNTs. Graphenes have similar G<sup>+</sup> and G<sup>-</sup> bands. A band observed near 1355 cm<sup>-1</sup> is called the *D band*, which reflects defects or disorder in them, such as amorphous carbon, vacancies, and heteroatoms. The origin of the D band is thought to be a double-resonance process. The G band, which is the overtone of the D band, is located at around 2700 cm<sup>-1</sup>.

Raman spectroscopy is also very useful for exploring the structure, interface interactions, and physical properties of CNT-based polymer nanocomposites [7–10]. In a polymer nanocomposite, the interaction between CNTs and polymers

is reflected by a peak shift or a change in the peak intensity or width in a Raman spectrum [7,9]. Bokobza et al. [8] studied the strain dependence of Raman spectra of multiwalled CNT (MWCNT)/styrene-butadiene rubber (SBR) composites and observed a shift of the G band to a lower-wave number side, which indicates a stress transfer interaction between the CNTs and the polymer. Cooper et al. investigated the deformation micromechanics of SWCNTs and MWCNTs in epoxy resin nanocomposites using Raman spectroscopy [10]. They reported that stress-induced Raman band shifts of the CNTs demonstrated the transfer of stress between CNTs and the polymer (epoxy) and that the effective moduli of the SWCNTs and MWCNTs dispersed in the composites could be more than 1 TPa and approximately 0.3 TPa, respectively.

However, spatial resolution of Raman spectroscopy is restricted by the diffraction limit of light. Thus, the spectroscopic techniques that realize higher spatial resolution have been greatly preferred recently. Tip-enhanced Raman scattering (TERS) spectroscopy is a technique that employs near-field enhancement from a metallic nanotip to measure Raman spectra with spatial resolution surpassing the diffraction limit [4–6,11,12]. The mechanism of TERS is generally the same as that of surface-enhanced Raman scattering, because both effects happen at a metallic tip apex at the junction of metallic nanoaggregates, which produces an electromagnetic (EM) enhancement effect and a chemical enhancement effect. The EM enhancement is generated by the coupling of light and radiative plasmon modes (mainly dipole modes) on a tip [13], while the chemical enhancement is produced by the formation of a charge-transfer complex between molecules and a tip surface [14]. In the cases reported in this review, only the EM enhancement is important because the chemical enhancement can only occur when the tip is operated in a contact mode, while a noncontact mode is used in the present cases [15].

To achieve a good enhancement, the size, shape, and material of a tip must be carefully chosen to ensure plasmon resonance with the excitation laser light [16,17]. The evanescent field from this resonance is confined to a small area around the tip, resulting in the improvement of spatial resolution [11]. For a TERS measurement, the size of the TERS probe is generally about 30–100 nm, and the size of the laser spot on the interaction area can be reduced to 10–50 nm to achieve much higher spatial resolution. Therefore, much more detailed information about the interface of composites in the local area is expected to be gained by measuring point-dependent TERS spectra.

CNTs hold remarkable electronic, thermal, optical, and mechanical properties [18–20]. Their unique tubular structure prevents the propagation of cracks and dislocations, which provides CNTs with great potential as materials with high Young's moduli [21]. The partial  $sp^2$ – $sp^3$  hybridization of the C–C bonds of CNTs can induce high flexibility [10,22]. Thus, the potential applications of CNTs have been matters of keen interest. CNTs are also excellent nanofillers for polymer nanocomposites [23,24]. Even a small amount of CNTs added to a polymer can markedly improve its mechanical properties and can even turn an electrically insulating polymer into a conductive composite [25,26].

A number of studies have been reported for the physical properties and structure of CNT-based polymer nanocomposites. For example, Bokobza et al. [27] found a 45% increase in modulus and a 70% increase in tensile length by incorporating 1% w/w of MWCNT into SBR. They also investigated MWCNT/poly (dimethylsiloxane) (PDMS) composites, reporting that well-dispersed CNT allows the formation of a conductive interconnecting filler network, even at very small loadings (5 wt%). Marked improvements in the physical and chemical properties of polymer nanocomposites are induced by the interaction between a polymer and a nanofiller and/or a change in the local structure of the polymer [28,29]. However, the mechanism by which the properties are improved has not fully been elucidated. In order to explore the interactions in nanocomposites occurring at the interface between a polymer and a nanofiller, TERS spectroscopy is very suitable.

In this chapter, we outline three recent Raman and TERS studies of polymer nanocomposites.

---

## 4.2 EXAMPLES OF RAMAN STUDIES OF POLYMER NANOCOMPOSITES

### 4.2.1 A RAMAN SPECTROSCOPY STUDY ON SWCNT/POLYSTYRENE NANOCOMPOSITES: MECHANICAL COMPRESSION TRANSFERRED FROM THE POLYMER TO SWCNTS

Raman spectroscopy was used to elucidate the interactions between SWCNTs and polystyrene (PS) inside the nanocomposites. It was found that the  $G^-$ ,  $G^+$ , and  $G'$  SWCNT bands shifted to higher wave numbers when incorporated into the nanocomposites [8,30–32]. Yan et al. [33] concluded that this upshift was induced exclusively by a mechanical compression transfer from PS to the SWCNTs. The mechanical compression transfer was estimated to be  $\sim 518$  MPa from the magnitude of the upshift.

Figure 4.1a–c shows Raman spectra of pristine SWCNTs, SWCNT/PS composite (3 wt%), and PS, respectively [33]. The RBM band,  $G^-$  and  $G^+$  bands, D band, and  $G'$  band are observed at 178, 1566, 1590, 1333, and 2667  $\text{cm}^{-1}$ , respectively. The shape of the G bands suggested that the SWCNTs were semiconducting in nature [34–36]. Comparison among the Raman spectra of SWCNT, SWCNT/PS composite, and pristine PS, reveals that the spectrum of SWCNT/PS composites is dominated by SWCNT bands, and the intensities of Raman bands due to PS are much weaker. Most of the Raman peaks of SWCNTs in the SWCNT/PS composite spectrum appeared at higher wave numbers as compared to the peaks in the spectrum of pristine SWCNTs. For example, the G bands shifted from 1566 and 1590 to 1568 and 1593  $\text{cm}^{-1}$ , respectively.

To investigate the Raman band shifts of SWCNTs in the SWCNT/PS composites, Yan et al. [33] prepared SWCNT/PS composites with three different

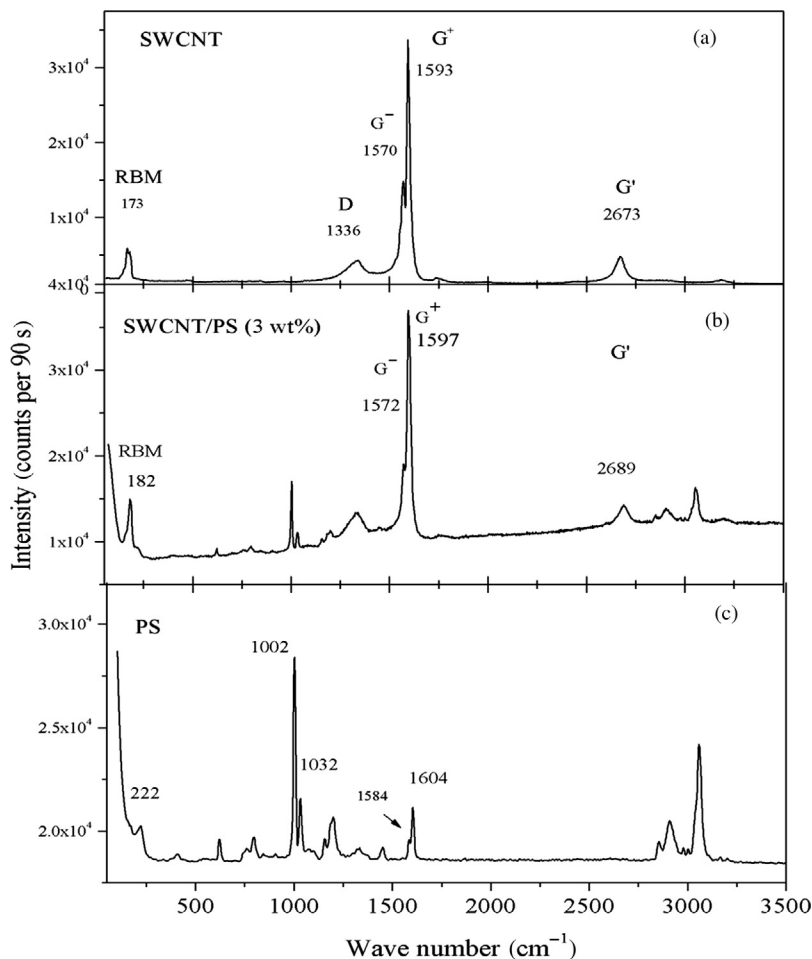


**FIGURE 4.1**

Raman spectra of (a) SWCNTs, (b) 3 wt% SWCNT/PS, (c) PS.

*Ref. [32]. Copyright 2012. Reprinted with permission from American Chemical Society.*

loadings of SWCNTs: 0.5, 1, and 3 wt%. Figure 4.2a–c depicts Raman spectra in the 275–50, 1700–1450, and 3000–2500  $\text{cm}^{-1}$  regions of pure SWCNTs and the three kinds of SWCNT/PS composites, respectively [33]. The RBM band region of pristine SWCNTs shows two peaks at 178 and 164  $\text{cm}^{-1}$  (Figure 4.2a). The stronger one, at 178  $\text{cm}^{-1}$ , shifts to 182, 184, and 187  $\text{cm}^{-1}$  in the spectra of the 3, 1, and 0.5 wt% SWCNT/PS composites, respectively. The weaker one, at 164  $\text{cm}^{-1}$ , was marked by a solid dark circle (●) in Figure 4.2a. This peak also upshifts to higher wave numbers in the spectra of the 0.5 and 1 wt% composites. However, it is nearly missing in the spectrum of 3 wt% SWCNT/PS.

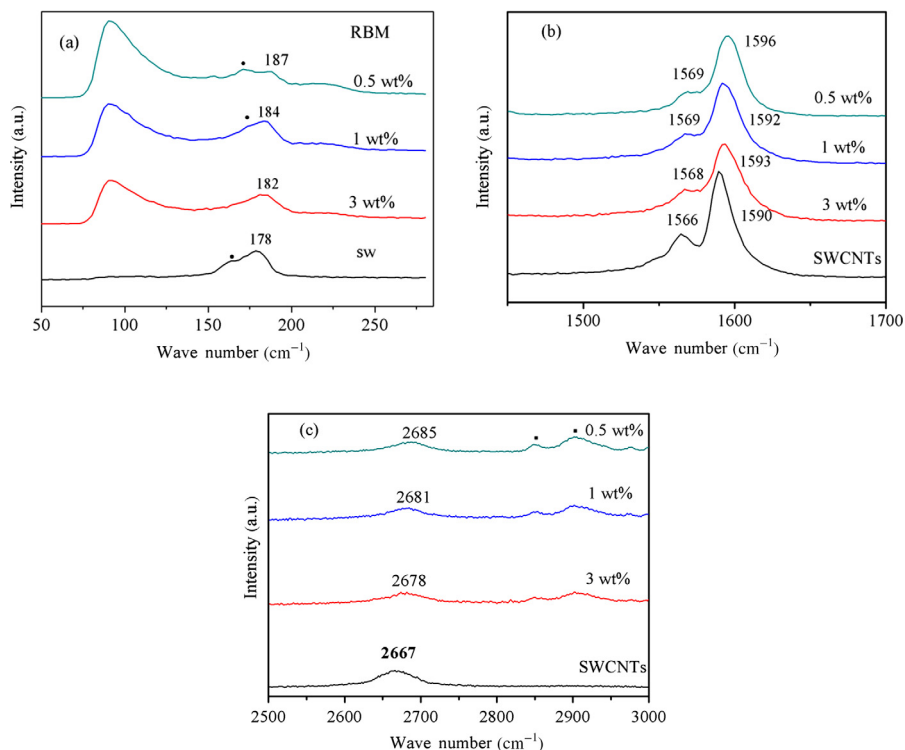


**FIGURE 4.2**

RBM in the Raman spectra of (a) SWCNT/PS, (b) the G band region in the Raman spectra of SWCNTs and SWCNT/PS with two different loadings of SWCNTs, and (c) the G' band region in the Raman spectra of SWCNTs and SWCNT/PS with three different loading of SWCNTs (0.5, 1, and 3 wt%).

*Ref. [32]. Copyright 2012. Reprinted with permission from American Chemical Society.*

This happens due to the fact that the pristine SWCNTs were not uniform in diameter and had a distribution of  $\leq 2$  nm.

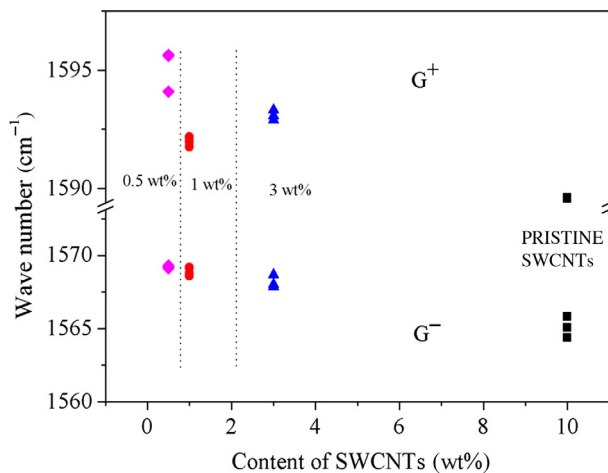
The G-band region of pristine SWCNTs and the SWCNT/PS composites are compared in Figure 4.2b. The G band of SWCNTs is composed of two sub-bands ( $G^-$  and  $G^+$ ) attributed to carbon vibrations along the circumferential and axial directions of SWCNTs, respectively. Figure 4.2c yields the corresponding spectra in the G' band region. Two additional peaks at 2850 and 2904  $\text{cm}^{-1}$  marked by solid dark square (■) are due to symmetric  $\nu_s$  ( $\text{CH}_2$ ) and antisymmetric  $\nu_s$  ( $\text{CH}_2$ ) stretching modes of PS, respectively. Figure 4.2b and c reveals that the two G bands and the G' band yield higher wave number shifts of different degrees, similar to the shift behavior of RBM. It also shows that the 0.5 wt% SWCNT/PS composite gives a larger shift than the composites with the 3 and 1 wt% SWCNT loading.

The shifts observed in the Raman bands of SWCNTs may be due to three possible mechanisms: chemical action between SWCNTs and matrix, such as charge transfer or chemical bonds; [30] changes in the tube–tube interactions due to the distribution of SWCNTs; [37] and mechanical compression from the polymer matrix [31,38,39]. As for the first possibility, it has been shown that charge transfer induced by doping, or chemical bonds formed between CNTs and the polymer, can induce a higher wave number shift in the Raman peaks of CNTs by several tens of  $\text{cm}^{-1}$  (Br doped) or a lower wave-number shift by  $100 \text{ cm}^{-1}$  (K, Rb doped). However, in the current system, it is very unlikely that the Raman shift resulted from this kind of action because the SWCNTs used were not functionalized or doped. Another possibility is that CH interactions may be involved between CNTs with a  $\pi$ -electron-rich surface and polymer chains with methyl or methylene groups [40,41].

This type of interaction can be studied by using infrared (IR) spectroscopy, as the  $\text{CH}_2$  band shifts by roughly  $10 \text{ cm}^{-1}$  [8]. Yan et al. [33] investigated the IR spectra of pure PS and 1 and 3 wt% SWCNT/PS composites. The  $\text{CH}_2$  bands of PS are located at 2924, 2850, and  $1371 \text{ cm}^{-1}$ . However, the bands did not show any shift, indicating that CH interactions do not occur or play only a weak role in these samples. Thus, charge transfer cannot be used to explain the observed Raman shifts. Van der Waals interactions are known to occur among the tubes within SWCNT bundles. However, it was found that van der Waals interactions are also not suitable for explaining the Raman shifts observed in the system.

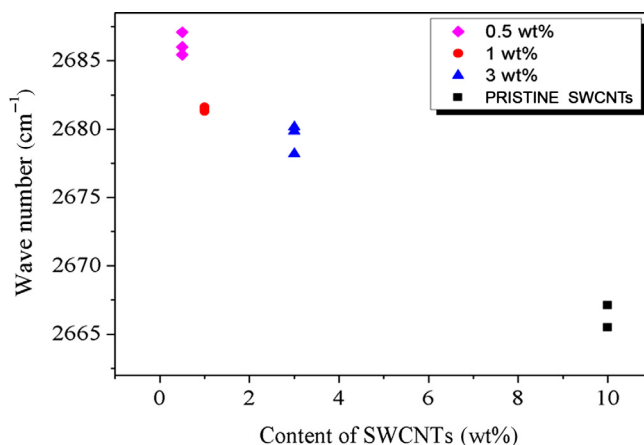
Thus, Yan et al. [33] concentrated on the last possible mechanism. It is well-known that the elongation or shrinkage of carbon atom vibrations causes shifts in Raman bands of SWCNTs by several wave numbers. When SWCNTs are embedded into another system, such as a liquid and polymer, SWCNTs are subjected to hydrostatic pressure [31,38,39]. The hydrostatic pressure induces higher wave number shifts of Raman bands of SWCNTs. Loa [42] carried out a comprehensive study of SWCNTs under different high pressures using Raman spectroscopy. The results showed that pressure can induce a reversible change in the lattice dynamics and structure of SWCNT, and that it is also possible to transform SWCNTs into diamond and other “superhard” phases by applying pressure. Yan et al. [33] concluded that the SWCNTs underwent mechanical compression from the PS matrix during the process of generating the composites. They estimated the magnitude of compression to be 518 MPa from the Raman shifts observed between pure SWCNTs and those in 1 wt% SWCNT/PS composites.

Figures 4.3 and 4.4 show the shift behaviors of the G and  $G'$  bands, respectively, at different positions within the samples [33]. Figure 4.3 reveals that the  $G^+$  band shifted more than the  $G^-$  band. This indicates that the carbon-carbon atom vibrations along the axial direction were more sensitive to mechanical pressure than the vibrations along the circumferential direction. It is apparent from Figure 4.4 that the  $G'$  band shifted more than the two G bands, which shows that the  $G'$  band is an excellent indicator of the interaction between SWCNTs and the polymer. The shift behavior of the  $G'$  band, as a detector for stress transfer from polymer to CNTs, has been studied using strain-dependent Raman spectroscopy.

**FIGURE 4.3**

A Raman shift of the  $G^+$  and  $G^-$  bands for SWCNT/PS composites containing different loadings of SWCNTs. Corresponding symbols indicate results detected from different points in the same sample.

*Ref. [32]. Copyright 2012. Reprinted with permission from American Chemical Society.*

**FIGURE 4.4**

A Raman shift of the  $G'$  bands versus the SWCNT loading in SWCNT/PS composites. Corresponding symbols indicate results detected from different points in the same sample.

*Ref. [32]. Copyright 2012. Reprinted with permission from American Chemical Society.*

When CNTs undergo strain, the  $G'$  band experiences a large downshift. Lower loadings of SWCNTs produce larger shifts (Figures 4.3 and 4.4) because lower loadings induce better alignment or distribution of the SWCNTs. At higher

loadings, the aggregation of SWCNTs increases, which causes the SWCNTs to undergo a lower mechanical compression than the well-dispersed SWCNTs.

#### 4.2.2 RAMAN STUDY OF INTERFACIAL LOAD TRANSFER IN GRAPHENE NANOCOMPOSITES

Srivastava et al. [43] investigated the strain-sensitive characteristic Raman G-band shift of graphene platelets (GPLs) in PDMS nanocomposites to reveal the filler-to-matrix interactions. They obtained large debonding strains of  $\sim 7\%$  for graphene in PDMS, with the peak shift rate with strain being  $\sim 2.4 \text{ cm}^{-1}/\text{composite strain } \%$  in comparison to SWCNT composites, where a relatively low rate of  $\sim 0.1 \text{ cm}^{-1}/\text{composite strain } \%$  was obtained. This result indicates enhanced load-transfer effectiveness for graphene.

Srivastava et al. [43] used Raman spectroscopy to directly study interfacial load transfer in a PDMS matrix with GPLs and SWCNT fillers under both tensile and compressive loading. The results indicated improved load transfer for GPLs in comparison to SWCNTs.

A scanning electron microscopy (SEM) of typical GPL filler embedded in the PDMS matrix is depicted in Figure 4.5a, and its inset shows a high-resolution SEM image revealing the wavy edge structure of the graphene. *In situ* straining of the sample under SEM observation showed that GPL debonds from the PDMS matrix for strain levels  $\sim 7\%$ , as indicated in Figure 4.5b. This high strain to debonding is indicative of a strong interface.

Figure 4.5c shows typical Raman G-band peak shift response of the GPL/PDMS nanocomposite with applied strain. It is noted that the G band of GPLs shifted as a function of strain applied, and that after  $\sim 7\%$  strain, the G band reverted close to the original unstrained peak position due to relaxation of the GPL upon debonding from the matrix. Figure 4.6a shows comparison of Raman G-band peak shift of GPL/PDMS, SWNT/PDMS, and GPL/PS nanocomposites below 2% applied strain. Data is shown for both tensile and compressive loading at a constant nanofiller weight fraction of  $\sim 0.1\%$ . Figure 4.6a shows the results within the elastic regime, while Figure 4.6b depicts the response for large strains. In the elastic region ( $<1.5\%$  strain) the G band showed a low wave number shift with applied tensile strain and showed a high wave number shift under compressive deformation. The rate of peak shift with strain was  $\sim 2.4 \text{ cm}^{-1}/\text{composite strain } \%$  in tension and  $\sim 1.8 \text{ cm}^{-1}/\text{composite strain } \%$  under compression.

For large deformations ( $<2\%$  strain) in the plastic domain (Figure 4.6b), particular note was that the GPL fillers went into compression under uniaxial tensile loading and vice versa. Thus, the G-band shifts to higher wave numbers under tensile load and is downshifted to lower wave numbers under compressive strain, as indicated for a representative sample in Figure 4.6b. This behavior was highly reproducible and was verified for more than 10 different samples, as shown in the form of a standard deviation in Figure 4.6c. This occurs because, in comparison to low tensile strain when there is efficient elastic strain transfer from the matrix to GPL, at higher strain the mobile PDMS chains.

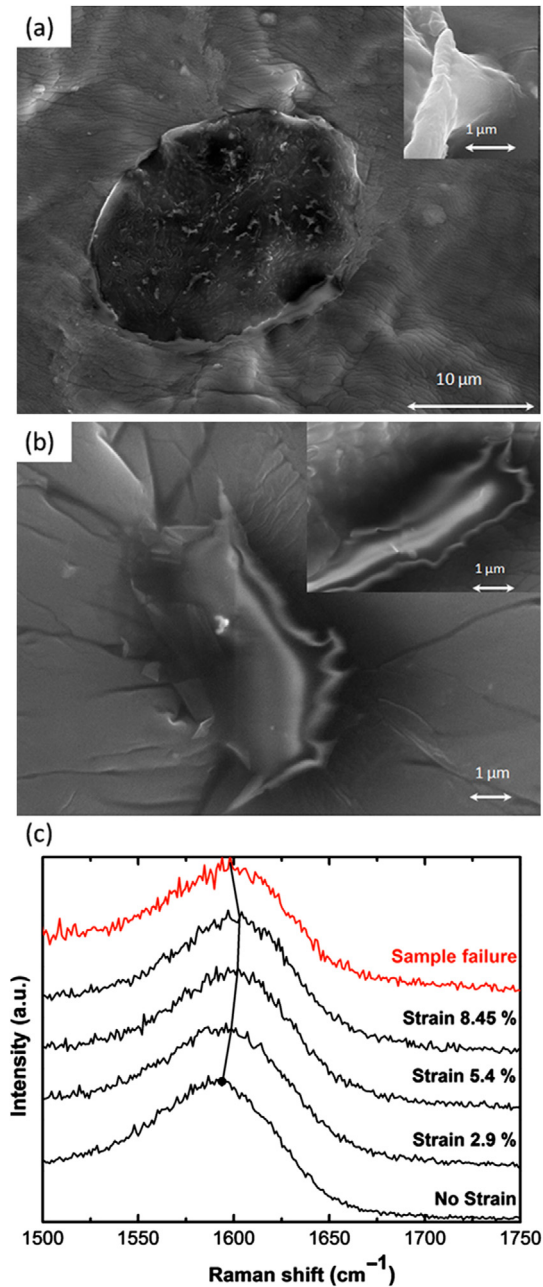


**FIGURE 4.5**

(a) SEM image of a typical GPL flake embedded in the PDMS matrix. The flake is an aggregate of several individual GPL platelets and is several microns in dimension. Inset; a higher resolution SEM image indicating a substantial polymer coating on the GPL. (b) Sample was strained *in situ* while under SEM observation. Image shows interfacial debonding at a strain level of  $\sim 7\%$ . Inset; similar debonding behavior for another GPL filler at  $\sim 7\%$  strain. (c) Typical G-band shift response of the GPL/PDMS nanocomposite with applied strain.

*Ref. [43]. Copyright 2011. Reprinted with permission from American Institute of Physics.*

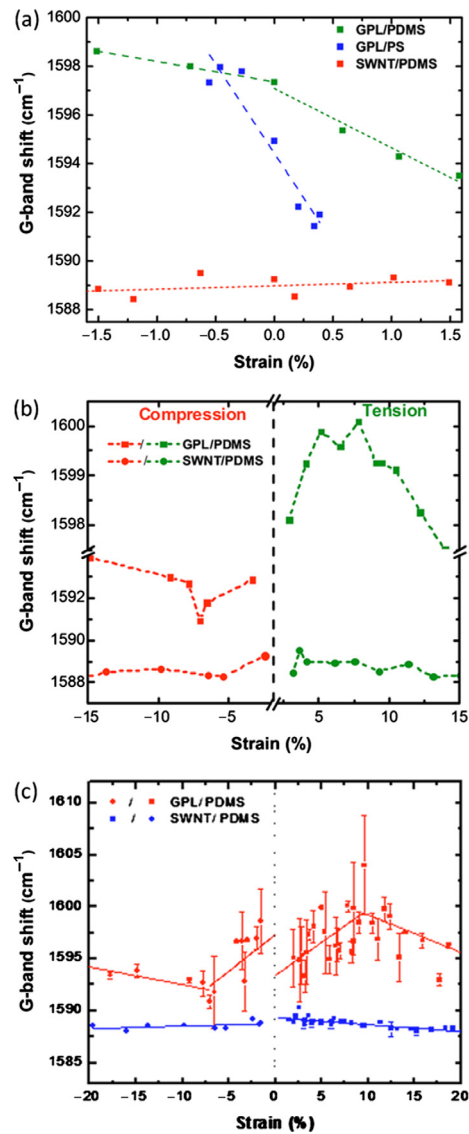


**FIGURE 4.6**

(a) Comparison of G-band shift of GPL/PDMS, SWNT/PDMS, and GPL/PS nanocomposites below 2% applied strain. (b) Corresponding G-band shift for strains greater than 2% for the GPL/PDMS and SWNT/PDMS nanocomposites for a representative sample. The strain level at which debonding appears to take place under both tension and compression is  $\sim 7\%$ . (c) The best fit plot taken from the average Raman peak shifts for the nanocomposites was for a sample data set of more than 10.

*Ref. [43]. Copyright 2011. Reprinted with permission from American Institute of Physics.*

Srivastava et al. concluded that the G-band shift rate in GPL/PDMS composites was at least an order of magnitude higher than its SWNT counterpart at the same loading fraction of  $\sim 0.1\%$  by weight. There may be several reasons for this which includes enhanced specific surface area of graphene, the rough/wrinkled surface texture of graphene which can lead to mechanical interlocking, and the abundance of defects in graphene which may provide chemical handles for covalent interactions with polymer chains.

### 4.3 RAMAN AND TERS SPECTROSCOPY STUDIES OF POLYMER NANOCOMPOSITES

#### 4.3.1 INTERACTION OF SWCNT AND PS AT THE INTERFACE IN SWCNT/PS NANOCOMPOSITES STUDIED BY RAMAN AND TERS SPECTROSCOPY

Raman and TERS spectra of SWCNT/PS were measured to investigate the distribution of SWCNTs in the nanocomposites and local interactions at an interface between SWCNTs and PS [33]. The Raman spectra of the nanocomposites did not show a significant point-to-point variation, while the corresponding TERS spectra show obvious point-to-point shifts. Raman spectra of (a) pristine SWCNT and (b) SWCNT/PS composites are compared in Figure 4.7 [33]. The region of

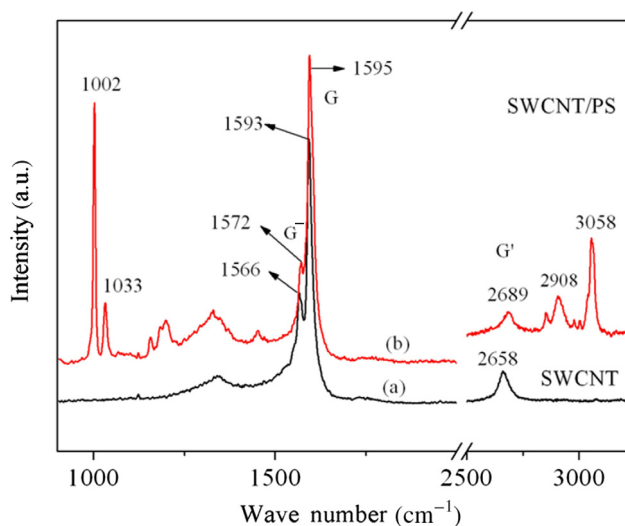


**FIGURE 4.7**

Raman spectra of pristine SWCNTs and 0.5 wt% SWCNT/PS composites.

*Ref. [33]. Copyright 2013. Reprinted with permission from the Royal Society of Chemistry.*

1700–1500  $\text{cm}^{-1}$  of the Raman spectrum of SWCNT is dominated by the G band that splits into two sub-bands. The shape of two G bands in Figure 4.7a and previous studies reveal that the SWCNTs belong to a semiconductor type of CNTs. For semiconductor SWCNTs, the peak at 1566  $\text{cm}^{-1}$  is due to the  $G^-$  band, which corresponds to a carbon vibration along the circumferential direction, and that, at 1595  $\text{cm}^{-1}$ , is assigned to the  $G^+$  band, which arises from a carbon vibration along the nanotube axis [44].

The Raman spectrum of the SWCNT/PS nanocomposites (Figure 4.7b) shows shifts of several bands of SWCNTs. It is noted that the  $G^-$  and  $G^+$  bands shift from 1566 to 1572  $\text{cm}^{-1}$  and from 1593 to 1595  $\text{cm}^{-1}$ , respectively, and that the  $G'$  band has the largest shift from 2658 to 2689  $\text{cm}^{-1}$ . The shifts of the G and  $G'$  bands from the Raman spectrum of pristine SWCNTs to that of the SWCNT-based polymer composites reflect mechanical compression of the CNTs by the polymer [39,45].

Figure 4.8a depicts the far-field and near-field Raman spectra of the SWCNT/PS composites in the 3500–900  $\text{cm}^{-1}$  region [33]. The far-field Raman spectrum was measured under tip-retracted conditions, while the near-field Raman spectrum was obtained under tip-approaching conditions. Figure 4.8b depicts a TERS spectrum calculated by subtracting the far-field Raman spectrum from the near-field Raman spectrum.

Figure 4.9a exhibits Raman spectra in the G-band region of the SWCNT/PS composites collected at different points ( $P_1$ ,  $P_2$ ,  $P_3$ ,  $P_4$ ,  $P_5$ ,  $P_6$ ,  $P_7$ ,  $P_8$ , and  $P_9$ ) [33]. The normal Raman spectra do not show a significant point-dependent difference in terms of band positions and relative band intensities. The G band shows only a negligible shift of less than 2  $\text{cm}^{-1}$  at the different points. Figure 4.7b displays the corresponding TERS spectra of the SWCNT/PS composites. The G bands at around 1564 and 1589  $\text{cm}^{-1}$  show a shift from point to point in the TERS spectra (Figure 4.3a).

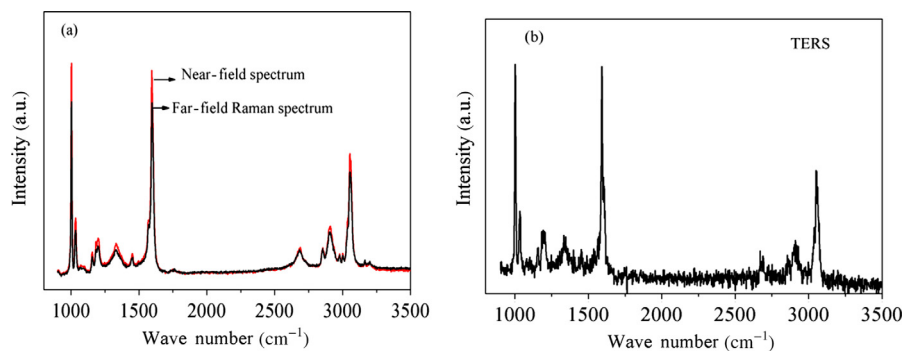


**FIGURE 4.8**

- (a) Far-field and near-field Raman spectra of 0.5 wt% SWCNT/PS nanocomposites;  
(b) TERS spectrum of 0.5 wt% SWCNT/PS nanocomposites.

*Ref. [33]. Copyright 2013. Reprinted with permission from Royal Society of Chemistry.*

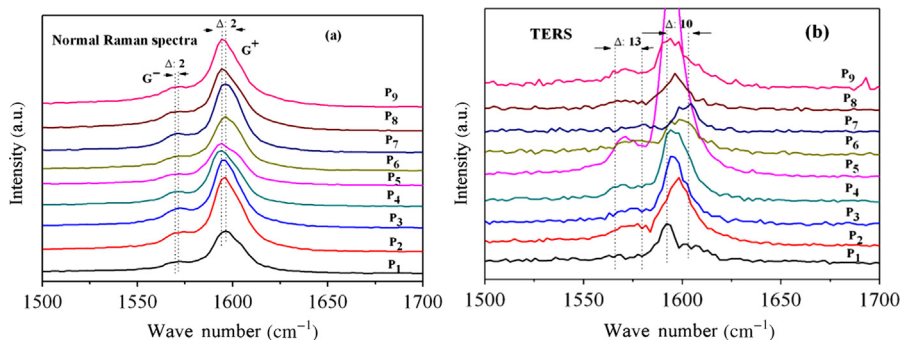


**FIGURE 4.9**

(a) Raman, and (b) TERS spectra in the region of 1700–1500  $\text{cm}^{-1}$  of 0.5 wt% SWCNT/PS nanocomposites measured at nine points.

*Ref. [33]. Copyright 2013. Reprinted with permission from Royal Society of Chemistry.*

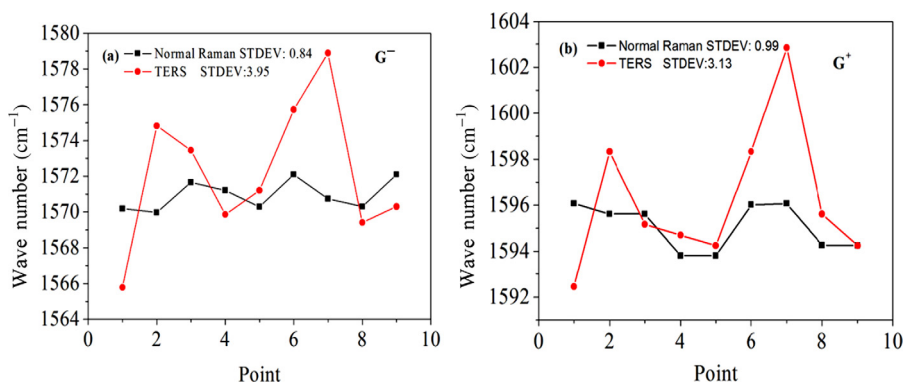


**FIGURE 4.10**

Point-dependent changes of wave number of  $G^-$  (a) and  $G^+$  (b) bands in normal Raman spectra (solid square) and TERS spectra (solid circle).

*Ref. [33]. Copyright 2013. Reprinted with permission from Royal Society of Chemistry.*

Figure 4.10a and b plots the peak positions of the  $G^-$  and  $G^+$  bands versus each point for the Raman (solid squares) and TERS (solid circles) spectra. It is noted that the TERS spectra show the largest shift of the  $G^-$  peak by approximately  $13 \text{ cm}^{-1}$ , and its standard error value (STDEV) is  $3.95 \text{ cm}^{-1}$ , whereas the corresponding shift is only  $2 \text{ cm}^{-1}$  in the normal Raman spectra, and the STDEV is  $0.84 \text{ cm}^{-1}$ . For the  $G^+$  peak, the largest shift is about  $10 \text{ cm}^{-1}$  for the TERS, and the STDEV is  $3.13 \text{ cm}^{-1}$ , whereas it is about  $2 \text{ cm}^{-1}$  for the normal Raman spectra, and the STDEV is  $0.99 \text{ cm}^{-1}$ .

The Raman band shifts of SWCNTs may be ascribed to three chemical interactions between SWCNTs and the matrix, such as charge transfer, changes in the

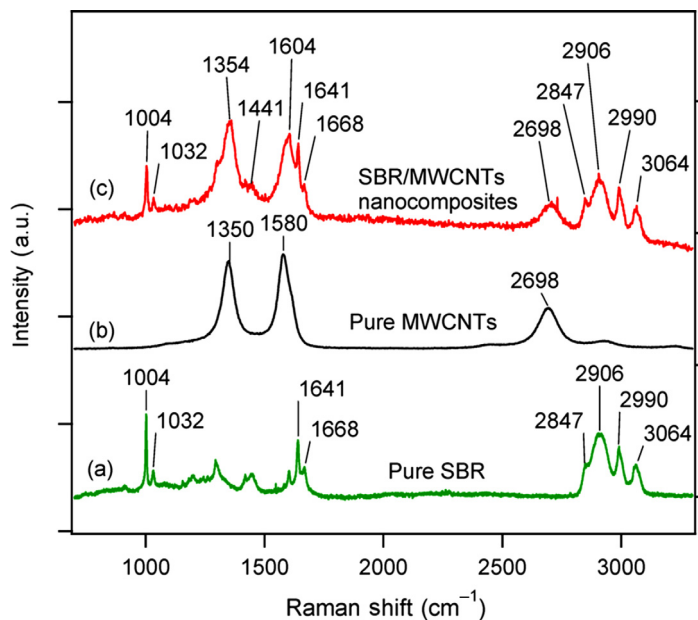
tube–tube interactions due to the distribution of SWCNTs, and mechanical compression from the polymer matrix to the CNTs.

Figure 4.10 demonstrates that the G bands in the TERS show a point-to-point dependent shift with similar shift degree [33]. The G' band has been known to be more sensitive to the mechanical compression than the G band, and shifts by much larger degree than the G bands under compression. In this study, the shift of G' band indicates that mechanical compression from the PS matrix to SWCNTs changes from point to point in the local area [33]. The disentanglement of CNTs and the penetration of a polymer into CNT bundles during melt mixing would cause a G-band shift. SWCNTs have an inhomogeneous distribution in the SWCNT/PS system, and thus, polymer chains penetrate into the bundle of SWCNTs at some points, while at other points, SWCNTs exist in aggregation states. This dispersion of SWCNTs in the PS matrix would induce a different effect on the molecular vibrations of SWCNTs. Therefore, Yan et al. [33] concluded that the G-band shift behavior in the TERS spectra is caused by both the distribution of SWCNTs in the PS matrix and the point-dependent mechanical compression from the PS matrix.

#### 4.3.2 TERS SPECTROSCOPY STUDY OF LOCAL INTERACTIONS AT THE INTERFACE OF SBR/MWCNT NANOCOMPOSITES

Local molecular interaction in the nanocomposite SBR and MWCNTs films were explored using TERS spectroscopy [46]. It was found that TERS bands due to SBR phenyl groups were strong when MWCNT bands were strong, whereas vinyl-group bands were strong when the MWCNT bands were weak. These findings suggested that the local distribution of polymer chains is modified with changes in the orientation of the phenyl rings by  $\pi$ – $\pi$  interactions between the polymer chains and the MWCNTs. Bokobza et al. investigated SBR polymer nanocomposites containing MWCNTs and carbon black using Raman spectroscopy and discussed the dispersion of the fillers [47]. Although the study was important, it did not provide new insights into the structure of SBR/MWCNT nanocomposites. SBR/MWCNT nanocomposites containing 1 phr MWCNTs were generous gifts from Professor L. Bokobza (ESPCI ParisTech, Paris, France). (The unit “phr” stands for parts per hundred parts of number by weight.)

Figure 4.11a–c shows Raman spectra of pure SBR, pure MWCNTs, and 1 wt % SBR/MWCNT nanocomposites, respectively [46]. A comparison of the three spectra in Figure 4.11 reveals that bands at 2698, 1604, and 1354  $\text{cm}^{-1}$  in the Raman spectrum of SBR/MWCNTs are due to the G', G, and D bands, respectively, of the MWCNTs [48]. Raman bands at 2990, 1668, and 1641  $\text{cm}^{-1}$  in the same spectrum arise from the vinyl C–H stretching and *trans* and *cis* C=C stretching modes of SBR, respectively [49]. A Raman band at 3064  $\text{cm}^{-1}$  and those at 1032 and 1004  $\text{cm}^{-1}$  are assigned to the aromatic C–H stretching and the phenyl ring modes of SBR, respectively, and that a Raman band at



**FIGURE 4.11**

Raman spectra of (a) pure SBR, (b) pure MWCNTs, and (c) 1 wt% SBR/MWCNT nanocomposites.

*Ref. [46]. Copyright 2013. Reprinted with permission from American Chemical Society.*

2906  $\text{cm}^{-1}$  is due to aliphatic C–H groups. Table 4.1 summarizes the assignment of Raman bands of 1 phr SBR/MWCNT nanocomposites [46].

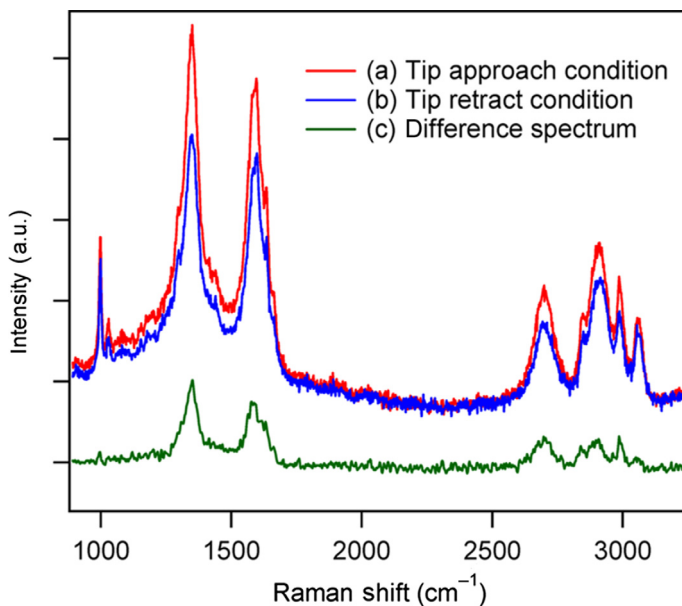
It is noted that the G band in the SBR/MWCNT spectrum shifted to a higher wave number compared with that in the pure MWCNT spectrum. A shift in the G band of a Raman spectrum of CNTs has been ascribed to the shrinkage of the CNTs induced by the pressure from the matrix of the polymer [33,40].

Raman spectra of SBR/MWCNT nanocomposites observed under tip-approaching and tip-retracted conditions are shown in Figure 4.12a and b, respectively. A TERS spectrum was calculated by subtracting the spectrum observed under tip-retracted conditions from that collected under tip-approaching conditions as shown in Figure 4.12c. Figure 4.13a and b compares normal Raman and TERS spectra of 1 wt% SBR/MWCNT nanocomposites collected at the same eight points: Position (1), (2), (3), (4), (5), (6), (7), and (8) [46].

The Raman spectra in Figure 4.13a show point-dependent changes. For example, at Position 7, the Raman signals assigned to SBR are relatively strong, while the spectrum collected at Position 3 yield relatively strong MWCNT signals. However, the point-dependent spectral differences are rather small, and one cannot extract structural information or information about the interaction at the interface between the MWCNTs and the SBR from the Raman spectra in Figure 4.13a.

**Table 4.1** Assignment of Raman Bands of 1 phr SBR/MWCNT Nanocomposites [46]

Wave Number (cm <sup>-1</sup> )	Assignment
1004	Phenyl ring breathing SBR (phenyl)
1032	Phenyl ring stretching SBR (phenyl)
1354	D band MWCNTs
1604	G band MWCNTs
1641	<i>Cis</i> C=C stretching SBR (C=C)
1668	<i>Trans</i> C=C stretching SBR (C=C)
2698	G'-band MWCNTs
2847	Aliphatic CH symmetric stretching SBR (main chain)
2906	Aliphatic CH asymmetric stretching SBR (main chain)
2990	Vinyl C-H stretching SBR (C=C)
3064	Aromatic C-H stretching SBR (phenyl)

**FIGURE 4.12**

Raman spectra of SBR/MWCNT nanocomposites measured under (a) tip-approaching and (b) tip-retracted conditions. (c) Difference spectrum calculated by subtracting spectrum (b) from spectrum (a) which is the TERS spectrum.

Ref. [46]. Copyright 2013. Reprinted with permission from American Chemical Society.

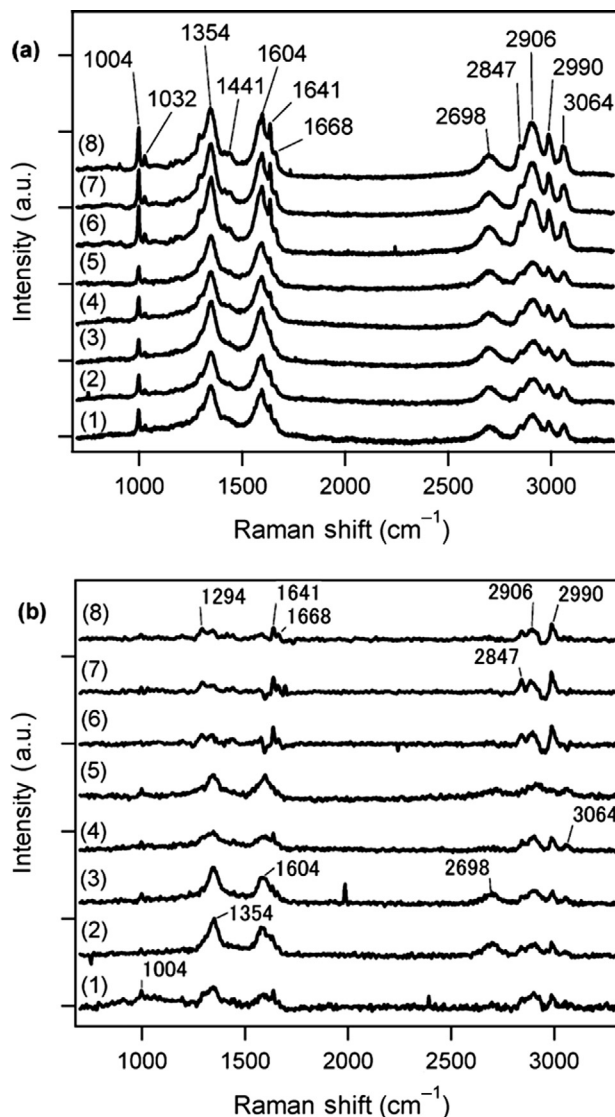


**FIGURE 4.13**

(a) Raman and (b) TERS spectra of 1 wt% SBR/MWCNT nanocomposites measured at the eight points.

*Ref. [46]. Copyright 2013. Reprinted with permission from American Chemical Society.*

The TERS spectra measured at the eight points are markedly different from each other. For example, in the spectrum at Position 7, TERS signals due to SBR were observed at 2990, 2904, 2847, 1668, and 1641  $\text{cm}^{-1}$  but a TERS signal at 1354  $\text{cm}^{-1}$  assigned to MWCNTs (D bands) is considerably weaker than the corresponding peak in the Raman spectrum.

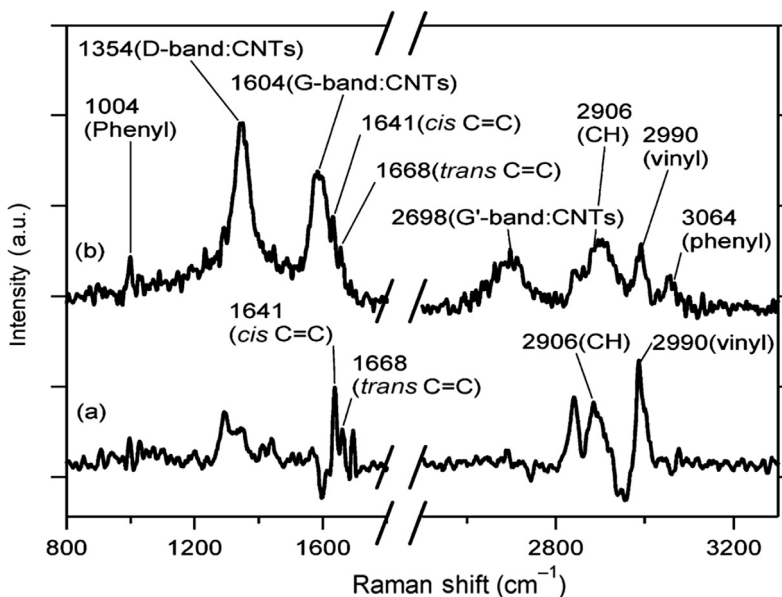


**FIGURE 4.14**

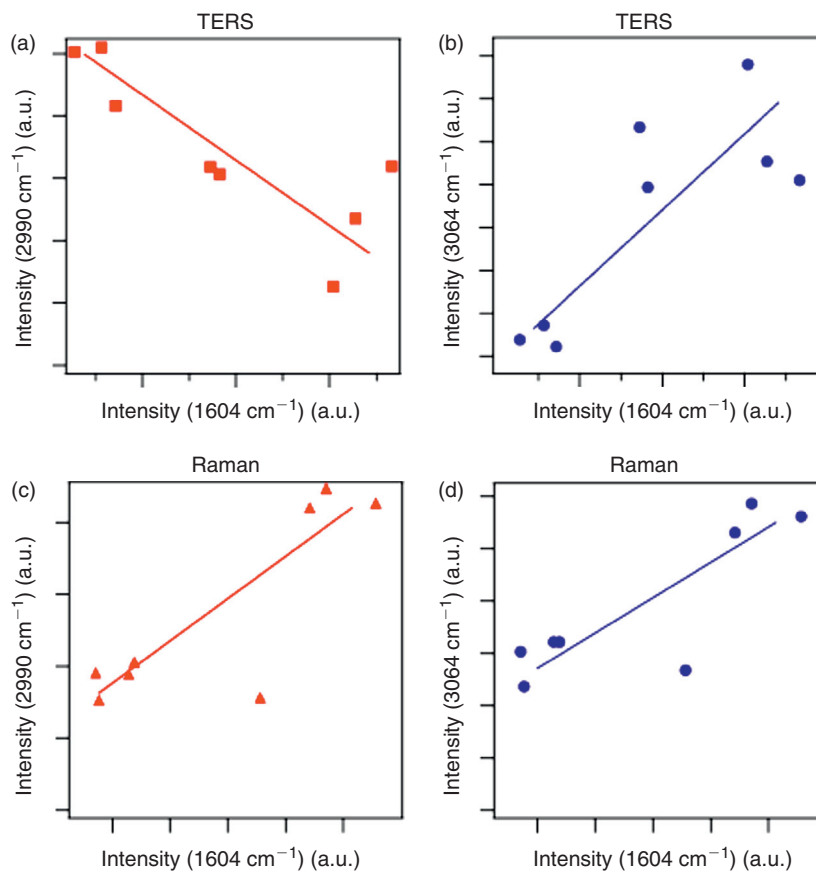
Enlarged TERS spectra of 1 wt% SBR/MWCNTs from Figure 4.12: (a) spectrum (7), (b) spectrum (3).

*Ref. [46]. Copyright 2013. Reprinted with permission from American Chemical Society.*

Moreover, those due to the G band ( $1604\text{ cm}^{-1}$ ) and G' band ( $2698\text{ cm}^{-1}$ ) were not observed in the spectrum collected at Position 7. On the other hand, in the TERS spectrum measured at Position 3, signals arising from SBR are observed at  $3064$ ,  $2990$ ,  $2904$ , and  $2847\text{ cm}^{-1}$  and those due to MWCNTs were identified at  $2698$ ,  $1604$ , and  $1354\text{ cm}^{-1}$ .

The MWCNT content, at 1 wt%, was considerably lower than the polymer content. Therefore, it was expected that there would be areas containing only SBR as well as areas that contained both SBR and MWCNTs. It is very likely that the TERS measurements detected the distribution clearly.

Figure 4.14 shows the  $1800 - 800$  and  $3200 - 2500\text{ cm}^{-1}$  regions of TERS spectra obtained at Positions 7 and 3, respectively, in Figure 4.13b [46]. In the corresponding Raman spectra for Positions 7 and 3 in Figure 4.11a, the signal intensity at  $1004\text{ cm}^{-1}$  was stronger than those at  $1668$  and  $1641\text{ cm}^{-1}$ . On the other hand, in the TERS spectra, the latter two signals are stronger than the former signal (Figure 4.13b). Moreover, in the higher-wave number region, four SBR peaks were observed at  $3064$ ,  $2990$ ,  $2906$ , and  $2847\text{ cm}^{-1}$  in the normal Raman spectrum (Figure 4.13a). In contrast, in the TERS spectrum in Figure 4.11b, the signal at  $3064\text{ cm}^{-1}$  was nearly missing, and the relative intensity of the signal at  $2990\text{ cm}^{-1}$  became stronger than that of the corresponding signal in the Raman spectrum. The  $3064$  and  $1004\text{ cm}^{-1}$  bands that were

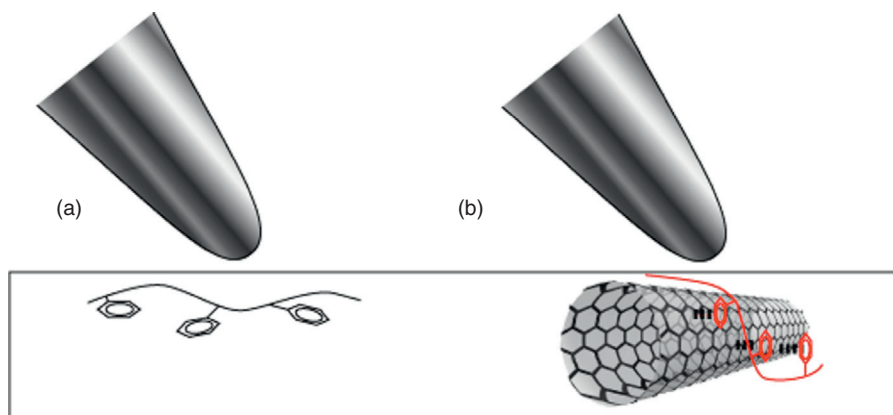
**FIGURE 4.15**

Peak intensity plots of (a) the vinyl band ( $2990\text{ cm}^{-1}$ ) versus the G band ( $1604\text{ cm}^{-1}$ ) in the TERS spectrum, (b) the phenyl band ( $3064\text{ cm}^{-1}$ ) versus the G band ( $1604\text{ cm}^{-1}$ ) in the TERS spectrum, (c) the vinyl band ( $2990\text{ cm}^{-1}$ ) versus the G band ( $1604\text{ cm}^{-1}$ ) in the normal Raman spectrum, and (d) the phenyl band ( $3064\text{ cm}^{-1}$ ) versus the G band ( $1604\text{ cm}^{-1}$ ) in the normal Raman spectrum.

*Ref. [46]. Copyright 2013. Reprinted with permission from American Chemical Society.*

relatively weak in the TERS spectrum arose from the aromatic C–H groups and the phenyl rings of the polymer side chains, respectively.

In contrast to Figure 4.14a, it is noted in Figure 4.14b that the TERS signals due to MWCNTs appear strongly at  $2698$ ,  $1604$ , and  $1354\text{ cm}^{-1}$ , and a peak at  $3064\text{ cm}^{-1}$  due to the clearly observed aromatic C–H. Figure 4.15 plots the intensities of the  $3064$  and  $2990\text{ cm}^{-1}$  bands versus that of the  $1604\text{ cm}^{-1}$  band. Figure 4.15a and b is concerned with the TERS spectra, while Figure 4.15c and d is from the Raman spectra.

**FIGURE 4.16**

Schematic diagram of the surface structure of SBR/MWCNT nanocomposites: (a) far from and (b) near the CNT area. At the interface between the polymer and the filler, the phenyl ring should be oriented perpendicular to the surface through a  $\pi-\pi$  interaction between the CNT and the phenyl ring.

*Ref. [46]. Copyright 2013. Reprinted with permission from American Chemical Society.*

It is noted from [Figure 4.15a and b](#) that in the TERS spectra, the  $2990\text{ cm}^{-1}$  signal (vinyl) decreases as the  $1604\text{ cm}^{-1}$  signal (G band) increases ([Figure 4.13a](#)), while the signal intensity at  $3064\text{ cm}^{-1}$  (phenyl) increases as the G-band signal increases ([Figure 4.13b](#)). In the Raman spectra, both signals at  $2990$  (vinyl) and  $3064$  (phenyl)  $\text{cm}^{-1}$  increase with an increase in the intensity of the  $1604\text{ cm}^{-1}$  signal ([Figure 4.13c and d](#)). These results suggest that the local distribution of polymer nanocomposites at the interface between the polymer and the filler is different from that of polymer areas without CNTs. The depth resolution of TERS is much smaller than the spatial resolution ( $\sim 100\text{ nm}$ ). It was reported that the intensity of the TERS signal decays exponentially from a surface with a decay length of  $2.8\text{ nm}$  [50]. Thus, the TERS experiments seem to measure a region several nanometers in depth from the surface of the nanocomposites.

The TERS spectral differences generated by SBR between the spectra in [Figure 4.15a and b](#) suggested that the local orientation of the polymer nanocomposites at the interface between the polymer and the filler is different from that of the polymer areas without MWCNTs in the surface region.

Based on the observed TERS spectral variations induced by SBR, Suzuki et al. described the following possibility. [Figure 4.16](#) illustrates a schematic diagram of the expected surface structure of SBR/MWCNT nanocomposites; (a) far from and (b) near CNT area. In the polymer nanocomposites areas where MWCNTs are not located, it is very likely that the  $\text{C}=\text{C}$  groups and the phenyl rings would be parallel to the polymer surface. In this orientation, the  $\text{C}=\text{C}$  signal would be much more enhanced than that of the phenyl ring. On the other

hand, at the interface of the polymer and the filler (Figure 4.16b), MWCNTs seem to have a significant interaction with the phenyl rings of the polymer through  $\pi$ - $\pi$  interactions. These interactions induce differences in the orientations of the polymer chain and its side residue. The orientation of the phenyl rings at the interface may be perpendicular to the surface because of the  $\pi$ - $\pi$  interaction between the CNTs and the phenyl rings shown in Figure 4.16b.

---

## 4.4 CONCLUSIONS

The above three studies demonstrated that Raman and TERS spectroscopy has great potential in exploring interactions at interfaces in polymer nanocomposites. TERS spectroscopy is particularly useful. We measured TERS spectra of SBR/MWCNT nanocomposites at different positions and observed marked position-dependent spectral variations. In the TERS spectra, the relative intensities of the MWCNT and SBR bands changed from place to place, and the relative intensities of the vinyl and phenyl bands also changed by location. The former finding reflects the dispersion of MWCNTs in the polymer nanocomposites, and the latter finding suggests that the  $\pi$ - $\pi$  interaction between the phenyl rings and MWCNTs affects the orientation of the phenyl rings, leading to a modification of the local orientation of the polymer chains.

---

## REFERENCES

- [1] Terekhov SV, Obratsova ED, Lobach AS, Konov VI. Laser heating method for estimation of carbon nanotube purity. *Appl Phys A: Mater Sci Process* 2002;74:393–6.
- [2] Zhang Y, Shi Z, Gu Z, Iijima S. Structure modification of single-wall carbon nanotubes. *Carbon* 2000;38:2055–9.
- [3] Alvarez L, Righi A, Guillard T, Rols S, Anglaret E, Laplaze D, et al. Resonant Raman study of the structure and electronic properties of single-wall carbon nanotubes. *Chem Phys Lett* 2000;316:186–90.
- [4] Ghislandi M, Hoffmann GG, Tkalya E, Xue LJ, De With G. Tip-enhanced Raman spectroscopy and mapping of graphene sheets. *Appl Spectrosc Rev* 2012;47:371–81.
- [5] Wang P, Zhang D, Li L, Li Z, Zhang L, Fang Y. Reversible defect in graphene investigated by tip-enhanced Raman spectroscopy. *Plasmonics* 2012;7:555–61.
- [6] Hayazawa N, Yano T, Watanabe H, Inouye Y, Kawata S. Detection of an individual single-wall carbon nanotube by tip-enhanced near-field Raman spectroscopy. *Chem Phys Lett* 2003;376:174–80.
- [7] Barraza HJ, Pompeo F, O'Rear EA, Resasco DE. SWNT-filled thermoplastic and elastomeric composites prepared by miniemulsion polymerization. *Nano Lett* 2002;2:797–802.
- [8] Bokobza L. Vibrational spectroscopic and mechanical investigation of carbon nanotube-reinforced styrene-butadiene rubbers. *Macromol Symp* 2011;305:1–9.

- [9] Zhao Q, Wood JR, Wagner HD. Using carbon nanotubes to detect polymer transitions. *J Polym Sci, Part B: Polym Phys* 2001;39:1492–5.
- [10] Cooper CA, Young RJ, Halsall M. Investigation into the deformation of carbon nanotubes and their composites through the use of Raman spectroscopy. *Composites Part A* 2001;32:401–11.
- [11] Bailo E, Deckert V. Tip-enhanced Raman scattering. *Chem Soc Rev* 2008;37:921–30.
- [12] Wang R, Wang J, Hao FH, Zhang MQ, Tian Q. Tip-enhanced Raman spectroscopy with silver-coated optical fiber probe in reflection mode for investigating multiwall carbon nanotubes. *Appl Opt* 2010;49:1845–8.
- [13] Itoh T, Biju V, Ishikawa M, Kikkawa Y, Hashimoto K, Ikehata A, et al. Surface-enhanced resonance Raman scattering and background light emission coupled with plasmon of single Ag nanoaggregates. *J Chem Phys* 2006;124 134708-1-6.
- [14] Doering WE, Nie SM. Single-molecule and single-nanoparticle SERS: examining the roles of surface active sites and chemical enhancement. *J Phys Chem B* 2002;106:311–17.
- [15] Yano TA, Inouye Y, Kawata S. Nanoscale uniaxial pressure effect of a carbon nanotube bundle on tip-enhanced near-field Raman spectra. *Nano Lett* 2006;6:1269–73.
- [16] Wu X, Zhang M, Wang J, Tian Q. Experimental research on double-walled carbon nanotubes using tip-enhanced Raman spectroscopy. *J Korean Phys Soc* 2010;56:1103–8.
- [17] Domke KF, Zhang D, Pettinger B. Tip-enhanced Raman spectra of picomole quantities of DNA nucleobases at Au(111). *J Am Chem Soc* 2007;129:6708–9.
- [18] Bethune DS, Johnson RD, Salem JR, Devries MS, Yannoni CS. Atoms in carbon cages: the structure and properties of endohedral fullerenes. *Nature* 1993;366:123–8.
- [19] Popov VN. Carbon nanotubes: properties and application. *Mater Sci Eng, R* 2004;43:61–102.
- [20] Sgobba V, Guldi DM. Carbon nanotubes—electronic/electrochemical properties and application for nanoelectronics and photonics. *Chem Soc Rev* 2009;38:165–84.
- [21] Krishnan A, Dujardin E, Ebbesen TW, Yianilos PN, Treacy MMJ. Young's modulus of single-walled nanotubes. *Phys Rev B* 1998;58:14013–19.
- [22] Falvo MR, Clary GJ, Taylor RM, Chi V, Brooks FP, Washburn S, et al. Bending and buckling of carbon nanotubes under large strain. *Nature* 1997;389:582–4.
- [23] McNally T, Pötschke P. Polymer-carbon nanotube composites. UK: Woodhead Publishing; 2011.
- [24] Coleman JN, Khan U, Blau WJ, Gun'ko YK. Small but strong: a review of the mechanical properties of carbon nanotube–polymer composites. *Carbon* 2006;44:1624–52.
- [25] Kanzaki K, Suzuki S, Inokawa H, Ono Y, Vijayaraghavan A, Kobayashi Y. Mechanism of metal-semiconductor transition in electric properties of single-walled carbon nanotubes induced by low-energy electron irradiation. *J Appl Phys* 2007;1017 034317-1-4.
- [26] Pötschke P, Brunig H, Janke A, Fischer D, Jehnichen D. Orientation of multiwalled carbon nanotubes in composites with polycarbonate by melt spinning. *Polymer* 2005;46:10355–63.
- [27] Bokobza L. Multiwall carbon nanotube elastomeric composites: a review. *Polymer* 2007;48:4907–20.

- [28] Zhang G, Shi Q. Impacts of image force on the Schottky barrier height at metal-carbon nanotube contacts. *Appl Phys Lett* 2012;100 173104-1-3.
- [29] Akita S, Nishijima H, Nakayama Y, Tokumasu F, Takeyasu K. Carbon nanotube tips for a scanning probe microscope: their fabrication and properties. *J Phys D: Appl Phys* 1999;32:1044–8.
- [30] Rao AM, Eklund PC, Bandow S, Thess A, Smalley RE. Evidence for charge transfer in doped carbon nanotube bundles from Raman scattering. *Nature* 1997;388:257–9.
- [31] Li HD, Yue KT, Lian ZL, Zhan YL, Zhou X, Zhang SL, et al. Temperature dependence of the Raman spectra of single-wall carbon nanotubes. *Appl Phys Lett* 2000;76:2053–5.
- [32] Yan X, Itoh T, Kitahama Y, Suzuki T, Sato H, Miyake T, et al. A Raman spectroscopy study on single-wall carbon nanotube/polystyrene nanocomposites: mechanical compression transferred from the polymer to single-wall carbon nanotubes. *J Phys Chem C* 2012;116:17897–903.
- [33] Yan X, Suzuki T, Kitahama Y, Sato H, Itoh T, Ozaki Y. A study on the interaction of single-walled carbon nanotubes (SWCNTs) and polystyrene (PS) at the interface in SWCNT–PS nanocomposites using tip-enhanced Raman spectroscopy. *Phys Chem Chem Phys* 2013;15:20618–24.
- [34] Jorio A, Pimenta MA, Souza AG, Saito R, Dresselhaus G, Dresselhaus MS. Characterizing carbon nanotube samples with resonance Raman scattering. *New J Phys* 2003;5 139-1-17.
- [35] Brown SDM, Jorio A, Corio P, Dresselhaus MS, Dresselhaus G, Saito R, et al. Origin of the Breit–Wigner–Fano line shape of the tangential G-band feature of metallic carbon nanotubes. *Phys Rev B* 2001;63 155414-1-8.
- [36] Pimenta MA, Marucci A, Empedocles SA, Bawendi MG, Hanlon EB, Rao AM, et al. Raman modes of metallic carbon nanotubes. *Phys Rev B* 1998;58:16016–19.
- [37] Rao AM, Chen J, Richter E, Schlecht U, Eklund PC, Haddon RC, et al. Effect of van der Waals interactions on the Raman modes in single walled carbon nanotubes. *Phys Rev Lett* 2001;86:3895–8.
- [38] Lourie O, Wagner HD. Evaluation of Young’s modulus of carbon nanotubes by micro-Raman spectroscopy. *J Mater Res* 1998;13:2418–22.
- [39] Wood JR, Frogley MD, Meurs ER, Prins AD, Peijs T, Dunstan DJ, et al. Mechanical response of carbon nanotubes under molecular and macroscopic pressures. *J Phys Chem B* 1999;103:10388–92.
- [40] Beigbeder A, Linares M, Devalckenaere M, Degee P, Claes M, Beljonne D, et al. CH- $\pi$  interactions as the driving force for silicone-based nanocomposites with exceptional properties. *Adv Mater* 2008;20:1003–7.
- [41] Bokobza L, Rahmani M. Carbon nanotubes: exceptional reinforcing fillers for silicone rubbers. *Kautsch GummiKunstst* 2009;62:112–17.
- [42] Loa I.J. Raman spectroscopy on carbon nanotubes at high pressure. *Raman Spectrosc* 2003;34:611–27.
- [43] Srivastava I, Mehta RJ, Yu Z, Schadler L, Koratkar N. Raman study of interfacial load transfer in graphene nanocomposites. *Appl Phys Lett* 2011;98 063102-1-3.
- [44] Dresselhaus MS, Dresselhaus G, Jorio A, Souza AG, Saito R. Raman spectroscopy on isolated single wall carbon nanotubes. *Carbon* 2002;40:2043–61.
- [45] Sandler J, Shaffer MSP, Windle AH, Halsall MP, Montes-Moran MA, Cooper CA, et al. Variations in the Raman peak shift as a function of hydrostatic pressure

- for various carbon nanostructures: a simple geometric effect. *Phys Rev B* 2003;67:035417-1-8.
- [46] Suzuki T, Yan X, Kitahama Y, Sato H, Itoh T, Miura T, et al. Tip-enhanced Raman spectroscopy study of local interactions at the interface of styrene–butadiene rubber/multiwalled carbon nanotube nanocomposites. *J Phys Chem C* 2013;117:1436–40.
- [47] Bokobza L, Rahmani M, Belin C, Bruneel JL, EI Bounia NEJ. Blends of carbon blacks and multiwall carbon nanotubes as reinforcing fillers for hydrocarbon rubbers. *Polym Sci B: Polym Phys* 2008;46:1939–51.
- [48] Jorio A, Saito R, Dresselhaus G, Dresselhaus MS. Determination of nanotubes properties by Raman spectroscopy. *Philos Trans R Soc, A* 2004;362:2311–36.
- [49] Martínez-Barrera G, López H, Castaño VM, Rodríguez R. Studies on the rubber phase stability in gamma irradiated polystyrene-SBR blends by using FT-IR and Raman spectroscopy. *Phys Chem* 2004;69:155–62.
- [50] Ichimura T, Fujii S, Verma P, Yano T, Inouye Y, Kawata S. Subnanometric near-field Raman investigation in the vicinity of a metallic nanostructure. *Phys Rev Lett* 2009;102:186101-1-4.

## 5

## Infrared and Fourier transform infrared spectroscopy for nanofillers and their nanocomposites

**B. Jaleh and P. Fakhri***Department of Physics, Bu Ali Sina University, Hamedan, Iran*

---

**5.1 INTRODUCTION**

Infrared (IR) spectroscopy is one of the most important techniques available for materials analysis. It is based on the absorption of electromagnetic (EM) radiation of a specified motion of chemical bonds by matter. An IR spectrum is commonly obtained by passing IR radiation through a sample and determining what fraction of the incident radiation is absorbed at a particular energy level. IR spectroscopy is advantageous as an analytical tool for polymers, because it provides a wealth of information about complex macromolecules with respect to composition, structure, conformation, and intermolecular interactions by utilizing simple sampling techniques [1–4].

---

**5.2 INTRODUCTION TO IR SPECTROSCOPY**

The IR spectrum of a sample is recorded by passing a beam of IR light through the sample. The IR region can be divided into three main regions: the far-IR ( $<400\text{ cm}^{-1}$ ), the mid-IR ( $4000\text{--}400\text{ cm}^{-1}$ ), and the near-IR ( $14,000\text{--}4000\text{ cm}^{-1}$ ). The mid IR region is commonly used for IR spectroscopy because the most compounds show characteristic absorption/emission within this region. This region can be divided into the functional group region ( $4000\text{--}1400\text{ cm}^{-1}$ ) and the fingerprint region ( $400\text{--}1400\text{ cm}^{-1}$ ). The functional group regions may be similar for two different molecules because they have similar functional groups, but the spectra for different molecules are usually quite different in the fingerprint region [2].

### 5.2.1 BASIS OF INFRARED SPECTROSCOPY

The vibrations of the atoms of a molecule are the basis of IR spectroscopy. There are two main types of molecular vibrations, stretching and bending. In stretching mode, bond length changes, and can either be symmetric or asymmetric. Bending vibration changes the bond angle. As IR radiation is passed through a sample it can be absorbed by the molecule when the frequency of the IR is equal to the frequency of the specific bond vibration of the molecule. Therefore, the energy of the absorbed IR light that corresponds to specific values can identify various functional groups within a molecule. Thus, IR is useful technique in determining chemical structure. The IR spectrum is a plot of % transmittance (or absorbance) of the radiation through the molecule versus wave number of the radiation. A peak on the plot represents absorption at a specific wave number [2,3].

### 5.2.2 INFRARED INSTRUMENTS

There are two types of IR spectrophotometer: dispersive (IR) and interferometric (Fourier transform infrared, or FTIR).

#### 5.2.2.1 Dispersive IR spectrometers

The traditional IR instruments were dispersive. An IR spectrometer consists of three basic components: radiation source, monochromator, and detector. The monochromator is a device used to disperse a broad spectrum of radiation and provide a continuous calibrated series of EM energy bands of determinable wavelength or frequency range. Prisms or gratings are the dispersive components used in conjunction with variable-slit mechanisms, mirrors, and filters. Dispersive spectrometers often have a double-beam arrangement in which radiation from a source is divided into two beams. One beam will pass through the sample, while the other beam will pass through a reference species. These two beams are reflected to a chopper to moderate the energy reaching the detector, and directed to a diffraction grating. The grating or prism separates the wavelengths of radiation into individual wavelength components and directs specific spectral elements through a slit to the detector. Then, by moving the grating to select the wavelength after passing through the sample, the IR spectrum is obtained [3,4].

#### 5.2.2.2 Interferometric IR spectrometers: FTIR

FTIR spectrometers have recently replaced dispersive instruments for most applications. There are three basic spectrometer components in an FTIR system: radiation source, interferometer, and detector. The major difference between an FTIR spectrometer and a dispersive IR spectrometer is the interferometer. The most commonly used interferometer is a Michelson interferometer. The incoming light is split inside an interferometer to two beams so that the paths of the two beams are different. One beam going to an internal fixed mirror and the other to a moving mirror. After reflection, the Michelson interferometer recombines the two

beams to produce an interference pattern and direct them to the detector. Then, it is necessary to perform a mathematical transform operation (a Fourier transform) on the data to present it in a usable interface [3,4].

### 5.2.2.3 Advantages of FTIR over dispersive IR

Currently, dispersive instruments are used only in selected applications due to the fact that interferometric instruments have a number of advantages for most applications. There are two significant advantages for a FTIR spectrometer over dispersive instruments:

1. The multiplex advantage: This advantage is due to an improvement in the signal-to-noise per unit time. The signal-to-noise ratio is a measure of the quality of a peak that is proportional to the square root of the number of scans used to measure a spectrum. Many FTIR instruments measure 100 scans in about 2 min that result in an improvement in spectral quality. Scanning a sample with a conventional IR spectrometer over the whole spectrum typically takes 30–60 min.
2. The throughput advantage: Throughput is a measure of the amount of light from the source that reaches to the detector. In a dispersive instrument, light may pass through slits, prisms, and gratings that decrease the intensity of the beam and thus reduce throughput. In an FTIR, the interferometer throughput is determined only by the diameter of the collimated beam coming from the source [1,3].

The FTIR spectrometer is now predominantly used because of these advantages.

## 5.2.3 SAMPLE PREPARATION

The first step for use of FTIR spectroscopy is to select appropriate sample preparation methods for different types of samples. The samples discussed in this chapter are in powder or film form. Therefore, the sample preparation method for these samples will be explained.

To prepare a powder sample and anything that can be ground into a powder for the FTIR spectrometer, the standard method is to use KBr. KBr is used because it is inert and transparent above  $400\text{ cm}^{-1}$  and is also low cost. At first, to minimize band distortion due to scattering of radiation, KBr should be ground for at least 1 min to reduce the particle size to less than  $2\text{ }\mu\text{m}$  in diameter. Then approximately 2 mg of the sample and 200 mg of KBr should be mixed together and ground. The mixture is then pressed hydraulically into transparent discs which can be measured directly. Then a background spectrum from the KBr should be obtained. The background spectrum will contain information about the species of gases and solvent molecules, which may then be subtracted from our sample spectrum in order to gain information about only the sample. The amount

of water in the disk should be kept to a minimum and spectra must be taken quickly to prevent the absorption of water from the atmosphere.

For film, such as polymeric and nanocomposite films, the sample can be measured directly. The film must not be too thick because thick films transmit too little radiation. A microtome equipped with a special knife can be used to prepare a thin film of the sample. For samples in film form, the background spectrum would be run on the empty film holder [1–3].

---

## 5.3 FTIR SPECTROSCOPY FOR NANOFILLERS AND THEIR NANOCOMPOSITES

Nanofillers and their nanocomposites' materials have recently received great attention in both scientific and industrial communities due to their extraordinary enhanced properties. However, from the experimental point of view, it is a great challenge to characterize the structure of filler and nanocomposites. One of the main processes to characterization is structure analysis that is carried out using a variety of microscopic and spectroscopic techniques such as x-ray diffraction (XRD), scanning electron microscopy (SEM), transmission electron microscopy (TEM), atomic force microscopy (AFM), scanning tunneling microscope (STM), UV-vis spectroscopy, and FTIR spectroscopy [5]. IR spectroscopy is widely used due to its many advantages such as: informative spectra, fast and easy spectra recording, relatively inexpensive nature, and that the minimum amount of material is required to yield a usable spectrum. Moreover, IR spectroscopy is almost universal. In addition, it is possible to obtain an IR spectrum from different types of samples including solids, liquids, and gases [1]. In this section FTIR spectroscopy has been extensively used in both qualitative and quantitative analyses of nanofillers and their polymer nanocomposites.

### 5.3.1 QUALITATIVE ANALYSIS

The qualitative aspects of IR spectroscopy are one of the most powerful attributes of this versatile analytical technique, where IR spectra are used to identify molecular structure (i.e., functional group and bond) qualitatively according to the characteristic frequencies. The vibrational spectrum of a molecule is considered to be a unique physical property and is characteristic of the molecule. As such, the IR spectrum can be used as a fingerprint for identification by the comparison of the spectrum from an unknown with previously recorded reference spectra. This is the basis of computer-based spectral searching. In the absence of a suitable reference database, it is possible to effect a basic interpretation of the spectrum from first principles, leading to characterization, and possibly even identification of an unknown sample. This first principles approach is based on the fact that structural features of the molecule, whether they are the

backbone of the molecule or the functional groups attached to the molecule, produce characteristic and reproducible absorptions in the spectrum. This information can indicate whether there is backbone to the structure and, if so, whether the backbone consists of linear or branched chains. Next, it is possible to determine if there is unsaturation and/or aromatic rings in the structure. Finally, it is possible to deduce whether specific functional groups are present. If detected, one can also determine local orientation of the group and its local environment and/or location in the structure. The origins of the sample, its pre-history, and the manner in which the sample is handled all have an impact on the final result [6].

However, it is not always possible to unequivocally identify a compound by examining its IR spectrum alone. It is normal to use IR spectroscopy in conjunction with other techniques, such as chromatographic methods, mass spectrometry, nuclear magnetic resonance (NMR) spectroscopy, and various other spectroscopic techniques [2].

In this chapter, FTIR spectroscopy is used for the characterization of nanofillers and nanocomposites. A variety of nanofillers—such as metal oxide nanoparticles, clay, carbonaceous nanofiller, and nanofiller synergy, along with their polymer nanocomposites—will be explored by FTIR spectroscopy based on the authors' research and the efforts of other researchers.

### 5.3.1.1 Nanofiller identification

#### 5.3.1.1.1 Metal oxides nanofiller

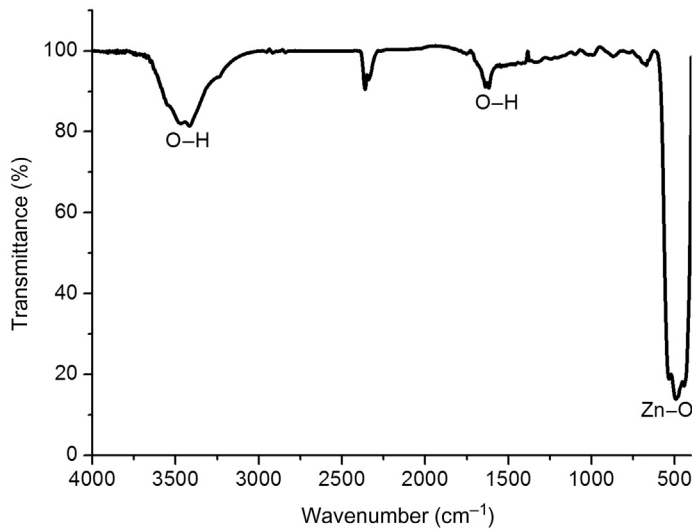
Oxides and hydroxides of metal nanoparticles generally give an absorption peak in the fingerprint region: that is, below a wavelength of  $1400\text{ cm}^{-1}$  arising from interatomic vibrations. In this section, the IR bands of a number of common classes of metal oxides nanofillers will be discussed.

- $\text{Fe}_3\text{O}_4$  nanoparticle

$\text{Fe}_3\text{O}_4$  nanoparticles were synthesized using a coprecipitation method, and then annealed at various temperatures between 50 and 850 °C for 1 h in air [7].  $\text{Fe}_3\text{O}_4$  is known as black iron oxide and is the oldest known magnetic oxide material.  $\gamma\text{-Fe}_2\text{O}_3$  is another kind of iron oxide that has the same crystalline structure as  $\text{Fe}_3\text{O}_4$ .  $\alpha\text{-Fe}_2\text{O}_3$  is the most frequent polymorph corundum-type crystal structure, having a rhombohedral-hexagonal shape.  $\text{Fe}_3\text{O}_4$  nanoparticles can be converted to  $\gamma\text{-Fe}_2\text{O}_3$  by annealing at 250 °C for 1 h, and then to  $\alpha\text{-Fe}_2\text{O}_3$  on annealing in the range of 550–650 °C [7]. In general, XRD can also be used to characterize the crystal structure of nanoparticles. However,  $\text{Fe}_3\text{O}_4$  and  $\gamma\text{-Fe}_2\text{O}_3$  have an extreme similarity in crystal structure, and XRD is not sensitive enough to differentiate between them. These two bands can be easily identified from their IR patterns [7]. FTIR spectroscopy is employed to illustrate phase transition of  $\text{Fe}_3\text{O}_4$  in oxidation processes. The characteristic peaks of  $\text{Fe}_3\text{O}_4$ ,  $\gamma\text{-Fe}_2\text{O}_3$ , and  $\alpha\text{-Fe}_2\text{O}_3$  are listed in Table 5.1.

**Table 5.1** Band Assignment in the FTIR Spectra of Iron Oxide

Iron Oxide	Assigned Vibrations ( $\text{cm}^{-1}$ )
$\text{Fe}_3\text{O}_4$	600, 440
$\gamma\text{-Fe}_2\text{O}_3$	639, 588
$\alpha\text{-Fe}_2\text{O}_3$	537, 458

**FIGURE 5.1**

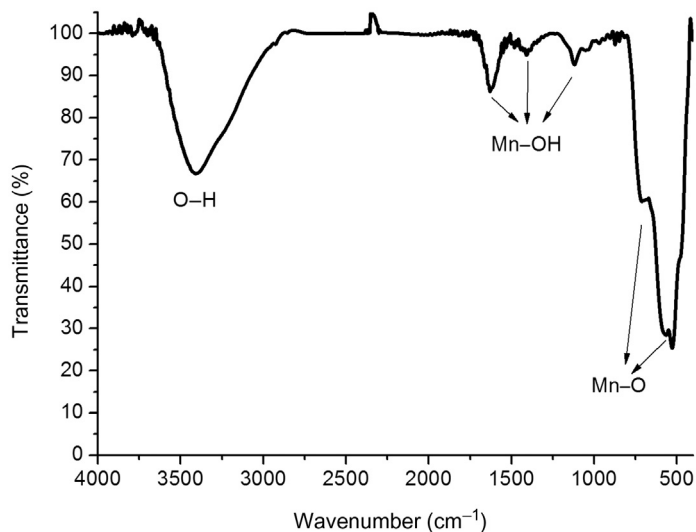
FTIR spectrum of ZnO nanoparticle.

- ZnO nanoparticle:

ZnO nanocrystal powders have been synthesized by using zinc acetate dehydrate as a precursor and sol-gel method [8]. The FTIR spectrum of ZnO nanoparticle in KBr matrix is shown in Figure 5.1. There is a broad band with very low intensity at  $3392\text{ cm}^{-1}$  corresponding to the vibration mode of water's OH group, which indicates the presence of a small amount of water adsorbed on the ZnO nanocrystal surface. The band at  $1608\text{ cm}^{-1}$  is due to the OH bending of water. A strong band at  $465\text{ cm}^{-1}$  is attributed to the Zn-O stretching band [9].

- $\text{MnO}_2$  nanocrystals:

$\gamma\text{-MnO}_2$  nanocrystals were prepared by solid-state reaction route [10]. Figure 5.2 shows the FTIR spectra of the  $\gamma\text{-MnO}_2$ . The band at  $3439\text{ cm}^{-1}$  should be attributed to the -OH stretching vibration, and the bands at 1644,

**FIGURE 5.2**

FTIR spectrum of MnO<sub>2</sub> nanoparticle.

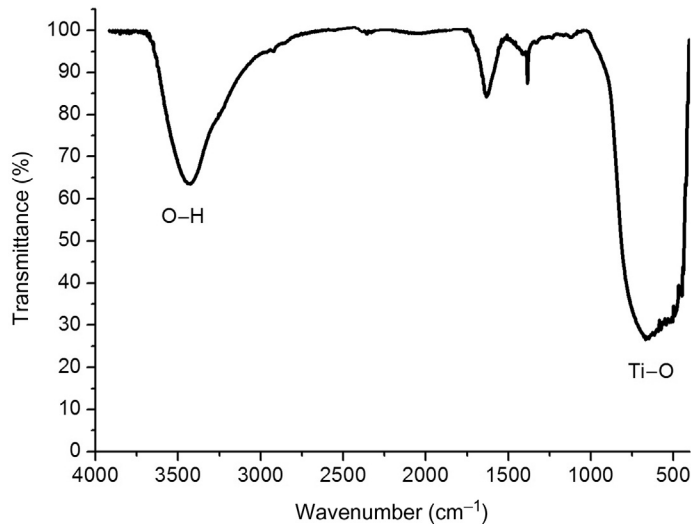
1430, and 1136 cm<sup>-1</sup> are usually attributed to the -OH bending vibrations combined with Mn atoms. While the bands at 560 and 530 cm<sup>-1</sup> should be ascribed to the Mn-O vibrations. The FTIR results suggest the presence of bound water in the MnO<sub>2</sub> structure, which is believed to be a typical characteristic of MnO<sub>2</sub> with  $\gamma$ -type structure [11].

- TiO<sub>2</sub> nanoparticle

The titanium dioxide (TiO<sub>2</sub>) nanoparticles catalyst was synthesized via sol-gel method. The FTIR spectrum of a TiO<sub>2</sub> nanoparticle is shown in Figure 5.3. Between 3800 to 3000 cm<sup>-1</sup> a broad band was observed which related to stretching hydroxyl (O-H), representing the water as moisture. The other peaks at 1635 cm<sup>-1</sup> were attributed to the stretching of titanium carboxylate, which stemmed from titanium tetra isopropoxide (TTIP) and ethanol. The peak between 800 and 450 cm<sup>-1</sup> was assigned to the Ti-O stretching bands [12].

#### 5.3.1.1.2 Clay

The IR spectra of clay minerals (which are not discussed in this chapter) show well-defined absorption bands corresponding to fundamental stretching and bending vibrations of their structural units: for example, OH and Si-O groups. The stretching and bending vibrations of OH groups absorb in the 3700–3500 and 950–650 cm<sup>-1</sup> regions, respectively. The Si-O stretching modes occur in the 1050–1000 cm<sup>-1</sup>, while the most intense bending bands appear in the 550–400 cm<sup>-1</sup> region [13].

**FIGURE 5.3**

FTIR spectrum of TiO<sub>2</sub> nanoparticle.

#### 5.3.1.1.3 Carbonaceous nanofiller

- Carbon nanotube (CNT)

Branca et al. [14] investigated the single-walled nanotubes (SWNTs) industrially produced and multiwalled nanotubes (MWNTs) they produced by FTIR spectroscopy. In the range between 700 and 2500 cm<sup>-1</sup> the two SWNT spectra present the same vibrational modes but shifted in energy and with different intensity. In particular, the peaks at 1110 cm<sup>-1</sup>, 1535 cm<sup>-1</sup>, and 1700 cm<sup>-1</sup> observed in the Aldrich sample are shifted to higher wave numbers in the CNTs-ILJIN sample by 25 cm<sup>-1</sup>, 20 cm<sup>-1</sup>, and 18 cm<sup>-1</sup>, respectively. Moreover, a very low shoulder is observable in both the spectra between 820 and 840 cm<sup>-1</sup>. This latter mode, together with the mode around 1540 cm<sup>-1</sup>, resembles the characteristic modes of graphite at 868 and 1590 cm<sup>-1</sup>. The FTIR investigation revealed the presence in all the spectra of strong structures near the graphite modes but shifted toward lower wave numbers.

- Graphite, graphene oxide (GO), reduced graphene oxide(rGO)

At times, surface modification of fillers is needed to promote better dispersion of fillers and to enhance the interfacial adhesion between the matrix and fillers. Graphene, a single hexagonally flat layer graphite sheet that consists of sp<sup>2</sup> carbon atoms covalently bonded in a honeycomb crystal lattice, has been intensively studied due to its unique structural and electronic properties and applications [15]. GO, a delaminated layer of graphite oxide, is typically prepared by the exhaustive oxidation of graphite to graphite oxide

using strongly acidic and oxidizing conditions, followed by the subsequent mechanical/chemical or thermal exfoliation of graphite oxide to GO sheets [15]. The GO consists of intact graphitic regions interspersed with  $sp^3$ -hybridized carbons containing carboxyl, hydroxyl, and epoxide functional groups on the edge, top, and bottom surface of each sheet and  $sp^2$ -hybridized carbons on the aromatic network. The presence of the abundant oxygen functional groups provides GO sheets with a large capability to load organic molecules through covalent or noncovalent approaches, facilitating the development of a broad, novel class of materials with enhanced properties which can even introduce new functionalities to GO sheets [16]. FTIR is a powerful technique to identify a functional group. While no significant peak was found in FTIR spectra of graphite, the presence of different type of oxygen functionalities in GO was confirmed at  $3400\text{ cm}^{-1}$  (O–H stretching vibrations), at  $1720\text{ cm}^{-1}$  (stretching vibrations from C–O), at  $1600\text{ cm}^{-1}$  (skeletal vibrations from unoxidized graphitic domains), at  $1220\text{ cm}^{-1}$  (C–OH stretching vibrations), and at  $1060\text{ cm}^{-1}$  (C–O stretching vibrations). The FTIR peak of reduced graphene shows that O–H stretching vibrations observed at  $3400\text{ cm}^{-1}$  was significantly reduced due to deoxygenation. However, stretching vibrations from C–O at  $1720\text{ cm}^{-1}$  were still observed and C–O stretching vibrations at  $1060\text{ cm}^{-1}$  became sharper, which was caused by remaining carboxyl groups even after hydrazine reduction [17].

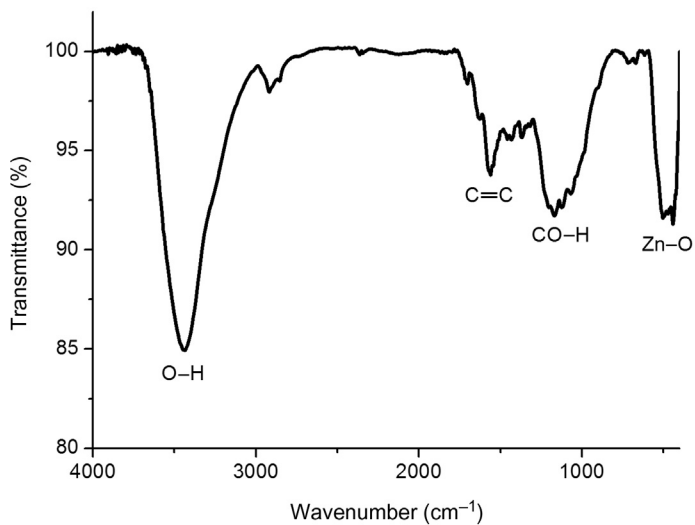
#### 5.3.1.1.4 Nanofiller synergy

Metal and metal oxide nanoparticles easily approach the surface of GOs because of the presence of carboxyl, hydroxyl, and epoxide functional groups on the edge, top, and bottom surface of each sheet. This nanocomposite can be used as a filler.

- GO/ZnO nanocomposite

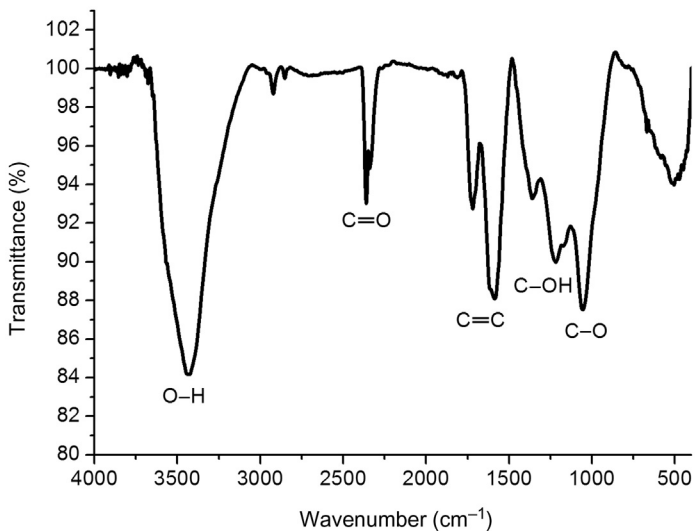
The GO/ZnO nanocomposite was synthesized with a weight ratio of (1:1) between GO and Zn. To synthesize GO/ZnO, zinc acetate ( $\text{Zn}(\text{CH}_3\text{CO}_2) \cdot 2\text{H}_2\text{O}$ ) and sodium hydroxide (NaOH) were successively dissolved in the GO suspension in water, followed by sonication. Then, this suspension stirred, filtered, and finally washed and dried the nanocomposite [18]. Figure 5.4 [18] shows the FTIR spectra of the GO/ZnO nanocomposite. The peaks at  $3431$ ,  $1582$ , and  $1211\text{ cm}^{-1}$  are related to O–H, C–C, and C–OH, respectively. In addition, the peak at  $431\text{ cm}^{-1}$  corresponds to Zn–O [18].

As described previously, FTIR spectra shows the chemical bonds and the molecular structure of the sample material. Therefore, FTIR is a failure analysis on a variety of materials such as metals because metal-metal bonds can not be observed by FTIR. For example, Figure 5.5 shows the FTIR spectra of the GO/Au nanoparticle nanocomposite [16]. As evidenced from the figure, only the peaks that are related to the GO were observed. Metal-metal bonds are often identified by their characteristic vibrations. They are usually observed in the Raman spectrum or in the Resonance Raman (RR) spectrum.

**FIGURE 5.4**

FTIR spectra of GO/ZnO nanocomposite.

*Ref. [18] Copyright 2014. Reprinted with permission from the Royal Society of Chemistry.*

**FIGURE 5.5**

FTIR spectra of GO/Au nanocomposite.

*Ref. [16] Copyright 2014. Reprinted with permission from the Royal Society of Chemistry.*

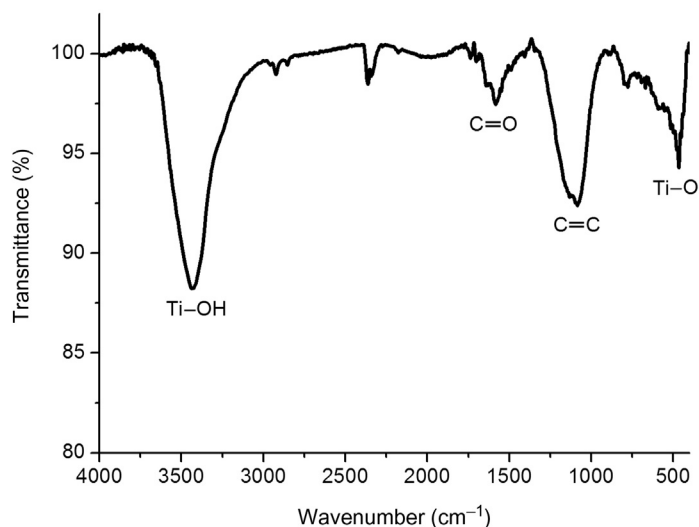


**FIGURE 5.6**

FTIR spectra of GAC/TiO<sub>2</sub> nanocomposite.

*Ref. [19] Copyright 2015. Reprinted with permission from Elsevier Ltd.*

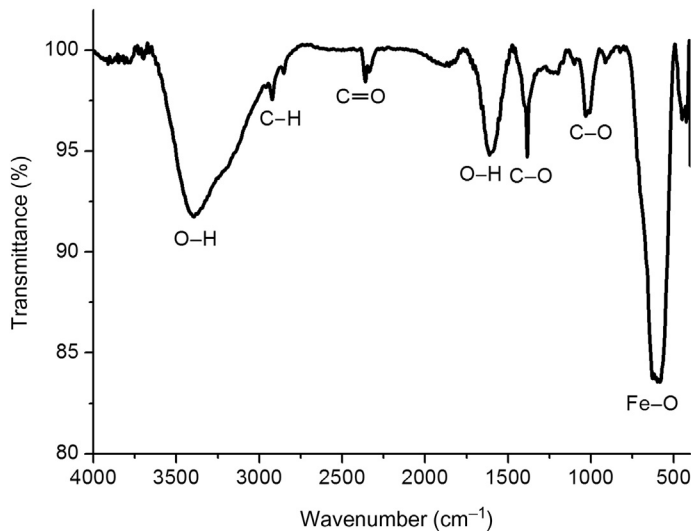
Therefore, FTIR spectroscopy is not sufficient to characterize this nanocomposite nanofiller, hence other characterization techniques such as XRD and UV spectroscopy can be employed. Raman spectroscopy was also used successfully to characterize metal-metal bonds.

- Granular activated carbon/TiO<sub>2</sub> (GAC/TiO<sub>2</sub>)

A dip-coating sol-gel impregnation technique was used to coat TiO<sub>2</sub> on granular activated carbon (GAC). **Figure 5.6** [19] shows the FTIR spectrum of GAC/TiO<sub>2</sub> nanocomposite. Two major bands in the region of 1000–1200 and 1200–1700 cm<sup>-1</sup> can be assigned to C–O–C, C–C, and C–O bonds associated with the GAC surface species. Furthermore, the spectrum of TiO<sub>2</sub> is also seen from the figure with a strong peak located between 3200 and 3600 cm<sup>-1</sup>, which can be attributed to the stretching vibration of Ti–OH bonds [19].

- GO/Fe<sub>3</sub>O<sub>4</sub>

The GO was prepared from graphite powder using a modified Hummers–Offeman method. Subsequently, the synthesis of the GO/Fe<sub>3</sub>O<sub>4</sub> nanocomposite was carried out by ultrasound-assisted coprecipitation of iron (II) and (III) chlorides in the presence of GO. **Figure 5.7** shows the FTIR spectrum of GO/Fe<sub>3</sub>O<sub>4</sub>. The peaks related to GO was observed and specified in spectrum. In addition, the band at 588 cm<sup>-1</sup>, which corresponds to the vibration of the Fe–O bonds in Fe<sub>3</sub>O<sub>4</sub> is observed [20].

**FIGURE 5.7**

FTIR spectra of GO/Fe<sub>3</sub>O<sub>4</sub> nanocomposite.

### 5.3.1.2 Polymer nanocomposite identification

Polymers play an enormously important role in modern society; these materials are fundamental to most aspects of modern life, such as building, communication, transportation, clothing, and packaging. Thus, an understanding of the structures and properties of polymers is vital. One of the fundamental problems in polymer science is the determination of the chemical structure of the repeat unit; this moiety determines all of the chemical properties such as reactivity, stability, and weatherability. Vibrational spectroscopic techniques are advantageous as a method of determining structure because the methods are applicable to all polymers regardless of the state of order. The IR spectroscopy method is accurate, faster than chemical analysis, and reduces exposure to irritating, toxic, and corrosive chemicals. The polymer nanocomposites are a mixture of polymers and fillers. If two components are immiscible, the IR spectrum should be the sum of the spectra of the two components. If the components are miscible, there is the possibility of chemical interactions between the individual polymer chains. Such interactions may lead to differences between the spectra of the polymers in the nanocomposite and the pure components. Generally, wave number shifts and band broadening are seen as evidence of chemical interactions between the components in a composite and are indicative of miscibility [2]. A variety of types of nanofillers can be used to prepare polymer nanocomposites with enhanced properties. Some examples are presented next:

- Polystyrene/TiO<sub>2</sub> (PS/TiO<sub>2</sub>)

Thin films of polystyrene (PS) and PS/TiO<sub>2</sub> nanocomposites were prepared by spin coating from a polystyrene solution in which TiO<sub>2</sub> nanoparticles were

dispersed by mechanical mixing. In the FTIR spectrum of PS and PS/TiO<sub>2</sub> nanocomposite [21], the main bands of PS are five peaks over the 2800–3100 cm<sup>-1</sup> range, which is attributed to C–H stretching vibrations in the main chain and in aromatic rings, and the peaks at 1601, 1492, 1451, 1027, 757, and 698 cm<sup>-1</sup> are due to deformation and skeletal vibrations of C–H in PS. The IR spectra of the pure PS film and low percentage PS/TiO<sub>2</sub> nanocomposite films (about 1%) were the same. It shows that the IR spectral characteristics of the polymeric matrix is not affected by the embedded TiO<sub>2</sub> particles, but at higher TiO<sub>2</sub> percentages, as expected, the characteristic peaks of TiO<sub>2</sub> appear in the spectrum of the PS/TiO<sub>2</sub> nanocomposite film.

The figure also shows the spectral bands at 3081, 3060, 3026, 1602, and 1493 cm<sup>-1</sup>, that are due to aromatic ring vibrations, and 2922, 2851, and 1452 cm<sup>-1</sup>, which are due to the aliphatic backbone of the PS macromolecule [21].

- Polycarbonate/TiO<sub>2</sub> (PC/TiO<sub>2</sub>) nanocomposite

Figure 5.8 shows the FTIR spectrum of PC and PC/TiO<sub>2</sub> nanocomposite films [22]. The characteristic peaks of PC were observed at 3684 cm<sup>-1</sup> (free alcohols), 3059 cm<sup>-1</sup> (C–H stretching), 2411 cm<sup>-1</sup>, and 2052 cm<sup>-1</sup> (asymmetric stretching mode of CO<sub>2</sub>), 1604 cm<sup>-1</sup> (phenyl ring stretching), 1512 cm<sup>-1</sup> (skeletal vibration of phenyl compounds), and 852 cm<sup>-1</sup> (bending mode of CO<sub>2</sub>) [22].

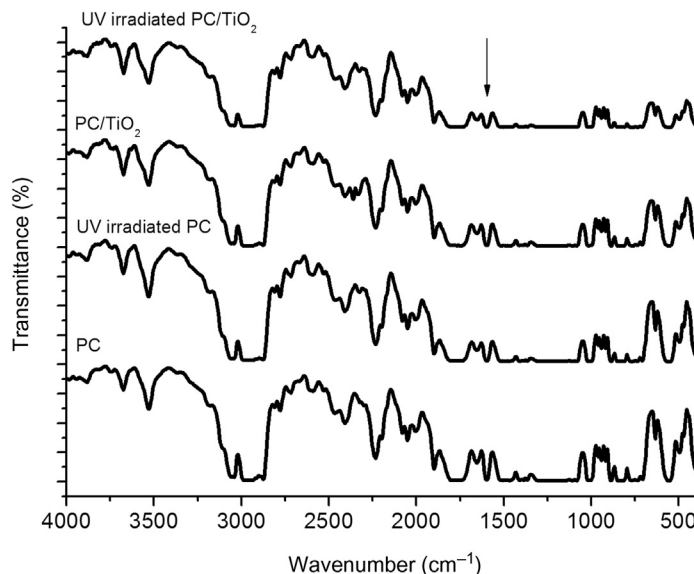


**FIGURE 5.8**

FTIR spectra of PC, UV irradiated PC, PC/TiO<sub>2</sub> nanocomposite, and UV irradiated PC/TiO<sub>2</sub> nanocomposite.

For the PC/TiO<sub>2</sub> sample, no new peak or peak shift was observed. Existence of TiO<sub>2</sub> nanoparticles in a sample lead to a decrease in intensity of peaks at 436 cm<sup>-1</sup> (Ti–O–Ti band), 650 cm<sup>-1</sup> (Ti–O band), and 1681 cm<sup>-1</sup> (C–O) band [22,23].

In addition, FTIR spectroscopy has been an important technique in the examination of physical and chemical characteristics that take place in the polymeric material due to irradiation. The spectra of bare PC, UV irradiated PC, PC/TiO<sub>2</sub> nanocomposite (1 wt.%), and UV irradiated PC/TiO<sub>2</sub> nanocomposite (1 wt.%) are included in Figure 5.8 [23]. When the samples were exposed to UV-radiation by 10 h, the intensity of the peak band to the carbonyl group (C–O) at 1681 cm<sup>-1</sup> decreases slightly, which shows the increases in absorbance of the peak. This decrease in intensity may be due to bond breakage at the carbonate site with the elimination of carbon monoxide/carbon dioxide [23].

- Polypropylene/clay nanocomposite

The nanocomposites obtained from clay minerals have intercalated or exfoliated structures when mixed with polymers, while, in the case of poor interactions, a conventional microcomposite structure is formed. Though the IR spectroscopy is often used to examine clay minerals, its use for characterizing nanoclay exfoliation has been explored. The shape of the Si–O band envelope of clay mineral in the 1350–750 cm<sup>-1</sup> region was used as an indicator of clay intercalation in a polymeric matrix. The complex Si–O stretching band of montmorillonite was composed of four components. Three of them (near 1015, 1045, and 1120 cm<sup>-1</sup>) were assigned to Si–O in plane vibrations, while the fourth one near 1070 cm<sup>-1</sup> was due to Si–O out of plane vibration [13].

### 5.3.2 QUANTITATIVE ANALYSIS

An important application of FTIR is quantitative spectroscopy, where IR spectra are used to determine the concentrations of chemical species in samples. Quantitative IR spectroscopy can provide certain advantages over other analytical techniques. This approach may be used for the analysis of one component of a mixture [1,2]. For quantitative analysis, the FTIR spectrum must be plotted in absorbance units, because absorbance is linearly proportional to concentration:

$$A = E_m C l \quad (5.1)$$

This formula is the Beer–Lambert law.  $E_m$  is the molar absorption coefficient,  $C$  is the concentration, and  $l$  is the path length through the sample. The height of a peak in an absorbance spectrum is proportional to concentration. The Beer–Lambert law shows that the intensity of an IR band is related to the amount of analyte present.

The absorbance is equal to the difference between the logarithms of the intensity of the light entering the sample ( $I_0$ ) and the intensity of the light transmitted ( $I_t$ ) by the sample [2]:

$$A = \log I_0 - I_t = \log \frac{I_0}{I_t} \quad (5.2)$$

Transmittance is defined as follows:

$$T = \frac{I_t}{I_0} \quad (5.3)$$

Thus:

$$A = -\log T \quad (5.4)$$

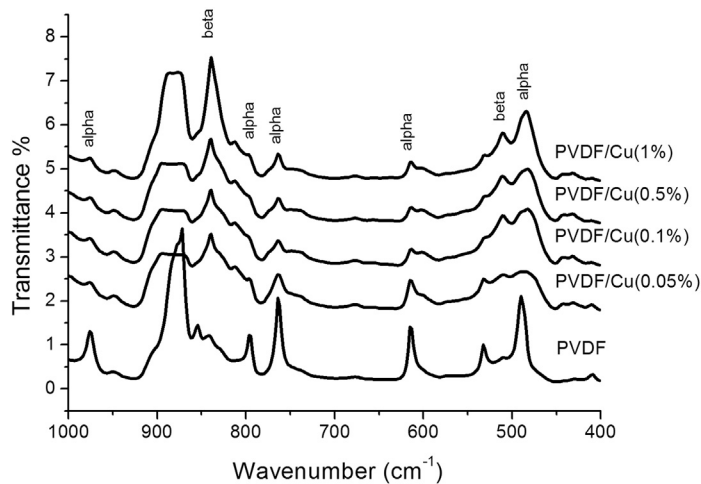
Absorbance and transmittance are mathematically related to each other. The spectra in this section will be plotted in absorbance units, and we will only focus on the fingerprint region of FTIR spectrum because the change in intensity of bands is typically found in this region.

- PVDF/Cu nanocomposite

Polyvinylidene fluoride (PVDF) and its copolymers have the best all-around electroactive properties, and are therefore the polymer of choice for the increasing number of possible applications [5–8]. This semicrystalline polymer shows a complex structure and can present five distinct crystalline phases include  $\alpha$ ,  $\beta$ ,  $\gamma$ ,  $\delta$ , and  $\varepsilon$ . Since the  $\beta$  and  $\gamma$  phases are the most electrically active phases, their promotion within the material is an ongoing pursuit. Different strategies have been therefore developed to obtain the electroactive phases of PVDF, mainly focusing on the development of specific processing procedures and the inclusion of specific fillers [24].

We will now discuss the effect of the copper nanoparticles on the phase transformation of PVDF nanocomposite films through FTIR spectroscopy. Nanocomposite films with different concentrations of Cu nanoparticles were prepared by a solution casting technique, then FTIR spectra of the films with air background were performed [25]. Figure 5.9 shows the FTIR spectrums of the pure PVDF and PVDF/Cu nanocomposites with different concentrations of Cu [25]. Vibrational bands at  $489 \text{ cm}^{-1}$  ( $\text{CF}_2$  bending),  $530 \text{ cm}^{-1}$  ( $\text{CF}_2$  bending),  $615$  and  $763 \text{ cm}^{-1}$  ( $\text{CF}_2$  bending and skeletal bending),  $795 \text{ cm}^{-1}$  ( $\text{CH}_2$  rocking), and  $975 \text{ cm}^{-1}$  ( $\text{CH}_2$  twisting) refer to  $\alpha$ -phase. Vibrational bands at  $509 \text{ cm}^{-1}$  ( $\text{CF}_2$  bending) and  $840 \text{ cm}^{-1}$  ( $\text{CH}_2$  rocking) correspond to  $\beta$ -phase [26].

The significant differences between FTIR spectra of pure PVDF and PVDF nanocomposites are the decreasing intensity of the vibration modes characteristic for  $\alpha$ -phase and the appearance and increase of new vibration modes characteristic for  $\beta$ -phase (at  $510$  and  $840 \text{ cm}^{-1}$ ) [25]. The technique of FTIR spectroscopy is a well-known technique for quantitative determination of PVDF crystalline polymorphs. In this technique, different absorption bands are assigned to different

**FIGURE 5.9**

FTIR spectra of PVDF and PVDF/Cu nanocomposite film.

Ref. [25] Copyright 2012. Reprinted with permission from Springer.

**Table 5.2** The Variations of  $\beta$ -phase Content with Increased Concentrations of Cu Nanoparticles

Concentration of Cu Nanoparticles (%)	$\beta$ -Phase Content $F(\beta)$ (%)
0	31.6
0.05	50.5
0.1	64.3
0.5	67
1	73.4

crystalline PVDF polymorphs. According to the technique, the peak heights (areas) at  $763\text{ cm}^{-1}$  ( $\alpha$ -form) and  $840\text{ cm}^{-1}$  ( $\beta$ -form) were extracted from the spectra shown in Figure 5.9 [27]. Using Eqn (5.5), the *beta* content of the nanocomposites was calculated:

$$F(\beta) = \frac{A_{\beta}}{1.26A_{\alpha} + A_{\beta}} \quad (5.5)$$

The percentage of  $\beta$ -phase for pure PVDF and PVDF/Cu nanocomposites are listed in Table 5.2. It is observed that by increasing concentration of Cu nanoparticles, the  $\beta$ -phase content is also increased [27].

---

## 5.4 CONCLUSION

IR spectroscopy is an excellent chemical analysis technique. The IR spectrum, showing absorption or transmission versus incident IR frequency, can offer a fingerprint of the structure of the molecule. As IR radiation is passed through a sample, it can be absorbed by the vibrational state, bending or stretching, of the molecule. Traditionally, dispersive instruments were used to obtain IR spectra. FTIR, which is currently preferred over IR, is based on the idea of the interference of radiation. FTIR spectrometers have several major advantages over older dispersive instruments such as higher signal-to-noise ratio and higher speed. FTIR spectra can provide qualitative and quantitative information about the structure of matter at the molecular scale. Therefore, FTIR spectroscopy is one of the best methods for identifying molecular structure, such as functional group and bond, qualitatively according to the characteristic frequencies. In addition, FTIR spectra can determine the component content of the sample quantitatively according to band intensity.

---

## REFERENCES

- [1] Brian CS. *Fundamental of Fourier transform spectroscopy*. United States of America: Taylor & Francis Group; 2011.
- [2] Stuart HB. *Infrared spectroscopy: fundamentals and applications*. John Wiley & Sons; 2004.
- [3] Sherman HC. *Handbook of instrumental techniques for analytical chemistry*. Prentice Hall; 1997.
- [4] Koenig JL. *Infrared and Raman spectroscopy of polymers*. Smithers Rapra Technology; 2001.
- [5] Sabu T, Kuruvilla J, Malhotra SK, Koichi G, Sreekalam MS. *Polymer composites*. Boschstr, Germany: VCH Verlag GmbH & Co. KGaA; 2013.
- [6] Coates J. *Interpretation of infrared spectra, a practical approach*. Chichester: John Wiley & Sons Ltd.; 2000.
- [7] Jaleh B, Ashrafi G, Gholami N, Azizian S, Golbedaghi R, Habibi S, et al. Study of heating effect on specific surface area, and changing optical properties of ZnO nanocrystals. *Adv Mater Res* 2012;403:1205–10.
- [8] Bagabas A, Alshammari A, Aboud MF, Kosslick H. Room-temperature synthesis of zinc oxide, nanoparticles in different media and their application in cyanide photodegradation. *Nanoscale Res Lett* 2013;8:516–26.
- [9] Yuan A, Wang X, Wang Y, Hu J. Textural and capacitive characteristics of MnO<sub>2</sub> nanocrystals derived from a novel solid-reaction route. *Electrochim Acta* 2009;54:1021–102.
- [10] Yuan A, Wang X, Wang Y, Hu J. Comparison of nano-MnO<sub>2</sub> derived from different manganese sources and influence of active material weight ratio on performance of nano-MnO<sub>2</sub>/activated carbon supercapacitor. *Energy Conversion Manage* 2010;51:2588–94.

- [11] Ba-Abbad MM, Kadhum AAH, Mohamad AB, Takriff MS, Sopian K. Synthesis and catalytic activity of TiO<sub>2</sub> nanoparticles for photochemical oxidation of concentrated chlorophenols under direct solar radiation. *Int J Electrochem Sci* 2012;7:4871–88.
- [12] Jafari S, Shayesteh SF, Salouti M, Boustani K. Effect of annealing temperature on magnetic phase transition in Fe<sub>3</sub>O<sub>4</sub> nanoparticles. *J Magn Magn Mater* 2015;379:305–12.
- [13] Yarwood J, Douthwaite R, Duckett B. Spectroscopic properties of inorganic and organometallic compounds techniques, materials and applications. RSC Publishing; 2009. p. 41.
- [14] Branca C, Frusteri F, Magazu V, Mangione A. Characterization of carbon nanotubes by TEM and infrared spectroscopy. *J Phys Chem B* 2004;108:3469–73.
- [15] Fakhri P, Jaleh P, Nasrollahzadeh M. Synthesis and characterization of copper nanoparticles supported on reduced graphene oxide as a highly active and recyclable catalyst for the synthesis of formamides and primary amines. *J Mol Catal A: Chem* 2014;383:17–22.
- [16] Fakhri P, Nasrollahzadeh M, Jaleh B. Graphene oxide supported Au nanoparticles as an efficient catalyst for reduction of nitro compounds and Suzuki–Miyaura coupling in water. *RSC Adv* 2014;4:48691–7.
- [17] Eun YC, Tae HH, Ji Hyun H, Ji EK, Sun HL, Hyun WK, et al. Noncovalent functionalization of graphene with end-functional polymers. *J Mater Chem* 2010;4:1907–12.
- [18] Nasrollahzadeh M, Jaleh B, Jabbari A. Synthesis, characterization and catalytic activity of graphene oxide/ZnO nanocomposites. *RSC Adv* 2014;4:36713–20.
- [19] Abedi K, Ghorbani FS, Jaleh B, Bahrami A, Yarahmadi R, Haddadi R, et al. Decomposition of chlorinated volatile organic compounds (CVOCs) using NTP coupled with TiO<sub>2</sub>/GAC, ZnO/GAC, and TiO<sub>2</sub>/ZnO/GAC in a plasma-assisted catalysis system. *J Electrostatics* 2015:80–8.
- [20] Deosarkara MP, Pawara SM, Bhanvase BA. *In situ* sonochemical synthesis of Fe<sub>3</sub>O<sub>4</sub>–graphene nanocomposite for lithium rechargeable batteries. *Chem Eng Process* 2014;73:49–55.
- [21] Jaleh B, Shayegani MM, Farshchi TM, Habibi S, Golbedaghi R, Keymanesh MR. UV-Degradation effect on optical and surface properties of polystyrene-TiO<sub>2</sub> nanocomposite film. *J Iran Chem Soc* 2011;8:161–168.
- [22] Motaung TE, Luyt AS, Saladino ML, Caponetti E. Study of morphology, mechanical properties, and thermal degradation of polycarbonate-titania nanocomposites as function of titania crystalline phase and content. *Polym Composites* 2013;34:164–72.
- [23] Jaleh B, Shahbazi N. Surface properties of UV irradiated PC-TiO<sub>2</sub> nanocomposite film. *Appl Surface Sci* 2014;313:251–8.
- [24] Martins P, Lanceros-Mendez S. Electroactive phases of poly(vinylidene fluoride): determination, processing and applications. *Progress Polym Sci* 2014;39:683–706.
- [25] Jaleh B, Fakhri P, Noroozi M, Muensit N. Influence of copper nanoparticles concentration on the properties of poly(vinylidene fluoride)/Cu nanoparticles nanocomposite films. *J Inorg Organomet Polym* 2012;22:878–85.
- [26] Jaleh B, Jabbari A. Evaluation of reduced graphene oxide/ZnO effect on properties of PVDF nanocomposite films. *Appl Surface Sci* 2014;320:339–47.
- [27] Yousefi AA. Hybrid polyvinylidene fluoride/nanoclay/MWCNT nanocomposites: PVDF crystalline transformation. *Iran Polym J* 2011;20:725–33.

## 6

## Ultraviolet and visible spectroscopy studies of nanofillers and their polymer nanocomposites

**Sridevi Venkatachalam***Department of Chemistry, Lady Doak College, Madurai, Tamil Nadu, India***6.1 INTRODUCTION**

Composites are multiphase materials prepared by combining two different compounds with the objective of enhancing the properties of the mixture in a desirable way. These materials have wider scope in a variety of fields ranging from packaging to biomedical applications. The composites are made by mixing chemically dissimilar compounds which are separated by distinct interfaces. A minimum of two phases is required to prepare a composite. One phase acts as matrix which is considered to be the continuous phase in which another phase is widely dispersed. The properties of the composites then depend on the properties of the constituent phases which can be optimized by varying the ratio of the matrix material with that of the dispersed material. With the advent of nanoscience and nanotechnology, nanocomposites have emerged as high-performance materials with the unique properties of the materials at nanoscale. Nanocomposites are composites in which at least one of the phases shows dimension in the nanometer scale (1–100 nm). The properties of nanocomposites depend on the dimensions of the matrix material which can be in the nanoscale, loading, size, shape, orientation, and degree of dispersion of the second phase, which can also be in the nanoscale. The interaction between the matrix and the dispersed phase also plays a crucial role in enhancing the desired properties of the nanocomposites.

**6.2 TYPES OF NANOCOMPOSITES**

Nanocomposites are classified into three major types based on the matrix material:

1. Ceramic matrix nanocomposites (CMCs)
2. Metal matrix nanocomposites (MMCs)
3. Polymer matrix nanocomposites (PMCs)

### 6.2.1 POLYMER MATRIX NANOCOMPOSITES

Out of the three types, PMCs are more suitable for industrial applications due to their light weight and ductile nature. However, they exhibit poor thermal, mechanical, electrical, and other physical properties when compared to CMC and MMC. These properties can be improved significantly by reinforcing the matrix with a suitable nanomaterial, usually called nanofillers, as the second phase. Nanofillers can suitably alter the properties of the polymer matrix when incorporated using appropriate synthesis procedures such as *in-situ* polymerization, melt intercalation, template synthesis, and sol-gel process. Some of the commonly employed nanofillers in PMC are nano clays, nano oxides, carbon nanotubes (CNTs), graphenes, and metallic nanoparticles. Polymer matrices reinforced with nanofillers are widely studied for their special and unique properties exhibited in synergy between the matrix and nanofiller. This has paved way for researchers to prepare PMC with tunable properties such as thermal, electrical, mechanical, and optical properties.

### 6.2.2 CHARACTERIZATION TECHNIQUES

Characterization of PMC prepared using suitable techniques is very important to further its use for any application. The choice of the technique depends on the property of study and application of the nanocomposite. A wide range of techniques such as X-ray diffraction (XRD), scanning electron microscope (SEM), transmission electron microscope (TEM), Fourier transform-infrared (FT-IR), Raman, UV-Vis spectroscopy, X-ray photo electron spectroscopy (XPS), nuclear magnetic resonance spectroscopy (NMR), thermal techniques such as thermogravimetric analysis or thermal gravimetric analysis (TGA), differential thermal analysis (DTA), and differential scanning calorimetry (DSC) are commonly employed to ascertain the structure and properties of the nanocomposites. The structural properties are best studied using XRD, XPES, FT-IR, and NMR techniques. Thermal properties of the composites are evaluated using TGA, DTA, and DSC. The shape, size, and morphology of the nanofillers in the polymer matrix is identified using field emission scanning electron microscopy (FESEM), and high-resolution transmission electron microscopy (HRTEM). UV-Vis spectroscopy is a powerful tool to understand the optical properties of the nanocomposites. However, it cannot be used as a singular technique to evaluate the viability of the PMC for any suitable application and thus, is usually coupled with other suitable characterization methods.

### 6.2.3 OPTICAL PROPERTIES OF PMC

PMC with tunable optical properties are of great significance to develop materials for potential applications, such as light emitting diodes, solar cells, polarizers, color-filters, optical communication and data storage devices, optical sensors, and in the biomedical field. The following are some of the important optical properties of PMC which are explored for the above applications.

1. *Refractive index*: The index of refraction of the polymer matrix can be controlled by tailoring the volume fraction of the nanoparticle added to it. Polymer matrices impregnated with nanofillers such as gold (for low index matrix) and lead sulfide (PbS) (for very high index matrix), finds application in filters, optical wave guides, optical adhesives, and solar cells.
2. *UV absorption*: Transparent UV absorbing nanocomposites used in paints, lacquers, and pigments are designed by mixing strong UV absorbing nanoparticles, such as Titanium dioxide (TiO<sub>2</sub>), Zinc oxide (ZnO), and Zirconium dioxide (ZrO<sub>2</sub>) in a polymer matrix.
3. *Transparency*: Transparent polymer matrices can be prepared by adding small-sized nanoparticles to minimize scattering effect and improve the optical transparency.
4. *Luminescence*: Luminescent polymer nanocomposites can be prepared by adding semiconducting quantum dots (QDs) cadmium selenide (CdSe), cadmium telluride (CdTe), and lead selenide (PbSe), coated with zinc sulfide (ZnS), which exhibit strong emission characteristics.

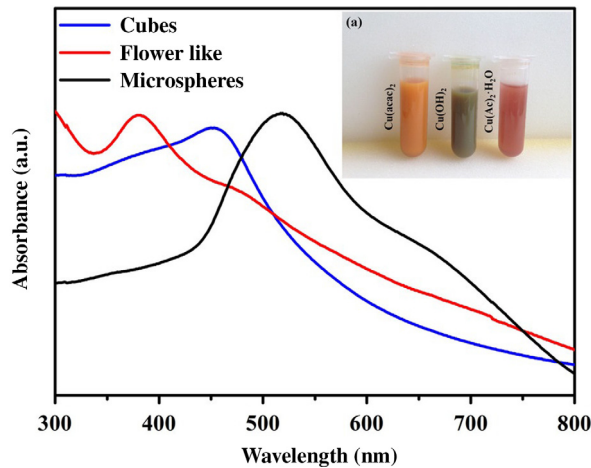
---

### 6.3 NANOFILLERS IN PMC

Though there are different types of nanofillers, integration of inorganic nanoparticles into a polymer matrix, forming polymer-inorganic nanocomposites [1] is of technological interest because of their potential applications as optoelectronic and magneto-optic devices. Frequently, employed inorganic nanofillers include metals and metal alloys (e.g., gold (Au), silver (Ag), copper (Cu), Germanium (Ge), platinum (Pt), iron (Fe), cobalt-platinum alloy (CoPt)), semiconductors (e.g., PbS, cadmium sulfide (CdS)), oxides (e.g., ZnO, TiO<sub>2</sub>), and clay minerals (e.g., montmorillonite, vermiculite, hectorite). These nanofillers are widely used in different types of polymers to enhance the optical properties. The next section reviews the application of UV-Vis spectroscopy to understand the optical properties of metal and semiconductor nanoparticle-reinforced polymer nanocomposites.

#### 6.3.1 METAL NANOPARTICLES AS NANOFILLERS

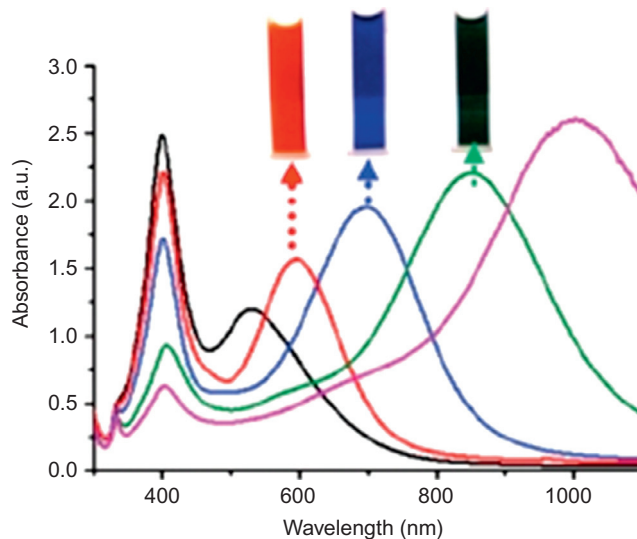
The free electrons in the metals when quantized are called plasmons and interact with the light to produce surface plasmon resonance (SPR) absorption. The oscillation frequency of the surface plasmons are in the visible region for noble metals like gold, silver, copper, and a few alloys, which leads to a typical color for each metallic cluster at the nanoscale. The oscillation modes of the surface plasmons depend heavily on the shape and slightly on the size of the metallic nanoparticles. Spherical nanoparticles interact with light in an isotropic manner and hence show a single SPR absorption peak in the UV-Vis spectrum. However, anisotropic particles (ellipsoids and rods) show two peaks: (i) transverse peak, independent of



**FIGURE 6.1**

SPR absorption peaks for copper nanoparticles [2].

*Copyright 2015. Reproduced with permission from Scientific Reports (open access).*

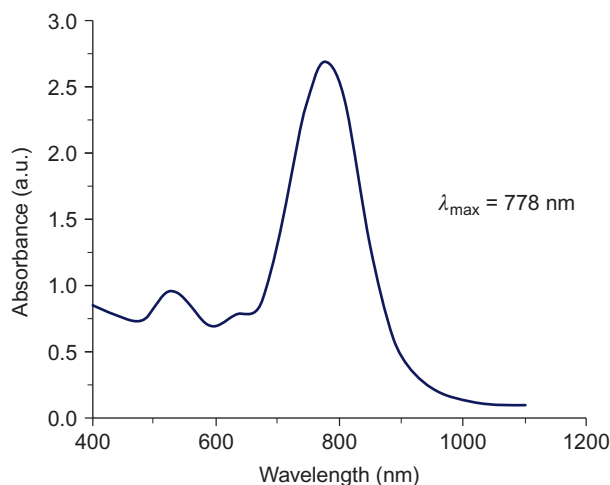


**FIGURE 6.2**

SPR absorption peaks for silver nanoparticles [3].

*Copyright 2008. Reproduced with permission from Royal Society of Chemistry.*

the aspect ratio, as found in spherical particles, and (ii) longitudinal peak at a longer wavelength, characteristic of the aspect ratio (Figures 6.1, 6.2, and 6.3). The transverse and longitudinal SPR absorption wavelengths for Cu, Ag, and Au are given in Table 6.1. The presence and/or absence of these SPR peaks, peak

**FIGURE 6.3**

SPR absorption peaks for gold nanoparticles [4].

Copyright 2012. Reproduced with permission from Royal Society of Chemistry.

**Table 6.1** SPR Characteristics of Noble Metal Nanoparticles

Metal Nanoparticle	SPR $\lambda_{\max}$ (nm)		UV-Vis Spectrum of the Metallic Nanocolloids
	Transverse Wavelength	Longitudinal Wavelength	
Copper	560	>700	[2]
Silver	420	>650	[3]
Gold	520	>700	[4]

position, peak intensity, and peak width offer enormous and valuable information about the metal nanoparticles. When these metal nanoparticles are used as nanofillers in the polymer matrices, UV-Vis spectroscopy can be one of the most important characterization methods to understand the size and dispersity of the nanofiller in the matrix, stability of the nanocomposite, and the interaction between the matrix and the filler.

Zhu and Zhu [5] prepared polyacrylamide-metal (i.e., Pt, Ag, Cu) nanocomposites with homogeneously dispersed metal nanoparticles in the polymer matrix using microwave heating. The PMC has been prepared by the simultaneous formation of metal nanoparticles and polymerization of the acrylamide monomer (AM) through a single step, leading to a homogeneous distribution of metal nanoparticles in the polyacrylamide matrix. Ethylene glycol (EG) is used as both a

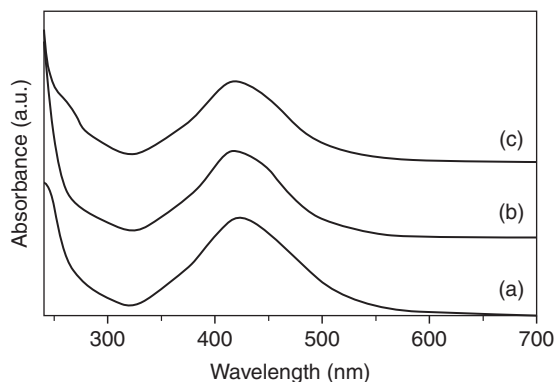


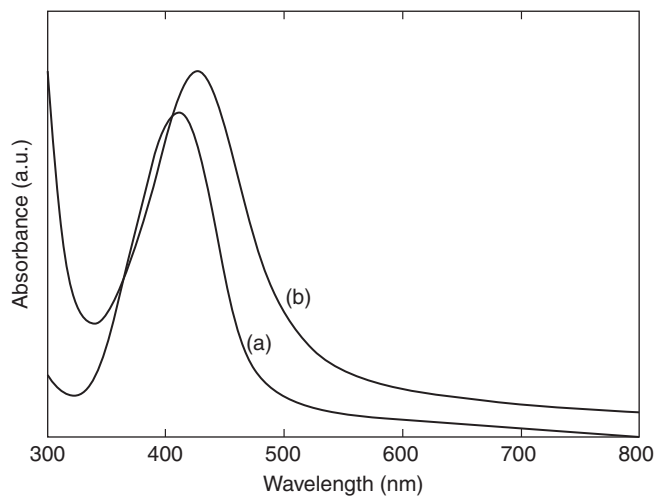
**FIGURE 6.4**

UV-Vis absorption spectra of (a) nanocomposite colloidal solution prepared by microwave heating a EG solution of 0.01 M  $\text{AgNO}_3$  and 3 M AM at 125 °C for 15 min; (b) after 8 months aging of the colloidal solution from part a; and (c) the redispersed nanocomposite colloidal EG solution [5].

Copyright 2006. Reproduced with permission from American Chemical Society.

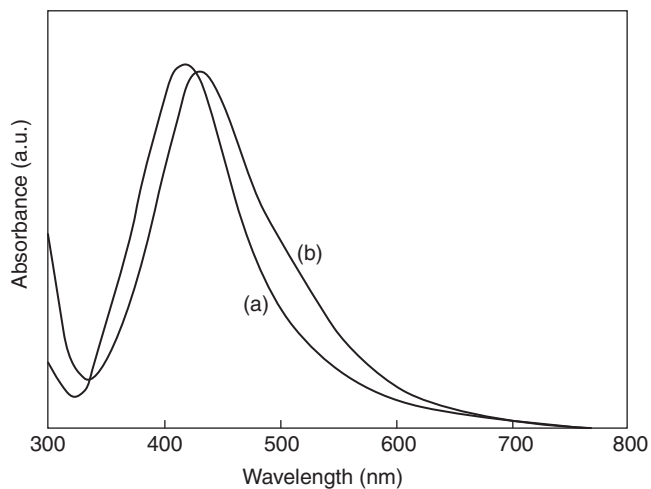
reducing reagent and solvent, and thus, no additional reductant has been added. The stability of the prepared nanocomposite colloidal solution is studied using UV-Vis spectroscopy by following the SPR absorption peak of Ag nanoparticles. Spherical silver nanoparticles show a typical SPR absorption maximum of around 410–420 nm. In the present study, the nanocomposite showed a peak around 423 nm, confirming the presence of the Ag nanoparticle in the polymer matrix. UV-Vis absorption spectra were also compared for the newly prepared sample after 8 months of storage (Figure 6.4a and b). The absorption band around 423 nm due to the surface plasmon absorption of Ag nanoparticle did not show any shift in both cases, indicating the high stability and nonaggregation of silver nanoparticles in the polymer matrix.

Dispersion of Ag nanoparticles in poly(vinylalcohol) (PVA) matrix via *in situ* reduction of silver salt by employing two different reducing agents namely, hydrazine hydrate (HH) and sodium formaldehyde sulfoxylate (SFS), has been attempted by Khanna et al. [6] Here UV-Vis spectroscopy is employed to understand the quality of nanoparticles formed with two different reducing agents. The SPR peaks of the Ag nanoparticles prepared using HH and SFS in the PVA matrix are at 418 nm, indicating the formation of Ag nanoparticles in the polymer matrix. However the absorption pattern is sharp for the Ag nanoparticles formed using SFS (Figure 6.5), indicating a narrow particle size distribution, though it is slightly broader when HH (Figure 6.6) is used as the reducing agent, which indicates uneven particle size distribution. Moreover, the peak width at half of maxima (PWHM) is a very useful parameter in UV-Vis spectroscopy. In this study, it

**FIGURE 6.5**

UV-Vis absorption spectra of Ag/PVA nanocomposite prepared using SFS: (a) solution, (b) film [6].

*Copyright 2005. Reproduced with permission from Elsevier Ltd.*

**FIGURE 6.6**

UV-Vis absorption spectra of Ag/PVA nanocomposite prepared using HH: (a) solution, (b) film [6].

*Copyright 2005. Reproduced with permission from Elsevier Ltd.*

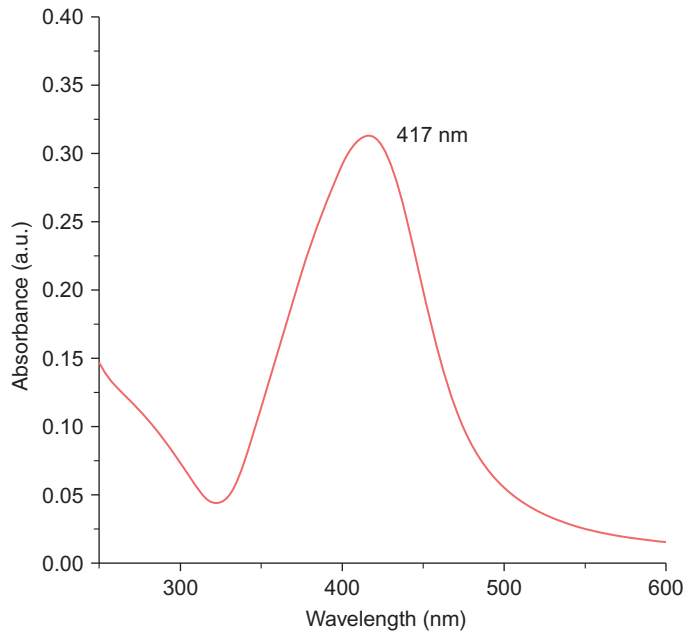


**FIGURE 6.7**

UV-Vis absorption spectra of colloidal solution of Ag nanoparticles [7].

*Copyright 2012. Reproduced with permission from Scientific Research Publishing.*

is used to understand the particle size and their distribution within the medium and matrix. The PWHM for the Ag nanoparticles prepared using HH turn out to be approximately 110 nm, which is much higher than the nanocomposite solution prepared using SFS, where the PWHM is only 85 nm. Thus UV-Vis spectral analysis has been used to confirm the narrow size distribution of the nanoparticles in the polymer matrix. Among the two reduction pathways, SFS yields better quality Ag nanoparticles in PVA than HH.

Polymeric composites of polypyrrole (PPy), PVA, and carboxymethyl cellulose (CMC) with preformed silver nanoparticles were prepared by mixing the colloidal solution of Ag nanoparticles with the aqueous solution of the respective polymers. UV-Vis spectroscopy is effectively used to understand the interaction between the nanofiller and the three polymer nanocomposites by following the SPR absorption peak for Ag nanoparticles in the pure and composite suspensions [7]. The SPR maximum of pure Ag nanoparticle colloidal suspension is 417 nm (Figure 6.7). This peak disappears when dispersed in the pyrrole solution due to the formation of black-colored PPy around the Ag nanoparticles (Figure 6.8).

The PVA/Ag nanocomposite films of various compositions of Ag show interesting results when characterized using their SPR absorption patterns.

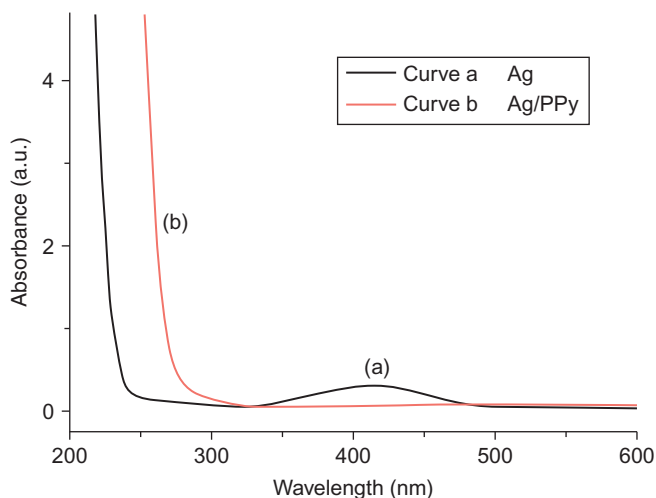


**FIGURE 6.8**

(a) UV-Vis absorption spectra of colloidal solution of Ag nanoparticles; (b) Ag/PPy nanoparticle [7].

*Copyright 2012. Reproduced with permission from Scientific Research Publishing.*

The composite films exhibit a broad surface plasmon absorption band, peaking at approximately 420 nm (Figure 6.9). The shift to the longer wavelength and broadening of the band upon incorporation of Ag nanoparticles into PVA has been attributed to the agglomeration of the Ag nanoparticles or change of the dielectric properties of the surrounding environment. A similar absorption pattern is also observed for CMC/Ag nanocomposites.

Biswas et al. [8] have introduced a novel and simple method of vapor phase codeposition of Teflon with Cu, Ag, and Au nanoparticles at elevated target temperatures, coupled with selective masking technique to produce a multi component optical material with seven different UV-Vis optical active planes arising from Teflon AF/Ag, Teflon AF/Au, and Teflon AF/Cu interfaces (Figure 6.10). The evolved systems are capable of showing tunable multiple SPR response at different UV-Vis wavelengths originating from various optically active planes of such systems. Teflon AF has been chosen as the polymer matrix due to its high resistance toward chemical attack and excellent transparency. The UV-Vis spectrum of Teflon Ag/Au nanocomposites optical system shows a double wavelength plasmon response which is tunable from 437 to 543 nm (Figure 6.11). The lower wavelength limit is governed by the characteristics of Ag nanoparticles and higher wavelength by Au nanoparticles. Similar response in the UV-Vis spectrum was also obtained with Teflon Au/Cu and Teflon Ag/Cu nanocomposite systems (Figure 6.12). When all three nanoparticles are embedded in the polymer matrix, a tunable optical response from 465 to 472 nm is observed in the UV-Vis

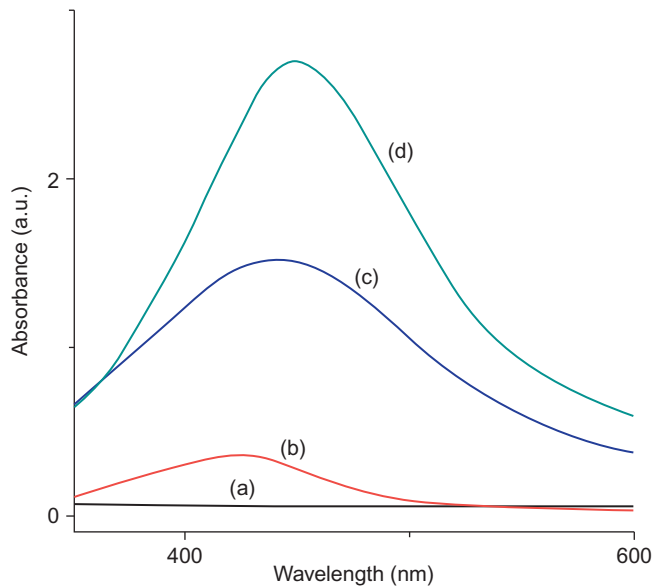


**FIGURE 6.9**

UV/Vis spectra of PVA/Ag nanocomposites of different concentrations: (a) control PVA; (b) 0.2% Ag content; (c) 0.5% Ag content; (d) 1.0% Ag content [7].

*Copyright 2012. Reproduced with permission from Scientific Research Publishing.*

spectrum. Such polymer-metal nanocomposite materials with tunable optical response can find applications as multi-color filters and gas sensors.

Saini et al. [9] have used absorption spectroscopy to understand the optical properties of Ag-PVA nanocomposites. Optical properties such as absorption coefficient, refractive index, and dielectric constant have been calculated from absorption spectroscopy. It was discovered that the refractive index of PVA increases with increasing concentration of Ag nanoparticles. Figure 6.13A and B presents the UV-Vis absorption spectra of colloidal Ag nanoparticles and Ag-PVA nanocomposite films with varying concentrations of Ag nanoparticles. The SPR peak for pure Ag nanoparticle colloids is around 395 nm (Figure 6.13A) which gets red-shifted to a slightly broader peak around 405 nm for Ag-PVA films (Figure 6.13B). This red shift in the SPR peak obtained for Ag-PVA film is attributed to the increase in the particle size and/or due to wider size distribution of the nanoparticles within the polymer because the band width, intensity, and position of the SPR wavelength of these metallic particles varies with particle size, shape, and with their surrounding matrix.

Biopolymer matrices are also widely used to prepare metal-based nanocomposites because of their biocompatible and nontoxic properties. Cellulose [10], gelatine [11], starch [12], and chitosan [13] are a few biopolymers which are converted into bionanocomposites using suitable nanofillers. Metal dendrimer

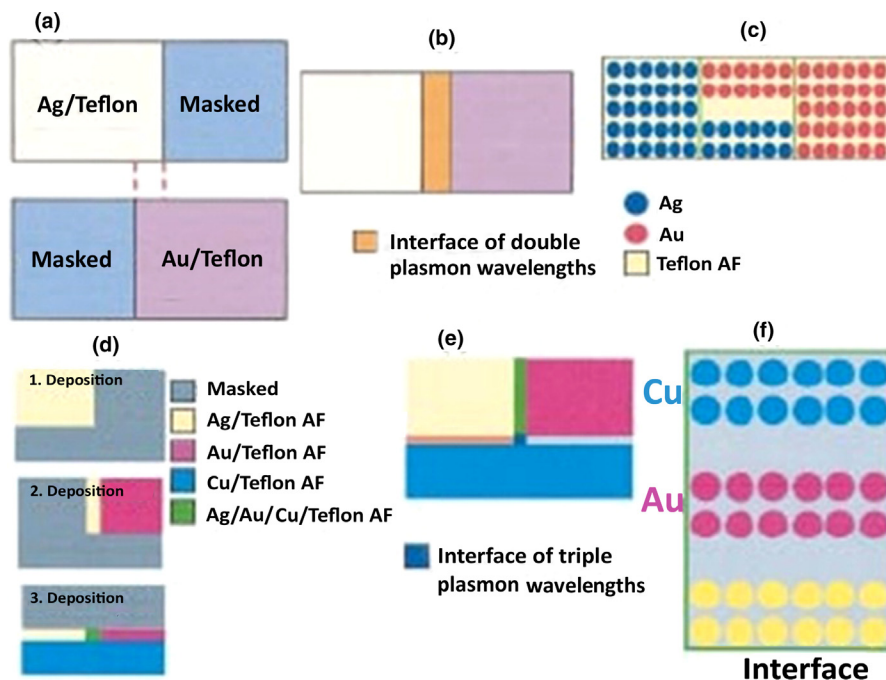


**FIGURE 6.10**

(a)–(c) Schematics of the masking technique to generate a combined polymer-metal nanocomposite structure with an interface producing junction of two different nanocomposites. (d)–(f) Serial masking to produce an optical system with seven different optical active planes. The method of generation of a junction of three different nanocomposites with a layered structure is also shown schematically [8].

*Copyright 2004. Reproduced with permission from American Institute of Physics.*

nanocomposites have been synthesized with poly(styrene sulfonate) [14], poly-amidoamine (PAMAM) [15], and such bionanocomposites offer ample scope in the biomedical field and environmental remediation. Huang et al. [16] have synthesized various metal–chitosan nanocomposites with silver Ag, Au, Pt, and Pd nanoparticles in aqueous solutions. The optimum concentration of chitosan and Ag nanoparticles in the nanocomposite is determined by analyzing the SPR peak of Ag nanoparticles in the polymer matrix in the UV-Vis spectra. When the concentration of chitosan is increased, the intensity of the absorption band decreases and then increases again with a further increase of the chitosan concentration, as shown in Figure 6.14a. At the same time, the center of absorption band gets shifted slightly with the change in chitosan concentration. All these changes in UV-Vis absorption indicate that the size of silver nanoparticles formed altered with the concentration of chitosan, which operates as a controller of nucleation as well as a stabilizer. As the concentration of  $\text{Ag}^+$  is increased, the peak intensity increases due to

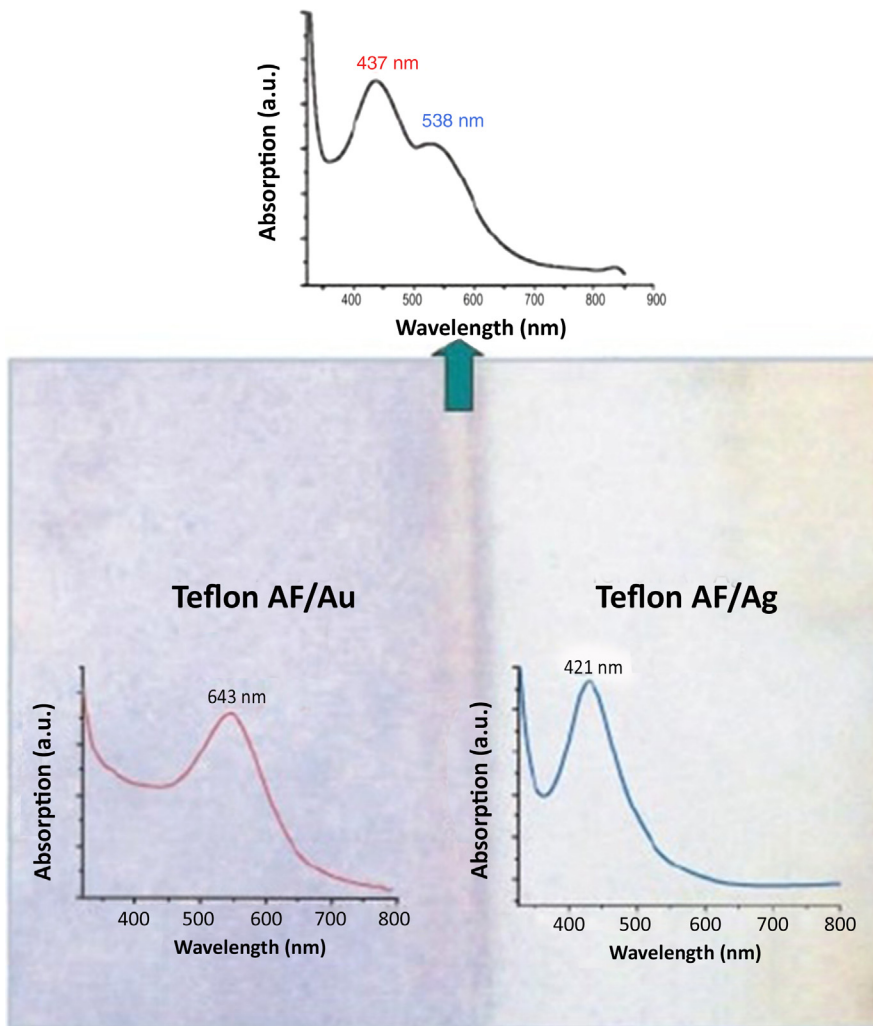


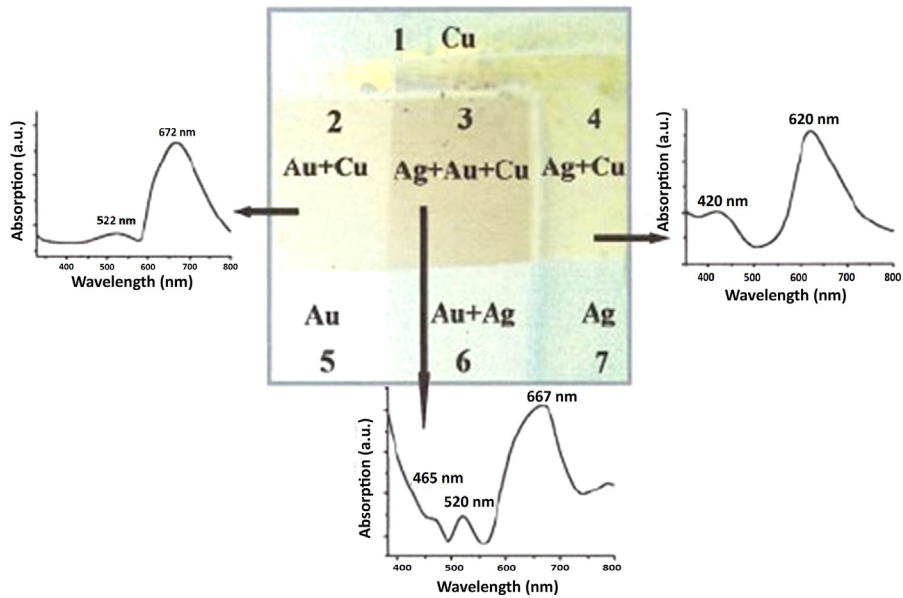
**FIGURE 6.11**

Particle plasmon resonances originating from the different planes of Teflon AF/Ag and Teflon AF/Au nanocomposites optical system [8].

*Copyright 2004. Reproduced with permission from American Institute of Physics.*

the formation of more Ag nanoparticles in the matrix (Figure 6.14b). The absorbance band for Ag nanoparticles is around 417 nm and is around 520 nm for Au nanoparticles. Platinum and palladium nanoparticles did not show any plasmon absorbance in the UV-Vis region of the spectrum (Figure 6.15).

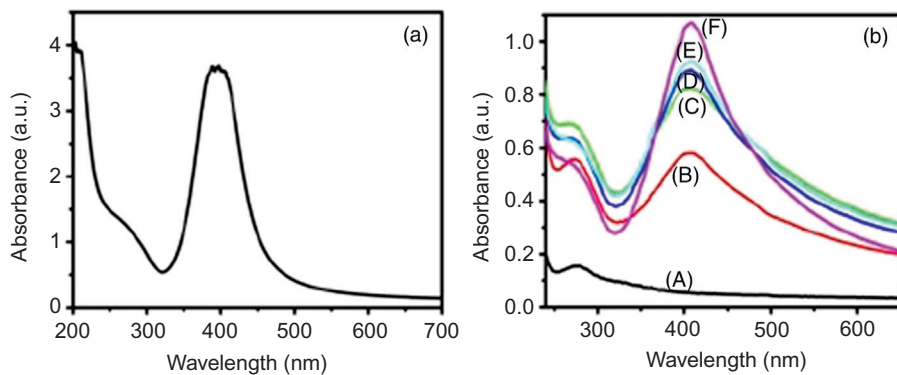
The glycogen biopolymer from the bovine liver has been used as a stabilization agent for the growth of silver nanoparticles by Božanić et al. [17]. Samples



**FIGURE 6.12**

The generated system consists of combined structures of three different nanocomposites of Teflon AF/Ag, Teflon AF/Au, and Teflon AF/Cu [8].

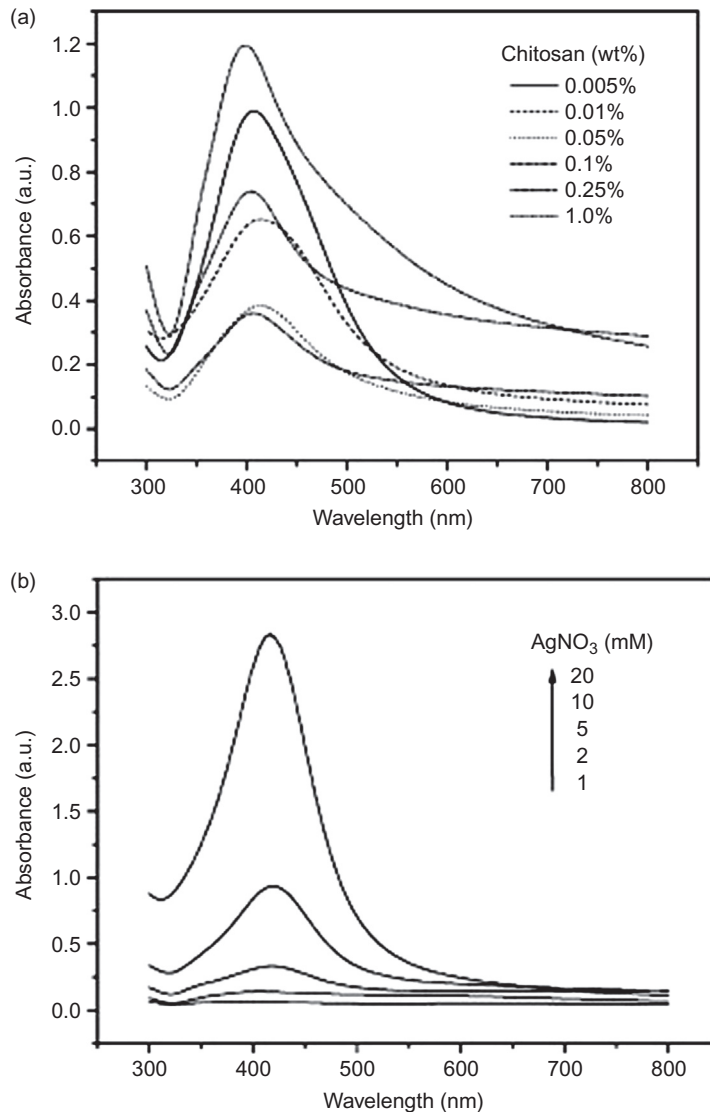
*Copyright 2004. Reproduced with permission from American Institute of Physics.*



**FIGURE 6.13**

(a) Absorption spectra of colloidal Ag nanoparticles, and (b) absorption spectra of: (A) virgin PVA and Ag-PVA nanocomposite films containing (B) 0.02 wt%, (C) 0.04 wt%, (D) 0.048 wt%, (E) 0.056 wt%, (F) 0.062 wt% of Ag nanoparticles in PVA [9].

*Copyright 2013. Reproduced with permission from Elsevier Ltd.*

**FIGURE 6.14**

UV-Vis absorption spectra of Ag–chitosan nanocomposites prepared with various concentrations of chitosan (a) and silver salt (b) [16].

Copyright 2004. Reproduced with permission from Elsevier Ltd.

with various contents of silver were prepared by two different procedures that include fast (using microwave radiation) and slow (conventional) heating of the reaction mixtures. Here UV-Vis spectroscopy is used to evaluate the quality of nanoparticles formed using the biopolymer by two different procedures.

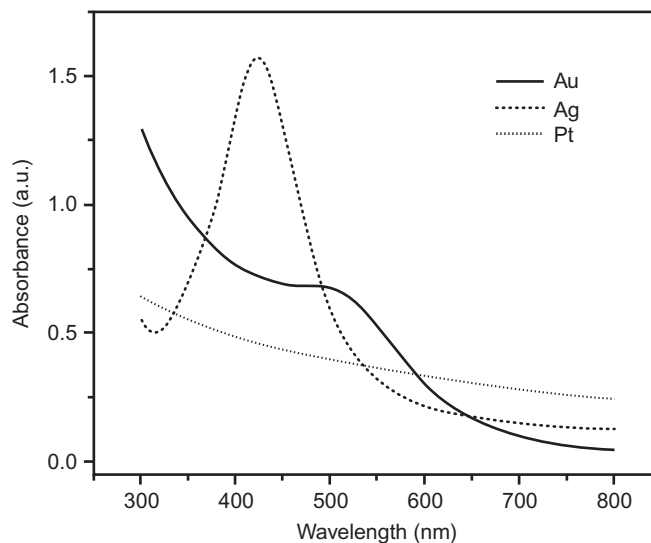


**FIGURE 6.15**

UV-Vis absorption spectra of metal (Ag, Au, and Pt)–chitosan nanocomposites prepared with 20 mM corresponding metal salts. The absorption spectrum of Pd–chitosan nanocomposite is not shown, but is similar to that of Pt [16].

*Copyright 2004. Reproduced with permission from Elsevier Ltd.*

The samples prepared using microwave radiation exhibited narrower SPR peaks (Figure 6.16), indicating the formation's better particle size distribution than those formed with the slow heating method.

Thin films of chitosan/Ag bionanocomposite have been fabricated by the spin-coating method for application as planar optical waveguides by Mironenko et al. [18]. Silver nanoparticles of less than 10 nm in size were distributed homogeneously in the chitosan matrix through an *in situ* synthesis of silver nanoparticles in the polymer matrix by sodium borohydride. The bionanocomposite was also cast into a thin film. UV-Vis spectroscopy is used to confirm the spherical nature of the nanoparticles in the film and in solution, as indicated by a single narrow absorption band at 412–413 nm in the spectra (Figure 6.17). The refractive index of the film increases from 1.53 to 1.69 with the increase of the silver volume fraction up to 2.55%. The prepared nanocomposite films have waveguiding properties up to a silver volume fraction of 1.3% with a refractive index of 1.58.

### 6.3.2 SEMICONDUCTOR NANOCRYSTALS AS NANOFILLERS

Nanocomposites with semiconducting nanoparticles as fillers are attracting attention in recent years due to their absorption and luminescence properties. The mechanism of light absorption is entirely different from that of metal

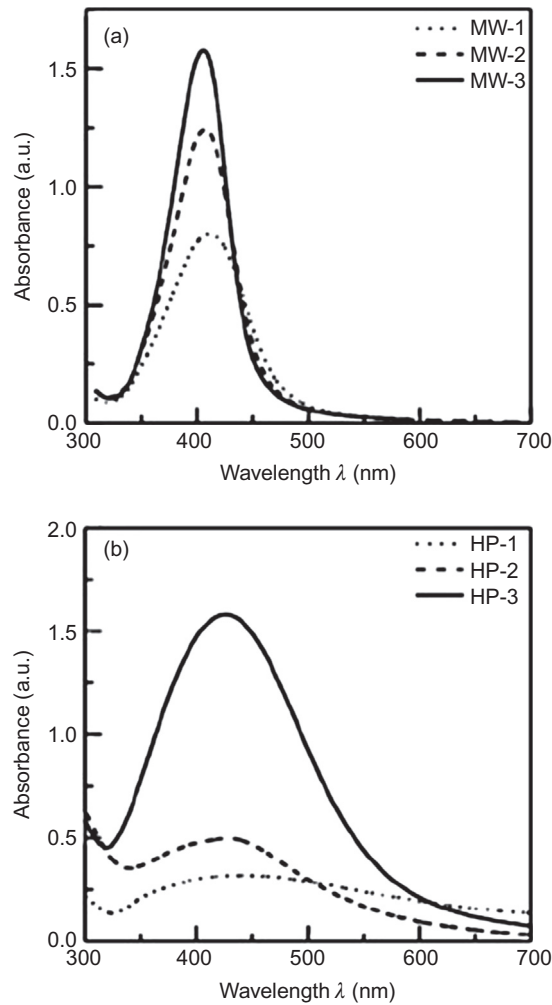


**FIGURE 6.16**

Absorption spectra of (a) MW, and (b) HP silver–glycogen nanocomposite solutions with various silver contents (dotted line (0.5 mM), dashed line (1 mM), and solid line (2 mM)) [17].

Copyright 2011. Reproduced with permission from Elsevier Ltd.

nanoparticles. As extremely small nanoparticles can be prepared, semiconductors obey the process of quantum confinement during the absorption of light. The semiconductor nanoparticles form an electron-hole pair called an exciton during their interaction with light. The radius of the exciton, which depends on the band gap of the material, is very sensitive to the size of the nanoparticle and similar to the SPR absorption in metal nanoparticles which is very sensitive to the shape of

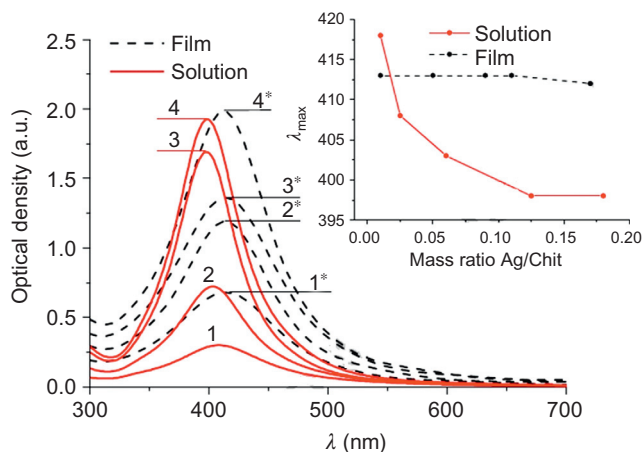


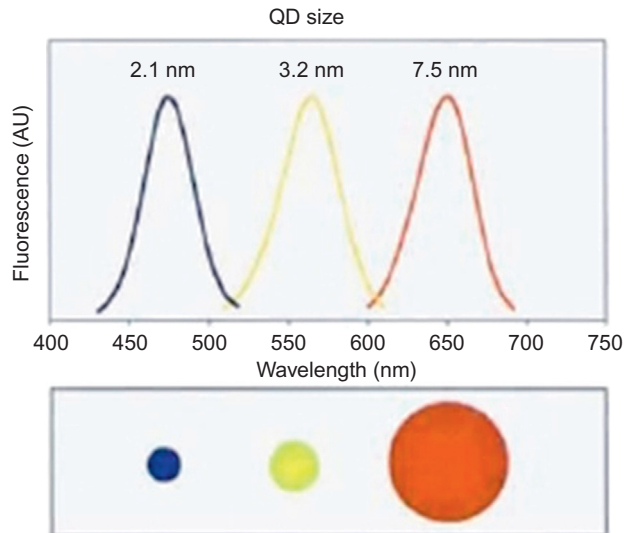
**FIGURE 6.17**

Absorption spectra of chitosan/Ag composites and dependence of absorption maximum wavelength on Ag/Chitosan mass ratio (inset). Ag/Chitosan mass ratios in spectra were 0.025 (1), 0.06 (2), 0.125 (3), 0.18 (4), 0.05 (1\*), 0.09 (2\*), 0.11 (3\*), 0.17 (4\*) [18].

Copyright 2014. Reproduced with permission from Elsevier Ltd.

the nanoparticle. Thus the band gap of the semiconducting nanoparticle can be tuned toward desired properties by tuning the size of the nanoparticle. The influence of particle size is found not only in the band gap but also in the wavelength of the emitted photons. The size of the semiconductor nanoparticle called QD is directly related to the absorption wavelength. These QDs also exhibit photoluminescence (PL) in the visible region. The emission spectra of CdSe nanoparticles with different sizes are shown in Figure 6.18, where the blue shift of the emission for decreasing particle size is clearly apparent [19]. A similar kind of observation is observed in the zinc oxide nanoparticle, where the absorbance of ZnO shows a blue shift with decreasing particle size from 12 to 3 nm (Figure 6.19) [20]. These examples clearly demonstrate the possibility of tailoring the optical properties of semiconducting nanoparticles simply by tuning the particle size. When such nanoparticles are used as nanofillers in polymer matrices, they offer excellent scope toward various optical applications. UV-Vis spectroscopy is one of the important techniques to understand the optical properties of such semiconductor-based nanofillers in polymer nanocomposites. The absorption and emission characteristics of the nanofillers in the UV-Vis region throws light on the particle size, band gap, and dispersity in the polymer matrix.

The absorption spectra in the UV-Vis region can reflect the size and size distribution of QDs such as CdSe or CdS embedded in a given polymer matrix. By increasing the diameter of incorporated CdS particles, the absorption peak shifts to a higher wavelength regime, as reported by Wu et al. [21]. Moreover, the absorption peak becomes broader as the polydispersibility of CdS particles

**FIGURE 6.18**

Size and composition tuning of optical emission for binary CdSe QD [19].

Copyright 2004. Reproduced with permission from John Wiley & Sons.

increases. A sharper peak often occurs for monodispersed CdS particles attached onto polymer cores. Tamborra et al. [22] investigated the optical properties of CdS nanocrystals embedded in optically transparent polystyrene (PS) and PMMA. A comparison of the absorption spectra of the CdS nanoparticles in chloroform solution and in PS and PMMA matrices indicate that both PS and PMMA polymer matrices do not affect the optical properties of native CdS nanocrystals. Except for a slight reduction in the optical transparency in the polymer films, the optical absorption spectra of CdS are same in solution and films. Thus, it is concluded that the PS and PMMA polymers act only as stabilizers for the QDs.

PbS is another interesting semiconducting nanoparticle whose band gap increases from 0.41 eV in bulk crystals up to a few electron volts in nanoparticles. Hence bulk PbS absorbs throughout the visible region and thus appears black. However, with decreasing crystal size, the color changes to dark brown and a suspension of PbS nanoparticles are clear and reddish. Reifeld [23] has dispersed PbS nanoparticles in glass using sol-gel method. The composite exhibits interesting optical properties, showing a blue shift in its UV-Vis spectrum with decreasing particle size (Figure 6.20a). The absorption spectrum is used to calculate the band gap of the nanoparticle and it is observed that as the particle size decreases, the band gap widens from 1.42 to 1.92 eV (Figure 6.20b). The luminescence properties of PbS in PS have been studied by Lim et al. [24]. The composite shows PL in the IR region and the luminescence intensity increases with decreasing particle size of the PbS nanoparticle.

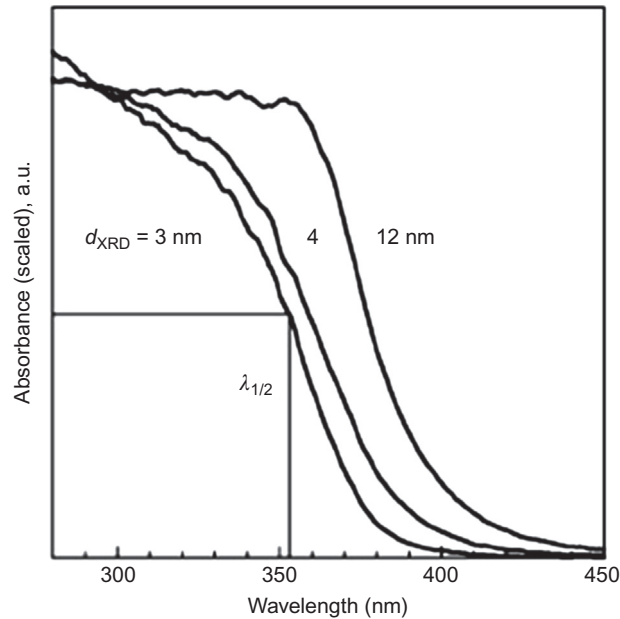


**FIGURE 6.19**

Optical absorbance spectra of as-prepared flame-made ZnO nanoparticles showing the blue shift associated with decreasing crystallite size [20].

*Copyright 2002. Reproduced with permission from American Institute of Physics.*

Hammad et al. [25] synthesized PVA-capped PbS nanoparticles using a wet chemical method. The PbS nanoparticles show a significant “blue shift” from bulk material in their UV-Vis spectra. The prepared PMC exhibit PL properties and a 10-fold increase in PL intensity is reached at 4 g of PVA addition. An obvious blue shift of the absorption edges can be observed in the capped PbS samples from 442 to 310 nm of PVA-capped PbS nanoparticles with concentrations from 0 to 4 g. The band gap energy increases from 2.8 to 4 eV for uncapped PbS and 3 g PVA-capped PbS, respectively. Their study indicates that the PVA matrix plays a vital role in the quantum confinement and it is believed that the PVA matrix arrests the growth of the nanoparticles with further size reduction of the PVA-capped PbS nanoparticles.

### 6.3.3 NANO OXIDES AS NANOFILLERS

Oxides such as ZnO, SnO<sub>2</sub>, TiO<sub>2</sub> nanoparticles, and others are widely used as nanofillers in polymer matrices to enhance the absorption of UV and optical transparency. In such studies, UV-Vis spectroscopy is an indispensable characterization method to evaluate the optical property of the PMC.

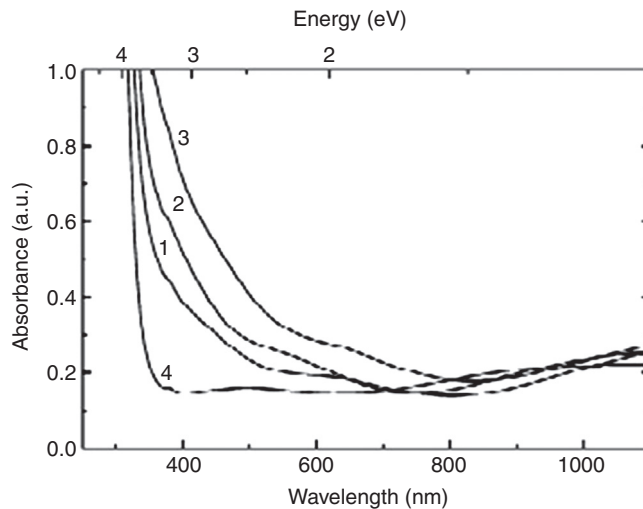


**FIGURE 6.20**

Absorption spectra of 20% PbS nanocrystallites annealed at: (1) 200, (2) 250, (3) 300 °C, and (4) zirconia substrate. [23].

*Copyright 2002. Reproduced with permission from Elsevier Ltd.*

The optical properties of polyvinylidenedifluoride (PVDF)–ZnO nanocomposite have been investigated by Indolia and Gaur [26]. The change in the optical band gap of PMC upon incorporation of ZnO nanoparticles was followed using UV-Vis spectroscopy. There is a significant, continuous decline in optical band gap and optical activation energy, while there is an increase in refractive index upon incorporating ZnO nanoparticles into the polymer. Moreover, the UV absorption characteristics of the polymer matrix with and without ZnO nanoparticles was also analyzed using the absorption spectrum in the UV region. The composite is very effective at shielding UV radiation due to the enhanced absorption capacity of ZnO nanoparticles in the polymer matrix. The UV-Vis spectrum indicates the limited UV absorbance of PVDF, which is enhanced with the addition of ZnO. Higher values of UV absorbance were obtained in the region between 300 and 400 nm, when ZnO content is 9 wt% (Figure 6.21).

Alam et al. [27] have prepared a polyaniline(PANI)/tin oxide (SnO<sub>2</sub>) hybrid nanocomposite through a coprecipitation process. UV-Vis spectroscopy was employed to characterize the optical properties of the synthesized nanocomposite materials. Figure 6.22 shows the results of optical absorption spectra of SnO<sub>2</sub>, PANI, and PANI/SnO<sub>2</sub> nanocomposite materials in visible region. SnO<sub>2</sub> nanoparticles show strong absorption in the UV light region (Figure 6.22a), and PANI shows three characteristic absorption bands at 274, 370, and 573 nm wavelengths, which are attributed to  $\pi-\pi^*$  conjugated ring systems, polaron- $\pi^*$  and  $\pi$ -polaron benzenoid to quinoid excitonic transition, respectively of the emeraldine base

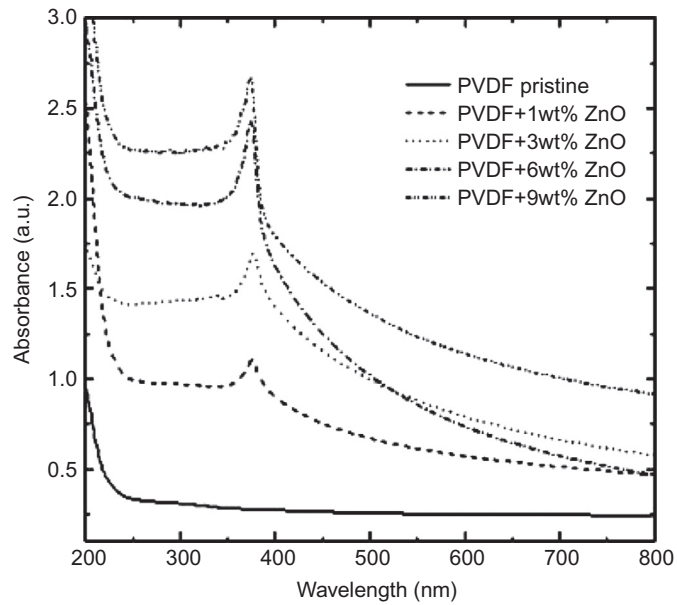


**FIGURE 6.21**

UV-Vis absorption spectra of PVDF pristine and PVDF–ZnO nanocomposites [26].

Copyright 2012. Reproduced with permission from Springer.

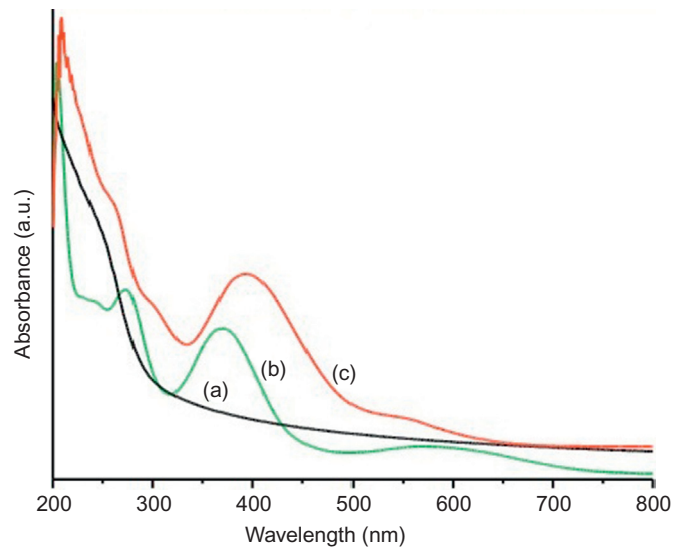


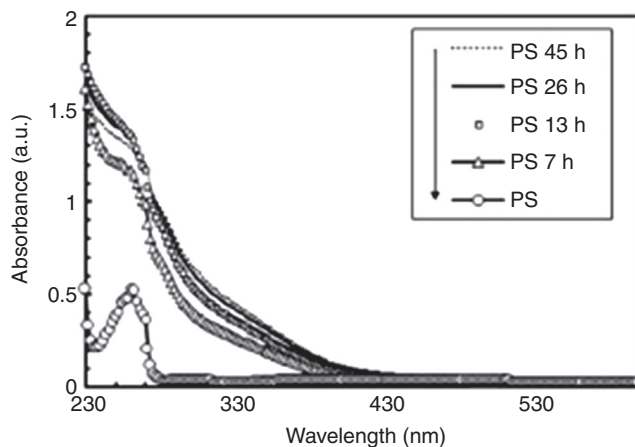
**FIGURE 6.22**

UV-Vis spectra of (a)  $\text{SnO}_2$ , (b) PANI, and (c) PANI/ $\text{SnO}_2$  nanocomposites [27].

Copyright 2013. Reproduced with permission from Elsevier Ltd.

(Figure 6.22b). The absorption band around 200–300 nm due to the conjugated system and  $\pi$ -polaron band around 500–750 nm gradually disappeared in the nanocomposites' spectrum and a new band around 400 nm emerged. The absorption band at 400 nm is attributed to the excitation from the highest occupied molecular orbital of the benzenoid to the lowest unoccupied molecular orbital of the localized quinoid ring and the two surrounding imine nitrogens in the emeraldine base form of PANI (Figure 6.22c). Furthermore, when tin oxide nanoparticles are dispersed in the PANI matrix, a significant change is measured in the absorption spectrum. The red shift of the absorption transition to higher wavelength may be due to the successful interaction of metal nanoparticles with the polymer chain. The characteristic features of absorption spectrum indicate that PANI/SnO<sub>2</sub> nanocomposite is in the conducting state.

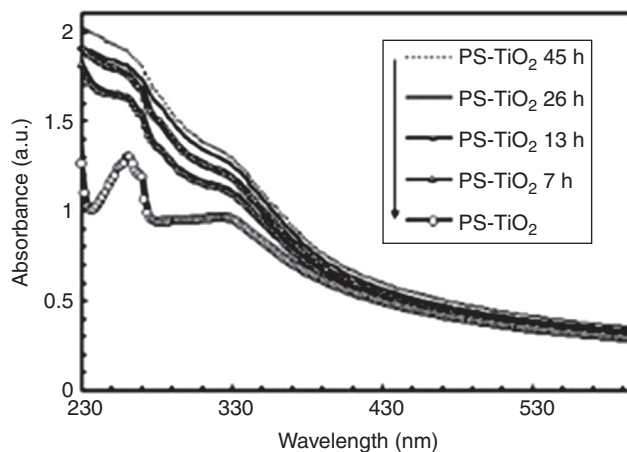
TiO<sub>2</sub> nanoparticles embedded PMC are the best candidates for the preparation of transparent UV filters and high refractive index materials. TiO<sub>2</sub> nanoparticles in polymer matrices also promote the photocatalytic degradation of the composite. Solid-phase photocatalytic degradation of PS plastic with TiO<sub>2</sub> as photocatalyst has been investigated under ambient conditions using UV light irradiation by Jaleh et al. [28]. They fabricated thin films of PS-TiO<sub>2</sub> nanocomposite using a spin coating method from a solution of PS in which TiO<sub>2</sub> nanoparticles were dispersed by mechanical mixing. UV-Vis spectroscopy has been effectively utilized to follow the photocatalytic degradation. The optical absorbance spectrum of PS and PS-TiO<sub>2</sub> nanocomposite films with similar thicknesses and different irradiation times over the wavelength ( $\lambda$ ) range 230–600 nm are shown in Figures 6.23 and 6.24. The absorption of the PS-TiO<sub>2</sub> film is increased due to the UV absorption of TiO<sub>2</sub> nanoparticles. The trend observed for all mentioned wavelengths is



**FIGURE 6.23**

UV-Vis spectra of PS film under UV-irradiation for 0, 7, 13, 26, and 45 h [28].

Copyright 2011. Reproduced with permission from Springer.

**FIGURE 6.24**

UV-Vis spectra of PS-TiO<sub>2</sub> film under UV irradiation for 0, 7, 13, 26, and 45 h [28].

Copyright 2011. Reproduced with permission from Springer.

similar (Figure 6.24). The changes of absorbance are significantly higher for photo-degraded nanocomposites than those for PS alone, exposed for the same time periods under the same conditions.

### 6.3.4 CARBON-BASED NANOMATERIALS AS NANOFILLERS

CNTs and graphenes are two technologically important carbon-based nanomaterials which are expected to revolutionize the field of electronics and energy sector in the near future. However, the lack of solubility and processability in common solvents and matrices limit the scope of these materials toward any commercial applications. Several approaches have been attempted to disperse CNTs and graphenes into solvents and matrices. One of the approaches, included the use of a suitable polymer matrix to disperse the carbon-based nanomaterials. The dispersant binds to the surface of the carbon framework through noncovalent interactions and prevents the material from aggregating, thereby enhancing dispersion. Conjugated block copolymers like poly(3-hexylthiophene) (P3HT) block copolymers are widely used because of the  $\pi$ - $\pi$  interaction between the carbon framework of CNTs and graphenes with the  $\pi$  conjugation of the conducting polymers [29]. Poly(3-hexylthiophene)-b-polystyrene (P3HT-b-PS) is one of the effective polymeric dispersants in chloroform for both single-walled CNTs (SWCNTs) and multiwalled CNTs (MWCNTs). Stronger the  $\pi$ - $\pi$  interaction between the P3HT block and CNTs, higher will be the dispersion of CNTs in the solvent chloroform. UV-Vis spectroscopy can be effectively used to investigate the extent of  $\pi$ - $\pi$  interaction between the polymer and CNTs. The UV-Vis absorption spectrum of P3HT-b-PS/SWCNT dispersion compared with P3HT-b-PS in solution and solid

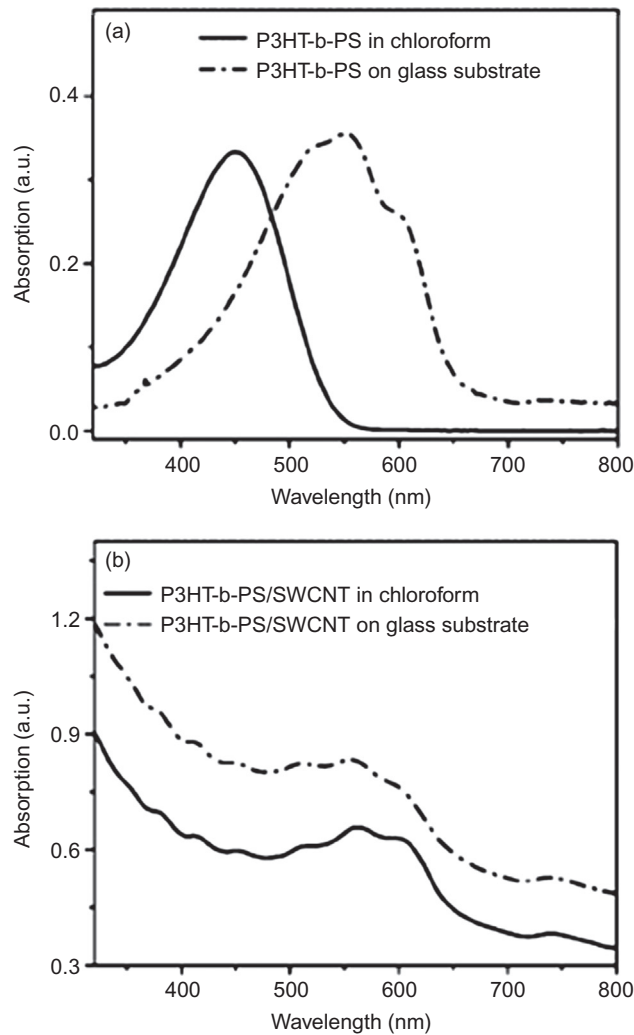


**FIGURE 6.25**

UV-Vis spectra of: (a) P3HT-b-PS in chloroform and a cast film on a glass substrate; (b) P3HT-b-PS/SWCNT (2:1) in chloroform and a cast film on a glass substrate [29].

Copyright 2012. Reproduced with permission from John Wiley & Sons.

phase is given in [Figure 6.25 a and b](#). P3HT-b-PS exhibits an absorption band at 454 nm in chloroform and three peaks (513, 560, and 604 nm) in solid state, which is due to increased coplanarity and extended  $\pi$  conjugation of the conducting block in the solid state ([Figure 6.25a](#)). The UV-Vis spectrum of P3HT-b-PS/SWCNT dispersion in the solution and solid state is similar to that of the solid state P3HT-b-PS

spectrum, with three absorption peaks at 513, 560, and 604 nm (Figure 6.25b). The results indicate that the P3HT block binds to the CNT surface in a coplanar geometry and this binding is not disturbed both in the solution and solid state obtained by solvent drying.

Similarly, Zhang et al. [30] have prepared PVA composite containing reduced graphene oxide (r-GO)/acid treated MWCNTs hybrids (t-CNT) (the hybrid abbreviated as G-CNT) by a simple water casting method. Here, two kinds of nanofillers, r-GO and t-CNTs are dispersed in the polymer to yield a high performance polymer nanocomposite. The synergistic interaction between the two kinds of nanofillers is studied using the UV-Vis spectral technique. The UV-vis spectra of GO sheets, r-GO sheets, t-CNTs, and G-CNT hybrids are shown in Figure 6.26. The t-CNTs exhibit a broad band around  $245\text{ cm}^{-1}$  due to the extended  $\pi$  conjugation of the CNT framework. The GO sheets exhibit two peaks at 228 and 300 nm due to  $\pi-\pi^*$  transition of aromatic C–C bonds and  $n-\pi^*$  transitions of C–O bonds, respectively. When GO sheets are reduced in the presence of t-CNTs, the r-GO does not show any peak in the UV-Vis region whereas the G-CNT hybrid prepared with r-GO and t-CNT (1:1) exhibits a peak around 250 nm, like that of pure t-CNT with a slight red shift. The results indicate that GO is completely reduced and present as r-GO in the polymer matrix along with t-CNTs.

UV-Vis spectroscopy is also used to study the optical properties, such as transmittance, absorbance, and reflection of polymer thin films after incorporation of clays like montmorillonite [31], bentonite, smectite, hectorite, and halloysite as nanofillers. The polymers widely used for such studies are PMMA [32], PVDF, polylactide [31], and other similar polymer matrices.

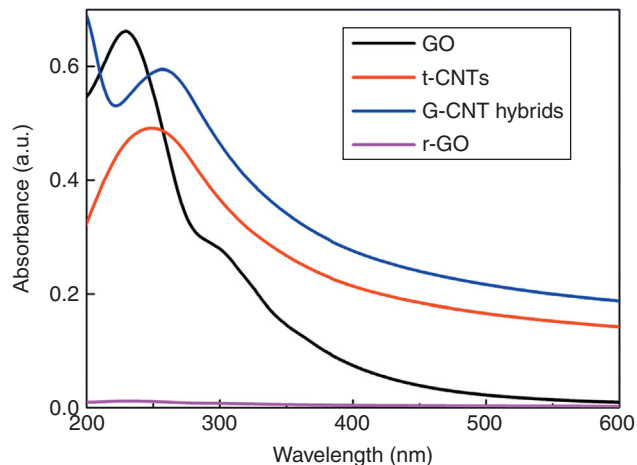


**FIGURE 6.26**

UV-Vis absorption spectra of the supernatants of GO sheets, t-CNTs, r-GO sheets, and G-CNT (1:1) hybrids [30].

Copyright 2012. Reproduced with permission from Royal Society of Chemistry.

---

## 6.4 CONCLUSION

UV-Vis spectroscopy is one of the important characterization techniques to study the optical properties of PMCs. It helps to understand the interaction between the matrix and the nanofiller and analyzes the role of nanofillers in enhancing the property of the nanocomposites. Coupled with other characterization methods, UV-Vis spectroscopy is an indispensable tool to evaluate the desired optical properties of nanofillers in a polymer matrix. Based on the analysis of the absorption characteristics of the PMC, further fine tuning of the desired optical properties can be achieved by careful selection of the type and composition of nanofiller in a polymer matrix. The chapter reveals the importance of the UV-Vis spectroscopic technique to characterize the polymer nanocomposites with some of the optically responsive nanofillers, such as metals, semiconductor nanocrystals, and nano oxides; toward development of functional materials with technologically important applications.

---

## REFERENCES

- [1] Li S, Lin MM, Toprak MS, Kim DKK, Muhammed M. Nanocomposites of polymer and inorganic nanoparticles for optical and magnetic applications. *Nano Rev* 2010;1:5214. Available from: <http://dx.doi.org/10.3402/nano.v1i0.5214>.
- [2] Chen L, Zhang Y, Zhu P, Zhou F, Zeng W, LuD D, et al. Copper salts mediated morphological transformation of Cu<sub>2</sub>O from cubes to hierarchical flower-like or microspheres and their supercapacitors performances. *Sci Rep* 2015;5. Available from: <http://dx.doi.org/10.1038/srep09672>.
- [3] Cao Z, Fu H, Kang L, Huang L, Zhai T, Ma Y, et al. Rapid room-temperature synthesis of silver nanoplates with tunable in-plane surface plasmon resonance from visible to near-IR. *J Mater Chem* 2008;18:2673–8.
- [4] Saute B, Premasiri R, Ziegler L, Narayanan R. Gold nanorods as surface enhanced Raman spectroscopy substrates for sensitive and selective detection of ultra-low levels of dithiocarbamate pesticides. *Analyst* 2012;137:5082–7.
- [5] Zhu JF, Zhu YJ. Microwave-assisted one-step synthesis of polyacrylamide-metal (M) Ag, Pt, Cu) nanocomposites in ethylene glycol. *J Phys Chem B* 2006;110:8593–7.
- [6] Khanna PK, Singh N, Charan S, Subbarao VVVS, Gokhale R, et al. Synthesis and characterization of Ag/PVA nanocomposite by chemical reduction method. *Mater Chem Phys* 2005;93:117–21.
- [7] Chitte HK, Bhat NV, Karmakar NS, Kothari DC, Shinde GN. Synthesis and characterization of polymeric composites embedded with silver nanoparticles. *World J Nano Sci Eng* 2012;2:19–24.
- [8] Biswas A, Aktas OC, Schürmann U, Saeed U, Zaporozhchenko V. Tunable multiple plasmon resonance wavelengths response from multicomponent polymer-metal nanocomposite systems. *J Appl Phys Lett* 2004;84:2655–7.
- [9] Saini I, Rozra J, Chandak N, Aggarwal S, Sharma PK, Sharma A. Tailoring of electrical, optical and structural properties of PVA by addition of Ag nanoparticles. *Mater Chem Phys* 2013;139:802–10.

- [10] Petersson L, Oksman K. Biopolymer based nanocomposites: comparing layered silicates and microcrystalline cellulose as nano reinforcement. *Composites Sci Technol* 2006;66:2187–96.
- [11] Kim HW, Song JH, Kim HE. Nanofiber generation of gelatin–hydroxyapatite biomimetics for guided tissue regeneration. *Adv Funct Mater* 2005;15:1988–94.
- [12] Zhao R, Torley P, Halley PJ. Emerging biodegradable materials: starch- and protein-based bio-nanocomposites. *J Mater Sci* 2008;43:3058–71.
- [13] Wang SF, Shen L, Tong YJ, Chen L, Phang IY, Lim PQ, et al. Biopolymer chitosan/montmorillonite nanocomposites: preparation and characterization. *Polym Degrad Stabil* 2005;90:123–31.
- [14] Balogh LP, Redmond SM, Balogh P, Tang H, Martin DC, Rand SC. Self-assembly and optical properties of dendrimer nanocomposite multilayers. *Macromol Biosci* 2007;7:1032–46.
- [15] Vasile E, Serafim A, Petre D, Giol D, Dubruel P, Iovu H, et al. Direct synthesis and morphological characterization of gold-dendrimer nanocomposites prepared using PAMAM succinamic acid dendrimers: preliminary study of the calcification potential. *Sci World J* 2014. Available from: <http://dx.doi.org/10.1155/2014/103462>.
- [16] Huang H, Yuan Q, Yang X. Preparation and characterization of metal–chitosan nanocomposites. *Colloids Surf B Biointerfaces* 2004;39:31–7.
- [17] Božanić DK, Branković SD, Bibića N, Luyte AS, Djoković V. Silver nanoparticles encapsulated in glycogen biopolymer: morphology, optical and antimicrobial properties. *Carbohydr Polym* 2011;83:883–90.
- [18] Mironenko A, Modin E, Sergeev A, Voznesenskiy S, Bratskaya S. Fabrication and optical properties of chitosan/Ag nanoparticles thin film composites. *Chem Eng J* 2014;15:457–63.
- [19] Smith AM, Gao X, Nie S. Quantum dot nanocrystals for *in vivo* molecular and cellular imaging. *Photochem Photobiol* 2004;80:377–85.
- [20] Mädler L, Stark WJ, Pratsinis SE. Rapid synthesis of stable ZnO quantum dots. *J Appl Phys* 2002;92:6537–40.
- [21] Wu XC, Bittner AM, Kern K. Synthesis, photoluminescence, and adsorption of CdS/dendrimer nanocomposite. *J Phys Chem* 2005;B109:230–9.
- [22] Tamborra M, Striccoli M, Comparelli R, Curri ML, Petrella A, Agostino A. Optical properties of hybrid composite based on highly luminescent CdS nanocrystals in polymer. *Nanotechnology* 2004;15:S240–4.
- [23] Reisfeld R. Nanosized semiconductor particles in glasses prepared by the sol–gel method: their optical properties and potential uses. *J Alloys Comp* 2002;341:56–61.
- [24] Lim WP, Low HY, Chin WS. IR-luminescent PbS-polystyrene nanocomposites prepared from random ionomers in solution. *J Phys Chem* 2004;B108:13093–9.
- [25] Hammad TM, Salem JK, Kuhn S, Abu NM, Hempelmann SR. Surface morphology and optical properties of PVA/PbS nanoparticles. *J Luminescence* 2015;157:88–92.
- [26] Indolia AP, Gaur MS. Optical properties of solution grown PVDF-ZnO nanocomposite thin films. *J Polym Res* 2012;20:1–8.
- [27] Alam M, Ansari AA, Shaik MR, Alandis NM. Optical and electrical conducting properties of polyaniline/tin oxide nanocomposite. *Arab J Chem* 2013;6:341–5.
- [28] Jaleh B, Shayegani Madad M, FarshchiTabrizi M, Habibi S, Golbedaghi R, Keymanesh MR. UV-degradation effect on optical and surface properties of polystyrene-TiO<sub>2</sub> nanocomposite film. *J Iran Chem Soc* 2011;8:S161–8.

- [29] Zou J, Liu L, Chen H, Khondaker SI, McCullough RD, Huo Q, et al. Dispersion of pristine carbon nanotubes using conjugated block copolymers. *Adv Mater* 2008;20:2055–60.
- [30] Zhang C, Huang S, Tjiu WW, Fan W, Liu T. Facile preparation of water-dispersible graphene sheets stabilized by acid-treated multi-walled carbon nanotubes and their poly(vinyl alcohol) composites. *J Mater Chem* 2012;22:2427–34.
- [31] Morlat S, Mailhot B, Gonzalez D, Gardette JL. Photo-oxidation of polypropylene/montmorillonite nanocomposites. I. Influence of nanoclay and compatibilizing agent. *Chem Mater* 2004;16:377–83.
- [32] Park JH, Jana SC. The relationship between nano- and micro-structures and mechanical properties in PMMA–epoxy–nanoclay composites. *Polymer* 2003;44:2091–100.

## 7

Fluorescence spectroscopy  
of nanofillers and their  
polymer nanocomposites

**Rohit Ranganathan Gaddam, Ramanuj Narayan and KVS N Raju**

*Polymers and Functional Materials Division, CSIR-Indian Institute of Chemical Technology, Hyderabad, India*

## 7.1 INTRODUCTION

Fluorescence spectroscopy is a versatile technique which provides exceedingly sensitive instrumentation for measuring different sensing approaches like intensity, polarization, and lifetime of a sample [1]. Intracellular monitoring of different samples via fluorescence microscopy has made many medical and biological studies possible. Fluorescence studies on organic dyes are simple, well-established, diverse, non-destructive, and can provide real time dynamic information. These dyes are characterized by low absorption coefficients and weak signals that hinder the sensitivity and response of the measurement. Their long-term tracking and short fluorescent times are limited by the inherent poor resistance to photo bleaching, which in turn is a serious drawback for many applications. Photo bleaching is a process by which an organic dye or any fluorophore permanently loses its ability to fluoresce due to photochemical alterations. This is generally caused by cleavage of bonds or nonspecific reaction between the dye and the surrounding molecule. Organic dyes are found to be more susceptible to photo bleaching. Therefore, development of new fluorescent probes with higher brightness levels and photo-stability is highly desirable [2].

The recent advances in nanotechnology, especially the development of new nanomaterial have encouraged the blending of analytical chemistry and fluorescence spectroscopy for effective design as chemical and biological probes [3]. Nanoparticle-based design platforms show clear advantage over traditional approaches in terms of sensitivity, stability, and capacity of multiplexing. Therefore, instead of using simple organic dye probes, they are embedded in a particle matrix. This embedded nanoparticle probe overcomes the drawback of organic dyes by instilling more photostability and biocompatibility. It is not always necessary to have organic dyes to provide fluorescence to nanoparticles.

For instance, semiconducting nanocrystal fluoresce when their size becomes comparable to that of bohr exciton radius, which are called quantum dots.

Semiconducting quantum dots (QDs) are intrinsically fluorescent and also provide excellent optical properties. The fluorescence properties of these QDs are attributed to their small size comparable to their Bohr exciton radius. Higher quantum confinement leads to better fluorescent property. These QDs provide a high signal-to-noise ratio along with the signal amplification, which therefore provides high sensitivity and quick response time [4]. These QDs are stable fluorophores due to their inorganic configuration, which diminishes the effect of photobleaching when compared with organic dyes. As an added advantage, the fluorescence time for QDs is about 10–40 ns, which is longer than that of organic dyes whose fluorescence is only a few nanoseconds. The inorganic composition of QDs also makes them more robust towards metabolic degradation, which contributes to their longevity *in vivo*. The large Stokes shift (difference between peak absorption and peak emission wavelengths) reduces autofluorescence which increases sensitivity.

Many approaches exist for the fabrication of nanoparticles with different geometries using a range of organic or inorganic materials based on different synthesis strategy [5]. Even polymers like polystyrene (PS) [6], acrylate derivatives [7,8], and dendrimers-based nanoparticles have been synthesised and reported. More recently, there are even reports of fluorescent carbon QDs: that is, a carbon nanoparticle typically in the range of 1–10 nm which self-fluoresces under ultraviolet (UV) light [9]. As fluorescent nanoparticles have become available, they have quickly been substituted for the traditional organic dyes for biological, polymer, and electronic applications.

In order to be used in functional devices, these nanoparticles need to be incorporated into a solid-state matrix. Such multicomponent material is called a nanocomposite. These materials have the advantage of combining the exceptional property of the nanomaterials along with the technological feasibility of the matrix. Among the available matrices polymer, owing to its easy availability, processability, and tunability, is a very promising material for the dispersion of nanoparticles [10]. The term polymer nanocomposite in a broad sense can be used to represent a nanoscale polymer matrix with nanoparticle filler (typically a core-shell like geometry) or bulk polymer matrix with nanoscale dispersion. In both the cases the nanofiller plays a major role in enhancing the property of the obtained composite. Therefore, fluorescence spectroscopy provides us the opportunity to investigate the structure and dynamics of the nanocomposite [11].

This chapter focuses mainly on the importance of fluorescence spectroscopy of nanofillers and their respective nanocomposites. Brief descriptions of the fluorescent experiments are discussed to showcase their importance of fluorescence in characterizing nanomaterials and their polymer nanocomposite and also the type of information that can be obtained from such measurements. Different areas and practicality of these experiments for providing information on nanocomposites are also discussed. Types of fluorescent nanocomposites are briefed. The advances in fluorescent measurement technologies are provided to outline the various possibilities that fluorescence offers to characterize nanomaterials and their respective composites.

## 7.2 MECHANISM OF FLUORESCENCE

A majority of molecules generally exists in the ground state at room temperature. When exposed to electromagnetic (EM) radiation, the molecules can absorb energy and get promoted to higher-energy state called the excited state. As a result of absorbing the radiation, the molecule can be at any subvibrational levels within the defined electronic state. Since the radiation absorbed is discrete in quanta, it might be judicious to consider series of absorption bands in the absorption spectrum. However, there are a series of rotational energy levels, which are superimposed on the vibrational energy levels that make it impractical to depict individual bands in the spectrum. Therefore broad absorption spectra with no sharp features are observed in most of the compounds (excluding planar and aromatic compounds) [12].

An excited molecule in the highest vibrational state is unstable and loses part of its energy by molecular collision and eventually reduces to the lowest vibrational energy of its excited state. Subsequently, a molecule will undergo an internal conversion where there is an energy transfer at the lowest vibrational energy at the upper excited state and highest vibrational energy at the lower excited state. This process repeats until the molecule finally reaches its lowest vibrational energy at its first excited state. From this level, a molecule can come down to any energy level by release of a photon of energy in the form of fluorescence. If all the excited molecules returns to the ground state, then the efficiency of the overall quantum phenomena is unity. Also, the emission of photons while returning to the ground state is the opposite of absorption. Therefore emission spectrum of fluorescence can be expected to coincide with that of the absorption spectrum. Nevertheless, such coincidence rarely occurs due to energy losses associated with the solvent or solute molecules [12].

The process that occurs in the absorption and emission of photon is generally depicted by the Jablonski diagram (Figure 7.1). The singlet states are represented

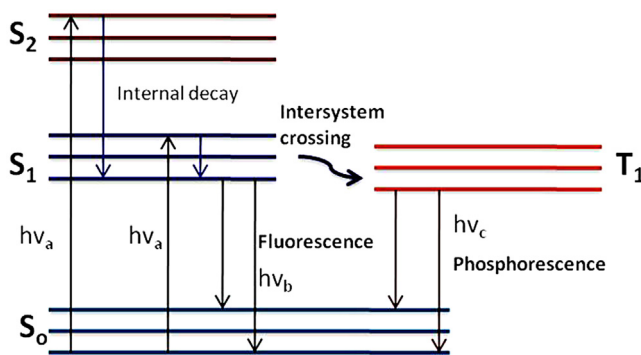


FIGURE 7.1

Jablonski diagram representing fluorescence and phosphorescence phenomena.

by  $S_0$ ,  $S_1$ , and  $S_2$  for ground first and second excited state. Each of these states contains subvibrational states. Transitions occur in the range of  $10^{-5}$  ns in accordance, which is too short for significant displacement of nuclei. The fluorescence follows a singlet-singlet transition. However, molecules in the  $S_1$  state can undergo a spin conversion to first triplet state  $T_1$ . The emission from  $T_1$  to the ground state (called *phosphorescence*) takes place through longer wavelengths (lower energy) with respect to that of fluorescence. The occurrence is an intersystem crossing and a triplet to singlet transition is generally forbidden. As a result, the rate constant for triplet state is several orders of magnitude smaller than those for fluorescence. The important parameter of a fluorescence measurement is the fluorescence lifetime and quantum yield. Quantum yield depicts the number of photons emitted, relative to those absorbed. The lifetime of a fluorophore is important to determine its interaction with the environment [13].

---

### 7.3 INSTRUMENTATION FOR FLUORESCENCE SPECTROSCOPY

A fluorescence spectrophotometer (Figure 7.2) contain three major components; a source of light, a sample holder, and a detector. For accuracy and precision, the incident radiation needs to be selectable and the detector should be highly sensitive to manipulation and selection. Generally, two types of fluorometers exist: filter fluorometers (which use filters to isolate the incident light and fluorescent light) and spectrofluorometers (which use diffraction-grating monochromators to isolate the incident light and fluorescent light).

Both the previously mentioned fluorometers use the following scheme for measurement: the light incident from the source passes through a filter and strikes the sample. A portion of the light incident on the sample is absorbed and some of the molecules in the samples fluoresce. The fluoresced light emitted is again passed through a filter or a monochromator to a detector. The detector is usually placed at a right angle to the incident light beam to minimize the risk of a transmitted or reflected incident beam reaching the detector. In order to achieve good

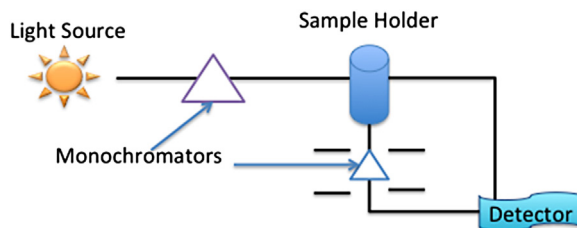


**FIGURE 7.2**

A typical setup of fluorescence spectroscopy.

sensitivity, filters that allow total range of wavelengths of emitted light from the sample to be collected with highest intensity source are preferred [13].

### 7.3.1 LIGHT SOURCE

The light source generally employed has spectral outputs as a continuum of energy in fluorescence spectrometry or discrete lines. Various light sources may be used as excitation sources like lasers, light emitting diodes, arc lamps, xenon lamps, and mercury vapor lamps. The mercury lamps are among the most commonly used light source whose EM radiation relies on the pressure of the filler gas. Low-pressure mercury lamps produce spectra in the UV range. Therefore, high- and medium-pressure lamps are used, which can generate spectra covering the whole UV-visible (Vis) region. Xenon bulbs can be used on either a continuous direct current (DC) basis or stroboscopically. The use of these bulbs offers advantages of cost and tenability in size of the lamp. The output is a continuum on which a number of sharp lines are superimposed allowing the feasibility of selecting wavelengths within the whole of UV-Vis spectrum. Arc lamps are more stable than discharge lamps. For long-term stability, a method for compensating for drifts is advisable [14].

### 7.3.2 SAMPLE HOLDER

The majority of fluorescence measurement is carried out in solution form, which is held in cuvettes of various geometries. Square cuvettes are generally used to facilitate easy maintenance of path-length. Round cuvettes are also regularly used as they are easily available at cheaper rates. The cuvette is placed normal to the incident beam. The sample is excited and fluorescence is given off equally in all directions, which can be collected from the front surface of the cell opposite to the incident beam or in-line with the incident beam. There is also a possibility to choose the type of measurement preferred depending on the loaded sample [14,15].

Fluorescence occurs from every point along the path of light in the sample. However, only a small part of this fluorescence is transmitted and passed onto the detector. Therefore much of the solution does not contribute to fluorescence measurement. Thus, the same intensity is observed from a relatively smaller quantity of sample. Also, some samples might not show fluorescence if the concentration is too high. Before checking the fluorescence, it is always better to consider checking absorbance for unknown samples.

### 7.3.3 DETECTOR

All fluorescence instruments use photomultiplier tubes as detectors, and a wide variety of such types are available. The material from which the photocathode is made determines the spectral range of photomultiplier, and generally, two tubes are required for UV-Vis range. The level of dark current might cause alterations

in the sensitivity of photomultiplier. The dark current is caused by thermal activation and can usually be reduced by cooling the photomultiplier. The spectral response of all photomultipliers varies with wavelength, however it is sometimes necessary to determine the actual quantum intensity of the incident radiation and a detector insensitive to changes in radiation is required [16].

---

## 7.4 FLUORESCENCE MEASUREMENT TYPES

Fluorescence measurements are broadly classified into two types: namely, steady-state and time-resolved [17].

### 7.4.1 STEADY-STATE FLUORESCENCE

The steady-state measurements involve constant illumination of the sample and observation of the emission. The time scale of fluorescence is in fractions of a nanosecond and therefore most of the measurements made are steady state in nature. The sample also reaches the steady state almost instantaneously upon illumination [18]. The shape of the obtained spectrum and the position of the emission maxima can provide insights into the polarity and mobility. The energy transfer, as a measure of distance between two fluorescent species can be studied through the emission spectra. Excitation of the fluorophore with a polarized light along with a sensitive detection allows anisotropy measurements for information on the rotational mobility of the probe molecule. The emission spectra can also be used to study dynamical processes by embedding probes within the polymer of interest. However quantifying the emission intensity from a polymer sample is difficult. Therefore, for dynamical studies, time-resolved fluorescence measurements are generally preferred.

### 7.4.2 TIME-RESOLVED FLUORESCENCE

In a time-resolved measurement, the sample is exposed to a pulse of light where the pulse width is typically shorter than the decay time of the sample. The intensity decay or anisotropy decay is measured in this kind of measurement using high-speed detectors. Considering the fact that time-resolved measurement provides data on intensity decay, the average of these decays could be seen as steady-state phenomena.

Although steady-state measurements are simple, unlike time-resolved measurements of fluorescence, which require sophisticated instrumentation, they cannot provide complex information about fluorescence measurement. This is because much of the molecular information is lost during the time-averaging process. The excited state decay of fluorescence typically ranges in fractions of a nanosecond to picoseconds. The dynamical processes, which occur in this timescale, can be

measured by time-resolved study. Also, time-resolved fluorescence studies reveal whether the quenching of a sample occurs due to diffusion or formation of a complex [19–21]. The conformational changes in the molecule and viscosity of the polymer are more directly measured by time-resolved fluorescence.

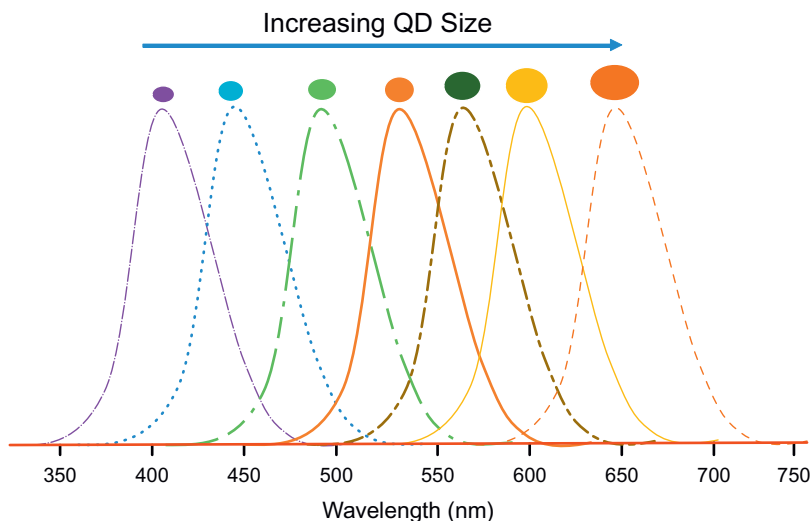
---

## 7.5 FLUORESCENCE SPECTROSCOPY FOR MATERIAL CHARACTERISTICS

Many interesting conclusions can be drawn based upon the emission spectra, stokes shift, and fluorescence quenching profiles studied by the fluorescence spectroscopy. They can provide us an insight into the molecular phenomena and dynamic processes, which can occur in different materials.

The quantum size effects in nanomaterials could be observed from the emission spectra. The quantization of the material can be deduced from the optical absorption and emission spectra, especially while using semiconductor nanofiller. In such nanofillers, the band gap  $E_g$  between the highest occupied electronic state (also called valence band) and lowest occupied electronic state (also called the conduction band) decrease with the particle size. Also the energy required to create an electron-hole pair (exciton) is directly related to  $E_g$  of the material. The exciton formed has a limited lifetime and therefore recombines [22]. The recombination releases energy which is too large to be dissipated by vibrational modes and is therefore released in the form of photons. The radioactive decay in the form of photons (i.e., fluorescence) is highly probable in the case of semiconducting QDs [23,24]. The semiconductor nanoparticles cannot absorb light with energy less than that of  $E_g$  to form an exciton. Therefore, the absorption is directly related to the size of nanofiller. In most cases a blue shift in emission spectra is found when the size of semiconductor nanomaterial decreases (Figure 7.3). This property can provide us information on the color of semiconductor, which is a material-specific property that becomes size-specific and paves the way for different colors among the same material over the whole visible EM spectrum. In addition, the lowest absorption energy, the lowest peak of optical excitation and emission energy (i.e., the wavelength of fluorescence) is not identical and can be used in deducing the material characteristics. The red shift in emission, also called the stokes shift, is strongly dependent on the surface properties of the particles. In order to utilize the nanomaterials in functional devices, they are dispersed into a solid-state matrix—generally a polymer.

Fluorophores absorb light in a particular direction along the molecular axis. The extent to which the fluorophore rotates during the excited state determines its fluorescence and anisotropy. This phenomenon can be used to determine the volume or molecular weight of the polymer [13]. This measurement is possible because the polymers are large molecules and therefore rotate slowly. Hence

**FIGURE 7.3**

Shift in the fluorescence emission peak with increase in QD size [13].

*Copyright 2014. Reprinted with permission from Elsevier Ltd.*

during mutual interaction of polymers, the rotation rate decreases and the anisotropy increases. The rotational axis is generally described by the correlation time  $t$ :

$$t = \frac{\eta V}{RT} \quad (7.1)$$

where  $R$  is the gas constant,  $T$  is the temperature,  $\eta$  is the viscosity, and  $V$  is the molecular volume. Owing to the relation between steady-state anisotropy,  $r$  and the rotational correlation time,  $t$ , any mutual interaction between polymers cause increase in the anisotropy. Therefore, fluorescence is an aspect which allows investigation of dynamic processes occurring in polymer science, such as different types of polymerizations, cross linkings, film formations, glass transition, phase separation, interpenetration, and diffusion of polymer chains.

The combination of monomers (which have low molecular weight and are less viscous) forms polymers. Once the monomers are linked together, they form polymers where the viscosity and the molecular weight increase rapidly. The polymerization process may occur either by chain growth or a step-growth mechanism.

Step-growth polymerization has a higher conversion rate due to controlled kinetics [25]. In any method of polymerization a general observation is that the viscosity of the material increases, and this can be effectively followed by fluorescent probes or nanofillers, which are sensitive to the mobility and rigidity of the medium. The increase in the viscosity can be detected in different ways. When the molecular rotation is hindered on the time scale of excited state

lifetime, the fluorescence emission is anisotropic in nature. Rigidochromic probes fluoresce weakly, due to radiationless decay, and this is suppressed when the viscosity increases. Solvatochromic fluorescent probes are also sensitive to viscosity because the formed excited state dipole requires stabilization, which is accomplished by the reorganization of the medium. Translational diffusion can be effectively probed by diffusive quenching processes [26].

Another important parameter of interest is the resonance energy transfer. This phenomenon occurs whenever the emission spectrum of the nanofiller (donor) overlaps with the absorption spectrum of the polymer (acceptor). It is important to understand that the phenomena does not require polymer to be fluorescent. The nanofiller also need not emit light. The donor and acceptor are coupled by dipole–dipole interaction. The distance between the donor and acceptor, and the extent of spectral overlap determines the extent of energy transfer. The efficiency of energy transfer for a single donor–acceptor pair is given at a fixed distance by Eqn (7.2):

$$E = \frac{A^6}{A^6 + r} \quad (7.2)$$

where  $A$  is the Förster distance and the extent of transfer depends on distance  $r$ .

The Förster distances are comparable to that of macromolecules. The field of resonance energy transfer is large and complex. If two monomers combine together to form a dimer, then the Förster distance is determined by the spectral overlap of the donor emission with that of the acceptor absorption (Figure 7.4). During this association a resonance energy transfer occurs which decreases the intensity of donor emission. The extent of donor quenching can be used to calculate the donor-to-acceptor quenching.

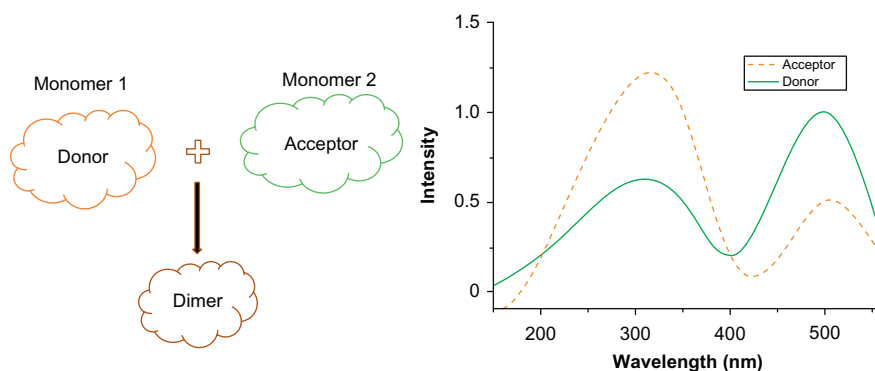


**FIGURE 7.4**

Energy transfer between donor and acceptor monomer to form a dimer.

## 7.6 FLUORESCENCE STUDIES OF NANOFILLER AND POLYMER NANOCOMPOSITES

In a polymer nanocomposite, the fluorescence can be credited to either the polymer matrix, the nanofiller, or both. The fluorescent nanofillers used can be semiconducting QDs, metals, rare-earth elements, and other inorganic nanomaterials. Polymers themselves can also be fluorescent. The interface between polymer and nanofiller may also generate fluorescence, such as in the examples provided in the next discussion. Various types of nanocomposites and their fluorescence studies are also described.

### 7.6.1 POLYMER COMPOSITE WITH FLUORESCENT SEMICONDUCTING NANOFILLER

This polymer composite mostly introduces semiconducting QDs (i.e., CdSe, ZnS, PbS, GaN, and InAs) or other nanoparticles (i.e., ZnO, TiO<sub>2</sub>) into polyurethanes, methacryl-based polymers, or polyvinyl alcohols. The color of fluorescence emitted can be well tuned according to the geometry of nanoparticle used. Khanna et al. [26] showed that embedding CdS nanoparticles in polyvinyl alcohol produced yellow and orange light emission. In another report a fluorescence maximum of 630 nm was found when CdS nanoparticles were dispersed in a polyethylene oxide matrix.

Studies were also carried out in order to showcase the effect of particle size on fluorescence. Tamborra et al. [27] demonstrated that the CdS and CdSe/ZnS nanoparticles dispersed in a poly methyl methacrylate matrix can have a broad range of emission maxima from red to blue depending on the size. Biocompatible fluorescent nanocomposites using polylactic acid and CdS nanofillers are also developed. Fang et al. [28] reported a CdS/poly(*n*-methylol acrylamide) composite which exhibited a fluorescence at 530 nm. The fluorescence, which appeared at 350 nm, was attributed to that of the polymer.

ZnO is a versatile material, which can be used to develop a large variety of fluorescent nanocomposites. The fluorescence of a ZnO-based polymer nanocomposite is generally observed in the UV region and can be utilized in a variety of applications, ranging from sensors to early corrosion detection. ZnO-based PMMA [29,30], epoxy [31], and polyurethane [32] are well reported. Kantheti et al. [31] has reported the formation of a ZnO-based triazole rich, hyperbranched polyurethane with a fluorescence emission around 350–400 nm (far-UV region) for corrosion and microbe resistant composite. The work also suggests a possibility for early corrosion detection (Figure 7.5).

Figure 7.5a and b gives the UV absorption and fluorescence emission spectral analysis of the pyrene-attached ZnO nanoparticles, 10% PyZnO and 20% PyZnO, respectively. From UV analysis, the spectral features at 266, 277, 328, and 344 nm correspond to  $\pi \rightarrow \pi^*$  electronic transitions of pyrene aromatic ring

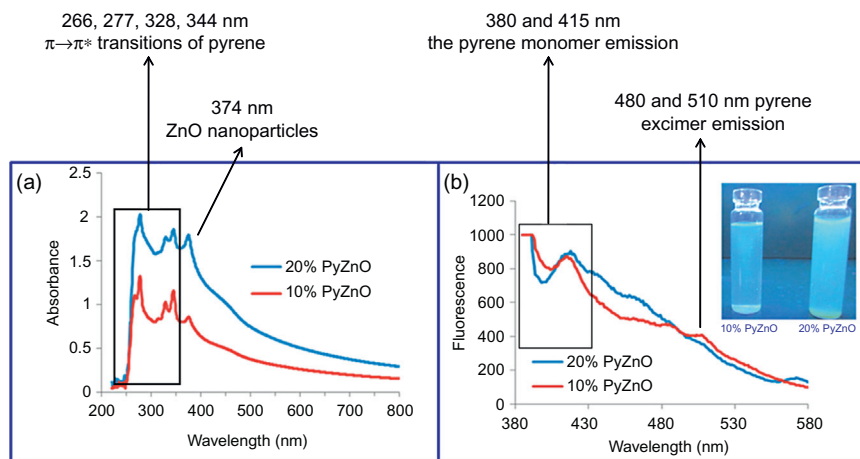


**FIGURE 7.5**

(a) UV spectral analysis, and (b) fluorescence spectra of 20% and 10% pyrene-capped ZnO nanoparticles.

electrons, and the peak at 374 nm corresponds to ZnO nanoparticles. This observation, along with the disappearance of azide stretching frequency in PyZnO Fourier transform infrared (FT-IR) spectra, clearly indicates the occurrence of click reactions between azide-functionalized ZnO nanoparticles with propargyl pyrene molecules. It was observed that, with an increase in concentration of pyrene units on the surface of ZnO nanoparticles, the UV absorption intensity also increases. From fluorescence emission data (Figure 7.5b), the highest intense peak was observed at 380 and 415 nm, which correspond with the pyrene monomer emission, whereas the lowest intense peaks observed at 480 and 510 nm correspond with pyrene excimer emission. The lower intensity of the excimer emission can be attributed to the immobilization of pyrene units on the hydrophobic ZnO nanoparticle surface. From this, it is clear that the attachment of pyrene units onto the ZnO surface results in the formation of fluorescent active ZnO nanoparticles in the UV region. Therefore, fluorescence spectroscopy can be used as a tool to characterize the attachment of fluorophore onto the surface of ZnO nanoparticles [32].

The polyurethane nanocomposites, such as 2% PyPU, 5% PyPU, and 10% PyPU, were also tested for the UV absorption and fluorescence emission spectroscopic studies. Figure 7.6a and b gives the UV absorption and fluorescence emission spectral analysis of the PyPU nanocomposites respectively. From UV analysis of films; it was observed that with increase in the loading of the PyZnO nanoparticles, the resulting nanocomposites show an improvement in the absorption intensity (Figure 7.6a). The peaks observed around 250–300 and 320 nm correspond to pyrene units, and peaks observed around 340 nm correspond to the ZnO nanoparticles. Similarly in fluorescence spectroscopy, the fluorescence

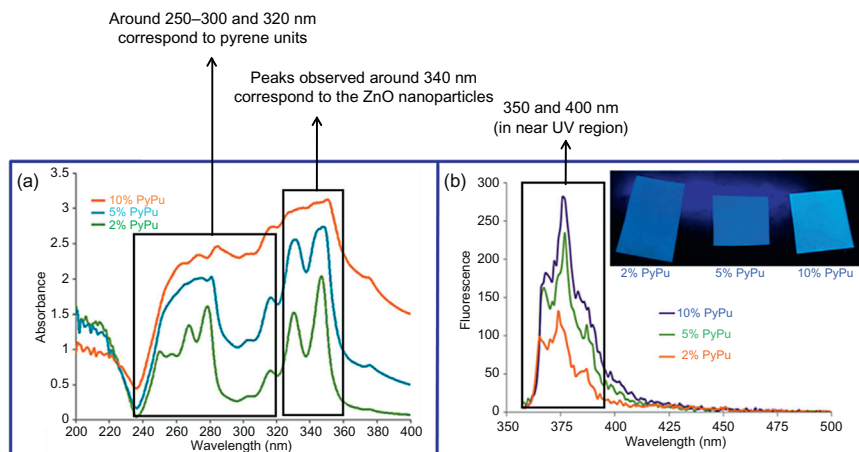


**FIGURE 7.6**

(a) UV spectral analysis, and (b) fluorescence spectra of 2%, 5%, and 10% nanoparticle-incorporated polyurethane hybrid films.

emission of the resulting nanocomposite increases gradually with loading of pyrene-grafted ZnO nanoparticles (Figure 7.6b). All these films show good fluorescence emission between 350 and 400 nm (in the near-UV region). In polyurethane film, fluorescence emission of pyrene monomers was observed, whereas the fluorescence of pyrene excimer (at 480 nm) was completely quenched, which may be due to the presence of hydrophobic urethane groups [32]. Therefore, Kantheti et al. [31] showed the importance of fluorescence spectroscopy in real-time analysis of polyurethane nanocomposites.

Another interesting example of semiconducting nanofiller is PbS. IR luminescent PbS/PS [33] can have emission in the visible and IR regime, which has strong effect on particle size. Syed et al. [33] studied the quantum size effect and exploited the fluorescence of PbS QDs in a different way. The optoimpedance spectroscopic studies were carried out in order to establish the optoelectronic properties of PbS QDs in the strongly, weakly, and the intermediately confined systems. Using the FT-IR spectroscopy, the strongly confined PbS was found to exhibit pronounced electron-lattice coupling characteristics. Optoimpedance characteristics suggest the enhanced mobility of charges like the supra band gap excitation for strongly confined QDs.

### 7.6.2 CORE/SHELL NANOFILLER-INCORPORATED POLYMER COMPOSITE

Core-shell nanofillers are generally used in order to exploit the property of both the core and shell material in a polymer matrix. Sometimes the shell also acts as

a protective layer so as to avoid agglomeration of cores. The core and the shell are typically composed of type II–VI, IV–VI, and III–V semiconductors in various combinations. Organically passivated QDs have low fluorescence quantum yield due to surface related trap states. Depending on the position of the valence and conduction band and the essential energy gap between them in the semiconductors, different categories of core-shells exist (Figure 7.7). The core could have a larger band gap than the shell (type I) or vice versa (inverse type I), or the conduction band or valence band of the core could be located within the band gap of the shell (type II). Core-shell nanoparticles are more desirable for biological applications as the core being passivated by the shell (usually a wider band-gap material) improves fluorescent properties and prevents leaching [34]. (CdSe)ZnS functionalized with polyamidoamine (PAMAM) and polyisoprene have shown great potential for applications in cancer targeting and molecular imaging, such as gastric cancer cells, because of their fluorescence [35]. TOPO-capped CdSe QDs dispersed in poly(2-methoxy, 5-(2-ethyl-hexyloxy)-1,4-phenylene vinylene) (MEH-PPV) and poly(3-hexylthiophene) (P3HT) were used by Umesh et al. [35].

Vollath et al. [36] presented experimental evidence for fluorescence generated due to the interface between core-shell nanoparticles. In PMMA-functionalized core-shell nanoparticles it was found that the carboxylic group present between the nanofiller and matrix was responsible for fluorescence. A similar conclusion was also drawn by Xiong et al. [37]. In addition, with a decrease in the size of particle, the surface to volume ratio (i.e., the surface area) increases and therefore the number of carboxylic groups on the interface increases, which results in a pronounced increase in fluorescence. The nature of the core and the surface modifications on the nanofiller also play a significant role in tuning the fluorescence.

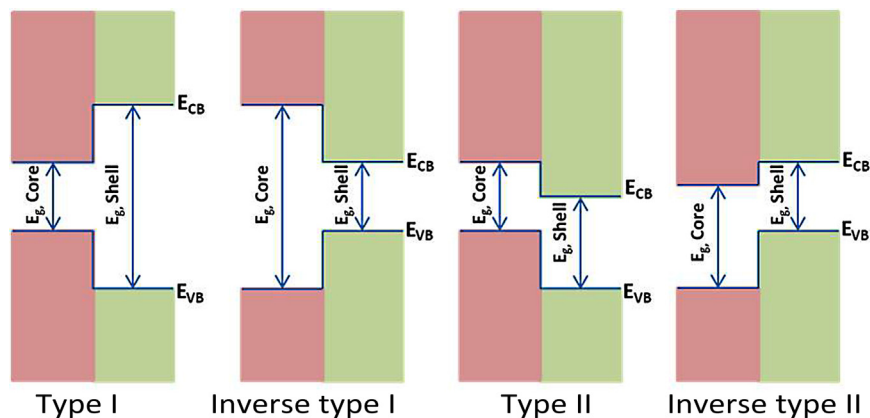


**FIGURE 7.7**

Types of core-shell QDs [30].

Apart from the traditional core-shell nanofillers several multifunctional fillers have surfaced in the present research. For biological and medicinal applications fluorescence is generally combined with magnetism. The synthesis of magnetic and fluorescent nanofiller simultaneous enables optimization of properties. Therefore, several possibilities exist in the field of fluorescence, and tuning the nanofiller properties through fluorescence via size or surface modifications.

### 7.6.3 OTHER FLUORESCENT NANOFILLER-BASED POLYMER NANOCOMPOSITE

Utilizing rare earth element-based fluorescent nanofillers can also provide insight into the characteristics of polymer composites. These types of composites find applications in optoelectronic devices, light emitting diodes, and lasers. Luminescent silica-coated  $Y_2O_3:Eu^{3+}$  nanopowders (particle size  $\sim 10$  nm) synthesized via sol-gel methods showed a photoluminescence around 610–620 nm [38]. A similar approach by Macedo et al. [38] used silica-coated  $Gd_2O_3:Eu^{3+}$ , grafted with an organosilane methacrylate and added styrene prior to radical polymerization. Depending on the excitation wavelength, different photoemission spectra in the visible range could be measured. Tang et al. [39] hybridized the cationic conjugated polymer with gold-SiO<sub>2</sub> nanoparticles and observed an enhancement in the intensity of fluorescence. The material was found to have potential for applications in selective biological sensing and imaging.

Another interesting material, which has recently surfaced as the allotrope of carbon, is carbon dot (Figure 7.8). Carbon and its allotropes are generally expected to be black in color, with little or no fluorescence and inherent water insolubility [36,40,41]. Carbon dot defies all these rules. They are nontoxic, cheap, fluorescent, water-soluble, and typically in the size range of 1–10 nm. It is no surprise that these materials are preferred as effective filler and a

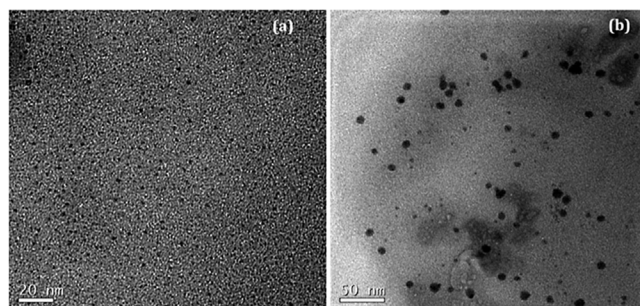


**FIGURE 7.8**

Transmission electron micrographs of carbon dots (a) before, and (b) after dialysis revealing a size range between 1 and 10 nm. [9].

*Copyright 2014. Reprinted with permission from the Royal Society of Chemistry.*

replacement to the traditional semiconducting nanofillers in polymer matrices. Carbon dot-based polymer composites can be used as fluorescent inks, anticounterfeit applications, UV-light detection systems, and light emitting diodes. A variety of polymers' linear and hyperbranched systems have been used in the preparation of carbon dot-based nanocomposites [41–45].

---

## 7.7 PROPERTIES OF POLYMER NANOCOMPOSITES STUDIED FROM FLUORESCENCE

The incorporation of nanomaterial into polymer changes the overall physical properties; such as conductivity, toughness, and permeability, which paves the path for latent industrial applications ranging from microwave to fuel cells. The enhancement of properties in a polymer nanocomposite is difficult to understand as it involves complex interactions between the nanoparticle and polymer. Fluorescence spectroscopy is one tool that can make such complex studies easier.

The glass transition temperature  $T_g$  is the most important parameter for a polymer. Above the glass transition state, the polymer exists in a rubbery state where the polymer chains are mobile and have larger free volume [46–49]. The  $T_g$  of a polymer depends on the thickness, and varies when the films are made ultrathin or thicker. Ellison et al. [50] first reported the use of the fluorescence method to determine the effect of decreasing film thickness on  $T_g$ . Pyrene-doped polymer films of PS, poly-isobutyl methacrylate, and polyvinyl pyridine spin coated on glass were studied for the above experiment. The fluorescence intensities was found to be inversely proportional to the temperature. This generally occurs because the nonradiative decay of the fluorophore increases the thermal energy of the system. The temperature and intensity relationship was found to be different in the glassy and rubbery state. The value of  $T_g$  was obtained from the intensity of the line associated with linear temperature dependences of fluorescence intensities in the two states. When hydrogen bonds are present between the polymer, interface confinement effect can lead to the enhancement of  $T_g$ . The  $T_g$  of polymer nanocomposites can be enhanced or decreased by tuning the nanoparticle–polymer interactions.

The mechanism of film formation in an organic coating can also be observed from fluorescence measurements. The formation of polymer film takes place in several steps. In the case of a water-borne polymer, the water evaporates and the spherical dispersion comes into an irreversible contact. In the final stage, the particle coalesces and forms a coherent film [51]. Fluorescence resonance energy transfer (FRET) is an excellent tool for understanding interdiffusion in polymers [52]. In FRET, energy donor and energy acceptors are required. Therefore two fluorophores could be used. For investigation of film formation, nearly the same amount of latex particles are labeled with each of the fluorophore. Prior to the

film formation, the two fluorophores are at a sufficient distance and no energy transfer occurs. After the formation the fluorophores come into contact and the distance is small enough for the energy transfer to occur. Therefore, studying FRET provides clear information about the film formation [52].

---

## 7.8 ADVANCES IN FLUORESCENCE TECHNOLOGIES

Several years of research have catered new technological advancements in the uses of fluorescence. These technologies are being quickly adapted and are also considered in mainstream measurements [13].

### 7.8.1 MULTIPHOTON FLUORESCENCE MICROSCOPY

Multiphoton fluorescence microscopy is a microscopic technique that may be used for imaging QDs, as well as other fluorophores. Fluorescence generally occurs when the fluorophore is excited by absorption of a single photon of a wavelength within the absorption range of the fluorophore. Fluorophores can be excited by two-photon absorption using pulsed lasers with femtosecond pulse widths. Such lasers have become easy to use and are available with microscopes. If the intensity of light from a laser is very high, then the fluorophore can easily absorb two photons and immediately go to first singlet state. The process is dependent on the laser intensity and is predominantly found at the focal point of the laser beam. Localized excitation from two-photon excitation has found wide use in fluorescence microscopy. Multiphoton excitation allows imaging from the focal plane of the microscope [53]. Unlike traditional fluorescence microscopy, the excitation wavelength is longer than the emission wavelength. Through this technique, a depth resolution of about 800  $\mu\text{m}$ , three-dimensional data acquisition, cell imaging for extended periods of time, and high spatial resolution is possible. The technique is noninvasive with little or no phototoxicity, which makes it appealing for the ranostic applications.

QDs can be used in conjugation with multiphoton microscopy. Lee et al. [54] examined an infusion of  $-\text{COOH}$  coated QD and QD-polyethylene glycol in isolated perfused skin with inductively coupled plasma emission spectrometry as well as fluorescence spectroscopy [54]. The images obtained from a multiphoton excitation spectroscopy are because there is no actual phase fluorescence that decreases the contrast in nonconfocal fluorescence microscopy. Biological multiphoton fluorescence emission microscopy has been well known for its advantages in increased depth penetration because of the low linear absorption coefficient of the analyte in the near-IR region. In addition the scattering decreases more in near-IR compared to that in the UV region.

## 7.8.2 FLUORESCENCE CORRELATION SPECTROSCOPY

Fluorescence correlation spectroscopy (FCS) is based on temporal fluctuations occurring in a small volume. Femtoliter volumes can be obtained by localized multiphoton excitation (Figure 7.9). Many photons can be observed as a single fluorophore diffuses in and out of the laser beam. This method is highly sensitive because the number of fluorophores observed is limited to a very few at a

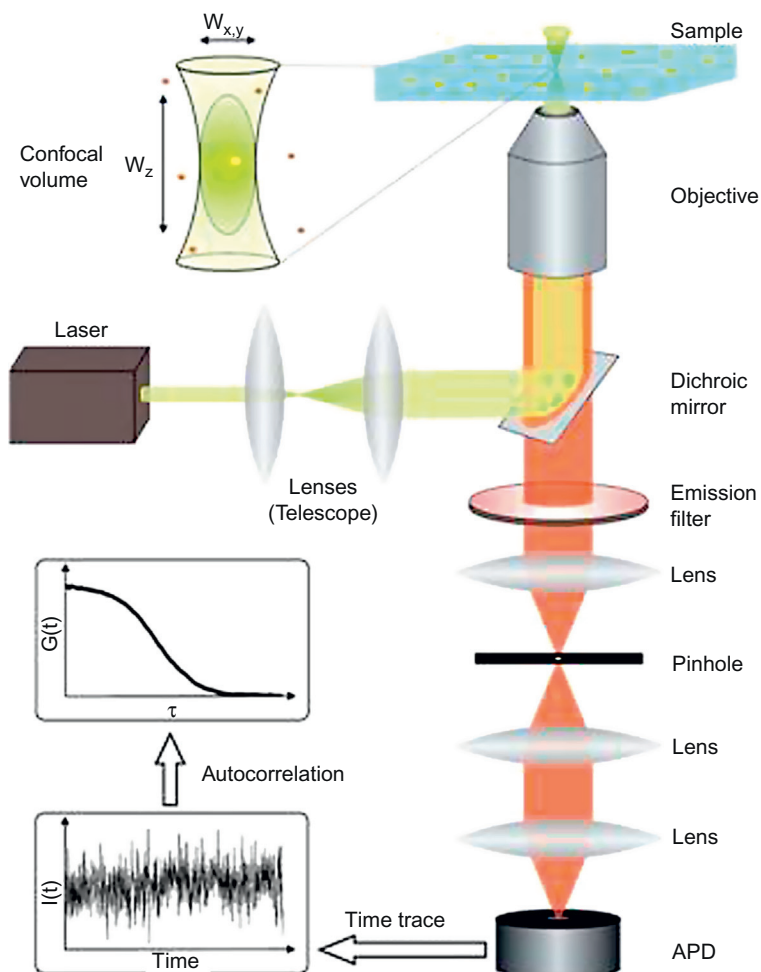


**FIGURE 7.9**

Instrumentation for fluorescence correlation spectroscopy [55].

Copyright 2014. Reprinted with permission from the Royal Society of Chemistry.

given time. FCS cannot be performed if the solution is too concentrated. Less fluorophores result in more fluctuations and vice versa. FCS is performed by observing the intensity fluctuations with time [55]. The rate of fluctuation is inherently dependent on the rate of diffusion. As the diffusion increases so does the intensity fluctuation. A slow diffusion enables the fluorophore to remain in the observed volume for a longer period of time and the fluctuation intensity occurs more slowly. The amplitude and speed of fluctuation is essential in determining the correlation function. The average number of fluorophores observed is inversely proportional to the height of the curve. FCS is especially suited to evaluate the dynamics of polymers. The diffusion of single molecules and nanoparticles provide important information about the local mechanical and viscoelastic properties of polymer solutions (i.e., their nanorheology). Nanoviscosity refers to the diffusion or drag of small objects like nanofillers in a polymer matrix. Therefore, viscosity is strongly correlated with the length scale at which it is probed. Another technique to investigate the dynamics of polymers, micelles, and aggregates is dynamic light scattering (DLS). FCS require very little fluorescent nanofiller or probing to study dynamics. In contrast, DLS requires three to four times more fluorescent probe than to FCS. Therefore, this minuscule probe helps in simultaneous analysis of micelles, free dyes, and large aggregates in a straightforward method. The scattered intensity in DLS is proportional to the particle mass and concentration. Thus small aggregates cannot be precisely detected in the presence of larger ones. The hydrodynamic size and radius is also better when measured by FCS. FCS provides the number average molecular weight of polymers unlike DLS, which provide weight average molecular weight.

### 7.8.3 SINGLE MOLECULE DETECTION

Single molecule analysis via fluorescence is the highest sensitivity analysis obtained at present. Highly fluorescent fluorophores with good quantum yield are chosen and immobilized for measurements [56,57]. A typical instrument for single molecule detection uses a laser excitation via microscope objective, a scanning stage to move the sample, and confocal optics to reject unnecessary signals. Single molecule detection can also now be extended to include UV-absorbing fluorophores. In the absence of such detection, the whole system is considered as an ensemble. Therefore, ensemble average of overall property is obtained. When a single molecule is observed, no averaging is done, therefore individual molecules could be clearly studied. At present single molecule experiments are performed on ultra-clean surfaces to minimize background. Single molecule detection can be applied to intracellular molecules if they don't diffuse too rapidly. Single molecule detection is a powerful technology which bypasses ensemble averaging and provides direct information and behavior (i.e., kinetics and dynamics) of single molecules.

Diffraction unlimited imaging based on single molecule fluorescence spectroscopy depends on the insight of the individual emitters which can be isolated and localized with nanometer-scale precision by simply determining the centroid of the emission distribution. It is also possible to generate an image of the sample with nanoscale precision from the calculation of emitter positions in the sample if the emission of a single isolated emitter is being considered. Therefore, in order to study samples containing many fluorophores in nanometer proximity one has to apply this localization to single emission events separated in time so that only a single fluorophore emits within a diffraction limited region at any instant. If stochastic process like photo-activation, photo-switching, photo-bleaching, etc., occur due to a photo-induced process in a single molecule, they can be used to separate emission events in time. Depending on the experimental parameters, images with features as small as 10 nm can be obtained by this method. Single molecule detection opens up various possibilities to probe dynamics and heterogeneities with molecular resolution in a wide range of time scales, which makes it ideal to address many characteristics of polymers that have remained unsolved [58].

Single molecule detection allows for the determination of the distributions of these properties, but more importantly, enables the determination of fluctuations of the properties measured on an ensemble of molecules, such as spectrum, polarization, and decay time monitored on time scales from milliseconds to few hours. For instance, the fluctuations in the emission rate can be correlated with that of local density fluctuations. Molecules embedded in polymer films show rearrangement on time scales of seconds and longer at temperatures near and above  $T_g$ . These can be observed by fluorescent measurement of light and more precisely by wide-field imaging techniques, through which direction of transition dipole moments can be established.

---

## 7.9 CONCLUSION

Fluorescence spectroscopy has a wide reach among polymer chemists and nanotechnologists. Their measurements can provide a wide range of detailed information regarding the molecular processes, including the solvent combinations in nanocomposite, rotational diffusion of molecules, distances between the nanofillers, conformational changes, and interaction of nanofiller with the polymer matrix. Recent advances in technology for cellular imaging, drug delivery, and single molecule detection, further extend the use of fluorescence. Also, the technological advances in fluorescence spectroscopy significantly reduce the need for complex technologies and exorbitantly-priced instruments. It is, therefore, sagacious to consider that fluorescence spectroscopy will contribute its fullest to the rapid advancements in biology, biotechnology, polymer chemistry, and nanotechnology.

---

## REFERENCES

- [1] Somers RC, Bawendi MG, Nocera DG. CdSe nanocrystal based chem-bio-sensors. *Chem Soc Rev* 2007;36:579–91.
- [2] Ruedas-Rama MJ, Walters JD, Orte A, Hall EA. Fluorescent nanoparticles for intracellular sensing: a review. *Anal Chim Acta* 2012;751:1–23.
- [3] Goesmann H, Feldmann C. Nanoparticulate functional materials. *Angew Chem Int Ed* 2010;49:1362–95.
- [4] Bera D, Qian L, Tseng TK, Holloway PH. Quantum dots and their multimodal applications: a review. *Materials* 2010;3:2260–345.
- [5] Gaddam RR, Kantheti S, Narayan R, Raju KVS. Graphitic nanoparticles from thermal dissociation of camphor as effective filler in polymeric coatings. *RSC Adv* 2014;4:23043–9.
- [6] Schmäzlin E, van Dongen JT, Klimant I, Marmodée B, Steup M, Fisahn J, et al. An optical multifrequency phase-modulation method using microbeads for measuring intracellular oxygen concentrations in plants. *Biophys J* 2005;89:1339–45.
- [7] Cao Y, Koo YEL, Kopelman R. Poly (decyl methacrylate)-based fluorescent PEBBLE swarm nanosensors for measuring dissolved oxygen in biosamples. *Analyst* 2004;129:745–50.
- [8] Ruedas-Rama MJ, Hall EA.  $K^+$ -selective nanospheres: maximising response range and minimising response time. *Analyst* 2006;131:1282–91.
- [9] Gaddam RR, Vasudevan D, Narayan R, Raju KVS. Controllable synthesis of bio-sourced blue-green fluorescent carbon dots from camphor for the detection of heavy metal ions in water. *RSC Adv* 2014;4:57137–43.
- [10] Liff SM, Kumar N, McKinley GH. High-performance elastomeric nanocomposites via solvent-exchange processing. *Nat Mater* 2007;6:76–83.
- [11] Valeur B, Berberan-Santos MN. *Molecular fluorescence: principles and applications*. John Wiley & Sons; 2012.
- [12] Mondal PP, Diaspro A. *Fundamentals of fluorescence microscopy: exploring life with light*. Springer Science & Business Media; 2013.
- [13] Lakowicz JR. *Principles of fluorescence spectroscopy*. Springer Science & Business Media; 2007.
- [14] Eisinger J, Flores J. Front-face fluorometry of liquid samples. *Anal Biochem* 1979;94:15–21.
- [15] Sharma A, Schulman SG. *Introduction to fluorescence spectroscopy*. Wiley Interscience; 1999.
- [16] Gauglitz G, Vo-Dinh T. *Handbook of spectroscopy*. Wiley-VCH; 2003.
- [17] Beechem JM, Gratton E, Ameloot M, Knutson JR, Brand L. The global analysis of fluorescence intensity and anisotropy decay data: second-generation theory and programs. *Topics in fluorescence spectroscopy*. Springer; 2002. p. 241–305.
- [18] Groot ML, Pawlowicz NP, van Wilderen LJ, Breton J, van Stokkum IH, van Grondelle R. Initial electron donor and acceptor in isolated photosystem II reaction centers identified with femtosecond mid-IR spectroscopy. *Proc Natl Acad Sci U S A* 2005;102:13087–92.
- [19] Fölling J, Bossi M, Bock H, Medda R, Wurm CA, Hein B, et al. Fluorescence nanoscopy by ground-state depletion and single-molecule return. *Nat Methods* 2008;5:943–5.

- [20] Ruedas-Rama MJ, Orte A, Hall EA, Alvarez-Pez JM, Talavera EM. A chloride ion nanosensor for time-resolved fluorimetry and fluorescence lifetime imaging. *Analyst* 2012;137:1500–8.
- [21] Heitz R, Born H, Guffarth F, Stier O, Schliwa A, Hoffmann A, et al. Existence of a phonon bottleneck for excitons in quantum dots. *Phys Rev B* 2001;64(24):241305.
- [22] Kambhampati P. Multiexcitons in semiconductor nanocrystals: a platform for optoelectronics at high carrier concentration. *J Phys Chem Lett* 2012;3:1182–90.
- [23] Ellingson RJ, Beard MC, Johnson JC, Yu P, Micic OI, Nozik AJ, et al. Highly efficient multiple exciton generation in colloidal PbSe and PbS quantum dots. *Nano Lett* 2005;5:865–71.
- [24] Bosch P, Catalina F, Corrales T, Peinado C. Fluorescent probes for sensing processes in polymers. *Chem-A Eur J* 2005;11:4314–25.
- [25] Loutfy RO. Fluorescence probes for polymer free-volume. *Pure Appl Chem* 1986;58:1239–48.
- [26] Khanna PK, Gokhale RR, Subbarao VVVS, Singh N, Jun KW, Das BK. Synthesis and optical properties of CdS/PVA nanocomposites. *Mater Chem Phys* 2005;94:454–9.
- [27] Tamborra M, Striccoli M, Curri ML, Agostiano A. Hybrid nanocomposites based on luminescent colloidal nanocrystals in poly(methyl methacrylate): spectroscopical and morphological studies. *J Nanosci Nanotechnol* 2008;8:628–34.
- [28] Fang Y, Chen L, Wang CF, Chen S. Facile synthesis of fluorescent quantum dot-polymer nanocomposites via frontal polymerization. *J Polym Sci Part A: Polym Chem* 2010;48:2170–7.
- [29] Sato M, Kawata A, Morito S, Sato Y, Yamaguchi I. Preparation and properties of polymer/zinc oxide nanocomposites using functionalized zinc oxide quantum dots. *Eur Polym J* 2008;44:3430–8.
- [30] Vasudevan D, Gaddam RR, Trinch A, Cole I. Coreshell quantum dots: properties and applications. *J Alloys Compounds* 2015;636:395–404.
- [31] Kantheti S, Narayan R, Raju KVS. Pyrene-anchored ZnO nanoparticles through click reaction for the development of antimicrobial and fluorescent polyurethane nanocomposite. *Polym Int* 2015;64:267–74.
- [32] Lim WP, Low HY, Chin WS. IR-luminescent PbS-polystyrene nanocomposites prepared from random ionomers in solution. *J Phys Chem B* 2004;108:13093–9.
- [33] Ziaudeen SA, Gaddam RR, Pallapothu PK, Sugumar MK, Rangarajan J. Supra gap excitation properties of differently confined PbS-nano structured materials studied with opto-impedance spectroscopy. *J Nanophotonics* 2013;7:073075.
- [34] Hines DA, Kamat PV. Quantum dot surface chemistry: ligand effects and electron transfer reactions. *J Phys Chem C* 2013;117:14418–26.
- [35] Kumar U, Kumari K, Sharma SN, Kumar M, Vankar VD, Kakkar R, et al. Role of surface modification of colloidal CdSe quantum dots on the properties of hybrid organic–inorganic nanocomposites. *Coll Polym Sci* 2010;288:841–9.
- [36] Vollath D, Szabó DV, Schlabach S. Oxide/polymer nanocomposites as new luminescent materials. *J Nanopart Res* 2004;6:181–91.

- [37] Xiong M, Zhou S, Wu L, Wang B, Yang L. Sol–gel derived organic–inorganic hybrid from trialkoxysilane-capped acrylic resin and titania: effects of preparation conditions on the structure and properties. *Polymer* 2004;45:8127–38.
- [38] Macedo AG, Martins MA, Fernandes SE, Barros-Timmons A, Trindade T, Carlos LD, et al. Luminescent SiO<sub>2</sub>-coated Gd<sub>2</sub>O<sub>3</sub>: Eu<sub>3+</sub>nanorods/poly (styrene) nanocomposites by *in situ* polymerization. *Opt Mater* 2010;32:1622–8.
- [39] Tang F, He F, Cheng H, Li L. Self-assembly of conjugated polymer-Ag@ SiO<sub>2</sub> hybrid fluorescent nanoparticles for application to cellular imaging. *Langmuir* 2010;26:11774–8.
- [40] Kantheti S, Gaddam RR, Narayan R, Raju KVS. Hyperbranched polyol decorated carbon nanotube by click chemistry for functional polyurethane urea hybrid composites. *RSC Adv* 2014;4:24420–7.
- [41] Gaddam RR, Kantheti S, Narayan R, Raju KVS. Bulk synthesis of green carbon nanomaterials from *Desmostachya bipinnata* for the development of functional polyurethane hybrid coatings. *Prog Org Coatings* 2015;79:37–42.
- [42] De B, Voit B, Karak N. Transparent luminescent hyperbranched epoxy/carbon oxide dot nanocomposites with outstanding toughness and ductility. *ACS Appl Mater Interfaces* 2013;5:10027–34.
- [43] Deng Y, Zhao D, Chen X, Wang F, Song H, Shen D. Long lifetime pure organic phosphorescence based on water soluble carbon dots. *Chem Commun* 2013;49:5751–3.
- [44] Dong Y, Wang R, Li H, Shao J, Chi Y, Lin X, et al. Polyamine-functionalized carbon quantum dots for chemical sensing. *Carbon* 2012;50:2810–15.
- [45] Wang F, Xie Z, Zhang H, Liu CY, Zhang YG. Highly luminescent organosilane-functionalized carbon dots. *Adv Funct Mater* 2011;21:1027–31.
- [46] deGennes PG. Glass transitions in thin polymer films. *Eur Phys J E* 2000;2:201–3 68.
- [47] Priestley RD, Ellison CJ, Broadbelt LJ, Torkelson JM. Structural relaxation of polymer glasses at surfaces, interfaces and in between. *Science* 2005;309:456–9 69.
- [48] Rittigstein P, Priestley RD, Broadbelt LJ, Torkelson JM. Model polymer nanocomposites provide an understanding of confinement effects in real nanocomposites. *Nat Mater* 2007;6:278–82 70.
- [49] Keddie JL, Jones RAL, Cory RA. Size-dependent depression of the glass-transition temperature in polymer-films. *Eur Phys Lett* 1994;27:59–64 71.
- [50] Ellison CJ, Kim SD, Hall DB, Torkelson JM. Confinement and processing effects on glass transition temperature and physical aging in ultrathin polymer films: novel fluorescence measurements. *Eur Phys J E* 2002;8:155–66.
- [51] Kara S, Pekcan O, Sarac A, Arda E. Film formation stages for poly(vinylacetate) latex particles: a photon transmission study. *Colloid Polym Sci* 2006;284:1097–105.
- [52] Felorzabih N, Froimowicz P, Haley JC, Bardajee GR, Li BX, Bovero E, et al. Determination of the Förster distance in polymer films by fluorescence decay for donor dyes with a nonexponential decay profile. *J PhysChem B* 2009;113:2262–72.
- [53] Weissleder R, Pittet MJ. Imaging in the era of molecular oncology. *Nature* 2008;452:580–9.

- [54] Lee HA, Imran M, Monteiro-Riviere NA, Colvin VL, Yu WW, Riviere JE. Biodistribution of quantum dot nanoparticles in perfused skin: evidence of coating dependency and periodicity in arterial extraction. *Nano Lett* 2007;7:2865–70.
- [55] Wöll D. Fluorescence correlation spectroscopy in polymer science. *RSC Adv* 2014;4:2447–65.
- [56] Rigler R, Orrit M, Basché T. *Single molecule spectroscopy*. Berlin: Springer; 2001.
- [57] Zander C. Single-molecule detection in solution: a new tool for analytical chemistry. *Fresenius' J Anal Chem* 2000;366:745–51.
- [58] Wiley Vch, Wöll D, Braeken E, Deres A, De Schryver FC, Uji-i H, et al. Polymers and single molecule fluorescence spectroscopy, what can we learn? *Chem Soc Rev* 2009;38:313–28.

# NMR spectroscopy of polymer nanocomposites

# 8

Kishor Kumar Sadasivuni<sup>1</sup>, John-John Cabibihan<sup>2</sup>  
and Mariam Ali SA Al-Maadeed<sup>1,3</sup>

<sup>1</sup>Center for Advanced Materials, Qatar University, Doha, Qatar

<sup>2</sup>Department of Mechanical and Industrial Engineering, Qatar University, Doha, Qatar

<sup>3</sup>Materials Science and Technology Program, Qatar University, Doha, Qatar

## 8.1 INTRODUCTION

The area of polymer nanocomposites is an ever-growing field of supreme applications where the incorporated nanometer-sized filler particles (1–500 nm in size) in polymer matrices make extraordinary discoveries. Very small percentages of nanoparticles are enough to create large variations in the polymer properties. Other than exhibiting potential technological applications, polymer nanocomposites also provide information about the fundamental scientific issues regarding polymers. With enhanced mechanical, thermal, physical, electrical, and gas permeability properties, polymer nanocomposites have applications in the automotive, food packaging, sensing, and biomedical industries. Thus, this specific area of nanocomposites—both synthesis and characterization—draws significant attention because there is a huge need for efficient combinations of structural and functional basic elements. However, the technical challenges for preparing the materials must be solved properly prior to the manufacturing.

Generally, polymer nanocomposites [1–6] are prepared by solution mixing, *in situ* polymerization, or by melt compounding [7,8]. A high level of dispersion of nanofillers is the goal of each of these preparations. The typical properties of such materials are due to the significantly strengthened interfacial interactions between the polymer chains and nanoparticles; with the latter dispersed well within the former medium [2,9–19]. Based on the extent of dispersion, two categories of nanocomposites—intercalated and exfoliated—are distinguished [2,20]. A superior level of filler exfoliation and, thus, maximum characteristic properties depend on various parameters like the nature of the filler (its shape and size), degree of mixing, interfacial adhesion between the filler and matrix, and property of polymer chains (i.e., conformation, relaxation, crystallization) at the interface [21]. Therefore, characterizing the abovementioned factors is very much essential and strongly influences the molding of composite applications.

Almost all kinds of spectroscopy have similar importance in detecting the nanocomposite properties. However the nuclear magnetic resonance (NMR) spectroscopy is very powerful in monitoring the structure and dynamics of a variety of macromolecular composite systems. The six Nobel prizes in this particular field illustrate NMR's usefulness in science and technology. NMR spectroscopy elucidates the delicate interplay of structure and dynamics in polymers and supra-molecules, since many different atomic spin-bearing nuclei constitute abundant probes of structure and dynamics and noninvasive strategies [22]. Though NMR provides significant contributions toward exploring the structure of the composites, certain challenges also exist in this field. For instance, solid-state NMR has some limitations in studying polymer nanocomposites in bulk state.

NMR is a broad method and a lot of individual analysis comes under its umbrella. The very first analysis of molecules in this technique was through observing its proton wide-line spectra [23]. However at a later stage, the deuterium ( $2H$ ) NMR gained attention in elucidating the molecular processes within the functional polymers [24]. The solid-state NMR went toward the bulk of the polymer through methods of  $^{13}C$  cross-polarization (CP) magic-angle spinning (MAS) [25]. The high-resolution (HR)  $^1H$  NMR has recently developed to its pinnacle, with higher MAS frequencies and stronger magnetic fields [26]. The concept of two-dimensional (2D) NMR [27] made the quantitative study of intermolecular spin-spin distances and molecular reorientations of naturally abundant nuclei such as  $^{13}C$ ,  $^{15}N$ , or  $^{31}P$ , possible [28].

This chapter is written as a critical review to address almost all issues in polymer nanocomposites; such as the polymer chain dynamics in composites, molecular motions, phase structures of multiphase materials, transverse relaxation, and residual dipolar interaction within entangled nanocomposites; in addition to the basic NMR theories and its importance in characterizing the polymers and nanocomposites. Based on different types of polymers and nanofillers, the concepts of solid-state NMR for investigating the orientation and distance dependence of spin interactions are mentioned. Multidimensional NMR is useful for observing the relaxation phenomena [29,30] in terms of molecular rotations, chemical structures, and conformational changes within the material. The theoretical concepts are also sometimes correlated with the experimental findings based on the mode of sample preparation and testing conditions.

---

## 8.2 THEORETICAL BACKGROUNDS OF NMR

NMR happens when certain atomic nuclei situated in a static magnetic field are exposed to another oscillating magnetic field. The nuclei possess spin angular momentum due to the protons and neutrons inside, and thus experience different energy levels when placed in the magnetic field. A nucleus can have three spin values ( $I = \frac{1}{2}$ , 1, or 0) based on the net spin of the nucleons and in the external field its energy level splits according to their spin values. For example, a nucleus with  $\frac{1}{2}$  spin has two orientations and energy levels  $\pm \frac{1}{2}$ . In the absence of an

external field, the orientations have equal energy whereas in the presence of the field, the energy levels vary with the lower level highly populated. An electromagnetic radiation (radio waves) of specific frequency is irradiated on a nucleus in a particular situation and it starts flipping from the spin-aligned low energy state to the spin-opposed high energy state. The energy required for this transition depends on the applied magnetic field strength.

The spin angular momentum ( $L$ ) of the nucleus is expressed by Eqn (8.1).  $L$  is also proportional to the nucleus' intrinsic magnetic momentum.

$$L = m\hbar \quad (8.1)$$

where  $m$  is the spin quantum number with  $(2I + 1)$  possible values ( $m = -I, -I + 1, \dots, I - 1, I$ ) and  $\hbar$  is Planck's constant.

For a given nucleus, the magnetic moment ( $\mu$ ) along the field direction  $z$  is related to the gyromagnetic ratio ( $\gamma$ ):

$$\mu_z = \gamma L \quad (8.2)$$

and thus Eqn (8.3) can be written as

$$\mu_z = \gamma m\hbar \quad (8.3)$$

In the presence of a magnetic field of strength  $H_0$ , the spinning nucleus undergoes a precessional motion with a frequency called the Larmor frequency ( $\omega$ ):

$$\omega = 2\pi\nu = \gamma H_0 \quad (8.4)$$

The magnetic moment is also related to  $H_0$  by Eqn (8.5):

$$E = -\mu_z H_0 \quad (8.5)$$

This can also be written as:

$$E = -\gamma m\hbar H_0 \quad (8.6)$$

Considering the flipping of an electron between two consecutive energy levels, the energy difference is expressed as Eqn (8.7):

$$\Delta E = E_2 - E_1 = \gamma\hbar H_0 \quad (8.7)$$

Figure 8.1 illustrates the splitting of the energy levels in an external magnetic field  $H_0$ . When the Larmor frequency equals the applied radio frequency, resonance occurs and the nucleus excites from a lower to higher energy state by absorbing energy [31]. The NMR spectrum is usually taken at this level.

$\Delta E$  is also related to the population at higher ( $N_1$ ) and lower energy states ( $N_0$ ), as per the Boltzmann statistics (Eqn (8.8)):

$$\frac{N_+}{N_-} = \exp(-\Delta E/K_B T) \quad (8.8)$$

where  $K_B$ , is the Boltzmann constant and  $T$  is the absolute temperature.

NMR spectra provide both qualitative and quantitative information. The connectivities of atoms or groups of atoms and their magnetic equivalence come under the

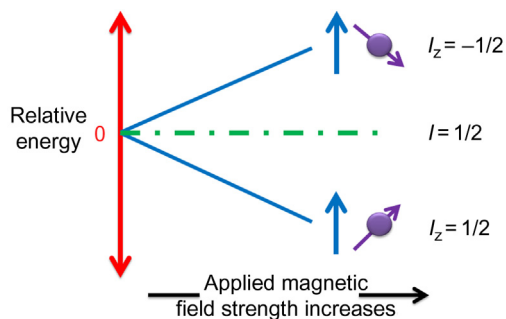


**FIGURE 8.1**

The energy difference between two adjacent energy levels as a function of the magnetic flux density.

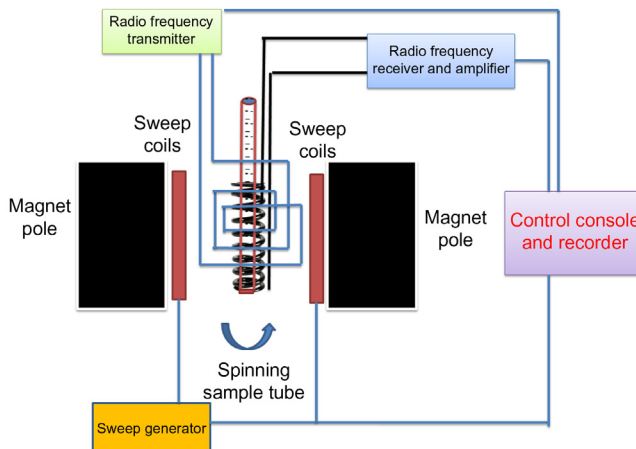


**FIGURE 8.2**

Block diagram of NMR spectrometer.

qualitative parameters whereas J-coupling constant and cross-relaxation rates are useful to understand the conformation, distances, bond angle, and local mobility of atoms, and contribute the quantitative values [32]. Figure 8.2 shows the schematic of an NMR spectroscopy with a radio frequency source, stable magnet, sample tube, phase sensitive detector, and unit to control and record the data (computer).

### 8.3 NMR ANALYSIS OF POLYMER COMPOSITES

Gutowksy et al. [33] conducted the first report of HR  $^1\text{H}$  NMR spectroscopy on uncured Heva rubber in  $\text{CS}_2$ , and since then the technique is often used to explore

the polymer and its nanocomposite characterization [34]. The  $T_2$  relaxometry is used to learn about the polymer mobilities in nanocomposites and the immobilized polymer chains surrounding the filler particles [35–40]. The data from NMR of various polymer composites are classified on the basis of the type of polymers and will be discussed in the next section.

### 8.3.1 ELASTOMER NANOCOMPOSITES

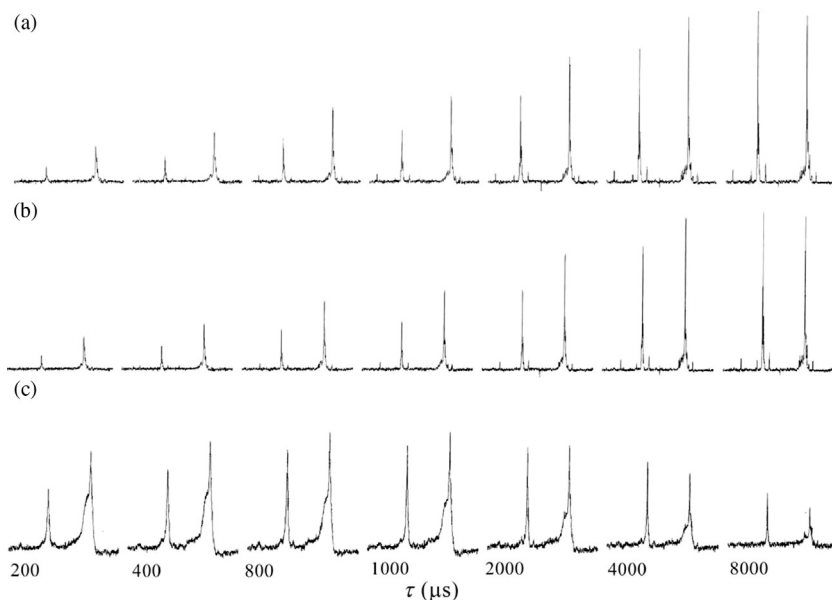
Incorporation of solid fillers into rubber improves the elastic modulus, fracture, and abrasion resistance of the base matrix; however it is dependent on the polymer dynamics near the filler interface [41–44]. NMR is a very useful and necessary technique in exploring the polymer mobility around the fillers since the potential formation of glassy bridges between such polymer layers with filler particles regulates the nanocomposite behavior. The immobilized rubber chains measured from the NMR data are theoretically related with a model which describes the glass transition temperature ( $T_g$ ) [45–47]. If the polymer films deposited on a substrate have stronger interactions (like hydrogen bonds), [48] the  $T_g$  increases with a decrease in polymer film thickness. This is explained by a  $T_g$  gradient, as given in Eqn (8.9) [49]:

$$T_g^f(z) = T_g^f(1 + (\delta/z)) \quad (8.9)$$

where  $T_g^f(z)$  represents the  $T_g$  at a distance  $z$  from the substrate at frequency  $f$ ,  $T_g^f$  the  $T_g$  of bulk polymer,  $\delta$  a length related to the amplitude of the gradient, and  $v$  an exponent of value 1.

Techniques like solid-echo and the Hahn echo pulse sequence are used to study the polymer mobility in nanocomposites respectively for the rigid and mobile polymer fraction, but are limited due to inapplicable fitting models and parameter interdependencies [50,51]. The magic-sandwich echo (MSE) is a better method to study the polymer relaxation especially at short time scales ( $<0.2$  ms). The method works by refocusing multispin dipolar interactions in the initial part of the free-induction decay (FID) [52,53]. Multiple quantum (MQ) measurements also provide quantitative information on cross-links and/or entanglements limiting the segmental mobility at 0.1–3 ms time scale and determines the residual dipolar coupling and local dynamic order parameter [50,54–57]. While MSE measures the immobilized polymer fraction, MQ NMR determines the cross-link density and homogeneity of nanocomposites, thus facilitating a complete survey of the filler distribution within the base matrix.

The effect of silica on the polymer properties is studied by fabricating two kinds of composites: one covalently bonded and the other with hydrogen bonding interaction via surface modification between the silica and polymer. Using NMR, the influence of a coupling agent on the polymer dynamics is studied by varying the silica content and the particles diameter [45–47]. MSE-refocused FIDs allowed the determination of even slower polymer dynamics for samples with

**FIGURE 8.3**

$^{13}\text{C}$  NMR CP/MAS spectra with variable contact-time experiment: (a) SBR, (b) SBR/TiO<sub>2</sub> nanocomposite and (c) SBR/TiO<sub>2</sub> photo degraded nanocomposite [60].

Copyright 2009. Reprinted with permission from Elsevier Ltd.

weaker filler-polymer bonding and was in agreement with gradient of mobility. Polymer relaxation at longer time scales by Hahn or pseudo solid spin-echoes [58] revealed the role of filler particles on the effective cross-link density of nanocomposites. MQ NMR also substantiate this result, with the additional information that up to 30% of the polymer in the vicinity of the filler particles has a far larger cross-link density. This can be due to the good filler dispersion within the polymer samples [59].

The  $^{13}\text{C}$  CP/MAS NMR spectra of styrene-butadiene rubber (SBR), its titania composites BR/TiO<sub>2</sub>, and photodegraded SBR/TiO<sub>2</sub> are shown in Figure 8.3. High power proton decoupling was performed with short delays between 90 pulses and all the nanocomposites showed an upshift of 5 ppm, indicating a strong interaction between the polymer chains and the TiO<sub>2</sub> nanoparticles [61,62]. Broadening of the peaks for the SBR/TiO<sub>2</sub> photodegraded nanocomposite without the characteristic butadiene data shows the photodegradation of the butadienic chain. By calculating the variation contact time and the proton spin-lattice relaxation time, the dynamic molecular motions of the samples were evaluated and the influence of nanoparticles on the polymer chain organization is established.

The semiquantitative analysis of segmental dynamics near the polymer interface is done for carboxyl-terminated polybutadiene (CTPB)/organo – clay

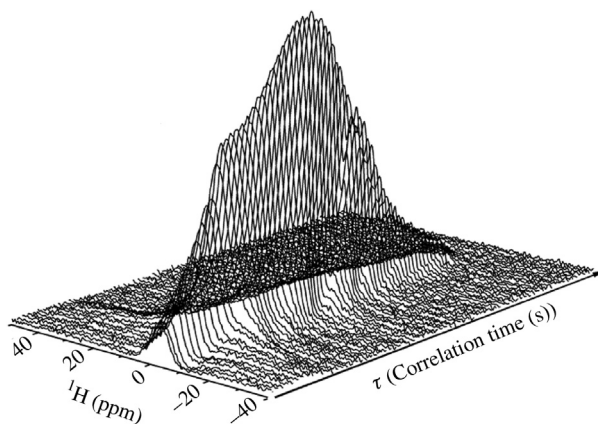


**FIGURE 8.4**

Typical  $^1\text{H}$  quasi-threshold dose (DQ) coherence NMR spectra of a structurally equilibrated CTPB/C18 – clay (CTPB = 60 wt%) nanocomposite at 30 °C [63].

*Copyright 2014. Reprinted with permission from American Chemical Society.*

(C18 – clay) composites using  $^1\text{H}$  DQ NMR. The critical concentration was observed as 60 wt% CTPB, which was the same as observed by the fully refocused  $^1\text{H}$  NMR FID. This observation enabled the determination of the critical concentration of a polymer/clay composite at molecular scale and explained the saturation effect for the surface-adsorbed polymer. The dynamic behavior of the composite changed with the removal of the CTPB end group and with an increased temperature. The nonreversible exfoliation happening in CTPB/clay is explained on the basis of such homogeneous to heterogeneous dynamic changes. The CTPB is varied between 1 and 100 wt% and the spectrum for the composite at 60 wt% is shown in Figure 8.4. After a  $90^\circ$  pulse, the DQ buildup curves are normalized to the integral intensity of the NMR signal and the curve of the pure C18 – clay showed a single maximum at  $\tau_{\text{max}} = 14 \mu\text{s}$ . This was attributed to the reduced mobility of the components and when the intensity reaches zero at around  $200 \mu\text{s}$ , the modifier is completely immobilized by the clay surface. When the cCTPB concentration was less than 20 wt%, the first maximum position was at  $\tau_{\text{max}} = 14 \mu\text{s}$ , indicating the same segmental immobilization near the interface for all samples and the presence of a rigid component on the clay surface. At greater than 30 wt%,  $\tau_{\text{max}}$  became larger which indicated increased molecular mobility. For 95 and 10 wt% cCTPB, the first maximum was not detectable and the intensity almost nullified. All these data are attributed to the fact that the CTPB/C18 – clay nanocomposites possess a concentration-dependent multimode dynamics.

The profiles of  $\tau_1$  relaxation times for polyurethane PEO-based hydrogels containing Cloisite 30B observed using  $^1\text{H}$  NMR spectroscopy are illustrated in Figure 8.5. The molecular dynamics of the nanocomposite hydrogel depended on

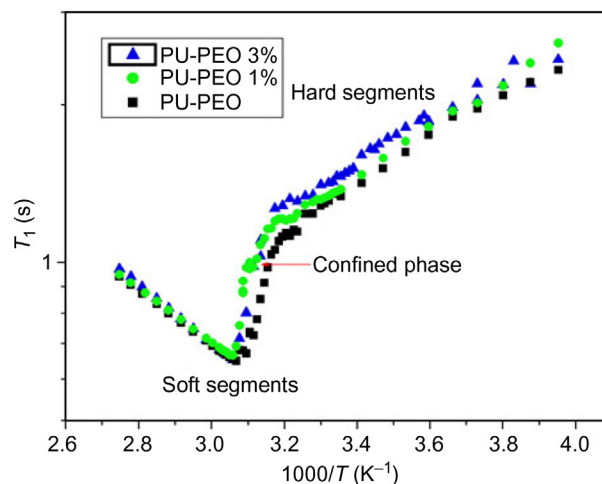


**FIGURE 8.5**

$T_1$  relaxation times profiles for PU-PEO nanocomposite samples. Molecular dynamics studies of polyurethane nanocomposite hydrogels [64].

Copyright 2013. Reprinted with permission from Springer.

the interaction of Cloisite 30B nanoparticles with soft segments of polyurethanes. All spectra contained one symmetric line of proton nuclei and the half-width of NMR peaks showed a decrease with temperature. Temperature activates the molecular motions within the polymer composite and for a pure PU-PEO sample and PU-PEO nanocomposites, two and three relaxation processes were respectively observed. The biomedical applicability of the synthesized hydrogel was also established.

### 8.3.2 THERMOPLASTIC NANOCOMPOSITES

Bilaterally sulfur-functionalized PS, SCH<sub>3</sub>-polystyrene-SH synthesized by anionic polymerization, and its nanocomposite with gold nanoparticles (AuNPs) were studied using NMR and their 500 MHz <sup>1</sup>H NMR spectra are compared in Figure 8.6. In Figure 8.6a, the 6.5–7.3 ppm chemical shift (d) of benzene rings and the peaks f and g in 2.6–2.8 ppm for thioli group of SCH<sub>3</sub>-PS-SH are seen. Due to the very low concentration of thiomethylprotons, the peak of SCH<sub>3</sub> is not clearly observed, but its existence is confirmed with <sup>13</sup>C NMR spectroscopy (Figure 8.6c). Other than the characteristic peak of SCH<sub>3</sub> in SCH<sub>3</sub>-PS at 26 ppm, all peaks in both spectra are nearly the same. The chemical shift (d) at 18 ppm is due to dimethyl sulfide and it shifts from ppm 18 to 26 ppm by the effect of bonded PS.

Islam et al. used a combination of reversible addition fragmentation chain transfer polymerization (RAFT) and click chemistry to synthesize a hybrid poly

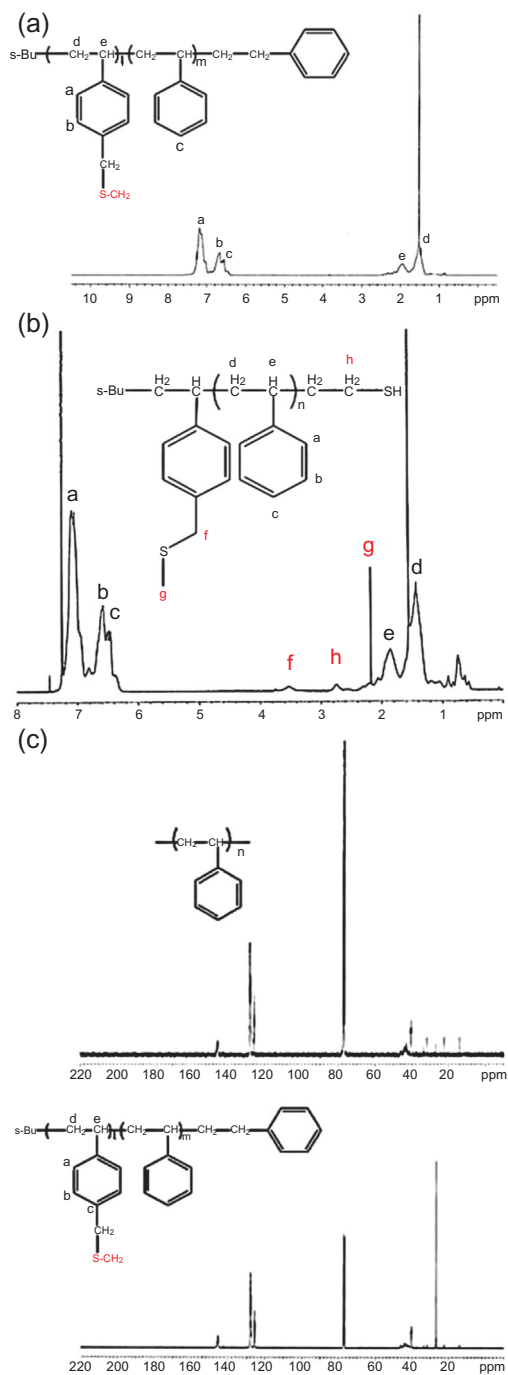


**FIGURE 8.6**

(a)  $^1\text{H}$  NMR spectrum of SCH3-PS; (b)  $^1\text{H}$  NMR spectrum of SCH3-PS-SH; (c) Comparison between  $^{13}\text{C}$ -NMR charts of PS and SCH3-PS [65].

Copyright 2015. Reprinted with permission from John Wiley & Sons.

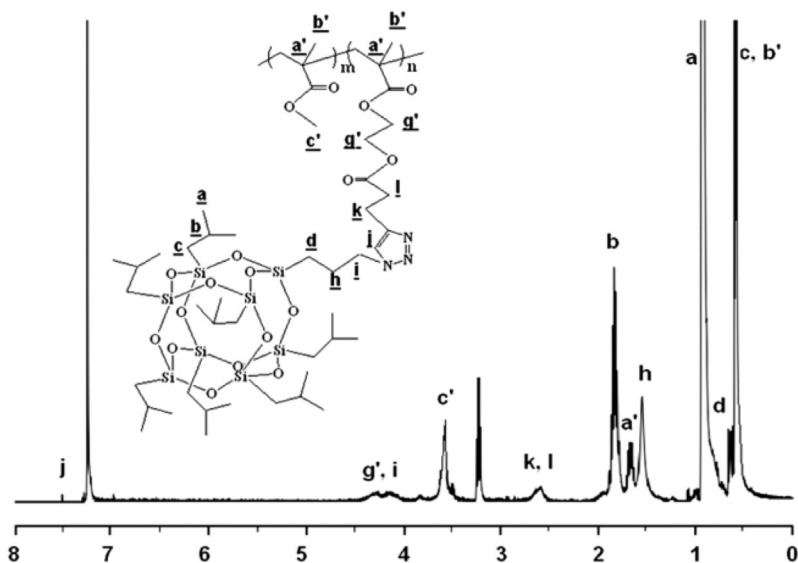


**FIGURE 8.7**

$^1\text{H}$  NMR spectra of poly(HEMA-co-MMA)-g-POSS (in ppm) [66].

Copyright 2013. Reprinted with permission from John Wiley & Sons.

(hydroxyethyl methacrylate-co-methyl methacrylate)-g-polyhedral oligosilsesquioxane (poly(HEMA-co-MMA)-g-POSS) nanocomposite from HEMA, MMA, and POSS. They applied  $^1\text{H}$ -NMR studies to identify the product poly(HEMA-co-MMA)-g-POSS (Figure 8.7) and the peaks at 7.55 (j), 4.16, 2.61, and 3.60 ppm are respectively assigned to the proton in the triazole ring, methylene protons I and k adjacent to the triazole ring, and methyl protons ( $\text{ACOOCH}_3$ ) of the MMA segment. The successful synthesis of poly(HEMA-co-MMA)-g-POSS was also evidenced from the peaks at 0.62 (d) and 0.59 (c) ppm attributed to the POSS pendent in the matrix with shielded methylene protons adjacent to the silicon atom. Concentration of POSS in the matrix was also determined to be 27% by a  $^1\text{H}$ -NMR spectrum. In addition,  $^{29}\text{Si}$ -NMR analysis of poly(HEMA-co-MMA)-g-POSS nanocomposites showed peaks at 67.58, 67.87, 96.54, 100.77, and 105.76 ppm, because of the presence of the AOASiAO framework.

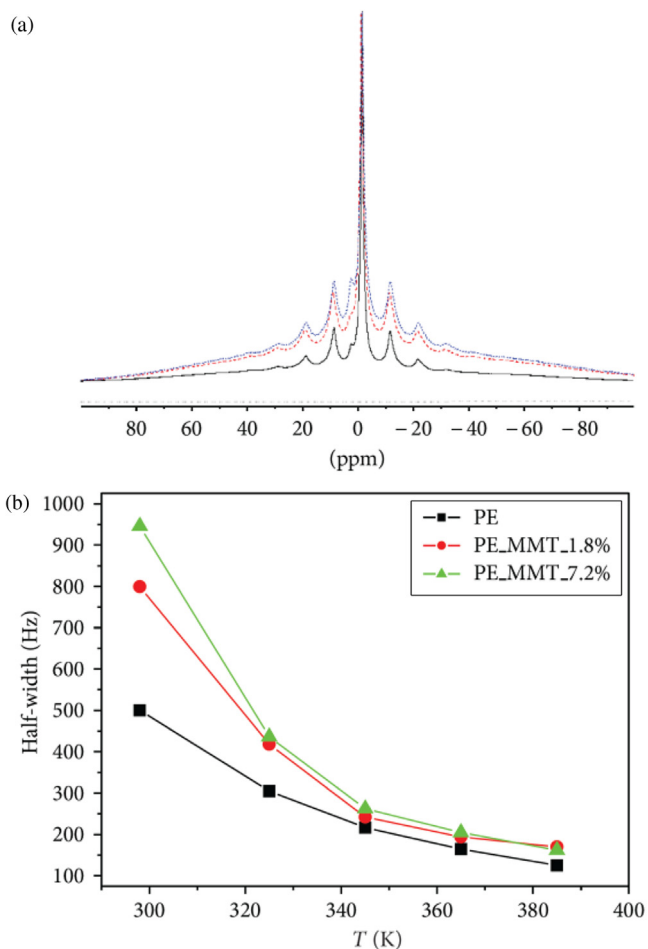
In the case of polymer clay nanocomposites, NMR provides information on polymer-surfactant-clay intercalation, polymer chain conformation and mobility, length of polymer chain, nature of the head group, and structure and charge of the mineral. The paramagnetic effect from the ions of the clay structure also influences the clay dispersion and thus, its characterization. Intercalated clay nanocomposites of modified saponites (HDTASAP0.75) with PCL were fabricated by the *in situ* polymerization of  $\epsilon$ -caprolactone and the typical  $^{13}\text{C}$  CP MAS NMR spectra of the composites [67].

The signals at 174 (O—CO), 66 (O—CH<sub>2</sub>), 34 (CO—CH<sub>2</sub>), 30 (OC—CH<sub>2</sub>—CH<sub>2</sub>), and 26 ppm (methylene groups) correspond to the polymer with a spinning side band at 125 ppm. The shifts at 68 (N—CH<sub>2</sub>), 54 (NCH<sub>3</sub>), 34 (H<sub>2</sub>C<sub>4-14</sub> in the all-*trans* conformation), 32 (H<sub>2</sub>C<sub>4-14</sub> in the dynamically exchanged *trans*/gauche conformation), 29 (H<sub>2</sub>C<sub>2</sub>), 25 (H<sub>2</sub>C<sub>3</sub>), and 17 ppm (terminal H<sub>3</sub>C<sub>16</sub> group) [67]. The greater polymer mobility is observed from the decrease of the *trans* conformer population in the HDTA (HDTP) chain and the variation of the <sup>31</sup>P relaxation times of the intercalated HDTP. Moreover, the shorter dipolar relaxation times for the extracted PCL than those of the nanocomposite, indicate greater mobility in the nanocomposite than in the bulk phase. The layer charge of the saponites did not affect the structure and dynamics of the intercalated nanocomposites, but did affect its yield.

The phase structure and molecular mobility of exfoliated and interacted PE/montmorillonite (MMT) nanocomposites were investigated by proton and carbon NMR spectroscopies under static and MAS conditions. MMT enhanced the polyethylene crystallinity and the orthorhombic and monoclinic phases were detected by <sup>13</sup>CP/MAS NMR. The polymer chain mobility of crystalline phase, interphase, and amorphous phase was hindered in the nanocomposites and the phase structure quantification was done by changing the temperature as well. From Figure 8.8, the line width of the 1H signal is dominated for polyethylene by the dipolar interactions between protons. A HR in the <sup>1</sup>H spectrum by MAS at a speed of 5 kHz for dipolar interactions is achieved. The higher half width of the PE nanocomposites spectrum compared with the PE bulk is also attributed to the rigidity attained for the chains with filler addition. From Figure 8.8b, the difference in line widths of the composites is disappearing with lower temperatures, while they showed similar line widths at 365 and 385 K near to the melting point. This typical behavior is not substantially proved and needs to be studied further.

In another work the nuclear magnetic relaxation is correlated with interparticle spacings of paramagnetic-impurity-containing clay nanoparticles in their polypropylene (PP) nanocomposites using 1H NMR relaxometry and the results are compared with transmission electron microscopy (TEM) images. Figure 8.9a shows slightly larger values for the DNMR than the DTEM\_rms values for all of the stretched samples. This is attributed to the nonuniform spatial distribution of MMT particles in the composites (PP—MMT-2.7).

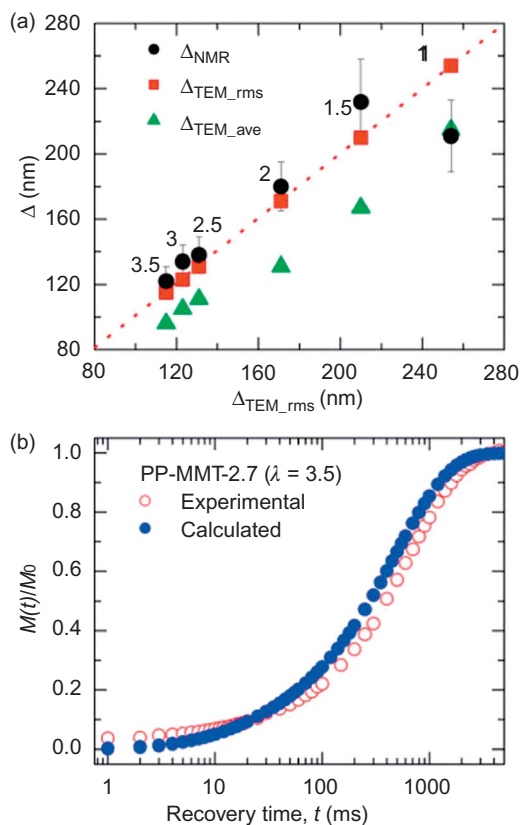
The NMR experimental magnetization growth profile in Figure 8.9b (open circles) shows faster recovery in the short-time regime and slower recovery in the long-time regime. Mathematical models are also used to identify the consistency of the behavior and found a broader distribution in NMR data compared to TEM. This might be due to the absence of bulk analysis in TEM and global averaging of NMR measurements over a much larger portion of the sample. The asymmetric shape of the distribution with smaller values indicates TEM of localized region are exhibiting smaller average interparticle spacings. Both the DNMR and DTEM\_ave values were equal for unstretched samples which rejects the overall quality or homogeneity of clay dispersion in bulk materials.

**FIGURE 8.8**

$^1\text{H}/\text{MAS}$  spectrum of polyethylene (PE) and PE nanocomposites. (a) A typical  $^1\text{H}/\text{MAS}$  spectrum measured at room temperature; (b) half-width of the  $^1\text{H}$  MAS spectra dependence on the temperature [68].

Copyright 2013. Reprinted with permission from Springer.

Finally, the NMR derived values reflected the overall properties of the nanocomposites better than the TEM data, and this can also be extended to rod-like or sphere-like particles. In such cases if their surface nuclei relaxes quickly, their magnetization growth profiles can be described by a 2D or three-dimensional model that is expressed as the product of a one-dimensional profile along two or three orthogonal directions.

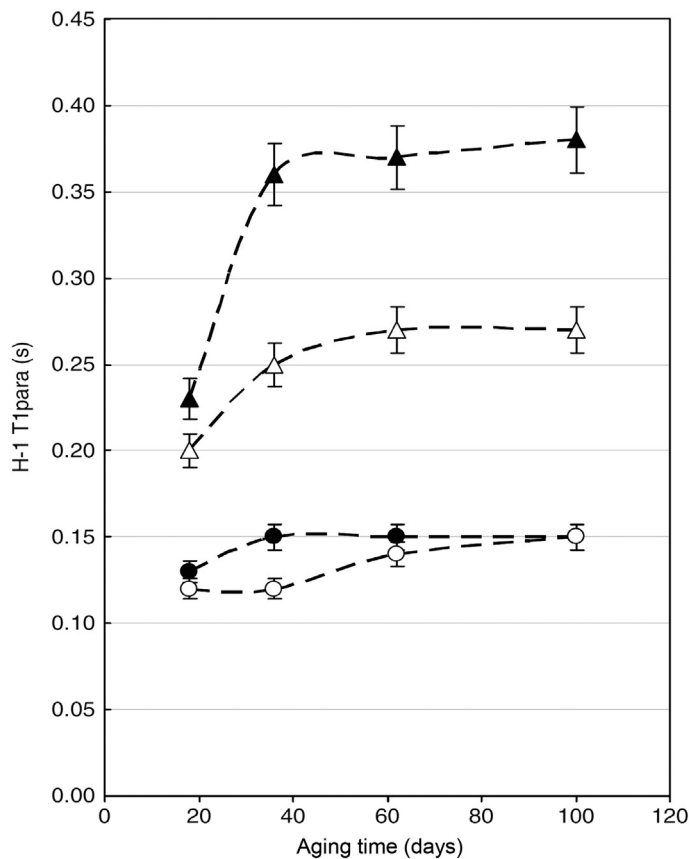
**FIGURE 8.9**

(a) Comparison between the NMR-derived (circles,  $\Delta_{\text{NMR}}$ ) and TEM-measured interparticle spacings in PP–MMT nanocomposites films (stretch ratios shown above the data): the TEM arithmetic average (triangles,  $\Delta_{\text{TEM\_ave}}$ ) and the TEM quadratic mean (squares,  $\Delta_{\text{TEM\_rms}}$ ). (b) Magnetization growth profiles for the PP–MMT-2.7 sample. The calculated profile was created using the TEM IPS distribution, and the same parameters were used and determined from fitting the NMR experimental profile ( $D = 0.24 \text{ nm}^2 \text{ ms}^{-1}$ ,  $T_{1,m} = 806 \text{ ms}$ , and  $T_{1,s} = 6.1 \text{ ms}$ ) [69].

Copyright 2014. Reprinted with permission from Royal Society of Chemistry.

### 8.3.3 BIOPOLYMER NANOCOMPOSITES

Bulk analysis of clay dispersion in starch–clay nanocomposites was done by HR solid-state NMR. At 2.5 wt% nanoclay concentration, complete exfoliation of clay particles were observed with an average interlayer distance of 40 nm. Figure 8.10 shows the  $^1\text{H}$   $T_1$  values of the starch matrix and moisture in samples,

**FIGURE 8.10**

$^1\text{H}$   $T_1$  para data of ST-N5.0 (starch; J, moisture) and SP-N5.0 (m, starch; n, moisture) over the aging period of 105 days [70].

Copyright 2010. Reprinted with permission from Springer.

ST-N5.0 and SP-N5.0, at relative humidity 50% and at room temperature along with their corresponding  $T_1$  para values.

The  $T_1$  para values showed an increase for the initial 40 days suggesting a decrease in the degree of exfoliation, and later during 40–60 days it became constant. This indicates that the recrystallization effect of starch during aging did not reduce the clay dispersion. For the SP-N5.0 system, the  $T_1$  para value of the starch matrix increased 60% during the initial 60 days of aging with variation in interlayer space from 33 nm to 55 nm. This suggests the participation of water molecules in retaining the strong interaction with the clay surface, the effect of which is more than the influence of polyvinyl alcohol (PVA) in the composite to decrease the degree of clay exfoliation within starch. The study addressed the effect of moisture, starch molecular

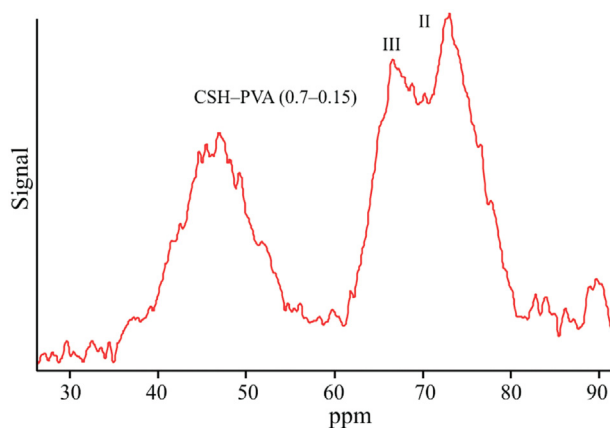


**FIGURE 8.11**

$^{13}\text{C}$  CP NMR spectra of C–S–HPN material (CSH–PVA (0.7–0.15)), in ppm [71].

Copyright 2006. Reprinted with permission from Springer.

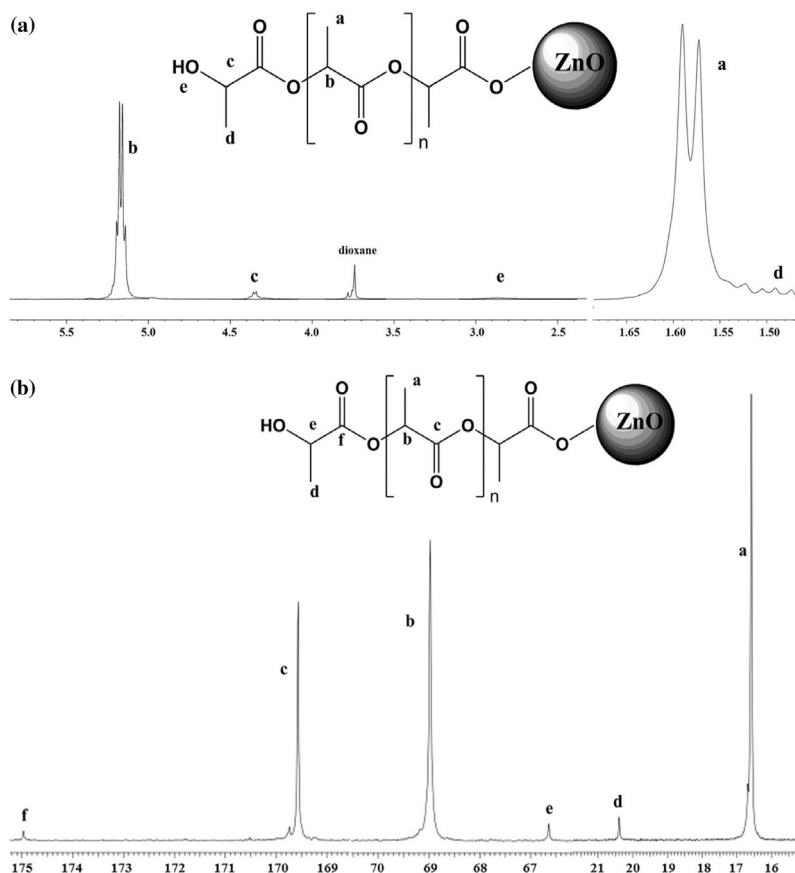
motions, starch-clay-polyvinylalcohol interactions, and starch recrystallization on clay dispersion during aging process in terms of the effect of paramagnetic impurity  $\text{Fe}^{3+}$  ions in the clay.

The behavior of calcium silicate hydrate (CSH)/PVA nanocomposite (C–S–HPN) material was characterized by  $^{13}\text{C}$  CP NMR ( $^{13}\text{C}$  CP NMR) as given in Figure 8.11.

In the spectrum, the methine carbon resonances are observed at 77 (peak I), 71 (peak II), and 65 ppm (peak III) respectively attributed to heterotactic triads with two intramolecular hydrogen bonds, heterotactic triads with one intramolecular hydrogen bond, and syndiotactic triads with no intervening intramolecular hydrogen bonds. In the C–S–HPN composite, signals at 46 ppm (methylene signal) and at 72 and 66 ppm (two methine carbon resonances) are seen and when comparing with pure PVA, makes out the interactions between PVA and CSH in aqueous media as a function of the degree of tacticity and the gelation procedure.

Multifunctional organic/ inorganic PLLA/ZnO nanocomposites with different ZnO concentrations characterized by  $^1\text{H}$  NMR also substantiate the importance of this particular technique in exploring the molecular interactions. Without any surface modification, ZnO nanoparticles (2–10 nm) were distributed in PLLA and the spectrum (Figure 8.12) was taken by dispersing the nanocomposite in  $\text{CDCl}_3$ . The  $^1\text{H}$  NMR showed signals at 1.56 and 5.18 ppm, respectively, corresponding to methyl and methine protons of PLLA.

A weak quartet at 4.35 ppm is assigned to the methine proton attached to the terminal –OH and the peak at 1.35 ppm to the methyl group in the vicinity of terminal –OH. Broad peaks at 3.5–3.8 ppm are due to –OH end groups.

**FIGURE 8.12**

(a)  $^1\text{H}$  NMR spectrum of PLLA/ZnO nanocomposites (2%), in ppm; (b)  $^{13}\text{C}$  NMR spectrum of PLLA/ZnO (2%) nanocomposites [72].

Copyright 2014. Reprinted with permission from Elsevier Ltd.

The quartet at 5.18 indicates the optical purity of PLLA and thus the absence of racemization during the polymerization. The  $^{13}\text{C}$  NMR was also in agreement with the  $^1\text{H}$  NMR, in which the signals at 16.59 and 68.98 ppm were due to methyl and methine protons of the repeating monomer and the weak peaks at 66.6, 20.3, and 174.5 ppm due to methine, methyl, and carbonyl carbon of the  $-\text{OH}$  end terminal. Another strong peak at 169.57 with a small shoulder at 169.74 comes from the carbonyl carbon and is attributed to the highly isotactic polymerization. The absence of carboxylic end groups and methyl and methane groups next to it both in the  $^{13}\text{C}$  and  $^1\text{H}$  NMR confirmed the bonding of the carboxylate group to the ZnO surface.

Many recent studies of NMR spectra and  $^1\text{H}$   $T_1$  proton spin-lattice relaxations on polymer nanocomposites identified the filler-polymer interactions as well as nature and rate of filler dispersion [73–77].

---

## 8.4 CONCLUSION

The significance of different types of nuclear magnetic spectroscopic techniques is demonstrated in this chapter via the example of various polymer nanocomposites. The use of NMR in characterizing the nanocomposite does not depend on the nature of the polymer or filler. However, in most of the composite cases—such as elastomers, thermoplastics, and biopolymers—NMR explains the polymer-filler interfacial interactions, nature of dispersion, interspatial distances of the filler particles, bonding, presence of voids, etc. in an almost similar way.

---

## REFERENCES

- [1] Giannelis EP. Polymer-layered silicate nanocomposites: synthesis, properties and applications. *Appl Organomet Chem* 1998;12:675–80.
- [2] LeBaron PC, Wang Z, Pinnavaia TJ. Polymer-layered silicate nanocomposites: an overview. *Appl Clay Sci* 1999;15:11–29.
- [3] Schmidt D, Shah D, Giannelis EP. New advances in polymer/layered silicate nanocomposites. *Curr Opin Solid State Mater Sci* 2002;6:205–12.
- [4] Bharadwaj RK, Mehrabi AR, Hamilton C, Trujillo C, Murga M, Fan R, et al. Structure–property relationships in cross-linked polyester–clay nanocomposites. *Polymer* 2002;43:3699–705.
- [5] Ray SS, Okamoto K, Okamoto M. Structure–property relationship in biodegradable poly(butylene succinate)/layered silicate nanocomposites. *Macromolecules* 2003;36:2355–67.
- [6] Rhim JW, Ng PKW. Natural biopolymer-based nanocomposite films for packaging applications. *Crit Rev Food Sci Nutr* 2007;47:411–33.
- [7] Vaia RA, Ishii H, Giannelis EP. Synthesis and properties of two-dimensional nanostructures by direct intercalation of polymer melts in layered silicates. *Chem Mater* 1993;5:1694–6.
- [8] Pinnavaia TJ, Beall BW. Polymer-clay nanocomposites. *Wiley Series in Polymer Science*; 2001; John Wiley & Sons, New York, ISBN: 978-0-471-63700-4.
- [9] Park H, Li X, Jin C, Park C, Cho W, Ha C. Preparation and properties of biodegradable thermoplastic starch/clay hybrids. *Macromol Mater Eng* 2002;287:553–8.
- [10] Park H, Lee W, Park C, Cho W, Ha C. Environmentally friendly polymer hybrids part I mechanical, thermal, and barrier properties of thermoplastic starch/clay nanocomposites. *J Mater Sci* 2003;38:909–15.
- [11] Wilhelm H, Sierakowski M, Souza G, Wypych F. Starch films reinforced with mineral clay. *Carbohydr Polym* 2003;52:101–10.
- [12] McGlashan S, Halley P. Preparation and characterisation of biodegradable starch based nanocomposite materials. *Polym Int* 2003;52:1767–73.

- [13] Fisher H. Polymer nanocomposites: from fundamental research to specific applications. *Mater Sci Eng* 2003;C23:763–72.
- [14] Kalambur S, Rizvi S. Starch-based nanocomposites by reactive extrusion processing. *Polym Int* 2004;53:1413–16.
- [15] Huang M, Yu J, Ma X. Studies on the properties of montmorillonite-reinforced thermoplastic starch composites. *Polymer* 2004;45:7017–23.
- [16] Chen B, Evans J. Thermoplastic starch–clay nanocomposites and their characteristics. *Carbohydr Polym* 2005;61:455–63.
- [17] Dean K, Yu L, Wu DY. Preparation and characterization of melt-extruded thermoplastic starch/clay nanocomposites. *Comp Sci Tech* 2007;67:413–21.
- [18] Dean K, Do M, Petinakis E, Yu L. Key interactions in biodegradable thermoplastic starch/poly(vinyl alcohol)/montmorillonite micro- and nanocomposites. *Comp Sci Tech* 2008;68:1453–62.
- [19] Alexson DE, Russell K. Characterization of polymers by means of  $^{13}\text{C}$  NMR spectroscopy. *Prog Polym Sci* 1985;11:221–82.
- [20] Bourbigot S, Vanderhart DL, Gilman JW, Bellayer S, Strett H, Paul DR. Solid state NMR characterization and flammability of styrene–acrylonitrile copolymer montmorillonite nanocomposites. *Polymer* 2004;45:7627–38.
- [21] Krishnamoorti R, Vaia RA. Polymer nanocomposites: synthesis, characterization and modeling. *ACS Symp Series* 2002;804:2758–79.
- [22] Spiess HW. Interplay of structure and dynamics in macromolecular and supramolecular systems. *Macromolecules* 2010;43:5479–91.
- [23] Bendeif EE, Gansmuller A, Hsieh KY, Pillet S, Woike Th, Zobel M, et al. Structure determination of molecular nanocomposites by combining pair distribution function analysis and solid-state NMR. *RSC Adv* 2015;5:8895–902.
- [24] Spiess HW. Molecular dynamics of solid polymers as revealed by deuterium NMR. *Colloid Polym Sci* 1983;261:193–209.
- [25] Schaefer J, Stejskal EOJ.  $^{13}\text{C}$  NMR of polymers spinning at magic angle. *Am Chem Soc* 1976;98:1031–2.
- [26] Grant DM, Harris RK, editors. *Encyclopedia of nuclear magnetic resonance*, vol. 3. Chichester, UK: Wiley; 2002. p. 1574. 101.
- [27] Ernst RR, Bodenhausen G, Wokaun A. *Principles of NMR in one and two dimensions*. Oxford, UK: Clarendon Press; 1987. p. 610.
- [28] Schmidt-Rohr K, Spiess HW. *Multidimensional solid-state NMR and polymers*. London, UK: Academic Press; 1994. p. 385–403.
- [29] Callaghan PT. *Principles of nuclear magnetic resonance microscopy*. Oxford, UK: Clarendon Press; 1993.
- [30] Kimmich R. *NMR: tomography, diffusometry, relaxometry*. Berlin, Germany: Springer; 1997. p. 5261997.
- [31] Ponnamma D, Sadasivuni KK, Thomas S. NMR studies of natural rubber composites from macro- to nanoscales—a review, natural rubber materials: volume 2. *Composites Nanocomposites* 2013;2:683–702.
- [32] Reusch W. Nuclear Magnetic Resonance Spectroscopy (NMR)-Introduction. Michigan State University, <<http://www2.chemistry.msu.edu/faculty/reusch/VirtTxtJml/Spectrpy/nmr/nmr1.htm#nmr1>>.

- [33] Gutowsky HS, Saika A, Takeda M, Woessner DE. Proton magnetic resonance studies on natural rubber. II. Line shape and T<sub>1</sub> measurements. *J Chem Phys* 1957;27:537–42.
- [34] Schaefer J, Stejskal EO. In: Levy GC, editor. *Topics in carbon-13 NMR spectroscopy*, vol. 3. New York, NY: Wiley; 1979. p. 283.
- [35] Kaufman S, Slichter W, Davis DJ. Nuclear magnetic resonance study of rubber–carbon black interactions. *Polym Phys* 1971;9:829.
- [36] Kenny J, McBrierty V, Rigbi Z, Douglass D. Carbon black filled natural rubber. I. Structural investigations. *Macromolecules* 1991;24:436–43.
- [37] Ou Y, Yu Z, Vidal A, Donnet JJ. Effects of alkylation of silicas on interfacial interaction and molecular motions between silicas and rubbers. *Appl Polym Sci* 1996;59:1321–8.
- [38] Litvinov V, Steeman P. EPDM – carbon black interactions and the reinforcement mechanisms, as studied by low-resolution <sup>1</sup>H NMR. *Macromolecules* 1999;32:8476–90.
- [39] ten Brinke J, Litvinov V, Wijnhoven J, Noordermeer J. Low-field NMR investigations of nanocomposites: polymer dynamics and network effects. *Macromolecules* 2002;35:10026–37.
- [40] Leu G, Liu Y, Werstler D, Cory D. NMR characterization of elastomer – carbon black interactions. *Macromolecules* 2004;37:6883–91.
- [41] Wang M. Effect of polymer-filler and filler-filler interactions on dynamic properties of filled vulcanizates. *Rubber Chem Technol* 1998;71:520–89.
- [42] Chazeau L, Brown J, Yanyo L, Sternstein S. Modulus recovery kinetics and other insights into the payne effect for filled elastomers. *Polym Compos* 2000;21:202–22.
- [43] Heinrich G, Kluppel M. Recent advances in the theory of filler networking in elastomers, filled elastomers drug delivery systems. *Adv Polym Sci* 2002;160:1–44.
- [44] Kluppel M. *Filler-reinforced elastomers/scanning force microscopy; advances in polymer science*. Berlin, Heidelberg: Springer Verlag; 2003. p. 1–86164.
- [45] Berriot J, Montes H, Lequeux F, Long D, Sotta P. Evidence for the shift of the glass transition near the particles in silica-filled elastomers. *Macromolecules* 2002;35:9756–62.
- [46] Berriot J, Lequeux F, Monnerie L, Montes H, Long D, Sotta P. Filler–elastomer interaction in model filled rubbers. *J Non-Crystalline Solids* 2002;719:307–10.
- [47] Berriot J, Montes H, Lequeux F, Long D, Sotta P. Gradient of glass transition temperature in filled elastomers. *Europhys Lett* 2003;64:50–6.
- [48] Fryer D, Peters R, Kim E, Tomaszewski J, de Pablo J, Nealey P, et al. Dependence of the glass transition temperature of polymer films on interfacial energy and thickness. *Macromolecules* 2001;34:5627–34.
- [49] Long D, Lequeux F. Heterogeneous dynamics at the glass transition in van der Waals liquids, in the bulk and in thin film. *Eur Phys J E* 2001;4:371–87.
- [50] Saalwachter K, Kluppel M, Luo H, Schneider H. Chain order in filled SBR elastomers: a proton multiple-quantum NMR study. *Appl Magn Reson* 2004;27:401–17.
- [51] Saalwachter K. Artifacts in transverse proton NMR relaxation studies of elastomers. *Macromolecules* 2005;38:1508–12.

- [52] Maus A, Hertlein C, Saalwachter K. A robust proton NMR method to investigate hard/soft ratios, crystallinity, and component mobility in polymers. *Macromol Chem Phys* 2006;207:1150–8.
- [53] Mauri M, Thomann Y, Schneider H, Saalwachter K. Spin-diffusion NMR at low field for the study of multiphase solids. *Solid State Nucl Magn Reson* 2008;34:125–41.
- [54] Saalwachter KJ. Detection of heterogeneities in dry and swollen polymer networks by proton low-field NMR spectroscopy. *Am Chem Soc* 2003;125:14684–5.
- [55] Saalwachter K, Herrero B, Lopez-Manchado MA. Chain order and cross-link density of elastomers as investigated by proton multiple-quantum NMR. *Macromolecules* 2005;38:9650–60.
- [56] Lewinski P, Sosnowski S, Kazmierski S, Penczek S. L-Lactide polymerization studied by  $^1\text{H}$  NMR with diffusion-ordered spectroscopy (DOSY): a “One NMR Tube Experiment” providing data on monomer conversion, polymer structure,  $M_n$  and  $M_w$ . *Polym Chem* 2015;6:4353–7.
- [57] Valentin J, Posadas P, Fernandez-Torres A, Malmierca M, Gonzalez L, Chasse W, et al. Inhomogeneities and chain dynamics in diene rubbers vulcanized with different cure systems. *Macromolecules* 2010;43:4210–22.
- [58] Aurelie PA, Kay SK, Kerstin SK, Laurent GL, Francois LF, Montes H. Low-field NMR investigations of nanocomposites: polymer dynamics and network effects. *Macromolecules* 2011;44:913–22.
- [59] Berriot J, Martin F, Montes H, Monnerie L, Sotta P. Reinforcement of model filled elastomers: characterization of the cross-linking density at the filler-elastomer interface by  $^1\text{H}$  NMR measurements. *Polymer* 2003;44:1437–47.
- [60] Tatiane MA, Katyuscya VL, Maria IBT, Antonio GF, Elson L, Emerson RC. NMR study of styrene-butadiene rubber (SBR) and  $\text{TiO}_2$  nanocomposites. *Polym Test* 2009;28:490–4.
- [61] Nogueira RF, Tavares MIB. Carbon-13 NMR study of poly(alpha-methylstyrene). *Polym Test* 2001;20:379–82.
- [62] Sakdapipanich J, Kowitteerawut T, Seiichi K, Tanaka Y. Structural characterization of highly cis-1,4-polybutadiene: a comparing study in swollen and solid state using NMR technique. *Polym Bull* 2001;46:479–85.
- [63] Gao Y, Zhang R, Lv W, Liu Q, Wang X, Sun P, et al. Critical effect of segmental dynamics in polybutadiene/clay nanocomposites characterized by solid state  $^1\text{H}$  NMR spectroscopy. *J Phys Chem C* 2014;118:5606–14.
- [64] Strankowska J, Piszczyk L, Strankowski M, Danowska M, Szutkowski K, Jurga S, et al. Molecular dynamics studies of polyurethane nanocomposite hydrogels. *Eur Phys J Spec Top* 2013;222:2179–86.
- [65] Liou YS, Tsai HC, Yeh CY, Tsiang RCC. Polymeric nanocomposite comprising gold nanoparticles and bilaterally sulfur-functionalized polystyrene. *J Polym Sci Part A: Polym Chem* 2015;53:1268–77.
- [66] Islam MR, Bach LG, Park JM, Hong SS, Lim KT. Synthesis and characterization of poly(HEMA-co-MMA)-g-POSS nanocomposites by combination of reversible addition fragmentation chain transfer polymerization and click chemistry. *J Appl Polym Sci* 2013;127:1569–77.
- [67] Grandjean J. Solid-state NMR study of modified clays and polymer/clay nanocomposites. *Clay Miner* 2006;41:567–86.

- [68] Wei L, Linxi H, Zhongren C. An NMR investigation of phase structure and chain dynamics in the polyethylene/montmorillonite nanocomposites. *J Nanomater* 2013;937210:1–10.
- [69] Xu B, Leisen J, Beckham HW. Nanoparticle dispersion in polymer nanocomposites by spin-diffusion-averaged paramagnetic enhanced NMR relaxometry. *Nanoscale* 2014;6:1318.
- [70] Xiaoqing Z, Katherine D, Iko MB. A high-resolution solid-state NMR study on starch–clay nanocomposites and the effect of aging on clay dispersion. *Polym J* 2010;42:689–95.
- [71] Mojumdar SC, Raki L, Mathis N, Schimdt K, Lang S. Thermal, spectral and AFM studies of calcium silicate hydrate-polymer nanocomposite material. *J Therm Anal Calorimetry* 2006;85:119–24.
- [72] Harjinder K, Anuradha R, Shinu R. A study on ZnO nanoparticles catalyzed ring opening polymerization of L-lactide. *J Polym Res* 2014;21:537–40.
- [73] VanderHart DL, Asano A, Gilman JW. Solid-state NMR investigation of paramagnetic nylon-6 clay nanocomposites. 1. Crystallinity, morphology, and the direct influence of Fe<sup>3+</sup> on nuclear spins. *Chem Mater* 2001;13:3781–95.
- [74] Terenzi C, Prakobna K, Berglund LA, Furó I. Nanostructural effects on polymer and water dynamics in cellulose biocomposites: <sup>2</sup>H and <sup>13</sup>C NMR relaxometry. *Biomacromolecules* 2015;16:1506–15.
- [75] Bourbigot S, VanderHart DL, Gilman JW, Awad WH, Davis RD, Morgan AB, et al. Investigation of nanodispersion in polystyrene–montmorillonite nanocomposites by solid-state NMR. *J Polym Sci Part B: Polym Phys* 2003;41:3188–213.
- [76] Bertmer M, Wang M, Kruger M, Blumich B, Litvinov V, van Es M. Structural changes from the pure components to nylon 6–montmorillonite nanocomposites observed by solid-state NMR. *Chem Mater* 2007;19:1089–97.
- [77] Mao L, Imam S, Gordon S, Cinelli P, Chiellini E. Extruded cornstarch-glycerol polyvinyl alcohol blends: mechanical properties, morphology, and biodegradability. *J Polym Environ* 2000;8:205–11.

## 9

EPR spectroscopy  
of polymer:fullerene  
nanocomposites<sup>1</sup>

V.I. Krinichnyi

*Institute of Problems of Chemical Physics, Chernogolovka, Russian Federation*

## 9.1 INTRODUCTION

Nanoscale composites with a  $\pi$ -conjugated polymer matrix have attracted a lot of attention in recent years due to potential use of their unique physical and chemical properties in molecular electronics [1–3] and spintronics [4] for energy conversion and transport. Among elements of organic electronics based on nanomodified polymers, polymer:fullerene composites seem to be most suitable for polymer photovoltaics which explains their wide investigation [5–8]. Fullerene molecules embedded into polymer matrix of such systems form so-called bulk heterojunctions (BHJ) and perform as electron acceptors (electron transporter, *n*-type material) and as electron donors (hole transporter, *p*-type material), respectively. Composites of soluble derivatives of conjugated polymers and fullerene were proved [8] to be the most efficient systems for utilization in plastic devices. Beyond photoinduced charge exciting and separation, positive carriers are transported to electrodes by polarons diffusing in the polymer phase and electrons hopping between fullerene domains embedded into the polymer matrix. A definitive advantage of BHJ is that it can be made by simply mixing the materials in an organic solvent, and casting with standard solution deposition techniques, such as spin coating [9].

The irradiation of such BHJ by visible light with photon energy  $h\nu_{\text{ph}}$  higher than the  $\pi$ - $\pi^*$  energy gap  $E_{\text{g}}$  of the polymer matrix leads to the formation of ion radical quasipairs, polaron  $P^{+\bullet}$  on a polymer chain (donor, *D*) and fullerene  $F_{60}^{-\bullet}$  (acceptor, *A*), and charge separation during the following successive stages [10]:

- (i) excitation of polaron on polymer chain:  $D + A \xrightarrow{h\nu} D^* + A$ ,
- (ii) excitation delocalization on the complex:  $D^* + A \xrightarrow{h\nu} (D + A)^*$ ,
- (iii) initiation of charge transfer:  $(D - A)^* \rightarrow (D^{\delta+} - A^{\delta-})$ ,

<sup>1</sup>This chapter is dedicated to my beautiful daughters, Natalia and Ksenia.

- (iv) formation of ion-radical pair:  $(D^{\delta+} - A^{\delta-})^* \rightarrow (D^{+\bullet} - A^{-\bullet})$ ,  
 (v) charge separation:  $(D^{+\bullet} - A^{-\bullet}) \rightarrow D^{+\bullet} - A^{-\bullet}$ .

The donor and acceptor units are spatially close, but not covalently bonded. At each step, the  $D$ - $A$  system can relax back to the ground state, releasing energy to the “lattice” in the form of either heat or emitted light. This process, revealed by time-resolved optical spectroscopy occurs in the femtosecond time domain [11,12] (e.g., about 100 fs in optimized polymer:fullerene BHJ [13], whereas the electron back transfer with charge annihilation is much slower, possibly due to dynamics and the relatively slow structural relaxation in such a system of lowered dimensionality. Understanding of photoexcitation, recombination of charge carriers, and other electronic processes realized in conjugated polymers is of fundamental interest for both material characterization and molecular device fabrication.

BHJs are characterized by efficient light-excited charge generation at the interface between two organic materials with different electron affinities. Figure 9.1 illustrates the energy diagram of two intrinsic semiconductors, poly(3-alkylthiophene) (P3AT) and [6,6]-phenyl- $C_{61}$ -butanoic acid methyl ester (PC<sub>61</sub>BM), most widely used in polymer:fullerene composites, before making a contact between

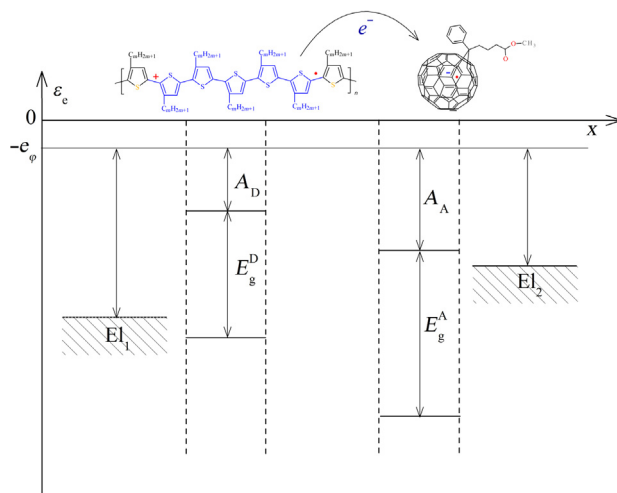


**FIGURE 9.1**

Schematic band diagram of two semiconductors with different electron affinities before forming the BHJ between them. The electron donor ( $A_D$ ) and electron acceptor ( $A_A$ ) affinities are defined as compared with the electron energy in vacuum at the same electrical potential.  $E_g^D$  and  $E_g^A$  are the band gap energies of the electron donor and electron acceptor, respectively. At the top of the figure, the P3AT and PC<sub>61</sub>BM are schematically shown as electron donor and electron acceptor, respectively. The appearance of the polaron quasiparticle with a spin  $S = \frac{1}{2}$  and an elemental positive charge in a P3AT chain and ion radical with an elemental negative charge and a spin  $S = \frac{1}{2}$  on a PC<sub>61</sub>BM are also shown.

them. A heterojunction formed by these materials inserted between a high work-function electrode ( $E_{I_1}$ ) matching the highest occupied molecular orbital level of the donor ( $HOMO_D$ ) and a low work-function electrode ( $E_{I_2}$ ) matching the lowest unoccupied molecular orbital level of the electron acceptor ( $LUMO_A$ ) should, in principle, act as a diode with rectifying current–voltage characteristics. Under the forward bias (the low work-function electrode is biased negative in respect to the high work-function electrode) the electron injection into the  $LUMO_A$  layer from the low work-function electrode as well as the electron extraction out of the  $HOMO_D$  by the high work-function electrode is energetically possible and a high current may flow through the heterojunction. Under reverse bias (the low work-function electrode is biased positive in respect to the high work-function electrode), the electron removal from the electron donor and electron injection to the electron acceptor is energetically unfavorable. The formation of the polaron  $P^{+\bullet}$  and fullerene  $F_{61}^{\bullet-}$  charge carriers is shown in Fig. 9.1.

The mobility and stability of charge carriers was found [14] to be considerably higher in the BHJ formed by poly(3-hexylthiophene) (P3HT) with  $PC_{61}BM$  globes as compared with other polymer:fullerene composites. The much longer charge carrier lifetime achieved in the P3HT: $PC_{61}BM$  films should, therefore, lead to a higher concentration of charge carriers and their reduced recombination rate. Specific nanomorphology of such composites could result in screened Coulomb potential between the radical pairs photoexcited in their BHJ and facilitate their splitting into noninteracting charge carriers with a reduced probability of their further annihilation. An example of such nanomorphology is better structural order in the presence of interface dipoles, which would provoke the creation of a potential barrier for carrier recombination in this composite. This implies that longer charge carrier lifetime can be achieved at the same concentrations which finally result in higher photocurrent and larger power-conversion efficiency of such solar cells. For these reasons, PCBM has appeared to be most suitable electron acceptor to be used for an extended time in plastic solar-cell prototypes.

Efficiency of light conversion has already attained about 3% for the P3HT: $PC_{61}BM$  BHJ [15] and around 6–8% for other organic solar cells [16]. This parameter is governed by different factors. The first limitation originated from the high binding energy of polarons photoinduced in conjugated polymers upon light excitation, so by adding an electron acceptor, it becomes energetically favorable for the electron to escape a polymer macromolecule and to transfer to an acceptor. This requires the  $LUMO_D$  to be 0.3–0.5 eV higher than the  $LUMO_A$  [17,18]. However, such energy difference can be much higher for some polymer matrices, which decreases optimal open-circuit voltage, since the latter is ultimately limited by the difference between the  $HOMO_D$  and  $LUMO_A$  [19,20]. Raising the  $LUMO_A$ , for example, the efficiency factor of plastic solar cells increases without affecting their light absorption. This approach is theoretically more beneficial for a single-layer solar cell, and results in an estimated efficiency of 8.4% when the LUMO offset is reduced to 0.5 eV [21]. The structure of donor and acceptor as well as the conformation of respective BHJ can also affect charge

transport and recombination [22]. Lenes et al. [23] have suggested *bis*-PC<sub>62</sub>BM methanofullerene,  $bmF_{62}^{\bullet}$ , to use as electron acceptor, in which the fullerene cage is functionalized by two methanobridged PBM side groups, with a higher (by  $\sim 0.1$  eV) LUMO<sub>A</sub> than that of PC<sub>61</sub>BM. Indeed, quantum efficiency of plastic solar cells appeared [24,25] to be improved when PC<sub>61</sub>BM is replaced by *bis*-PC<sub>62</sub>BM. However, it was shown [26] that the photoluminescence dynamics became slower after the replacement due to the reorganization of BHJ. Quantum efficiency can also be reduced due to possible formation of triplets from intersystem crossing of the excitons or by intersystem crossing of the charge-separated states followed by charge recombination [27]. Another way to improve this important parameter is by decreasing the band gap of the active polymer matrix (near 1.9 eV for P3HT), which limits the absorbance of light photons with higher energy. Thus, to harvest more solar photons, which increases the power-conversion efficiency, one should use polymers with lower band gaps in such devices. Poly[*N*-9'-hepta-decanyl-2,7-carbazole-alt-5,5-(4',7'-di-2-thienyl-2',1',3'-benzothiadiazole)] (PCDTBT), with band gap less than 1.9 eV [28,29], was discovered [30] to be one of the most efficient low-band gap semiconducting polymers for use in organic thin film field-effect transistors and solar cells [31–33]. The light conversion efficiency of the PCDTBT:PC<sub>71</sub>BM composite layer reached 7.2% [34] due to a relatively low HOMO<sub>D</sub> level and an internal quantum efficiency approaching 100% [35]. Such outstanding results were explained [13] mainly by ultrafast charge separation in the PCDTBT:PC<sub>71</sub>BM composite before localization of the primary excitation to form a bound exciton in contrast with, for example, a P3HT-based one, where photoinduced charge separation happens after diffusion of the polymer exciton to a fullerene interface. The other important property, the morphology of the PCDTBT:PC<sub>71</sub>BM BHJ is [34,36] laterally oriented with a column-like, bilayer-ordered polymer matrix with methanofullerene embedded between its chains that improves the carrier mobility, and, in particular, its electron mobility [37]. The dimensionality of the PCDTBT backbone with such morphology should be higher than that of P3AT matrices. Gutzler and Perepichka [38] showed that higher  $\pi$ -overlapping in two-dimensional (2D) thiophene-based polymers hinders their torsional twisting and, therefore, lowers their band gap. This allows holes to form through such well-ordered bilayer PCDTBT surfaces so the anode and electrons can move to the cathode inside methanofullerene pools located between these bilayers. This is evidence that charge dynamics is another important parameter affecting device light conversion efficiency. Higher charge carrier mobility of the polymer increases the diffusion length of electrons and photoinitiated holes and decreases the probability of their recombination in the active layer.

A real polymer:fullerene system consists of domains with different band gaps (i.e., different LUMO<sub>A</sub>–HOMO<sub>D</sub>) determining its energetic disorder with Gaussian distributed density of states [39]. Another constraint comes due to the finite number and mobility of charge carriers in organic solar cells which are lower when compared with conventional semiconductors. These main parameters depend on the

structure and properties of a polymer matrix and fullerene derivative embedded [23,40–43]. This why their power-conversion efficiency is appears to be governed by an ultrafast electron transfer from photoexcited polymer to fullerene [12], a large interfacial area for charge separation due to intimate blending of the materials [9], and efficient carrier transport across a thin film. Unambiguously, to increase power-conversion efficiency it is necessary to photoinitiate a higher density of charge carriers. However, an increased carrier density causes a reduced lifetime due to bimolecular recombination and the efficiency of solar cells might be reduced [43].

Planarity and regioregularity of polymer matrix, which are governed by the structure of the polymer and methanofullerene side substitutes, play an important role in charge separation and transition in the polymer:fullerene composites. The presence of substituents additionally affects torsional and energetic disorder of polymer chains, thereby changing effective mobility of charge carriers. Side chain groups accelerate torsional and librational chain dynamics, modulating intrachain and interchain charge transfer, respectively. Ginder et al. [44] showed that the torsional reordering of the backbone rings of conjugated polymers determines their electronic structure and charge transfer mechanism. Sensitivity of the average ring torsion angle between adjacent thiophene rings  $\theta$  to steric repulsion and electron delocalization is manifested in the effects of derivatization and temperature on optical spectra of these materials. The less a torsion angle  $\theta$ , the higher transfer integral and effective crystallinity can be reached. The increase in planarity reduces band gap, increases charge mobility, stability, and interactions between parallel polymer planes. Modification of the P3HT:PC<sub>61</sub>BM composite with N- or B-doped carbon nanotubes [45] and self-assembled dipole molecule deposition in plastic light-emitting diodes [46] can, in principle, to enhance their power-conversion efficiency. Thermal annealing can also modify morphological structure of BHJ and increase its light converting efficiency [47]. Such a treatment leads to the formation of crystalline regions in an amorphous polymer matrix that is accompanied by the shift of its light absorption maximum (e.g., of the P3HT:PC<sub>61</sub>BM composite from  $h\nu_{\text{ph}} \approx 2.5\text{--}2.8$  eV to the lower photon energies, 1.9–2.3 eV). The observed shift should also evidence the increase in the conjugation length in crystallites, because the polymer molecules within such crystallites are perfectly oriented and there are no defects like chain kinks, which limit the conjugation length. This process can be controlled, by UV/vis spectroscopy, grazing-incidence X-ray diffraction, and atomic force microscopy [48–50].

Charge recombination is considered to be predominantly nongeminate process governing the efficiency of polymer:fullerene solar cells [51–53]. Normally, the delay of charge carriers consists of prompt and persistent contributions [54,55]. The excitation light intensity dependence of prompt process is of activation bimolecular type and implies mutual annihilation within the initially created radical pair [56]. The persistent contribution is independent on the excitation intensity and originates from deep traps due to disorder [54]. Bimolecular and quadrimolecular recombination was shown [57] to be dominant in the P3AT:fullerene composites at the lower and higher intensity of the excited light, respectively.

The lifetime of charge carriers is usually estimated from photocurrent transients after the excitation by a short light pulse. However, this method seems to be inaccurate in the case of organic materials because the photocurrent transients depend not only on the decay of charge carrier concentration, but also on the mobility relaxation within the broad density of states [58]. An estimate of lifetimes from transient absorption techniques is difficult to make because of the very large dispersion observed leading to power law decays [51]. Thus, the photoexciting of charge carriers and their recombination are the most interesting points.

Both the  $P^{+\bullet}$  and  $F_{61}^{-\bullet}$  charge carriers possess uncompensated spin  $S = 1/2$ . This accounts for the wide use of light-induced electron paramagnetic resonance (LEPR) spectroscopy as a direct method for the investigation of charge photoexciting, separation, transfer, and recombination in fullerene-modified conjugated polymers [56,57,59]. Intramolecular quasi-one-dimensional (Q1D) charge transfer by polaron along polymer chains and its quasi-three-dimensional (Q3D) hopping between polymer and/or fullerene domains, as well as a rotational librative motion of fullerene globes are realized in the polymer:fullerene system. All spin-assisted molecular and electronic processes are expected to correlate. LEPR measurements revealed the existence of two radicals with different line shapes, magnetic resonance parameters, and saturation behaviors. The photoinduced spins should coact with their own charged microenvironment through exchange or dipole–dipole interaction. Such interactions do not register in LEPR spectra of plastic solar cells, which can be interpreted as the recession of mobile polarons on a conjugated polymer backbone and the fullerene anions with the rate faster than  $10^{-9}$  s. That is the reason why both the charge carriers excited in main polymer:fullerene composites are characterized by considerably long lifetimes and can be registered separately. Understanding the basic physics underlying the electron relaxation and dynamic behavior of fullerene-modified organic polymers is essential for the optimization of devices based on these materials.

The optimization of structure and nanomorphology of BHJ as well as the understanding of photoexcitation, dynamics, and recombination of charge carriers in such systems is of fundamental interest for controlled fabrication of optimal molecular photovoltaic devices. Understanding the charge separation and charge transport in such materials at a molecular level is crucial for improving the efficiency of the solar cells. However, they are not yet understood in detail and there is no generally applicable model describing molecular, electronic, and relaxation processes in different polymer:fullerene composites and there are no generally applicable models available.

This chapter describes a multifrequency (9.7–140 GHz) LEPR study of magnetic, relaxation and charge transport properties of spin charge carriers stabilized and photoinduced in different organic polymer:fullerene composites that was mainly conducted at the Institute of Problems of Chemical Physics of the Russian Academy of Sciences.

It starts with a brief theoretical background necessary for the interpretation of main spectroscopic parameters of spin carriers transferring a charge cross polymer:fullerene BHJ. The main results obtained by the LEPR spectroscopy in

combination with the steady-state saturation of spin-packets in the study of the nature, relaxation, and dynamics of both types of spin charge carriers are summarized and analyzed in the next section. Some examples of the utilization of multispin polymer/polymer:fullerene composites in molecular electronics and spintronics finalize their review.

---

## 9.2 THEORETICAL BACKGROUNDS OF ELECTRON PARAMAGNETIC RESONANCE IN POLYMER COMPOSITES

Electron paramagnetic resonance (EPR) spectroscopy is one of the most widely used and productive methods in structural and dynamic studies of various model, biological and physical solids containing free radicals, ion radicals, molecules in triplet states, transition metal complexes, and other paramagnetic centers (PC) [60–67]. The method is based on the interactions of unpaired electron spins in a sample with microwave irradiation in a magnetic field. Electrons possess a property called “spin,” resulting in an angular momentum. Because the electron is charged, there is a magnetic moment which points in the opposite direction to the angular momentum vector associated with the angular momentum. In an external magnetic field, the spin processes around the field direction at the Larmor frequency and thus a component of the magnetic moment is either parallel or anti-parallel to the field direction. If a microwave field of this frequency is applied to a spin containing sample, then the spins can change their direction relative to the magnetic field. This results in absorption of the microwave field, which may be measured. Spin reorientation is also affected by microenvironment. Microwave absorption depends on the fundamental properties of spin reservoir previously described. Thus, EPR spectra can yield detailed information not only about spin properties of a sample, but also about its structure and composition.

A typical continuous wave (CW) EPR spectrometer consists of a source of microwave radiation, a cavity into which the sample is placed (to enhance the size of the microwave field), a detector to measure the microwave signal reflected from the cavity, and a magnet to induce the external field. A small modulation field allows the use of phase sensitive detection for the increased signal/noise ratio. In some cases pulse EPR techniques, accompanied by the Fourier transformation of the signal [68–71], can be used for the study of fast dynamics and spin transitions. Such techniques, which involve illuminating the sample with a sequence of short pulses and then observing what it reradiates, offer time-resolved experiments, the ability to resolve closely spaced lines, and are good for measuring relaxation. To excite the whole spectrum at once, however, requires very short, very high power pulses and requires the system dead-time (the time after the last illuminating pulse before measurement can begin) to be minimized. The system dead-time often means that the signal from any broad lines has decayed before measurement starts.

The parameters which can be directly obtained from CW EPR spectra of PC stabilized or initiated in polymer systems are described next.

### 9.2.1 LANDÉ FACTOR

The main magnetic resonance parameters directly obtained by EPR spectroscopy for PC in condensed systems are the Landé factor (or  $g$ -factor: that is the ratio of electron mechanic momentum to a magnetic moment), spin susceptibility, and line width. The first of them is characterized by the Zeeman interaction of an unpaired electron with an external magnetic field. If the fundamental resonance condition [72] is fulfilled, an unpaired electron absorbs an energy quantum and is transferred to a higher excited state. It can be seen that the higher  $B_0$  (or  $\omega_e$ ) value, the higher excited state an electron can reach and the higher spectral resolution can therefore be realized. It is stipulated by the distribution of spin density in a polymer unit, the energy of excited configurations, and its interaction with nearest nuclear. If the spin of polaron weakly interacts with own environments, its Landé-factor lies near  $g$ -factor of free electron,  $g_e = 2.00232$ . At higher interaction, environmental nuclei induce an additional magnetic field resulting tensoric character of its Landé-factor [63,73,74].

$$\hbar\omega_e = \gamma_e \hbar B_0 = g \mu_B B_0 \quad (9.1)$$

where  $\hbar = h/2\pi$  is the Planck constant,  $\omega_e = 2\pi\nu_e$  is the Larmor or electron spin precession angular frequency,  $\gamma_e$  is the gyromagnetic ratio for electron,  $B_0$  is the strength of an external magnetic field, and  $\mu_B$  is the Bohr magneton.

$$\mathbf{g} = \begin{vmatrix} g_{xx} & & \\ & g_{yy} & \\ & & g_{zz} \end{vmatrix} = \begin{vmatrix} 2 \left( 1 + \frac{\lambda\rho(0)}{\Delta E_{n\pi^*}} \right) & & \\ & & 2 \left( 1 + \frac{\lambda\rho(0)}{\Delta E_{\sigma\pi^*}} \right) \\ & & & & & 2 \end{vmatrix}, \quad (9.2)$$

where  $\lambda$  is the spin-orbit coupling constant,  $\rho(0)$  is the spin density,  $\Delta E_{n\pi^*}$  and  $\Delta E_{\sigma\pi^*}$  are the energies of the unpaired electron  $n \rightarrow \pi^*$  and  $\sigma \rightarrow \pi^*$  transitions, respectively. Normally, polarons in organic conjugated polymers require a small energy of  $n \rightarrow \pi^*$  transition. This leads to deviation of its  $g_{xx}$  and  $g_{yy}$  values from  $g_e$ , so then the inequality  $g_{xx} > g_{yy} > g_{zz} \approx g_e$  holds for these PC.

Weak interaction of an unpaired electron delocalized on polaron over  $L$  lattice units with heteroatoms involved in a polymer backbone provokes rhombic symmetry of spin density and, therefore, anisotropy of its magnetic resonance parameters. Since the backbone of a polymer can be expected to lie preferably parallel to the film substrate [75], the lowest principal  $g$ -value is associated with the polymer backbone. The macromolecule can take any orientation relative to the  $z$ -axis, that is, the polymer backbone direction as it derives from the presence

of both the  $g_{xx}$  and  $g_{yy}$  components in the spectra for all orientations of the film. Thus, the  $g$ -factor anisotropy is the result of inhomogeneous distribution of additional fields in such systems along the  $x$  and  $y$  directions within the plane of their  $\sigma$ -skeleton rather than along its perpendicular  $z$  direction. Multifrequency EPR spectroscopy allows the resolution of some PC with near  $g$ -factors or spectral components of PC with anisotropic  $g$ -factor [63,74,76–78]. Harmonic librations of polymer chains with localized polarons can modulate the charge transfer integrals in polymer composites as it is typical for organic molecular ordered systems [79]. This should change the effective  $g$ -factor as:

$$g = g_0 + \frac{A}{\hbar\omega_l} \coth\left(\frac{\hbar\omega_l}{2k_B T}\right), \quad (9.3)$$

where  $g_0$  and  $A$  are constants,  $\omega_l = \omega_0 \exp(-E_l/k_B T)$  is librational frequency,  $E_l$  is the energy required for activation of such a motion,  $k_B$  is the Boltzmann constant, and  $T$  is the temperature.

### 9.2.2 SPIN SUSCEPTIBILITY

A static paramagnetic susceptibility  $\chi$  is also an important characteristic of a paramagnetic system. Generally, this parameter of  $N$  spins consists of temperature-independent Pauli susceptibility of the Fermi gas  $\chi_P$  and temperature-dependent contributions of localized Curie PC  $\chi_C$  [80]. However, such a simple system has been questioned, especially for conjugated polymers and their composites. These systems are characterized by significant disorder which localizes spins [81,82]. This originates the appearance in effective  $\chi$  of additional contribution  $\chi_{ST}$  which may be due to a possible singlet-triplet spin equilibrium in the system [80], contribution  $\chi_{ECP}$  described in terms of an exchange-coupled pairs (ECP) model of spin exchange interaction in pairs randomly distributed in a polymer matrix [83,84], and contribution  $\chi_m$  coming due to polaron Q1D mobility characterized by mid-gap energy  $E_g = 2E_a$  near the Fermi level  $\varepsilon_F$  [85,86]. Finally, one can write the equation for sum  $\chi$  as:

$$\begin{aligned} \chi = \chi_P + \chi_C + \chi_{ST} + \chi_m + \chi_{ECP} = & N_A \mu_{\text{eff}}^2 n(\varepsilon_F) + \frac{C}{3k_B T} + \frac{k_1}{T} \left[ \frac{\exp(-J/k_B T)}{1 + 3 \exp(-J/k_B T)} \right]^2 \\ & + \frac{Ca_d}{3k_B T} \left[ 3 + \exp\left(-\frac{2J}{k_B T}\right) \right]^{-1} + C(1 - a_d) \left\{ \frac{J}{3k_B T} + \ln \left[ 3 + \exp\left(-\frac{2J}{k_B T}\right) \right] \right\} \\ & + k_2 \sqrt{\frac{E_a}{k_B T}} \exp\left(1 - \frac{E_a}{k_B T}\right) \end{aligned} \quad (9.4)$$

where  $N_A$  is the Avogadro's number,  $n(\varepsilon_F)$  is the density of states per unit energy (in eV) for both spin orientations per monomer unit at  $\varepsilon_F$ ,  $\mu_{\text{eff}} = \mu_B g \sqrt{S(S+1)}$  is the effective magneton,  $S$  is a spin normally equal to  $1/2$  for PC in organic

polymers,  $C = N\mu_B^2 g^2 S(S + 1)$  is the Curie constant per mole-C/mole-monomer,  $k_1$  and  $k_2$  are constants,  $J$  is the exchange coupling constant, and  $a_d$  is a fraction of spin pairs interacting in disordered polymer regions. The contributions of these terms to the total paramagnetic susceptibility depend on various factors, for example, on the nature and mobility of charge carriers that can vary at the system modification. A small value of  $J$  corresponds to spin localization in a strongly disordered matrix and increases at overlapping of wave functions of interacting spins in more ordered regions.

In most polymer semiconductors, polarons are formed as very stable quasiparticles as a result of their doping and/or treatment by, for example, annealing or irradiation. Such charge carriers can also be excited on polymer chains quite reversibly, and this effect is used for conversion of solar light [5,8]. The treatment of polymer semiconductors modified by some electron acceptor normally leads to the transfer of electrons from their chains to the acceptor that is accompanied by the formation of polarons on polymer chains and anion radicals on acceptors. PC charged positively and negatively recombine after an irradiation down. Therefore, an effective spin susceptibility of such a system is the sum of these two alternating processes [53].

In polymer:fullerene composites, both initiated charges diffusing to the opposite electrodes must reach them prior to recombination. If these chargers after their transfer are still bound by the Coulomb potential, which is typical for the compounds with low-mobile charge carriers described here, they cannot escape from each other's attraction and will finally recombine. When the carrier dissipation distance is longer than the Coulomb radius, the excitons initiated by, for example, light in their heterojunctions can be split into positive and negative charge carriers. To fulfill this condition, the Coulomb field must be shielded or charge carrier-hopping distance must exceed the Coulomb radius. In this case, charges are transferred to the electrodes either by the diffusion of appropriate carriers or by the drift induced by the electric field. In order to excite a radical pair by each photon, charge carrier transit time  $t_{tr}$  should be considerably shorter than the lifetime of a radical pair  $\tau$ , that is,  $t_{tr} \ll \tau$ . The former value is determined by charge carrier mobility  $\mu$ , sample thickness  $d$ , and electric field  $E$  inside the film,  $t_{tr} = d/\mu E$ . If photocurrent is governed by the carrier drift in the applied electric field, the drift distance  $l_{dr} = \mu\tau E$ . If this current is governed by carrier diffusion, the diffusion distance  $l_{diff} = (D\tau)^{1/2} = (\mu\tau k_B T/e)^{1/2}$ , where  $D$  is the diffusion coefficient, and  $e$  is the elemental electron charge. Thus, the  $\mu\tau$  product governs the average distance passed by the charge carrier before recombination and, therefore, is an important parameter determining whether the efficiency of solar cells is limited by charge transport and recombination. The latter, generally is described as a thermally activated bimolecular recombination [56] which consists of temperature-independent fast and exponentially temperature-dependent slow steps [55].

Let a polaron possessing a positive charge multihops along a polymer chain from one initial site  $i$  to other available site  $j$  close to a position occupied by a negatively charged fullerene globule. A charge hops easier between fullerenes

than from polaron and fullerene, and an effective charge recombination is still limited by the transport of polarons towards fullerene molecules. The recombination is mainly stipulated by sequential charge transfer by polaron along a polymer chain and its transfer from polymer chain to a site occupied by a fullerene. Polaronic dynamics in undoped and slightly doped conjugated polymers is highly anisotropic [77]. Therefore, the probability of a charge transfer along a polymer chain exceeds considerably that of its transfer between polymer macromolecules.

According to the tunneling model [87], positive charge on a polaron can tunnel from this carrier toward a fullerene and recombine with its negative charge during the time:

$$\tau(R_{ij}^{\downarrow}) = \frac{\ln X}{\nu_{pn}} \exp\left(\frac{2R_{ij}^{\downarrow}}{a_0}\right), \quad (9.5)$$

where  $R_{ij}^{\downarrow}$  is the spatial separation of sites  $i$  and  $j$ ,  $a_0$  is the effective localization (Bohr) radius,  $X$  is a random number between 0 and 1, and  $\nu_{pn}$  is the attempt to jump frequency for positive charge tunneling from polymer chain to fullerene. The charge can also be transferred by the polaron thermally assisted multistep tunneling through energy barrier  $\Delta E_{ij} = E_j - E_i$ , so then:

$$\chi(R_{ij}, E_{ij}) = \chi_0 \frac{\ln X}{\nu_{pp}} \exp\left(\frac{2R_{ij}}{a_0}\right) \exp\left(\frac{\Delta E_{ij}}{k_B T}\right), \quad (9.6)$$

where  $\nu_{pp}$  is the attempt frequency for a hole tunneling between the polymer chains. The values in the couples  $\nu_{pn}$ ,  $\nu_{pp}$ , and  $R_{ij}^{\downarrow}$ ,  $R_{ij}$  may be different due, for instance, to the different electronic orbits.

If one switches off light excitation of the polymer:fullerene system, the concentration of spin pairs excited in its BHJ starts to decrease. This leads to instantaneous collapse of radical pairs or their splitting into noninteracting charge carriers due to polaron diffusion. The rate of recombination of charge carriers with effective localization radius  $a$  separated by a distance  $R_0$  can be written as [88]:

$$\nu(R) = \nu_0 \exp\left(-\frac{2R_0}{a}\right), \quad (9.7)$$

where  $\nu_0$  is an attempt to recombine frequency. Undoubtedly, both charge carriers have different localization radii. The localization radius for a negatively charged carrier should be on the order of the radius of the fullerene globule. The distance  $R_0$  should depend, for example, on the length of a side alkyl chain substitute in a polymer:fullerene matrix [89]. Polaron stabilized in conjugated polymers normally covers near to five monomer units [55,90]. The nearest-neighbor distance of spin pair with the typical radiative lifetime  $\tau_0$  changes with time  $t$  as:

$$R_0(t) = \frac{a}{2} \ln\left(\frac{t}{\tau_0}\right). \quad (9.8)$$

Assuming that photoexcitation is turned off at some initial time  $t_0 = 0$  at a charge carrier concentration  $n_0$  and taking into account a time period of geminate recombination  $t_1 - t_0$ , one can determine for concentration of charge carriers with:

$$n(R) = \frac{n}{1 + \frac{4\pi}{3} n_1 (R_0^3 - R_1^3)}, \quad (9.9)$$

where  $R_0$  is specified by Eqn (9.8),  $R_1 = R(t_1)$  describes the distance between the nearest-neighbor charge carriers at time  $t_1$ , after which solely nongeminate recombination is assumed, and  $n_1$  is the charge carrier concentration at time  $t_1$ . It follows from Eqn (9.9) that the time dependence of residual carrier concentration does not follow a simple exponential decay but shows a more logarithmic time behavior. After very long times, that is, at large  $R_0$ , one obtains  $n(R_0) = (3/4\pi)R_0^{-3}$  which is independent of the initial carrier density  $n_1$  and also  $n_0$ . It follows from Eqn (9.7) that photoexcited charge carriers have comparable long lifetimes which are solely ascribed to the large distances between the remaining trapped charge carriers. The excited carrier concentration  $n_1$  follows directly from LEPR measurements, whereas the  $a$  and  $\tau_0$  values can be guessed in a physically reasonable range. Finally, the concentration of spin pairs should follow the relation [88]:

$$\frac{n(t)}{n_0} = \frac{\frac{n_1}{n_0}}{1 + \left(\frac{m}{m_0}\right) \frac{\pi}{6} n_0 a^3 \left[ \ln^3\left(\frac{t}{\tau_0}\right) - \ln^3\left(\frac{t_1}{\tau_0}\right) \right]}. \quad (9.10)$$

The analysis showed that the spin concentration initially photoexcited at  $t = 0$  is governed by certain factors. One factor is the number and distribution of spin traps inversely formed in a polymer matrix under irradiation. A number and a depth of such traps depend on the photon energy  $h\nu_{\text{ph}}$  [42,91]. At the latter step, a polaronic charge carrier can either be retrapped by a vacant trap site or recombine with an electron on a fullerene anion radical. Trapping and retrapping of a polaron reduces its energy, which results in its localization into deeper trap and in the increase in number of localized polarons with time. So, the decay curves presented can be interpreted in terms of bulk recombination between holes and electrons during their repeated trapping into and detrapping from trap sites with different depths in an energetically disordered semiconductor [92]. Analyzing LEPR spectra, it becomes possible to separate the decay of mobile and pinned spin charge carriers excited in the composite. The traps in such a system should be characterized by different energy depths and energy distribution  $E_0$ . Polarons translative diffuse quickly along a polymer backbone, and fullerene anion radicals can be considered to be immobilized between polymer chains. This approach predicts the following law for decay of charge carriers [92]:

$$\frac{n(t)}{n_0} = \frac{\pi\alpha\delta(1+\alpha)\nu_d}{\sin(\pi\alpha)} t^{-\alpha}, \quad (9.11)$$

where  $n_0$  is the initial number of polarons at  $t = 0$ ,  $\delta$  is the gamma function,  $\alpha = k_B T/E_0$ ,  $\nu_d$  is the attempt jump frequency for polaron detrapping.

Positive charge on a polaron is not required to be recombined with the first negative charge on the subsequent acceptor. Thus, the probability of annihilation of charges can differ from the unit. Q1D hopping of a positively charged polaron from site  $i$  to site  $j$  with the frequency  $\omega_{\text{hop}}$  may collide with the acceptor located near the polymer matrix. While the polaron is mobile, the molecule of the acceptor can be considered as a translative fixed, but librating near its own main molecular axis. In this case, the spin flip-flop probability  $p_{\text{ff}}$  during a collision should depend on the amplitude of exchange and  $\omega_{\text{hop}}$  value as shown by [93,94]:

$$p_{\text{ff}} = \frac{1}{2} \cdot \frac{\alpha^2}{1 + \alpha^2} \quad (9.12)$$

where  $\alpha = (3/2) 2\pi J_{\text{ex}}/\hbar\omega_{\text{hop}}$  and  $J_{\text{ex}}$  is the constant of exchange interaction of spins in a radical pair. In the polymer composites weak and strong exchange limits can be realized when the increase of  $\omega_{\text{hop}}$  may result in decrease or increase in exchange frequency, respectively. If the ratio  $J_{\text{ex}}/\hbar$  exceeds the frequency of collision of both types of spins, the condition of strong interaction is realized in the system leading to the direct relation of spin–spin interaction and polaron diffusion frequencies, so then  $\lim(p) = 1/2$ . In the opposite case  $\lim(p) = 9/2 (\pi/\hbar)^2 (J_{\text{ex}}/\omega_{\text{hop}})^2$ . It is evident that the longer both the above tunneling times and/or the lesser the probability  $p_{\text{ff}}$ , the smaller the number of ion-radical pairs possible to recombine and, therefore, higher spin susceptibility should be reached. A combination of the two previous equations gives:

$$\chi_{\text{p}} = \chi_{\text{pn}} + \chi_{\text{p}}^0 \frac{\hbar}{J_{\text{ex}}} \left( \alpha + \frac{1}{\alpha} \right). \quad (9.13)$$

Assuming the above-introduced activation character for polaron multistep hopping with the frequency  $\omega_{\text{hop}} = \omega_{\text{hop}}^0 \exp(-\Delta E_{\text{r}}/k_{\text{B}}T)$  and the absence of dipole–dipole interaction between fullerene anion radicals, one can determine  $\Delta E_{\text{r}}$  from temperature dependences of paramagnetic susceptibility.

### 9.2.3 LINE SHAPE AND WIDTH

In contrast with a solitary and isolated spin characterized by  $\delta$ -function absorption spectrum, the spin interaction with a particle's own environment in a real system leads typically to the change in line shape and increase of line width. Analyzing the shape and intensity of the experimental spectrum it is possible to obtain direct information on electronic processes in polymer systems. An electron spin is affected by local magnetic fields, induced by another nuclear and electron  $n$   $r_{ij}$ -distanced spins [95]:

$$B_{\text{loc}}^2 = \frac{1}{4n} \gamma_{\text{e}}^2 \hbar^2 S(S+1) \sum_{ij} \frac{(1 - 3 \cos^2 \theta_{ij})}{r_{ij}^6} = \frac{M_2}{3\gamma_{\text{e}}^2}, \quad (9.14)$$

where  $M_2$  is the second moment of a spectral line. If a line broadening is stipulated by a local magnetic field fluctuating faster than the rate of interaction of a spin with the nearest environment, the first derivative of the Lorentzian resonant line with a distance between positive and negative peaks  $\Delta B_{pp}^L$  and maximum intensity between these peaks  $I_L^{(0)}$  is registered at resonance frequency  $\omega_e^{(0)}$  [96,97]

$$I_L' = \frac{16}{9} I_L^{(0)} \frac{(B - B_0)}{\Delta B_{pp}^L} \left[ 1 + \frac{4(B - B_0)^2}{3(\Delta B_{pp}^L)^2} \right]^{-2} \quad (9.15)$$

whereas at slower fluctuation of an additional local magnetic field, the spectrum is defined by Gaussian function of distribution of spin packets:

$$I_G' = \sqrt{e} I_G^{(0)} \frac{(B - B_0)}{\Delta B_{pp}^G} \exp \left[ -\frac{2(B - B_0)^2}{(\Delta B_{pp}^G)^2} \right]. \quad (9.16)$$

The EPR line shape due to dipole or hyperfine broadening is normally Gaussian. An exchange interaction between the spins in real system may result in the appearance of a more complicated line shape, described by a convolution of Lorentzian and Gaussian distribution function. This takes a possibility from the analysis of such a line shape to define the distribution, composition, and local concentrations of spins in such a system. For example, if equivalent PC with concentration  $n$  are arranged chaotically or regularly in the system their line shape is described by the Lorentzian and Gaussian distribution function, respectively, with the width  $\Delta B_{pp}^L = \Delta B_{pp}^G = 4\gamma_e \hbar n$  [98]. In the mixed cases, the line shape transforms to Lorentzian at a distance from the center  $\delta B \leq 4\gamma_e \hbar / r^3$  (here,  $r$  is a distance between magnetic dipoles) with the width  $\Delta B_{pp}^L = 4\gamma_e \hbar n$  in the center and becomes Gaussian type on the tails at  $\delta B \geq \gamma_e \hbar / r^3$  with the width  $\Delta B_{pp}^G = \gamma_e \hbar \sqrt{n/r^3}$ .

Line width is mainly determined by transverse (spin–spin) relaxation time  $T_2$ . However, there are several relaxation processes in a polymer composite which cause the shortening of  $T_2$  and hence the broadening of the EPR line. One of them is spin longitudinal (spin–lattice) relaxation on the lattice phonons with time  $T_1$ , which shortens the lifetime of a spin state and therefore broadens the line. Representing all other possible relaxation processes by the time  $T_2^1$ , one can determine for effective peak-to-peak line width  $\Delta B_{pp}$  as [99]:

$$\Delta B_{pp} = \Delta B_{pp}^0 + \frac{2}{\sqrt{3}\gamma_e} \cdot \frac{1}{T_2} = \Delta B_{pp}^0 + \frac{2}{\sqrt{3}\gamma_e} \cdot \left( \frac{1}{T_2^1} + \frac{1}{2T_1} \right), \quad (9.17)$$

where  $\Delta B_{pp}^0$  is the line width at the absence of spin dynamics and interaction. The collision of these PC should broaden the EPR spectrum by [93,94]:

$$\delta(\Delta B_{pp}) = p_{ff} \omega_{hop} n_g = k_1 \omega_{hop} n_g \left( \frac{\alpha^2}{1 + \alpha^2} \right), \quad (9.18)$$

where  $p_{\text{ff}}$  is the flip–flip probability inserted above,  $n_g$  is the number of guest PC per each polymer unit,  $k_1$  is constant equal to  $\frac{1}{2}$  and  $16/27$  for  $S = \frac{1}{2}$  and  $S = 1$ , respectively. In this case the guest spin acts as a nanoscopic probe of the polaron dynamics. Note, that the  $n_g$  parameter is temperature dependent that should be taken into account when calculating the effective line width. According to the spin exchange fundamental concepts [93], if exchange interaction changes between weak and strong exchange limits (see above), an appropriate  $\delta(\Delta\omega)(T)$  dependency may demonstrate extremal dependence with characteristic temperature  $T_c$ . This should evidence the realization of high and low of spin–spin interaction at  $T \leq T_c$  and  $T \geq T_c$ , respectively, realized, for example, in highly doped polyaniline samples [94,100–102].

The rate of charge hopping between two adjacent polymer units can be estimated to a good approximation using a semiclassical Marcus theory adopted for conjugated polymers [103,104]

$$\omega_{\text{hop}} = \frac{4\pi^2}{\hbar} \frac{t_{1\text{D}}^2}{\sqrt{4\pi E_r k_B T}} \exp\left(-\frac{E_r}{4k_B T}\right) \quad (9.19)$$

where  $t_{1\text{D}}$  is electronic coupling between initial and final states (intrachain transfer integral) and  $E_r$  is both the inner- and outer-sphere reorganization energy of charge carriers due to their interaction with the lattice phonons. The  $t_{1\text{D}}$  value decreases slightly with temperature, whereas its distribution broadens a line due to thermal motion of polymer units [105], similar to that which happens in organic crystals [106,107]. Note that the  $n_g$  parameter is temperature dependent and should be included in the finalized equation. Combination of Eqns (9.18) and (9.19) yields:

$$\delta(\Delta\omega) = \frac{\pi t_{1\text{D}}^2 n_g(T)}{\hbar \sqrt{\frac{E_r k_B T}{\pi}}} \cdot \frac{\exp\left(-\frac{E_r}{4k_B T}\right)}{1 + \left[ \frac{3J_{\text{ex}}}{2t_{1\text{D}}^2} \sqrt{\frac{E_r k_B T}{\pi}} \exp\left(\frac{E_r}{4k_B T}\right) \right]^{-2}}. \quad (9.20)$$

Excluding fast electron spin diffusion, the EPR line can also be broadened by the acceleration of molecular dynamics processes, for example, oscillations or slow torsion librations of the polymer macromolecules. The approach of random walk treatment [108] provides that such Q1D, Q2D, and Q3D spin diffusion with respective diffusion coefficients  $D_{1\text{D}}$ ,  $D_{2\text{D}}$ , and  $D_{3\text{D}}$  in the motionally narrowed regime changes the respective line width of a spin-packet as [109]:

$$\Delta B_{\text{pp}} \approx \frac{\gamma_e^{1/3} (\Delta B_{\text{pp}}^0)^{4/3}}{D_{1\text{D}}^{1/3}}, \quad (9.21)$$

$$\Delta B_{\text{pp}} \approx \frac{\gamma_e (\Delta B_{\text{pp}}^0)^2}{\sqrt{D_{1\text{D}} D_{3\text{D}}}}, \quad (9.22)$$

$$\Delta B_{\text{pp}} \approx \frac{\gamma_e (\Delta B_{\text{pp}}^0)^2}{D_{3\text{D}}}. \quad (9.23)$$

This theory postulates that at the transition from Q1D to Q2D and then to Q3D spin motion the shape of the EPR line should transform from Gaussian to Lorentzian. This approach allows the evaluation of an effective dimension of the system under study, say from an analysis of temperature dependence of its EPR spectrum line width. For spin Q3D motion or exchange, the line shape becomes close to Lorentzian shape, corresponding to an exponential decay of transverse magnetization with time  $t$ , proportional to  $\exp(-\eta t)$ ; for a Q1D spin motion, this value is proportional to  $\exp(-\rho t)$  (here  $\eta$  and  $\rho$  are constants) [110]. In order to determine the type of spin dynamics in a Q1D system appropriate anamorphoses  $I_0^l/I(B)$  versus  $[(B-B_0)/\Delta B_{1/2}]^2$ , and  $I_0^l/I(B)$  versus  $[(B-B_0)/\Delta B_{pp}]^2$  (here  $\Delta B_{1/2}$  is the half-width of an integral line) [110] should be analyzed.

### 9.2.4 DYSONIAN SPECTRAL CONTRIBUTION

The EPR line of PC in conducting composites can be complicated by the fact that the magnetic term  $B_1$  of the microwave field used to excite resonance sets up eddy currents in the material bulk. These currents effectively confine the magnetic flux to a surface layer of thickness of order of the “skin depth.” This phenomenon affects the absorption of microwave energy incident upon a sample and results in less intensity of electron absorption per unit volume of material for large particles than for small ones. This also leads to the appearance of asymmetric Dyson-like contribution [111] in EPR spectra of some composites containing ordered domains embedded into an amorphous polymer matrix [43,102], as in the case of metal-like organic polymers [76,112,113]. Such an effect appears when the skin-layer thickness  $\delta$  becomes comparable or thinner than a characteristic size of a sample, for example, due to the increase of conductivity. In this case the time of charge carrier diffusion through the skin-layer becomes essentially less than a spin relaxation time and the Dysonian line with characteristic asymmetry factor  $A/B$  (the ratio of intensities of the spectral positive peak to the negative one) is registered. Such line shape distortion is accompanied by the line shift into higher magnetic fields and the drop in sensitivity of EPR technique.

Generally, the Dysonian line consists of dispersion  $\chi^l$  and absorption  $\chi^ll$  terms, therefore one can write for its first derivative the following equation:

$$\frac{d\chi}{dB} = A \frac{2x}{(1+x^2)^2} + D \frac{1-x^2}{(1+x^2)^2}, \quad (9.24)$$

where  $x = 2(B - B_0)/\sqrt{3}\Delta B_{pp}^l$ . The line asymmetry parameter  $A/B$  is correlated with the above coefficients  $A$  and  $D$  simply as  $A/B = 1 + 1.5 D/A$  independently on the EPR line width. Organic polymers are usually studied as powder and film. Appropriate coefficients of absorption  $A$  and dispersion  $D$  in Eqn (9.24)

for skin-layer on the surface of a spherical powder particle with radius  $R$  and intrinsic ac conductivity  $\sigma_{ac}$  can be calculated from equations [114]:

$$\frac{4A}{9} = \frac{8}{p^4} - \frac{8(\sinh p + \sin p)}{p^3(\cosh p - \cos p)} + \frac{8 \sinh p \sin p}{p^2(\cosh p - \cos p)^2} + \frac{(\sinh p - \sin p)}{p(\cosh p - \cos p)} - \frac{(\sinh^2 p - \sin^2 p)}{(\cosh p - \cos p)^2} + 1, \quad (9.25)$$

$$\frac{4D}{9} = \frac{8(\sinh p - \sin p)}{p^3(\cosh p - \cos p)} - \frac{4(\sinh^2 p - \sin^2 p)}{p^2(\cosh p - \cos p)^2} + \frac{(\sinh p + \sin p)}{p(\cosh p - \cos p)} - \frac{2 \sinh p \sin p}{(\cosh p - \cos p)^2}, \quad (9.26)$$

where  $p = 2R/\delta$ ,  $\delta = \sqrt{2/\mu_0\omega_e\sigma_{ac}}$ , and  $\mu_0$  is the magnetic permeability for a vacuum. In case of the formation of skin-layer on the flat plate with a thickness of  $2d$  the above coefficients can be determined from relations [114]:

$$A = \frac{\sinh p + \sin p}{2p(\cosh p + \cos p)} + \frac{1 + \cosh p \cos p}{(\cosh p + \cos p)^2}, \quad (9.27)$$

$$D = \frac{\sinh p - \sin p}{2p(\cosh p + \cos p)} + \frac{\sinh p \sin p}{(\cosh p + \cos p)^2}, \quad (9.28)$$

where  $p = 2d/\delta$ . The analysis of multifrequency EPR spectra with Dysonian term allows for the direct determination of the ac conductivity of conducting domains embedded into polymer matrix [76–78].

### 9.2.5 ELECTRON RELAXATION AND SPIN DYNAMICS

As the magnetic term  $B_1$  of the steady-state microwave field increases, the line width  $\Delta B_{pp}$  of a LEPR spectrum broadens and its intensity  $I_L$  first increases linearly, plateaus starting from some  $B_1$  value, and then decreases. This occurs due to manifestation of the microwave steady-state saturation effect in the LEPR spectrum of the composite. Polaron and fullerene anion radicals are noninteracting and, therefore, independent of one another. This allows us to use such effects for separate estimation of their spin–lattice  $T_1$  and spin–spin  $T_2$  relaxation times from relations [115]

$$\Delta B_{pp} = \Delta B_{pp}^{(0)} \sqrt{1 + \gamma_e^2 B_1^2 T_1 T_2} \quad (9.29)$$

and

$$I_L = I_L^{(0)} B_1 (1 + \gamma_e^2 B_1^2 T_1 T_2)^{-3/2}, \quad (9.30)$$

where  $I_L^{(0)}$  is intensity of nonsaturated spectrum and  $T_2 = 2/\sqrt{3}\gamma_e\Delta B_{pp}^{(0)}$ . Normally, the inflection point characteristic for polarons' saturation curve is distinct from that obtained for fullerene anion radicals. This is evidence of different relaxation parameters of these PC and also confirms their mutual independence.

The mechanism and the rate of electron relaxation depend on the structure and conformation of an initial and modified polymer:fullerene composites in which radical pairs are photoinduced in differently ordered domains with respective

band gaps. Various spin-assisted dynamic processes occur in polymer:fullerene composites, for example, polaron diffusion along and between polymer chains with coefficients  $D_{1D}$  and  $D_{3D}$ , respectively, and librative rotational motion of fullerene anion radicals near their own main molecular axis with coefficient  $D_{rot}$ . These processes induce additional magnetic fields in the whereabouts of electron and nuclear spins which, in turn, accelerates relaxation of both spin ensembles. Relaxation of the whole spin reservoir in organic conjugated polymers is defined mainly by dipole–dipole interaction between electron spins [116], so then these coefficients can be determined from the following equations [117]:

$$T_1^{-1}(\omega_e) = \langle \omega^2 \rangle [2J(\omega_e) + 8J(2\omega_e)], \quad (9.31)$$

$$T_2^{-1}(\omega_e) = \langle \omega^2 \rangle [3J(0) + 5J(\omega_e) + 2J(2\omega_e)], \quad (9.32)$$

where  $\langle \omega^2 \rangle = 1/10\gamma_e^4 \hbar^2 S(S+1)n \sum_{ij}$  is the constant of dipole–dipole interaction for powder,  $n$  is a number of polarons per each monomer,  $\sum_{ij}$  is the lattice sum for a powder-like sample,  $J(\omega_e) = (2D_{1D}^l \omega_e)^{-1/2}$  (at  $D_{1D}^l \gg \omega_e \gg D_{3D}$ ),  $J(0) = (2D_{1D}^l D_{3D})^{-1/2}$  (at  $D_{3D} \gg \omega_e$ ) are the spectral density functions for polaron longitudinal diffusion, and  $J(\omega_e) = \tau_c / (1 + \tau_c^2 \omega_e^2)$  is the spectral density function for fullerene rotational libration with correlation time  $\tau_c$ ,  $D_{1D}^l = 4D_{1D}/L^2$ , and  $L$  is a factor of spin delocalization over a polaron equal approximately to five monomer units in P3AT [55,90].

### 9.2.6 MECHANISM OF CHARGE TRANSPORT IN POLYMERS

To account for the LEPR mobility data obtained, different theoretical models can be used. Polaron dynamics in some nanomodified polymer composites can be characterized by strong temperature dependence. This can probably be due to the scattering of polarons on the lattice phonons of crystalline domains embedded into an amorphous matrix. According to the model proposed for charge dynamics in crystalline domains of doped conjugated polymers, such scattering should affect polaron intrachain diffusion with an appropriate coefficient [118,119]:

$$D_{3D}(T) = \frac{\pi^2 M t_0^2 k_B^2 T^2}{h^3 \alpha_{eph}^2} \cdot \left[ \sinh\left(\frac{E_{ph}}{k_B T}\right) - 1 \right] = D_{3D}^{(0)} T^2 \cdot \left[ \sinh\left(\frac{E_{ph}}{k_B T}\right) - 1 \right] \quad (9.33)$$

where  $M$  is the mass of a polymer unit,  $t_0$  is the transfer integral equal for  $\pi$ -electron to  $\sim 2.5-3$  eV,  $\alpha_{eph}$  is a constant of electron–phonon interaction, and  $E_{ph}$  is phonon energy.

Spin dynamics in a less-ordered polymer matrix of composites can be realized in the frames of the Elliot model based on spin hopping over energetic barrier  $E_b$  [120]. This model predicts the following temperature dependencies for diffusion coefficients of a charge carrier at direct and alternating currents:

$$D_{dc}(T) = D_{dc}^0 T \exp\left(\frac{E_b}{k_B T}\right) \quad (9.34)$$

$$D_{ac}(\omega, T) = D_{ac}^0 T^2 \omega_c^s \exp\left(\frac{E_b}{k_B T}\right) \quad (9.35)$$

where the exponent  $s = 1 - \alpha k_B T / E_b$  reflects system dimensionality and  $\alpha$  is a constant. Comparison of spin dynamic parameters obtained at direct current and at different spin precession frequencies  $\omega_c$  allows one to determine more precise details of charge transfer in organic polymer systems [76–78].

If spin traps are initiated in a polymer matrix, the dynamics of spin charge carriers can be explained in terms of the Hoesterey-Letson formalism modified for amorphous low-dimensional systems containing spin traps with concentration  $n_t$  and depth  $E_t$  [121]. Combining Eqns (9.18) and (9.25) in Ref. [121] and using from the modified Einstein relation of the trap-controlled interchain mobility  $\mu_t$  and diffusion coefficient  $D_t$  of a charge carrier  $\mu_t = e D_t d^2 / k_B T$ , one can obtain in the case of low trap concentration limit:

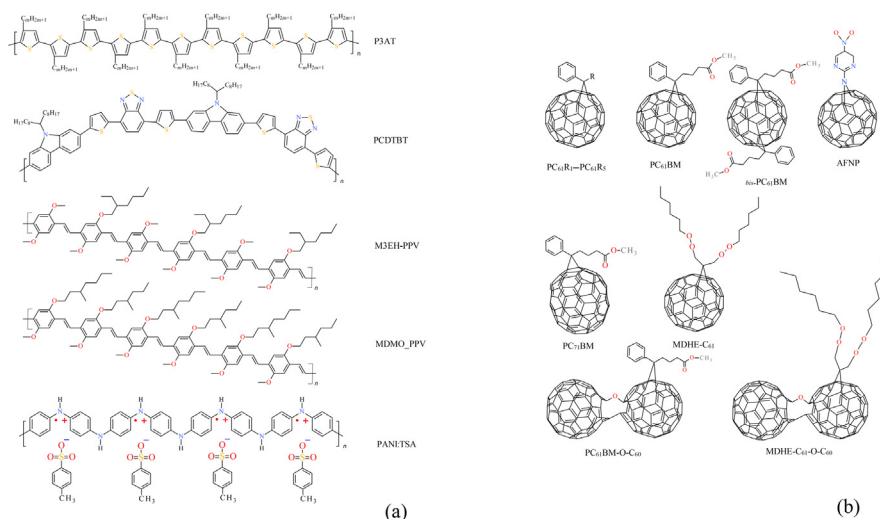
$$D_t(T) = \nu_0 \left(\frac{R_{ij}}{d}\right)^2 \exp\left(-\frac{2R_{ij}}{r}\right) \exp\left(\frac{E_t}{2k_B T_{cr}}\right) \exp\left[-\frac{E_t}{2k_B T} \left(\frac{\sigma_0}{k_B T}\right)^2\right] \quad (9.36)$$

where  $\nu_0$  is hopping attempt frequency,  $d$  is the lattice constant,  $T_{cr} = E_t / 2k_B \ln(n_t)$  is critical temperature at which the transition from trap-controlled to trap-to-trap hopping transport regimes occurs, and  $\sigma_0$  is the width of intrinsic energetic distributions of hopping states in the absence of traps.

### 9.3 MAGNETIC RESONANCE PARAMETERS OF SPIN CHARGE CARRIERS IN POLYMER:FULLERENE COMPOSITES

Once excitons are converted into polarons and ion radicals in the polymer:fullerene BHI, respective positive and negative charge carriers appear in the system. Both charge carriers possess spin, so then they are characterized by different magnetic resonance parameters. In addition, the energies of reorientation transition of these spins are affected by their local environment. Thus, EPR spectra can yield information about the type, number, state, etc., of spin charge carriers and also about their local environment in a sample.

Figure 9.2a shows schematic structures of the regioregular P3AT with hexyl ( $m = 6$ , P3HT), oktyl ( $m = 8$ , P3OT), dodecyl ( $m = 12$ , P3DDT) side groups, PCDTBT, poly[2,5-dimethoxy-1,4-phenylene-1,2-ethynylene-2-methoxy-5-(2-ethylhexyloxy)-(1,4-phenylene-1,2-ethynylene)] (M3EH – PPV), poly[2-methoxy-5-(3',7'-dimethyloctyloxy)-1,4-phenylenevinylene] (MDMO-PPV), and the emeraldine salt form of polyaniline (PANI-ES) heavily doped by paratoluenesulfonic acid (PANI:TSA) used as polymer matrices, whereas the [6,6]-phenyl-C<sub>61</sub>-R [PC<sub>61</sub>R where R ≡ –(CH<sub>2</sub>)<sub>2</sub>C(O)OCH<sub>2</sub>Ph (PC<sub>61</sub>R<sub>1</sub>), –(CH<sub>2</sub>)<sub>2</sub>C(O)O–CH<sub>3</sub> (PC<sub>61</sub>R<sub>2</sub>), –(CH<sub>2</sub>)<sub>2</sub>C(O)OCH<sub>2</sub>CH<sub>3</sub> (PC<sub>61</sub>R<sub>3</sub>), –(CH<sub>2</sub>)<sub>3</sub>C(O)OCH<sub>3</sub> (PC<sub>61</sub>R<sub>4</sub>), –(CH<sub>2</sub>)<sub>2</sub>C(O)O(CH<sub>2</sub>)<sub>2</sub>CH<sub>3</sub> (PC<sub>61</sub>R<sub>5</sub>)], PC<sub>61</sub>BM, *bis*-PC<sub>62</sub>BM, 2-(azahomo[60]

**FIGURE 9.2**

Schematic structures of the regioregular P3AT with hexyl ( $m = 6$ , P3HT), oktyl ( $m = 8$ , P3OT), dodecyl ( $m = 12$ , P3DDT) side groups, PCDTBT, M3EH – PPV, MDMO-PPV, and PANI:TSA (a) as well as fullerene derivatives  $mF_{1-5}$ ,  $PC_{61}BM$ , *bis*- $PC_{62}BM$ , AFNP,  $PC_{71}BM$ ,  $PC_{61}BM-O-C_{60}$ , MDHE- $C_{61}$ , and MDHE- $C_{61}-O-C_{60}$  (b) used in polymer composites.

fullereno)-5-nitropyrimidine (AFNP),  $PC_{71}BM$ ,  $PC_{61}BM-O-C_{60}$ , [6,6]-malonedihexyle-fullerene ester (MDHE- $C_{61}$ ), and MDHE- $C_{61}-O-C_{60}$ -fullerene derivatives embedded as electron acceptors into polymer composites are shown schematically in Fig. 9.2b. These materials and their composites were studied by multifrequency, X-, K-, W-, and D-bands EPR spectroscopy when spin precession frequency  $\omega_c/2\pi$  and resonant magnetic field  $B_0$  lie near 9.7 GHz and 3.4 kG, 24 GHz and 8.6 kG, 85 GHz and 33 kG, 140 GHz and 49 kG, respectively.

### 9.3.1 LINE SHAPE AND G-FACTOR

No EPR signal has been found in pure fullerene derivatives at 3-cm wave band in whole temperature range. Some initial P3AT samples, for example, P3HT demonstrates at 3-cm wave band EPR Lorentzian exchange-narrowed nearly symmetrical line with effective  $g_{\text{eff}} = 2.0029$  (Fig. 9.3). As in the cases of other regioregular P3AT with longer side chains, this fact was interpreted as stabilization in the polymer of mobile polarons during synthesis and/or its treating by oxygen of air [40,41]. As the sample is modified by methanofullerenes  $mF_1-mF_5$  two additional lateral lines appear in its spectrum (Fig. 9.3). This fact evidences the localization of part of polarons probably at cross-bonds and/or at ends of polymer chains during such a modification. The intensity of these components decreases in the series

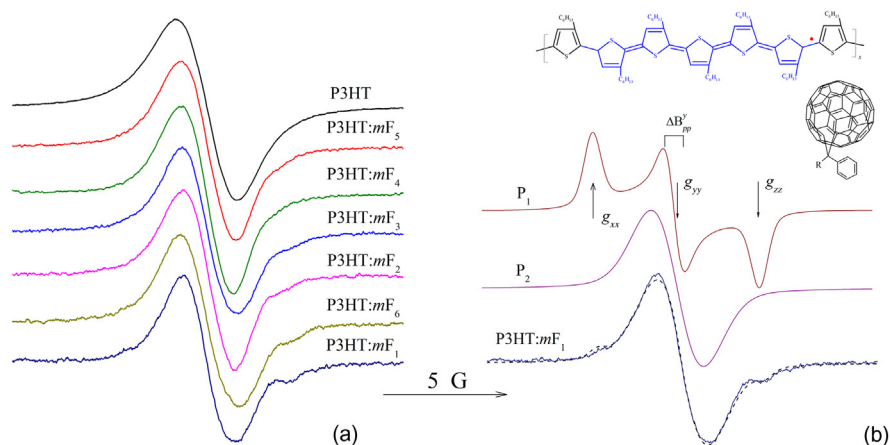


**FIGURE 9.3**

(a) Room temperature EPR spectra of the initial P3HT and P3HT: $mF_1$ –P3HT: $mF_6$  composites. (b) Experimental EPR spectrum of the sample P3HT: $mF_1$  (solid line) compared with sum theoretical spectrum (dashed line) of localized  $P_1^{+\bullet}$  and mobile  $P_2^{+\bullet}$  polarons with relative concentration ratio  $[P_1^{+\bullet}]/[P_2^{+\bullet}] = 0.089$  and  $f_1^0/f_2^0 = 0.3$  and 0.2, respectively. The formation of polaron in P3HT is shown schematically. The magnetic resonance parameters measured are shown as well.

P3HT: $mF_1$  → P3HT: $mF_6$  → P3HT: $mF_2$  → P3HT: $mF_3$  → P3HT: $mF_4$  → P3HT: $mF_5$ . A high-field/frequency EPR study shown [122–124] that the interaction of an unpaired electron of  $P^{+\bullet}$  with sulfur heteroatoms involving into the P3AT backbone leads to anisotropy of its magnetic resonance parameters.

Computer simulation and deconvolution of EPR spectra of P3HT: $mF_i$  showed that two types of PC are stabilized in the samples, namely, polarons localized at cross-bonds and/or on the short  $\pi$ -conjugated polymer chains  $P_1^{+\bullet}$  with  $g_{xx} = 2.0049$ ,  $g_{yy} = 2.0030$ ,  $g_{zz} = 2.0010$ , and line width  $\Delta B_{pp} = 0.66$  G, and a polaron moving along the main  $\pi$ -conjugated polymer chain  $P_2^{+\bullet}$  with  $g_{xx} = g_{yy} = g_{zz} = 2.0029$ , and  $\Delta B_{pp} = 2.15$  G. The principal  $x$ -axis is chosen parallel to the longest molecular  $c$ -axis, the  $y$ -axis lies in the thiophene rings plane, and the  $z$ -axis is perpendicular to the  $x$ - and  $y$ -axes. The best fit of the  $P_1^{+\bullet}$  signal was achieved using a nearly Gaussian line shape, which means that the transitions are inhomogeneously broadened mainly due to unresolved hyperfine interaction of unpaired spin with protons. Simulated spectra of  $P_1^{+\bullet}$  and  $P_2^{+\bullet}$  are also shown in Fig. 9.3. The isotropic  $g$ -factor of polarons  $P_1^{+\bullet}$  lies near to that of the  $P_2^{+\bullet}$  ones. This fact supports the supposition made previously about the nature of PC. Spin concentration ratio  $[P_1^{+\bullet}]/[P_2^{+\bullet}]$  lies near 0.089 for P3HT: $mF_1$  and decreases for other compounds (see Fig. 9.3a). Note that the existence of such polarons with different relaxation and dynamics was also determined in other conjugated polymers [77] and polymer composites [91].

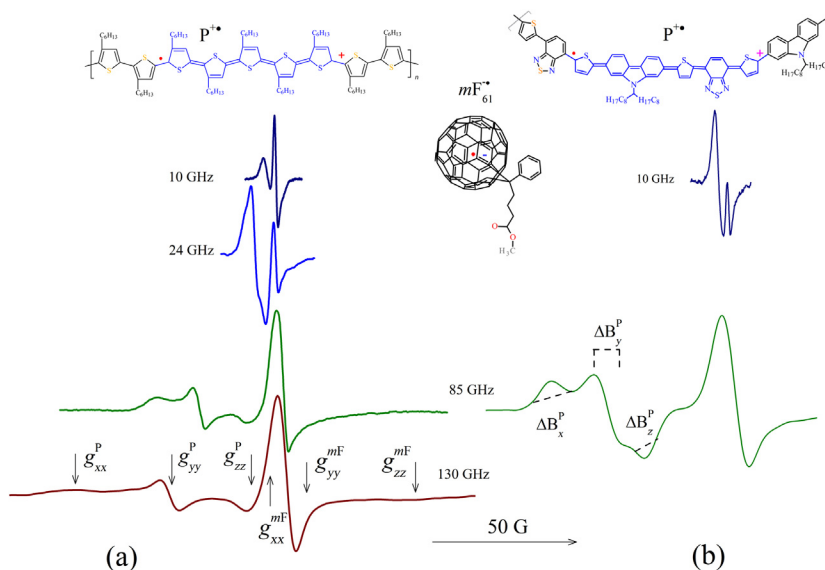


**FIGURE 9.4**

LEPR spectra of the P3HT:PC<sub>61</sub>BM (a) and PCDTBT:PC<sub>61</sub>BM (b) composites irradiated by laser registered at different spin precession frequencies  $\omega_e$  and low temperature. The appearance of a polaron P<sup>•+</sup> on polymer chain and methanofullerene ion radical  $mF_{61}^{-\bullet}$  embedded between polymer chains are shown. The main values of **g**-tensors of these PC are shown as well.

As a polymer with embedded fullerene derivative is irradiated at  $T \leq 200$  K by visible light directly in the cavity of the EPR spectrometer, in LEPR spectra two overlapping contributions appear, whose shape, relative intensity, and position depend on spin precession frequencies  $\omega_e$ . Figure 9.4 shows as an example the LEPR spectra of the P3HT:PC<sub>61</sub>BM and PCDTBT:PC<sub>61</sub>BM composites background irradiated by laser light at different  $\omega_e$  values [42,43,68,127,128]. Subsequent LEPR measurement cycles of heating up to the room temperature, cooling down to  $T \leq 200$  K, illumination with light, switching light off and heating up again yield identical data. The spectra registered in low and high fields can be attributed to positively charged polarons P<sup>•+</sup> and negatively charged methanofullerene  $mF_{61}^{-\bullet}$  photoinduced in BHJ of the composites, respectively. These PC are characterized by anisotropic magnetic resonance parameters more evidently manifesting at higher  $\omega_e$  as it follows from Eqn (9.1). These parameters measured at different  $\omega_e$  are also summarized in Table 9.1. The **g**-factor of the fullerene ion radicals lies near that of other fullerene anion radicals [133]. As in case of the initial C<sub>60</sub> molecule [134], the deviation of the C<sub>61</sub><sup>•-</sup> **g**-factor from that of free electron,  $g_e = 2.00232$ , is due to the fact that the orbital angular momentum is not completely quenched. Due to the dynamical Jahn-Teller effect

**Table 9.1** The Main Magnetic Resonance Parameters Obtained for Polymer Composites by the Light-Induced EPR Method at Different Wave Bands and Low (20–80 K) Temperatures When All Spin Motions Are Considered Frozen

Sample	$g_{xx}$	$g_{yy}$	$g_{zz}$	$g_{iso}$	$\Delta B_{pp}^x, G$	$\Delta B_{pp}^y, G$	$\Delta B_{pp}^z, G$	$\Delta B_{pp}^{iso}, G$	Wave band <sup>a</sup>	References
P3HT	2.0049	2.0030	2.0010	2.0030	6.6	6.6	6.6	6.6	X	[40]
P3HT	2.0030	2.0021	2.0011	2.0021	1.6	1.5	1.6	1.6	K	[125]
P3HT	2.0028	2.0019	2.0009	2.0019	10.7	5.3	6.4	7.5	W	[68]
P3HT	2.00380	2.00230	2.00110	2.00240					D	[126]
P3OT	2.00409	2.00332	2.00232	2.00324	8.2	7.8	8.8	8.3	D	[124]
P3DDT	2.0026	2.0017	2.0006	2.0016	2.5	1.4	1.5	1.8	X	[42]
PCDTBT	2.0031	2.0026	2.0010	2.0022	—	—	—	1.4	X	[127]
PCDTBT	2.00320	2.00240	2.00180	2.00247	—	—	—	—	D	[128]
M3EH-PPV	2.0034	2.0025	2.0024	2.0028	2.2	2.7	2.8	2.5	K	[125]
M3EH – PPV	2.00377	2.00275	2.00220	2.00291	4.0	4.0	4.0	4.0	W	[43]
(MDMO-PPV)	2.00341	2.00341	2.00241	2.00308	8.0	5.0	5.0	6.0	W	[129]
(MDMO-PPV)	2.0033	2.0022	2.0022	2.0026	9.6	8.2	8.2	8.7	W	[68]
<i>bis</i> -PC <sub>62</sub> BM	—	—	—	2.0007	—	—	—	1.3	X	[130]
PC <sub>61</sub> BM	2.0005	2.0004	1.9988	1.9999	1.2	1.1	2.9	1.7	K	[125]
PC <sub>61</sub> BM	2.00031	2.00011	1.99821	1.99954	2.3	1.3	8.8	4.1	W	[129]
PC <sub>61</sub> BM	2.00021	2.00000	1.99860	1.99960	5.0	4.0	17	8.7	W	[43]
PC <sub>61</sub> BM	2.00058	2.00045	1.99845	1.99983	—	—	—	—	D	[126]
PC <sub>71</sub> BM	2.0062	2.0031	2.0027	2.0040	—	—	—	1.4	X	[131]
PC <sub>71</sub> BM	2.0056	2.0023	2.0022	2.0034	—	—	—	—	X	[132]
PC <sub>71</sub> BM	2.00592	2.00277	2.00211	2.00360	—	—	—	—	D	[126]
PC <sub>61</sub> BM-O-C <sub>60</sub>	2.0004	2.0002	1.9984	1.9997	3.6	3.6	4.4	3.9	K	[125]
PC <sub>61</sub> BM-O-C <sub>60</sub>	2.00045	2.00004	1.99860	1.99970	5.7	5.8	16	9.2	W	[43]
MDHE-C <sub>61</sub>	2.00016	2.00000	1.99940	1.99985	2.1	1.9	10	4.7	W	[43]
MDHE-C <sub>61</sub> -O-C <sub>60</sub>	2.00050	2.00023	1.99910	1.99994	2.1	23	9.0	11.4	W	[43]

<sup>a</sup>The spin precession frequency  $\omega_d/2\pi$  and resonant magnetic field  $B_0$  at the X, K, W, and D wave bands are 9.7 GHz and 3.4 kG, 24 GHz and 8.6 kG, 85 GHz and 33 kG, and 140 GHz and 49 kG, respectively.

accompanying the structural molecular deformation, the isotropic nature of the icosahedral  $C_{60}$  molecule is distorted after formation of the  $F_{61}^{\bullet-}$  anion radical, resulting in an axial or even lower symmetry [135]. This is also realized in case of the  $F_{61}^{\bullet-}$  anion radical [129], where the high symmetry of the molecule is already decreased by the bond to the phenyl side chain prior to electron accepting. Asymmetrical distribution of spin density in polaron and fullerene anion radical leads also to tensor character of their line widths [123,129]. This should be taken into account in order to calculate more precisely an effective LEPR spectrum of the P3AT:PC<sub>61</sub>BM system.

If one includes Coulomb interactions, this should affect the activation energy for either defrosting or thermally assisted tunneling by an amount  $U_c = e^2/4\pi\epsilon\epsilon_0r$ , where  $e$  is elemental charge,  $\epsilon$  is a dielectric constant, and  $r$  is charge pair separation. Assuming, for example,  $\epsilon = 3.4$  for P3HT [136], minimum separation of charge carriers is equal to the radius of  $\pi$  electrons on the C atoms  $a$  which are two times longer than the Bohr radius, that is, 0.106 nm,  $r$  equal to interchain separation, 0.38 nm [137]. One obtains the decrease in  $U_c$  from  $\sim 0.4$  eV down to 0.02 eV during dissociation of an initial radical pair. Therefore, both the photoinduced polaron and the anion radical indeed should be considered noninteracting, which prolongs their life.

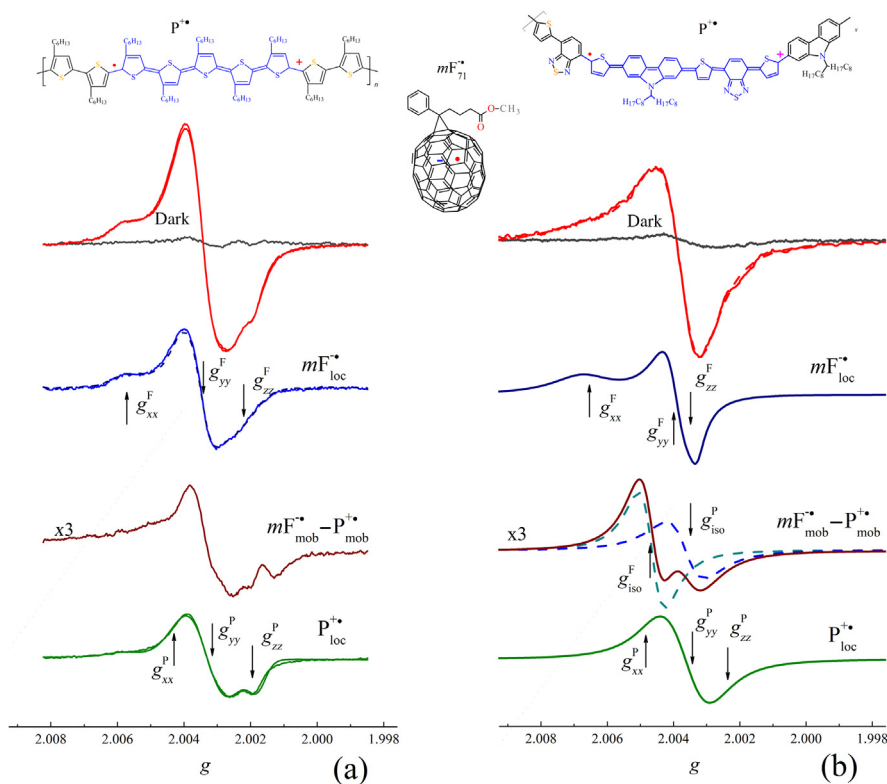
Electronic properties of plastic solar cell can also be improved, for example, by the increase of its light absorption coefficient. Photoluminescence and atomic force microscopy studies showed [138–140] that wider and stronger light absorption is reached in polymer:PC<sub>71</sub>BM composites. Since optical absorption is closely related to crystallinity of such systems, it was inferred that, for example, a P3HT:PC<sub>71</sub>BM composite is more crystalline than a P3HT:PC<sub>61</sub>BM one and, therefore, demonstrates higher (by  $\sim 33\%$ ) current density and power-conversion efficiency. Thus, the understanding of the elementary processes of exciton initiation, charge separation, stabilization, and recombination should be as a prerequisite for improving the efficiency of such photovoltaic systems. Indeed, the formation of  $C_{70}$  anion radicals initiates a subgap photoinduced absorption band at 0.92 eV [141], hidden in the spectra of polymer:PC<sub>71</sub>BM composites, which allows more exact studies of charge-separated states in such systems. On the other hand, comparative multifrequency EPR investigation of various polymer:fullerene composites have demonstrated [126,128] significant difference in deconvoluted LEPR spectra of both charge carriers. Indeed, the isotropic  $g$ -factor of the  $mF_{61}^{\bullet-}$  and  $mF_{71}^{\bullet-}$  methanofullerene anion radicals was obtained as equal to 1.99983 and 2.00360, respectively. Taking into account that isotropic (effective)  $g$ -factor,  $g_{\text{iso}} = (g_{xx} + g_{yy} + g_{zz})/3$  of polarons lies near 2.003, this should mean the decrease in spectral resolution at the PC<sub>61</sub>BM replacing by PC<sub>71</sub>BM counter ions. So, the effective  $g$ -factor of different  $F_{61}^{\bullet-}$  anion radicals is normally less than the  $g$ -factor of free electrons [42,126,129,130,142], and the  $g_{\text{iso}}$  value of the  $mF_{71}^{\bullet-}$  anion radical exceeds  $g_e$  [126,132]. This is in agreement with the study of respective anion radicals in crystalline ( $g_{\text{iso}} = 2.0047$ ) [143,144] and dissolved [144–147]  $C_{70}$ . Such an effect is supposed [148] to appear due to different Jahn-Teller dynamics

of C<sub>60</sub> and C<sub>70</sub> molecules, which might contribute to different signs of the  $g$ -value shifts. According to the classical Stone theory of  $g$ -factors [149], negative deviation of the  $g$ -factor from  $g_e$  is due to spin – orbit coupling with empty  $p$ - or  $d$ -orbitals, while spin-orbit coupling with occupied orbitals leads to positive  $g$ -factor deviation. The latter case is typical for most organic radicals. Thus, a difference in  $g$ -values of  $mF_{61}^{\bullet-}$  and  $mF_{71}^{\bullet-}$  anion radicals indicates the different electronic structure of their molecular orbitals. Positive shift of the  $g$ -factors in solution for  $mF_{61}^{\bullet-}$  relative  $mF_{71}^{\bullet-}$  can be explained in the framework of the static Jahn-Teller effect [148,150]. Jahn-Teller dynamics in the solid phase seems to be quite different for C<sub>60</sub> and C<sub>70</sub> globes, which might contribute to different signs of their  $g$ -value shifts [148]. However, there is not yet a unified theory that can explain  $g$ -tensors of both  $mF_{61}^{\bullet-}$  and  $mF_{71}^{\bullet-}$  radicals.

Nevertheless, the contribution of the  $mF_{71}^{\bullet-}$  charge carriers can be obtained by using the “light on-light off” method accompanied with the deconvolution of sum LEPR spectrum of both charge carriers into two individual spectra which can then be compared with those obtained at millimeter wave band EPR. Figure 9.5 shows X-band LEPR spectra of the P3HT:PC<sub>71</sub>BM and PCDTBT:PC<sub>71</sub>BM composites irradiated at  $T = 77$  K [127,151]. Assuming that each optical photon initiates a positively and a negatively charged carriers, the  $mF_{71}^{\bullet-}$  spectrum may simply be obtained by the extraction of the  $P^{\bullet+}$  spectrum from the initial LEPR one shown in Fig. 9.5.

In order to analyze all magnetic resonance parameters in detail as a function of different effects, sum LEPR spectra were deconvoluted by using numerical simulations as it was done in the case of other polymer:fullerene systems [42,126,131,142]. Such an algorithm in combination with the “light on-light off” method allowed for determining appropriate parameters of both charge carriers photoinduced in the P3HT:PC<sub>71</sub>BM composite (see Table 9.1). These values lie near those determined at higher spectral resolution [68,126]. This was used also for separate determination of all main magnetic resonance parameters of charge carriers stabilized and photoinitiated in other analogous BHJ at wide regions of the temperature, photon energy, and registration frequency. The best fit of such LEPR spectra was achieved using a convolution of Gaussian and Lorentzian line shapes, which means that electron excitation leads to inhomogeneous and homogeneous line broadening, respectively, due to unresolved hyperfine interaction of unpaired spin with neighboring protons and also to its different mobility.

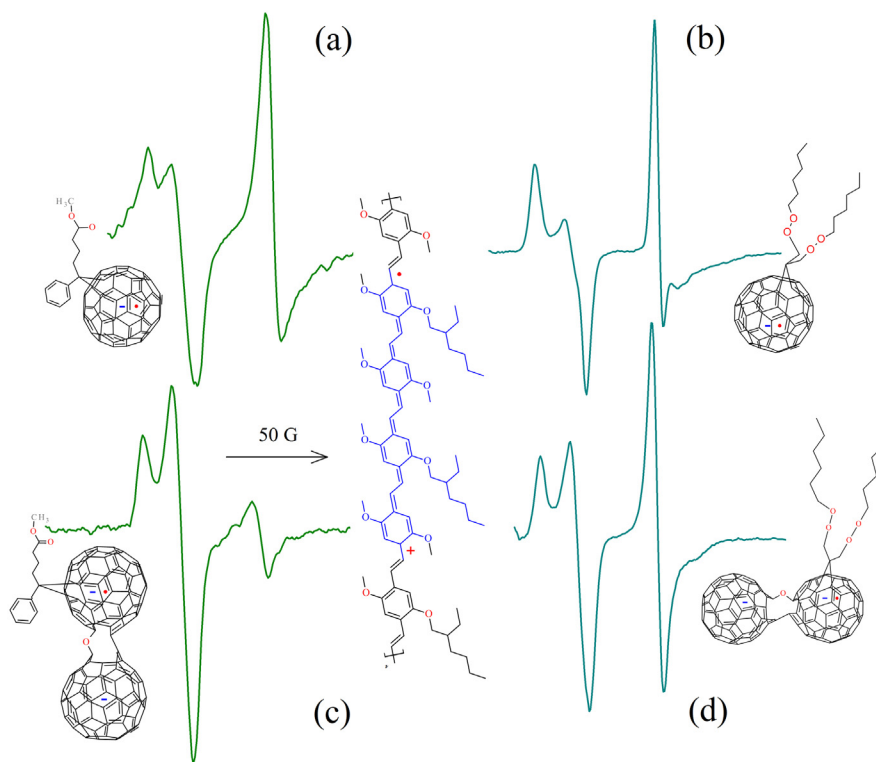
It was demonstrated [76–78] that the main parameters of spin charge carriers stabilized in conjugated polymers are governed by their structure as well as by different adducts embedded into the polymer matrix [91,113,152]. A similar effect should be probably reached by varying the number of electrons trapped by each acceptor of a polymer:fullerene composite. In order to test this assumption, the charge carriers photoinitiated in some BHJ formed by the M3EH-PPV macromolecules with different mono- and di-C<sub>60</sub>-fullerene derivatives were studied at W-band EPR [43]. Figure 9.6 shows W-band LEPR spectra of the M3EH-PPV:PC<sub>61</sub>BM, M3EH-PPV:PC<sub>61</sub>BM-O-C<sub>60</sub>, M3EH-PPV:MDHE-C<sub>61</sub>, and



**FIGURE 9.5**

X-band LEPR spectra of the P3HT:PC<sub>71</sub>BM (a) and PCDTBT:PC<sub>71</sub>BM (b) composites and their contributions due to mobile quasipairs  $mF_{71}^{-\bullet} - P_{\text{mob}}^{+\bullet}$  and localized polarons  $P_{\text{loc}}^{+\bullet}$  and methanofullerene anion radicals  $mF_{71}^{-\bullet}$  background photoinduced by photons with  $h\nu_{\text{ph}} = 2.10$  eV at  $T = 77$  K. Dashed lines show the spectra calculated using the terms of appropriate terms of their  $g$ -tensor, as presented in Table 9.1. Photoinitiation of a polaron on a polymer chain accompanied by electron transfer to a methanofullerene globe is schematically shown. The positions of photoinduced radicals and terms of their  $g$ -tensors are shown as well.

M3EH-PPV:MDHE-C<sub>61</sub>-O-C<sub>60</sub> composites. The main magnetic resonance parameters determined for both charge carriers in these systems are summarized in Table 9.1. It was shown that the increase of a number of elemental negative charge on fullerene molecules leads to the appearance of dispersion term in LEPR spectra of respective ion radicals (see Fig. 9.6). This effect was interpreted as the formation of highly ordered fullerene domains (conductive crystallites) in the amorphous phase of M3EH-PPV matrix. Interaction of conduction electrons with microwave field originates the appearance on the surface on the sample of skin

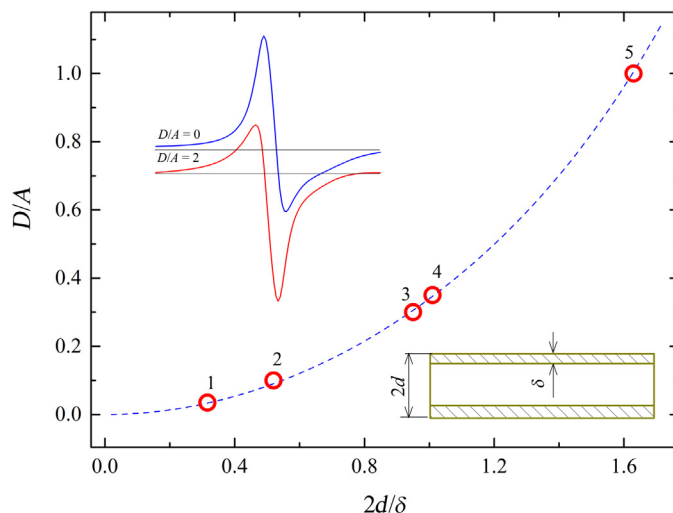


**FIGURE 9.6**

W-band LEPR spectra of charge carriers photoinitiated in BHJ formed by M3EH-PPV macromolecules with PC<sub>61</sub>BM (a), MDHE-C<sub>61</sub> (b), PC<sub>61</sub>BM-O-C<sub>60</sub> (c), and MDHE-C<sub>61</sub>-O-C<sub>60</sub> (d) irradiated by laser photons with the energy of 2.3 eV (wavelength  $\lambda_{\text{ph}} = 530 \text{ nm}$ ) at low temperature when molecular motion is frozen. The polaron formed on the polymer after transfer a charge from its chain to a fullerene molecule is shown schematically.

depth  $\delta$  and, therefore, Dysonian contribution in its LEPR spectrum described previously. Figure 9.7 shows that the data obtained for M3EH-PPV modified with both di-fullerene derivatives are well fitted by the dependence calculated from Eqns (9.24), (9.27), and (9.28). The conclusion made above is also confirmed by scanning electron microscopy [43]. This allowed a more complete investigation of magnetic, relaxation, and dynamic parameters of spin charge carriers depending on different properties of polymer composites and their ingredients. The skin-layer depth  $\delta$  was estimated for di-C<sub>62</sub>-fullerene to be near  $10 \mu\text{m}$  at  $\omega_c/2\pi = 95 \text{ GHz}$ . This allows the evaluation of the ac conductivity of the di-C<sub>60</sub>-fullerene domains.

Main resonance parameters of both charge carriers are governed by the energy of excitation photons  $h\nu_{\text{ph}}$ . Figure 9.8 demonstrates how this parameter affects

**FIGURE 9.7**

Dependence  $D/A(2d/\delta)$  calculated from Eqns (9.24), (9.27), and (9.28) (solid line) and obtained experimentally for the M3EH-PPV:PC<sub>61</sub>BM-O-C<sub>60</sub> (open points 2, 3, and 5) and M3EH-PPV:MDHE-C<sub>61</sub>-O-C<sub>60</sub> (open points 1 and 4) composites at their different plane thickness  $2d$  and spin precession frequencies  $\omega_e \sim \delta^{-2}$ . The inserts show X-band LEPR spectra and parameters of the samples.

the LEPR spectrum of the P3DDT:PC<sub>61</sub>BM composite at  $T \leq 200$  K. As in the case of other polymer:fullerene composites, sum spectra were attributed to radical quasipairs of polarons  $P^{+\bullet}$  with  $g_{\text{iso}} = 2.0023$ , and negatively charged anion radicals  $mF_{61}^{-\bullet}$  with  $g_{\text{iso}} = 2.0001$  [42,59,153–159]. The sum spectra calculated with the fitting magnetic parameters presented in Table 9.1 are also shown in Fig. 9.8.

In order to analyze the conjoint effect of the structure of fullerene derivative and the energy of initiating photons on electronic properties of a polymer:fullerene composite, P3HT:PC<sub>61</sub>BM and P3HT:*bis*-PC<sub>62</sub>BM composites were studied at X-band LEPR [130,142,160]. Their detached ingredients are characterized by the absence of both “dark” and photoinduced LEPR signals over the entire temperature range (77–340 K). As they form polymer:fullerene BHJ and irradiated by visible light directly in a cavity of the EPR spectrometer, two overlapping LEPR lines appear at  $T \leq 200$  K (Fig. 9.9). As in case of other polymer:fullerene systems, low- and high-field lines photoinduced in the P3HT:PC<sub>61</sub>BM composite consist of two Lorentzian contributions of mobile polarons,  $P_{\text{mob}}^{+\bullet}$ , and methanofullerene anion radicals,  $mF_{\text{mob}}^{-\bullet}$  (shown in Fig. 9.9 as radical quasipairs 2,  $P_{\text{mob}}^{+\bullet} - mF_{\text{mob}}^{-\bullet}$ ) as well as two Gaussian contributions of localized polarons,  $P_{\text{loc}}^{+\bullet}$ , and methanofullerene anion radicals,  $mF_{\text{loc}}^{-\bullet}$ , pinned in polymer traps. Analogous localized polarons  $P_{\text{loc}}^{+\bullet}$  with  $g_{\text{iso}}^{\text{P}} = 2.0023$  and quasipairs with  $g_{\text{iso}}^{\text{F}} = 2.0007$  also contribute to the LEPR spectra of the P3HT:*bis*-PC<sub>62</sub>BM composite, however, the

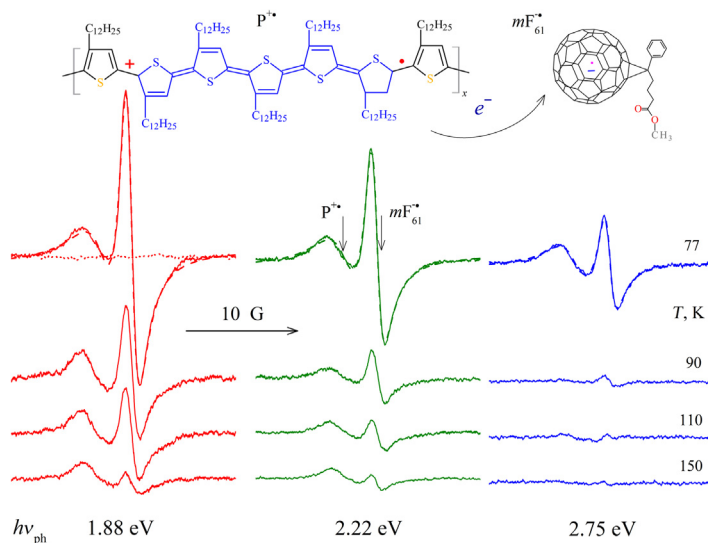


**FIGURE 9.8**

X-band LEPR spectra of the radical quasipairs photoinduced in the P3DDT:PC<sub>61</sub>BM system shown in the above insert by steady-state laser irradiation with different photon energy  $h\nu_{\text{ph}}$  and as function of temperature. By the left dotted line is shown the “dark” spectrum obtained before laser irradiation. Dashed lines show sum LEPR spectra calculated using magnetic resonance parameters presented in [Table 9.1](#).

contribution of pinned *bis*-methanofullerene radicals,  $bmF_{\text{loc}}^{+\bullet}$  is absent ([Fig. 9.9](#)). These values differ slightly from those obtained for P3HT:PC<sub>61</sub>BM, but are close to appropriate parameters determined for polarons stabilized in other fullerene-modified conjugated polymers [[91,154,155,161,162](#)] and fullerene anion radicals [[133](#)]. The absence of localized anion radicals in the P3HT:*bis*-PC<sub>62</sub>BM composite implies that the number of deep traps able to capture is sufficiently lower than that in the P3HT:PC<sub>61</sub>BM one due to the better order of the former, however, their depth depends on the energy of photons.

PCDTBT, in contrast with P3AT, is characterized by the “dark” EPR spectrum typical for localized PC which changed slightly under its irradiation by visible light over a wide temperature range. [Figure 9.10](#) shows LEPR spectra of charge carriers stabilized and reversibly photoinitiated in the PCDTBT:PC<sub>61</sub>BM sample under its background irradiation in a microwave cavity of the EPR spectrometer by light with a photon energy of 1.32 – 2.73 eV in comparison with its IR–vis absorption spectrum [[127](#)]. In the latter, the low energy, broad, and featureless absorption band with a peak at  $h\nu_{\text{ph}} = 2.23$  eV ( $\lambda_{\text{ph}} = 560$  nm) corresponds to the intramolecular charge transfer transition, whereas meanwhile the pronounced absorption lines in the higher energy region  $h\nu_{\text{ph}} = 3.09, 3.72,$  and  $4.70$  eV ( $\lambda_{\text{ph}} = 400, 333,$  and  $264$  nm) (the two latter lines are not shown) are attributed to

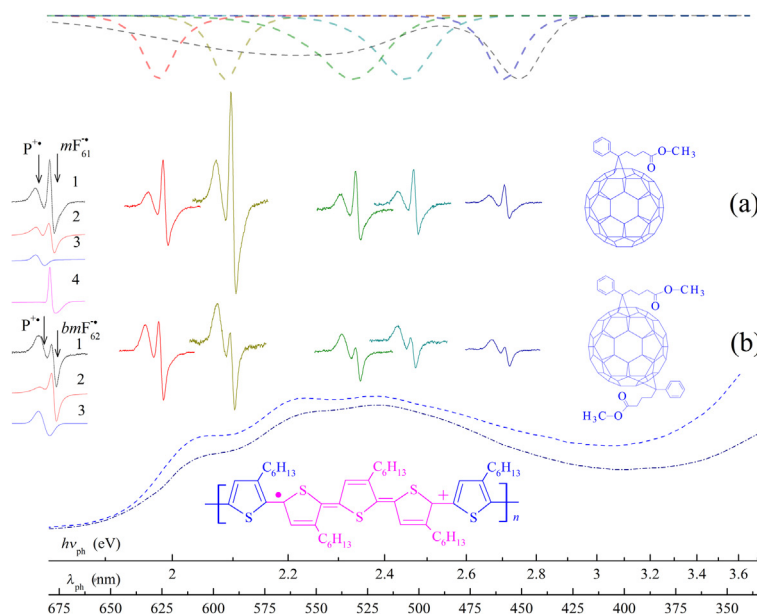


**FIGURE 9.9**

Normalized LEPR spectra of charge carriers background photoinduced at 77 K in BHJ formed by macromolecules of regioregular P3HT with globes of PC<sub>61</sub>BM and (a) *bis*-PC<sub>62</sub>BM (b) as a function of the photon energy  $h\nu_{\text{ph}}$  (wavelength  $\lambda_{\text{ph}}$ ). From left to right: the spectra obtained at irradiation of the samples by the white light and by the light with photon energy of 1.98, 2.10, 2.33, 2.45, 2.72 eV are shown. Above are shown irradiation spectra of the light sources. Below UV–vis absorption spectra of the P3HT:PC<sub>61</sub>BM and P3HT:*bis*-PC<sub>62</sub>BM composites are shown by dashed and dash-dotted lines, respectively. At the left are also shown theoretical sum spectra (1) and their Lorentzian contribution of mobile radical quasipairs,  $P_{\text{mob}}^{+\bullet} - bmF_{\text{mob}}^{-\bullet}$  (2), Gaussian contributions caused by localized polarons  $P_{\text{loc}}^{+\bullet}$  (3), and methanofullerene  $mF_{\text{loc}}^{-\bullet}$  (4), calculated using respective magnetic resonance parameters presented in Table 9.1 and concentration ratios  $[P_{\text{loc}}^{+\bullet}]:[P_{\text{mob}}^{+\bullet} - bmF_{\text{mob}}^{-\bullet}]:[mF_{\text{loc}}^{-\bullet}]$  of 6:57:1 for P3HT:PC<sub>61</sub>BM and 15:87 for P3HT:*bis*-PC<sub>62</sub>BM. The polaron formed on the P3HT chain after transfer of its charge to the methanofullerene is shown schematically. The positions of LEPR spectra of polarons,  $P^{+\bullet}$ , and methanofullerene anion radicals,  $bmF_{\text{mob}}^{-\bullet}$ , are shown as well.

the fullerene units. This leads to an increase in the intensity of the initial EPR spectrum and the appearance of the second line at higher magnetic fields (see Fig. 9.10). Following previous studies, these low- and high-field signals can be also assigned to  $P_{\text{mob}}^{+\bullet} - mF_{\text{mob}}^{-\bullet}$  quasipairs.

There were some unusual effects recorded which should be emphasized. The main one is that the LEPR signal of the sample appears under its irradiation even in the near infrared region,  $h\nu_{\text{ph}} = 1.32$  eV ( $\lambda_{\text{ph}} = 940$  nm), where the optical

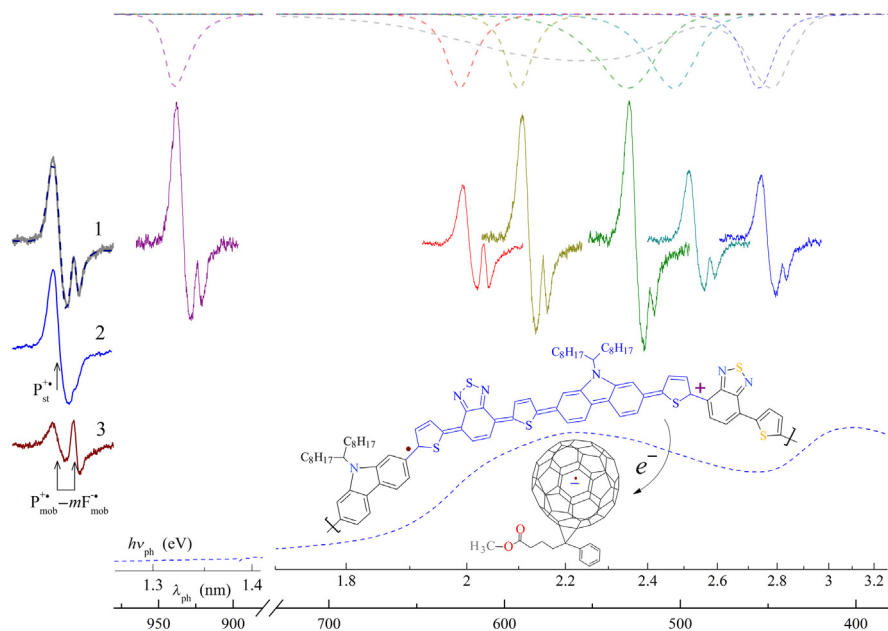


**FIGURE 9.10**

LEPR spectra of charge carriers background photoinduced at  $T = 77$  K in BHJ formed by macromolecules of PCDTBT with globes of PC<sub>61</sub>BM as function of the photon energy  $h\nu_{\text{ph}}$  (line width  $\lambda_{\text{ph}}$ ) normalized to the intensity of light sources. From left to right are shown the spectra obtained at irradiation of the samples by the white light and by the light with photon energy  $h\nu_{\text{ph}} = 1.32, 1.98, 2.10, 2.34, 2.46,$  and  $2.73$  eV. On the left are shown theoretical sum spectra (1, dashed lines) and their Lorentzian contributions caused by stabilized polarons  $P_{\text{st}}^{+\bullet}$  (2) and highly mobilized pair radicals,  $P_{\text{mob}}^{+\bullet}$  and  $mF_{\text{mob}}^{-\bullet}$  (3) numerically calculated using  $\Delta B_{\text{pp}}^{\text{P}} = 1.37$  G,  $\Delta B_{\text{pp}}^{mF} = 1.13$  G and a concentration ratio  $[P_{\text{st}}^{+\bullet}]:[P_{\text{mob}}^{+\bullet} - mF_{\text{mob}}^{-\bullet}] = 1:14$ . Above, dashed lines show irradiation spectra of the light sources and below dashed line shows IR–vis absorption spectrum of the PCDTBT:PC<sub>61</sub>BM composite. The charge transfer from PCDTBT to the methanofullerene accompanied by the formation on the polymer chain positively charged polaron  $P^{+\bullet}$  and negatively charged ion radical  $mF_{61}^{-\bullet}$  both with spin  $S = \frac{1}{2}$  is shown schematically. The positions of LEPR spectra of all charge carriers are also shown.

absorption band is nearly nulled (Fig. 9.10). The intensity of this signal is comparable to that obtained at higher photon frequencies. This fact can be originated, for example, by a nonlinear optical effect in the bulk of the PCDTBT:PC<sub>61</sub>BM composite converting the photon frequency/energy into the higher value, however, such a supposition was not supported under second harmonic illumination of the composite. Thus, it can be assumed that the formation of spin quasipairs indeed occurs in the sample BHJ under their excitation by infrared quanta. Besides, the comparison of an intensity of all LEPR and optical spectra presented shows that

the intensity of the former definitely does not correlate neither with the number of optical quanta reaching the sample surface nor with those absorbed by the sample. This does not confirm the conclusion made by Tong et al. [163] that the efficiency of carrier generation in the PCDTBT:fullerene BHJ should be essentially independent of the excitation wavelength. Various hypotheses can be supposed for explanation of these effects. One of them could be the interaction of charge carriers with a microwave field. Indeed, only for those relatively isolated excitons there is a reasonably high probability that a metastable PC will result from the optical production of an electron-hole pair by means of the trapping of one carrier and the hopping away of the other [164]. Thus, the separation and, therefore, lifetime of photoinitiated radical quasipairs  $P_{\text{mob}}^{+\bullet} - mF_{\text{mob}}^{-\bullet}$  will generally increase with electron spin precession frequency  $\omega_e$ . One, therefore, can take into account a combination of different processes affecting electronic transport through PCDTBT:PC<sub>61</sub>BM BHJ.

The best fit was achieved by supposing stabilization in a polymer backbone of polarons  $P_{\text{loc}}^{+\bullet}$ , characterized by the anisotropic Lorentzian spectrum 2 in the left of Fig. 9.10 with the main magnetic resonance parameters presented in Table 9.1. The anisotropic nature of the  $P_{\text{loc}}^{+\bullet}$  spectrum is *prima facie* evidence for its perceptible spin-orbit interaction with the nucleus of nitrogen and sulfur heteroatoms in the polymer network, as well as slow mobility. Under light irradiation of the composite, the number of such polarons somewhat increases and additionally highly mobile radical quasipairs  $P_{\text{mob}}^{+\bullet} - mF_{\text{mob}}^{-\bullet}$  with  $g_{\text{iso}}^{\text{P}} = 2.0022$  and  $g_{\text{iso}}^{\text{mF}} = 2.0006$  (contribution 3 in the left of Fig. 9.10) appear. The latter value lies close to that obtained for other fullerene anion radicals [126,128,133,165,166], however, it slightly exceeds that obtained for PC<sub>61</sub>BM embedded into P3AT matrices [42,91,157,161,162]. The absence of a Gaussian contribution in LEPR spectra of these charge carriers argues, as in case of the P3HT:*bis*-PC<sub>62</sub>BM composite, in favor of a smaller number of spin traps, as well as their faster dynamics in this sample. Two main differences of this composite from the known systems should be emphasized. Hyperfine polaron interaction with neighboring hydrogen and heteroatoms should broaden its spectrum and cause its Gaussian shape. Such a line shape is also characteristic of spins captured by energetically deep traps. This leads to the appearance of appropriate Gaussian contributions in LEPR spectra of P3HT:PC<sub>61</sub>BM and analogous composites. Both charge carriers stabilized and photoinitiated in the PCDTBT:PC<sub>61</sub>BM composite, however, are characterized by Lorentzian line shapes. This fact was not previously detected in LEPR study of various polymer:fullerene composites and should likely indicate a lower number of spin traps and higher spin dynamics in the PCDTBT:PC<sub>61</sub>BM system.

Methanofullerene anion radicals photoinduced, for example, in the P3HT:*bis*-PC<sub>62</sub>BM, P3HT:PC<sub>61</sub>BM, and PCDTBT:PC<sub>61</sub>BM systems demonstrate nearly temperature independent  $g_{\text{iso}}^{\text{F}}$ . On the other hand, this parameter of polaronic charge carriers,  $g_{\text{iso}}^{\text{P}}$ , was determined to be a function of temperature and, to a lesser extent, of photon energy  $h\nu_{\text{ph}}$  (see Figs 9.9 and 9.10). Figure 9.11 illustrates

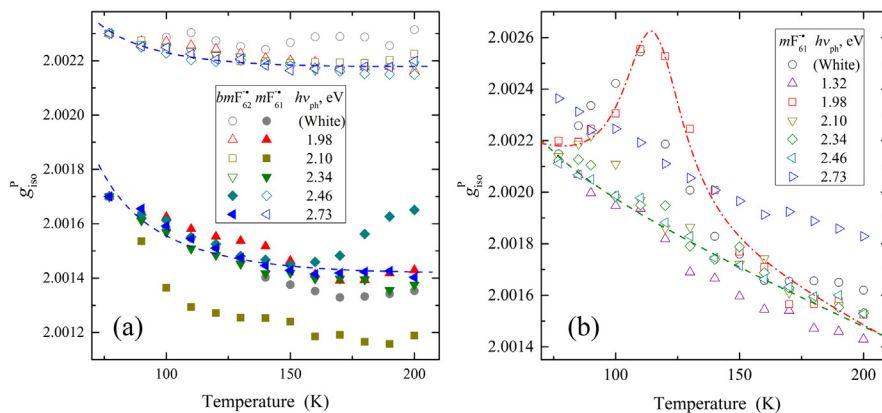


**FIGURE 9.11**

The value of  $g_{1so}^P$  for polarons photoinduced in the P3HT:*bis*-PC<sub>62</sub>BM, P3HT:PC<sub>61</sub>BM (a) and PCDTBT:PC<sub>61</sub>BM (b) BHJ as a function of photon energy  $h\nu_{ph}$  and temperature. The dashed line shows the dependences calculated from Eqn (9.3) with  $E_i$  equal to 9.5 meV (a, above line), 8 meV (a, below line), and 8 meV (b). The dash-dotted line (b) is drawn arbitrarily only for illustration to guide the eye.

that the temperature increase leads to the decrease in  $g_{1so}^P$ , especially in the two latter composites. It can be noted that as PC<sub>61</sub>BM counter ions are replaced by *bis*-PC<sub>62</sub>BM ones, the scattering in  $g_{1so}^P(T)$  dependences decreases, possibly due to the ordering of the polymer:fullerene composite. In other words, this parameter is strongly governed by the structure and conformation of conjugated  $\pi$ -electron system. Indeed, the HOMO energy level depends on the overlap of adjacent thiophene molecular orbits and, therefore, is expected to shift with ring angle [167] similarly to the valence band involved in the  $\pi-\pi^*$  transition. The band gap, LUMO–HOMO, slightly depends on both temperature [105] and torsion angle  $\theta$  [168], being near  $30^\circ$  in regioregular P3HT [169]. A decrease in  $g_{1so}^P$  occurs at electron excitation from the unoccupied shell to the antibonding orbit,  $\pi\rightarrow\sigma^*$  [170]. Comparing the data obtained, one may conclude that the energy of antibonding orbits decreases as *bis*-PC<sub>62</sub>BM is embedded into the P3HT matrix instead of PC<sub>61</sub>BM. This increases  $g_{1so}^P$  of the P3HT:*bis*-PC<sub>62</sub>BM composite and decreases the slope of its temperature dependency characteristic of more ordered system. Indeed, the changes in total energy with the torsion angle  $\theta$  appear as effective steric potential energy. The angular dependence of this energy is nonharmonic, with larger angles becoming more probable with the temperature increase. In this case the decrease of molecular regioregularity or a greater distortion of the thiophene rings out of coplanarity reduces charge mobility along the polymer chains [104]. This is usually attributed to a decrease in the effective conjugation lengths of the chain segments. The intrachain transfer integral  $t_{1D}$  is primarily

governed by the degree of overlap between the  $p_z$  atomic orbitals of the carbon atoms forming polymer units and, therefore, should evolve a square-cosine function of the torsion angle  $\theta$  between the planes of the neighboring thiophene rings [103]. This allows one to evaluate the decrease in the  $\theta$  value by nearly  $12^\circ$  at the replacement of the PCBM by *bis*-PCBM in appropriate polymer:fullerene system. Therefore, this indicates a more planar and ordered polymer matrix in the P3HT:*bis*-PC<sub>62</sub>BM composite than in the P3HT:PC<sub>61</sub>BM one. Peculiar extreme  $g_{\text{iso}}^{\text{P}}$  ( $T$ ) dependences obtained for polarons photoinitiated in PCDTBT:PC<sub>61</sub>BM BHJ by wideband white and monochromic light with photon energy  $h\nu_{\text{ph}} = 1.98$  eV was explained by competitive impact of the change in the energy transition of a spin from the unoccupied shell to the antibonding orbit  $\pi \rightarrow \sigma^*$  [170]. This effect can be explained by the change in effective dimensionality of the polymer matrix [38] and is additional evidence for the better ordering of PCDTBT:PC<sub>61</sub>BM BHJ in comparison with analogous P3AT composites.

Monotonic temperature dependences presented in Fig. 9.11, can be explained *inter alia* by joint harmonic librations of polymer units and chains together with localized polarons which change the backbone dimensionality [38], modulate charge transfer integrals [79], lift symmetry restrictions, and enable intrachain and interchain spin relaxation to cause broader polaron line width due to the relation  $\Delta B_{\text{pp}}^{\text{P}} \propto (\Delta g_{\text{iso}}^{\text{P}})^2$  [171]. Figure 9.11 indicates that the dependences calculated from Eqn (9.3) with respective  $E_1$  summarized in Table 9.2 are well fitted in the main experimental data. Such libration dynamics in the P3HT:*bis*-PC<sub>61</sub>BM and PCDTBT:PC<sub>61</sub>BM composites occurs mainly with the lower activation energy than in the P3HT:PC<sub>61</sub>BM one (see Table 9.2). Temperature sensitivity of the polaron  $g$ -factor decreases at  $T \geq 200$  K. The concentration of both types of charge carriers decreases dramatically at this temperature region and limits significantly the precision of determination for their main magnetic resonance parameters. Such effects can be attributed to fluctuations in local symmetry of side groups relative to the main polymer axis. These groups begin to move at the glass transition of the polymer matrix at  $T \approx 200$  K [172], their local relaxation contributes to the topological disorder in the polymer structure and leads to an increase in energy barriers for charge transport. The temperature dependence of  $g$ -factors is argued to be due to a coupling of the holes to local vibrations of the chains or/and side groups along a backbone of the polymer matrix. This means that photoinitiated spins act as a nanoscopic probe of molecular and polaron dynamics in polymer:fullerene composites. More detailed information can be obtained at higher spin precession frequencies  $\omega_e$  that are at higher spectral resolution. Thus, the absence in the LEPR spectra of Gaussian signals of localized charge carriers can evidence for higher ordering of PCDTBT layers and also for low number of energetically deep spin traps that facilitates charge transfer from the polymer chain to the methanofullerene cage. This is similar to cation radical single crystals with alternating organic and inorganic layers possessing a Lorentzian EPR spectra of their charge carriers, characteristic of free electrons [171].

**Table 9.2** The  $n_p$ ,  $n_f$  Values Determined for Polarons and Fullerene Ion Radicals, Energies  $E_i$  Determined from Eqn (9.3),  $\Delta E_{ij}$  Determined from Eqn (9.13),  $E_0$  Determined from Eqn (9.11),  $E_r$  Determined from Eqn (9.20),  $E_{ph}$  Determined from Eqn (9.33),  $E_b$  Determined from Eqn (9.35),  $\sigma_0$  and  $E_t$  Determined from Eqn (9.36) (all in eV) for the P3HT:PC<sub>61</sub>BM, P3HT:*bis*-PC<sub>62</sub>BM, and PCDTBT:PC<sub>61</sub>BM Composites Irradiated by Polychromatic White and Monochromatic Light with Different Photon Energy/Lineidth  $h\nu_{ph}/\lambda_{ph}$  (in eV nm<sup>-1</sup>)

Parameter	$h\nu_{ph}/\lambda_{ph}$						
	White	1.32/940	1.98/625	2.10/590	2.34/530	2.46/505	2.73/455
<b>P3HT:PC<sub>61</sub>BM</b>							
$n_p$	$4.9 \times 10^{-5}$	—	$3.9 \times 10^{-5}$	$9.7 \times 10^{-5}$	$4.2 \times 10^{-5}$	$4.3 \times 10^{-5}$	$2.4 \times 10^{-5}$
$n_f$	$4.2 \times 10^{-5}$	—	$2.5 \times 10^{-5}$	$7.7 \times 10^{-5}$	$3.1 \times 10^{-5}$	$3.4 \times 10^{-5}$	$2.1 \times 10^{-5}$
$E_i$	0.0098	—	0.0100	0.0097	0.0099	0.0056	0.0095
$\Delta E_{ij}^a$	0.0092	—	0.0054	0.0028	0.0017	0.0048	0.0066
$\Delta E_{ij}^b$	0.0607	—	0.0307	0.0476	0.0663	0.0793	0.0744
$\Delta E_{ij}^c$	0.0304	—	0.0258	0.0438	0.0540	0.0558	0.0569
$E_0^a$	0.0134	—	0.0519	0.0430	0.0088	0.0082	0.0318
$E_0^b$	0.0103	—	0.0181	0.0208	0.0113	0.0075	0.0163
$E_0^c$	0.0210	—	0.0236	0.0296	0.0307	0.0186	0.0169
$E_r$	0.0465	—	0.0460	0.0452	0.0351	0.0412	0.0473
$E_{ph}$	0.1132	—	0.1218	0.0822	0.1042	0.0709	0.0823
$\sigma_0$	0.0086	—	0.0144	0.0212	0.0109	0.0133	0.0183
$E_t$	0.1409	—	0.1441	0.1356	0.1335	0.1267	0.1404
$E_b$	0.0504	—	0.1024	0.0739	0.0551	0.0363	0.0454
<b>P3HT:<i>bis</i>-PC<sub>62</sub>BM</b>							
$n_p$	$9.7 \times 10^{-5}$	—	$7.6 \times 10^{-5}$	$1.6 \times 10^{-4}$	$7.0 \times 10^{-5}$	$6.5 \times 10^{-5}$	$4.9 \times 10^{-5}$
$n_f$	$7.2 \times 10^{-5}$	—	$5.2 \times 10^{-5}$	$7.7 \times 10^{-5}$	$3.3 \times 10^{-5}$	$3.2 \times 10^{-5}$	$2.2 \times 10^{-5}$
$E_i$	0.0053	—	0.0093	0.0066	0.0097	0.0088	0.0081

$\Delta E_{ij}^a$	0.0027	—	0.0014	0.0288	0.0140	0.0162	0.0177
$\Delta E_{ij}^c$	0.0171	—	0.0239	0.0404	0.0350	0.0375	0.0413
$E_0^a$	0.0309	—	0.0409	0.0272	0.0184	0.0144	0.0107
$E_0^c$	0.0080	—	0.0202	0.0136	0.0198	0.0222	0.0227
$E_r$	0.0453	—	0.0479	0.0495	0.0468	0.0509	0.0503
$E_{ph}$	0.0615	—	0.0765	0.0751	0.0909	0.0875	0.0650
$\sigma_0$	0.0193	—	0.0167	0.0219	0.0174	0.0160	0.0206
$E_t$	0.1228	—	0.1283	0.1294	0.1275	0.1189	0.1250
$E_b$	0.0627	—	0.0770	0.0423	0.0786	0.0565	0.0588

**PCDTB:PC<sub>61</sub>BM**

$E_l$	0.006 <sup>d</sup>	0.004	0.008 <sup>d</sup>	0.003	0.002	0.004	0.004
$\Delta E_{ij}^a$	0.018	0.005	0.056	0.050	0.032	0.072	0.059
$\Delta E_{ij}^c$	0.048	0.051	0.068	0.060	0.076	0.065	0.058
$E_r^a$	0.028	0.117	0.001	0.001	0.017	0.003	0.015
$E_r^c$	0.013	0.013	0.014	0.019	0.020	0.018	0.018
$E_{ph}$	0.121	0.098	0.049	0.074	0.080	0.043	0.120
$E_b$	0.079	0.093	0.067	0.081	0.110	0.141	0.178

<sup>a</sup>Determined for  $P_{loc}^{+\bullet}$ .

<sup>b</sup>Determined for  $mF_{loc}^{-\bullet}$ .

<sup>c</sup>Determined for  $mF_{mob}^{-\bullet}$ .

<sup>d</sup>Determined for monotonic part.

### 9.3.2 PHOTOINITIATION AND RECOMBINATION OF CHARGE CARRIERS IN POLYMER:FULLERENE COMPOSITES

Another important parameter of a nanomodified polymer composite, proportional to the number of both charge carriers is its paramagnetic susceptibility  $\chi$ .

In darkened P3HT:*m*F<sub>1</sub> BHJ, spin concentration ratio  $[P_1^{\bullet}]/[P_2^{\bullet}]$  of coupled polarons lies near 0.089 (see Fig. 9.3a) [40,41] and decreases for other compounds. Under light illumination the number of spin charge carriers increases sharply in composites and tend to recombine. This means that by illuminating a polymer:fullerene BHJ one can register only the net PC as a difference of forward initiating (fast) and reversed recombination (slow) processes [53]. The number of such centers depends mainly on the maximum number of polarons able to be formed at the first photoinitiation stage and also on recombination coefficient of charge carriers. To determine the limiting number of polarons able to be stabilized in a polymer matrix and to compare magnetic resonance parameters of polarons reversibly and irreversibly initiated in a polymer matrix, its modification by, for example, iodine molecules [68,129] can be used. However, this allows one to only modify an initial polymer. Such a procedure was used to obtain the limiting number of both polarons  $n_p$  and methanofullerene anion radicals  $n_f$  simultaneously formed per each polymer unit of the P3HT:PC<sub>61</sub>BM and P3HT:*bis*-PC<sub>62</sub>BM composites [142]. The former parameter was obtained for these systems at  $T = 77$  K to be 0.0028 and 0.0038, respectively. Note, that the  $n_p$  values obtained are considerably lower than those estimated for polarons excited, for example, in doped polyaniline,  $n_p \approx 0.05$  [94]. Limiting paramagnetic susceptibility  $\chi$  was determined for these systems to be  $8.7 \times 10^{-6}$  and  $1.1 \times 10^{-5}$  emu mol<sup>-1</sup>, respectively, at  $T = 310$  K. As the temperature decreases to 77 K, these values increase to  $8.7 \times 10^{-5}$  and  $9.9 \times 10^{-5}$  emu mol<sup>-1</sup>, respectively. The analysis also showed that the cooling of the samples leads to the appearance of anisotropic Gaussian term in their sum EPR spectra attributed to strongly frozen polarons. The ratio of a number of mobile to frozen polarons at 77 K is near 8:1 for P3HT:PC<sub>61</sub>BM and 7:1 for P3HT:*bis*-PC<sub>62</sub>BM. Mobile polarons initiated in these systems by the I<sub>2</sub>-doping at 310 K demonstrate single Lorentzian EPR spectra with line width  $\Delta B_{pp}$  of 4.0 and 5.6 G, respectively, which are much broader than those obtained for polarons in other conjugated polymers [77]. The broadening of the EPR transitions becomes most likely due to interaction between neighboring charged polarons. The contribution to line width due to such interaction can be estimated as  $\Delta B_{dd} = \mu_B R_0^{-3} = 4/3\pi\mu_B n_p$ , where  $R_0$  is a distance between polarons proportional to their concentration  $n_p$  on the polymer chain. At the transition from PC<sub>61</sub>BM to *bis*-PC<sub>62</sub>BM counter-anion, the  $\Delta B_{pp}$  value of mobile and trapped polarons characterized by Lorentzian and Gaussian distribution of spin packets, respectively, changes at 77 K from 1.9 and 2.3 G down to 1.8 and 1.9 G. Assuming intrinsic line width of polarons  $\Delta B_{pp}^0 = 1.5$  G in regioregular P3HT [173], one can obtain from the line broadening as a result of dipole–dipole interaction  $R_0 \approx 1.6$  nm for P3HT:PC<sub>61</sub>BM and

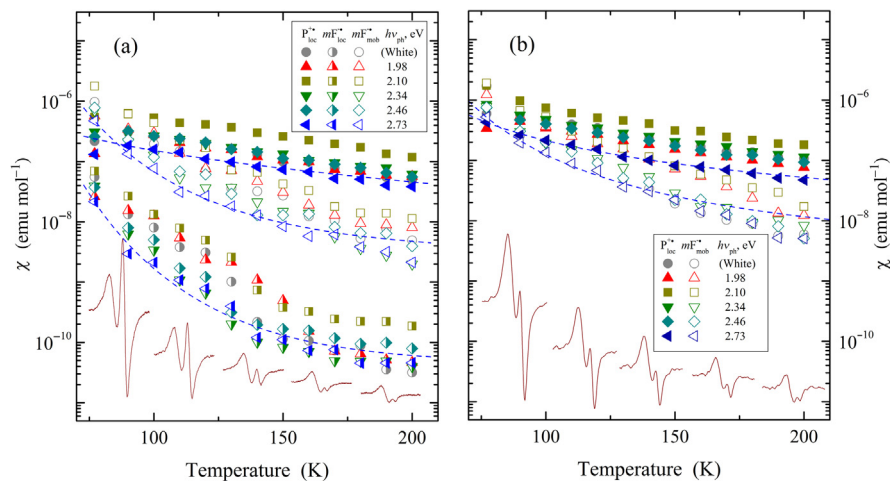
1.3 nm for P3HT:*bis*-PC<sub>62</sub>BM. Intrinsic concentration of doping-initiated polarons relying only upon polymer fraction in these composites was determined to be  $1.6 \times 10^{19}$  and  $2.2 \times 10^{19} \text{ cm}^{-3}$ , respectively, at 77 K. This value lies near  $2 \times 10^{19} \text{ cm}^{-3}$  obtained for concentration of acceptors in ZnO-treated P3HT [174], however, less sufficiently than  $10^{21} \text{ cm}^{-3}$  supposed for maximum polaron concentration in regioregular P3HT [55]. Effective concentration calculated for both polymer and fullerene phases in the P3HT:PC<sub>61</sub>BM and P3HT:*bis*-PC<sub>62</sub>BM composites is  $1.8 \times 10^{18}$  and  $2.1 \times 10^{18} \text{ cm}^{-3}$ , respectively. This allows one to evaluate an effective number of both types of charge carriers per each polymer unit initiated in these polymer:fullerene composites by I<sub>2</sub>-doping (described previously) and also by light irradiation. The values obtained for photoinitiated charge carriers are summarized in Table 9.2.

Figure 9.12 illustrates the changes in LEPR spectra of the P3HT:PC<sub>61</sub>BM and P3HT:*bis*-PC<sub>62</sub>BM composites with their heating and shows temperature dependences of all contributions into sum  $\chi$ . Since concentration of main charge carriers decreases dramatically at  $T > 200 \text{ K}$ , the precision of determination of their spin susceptibility falls significantly. The fitting of their double integrated sum LEPR spectra allowed us to separately obtain all terms of effective paramagnetic susceptibility  $\chi$ . This value consists of the contributions of mobile and localized polarons  $\chi_P$  and methanofullerene anion radicals  $\chi_F$ . The contribution of localized fullerene anion radicals into  $\chi$  of the P3HT:*bis*-PC<sub>62</sub>BM composite is absent within the whole temperature range used. Assuming the absence of a dipole–dipole interaction between fullerene anion radicals, one can evaluate energy  $\Delta E_{ij}$  from Eqn (9.13) for all charge carriers from temperature dependences of their paramagnetic susceptibility as a function of the energy of photons  $h\nu_{\text{ph}}$  (see Table 9.2). As is seen from Fig. 9.12, the net electronic processes in the composites can be described in terms of spin exchange with  $\Delta E_{ij}$  presented in Table 9.2.

It is evident that the energy required for polaron trapping in the P3HT matrix is lower than that obtained for other charge carriers.  $\Delta E_{ij}$  evaluated from  $\chi(T)$  for mobile radicals increases considerably indicating that higher energy is required for their trapping in the system. This value becomes larger for methanofullerene after its pinning in bulk of the P3HT:PC<sub>61</sub>BM matrix. The data obtained again evidences that all spin-assisted processes are governed mainly by the structure of anion radicals, as well as by the nature and dynamics of charge carriers photoinduced in BHJ of a composite. The  $\chi$  value of both charge carriers becomes distinctly higher at characteristic energy  $h\nu_{\text{ph}} \approx 2.1 \text{ eV}$  lying near the band gap of P3AT [175]. Such a dependence of spin concentration on photon energy can be explained either by the formation of spin pairs with different properties in homogeneous (higher-ordered) composite fragments or by the excitation of identical charge carriers in heterogeneous (lower-ordered) domains of the system. Different spin pairs can be photoinduced as a result of the photon-assisted appearance of traps with different energy depths in a polymer matrix. However, the revealed difference in the parameters of radicals seems to be a result of their interaction with their microenvironment in domains inhomogeneously distributed in a polymer:

**Table 9.3** The Spin–Lattice  $T_1$  and Spin–Spin  $T_2$  Relaxation Times (in s) of Polarons and Metanofullerene Anion Radicals Stabilized  $P_{loc}^{+\bullet}$ ,  $mF_{loc}^{-\bullet}$  and Mobile  $P_{mob}^{+\bullet}$ ,  $mF_{mob}^{-\bullet}$  Photoinduced in Some Polymer:Fullerene Composites at Different Photon Energy/Line Width  $h\nu_{ph}/\lambda_{ph}$  (in eV nm<sup>-1</sup>)

Parameter		$h\nu_{ph}/\lambda_{ph}$						
		White	1.32/940	1.98/625	2.10/590	2.34/530	2.46/505	2.73/455
<b>P3HT:PC<sub>61</sub>BM</b>								
$P_{loc}^{+\bullet}$	$T_1$	$2.8 \times 10^{-6}$	–	$2.6 \times 10^{-6}$	$1.9 \times 10^{-6}$	$2.3 \times 10^{-6}$	$1.9 \times 10^{-6}$	$1.4 \times 10^{-6}$
	$T_2$	$5.6 \times 10^{-8}$	–	$5.4 \times 10^{-8}$	$5.5 \times 10^{-8}$	$5.3 \times 10^{-8}$	$5.4 \times 10^{-8}$	$5.4 \times 10^{-8}$
$P_{mob}^{+\bullet}$	$T_1$	$1.8 \times 10^{-6}$	–	$1.2 \times 10^{-6}$	$1.5 \times 10^{-6}$	$1.7 \times 10^{-6}$	$1.7 \times 10^{-6}$	$2.6 \times 10^{-6}$
	$T_2$	$2.6 \times 10^{-8}$	–	$2.6 \times 10^{-8}$	$2.5 \times 10^{-8}$	$2.5 \times 10^{-8}$	$2.5 \times 10^{-8}$	$2.5 \times 10^{-8}$
$mF_{loc}^{-\bullet}$	$T_1$	$1.5 \times 10^{-6}$	–	$7.3 \times 10^{-7}$	$9.4 \times 10^{-7}$	$1.3 \times 10^{-6}$	$1.2 \times 10^{-6}$	$1.2 \times 10^{-6}$
	$T_2$	$8.9 \times 10^{-8}$	–	$8.9 \times 10^{-8}$	$9.1 \times 10^{-8}$	$8.9 \times 10^{-8}$	$9.4 \times 10^{-8}$	$8.9 \times 10^{-8}$
$mF_{mob}^{-\bullet}$	$T_1$	$1.6 \times 10^{-6}$	–	$1.3 \times 10^{-6}$	$1.6 \times 10^{-6}$	$1.4 \times 10^{-6}$	$1.6 \times 10^{-6}$	$1.5 \times 10^{-6}$
	$T_2$	$4.1 \times 10^{-8}$	–	$4.2 \times 10^{-8}$	$4.2 \times 10^{-8}$	$4.2 \times 10^{-8}$	$4.3 \times 10^{-8}$	$4.1 \times 10^{-8}$
<b>P3HT:bis-PC<sub>62</sub>BM</b>								
$P_{loc}^{+\bullet}$	$T_1$	$3.3 \times 10^{-6}$	–	$2.8 \times 10^{-6}$	$1.3 \times 10^{-6}$	$1.8 \times 10^{-6}$	$1.4 \times 10^{-6}$	$1.3 \times 10^{-6}$
	$T_2$	$5.6 \times 10^{-8}$	–	$5.4 \times 10^{-8}$	$4.9 \times 10^{-8}$	$4.7 \times 10^{-8}$	$4.8 \times 10^{-8}$	$4.8 \times 10^{-8}$
$P_{mob}^{+\bullet}$	$T_1$	$1.3 \times 10^{-6}$	–	$3.8 \times 10^{-6}$	$3.2 \times 10^{-6}$	$2.4 \times 10^{-6}$	$5.2 \times 10^{-6}$	$1.2 \times 10^{-6}$
	$T_2$	$2.6 \times 10^{-8}$	–	$2.5 \times 10^{-8}$	$2.3 \times 10^{-8}$	$2.2 \times 10^{-8}$	$2.2 \times 10^{-8}$	$2.2 \times 10^{-8}$
$mF_{mob}^{-\bullet}$	$T_1$	$1.2 \times 10^{-6}$	–	$2.1 \times 10^{-6}$	$1.4 \times 10^{-6}$	$1.1 \times 10^{-6}$	$1.3 \times 10^{-6}$	$1.1 \times 10^{-6}$
	$T_2$	$5.4 \times 10^{-8}$	–	$5.3 \times 10^{-8}$	$5.3 \times 10^{-8}$	$5.4 \times 10^{-8}$	$5.3 \times 10^{-8}$	$5.0 \times 10^{-8}$
<b>PCDTBT:PC<sub>61</sub>BM</b>								
$P_{loc}^{+\bullet}$	$T_1$	$1.9 \times 10^{-6}$	$2.1 \times 10^{-6}$	$2.9 \times 10^{-6}$	$2.1 \times 10^{-6}$	$2.2 \times 10^{-6}$	$1.6 \times 10^{-6}$	$2.3 \times 10^{-6}$
	$T_2$	$4.8 \times 10^{-8}$	$4.4 \times 10^{-8}$	$4.4 \times 10^{-8}$	$4.3 \times 10^{-8}$	$4.9 \times 10^{-8}$	$4.7 \times 10^{-8}$	$4.5 \times 10^{-8}$
$mF_{mob}^{-\bullet}$	$T_1$	$1.1 \times 10^{-6}$	$8.9 \times 10^{-7}$	$1.4 \times 10^{-6}$	$1.3 \times 10^{-6}$	$1.3 \times 10^{-6}$	$1.2 \times 10^{-6}$	$9.7 \times 10^{-7}$
	$T_2$	$5.8 \times 10^{-8}$	$5.8 \times 10^{-8}$	$5.6 \times 10^{-8}$	$5.4 \times 10^{-8}$	$5.3 \times 10^{-8}$	$5.5 \times 10^{-8}$	$5.9 \times 10^{-8}$



**FIGURE 9.12**

Temperature dependence of paramagnetic susceptibility of the  $P_{\text{loc}}^{+\bullet}$ ,  $mF_{\text{loc}}^{-\bullet}$ , and  $mF_{\text{mob}}^{-\bullet}$  charge carriers photoinduced in BHJ formed by P3HT chains with the PC<sub>61</sub>BM (a) and *bis*-PC<sub>62</sub>BM (b) methanofullerenes by photons with different energy  $h\nu_{\text{ph}}$ . Dashed lines show dependences calculated as an example for  $h\nu_{\text{ph}} = 2.73$  eV from Eqn (9.13) with  $\Delta E_{ij}$  summarized in Table 9.2. LEPR spectra of these heterojunctions registered at respective temperatures are shown at the bottom.

fullerene composite. Different ordering of these domains can be the reason for variation in their band gap energy which leads to their sensitivity to photons with definite but different energies. This can give rise to the change in the interaction of charge carriers with a lattice and other spins. Effective spin susceptibility of the P3HT:*bis*-PC<sub>62</sub>BM composite somewhat exceeds that obtained for the P3HT:PC<sub>61</sub>BM one. This effect and the absence of trapped anion radicals in the former support additionally higher ordering of BHJ in this system which interfere in the formation of traps in its matrix.

Figure 9.13 depicts appropriate contributions of charge carriers into an effective spin susceptibility of the PCDTBT:PC<sub>61</sub>BM composite as function of temperature and photon energy. The data presented can also be interpreted in terms of the exchange interaction of both charge carriers with the spin flip-flop probability  $p_{\text{ff}}$  previously introduced in Eqn (9.12). The figure illustrates that the spin–spin interaction processes in the composite can indeed be described by Eqns (9.6) and (9.13), so the energies  $\Delta E_{ij}$  evaluated for both charge carriers from their dependences can be determined (Table 9.2). It is evident that polaron diffusion in the PCDTBT matrix requires lower energy  $\Delta E_{ij}$  when compared with mobile methanofullerene anion radicals. It also shows that the  $\chi$  value of anion radicals becomes more temperature dependent when  $h\nu_{\text{ph}} \approx 1.98$  and 2.73 eV. The former value lies near the band gap obtained for PCDTBT (1.88 eV) [29]. Such a

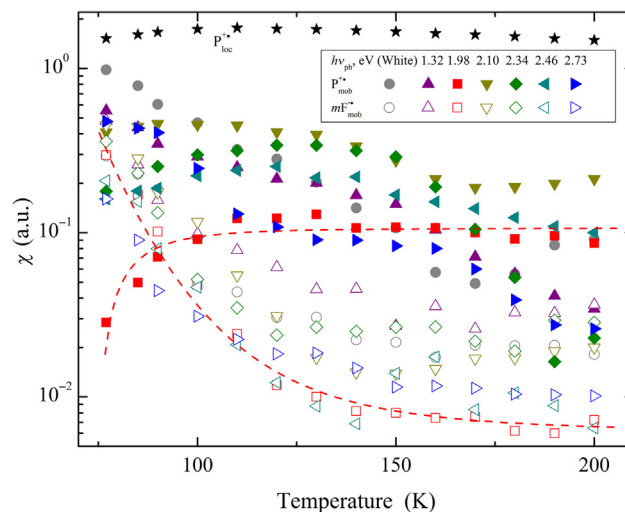


**FIGURE 9.13**

Temperature dependence of the paramagnetic susceptibility of polarons  $P_{loc}^{+\bullet}$  and  $P_{mob}^{+\bullet}$  (filled points) and methanofullerene anion radicals  $mF_{mob}^{-\bullet}$  (open points) photoinduced in PCDTBT:PC<sub>61</sub>BM BHJ by photons with different energy  $h\nu_{ph}$  normalized to illumination intensity of the light sources. The dashed lines show dependences calculated as an example for  $h\nu_{ph} = 1.98$  eV from Eqn (9.6) with  $\Delta E_{ji} = 0.056$  eV, and Eqn (9.13) with  $\Delta E_{ji} = 0.068$  eV.

dependence of spin concentration on photon energy should indeed be a result of different interaction of charge carriers with their microenvironment in domains inhomogeneously distributed in the composite causing sensitivity to photon energy. Figure 9.13 shows that the illumination of the PCDTBT:PC<sub>61</sub>BM composite by photons with  $h\nu_{ph} = 1.98$  eV induces the minimum number of traps for polarons that leads to formation of a larger number of mobile spin quasipairs at low temperatures. Such photon frequency selectivity is governed by the polymer structure, effective dimensionality, and also by the properties of an acceptor involved in BHJ. It can be used, for example, in plastic sensoric photovoltaics, whereas the composites with low selectivity seem to be more suitable for higher efficient conversion of solar energy.

When initiating background illumination is switched off, photoinitiation of charge carriers in some polymer:fullerene BHJ stops and the concentration of spin charge carriers excited starts to decrease. This is demonstrated in the insert of Fig. 9.14, where the decay of spin charge carriers in the P3HT:PC<sub>61</sub>BM, P3HT:*bis*-PC<sub>62</sub>BM, and P3DDT:PC<sub>61</sub>BM systems is shown. Lifetime of charge carriers seems to be much longer than the  $t \sim 0.1$   $\mu$ s obtained by optical absorption spectroscopy for relevant recombination times of mobile photoexcitations in organic solar cells [176,177]. Thus, the data obtained are mainly pertinent to carriers time-dependent separated or trapped in a polymer matrix [42,130,142,157,178,179].

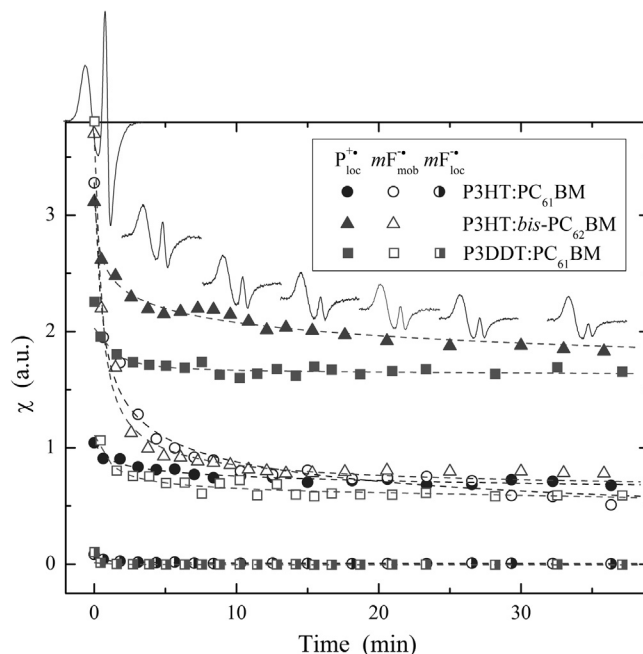


**FIGURE 9.14**

Decay of spin susceptibility of pinned polarons  $P_{loc}^{+\bullet}$  (filled points) as well as pseudorotating ( $mF_{mob}^{-\bullet}$ , open points) and pinned ( $mF_{loc}^{-\bullet}$ , semi-filled points) methanofullerenes photoinduced in the BHJ of P3HT:PC<sub>61</sub>BM (circles), P3HT:*bis*-PC<sub>62</sub>BM (triangles), and P3DDT:PC<sub>61</sub>BM (squares) systems at 77 K. Dashed lines show the dependences calculated for these carriers in the latter sample from Eqn (9.10) with  $n_0 a^3 = 2.1 \times 10^{-5}$  and  $\tau_0 = 0.27$  min,  $n_0 a^3 = 1.4 \times 10^{-7}$  and  $\tau_0 = 7.2 \times 10^{-5}$  min, and  $n_0 a^3 = 6.4 \times 10^{-6}$  and  $\tau_0 = 2.2 \times 10^{-5}$  min, respectively, as well as from Eqn (9.11) with  $\Delta E_0$  summarized in Table 9.2. Typical changes in the LEPR spectrum of a polymer:fullerene composite at appropriate time  $t$  is shown as well.

The decay of spin susceptibility of the P3DDT:PC<sub>61</sub>BM composite shown in Fig. 9.14 was interpreted [42] in terms of the above described approach of recombination of charge carriers with different effective localization radii,  $n_p = 1.2 \times 10^{-4}$ ,  $n_f = 6.3 \times 10^{-5}$  and separated by a time-dependent distance  $R_0$  [88]. Figure 9.14 evidences that the dependences calculated from Eqn (9.10) with respective  $n_0 a^3$  products and  $\tau_0$  values fit the experimental data obtained well. Therefore, the decay of long-living spin quasipairs photoinduced in the P3DDT:PC<sub>61</sub>BM composite can indeed be described in terms of this model, in which the low-temperature recombination rate is particularly strongly dependent on the spatial distance between photoinduced polarons and methanofullerene ion radicals. The long lifetimes are solely ascribed to the large spatial distances that buildup among the remaining photoinduced charge carriers, which did not recombine at a

shorter time. The product  $n_0 a^3$  decreases considerably as the methanofullerene acceptor is replaced by, for example, the azagomofullerene one [42]. This can be due to the higher probability of excitation of mobile polarons in the P3DDT:PC<sub>61</sub>BM system characterizing with prolonged radiative lifetime of spin quasi-pairs  $\tau_0$  that also corresponds to the lower constant of bimolecular recombination in this system.

The other data presented in Fig. 9.14 can be described in frameworks of the Tachiya concept [92] of bulk recombination of charge carriers during their repeated trapping into and detrapping from trap sites with different depths. The dependences calculated with  $E_0$  presented in Table 9.2 for charge carriers photoinduced in the BHJ studied are also shown in Fig. 9.14. It is shown that Eqn (9.11) fits the experimental data presented in the Fig. 9.14 well. Therefore, the decay of long-lived charge carriers originated from initial spin pairs photoinduced in the polymer:fullerene composite can successfully be described in terms of the above model in which the low-temperature recombination rate is strongly governed by temperature and the width of energy distribution of trap sites. The analysis of the experimental data allows one to support the crucial role of the photon energy on the formation and energetic properties of the traps in BHJ of such disordered systems. This parameter obtained for the sites occupied by both localized polarons and fullerene anion radicals in P3HT:PC<sub>61</sub>BM changes extremely, with  $h\nu_{\text{ph}}$  attaining the minimum at  $h\nu_{\text{ph}} \sim 2.4$  eV. The width of energy distribution of the traps in the P3HT:*bis*-PC<sub>62</sub>BM system decreases with growing  $h\nu_{\text{ph}}$ . On the other hand, mobile charge carriers are characterized by extremal  $E_0(h\nu_{\text{ph}})$  dependences with a maximum at  $h\nu_{\text{ph}} \sim 2.3$  eV for P3HT:PC<sub>61</sub>BM and a minimum at  $h\nu_{\text{ph}} \sim 2.1$  eV for P3HT:*bis*-PC<sub>62</sub>BM (Table 9.2). This indicates that the local structure and ordering govern the depth of spin traps and their distribution in these composites.

It should be noted that the other polymer:fullerene composites are characterized by much shorter-lived centers, making it impossible to register them just after their light excitation due to the higher ordering of such systems.

### 9.3.3 LEPR LINE WIDTH

Temperature dependences of effective LEPR line width  $\Delta B_{\text{pp}}^{(0)}$  of charge carriers photoinduced in different polymer:fullerene composites by light photons is presented in Figs 9.15 and 9.16. It should be noted that the value obtained for polarons photoinduced in the composites lies near 1.5–1.8 G, and is evaluated for respective charge carriers stabilized in different P3AT matrices [81]. However, this value is considerably lower than that determined for undoped polythiophene [81,180], which is evidence of weaker spin interaction with the P3AT lattice. The LEPR line width should reflect different processes occurring in a polymer:fullerene composite. One of them is the association of mobile polarons with the counter charges. Another process realized in the system is exchange interaction between mobile and trapped polarons and fullerenes that broadens the line by

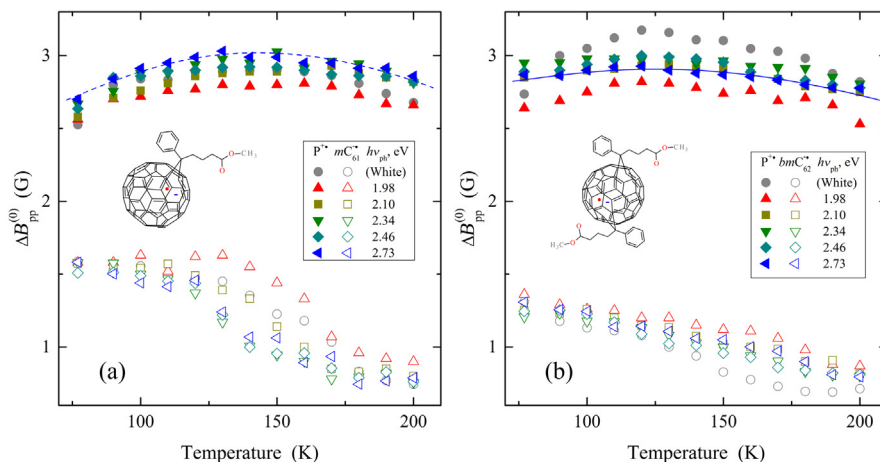


**FIGURE 9.15**

Line width of charge carriers photoinduced in the P3HT:PC<sub>61</sub>BM (a) and P3HT:*bis*-PC<sub>62</sub>BM (b) composites as a function of temperature and photon energy  $h\nu_{\text{ph}}$ . As an example, dashed lines show the dependences calculated from Eqn (9.20) with  $E_r = 0.047$  (a) and 0.050 eV (b). The symbol (0) in  $\Delta B_{\text{pp}}^{(0)}$  implies that the LEPR spectra were measured far from microwave saturation, when  $B_1 \rightarrow 0$ .

$\delta\Delta B_{\text{ex}} = \mu_B/R_0^3 = 4/3\pi\mu_B n_P$ , where  $R_0$  is the distance between dipoles proportional to polaron concentration  $n_P$  on the polymer chain. Assuming anisotropic character of the main magnetic resonance parameters of polarons discussed above, one can evaluate  $R_0 \approx 2.3\text{--}2.5$  nm for a distance between dipoles in the P3AT:PC<sub>61</sub>BM systems.

Figure 9.15 shows that the line width obtained for polarons in the P3HT:PC<sub>61</sub>BM and P3HT:*bis*-PC<sub>62</sub>BM systems is characterized by  $\cap$ -like temperature dependence with the extremes lying near 140 and 130 K, respectively, and remains almost unchanged at the exchange of the fullerene derivatives. Line width of the methanofullerene anion radicals demonstrates more monotonic temperature dependence and decreases with the system heating (Fig. 9.15).

The data presented were interpreted in terms of the exchange interaction of spins with different mobility in a polymer matrix. The dependences calculated from Eqn (9.20) with  $t_{1D} = 1.18$  eV [105] and  $E_r$  summarized in Table 9.2 are also presented in Fig. 9.15. The fitting is evidence of the applicability of these approaches for interpretation of electronic processes realized in these polymer composites. The energy  $E_r$  obtained for P3HT:PC<sub>61</sub>BM and P3HT:*bis*-PC<sub>62</sub>BM lies close to that evaluated for regioregular P3HT from its ac conductometric (0.080 eV) [181] and <sup>13</sup>C NMR (0.067–0.085 eV at  $T < 250$  K) [172] data. Figure 9.15 shows that line width of the PC<sub>61</sub>BM anion radicals decreases with the system heating. This value decreases with the replacement of the PC<sub>61</sub>BM

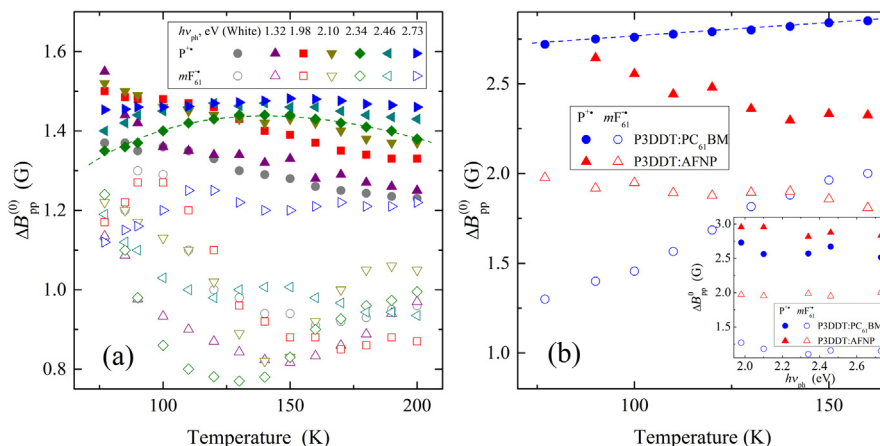


**FIGURE 9.16**

Line width of stabilized and mobile charge carriers photoinduced in the PCDTBT:PC<sub>61</sub>BM (a), P3DDT:PC<sub>61</sub>BM and P3DDT:AFNP (b) composites as a function of temperature and photon energy  $h\nu_{ph}$ . Dashed lines show the dependences calculated as an example from Eqn (9.20), with  $E_a$  equal to 0.017 (a) and 0.001 eV (b), respectively. The symbol (0) in  $\Delta B_{pp}^{(0)}$  implies that the LEPR spectra were measured far from microwave saturation, when  $B_1 \rightarrow 0$ .

acceptor by *bis*-PC<sub>62</sub>BM in such polymer:fullerene composites. The latter fact additionally indicates a more ordered structure of the P3HT:*bis*-PC<sub>62</sub>BM composite as compared with P3HT:PC<sub>61</sub>BM one.

Figure 9.16a shows the line widths of both charge carriers photoinitiated in the PCDTBT:PC<sub>61</sub>BM composite and those normalized to the unit concentration  $n_i$  as a function of temperature and photon energy  $h\nu_{ph}$ . One of the dependences calculated from Eqn (9.20) and fitting appropriate data are also presented in Fig. 9.16. This is also evidence of the applicability of the approach proposed above for interpretation of electronic processes realized in organic composites. It is seen from the figure that the line width of polarons and methanofullerene anion radicals differently depends not only on the temperature, but also on the energy of the initiated photons. These charge carriers also demonstrate a different sign of own temperature dependence. This can be due to their different nature and dynamics mechanism in domains inhomogeneously distributed in the composite. Such inhomogeneity seems to be more characteristic for methanofullerene domains than for polaronic phase, possibly because of more ordered, layer morphology of PCDTBT matrix. The energy necessary for activation of both the charge carriers change slightly as  $h\nu_{ph}$  exceeds the polymer band gap.

Respective dependences obtained for the P3DDT:PC<sub>61</sub>BM and P3DDT:AFNP composites are presented in Fig. 9.16b. The figure shows that the line width of polarons in the P3DDT:PC<sub>61</sub>BM composite broadens with the temperature,

however, this value oppositely depends on the temperature as P3DDT is modified by AFNP nanoadduct. The data obtained were also interpreted in terms of the previously mentioned approach of the collision of localized and mobile spins. Indeed, the dependences calculated from Eqn (9.20) with  $E_r$  summarized in Table 9.2 fits the experimental data presented well.

One can conclude that the energy required for initiation of polaron diffusion in the P3HT:PC<sub>61</sub>BM composite exceeds  $E_r$  obtained for both the PCDTBT:PC<sub>61</sub>BM and P3DDT:PC<sub>61</sub>BM ones. This parameter additionally decreases as PC<sub>61</sub>BM globes in P3DDT matrix are replaced by AFNP nanoadducts.

The data presented are additional evidence that relaxation and dynamics processes realized in the composites are governed mainly by the structure of polymer matrix and fullerene derivative, as well as by the nature and dynamics of charge carriers photoinduced in appropriate BHJ. As in the case of feature of spin susceptibility, variation in  $\Delta B_{pp}^{(0)}(h\nu_{ph})$  registered for charge carriers can also be attributed to inhomogeneous distribution of domains with different ordering (and, hence, band gap energies) in the polymer:fullerene BHJ. The photon-energy-correlation obtained for the main magnetic resonance parameters of the polymer:fullerene BHJ can be used in creation of organic molecular devices with spin-assisted (spintronic) properties.

### 9.3.4 ELECTRON RELAXATION AND DYNAMICS OF SPIN CHARGE CARRIERS

With the increase of the magnetic term  $B_1$  of microwave irradiation in a polymer:fullerene BHJ, the width and intensity of the LEPR spectra of both polarons and fullerene anion radicals shown in Figs 9.3–9.10 change according to Eqns (9.29) and (9.30), respectively. The slope of these dependences is evidently governed by the nature, electron relaxation, and mobility of these spin charge carriers. The insert of Fig. 9.17 shows changes at different  $B_1$  values, for example, the intensity of both the charge carriers photoinitiated in the P3HT:PC<sub>61</sub>BM composite [42]. These data are well described by Eqn (9.30). Since polarons and fullerene anion radicals carrying a charge through BHJ are found to be independent, this allows the separate determining of both their  $T_1$  and  $T_2$  relaxation times. One should only take into account the different distribution of spin packets in the LEPR spectra of mobile and localized charge carriers. Figure 9.17 shows as an example these parameters determined for charge carriers stabilized and photoinitiated in the P3HT:PC<sub>61</sub>BM and P3DDT:PC<sub>61</sub>BM composites in a wide temperature region. Both the  $T_1$  and  $T_2$  values of charge carriers photoinitiated in some polymer:fullerene composites at  $T = 77$  K are summarized in Table 9.3.

The analysis of the data presented shows that the interaction of most charge carriers with the lattice is characterized by monotonic temperature dependences, whereas  $T_1$  of fullerene anion radicals trapped by the P3DDT matrix demonstrates sharper temperature dependence. Spin–spin interaction is nearly temperature

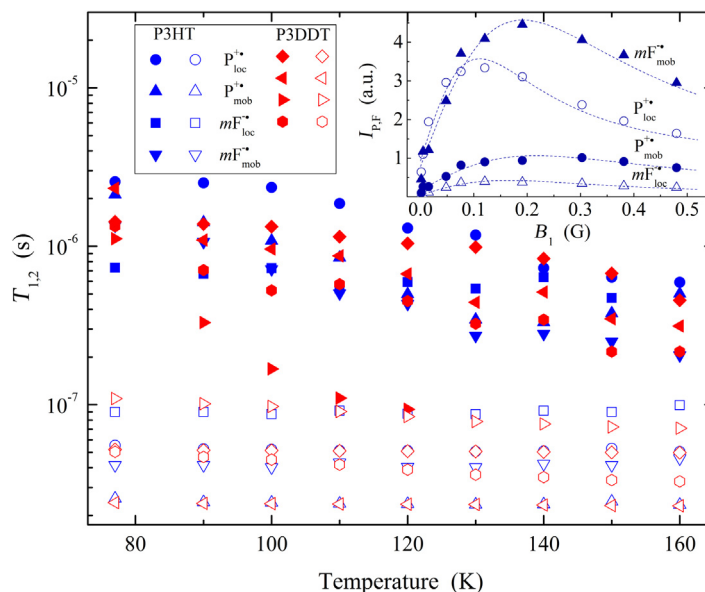


**FIGURE 9.17**

Temperature dependence of spin–lattice ( $T_1$ , filled points) and spin–spin ( $T_2$ , open points) relaxation times of charge carriers  $P_{loc}^{+\bullet}$  and  $mF_{loc}^{-\bullet}$ , as well as  $P_{mob}^{+\bullet}$  and  $mF_{mob}^{-\bullet}$  photoinduced in the P3HT:PC<sub>61</sub>BM and P3DDT:PC<sub>61</sub>BM composites by light with  $h\nu_{ph} = 1.98$  eV. The insert shows the changes in intensity of their contributions to the effective LEPR spectrum initiated in the P3HT:PC<sub>61</sub>BM BHJ by light with  $h\nu_{ph} = 1.98$  eV at 90 K as a function of the magnetic term  $B_1$  of microwave field as well as the dependences shown by dashed lines and calculated from Eqn (9.30) with  $T_1 = 2.5 \times 10^{-6}$  and  $T_2 = 5.3 \times 10^{-8}$  s,  $T_1 = 1.4 \times 10^{-6}$  and  $T_2 = 2.4 \times 10^{-8}$  s,  $T_1 = 1.1 \times 10^{-6}$  and  $T_2 = 4.2 \times 10^{-8}$  s,  $T_1 = 6.7 \times 10^{-7}$  and  $T_2 = 9.0 \times 10^{-8}$  s, respectively.

independent. However, it is governed by structural properties of a polymer:fullerene composite (Fig. 9.17).

Diffusion coefficients calculated from Eqns (9.31) and (9.32) for both types of charge carriers photoinduced in the P3HT:PC<sub>61</sub>BM and P3HT:*bis*-PC<sub>62</sub>BM composites using the relaxation and susceptibility data as well as the appropriate spectral density functions are presented in Fig. 9.18 as a function of temperature and  $h\nu_{ph}$ . Figure 9.18 shows that the coefficient of polaron intrachain diffusion  $D_{1D}$  is governed sufficiently by the energy of initiated photons  $h\nu_{ph}$ . The replacement of PC<sub>61</sub>BM by *bis*-PC<sub>62</sub>BM suppresses this effect. Such a replacement increases anisotropy of polaron diffusion  $D_{1D}/D_{3D}$  in the P3HT matrix. This fact additionally justifies better planarity of the matrix with *bis*-PC<sub>62</sub>BM molecules embedded. This is due to the fact that these more side-ramified methanofullerenes restrict the number of possible conformations able to be formed by two adjacent thiophene rings rotating about their shared C–C bond. As seen from the data presented,

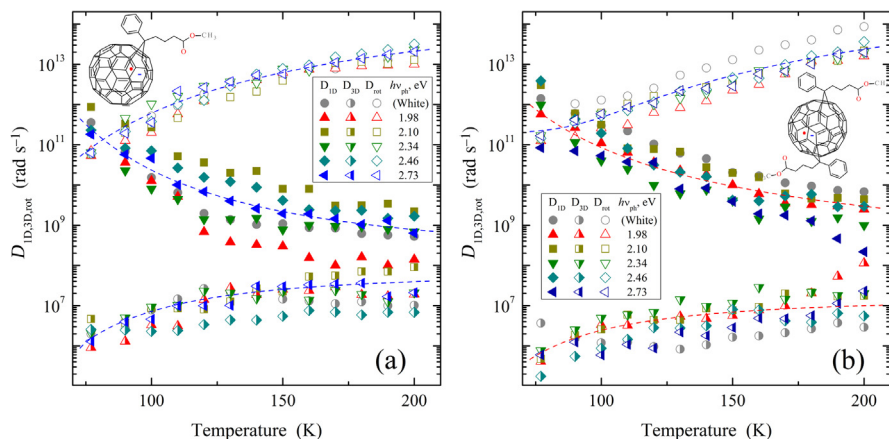


**FIGURE 9.18**

Temperature dependence of intrachain ( $D_{1D}$ , filled points), interchain ( $D_{3D}$ , semi-filled points), and rotational diffusion ( $D_{rot}$ , open points) coefficients of mobile charge carriers  $P_{mob}^{+\bullet}$  and  $mF_{mob}^{-\bullet}$  (left and right lines of the quasipairs 2 in Fig. 9.9, respectively) photoinduced in the P3HT:PC<sub>61</sub>BM (a) and P3HT:*bis*-PC<sub>62</sub>BM (b) composites by the polychromatic white and monochromatic light with different photon energy  $h\nu_{ph}$ . Dashed lines show the dependences calculated from Eqn (9.35) with  $E_b = 0.045$  eV, Eqn (9.33) with  $E_{ph} = 0.082$  eV, Eqn (9.36) with  $E_t = 0.140$  eV,  $\sigma_0 = 0.018$  eV (a) and from Eqn (9.35) with  $E_b = 0.059$  eV, Eqn (9.33) with  $E_{ph} = 0.077$  eV, Eqn (9.36) with  $E_t = 0.128$  eV,  $\sigma_0 = 0.017$  eV (b).

both fullerene anion radicals pseudorotate between the P3HT chains with approximately the same rate in the whole temperature range used (except charge carriers photoinduced in the P3HT:*bis*-PC<sub>62</sub>BM system by white light, see Fig. 9.18).

To account for the LEPR mobility data obtained, different theoretical models can be used. Intrachain polaron dynamics in the samples is characterized by strong temperature dependence (Fig. 9.18). Such a behavior can be associated, for example, with the scattering of polarons on the lattice phonons of crystalline domains embedded into an amorphous matrix. Figure 9.18 evidences that the  $D_{1D}$  obtained for a polaron from Eqn (9.31) follows well Eqn (9.33) with the phonon energy summarized in Table 9.2. This value lies near the energy of lattice phonons, 0.09–0.32 eV determined for other conjugated polymers [77].  $E_{ph}$  obtained for the P3HT:*bis*-PC<sub>62</sub>BM composite appears to be sensitive to the energy of illuminated photons attaining a maximum at  $h\nu_{ph} = 2.46$  eV.

The interchain spin hopping dynamics can be analyzed in terms of the previously discussed Hoesterey-Letson formalism of trap-controlled spin mobility. Figure 9.18 also shows exemplary temperature dependences calculated from Eqn (9.36) with  $T_{cr} = 111$ –126 K (P3HT:PC<sub>61</sub>BM),  $T_{cr} = 127$ –140 K (P3HT:*bis*-PC<sub>62</sub>BM),  $\sigma_0$  and  $E_t$  summarized in Table 9.2. The figure evidences

that interchain polaron dynamics can indeed be described in the frame of the previously mentioned theory. The  $E_t$  values obtained for P3HT:PC<sub>61</sub>BM prevail for those characteristics of P3HT:*bis*-PC<sub>62</sub>BM (Table 9.2), which is additional evidence of deeper traps reversible formed in the former polymer matrix. Moreover, the replacement of the PC<sub>61</sub>BM by the *bis*-PC<sub>62</sub>BM counter-ions somewhat increases  $T_{ct}$  of a polymer:fullerene system. This fact probably indicates the decrease in trap concentration due the increase in effective crystallinity (ordering) of the polymer matrix. The data presented show that the photon energy governs simultaneously both the  $T_{ct}$  and  $E_t$  parameters, which attain the maximal and the minimal values, respectively, at  $h\nu_{ph} \approx 2.5$  eV. Assuming all the electron wave functions exponentially decay, the interchain transfer integral,  $t_{\perp} = 2e^2r/3\epsilon a^2 \exp(-r/a)$  [182], was roughly estimated for P3HT to be equal to 0.12 eV. Comparing the data presented, one can note rather extremal  $E_t(h\nu_{ph})$  dependences with a minimum at  $h\nu_{ph} \approx 2.3-2.4$  eV.

The fullerene pseudorotational mobility data can be analyzed in the framework of Elliot's charge carrier-hopping model described previously. The energies,  $E_b$ , necessary to activate methanofullerene pseudorotational diffusion in the polymer:fullerene composites obtained from the fitting of experimental data by Eqn (9.35) are summarized in Table 9.2. Figure 9.18 illustrates the temperature dependences of dynamic parameters calculated from Eqn (9.35), with  $E_b$  determined approximately to fit the experimental data. These values depend on photon energy (see Table 9.2) and lie near those obtained, for example, from molecular dynamics in polycrystalline fullerene [183] and a triphenylamine fullerene complex [184].

Spin diffusion coefficients of both types of charge carriers photoinduced in the PCDTBT:PC<sub>61</sub>BM composite in wide temperature region and photon energy  $h\nu_{ph}$  calculated from Eqns (9.31) and Eqn (9.32) are presented in Fig. 9.19. The figure shows that the values and frequency dispersion of all diffusion coefficients are characterized by weak dependence on the  $h\nu_{ph}$  value, as in case of the P3HT/*bis*-PC<sub>62</sub>BM composite which appeared to become more ordered than P3HT/PC<sub>61</sub>BM and other known polymer:fullerene systems [142].

The anisotropy of polaron dynamics,  $A = D_{1D}/D_{3D}$ , in the PCDTBT:PC<sub>61</sub>BM composite is significantly lower than that obtained for analogous P3DDT:PC<sub>61</sub>BM and P3HT:*bis*-PC<sub>62</sub>BM (see above) that is typical for more ordered systems. This value determined at  $T = 77$  K is characterized by a U-like dependence on the photon energy  $h\nu_{ph}$  (see inset of Fig. 9.19). This can probably evidence the better ordering of the composite at intermediate  $h\nu_{ph}$  and  $A$  values. One can only note an unusual feature of this dependence, namely the evident increase of an anisotropy of the polaron diffusion at  $h\nu_{ph} = 2.10$  eV lying near the polymer band gap. This effect can probably be explained by stronger interaction of the polymer matrix with light photons. Indeed, the layer ordering of the polymer matrix allows longer polaron diffusion and formation of well-ordered PC<sub>61</sub>BM pools located between these layers [34,36]. This can, in principle, lead to resonant electronic response on photon energy. If the latter becomes comparable with the polymer band gap, the stronger polaron interaction with the lattice phonons can initiate the

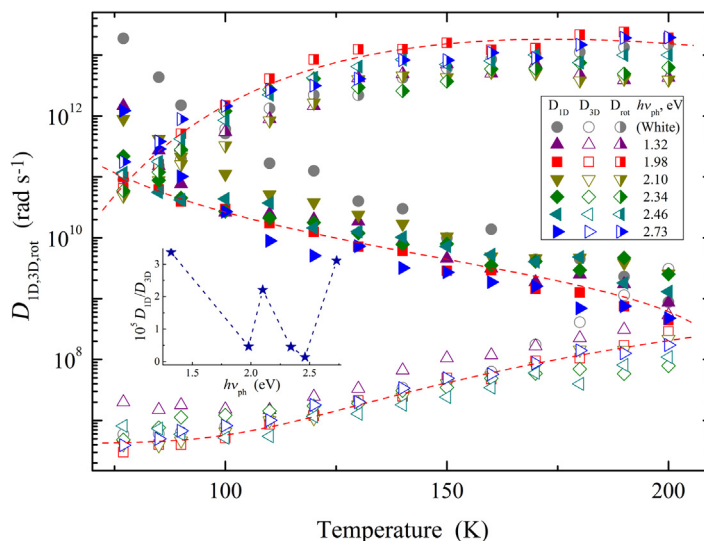


**FIGURE 9.19**

Temperature dependence of intrachain ( $D_{1D}$ , filled points), interchain ( $D_{3D}$ , open points), and rotational diffusion ( $D_{rot}$ , semi-filled points) coefficients of mobile charge carriers  $P_{mob}^{+\bullet}$  and  $mF_{mob}^{-\bullet}$  photoinduced in the PCDTBT:PC<sub>61</sub>BM composite by the polychromatic white and monochromatic light with different photon energy  $h\nu_{ph}$  determined at their appropriate unit concentration  $n_i$ . Top-to-bottom dashed lines show the dependences calculated from Eqn (9.19) with  $E_r = 0.102$  eV, Eqn (9.33) with  $E_{ph} = 0.049$  eV, and Eqn (9.35) with  $E_b = 0.067$  eV as well. The insert shows the anisotropy of polaron motion,  $A = D_{1D}/D_{3D}$  as function of  $h\nu_{ph}$ . The dash-dotted line shortly connects experimental points only for illustration to guide the eye.

observed change in its  $g$ -factor and diffusion anisotropy. An analogous decrease by two orders of magnitude in the anisotropy of polaron dynamics was detected under microwave-treatment of the P3HT:PC<sub>61</sub>BM composite [160]. This effect was explained by the increase of well-ordered polymer and methanofullerene clusters under such system modification that facilitates polaron diffusion, inhibits fullerene reorientation, and decreases interaction of charge carriers in photoinduced radical pairs. The formation of appropriate crystallites in an amorphous polymer matrix leads to the longer diffusion of charge carriers and higher light conversion efficiency. Thus, one can conclude better matrix planarity of the PCDTBT:PC<sub>61</sub>BM composite at illumination by such phonons that accelerate charge transport.

Intrachain polaron dynamics in the PCDTBT:PC<sub>61</sub>BM BHJ, as in the case of other polymer:fullerene composites, is characterized by a strong temperature dependence. Thus, the data presented in Fig. 9.19 can also be described in terms of polaron scattering on the phonons of crystalline lattice domains embedded into

an amorphous polymer matrix.  $E_{\text{ph}}$  obtained for polaron diffusion in the PCDTBT:PC<sub>61</sub>BM composite at different photon energy  $h\nu_{\text{ph}}$  is also summarized in Table 9.2. Figure 9.19 evidences that the  $D_{1\text{D}}$  obtained for polarons initiated by photons with, for example,  $h\nu_{\text{ph}} = 1.98$  eV follows Eqn (9.33) well, with  $E_{\text{ph}} = 0.049$  eV. This value lies near the energy of lattice phonons determined for various conjugated polymers (0.09–0.32 eV) [77] and plastic solar cells [91].

Interchain spin dynamics can also be analyzed in terms of the Hoesterey-Letson concept [121] of the trap-controlled charge hopping between polymer layers. The analysis of the data obtained, however, have showed that such an approach cannot be used for the interpretation of the  $D_{3\text{D}}(T)$  dependences presented in Fig. 9.19. These values, as well as methanofullerene reorientational diffusion coefficients  $D_{\text{rot}}(T)$ , can be explained in the frame of the Pike [185] and Elliott [186] models based on the carrier hopping over the energetic barrier  $E_{\text{b}}$  [187]. This may be due to a suggestion that the PC produced by the influence of light might be expected to have a large effect on the ac mobility of charge carriers [164]. The respective energies  $E_{\text{b}}$  required to activate polaron transverse diffusion in the PCDTBT:PC<sub>61</sub>BM composite are also summarized in Table 9.2.

Reorientational mobility of the methanofullerene cages can be described in the framework of the Marcus mechanism. Reorganization energies,  $E_{\text{r}}$ , obtained from Eqn (9.19) with  $t_{\text{r}} = 1.18$  eV [105] for charge carriers photoinitiated in the PCDTBT:PC<sub>61</sub>BM composite are also summarized in Table 9.2. The  $E_{\text{r}}$  values obtained exceed the energy required for activation of reorientation of C<sub>60</sub><sup>•-</sup> anions in polymethylmethacrylate (0.026 eV) and C<sub>70</sub> globes in cyclohexane [188], however, and lie near those determined for a motion of fullerene derivatives in conjugated polymer matrices [42,142]. It should be noted that the  $E_{\text{r}}$  value obtained for methanofullerene photoinitiated by achromatic (white) and monochromic (with the photon energy of 1.98 and 2.73 eV) light becomes compatible to that (0.224 eV) required for activating fullerene reorientational hopping or rotation in pure C<sub>60</sub> matrix [189]. The data described considers the dynamics of solitary polarons and fullerene. Undoubtedly, the interaction of these charge carriers with the nearest spins, lattice phonons, etc., may also affect their relaxation and, therefore, should also be taken into account when interpreting the results.

---

## 9.4 UTILIZATION OF POLYMER COMPOSITES IN SPIN-ASSISTED MOLECULAR ELECTRONICS

Conjugated polymers and their composites can successfully be used as a base for organic elements of molecular electronics and spintronics [4,8], including sensors for solution and gas components [190,191]. In order to construct such elements, the correlations of their electronic properties, selectivity, sensitivity, etc., with magnetic, relaxation, and dynamics properties of spin charge carriers should be analyzed.

Lubentsov et al. [192] found that PANI doped with sulfuric acid becomes sensitive to water molecules. The EPR data gave additional independent support for the conclusions presented above. X-band EPR spectrum of polarons in PANI sample is characterized by a symmetric Lorentzian solitary line with  $g_{\text{iso}} = 2.0031$ .

The saturation of the emeraldine base form of PANI with water vapor broadens its spectrum from 2.5 up to 9.0 G, however, its doping with the  $\text{H}_2\text{SO}_4$  molecules narrows the line down to 1.5 G; the saturation of the doped sample broadens its signal up to 5.2 G. At D-band EPR, its spectrum becomes Gaussian and the anisotropy of polaron's  $g$ -factor becomes more evident. At this wave band, the initial and modified samples reveal typical spectra of polarons with axially symmetrical distribution of unpaired electrons, which have effective relaxation times near  $3 \times 10^{-7}$  s. The saturation of the initial PANI sample with the water vapor causes the broadening of individual EPR lines from 4.6 up to 5.9 G, sustaining unchanged the  $g$ -tensor components,  $g_{\perp} = (g_{xx} + g_{yy})/2 = 2.00301$  and  $g_{\parallel} = g_{zz} = 2.00249$ . The doping of this sample with sulfuric acid is not found to lead to a noticeable change in its magnetic parameters. However, the exposure of doped PANI samples to a wet atmosphere resulted in the narrowing of the individual EPR components from 4.1 down to 3.2 G and, moreover, in a change of the spectrum shape when its  $g$ -tensor components shift to  $g_{\perp} = 2.00288$  and  $g_{\parallel} = 2.00271$ . This change in the spectrum shape indicates a significant rearrangement of the microenvironment of unpaired electrons localized on chains caused by the diffusion of water molecules into the polymer matrix bulk. Since the energy of the excited configuration of macromolecular systems is inversely proportional to the  $g$ -factor shift,  $\Delta E \propto (g_{\perp} - g_{\parallel})^{-1}$  [193,194], the above-mentioned change in the EPR spectrum shape may be explained by the growth of the ordering of the doped and water-vapor-saturated PANI, in accordance with the analogous conclusion made from the analysis of its X-ray phase data [192].

A highly sensitive and selective polymer sensor for water molecules with polyvinyl chloride matrix treated by fuming sulfuric acid was also constructed and studied by both the EPR and conductometry methods [195]. This material exhibited a Lorentzian weak EPR singlet with  $\Delta B_{\text{pp}} = 5.4$  G and  $g = 2.0031$  at room temperature, characteristic of  $\pi$ -electron systems. This is accompanied by the increase in the film conductivity, especially under its contact with the water molecules. The line width and signal intensity changed weakly while the temperature decreased down to  $T = 77$  K. Magnetic parameters of this material appeared to be close to those of solitons formed in a small amount of *trans*-polyacetylene, usually presented in *cis*-polyacetylene [112]. Thus, the change in electronic and paramagnetic properties of the film can be explained by dehydrochlorination during its oleum treatment with the formation of *trans*-polyacetylene regions with unpaired electrons in neutral solitons,  $[-\text{CHCl}-\text{CH}_2-]_m \rightarrow [-\text{CHCl}-\text{CH}_2-]_m - [\text{CH}=\text{CH}=\text{CH}=\text{CH}-]_k$ . Due to their status as weak electron acceptors, water molecules can partially accept the electron density from the solitary charge carriers [112], on the surface or in the bulk of the film, thus providing  $p$ -type conductivity of the sample. When the water molecules diffuse into the polymer bulk, they form bridge-type hydrogen bonds between the

conjugated chains. As a result, the solitons acquire a positive charge in the *trans*-polyacetylene fragments. Moreover, solitons which may occur in the spreading water associate [196] may also participate in charge transfer between polymer chains. Thus, the macroconductivity of the sample contacting water vapor increases considerably as a result of both intra- and interchain charge transfer. Other molecules are not able to form such associations which determines the selectivity of the sensor to water molecules only.

There were other utilizations of conducting polymers as an active matrix of organic sensors [190,197–199], Schottky diodes [200–202], etc. Since charge carriers in conjugated polymers and their composites possess spin, this feature can be used for creation of spintronic devices with spin-assisted electronic properties [4]. It was previously demonstrated that since both the charge carriers exchangeable spin-flip, their further recombination becomes dependent on their dynamics, number, polarization, and mutual separation. For large separations, when thermal energy exceeds the interaction potential, the charges are considered as noninteracting. Once the carriers become nearer than the inverted Coulombic interaction potential, their wave functions overlap and exchange interactions become non-negligible. This can originate a formation of singlet or triplet excitons in organic semiconductors. Such excited states can be detected in organic systems using optical (fluorescence and phosphorescence) and/or magnetic resonance [203] methods. However, other absorbing species are generally present in such systems, namely polaronic charge carriers, which themselves introduce efficient subgap optical transitions. Thus, a clear assignment to triplet excitations is not always possible.

The EPR method was proved [203] to be the most effective direct tool able to reveal the underlying nature of spin carriers excited in such systems. This method allows one to study various materials with weak spin-orbit coupling, where the differences in lifetime between the three excited-state triplet sublevels give rise to a spin-dependent buildup of macroscopic polarization [204], including spin charge carriers stabilized in conjugated polymers [77,81] and photoinduced in their fullerene-based compositions for photovoltaic applications [8,91]. The interaction between polarons and excitons increases under paramagnetic resonance [205]. Thus, singlet excitons are quenched to promote nonradiative decay to the ground state. The study of exchange effects in composites of two or more spin subsystems and their ingredients are expected to provide a good framework for understanding the underlying nature of exchange interactions among spins in such systems with different polaron lattices. However, there is no simple picture which would clarify spin resonance-assisted processes in organic semiconductors governed by spin-dependent exciton–charge interactions and consistent with the spin-dependent polaron pair recombination model [206]. The previously presented data prove that such processes are also governed by the energy of initiating photons due mainly to inhomogeneous distribution of polymer and fullerene domains in BHJ. It should also be noted that only very few data are published on molecular magnetic resonance spectroscopy related to actual problems in organic electronics.

The interaction between spin charge carriers affects electronic properties of organic polymers with spin charge carriers. In order to study exchange interaction in a multispin composite, P3DDT (previously used as an effective polymer matrix of organic solar cells) [42,154,155,157,158] was selected as one of a model spin reservoir [102]. PANI-ES was chosen to be a second suitable spin subsystem for the study of spin-assisted charge transfer in its composite with nanomodified P3DDT. The existence of two types of PC, namely polarons trapped on chains in amorphous polymer phase and polarons diffusing along and between chains of crystalline polymer clots was found [77,113] to be in typical PANI-ES. Polarons diffusing along polymer chains in such regions appeared to be accessible for triplet excitations injected into the polymer bulk. It was shown above that spin exchange interaction in polymer:fullerene composites leads to collision of domestic and guest spins, dramatically changing their magnetic, relaxation, and electronic dynamics parameters. This effect was not registered in main PANI-ES samples [77,113] except PANI:TSA, due to more accessibility of its spin ensemble for guest spins [100,101,207]. Unlike other PANI-ES, the latter system becomes Fermi glass with high density of states near the Fermi energy level  $\varepsilon_F$  [208,209] and its dc conductivity follows the 3D Mott's variable range hopping model [210]. This is why PANI:TSA demonstrates better material quality and therefore more metallic behavior with extended states near  $\varepsilon_F$ .

This section considers the results of a detailed LEPR study of main magnetic resonance parameters of polarons stabilized in highly doped PANI:TSA, as well as polarons and fullerene anion radicals background photoinduced in the PANI:TSA/P3DDT:PC<sub>61</sub>BM composite in a wide temperature range. Such study was expected to schedule the strategy of spin handling in organic complex nanocomposites for the further construction of novel molecular devices with spin-assisted electronic transport.

Initial PANI:TSA samples exhibit single X-band EPR spectrum (central spectrum shown in Fig. 9.20) attributed to polarons  $P_1^{\bullet+}$  with  $g_{iso} = 2.0028$  stabilized in its backbone. This value remains almost unchanged within a wide temperature range typical for crystalline high-conductive solids [77,211,212]. The P3DDT:PC<sub>61</sub>BM subcomposite does not demonstrate any EPR spectrum without light irradiation. When illuminated by visible light, it exhibits superposed lines attributed to positively charged diffusing polarons  $P_2^{\bullet+}$  with  $g_{iso} = 2.0018$  and negatively charged anion radicals  $mF_{61}^{\bullet-}$  with  $g_{iso} = 1.9997$  rotating around its own main axis (lower spectrum in Fig. 9.20). When combined, these systems form the PANI:TSA/P3DDT:PC<sub>61</sub>BM composite, of which the dark EPR spectrum mainly demonstrates contribution of polarons  $P_1^{\bullet+}$  (upper spectrum in Fig. 9.20). Under light illumination its shape and intensity change, as shown in Fig. 9.20. Such transformation was interpreted as the result of the appearance of photoinduced quasipair  $P_2^{\bullet+} - mF_{61}^{\bullet-}$  in its latter subsystem. In this case, two spin subsystems appear in the PANI:TSA/P3DDT:PC<sub>61</sub>BM composite, containing  $P_1^{\bullet+}$  and  $P_2^{\bullet+} - mF_{61}^{\bullet-}$  spin ensembles. As illumination is turned off, the spectra originated from the polarons  $P_1^{\bullet+}$  stabilized in PANI:TSA composite and polarons  $P_2^{\bullet+}$

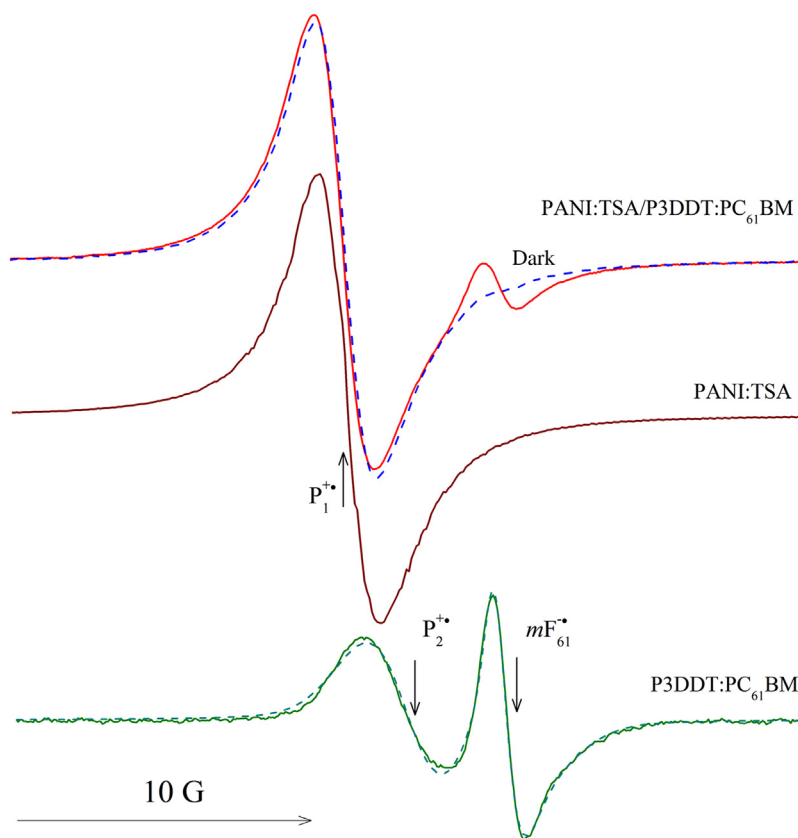


**FIGURE 9.20**

X-band LEPR spectra of the PANI:TSA/P3DDT:PC<sub>61</sub>BM composite illuminated by white light at  $T = 90$  K (above) as well as its contributions due to polarons  $P_1^{\bullet+}$  stabilized in PANI:TSA (center) and radical quasipairs  $P_2^{\bullet+} - mF_{61}^{\bullet-}$  (below). The above and below dashed lines show EPR spectra obtained in the absence of illumination and were calculated using  $\Delta B_{pp}^P = 2.67$  G,  $\Delta B_{pp}^{mF} = 1.17$  G, and  $[P_2^{\bullet+}]/[mF_{61}^{\bullet-}] = 2.0$ , respectively. The positions of PC are also shown.

pinned in P3DDT:PC<sub>61</sub>BM system are only detected. In order to study charge-separated states and spin–spin interactions in this composite, its sum spectrum was tentatively deconvoluted [102]. As in case of other organic systems [42,126,131,142,213,214], this allowed the obtaining of separate magnetic resonance parameters for all PC stabilizing in initial polymers, and their appropriate composites for analyzing of these parameters in PANI:TSA/P3DDT:PC<sub>61</sub>BM BHJ.

Figure 9.21a shows temperature dependences of the line width  $\Delta B_{pp}$  of polarons  $P_1^{\bullet+}$  stabilized in the PANI:TSA,  $P_2^{\bullet+}$  photoinitiated in P3DDT:PC<sub>61</sub>BM BHJ, and those values obtained for the darkened and illuminated PANI:TSA/P3DDT:PC<sub>61</sub>BM

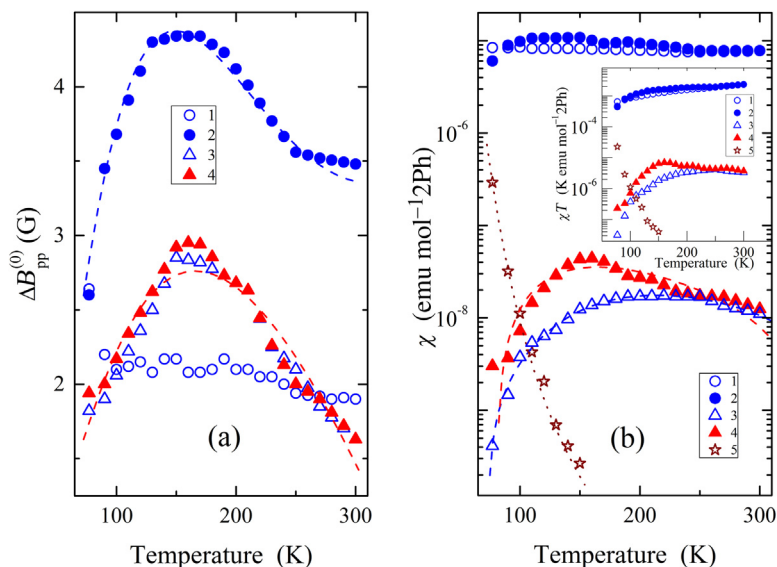


**FIGURE 9.21**

Temperature dependence of peak-to-peak line width  $\Delta B_{pp}^{(0)}$  (a), spin susceptibility  $\chi$  and  $\chi T$  product (inserts) (b) determined for domestic polarons  $P_1^{\bullet+}$  stabilized in the initial PANI:TSA backbone (1), PANI:TSA/P3DDT:PC<sub>61</sub>BM composite (2), polarons  $P_2^{\bullet+}$  stabilized in the darkened (3) and irradiated by white light (4) PANI:TSA/P3DDT:PC<sub>61</sub>BM composite, as well as methanofullerene radical anions  $mC_{61}^{\bullet-}$  (5) photoinitiated in the composite. The upper (0) symbol in  $\Delta B_{pp}^{(0)}$  implies that this parameter is to be measured far from the spectrum microwave saturation. Dashed lines in (a) show the dependences calculated from Eqn (9.18) with  $\omega_{hop}^0 = 1.2 \times 10^9 \text{ s}^{-1}$ ,  $E_r = 0.006 \text{ eV}$  (above line),  $\omega_{hop}^0 = 1.3 \times 10^9 \text{ s}^{-1}$ ,  $E_r = 0.012 \text{ eV}$  (below line),  $J_{ex} = 0.110 \text{ eV}$ , and  $n_p = 1.2 \times 10^{-4}$ . Above and below dashed lines in (b) show the dependences  $\chi_{ECP}$  calculated from Eqn (9.4) with  $C = 1.0 \times 10^{-8} \text{ emu mol}^{-1} \text{ 2Ph}$ ,  $a_d = 0.98$ ,  $J = 0.015 \text{ eV}$  and  $C = 9.8 \times 10^{-7} \text{ emu mol}^{-1} \text{ 2Ph}$ ,  $a_d = 0.98$ ,  $J = 0.010 \text{ eV}$ , respectively. The dotted line shows the dependences calculated from Eqn (9.13) with  $E_r = 0.050 \text{ eV}$ .

composite. The EPR line width for both polarons stabilized in these systems depends on the structure of polymer matrix. Indeed, the heating of the initial PANI:ES sample is accompanied by a monotonic decrease in  $\Delta B_{pp}$  of polarons  $P_1^{\bullet+}$  stabilized on its chains. However, this parameter for polarons  $P_2^{\bullet+}$  photoinitiated in the P3DDT:PC<sub>61</sub>BM BHJ shows an opposite temperature dependence when compared with that for polarons  $P_1^{\bullet+}$  (Fig. 9.21). This effect can be explained by different interaction of these polarons with appropriate polymer lattice. The formation of the PANI:TSA/P3DDT:PC<sub>61</sub>BM composite does not noticeably changes the line width for PC  $P_1^{\bullet+}$ . However, this originates the change in the temperature dependence of  $P_2^{\bullet+}$  charge carriers photoinitiated in the P3DDT matrix.

Spin properties of both polaronic reservoirs in this composite are strongly governed by the morphology of PANI chains which determines their main electronic properties [215]. Figure 9.21 shows that once both polymers form a composite, their polarons  $P_1^{\bullet+}$  and  $P_2^{\bullet+}$  start to demonstrate extreme temperature-dependent line widths characterized by appropriate critical point  $T_{ex} \approx 150$  K. A similar effect was observed in the EPR study of exchange interaction for polarons with guest oxygen biradicals  $\bullet O - O \bullet$  in highly doped PANI:HCl [94] and PANI:TSA [100,101]. This effect was identified [102] as exchange interaction in quasipairs formed by the guest spins with domestic polarons hopping across energy barrier  $E_b$ . Thus, the data, presented in Fig. 9.3b can be described in terms of the polaron exchange interaction hopping in the closely located solitary polymer chains.

The collision of both type spins should additionally broaden the absorption term of the EPR line expressed by Eqn (9.18). Indeed, this equation fits well the line width of both the polarons  $P_1^{\bullet+}$  and  $P_2^{\bullet+}$  at  $n_p = 1.2 \times 10^{-4}$  obtained for P3DDT:PC<sub>61</sub>BM BHJ [42] and  $E_r = 0.006$  and  $0.012$  eV, respectively (see Fig. 9.21a).

Figure 9.21b shows the temperature dependence of spin susceptibility  $\chi$  with contributions by polarons  $P_1^{\bullet+}$ ,  $P_2^{\bullet+}$  and methanofullerene radical anions  $mF_{61}^{\bullet-}$  forming spin quasipairs in the P3DDT:PC<sub>61</sub>BM and PANI:TSA/P3DDT:PC<sub>61</sub>BM BHJ. The analysis of the above data was performed in the framework of the above-mentioned ECP model for an ensemble of  $N_s/2$  interacting spin pairs with an uniform distribution of intrapair exchange characterized by coefficient  $J$ .  $\chi_{ECP}(T)$  dependences calculated from Eqn (9.4) with appropriate  $C$ ,  $a_d$ , and  $J$  values, which are presented in Fig. 9.21b. The model used provides an excellent fit to all the experimental data sets within all temperature ranges used.

Spin susceptibility determined for polarons  $P_1^{\bullet+}$  is close to that obtained for PANI highly doped by sulfonic [208] and hydrochloric [216] acids. The appropriate term of Eqn (9.4) is normally a function of distance. When polymer chains vibrate,  $J$  for polarons diffusing along neighboring chains would oscillate and should be described by a stochastic process [217]. However, such effect appears at low temperatures, when  $k_B T < J$ . Thus, it can be neglected within all temperature ranges used. Nevertheless, this constant increases as polarons  $P_1^{\bullet+}$  start to interact with polarons  $P_2^{\bullet+}$  in the composite. This is additional evidence of the strong interaction of polarons stabilized in both PANI:TSA and P3DDT matrices. When the Fermi energy  $\varepsilon_F$  is close to the mobility edge, the temperature dependence of spin susceptibility gradually changes from Curie-law behavior  $\chi_C \propto 1/T$  to temperature-independent Pauli-type behavior with increasing temperature. Corresponding density of states  $n(\varepsilon_F)$  for both spin directions per monomer unit at  $\varepsilon_F$  can be determined from the analysis of the  $\chi(T)T$  dependence for all polarons stabilized in both polymers (see insert in Fig. 9.21b). Krinichnyi et al. [100,101] showed that the transition-state approach (TSA)-treated system is characterized by higher  $n(\varepsilon_F)$  compared with other PANI-ES. This can be explained by the difference in their metallic properties and also by onsite electron–electron interaction [218].

Spin susceptibility obtained for methanofullerene radical anions  $mF_{61}^{\bullet-}$  photoinduced in the composite demonstrates sharper temperature dependence (Fig. 9.21b). This can be explained by the fast recombination of  $P_2^{\bullet+} - mF_{61}^{\bullet-}$  quasipairs. Effective paramagnetic susceptibility of this charge carrier should inversely depend on the probability of their recombination, which in turn is governed by polaron Q1D hopping between polymer units [219]. In this case, the  $\chi$  value should follow Eqn (9.13). The dependence calculated from Eqn (9.13) with  $E_r = 0.050$  eV is also presented in Fig. 9.21b. Therefore, the decay of long-lived charge carriers originated from initial spin pairs photoinduced in the PANI:TSA/P3DDT:PC<sub>61</sub>BM composite can indeed be described in terms of the above model. This process is also determined by the structure and morphology of a radical anion and its environment in a polymer backbone. The use, for example, of PCDTBT instead of P3DDT and PC<sub>71</sub>BM instead of PC<sub>61</sub>BM should facilitate the excitation to reach the polymer:fullerene interface for charge separation before it becomes spatially self-localized and bound within an exciton [36]. Therefore, the main properties of an exciton are irrelevant to ultrafast charge transfer and do not limit effective charge transfer in such composites.

Figure 9.21b shows that the spin susceptibility of polarons  $P_1^{\bullet+}$  stabilized in the initial PANI:TSA sample is characterized by weak temperature dependence without any anomaly. Interaction between neighboring polarons provokes extremal  $\chi$  versus  $T$  dependence obtained for both polarons  $P_1^{\bullet+}$  and  $P_2^{\bullet+}$  (see Fig. 9.21b). Such interaction increases the overlapping of their wave functions and the energy barrier which overcomes the polaron crossing BHJ. This affects the polaron intrachain mobility and, therefore, the probability of its recombination with a fullerene anion.

There are several relaxation and dynamic processes, for example, dipole–dipole, hyperfine, exchange interactions between PC of different spin-packets, etc., which cause the shortening of spin relaxation times and, hence, the change of the shape of an EPR line. Thus, the study of spin relaxation can supply us with important information about spin-assisted electronic processes carried out in the PANI:TSA/P3DDT:PC<sub>61</sub>BM composite. As previously demonstrated, the initial EPR line width is oppositely proportional to the spin–spin relaxation time in accordance with Eqn (9.17). Spin–lattice relaxation also shortens the lifetime of a spin state and broadens the line. Electron relaxation of spin charge carriers stabilized in, for example, PANI-SA [212,220], PANI:TSA [100,101,207], and P3DDT [42,154,155,157,158] was shown to be strongly defined by the structural, conformational, and electronic properties of their microenvironment. Thus, it would be important to analyze also how spin exchange affects spin–lattice relaxation of polarons in polymer matrix.

Figure 9.22 exhibits temperature dependencies of  $T_1$  and  $T_2$  values for polarons  $P_1^{\bullet+}$  stabilized in the PANI:TSA and PANI:TSA/P3DDT:PC<sub>61</sub>BM samples. Spin–spin relaxation was shown to be governed by the spin–spin exchange interaction. Spin–lattice relaxation time of the samples was measured at room temperature to be  $0.45 \times 10^{-7}$  and  $0.33 \times 10^{-7}$  s, respectively. These values are

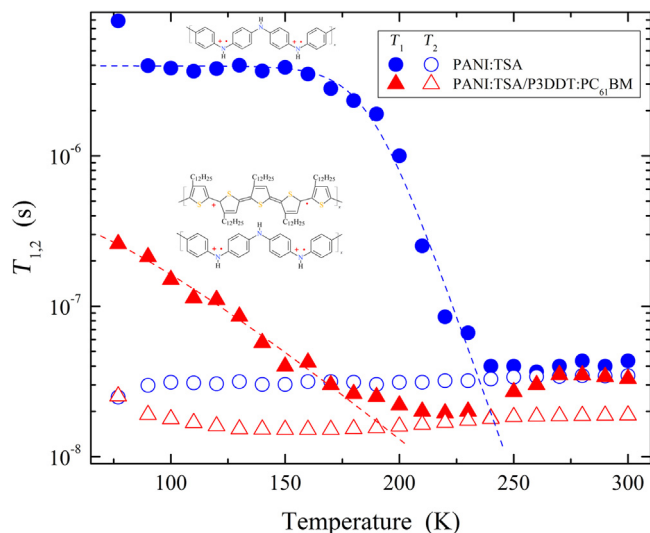


**FIGURE 9.22**

Temperature dependence of spin–lattice,  $T_1$ , and spin–spin,  $T_2$ , relaxation times determined for polarons  $P_1^{\bullet+}$  stabilized in the PANI:TSA backbone and respective PANI:TSA/P3DDT:PC<sub>61</sub>BM composite without light illumination.

in good agreement with  $T_1 = 0.98 \times 10^{-7}$  s obtained by Wang et al. [221] for highly doped PANI:HCl. It is seen that spin–lattice relaxation of  $P_1^{\bullet+}$  stabilized in the initial PANI:TSA changes weakly as the temperature increases to  $T \sim 180$  K, which is typical for organic ordered systems. This process accelerates suddenly near  $T \sim 210$  K, possibly due to a phase transition, and then plateaus at higher temperatures. As  $P_1^{\bullet+}$  start to interact with  $P_2^{\bullet+}$  in the PANI:TSA/P3DDT:PC<sub>61</sub>BM composite, their spin–lattice relaxation strongly accelerates and becomes more temperature-dependent (Fig. 9.22). This is more evidence of the exchange between polarons stabilized in different neighboring polymer chains. Figure 9.22 demonstrates that  $T_1$  tends to  $T_2$  at high temperatures. This is typical for organic systems of lower dimensionality and can be explained by the defrosting of macromolecular dynamics.

Therefore, light excitation of P3DDT:PC<sub>61</sub>BM BHJ in the PANI:TSA/P3DDT:PC<sub>61</sub>BM composite leads to charge separation and transfer from a P3DDT chain to methanofullerene globes. This is accompanied by the appearance of polarons  $P_2^{\bullet+}$  on the P3DDT backbone and anion radicals  $mF_{61}^{\bullet-}$  located between polymer chains. Polarons  $P_2^{\bullet+}$  moving in P3DDT solitary chains interact with  $P_1^{\bullet+}$  stabilized on neighboring PANI:TSA chains due to overlapping of their wave functions. Such interaction is governed mainly by nanomorphology of the conducting form of PANI:TSA subdomains. Exchange interaction and polaron relaxation are governed by Q1D activation hopping of  $P_2^{\bullet+}$  along domestic polymer chains.

Paramagnetic susceptibility of both polarons is described in frames of the model of exchange-coupled spin pairs differently distributed in appropriate polymer matrices. This deepens the overlapping of wave functions for these charge carriers and leads to an increase in the energy barrier which overcomes the polaron under its crossing through a BHJ. It is evident that EPR investigation of spin properties of domestic and photoexcited PC in a complex polymer:dopant/polymer:fullerene composite and its ingredients allows for control of its texture and other structural properties. This can open new opportunities in the creation of flexible and scalable organic molecular devices with spin-assisted electronic properties. They suggest an important role played by interchain coupling of different spin charge carriers on a handling of charge transfer through BHJ of the PANI:TSA/P3DDT:PC<sub>61</sub>BM and analogous multispin composites. Photoinitiation of additional spins allows the making such handling more delicate, which is a critical strategy in creating systems with spin-assisted charge transfer. The correlations established between dynamics, electronic, and structural parameters of these systems can be used for controllable synthesis of various organic spintronic devices with optimal properties.

---

## 9.5 SUMMARY

Light excitation of BHJ formed by organic polymer macromolecules with fullerene globes leads to fast formation of two long-living noninteracting PC with rhombic symmetry, namely the positively charged polaron  $P^{+\bullet}$  (hole) on the polymer backbone and the negatively charged fullerene anion radical  $F^{-\bullet}$  located between polymer chains. The main magnetic resonance, relaxation, and dynamic parameters of these charge carriers are governed by the structure, morphology, and ordering of BHJ, as well as by the energy of excited photons. Weak interaction of these charge carriers originated from the former radical quasipairs, stipulating a difference in their dynamics, interaction with their own microenvironment, and, hence, in their magnetic resonance parameters. Spatial separation due to charge distribution over the full fullerene globule additionally reduces the recombination rate of these charge carriers. This allows one to separately determine all their parameters.

LEPR spectroscopy was proved to be the powerful direct tool for detailed study of spin charge carriers and the processes that occurred with their participation. It is characterized, as other physical methods, by advantages and limitations. This is why the LEPR data should be discussed in comparison with those determined by other methods. The method becomes more informative at millimeter wave bands EPR. Therefore, complex organic composites should be investigated with the multifrequency EPR method. Polarons and fullerene anion radicals photoinitiated tend to recombine, and the probability of such a process depends on the rate of polaron diffusion, the energy of initiating photons, and properties of

their microenvironment. Illumination initiates the appearance in a polymer matrix of spin traps, whose number and energy depth are governed by the photon energy. Such selectivity can be used, for example, in plastic photovoltaic sensors. A part of charge carriers can be captured by such traps that decreases the conversion efficiency of a composite. The data obtained suggest the impact of the polymer ring-torsion and layer motions on the charge initiation, separation, and diffusion in disordered organic composites.

Optimization of the structure of polymer matrix and nanoadditives allows the improvement of the electronic properties of appropriate composite. The substitution, for example, PC<sub>61</sub>BM by *bis*-PC<sub>62</sub>BM increases the planarity and ordering of the P3HT matrix. It also decreases the number of traps, facilitates local molecular vibrations, and, therefore, accelerates charge transfer through a BHJ. On the other hand, the replacement of P3AT matrix by PCDTBT also increases the planarity and crystallinity of the polymer matrix, suppresses the appearance of spin traps, facilitates local site molecular vibrations that accelerates charge transfer through BHJ, minimizes the energy loss, and, therefore, increases the power-conversion efficiency. The illumination of this sample by photons with energy lying near the polymer band gap also decreases the number of such traps. This significantly reduces the anisotropy of polaron dynamics in such layer-ordered Q2D matrix due to collective interaction of charge carriers. This more noticeably affects the splitting of the polarons'  $\sigma$ ,  $\pi$ , and  $\sigma^*$  levels, increases the number of initial spin quasipairs, broadens the LEPR spectrum, slightly reduces spin interaction with the polymer network, and increases diffusion anisotropy in the polymer network.

A polaron diffusing along a polymer chain interacts with the spin of a counter anion radical which acts as a nanoscopic probe of such dynamics. This causes a variety of mechanisms of charge transport in appropriate polymer:fullerene composite. Charge transfer is governed by polaron scattering on the lattice phonons of crystalline domains embedded into an amorphous polymer matrix and its activation hopping between polymer layers. Fullerene cages reorientate between polymer units according to the Marcus mechanism. These spin-assisted processes are governed mainly by the structure of ingredients of a composite as well as by the nature and dynamics of photoinduced charge carriers. The specific structure of the polymer matrix changes the energy levels of the appropriate composite and shifts the competition between excited states in its BHJ. It was proven that the charge transfer in the polymer/polymer:fullerene composite can be handled by the interaction of polarons stabilized in both polymer backbones with fullerene anion radicals.

The LEPR study described contributes to a better understanding of the correlations of polymer:fullerene and polymer/polymer:fullerene composites and appropriate ingredients with their structural, magnetic, and transport properties. Such direct correlations seem to be important for a further development and optimization of plastic photovoltaic devices. The results presented suggest an important role played by interchain coupling of different spin ensembles on a handling of

charge transfer in BHJ. Initiation of spins by different photons allows making such handling more delicate, which is a critical strategy in creating optimal systems with spin-assisted charge transfer. Solitary spin carriers trapped in bulk of darkened polymer matrix can, in principle, be used as elemental dots for quantum computing. Since coherent spin dynamics in such organic BHJ is anisotropic, our strategy seems to make it possible to obtain complex correlations of anisotropic electron transport and spin dynamics from multifrequency EPR study for the further design of progressive molecular electronics and spintronics.

---

## ACKNOWLEDGMENTS

The author gratefully thanks Professor Dr H.-K. Roth and Dr E.I. Yudanova for the fruitful discussions, Dr B. Wessling for collaboration, Dr N.N. Denisov for the assistance in EPR experiments. The partial support by the Russian Foundation of Basic Researches, Grant No. 12-03-00148, and the Program of Fundamental Researches of Presidium of the Russian Academy of Sciences is also gratefully acknowledged.

---

## REFERENCES

- [1] Tjong SC, Mai Y-W, editors. *Physical properties and applications of polymer nanocomposites*. Cambridge: Woodhead Publishing; 2010.
- [2] Tjong SC, editor. *Polymer composites with carbonaceous nanofillers: properties and applications*. Weinheim: Wiley-VCH Verlag; 2012.
- [3] Zhang G, Manjooan N, editors. *Nanofabrication and its application in renewable energy*. Cambridge: The Royal Society of Chemistry; 2014.
- [4] Xu Y, Awschalom DD, Nitta J, editors. *Handbook of spintronics*. Berlin: Springer-Verlag; 2015.
- [5] Sun SS, Sariciftci NS, editors. *Organic Photovoltaics: mechanisms, materials, and devices (Optical Engineering)*. Boca Raton, FL: CRC Press; 2005.
- [6] Poortmans J, Arkhipov V, editors. *Thin film solar cells: fabrication, characterization and applications*. West Sussex: Wiley; 2006.
- [7] Pagliaro M, Palmisano G, Ciriminna R. *Flexible solar cells*. Weinheim: Wiley-WCH; 2008.
- [8] Brabec C, Scherf U, Dyakonov V, editors. *Organic photovoltaics: materials, device physics, and manufacturing technologies, vol. 1*. Weinheim: Wiley-VCH; 2014.
- [9] Shaheen SE, Brabec CJ, Sariciftci NS, Padinger F, Fromherz T, Hummelen JC. 2.5% efficient organic plastic solar cells. *Appl Phys Lett* 2001;78:841–3.
- [10] Hwang IW, Soci C, Moses D, Zhu ZG, Waller D, Gaudiana R, et al. Ultrafast electron transfer and decay dynamics in a small band gap bulk heterojunction material. *Adv Mater* 2007;19:2307–12.
- [11] Kraabel B, McBranch D, Sariciftci NS, Moses D, Heeger AJ. Ultrafast spectroscopic studied of photoinduced electron-transfer from semiconducting polymers to C-60. *Phys Rev B* 1994;50:18543–52.

- [12] Brabec CJ, Zerza G, Cerullo G, DeSilvestri S, Luzatti S, Hummelen JC, et al. Tracing photoinduced electron transfer process in conjugated polymer/fullerene bulk heterojunctions in real time. *Chem Phys Lett* 2001;340:232–6.
- [13] Banerji N, Cowan S, Leclerc M, Vauthey E, Heeger AJ. Exciton formation, relaxation, and decay in PCDTBT. *J Am Chem Soc* 2010;132:17459–70.
- [14] Pivrikas A, Sariciftci NS, Juska G, Osterbacka R. A review of charge transport and recombination in polymer/fullerene organic solar cells. *Progress Photovoltaics* 2007;15:677–96.
- [15] Kubis P, Lucera L, Machui F, Spyropoulos G, Cordero J, Frey A, et al. High precision processing of flexible P3HT/PCBM modules with geometric fill factor over 95%. *Org Electron* 2014;15:2256–63.
- [16] Green MA, Emery K, Hishikawa Y, Warta W, Dunlop ED. Solar cell efficiency tables (version 44). *Progress Photovoltaics: Res Appl* 2014;22:701–10.
- [17] Halls JJM, Cornil J, Dos Santos DA, Silbey R, Hwang DH, Holmes AB, et al. Charge- and energy-transfer processes at polymer/polymer interfaces: a joint experimental and theoretical study. *Phys Rev B* 1999;60:5721–7.
- [18] Brabec CJ, Winder C, Sariciftci NS, Hummelen JC, Dhanabalan A, van Hal PA, et al. A low-bandgap semiconducting polymer for photovoltaic devices and infrared emitting diodes. *Adv Funct Mater* 2002;12:709–12.
- [19] Brabec CJ, Cravino A, Meissner D, Sariciftci NS, Fromherz T, Rispeins MT, et al. Origin of the open circuit voltage of plastic solar cells. *Adv Funct Mater* 2001;11:374–80.
- [20] Koster LJA, Mihailetchi VD, Ramaker R, Blom PWM. Light intensity dependence of open-circuit voltage of polymer:fullerene solar cells. *Appl Phys Lett* 2005;86:123509.
- [21] Koster LJA, Mihailetchi VD, Blom PWM. Ultimate efficiency of polymer/fullerene bulk heterojunction solar cells. *Appl Phys Lett* 2006;88:093511–13.
- [22] Wu P-T, Ren G, Jenekhe SA. Crystalline random conjugated copolymers with multiple side chains: tunable intermolecular interactions and enhanced charge transport and photovoltaic properties. *Macromolecules* 2010;43:3306–13.
- [23] Lenes M, Wetzelaer GJAH, Kooistra FB, Veenstra SC, Hummelen JC, Blom PWM. Fullerene bisadducts for enhanced open-circuit voltages and efficiencies in polymer solar cells. *Adv Mater* 2008;20:2116–19.
- [24] Li G, Shrotriya V, Huang J, Yao Y, Moriarty T, Emery K, et al. High-efficiency solution processable polymer photovoltaic cells by self-organization of polymer blends. *Nat Mater* 2005;4:864–8.
- [25] Huang JH, Li KC, Chien FC, Hsiao YS, Kekuda D, Chen PL, et al. Correlation between exciton lifetime distribution and morphology of bulk heterojunction films after solvent annealing. *J Phys Chem C* 2010;114:9062–9.
- [26] Jarzab D, Cordella F, Lenes M, Kooistra FB, Blom PWM, Hummelen JC, et al. Charge transfer dynamics in polymer-fullerene blends for efficient solar cells. *J Phys Chem B* 2009;113:16513–17.
- [27] Dyer-Smith C, Reynolds LX, Bruno A, Bradley DDC, Haque SA, Nelson J. Triplet formation in fullerene multi-adduct blends for organic solar cells and its influence on device performance. *Adv Funct Mater* 2010;20:2701–8.
- [28] Berton N, Ottone C, Labet V, de Bettignies R, Bailly S, Grand A, et al. New alternating copolymers of 3,6-carbazoles and dithienylbenzothiadiazoles: synthesis, characterization, and application in photovoltaics. *Macromol Chem Phys* 2011;212:2127–41.

- [29] Kim J, Yun MH, Kim GH, Kim JY, Yang C. Replacing 2,1,3-benzothiadiazole with 2,1,3-naphthothiadiazole in PCDTBT: towards a low bandgap polymer with deep HOMO energy level. *Polym Chem* 2012;3:3276–81.
- [30] Blouin N, Michaud A, Leclerc M. A low-bandgap poly(2,7-carbazole) derivative for use in high-performance solar cells. *Adv Mater* 2007;19:2295–300.
- [31] Choy WCH, editor. *Organic solar cells: materials and device physics*. London: Springer; 2013.
- [32] Ostroverkhova O, editor. *Handbook of organic materials for optical and (Opto) Electronic devices: properties and applications*, vol. 39. New York, NY: Elsevier; 2013.
- [33] Huh YH, Park B. Interface-engineering additives of poly(oxyethylene tridecyl ether) for low-band gap polymer solar cells consisting of PCDTBT:PCBM70 bulk-heterojunction layers. *Opt Express* 2013;21:A146–56.
- [34] Lu XH, Hlaing H, Germack DS, Peet J, Jo WH, Andrienko D, et al. Bilayer order in a polycarbazole-conjugated polymer. *Nat Commun* 2012;3. Available from: <http://dx.doi.org/10.1038/ncomms1790>.
- [35] Park SH, Roy A, Beaupre S, Cho S, Coates N, Moon JS, et al. Bulk heterojunction solar cells with internal quantum efficiency approaching 100%. *Nat Photon* 2009;3:297–302.
- [36] Moon JS, Jo J, Heeger AJ. Nanomorphology of PCDTBT:PC<sub>70</sub>BM bulk heterojunction solar cells. *Adv Energy Mater* 2012;2:304–8.
- [37] Liu JG, Chen L, Gao BR, Cao XX, Han YC, Xie ZY, et al. Constructing the nanointerpenetrating structure of PCDTBT:PC70BM bulk heterojunction solar cells induced by aggregating of PC70BM via mixed-solvent vapor annealing. *J Mater Chem A* 2013;1:6216–25.
- [38] Gutzler R, Perepichka DF.  $\pi$ -Electron conjugation in two dimensions. *J Am Chem Soc* 2013;135:16585–94.
- [39] Bässler H. Charge transport in disordered organic photoconductors a Monte Carlo simulation study. *Phys Status Solidi (B)* 1993;175:15–56.
- [40] Krinichnyi VI, Troshin PA, Denisov NN. The effect of fullerene derivative on polaronic charge transfer in poly(3-hexylthiophene)/fullerene compound. *J Chem Phys* 2008;128:164715/01–164715/07.
- [41] Krinichnyi VI, Troshin PA, Denisov NN. Structural effect of fullerene derivative on polaron relaxation and charge transfer in poly(3-hexylthiophene)/fullerene composite. *Acta Mater* 2008;56:3982–9.
- [42] Krinichnyi VI, Yudanov EI, Spitsina NG. Light-induced EPR study of poly(3-alkylthiophene)/fullerene composites. *J Phys Chem C* 2010;114:16756–66.
- [43] Konkin A, Ritter U, Scharff P, Mamin G, Aganov A, Orlinskii S, et al. W-band ESR study on photo-induced ion radical formation in solid films of mono- and di-fullerenes embedded in conjugated polymers. *Carbon* 2014;77:11–17.
- [44] Ginder JM, Epstein AJ, MacDiarmid AG. Ring-torsional polarons in polyaniline and polyparaphenylene sulfide. *Synth Metals* 1991;43:3431–6.
- [45] Lee JM, Park JS, Lee SH, Kim H, Yoo S, Kim SO. Selective electron- or hole-transport enhancement in bulk-heterojunction organic solar cells with N- or B-doped carbon nanotubes. *Adv Mater* 2011;23:629–33.
- [46] Park JS, Lee BR, Lee JM, Kim J-S, Kim SO, Song MH. Efficient hybrid organic-inorganic light emitting diodes with self-assembled dipole molecule deposited metal oxides. *Appl Phys Lett* 2010;96:243306–8.

- [47] Padinger F, Rittberger RS, Sariciftci NS. Effects of postproduction treatment on plastic solar cells. *Adv Funct Mater* 2003;11:1–4.
- [48] Chirvase D, Parisi J, Hummelen JC, Dyakonov V. Influence of nanomorphology on the photovoltaic action of polymer-fullerene composites. *Nanotechnology* 2004;15:1317–23.
- [49] Chu CW, Yang HC, Hou WJ, Huang JS, Li G, Yang Y. Control of the nanoscale crystallinity and phase separation in polymer solar cells. *Appl Phys Lett* 2008;92:103306–8.
- [50] Dante M, Peet J, Nguyen TQ. Nanoscale charge transport and internal structure of bulk heterojunction conjugated polymer/fullerene solar cells by scanning probe microscopy. *J Phys Chem C* 2008;112:7241–9.
- [51] Montanari I, Nogueira AF, Nelson J, Durrant JR, Winder C, Loi MA, et al. Transient optical studies of charge recombination dynamics in a polymer/fullerene composite at room temperature. *Appl Phys Lett* 2002;81:3001–3.
- [52] Nogueira AF, Montanari I, Nelson J, Durrant JR, Winder C, Sariciftci NS. Charge recombination in conjugated polymer/fullerene blended films studied by transient absorption spectroscopy. *J Phys Chem B* 2003;107:1567–73.
- [53] Krebs FC. *Stability and degradation of organic and polymer solar cells*. Chichester: John Wiley & Sons; 2012.
- [54] Dyakonov V, Zorinians G, Scharber M, Brabec CJ, Janssen RAJ, Hummelen JC, et al. Photoinduced charge carriers in conjugated polymer-fullerene composites studied with light-induced electron-spin resonance. *Phys Rev B* 1999;59:8019–25.
- [55] Westerling M, Osterbacka R, Stubb H. Recombination of long-lived photoexcitations in regioregular polyalkylthiophenes. *Phys Rev B* 2002;66:165220/01–165220/07.
- [56] Brabec C, Dyakonov V, Parisi J, Sariciftci NS. *Organic photovoltaic: concepts and realization*. Berlin: Springer; 2003.
- [57] Marumoto K, Muramatsu Y, Kuroda S. Quadrimolecular recombination kinetics of photogenerated charge carriers in regioregular poly(3-alkylthiophene)/fullerene composites. *Appl Phys Lett* 2004;84:1317–19.
- [58] Bassler H. Charge transport in disordered organic photoconductors. *Phys Status Solidi B* 1993;175:15–56.
- [59] Sensfuss S, Konkin A, Roth HK, Al-Ibrahim M, Zhokhavets U, Gobsch G, et al. Optical and ESR studies on poly(3-alkylthiophene)/fullerene composites for solar cells. *Synth Metals* 2003;137:1433–4.
- [60] Schlick S, editor. *Advanced ESR methods in polymer research*. New York, NY: John Wiley & Sons, Inc.; 2006.
- [61] Eaton GR, Eaton SS, Barr DP, Weber RT. *Quantitative EPR*. Wien, New York, NY: Springer; 2010.
- [62] Ranby B, Rabek JF. *ESR spectroscopy in polymer research*. New York, NY: Springer; 2011.
- [63] Misra SK, editor. *Multifrequency electron paramagnetic resonance: theory and applications*. Weinheim: Wiley-VCH; 2011.
- [64] Lund A, Shiotani M, Shimada S. *Principles and applications of ESR spectroscopy*. New York, NY: Springer; 2011.
- [65] Lund A, Shiotan M, editors. *EPR of free radicals in solids I: trends in methods and applications*, vol. 1. Amsterdam: Springer; 2013.

- [66] Lund A, Shiotan M, editors. *EPR of free radicals in solids II: progress in theoretical chemistry and physics*, vol. 2. Amsterdam: Springer; 2013.
- [67] Baranov P. *Magnetic resonance of semiconductors and semiconductor nanostructures*. New York, NY: Springer; 2016.
- [68] Aguirre A, Gast P, Orlinskii S, Akimoto I, Groenen EJJ, El Mkami H, et al. Multifrequency EPR analysis of the positive polaron in I<sub>2</sub>-doped poly(3-hexylthiophene) and in poly[2-methoxy-5-(3,7-dimethyloctyloxy)]-1,4-phenylenevinylene. *Phys Chem Chem Phys* 2008;10:7129–38.
- [69] Behrends J, Sperlich A, Schnegg A, Biskup T, Teutloff C, Lips K, et al. Direct detection of photoinduced charge transfer complexes in polymer fullerene blends. *Phys Rev B* 2012;85:125206/01–125206/06.
- [70] Uvarov MN, Kulik LV. Electron spin echo of photoinduced spin-correlated polaron pairs in P3HT:PCBM composite. *Appl Magn Reson* 2013;44:97–106.
- [71] Uvarov MN, Popov AG, Lukina EA, Kulik LV. Spin relaxation and structure of light-induced spin-correlated PCBM-/P3HT(+) radical pairs. *J Struct Chem* 2014;55:644–50.
- [72] Assenheim HM. *Introduction to electron spin resonance*. New York, NY: Springer; 2014.
- [73] Buchachenko AL, Turton CN, Turton TI. *Stable radicals*. New York, NY: Consultants Bureau; 1995.
- [74] Misra SK, editor. *Handbook of multifrequency electron paramagnetic resonance: data and techniques*. New York, NY: Wiley; 2014.
- [75] Kim Y, Cook S, Tuladhar SM, Choulis SA, Nelson J, Durrant JR, et al. A strong regioregularity effect in self-organizing conjugated polymer films and high-efficiency polythiophene: fullerene solar cells. *Nat Mater* 2006;5:197–203.
- [76] Krinichnyi VI. *2-mm wave band EPR spectroscopy of condensed systems*. Boca Raton, FL: CRC Press; 1995. See also <<http://hf-epr.awardspace.us/publications.htm>>.
- [77] Krinichnyi VI. 2-mm Waveband electron paramagnetic resonance spectroscopy of conducting polymers (review). *Synth Metals* 2000;108:173–222 See also the references therein.
- [78] Krinichnyi VI. Advanced ESR methods. In: Schlick S, editor. *Polymer research*. Hoboken, NJ: Wiley; 2006. p. 307–38. See also the references therein.
- [79] Silinsh EA, Kurik MV, Chapek V. *Electronic processes in organic molecular crystals: the phenomena of localization and polarization (Russian)*. Riga: Zinatne; 1988.
- [80] Vonsovskii SV. *Magnetism. Magnetic properties of dia-, para-, ferro-, antiferro-, and ferrimagnetics*, vol. 1. New York, NY: John Wiley & Sons; 1974.
- [81] Mizoguchi K, Kuroda S. Magnetic properties of conducting polymers. In: Nalwa HS, editor. *Handbook of organic conductive molecules and polymers*. Chichester, New York: John Wiley & Sons; 1997. p. 251–317.
- [82] Raghunathan A, Kahol PK, Ho JC, Chen YY, Yao YD, Lin YS, et al. Low-temperature heat capacities of polyaniline and polyaniline polymethylmethacrylate blends. *Phys Rev B* 1998;58:R15955–8.
- [83] Kahol PK, Mehring M. Exchange-coupled pair model for the non-curie-like susceptibility in conducting polymers. *Synth Metals* 1986;16:257–64.
- [84] Clark WG, Tippie LC. Exchange-coupled pair model for the random-exchange Heisenberg antiferromagnetic chain. *Phys Rev B* 1979;20:2914–23.
- [85] Jonston DC. Thermodynamics of charge-density waves in quasi one-dimensional conductors. *Phys Rev Lett* 1984;52:2049–52.

- [86] Barnes SE. Theory of electron spin resonance of magnetic ions in metals. *Adv Phys* 1981;30:801–938.
- [87] Nelson J. Diffusion-limited recombination in polymer-fullerene blends and its influence on photocurrent collection. *Phys Rev B* 2003;67:155209/1–155209/10.
- [88] Schultz NA, Scharber MC, Brabec CJ, Sariciftci NS. Low-temperature recombination kinetics of photoexcited persistent charge carriers in conjugated polymer/fullerene composite films. *Phys Rev B* 2001;64:245210/01–245210/07.
- [89] Tanaka H, Hasegawa N, Sakamoto T, Marumoto K, Kuroda SI. Light-induced ESR studies of quadrimolecular recombination kinetics of photogenerated charge carriers in regioregular poly(3-alkylthiophene)/C-60 composites: alkyl chain dependence. *Jpn J Appl Phys Part 1-Regular Pap Brief Commun Rev Pap* 2007;46:5187–92.
- [90] Devreux F, Genoud F, Nechtschein M, Villeret B. On polaron and bipolaron formation in conducting polymers. In: Kuzmany H, et al., editors. *Electronic properties of conjugated polymers*. Berlin: Springer-Verlag; 1987. p. 270–6.
- [91] Krinichnyi VI. LEPR spectroscopy of charge carriers photoinduced in polymer/fullerene composites. In: Lechkov M, Prandzheva S, editors. *Encyclopedia of polymer composites: properties, performance and applications*. Hauppauge, New York, NY: Nova Science Publishers; 2009. p. 417–46.
- [92] Tachiya M, Seki K. Theory of bulk electron-hole recombination in a medium with energetic disorder. *Phys Rev B* 2010;82:085201/01–085201/08.
- [93] Molin YN, Salikhov KM, Zamaraev KI. *Spin exchange*. Berlin: Springer; 1980.
- [94] Houze E, Nechtschein M. ESR in conducting polymers: oxygen-induced contribution to the linewidth. *Phys Rev B* 1996;53:14309–18.
- [95] Roth HK, Keller F, Schneider H. *Hochfrequenzspektroskopie in der Polymerforschung*. Berlin: Akademie Verlag; 1984.
- [96] Blumenfeld LA, Voevodski VV, Semenov AG. *Application of electron paramagnetic resonance in chemistry (Russ)*. Novosibirsk: Izdat. SO AN SSSR; 1962.
- [97] Weil JA, Bolton JR, Wertz JE. *Electron paramagnetic resonance: elementary theory and practical applications*, vol. 2d. New York, NY: Wiley-Interscience; 2007.
- [98] Lebedev YS, Muromtsev VI. *EPR and relaxation of stabilized radicals (Russ)*. Moscow: Khimija; 1972.
- [99] Wertz JE, Bolton JR. *Electron spin resonance: elementary theory and practical applications*. London: Springer Verlag; 2013.
- [100] Krinichnyi VI, Roth HK, Schrödner M, Wessling B. EPR study of polyaniline highly doped by p-toluenesulfonic acid. *Polymer* 2006;47:7460–8.
- [101] Krinichnyi VI, Tokarev SV, Roth HK, Schrödner M, Wessling B. EPR study of charge transfer in polyaniline highly doped by p-toluenesulfonic acid. *Synth Metals* 2006;156:1368–77.
- [102] Krinichnyi VI, Yudanov EI, Wessling B. Influence of spin–spin exchange on charge transfer in PANI-ES/P3DDT/PCBM composite. *Synth Metals* 2013;179:67–73.
- [103] Van Vooren A, Kim J-S, Cornil J. Intrachain versus interchain electron transport in poly(flourene-alt-benzothiadiazole): a quantum-chemical insight. *Eur J Chem Phys Phys Chem* 2008;9:989–93.
- [104] Lan Y-K, Huang C-I. A theoretical study of the charge transfer behavior of the highly regioregular poly-3-hexylthiophene in the ordered state. *J Phys Chem B* 2008;112:14857–62.

- [105] Cheung DL, McMahon DP, Troisi A. Computational study of the structure and charge-transfer parameters in low-molecular-mass P3HT. *J Phys Chem B* 2009;113:9393–401.
- [106] Troisi A, Orlandi GJ. Dynamics of the intermolecular transfer integral in crystalline organic semiconductors. *J Phys Chem A* 2006;110:4065–70.
- [107] Kirkpatrick J, Marcon V, Nelson J, Kremer K, Andrienko D. Charge mobility of discotic mesophases: a multiscale quantum and classical study. *Phys Rev Lett* 2007;98:227402/01–227402/04.
- [108] Butler MA, Walker LR, Soos ZG. Dimensionality of spin fluctuations in highly anisotropic TCNQ salts. *J Chem Phys* 1976;64:3592–601.
- [109] Krasicky PD, Silsbee RH, Scott JC. Studies of a polymeric chromium phosphinate—electron-spin resonance and spin dynamics. *Phys Rev B* 1982;25:5607–26.
- [110] Hennessy MJ, McElwee CD, Richards PM. Effect of interchain coupling on electron-spin resonance in nearly one-dimensional systems. *Phys Rev B* 1973;7:930–47.
- [111] Dyson FJ. Electron spin resonance absorption in metals. II. Theory of electron diffusion and the skin effect. *Phys Rev B* 1955;98:349–59.
- [112] Bernier P. The magnetic properties of conjugated polymers: ESR studies of undoped and doped systems. In: Scotheim TE, editor. *Handbook of conducting polymers*. New York, NY: Marcel Dekker, Inc.; 1986. p. 1099–125.
- [113] Krinichnyi VI. Dynamics of spin charge carriers in polyaniline. *Appl Phys Rev* 2014;1:021305/01–021305/40.
- [114] Chapman AC, Rhodes P, Seymour EFW. The effect of eddy currents on nuclear magnetic resonance in metals. *Proc Phys Soc B* 1957;70:345–60.
- [115] Poole CP. *Electron spin resonance, a comprehensive treatise on experimental techniques*. New York, NY: John Wiley & Sons; 1983.
- [116] Krinichnyi VI, Pelekh AE, Tkachenko LI, Kozub GI. Study of spin dynamics in trans-polyacetylene at 2-mm waveband EPR. *Synth Metals* 1992;46:1–12.
- [117] Carrington F, McLachlan AD. *Introduction to magnetic resonance with application to chemistry and chemical physics*. New York, Evanston, London: Harrer & Row, Publishers; 1967.
- [118] Pietronero L. Ideal conductivity of carbon p-polymers and intercalation compounds. *Synth Metals* 1983;8:225–31.
- [119] Kivelson S, Heeger AJ. Intrinsic conductivity of conducting polymers. *Synth Metals* 1988;22:371–84.
- [120] Long AR, Balkan N. AC loss in amorphous germanium. *Philos Mag B* 1980;41:287–305.
- [121] Fishchuk II, Kadashchuk AK, Bäessler H, Weiss DS. Nondispersive charge-carrier transport in disordered organic materials containing traps. *Phys Rev B* 2002;66:205208/01–205208/12.
- [122] Roth HK, Krinichnyi VI. Spin and charge transport in poly(3-octylthiophene). *Synth Metals* 2003;137:1431–2.
- [123] Krinichnyi VI, Roth HK, Konkin AL. Multifrequency EPR study of charge transfer in poly(3-alkylthiophenes). *Phys B* 2004;344:430–5.
- [124] Krinichnyi VI, Roth HK. EPR study of spin and charge dynamics in slightly doped poly(3-octylthiophene). *Appl Magn Reson* 2004;26:395–415.
- [125] Konkin A, Ritter U, Scharff P, Roth H-K, Aganov A, Sariciftci NS, et al. Photo-induced charge separation process in (PCBM-C<sub>120</sub>O)/(M3EH-PPV) blend solid film

- studied by means of X- and K-bands ESR at 77 and 120 K. *Synth Metals* 2010;160:485–9.
- [126] Poluektov OG, Filippone S, Martín N, Sperlich A, Deibel C, Dyakonov V. Spin signatures of photogenerated radical anions in polymer-[70]fullerene bulk heterojunctions: high frequency pulsed EPR spectroscopy. *J Phys Chem B* 2010;114:14426–9.
- [127] Krinichnyi VI, Yudanova EI, Denisov NN. The role of spin exchange in charge transfer in low-bandgap polymer:fullerene bulk heterojunctions. *J Chem Phys* 2014;141:044906/01–044906/11.
- [128] Niklas J, Mardis KL, Banks BP, Grooms GM, Sperlich A, Dyakonov V, et al. Highly-efficient charge separation and polaron delocalization in polymer–fullerene bulk-heterojunctions: a comparative multi-frequency EPR and DFT study. *Phys Chem Chem Phys* 2013;15:9562–74.
- [129] De Ceuster J, Goovaerts E, Bouwen A, Hummelen JC, Dyakonov V. High-frequency (95 GHz) electron paramagnetic resonance study of the photoinduced charge transfer in conjugated polymer-fullerene composites. *Phys Rev B* 2001;64:195206/01–195206/06.
- [130] Krinichnyi VI, Yudanova EI. Light-induced EPR study of charge transfer in P3HT/bis-PCBM bulk heterojunctions. *AIP Adv* 2011;1:022131/01–022131/15.
- [131] Krinichnyi VI, Yudanova EI. Light-induced EPR study of charge transfer in P3HT/PC<sub>71</sub>BM bulk heterojunctions. *J Phys Chem C* 2012;116:9189–95.
- [132] Sensfuss S, Blankenburg L, Schache H, Shokhovets S, Erb T, Konkin A, et al. Thienopyrazine-based low-bandgap polymers for flexible polymer solar cells. *Eur Phys J-Appl Phys* 2010;51:303204/1–303204/5.
- [133] Eaton SS, Eaton GR. EPR spectra of C-60 anions. *Appl Magn Reson* 1996;11:155–70.
- [134] Allemand PM, Srdanov G, Koch A, Khemani K, Wudl F, Rubin Y, et al. The unusual electron-spin-resonance of fullerene C<sub>60</sub>. *J Am Chem Soc* 1991;113:2780–1.
- [135] Bietsch W, Bao J, Ludecke J, van Smaalen S. Jahn-Teller distortion and merohedral disorder of C-60(-) as observed by ESR. *Chem Phys Lett* 2000;324:37–42.
- [136] Deibel C, Mack D, Gorenflot J, Schöll A, Krause S, Reinert F, et al. Energetics of excited states in the conjugated polymer poly(3-hexylthiophene). *Phys Rev B* 2010;81:085202–6.
- [137] Chen TA, Wu XM, Rieke RD. Regiocontrolled synthesis of poly(3-alkylthiophenes) mediated by Rieke zink—their characterization and solid-state properties. *J Am Chem Soc* 1995;117:233–44.
- [138] Wienk MM, Kroon JM, Verhees WJH, Knol J, Hummelen JC, van Hal PA, et al. Efficient methano[70]fullerene/MDMO-PPV bulk heterojunction photovoltaic cells. *Angewandte Chemie-Int Edn* 2003;42:3371–5.
- [139] Yamanari T, Taima T, Sakai J, Saito K. Highly efficient organic thin-film solar cells based on poly(3-hexylthiophene) and soluble C-70 fullerene derivative. *Jpn J Appl Phys* 2008;47:1230–3.
- [140] Boland P, Sunkavalli SS, Chennuri S, Foe K, Abdel-Fattah T, Namkoong G. Investigation of structural, optical, and electrical properties of regioregular poly(3-hexylthiophene)/fullerene blend nanocomposites for organic solar cells. *Thin Solid Films* 2010;518:1728–31.

- [141] Sperlich A, Liedtke M, Kern J, Kraus H, Deibel C, Filippone S, et al. Photoinduced C(70) radical anions in polymer:fullerene blends. *Phys Status Solidi-Rapid Res Lett* 2011;5:128–30.
- [142] Krinichnyi VI, Yudanova EI. Structural effect of electron acceptor on charge transfer in poly(3-hexylthiophene)/methanofullerene bulk heterojunctions. *Solar Energy Mater Solar Cells* 2011;95:2302–13.
- [143] Pénicaud A, Pérez-Benitez A, Escudero R, Coulon C. Single crystal synthesis of  $[(C_6H_5)_4P]_2[C_{70}] [I]$  by electrocrystallization and experimental determination of the g-value anisotropy of  $C_{70}^{\bullet-}$  and  $C_{60}^{\bullet-}$  at 4.2 K. *Solid State Commun* 1995;96:147–50.
- [144] Reed CA, Bolskar RD. Discrete fulleride anions and fullerenium cations. *Chem Rev* 2000;100:1075–120.
- [145] Tanaka K, Zakhidov AA, Yoshizawa K, Okahara K, Yamabe T, Yakushi K, et al. Magnetic properties of TDAE-C-60 add TDAE-C-70 where TDAE is tetrakis (dimethylamino)ethylene. *Phys Rev B* 1993;47:7554–9.
- [146] Friedrich J, Schweitzer P, Dinse KP, Rapta P, Stasko A. EPR study of radical-anions of C-60 and C-70. *Appl Magn Reson* 1994;7:415–25.
- [147] Hase H, Miyatake Y. Comparative ESR study of C-60 and C-70 radical-anions produced in gamma-irradiated organic-solid solutions at 77 K. *Chem Phys Lett* 1995;245:95–101.
- [148] Adrian FJ. Spin-orbit effects in fullerenes. *Chem Phys* 1996;211:73–80.
- [149] Stone AJ. Gauge invariance of the g tensor. *Proc R Soc A: Math Phys Eng Sci* 1963;A271:424–34.
- [150] Dubois D, Kadish KM, Flanagan S, Haufler RE, Chibante LPF, Wilson LJ. Spectroelectrochemical study of the C60 and C70 fullerenes and their monoanions, dianions, trianions, and tetraanions. *J Am Chem Soc* 1999;113:4364–6.
- [151] Krinichnyi VI, Yudanova EI. Influence of morphology of low-band-gap PCDTBT: PC71BM composite on photoinduced charge transfer: LEPR spectroscopy study. *Synth Metals* 2015. Available from: <http://dx.doi.org/10.1016/j.synthmet.2015.09.019>.
- [152] Krinichnyi VI. Relaxation and dynamics of spin charge carriers in polyaniline. In: Wythers MC, editor. *Advances in materials science research*. Hauppauge, New York, NY: Nova Science Publishers; 2014. p. 109–60.
- [153] Krinichnyi VI, Roth HK, Sensfuss S, Schrödner M, Al Ibrahim M. Dynamics of photoinduced radical pairs in poly(3-dodecylthiophene)/fullerene composite. *Phys E* 2007;36:98–101.
- [154] Krinichnyi VI. Dynamics of charge carriers photoinduced in poly(3-dodecylthiophene)/fullerene composite. *Acta Mater* 2008;56:1427–34.
- [155] Krinichnyi VI. Dynamics of charge carriers photoinduced in poly(3-dodecylthiophene)/fullerene bulk heterojunction. *Solar Energy Mater Solar Cells* 2008;92:942–8.
- [156] Krinichnyi VI. An ESR study of photoinduced charge transport in the polymer/fullerene system. *High Energy Chem* 2008;42:572–5.
- [157] Krinichnyi VI, Yudanova EI. LEPR spectroscopy of charge carriers photoinduced in polymer/fullerene bulk heterojunctions. *J Renewable Sustain Energy* 2009;1:043110/01–043110/18.

- [158] Krinichnyi VI, Balakai AA. Light-induced spin localization in poly(3-dodecylthiophen)/PCBM composite. *Appl Magn Reson* 2010;39:319–28.
- [159] Krinichnyi VI. EPR study of charge transfer in the poly-3-dodecylthiophene-fullerene system. *Polym Sci, Ser A* 2010;52:26–32.
- [160] Yudanova EI, Krinichnyi VI. Influence of ultrasonic, microwave, and thermal effects on photoinduced charge transfer in poly(3-hexylthiophene)-methanofullerene composites: EPR study. *Polym Sci Ser A* 2013;55:233–43.
- [161] Marumoto K, Muramatsu Y, Takeuchi N, Kuroda S. Light-induced ESR studies of polarons in regioregular poly(3-alkylthiophene)-fullerene composites. *Synth Metals* 2003;135:433–4.
- [162] Janssen RAJ, Moses D, Sariciftci NS. Electron and energy transfer processes of photoexcited oligothiophenes onto tetracyanoethylene and C60. *J Chem Phys* 1994;101:9519–27.
- [163] Tong MH, Coates NE, Moses D, Heeger AJ, Beaupre S, Leclerc M. Charge carrier photogeneration and decay dynamics in the poly(2,7-carbazole) copolymer PCDTBT and in bulk heterojunction composites with PC70BM. *Phys Rev B* 2010;81:125210–15.
- [164] Kočka J, Elliott SR, Davis EA. AC conductivity and photo-induced states in amorphous semiconductors. *J Phys C—Solid State Phys* 1979;12:2589–96.
- [165] Tanaka K, Sato T, Kuga T, Yamabe T, Yoschizawa K, Okahara K, et al. Weak suppression of ferromagnetism in tetrakis(dimethylamino)ethylene-(C60)1-x(C70)x. *Phys Rev B Solid State* 1995;51:990–5.
- [166] Gotschya B, Gompper R, Klos H, Schilder A, Schütz W, Völkel G. Ferromagnetic versus molecular ordering in C60 charge transfer complexes. *Synth Metals* 1996;77:287–90.
- [167] Conwell EM, Duke CB, Paton A, Jeyadev S. Molecular conformation of polyaniline oligomers: optical absorption and photoemission of three-phenyl molecules. *J Chem Phys* 1988;88:3331–7.
- [168] Harigaya K. Long-range excitons in conjugated polymers with ring torsions: poly(para-phenylene) and polyaniline. *J Phys Condensed Matter* 1998;10:7679–90.
- [169] Łuźny W, Trznadel M, Proń A. X-Ray diffraction study of reoregular poly(3-alkylthiophenes). *Synth Metals* 1996;81:71–4.
- [170] Buchachenko AL, Vasserman AM. Stable radicals (Russ). Moscow: Khimija; 1973.
- [171] Williams JM, Ferraro JR, Thorn RJ, Carlson KD, Geiser U, Wang HH, et al. Organic superconductors (including fullerenes): synthesis, structure, properties, and theory. Englewood Cliffs, NJ: (Prentice-Hall, Inc.; 1992.
- [172] Yazawa K, Inoue Y, Shimizu T, Tansho M, Asakawa N. Molecular dynamics of regioregular poly(3-hexylthiophene) investigated by NMR relaxation and an interpretation of temperature dependent optical absorption. *J Phys Chem B* 2010;114:1241–8.
- [173] Breiby DW, Sato S, Samuelsen EJ, Mizoguchi K. Electron spin resonance studies of anisotropy in semiconducting polymeric films. *J Polym Sci Part B-Polym Phys* 2003;41:3011–25.
- [174] Marchant S, Foot PJS. Poly(3-hexylthiophene)-zinc oxide rectifying junctions. *J Mater Sci-Mater Electron* 1995;6:144–8.
- [175] Al Ibrahim M, Roth HK, Schrödner M, Konkin A, Zhokhavets U, Gobsch G, et al. The influence of the optoelectronic properties of poly(3-alkylthiophenes) on the device parameters in flexible polymer solar cells. *Org Electron* 2005;6:65–77.

- [176] So F, Kido J, Burrows P. Organic light-emitting devices for solid-state lighting. *Mater Res Soc Bull* 2008;33:663–9.
- [177] Sharma GD. Advances in nano-structured organic solar cells. In: Badescu V, Paulescu M, editors. *Physics of nanostructured solar cells*. New York, NY: Nova Science Publishers; 2010. p. 361–460.
- [178] Krinichnyi VI, Yudanova EI, Denisov NN. Light-induced EPR study of charge transfer in poly(3-hexylthiophene)/fullerene bulk heterojunction. *J Chem Phys* 2009;131:044515/01–044515/11.
- [179] Krinichnyi VI, Yudanova EI, Denisov NN. EPR study of charge transfer photoinduced in poly(3-hexylthiophene)/fullerene composite. *Polym Sci Ser A* 2010;52:715–26.
- [180] Krinichnyi VI, Grinberg OY, Nazarova IB, Kozub GI, Tkachenko LI, Khidekel ML, et al. Polythiophene and polyacetylene conductors in the 3-cm and 2-mm electron spin resonance bands. *Bull Acad Sci USSR Div Chem Sci* 1985;34:425–7.
- [181] Obrzut J, Page KA. Electrical conductivity and relaxation in poly(3-hexylthiophene). *Phys Rev B* 2009;80:195211/01–195211/07.
- [182] Shklovskii BI, Efros AL. *Electronic properties of doped semiconductors*. New York, NY: Springer-Verlag; 1984.
- [183] Tycko R, Dabbagh G, Fleming RM, Haddon RC, Makhija AV, Zahurak SM. Molecular dynamics and the phase transition in solid C<sub>60</sub>. *Phys Rev Lett* 1991;67:1886–9.
- [184] Denisov NN, Krinichnyi VI, Nadtochenko VA. Spin properties of paramagnetic centers photogenerated in crystals of complexes between C<sub>60</sub> and TPA. In: Kadish K, Ruoff R, editors. *Fullerenes. Recent advances in the chemistry and physics of fullerenes and related materials*. Pennington, NJ: The Electrochemical Society, Inc.; 1997. p. 139–47.
- [185] Pike GE. AC conductivity of scandium oxide and a new hopping model for conductivity. *Phys Rev B* 1972;6:1572–80.
- [186] Elliott SR. On the super-linear frequency dependent conductivity of amorphous semiconductors. *Solid State Commun* 1978;28:939–42.
- [187] Parneix JP, El Kadiri M. Frequency- and temperature-dependent dielectric losses in lightly doped conducting polymers. In: Kuzmany H, et al., editors. *Electronic properties of conjugated polymers*. Berlin: Springer-Verlag; 1987. p. 23–6.
- [188] Agostini G, Corvaja C, Pasimeni L. EPR studies of the excited triplet states of C<sub>60</sub>O and C<sub>60</sub>C<sub>2</sub>H<sub>4</sub>N(CH<sub>3</sub>) fullerene derivatives and C<sub>70</sub> in toluene and polymethylmethacrylate glasses and as films. *Chem Phys* 1996;202:349–56.
- [189] Morosin B, Hu ZB, Jorgensen JD, Short S, Schirber JE, Kwei GH. Ne intercalated C-60: diffusion kinetics. *Phys Rev B* 1999;59:6051–7.
- [190] Harsanyi G. *Polymer films in sensor applications*. Boca Raton, FL: CRC Press; 1995.
- [191] ElKaoutit M. Application of conducting polymers in electroanalysis. In: Motheo AJ, editor. *Aspects on fundamentals and applications of conducting polymers*. Rijeka: InTech; 2011. p. 43–66.
- [192] Lubentsov BZ, Timofeeva ON, Saratovskikh SL, Krinichnyi VI, Pelekh AE, Dmitrenko VV, et al. The study of conducting polymer interaction with gaseous substances. 4. The water-content influence on polyaniline crystal structure and conductivity. *Synth Metals* 1992;47:187–92.

- [193] Krinichnyi VI. Investigation of biological systems by high-resolution 2-mm wave band ESR. *J Biochem Biophys Methods* 1991;23:1–30.
- [194] Krinichnyi VI. Investigation of biological systems by high resolution 2-mm wave band EPR. *Appl Magn Reson* 1991;2:29–60.
- [195] Goldenberg LM, Krinichnyi VI. Water-sensitive sensor based on modified poly(vinylchloride). *Synth Metals* 1993;53:403–7.
- [196] Davydov AS. Solitons in molecular systems (Russ.). Kiev: Naukova Dumka; 1984.
- [197] Krinichnyi VI, Eremenko ON, Rukhman GG, Letuchii YA, Geskin VM. Sensors based on conducting organic polymers. Polyaniline. *Polym Sci USSR* 1989;31:1819–25.
- [198] Schuhmann W. Conducting polymers and their application in amperometric biosensors. In: Usmani AM, Akmal N, editors. *Diagnostic biosensor polymers*, ACS symposium series. Washington, DC: American Chemical Society; 1994. p. 110–23.
- [199] Arshak K, Velusamy V, Korostynska O, Oliwa-Stasiak K, Adley C. Conducting polymers and their applications to biosensors: emphasizing on foodborne pathogen detection. *IEEE Sens J* 2009;9:1942–51.
- [200] Goldenberg LM, Krinichnyi VI, Nazarova IB. The Schottky device based on doped poly(para-phenylene). *Synth Metals* 1991;44:199–203.
- [201] Nazarova IB, Krinichnyi VI, Goldenberg LM. Schottky diodes based on poly(para-phenylene) and poly(1,4-dipyrrolobenzene). *Synth Metals* 1993;53:399–402.
- [202] Cosnier S, Karyakin A, editors. *Electropolymerization: concepts, materials and applications*. New York, NY: Wiley; 2011.
- [203] Lupton JM, McCamey DR, Boehme C. Coherent spin manipulation in molecular semiconductors: getting a handle on organic spintronics. *Chem Phys Chem* 2010;11:3040–58.
- [204] Kinoshita M, Iwasaki N, Nishi N. Molecular spectroscopy of the triplet state through optical detection of zero-field magnetic resonance. *Appl Spectrosc Rev* 1981;17:1–94.
- [205] Lee MK, Segal M, Soos ZG, Shinar J, Baldo MA. Yield of singlet excitons in organic light-emitting devices: a double modulation photoluminescence-detected magnetic resonance study. *Phys Rev Lett* 2005;94:137403–6.
- [206] McCamey DR, van Schooten KJ, Baker WJ, Lee SY, Paik S-Y, Lupton JM, et al. Hyperfine-field-mediated spin beating in electrostatically bound charge carrier pairs. *Phys Rev Lett* 2010;104:017601–4.
- [207] Krinichnyi VI, Tokarev SV, Roth HK, Schrödner M, Wessling B. Multifrequency EPR study of metal-like domains in polyaniline. *Synth Metals* 2005;152:165–8.
- [208] Kahol PK. Magnetic susceptibility of polyaniline and polyaniline-polymethylmethacrylate blends. *Phys Rev B* 2000;62:13803–4.
- [209] Wessling B, Srinivasan D, Rangarajan G, Mietzner T, Lennartz W. Dispersion-induced insulator-to-metal transition in polyaniline. *Eur Phys J* 2000;2:207–10.
- [210] Kapil A, Taunk M, Chand S. Preparation and charge transport studies of chemically synthesized polyaniline. *J Mater Sci-Mater Electron* 2010;21:399–404.
- [211] Krinichnyi VI. The nature and dynamics of nonlinear excitations in conducting polymers. Heteroaromatic polymers. *Russ Chem Rev* 1996;65:521–36.
- [212] Krinichnyi VI. The nature and dynamics of nonlinear excitations in conducting polymers. Polyaniline. *Russ Chem Bull* 2000;49:207–33.
- [213] Takeda K, Hikita H, Kimura Y, Yokomichi H, Morigaki K. Electron spin resonance study of light-induced annealing of dangling bonds in glow discharge hydrogenated

- amorphous silicon: deconvolution of electron spin resonance spectra. *Jpn J Appl Phys Part 1-Regular Papers Short Notes Rev Paps* 1998;37:6309–17.
- [214] Yanilkin VV, Nastapova NV, Morozov VI, Gubskaya VP, Sibgatullina FG, Berezhnaya LS, et al. Competitive conversions of carbonyl-containing methanofullerenes induced by electron transfer. *Russ J Electrochem* 2007;43:184–203.
- [215] Wessling B. New insight into organic metal polyaniline morphology and structure. *Polymers* 2010;2:786–98.
- [216] Wang ZH, Ray A, MacDiarmid AG, Epstein AJ. Electron localization and charge transport in poly(o-toluidine)—a model polyaniline derivative. *Phys Rev B* 1991;43:4373–84.
- [217] Adrain FJ, Monchick L. Theory of chemically induced magnetic polarization. Effects of  $S-T_{\pm 1}$  mixing in strong magnetic fields. *J Chem Phys* 1979;71:2600–10.
- [218] Ginder JM, Richter AF, MacDiarmid AG, Epstein AJ. Insulator-to-metal transition in polyaniline. *Solid State Commun* 1987;63:97–101.
- [219] Yan B, Schultz NA, Efros AL, Taylor PC. Universal distribution of residual carriers in tetrahedrally coordinated amorphous semiconductors. *Phys Rev Lett* 2000;84:4180–3.
- [220] Krinichnyi VI, Roth HK, Hinrichsen G, Lux F, Lüders K. EPR and charge transfer in  $H_2SO_4$ -doped polyaniline. *Phys Rev B* 2002;65:155205/1–155205/14.
- [221] Wang ZH, Scherr EM, MacDiarmid AG, Epstein AJ. Transport and EPR studies of polyaniline—a quasi-one-dimensional conductor with 3-dimensional metallic states. *Phys Rev B* 1992;45:4190–202.

## 10

Dielectric spectroscopy  
and stimulated  
current analyses of  
polymer-ceramic  
nanocomposites**Sasidhar Siddabattuni<sup>1</sup> and Thomas P. Schuman<sup>2</sup>**

<sup>1</sup>Department of Chemistry, Sri Sathya Sai Institute of Higher Learning, Anantapur, Andhra Pradesh, India <sup>2</sup>Chemistry Department, Missouri University of Science and Technology (formerly the University of Missouri-Rolla), Rolla, MO, United States

---

**10.1 INTRODUCTION**

Nanodielectrics, composites containing nanometer-sized particulates, combine easily processed and highly insulating polymeric materials mixed with ceramic fillers of high dielectric permittivity [1–3]. Nanodielectrics with well-dispersed ceramic nanoparticles offer large interaction zones through large contact surface areas between nanoparticulate fillers and their surrounding matrix, compared with conventional composites employing microparticles. The interactions between a polymer matrix and nanoparticles alters polymer chemistry and dynamics in the interfacial regions [3], which brings about the significant changes in dielectrical properties of the nanodielectrics. Results reported in literature support the use of these new materials in applications ranging from power delivery to high energy storage density capacitors to electrical insulators of low loss and high breakdown resistance. The polymer-ceramic interface may have its own electrical and dielectrical properties, as a unique circuit element when under an applied electric field, thus changing the dielectric permittivity of the nanodielectric [4–7].

The dielectric analysis of nanodielectrics is of major importance in order to understand the interactions between the nanoparticles and polymers. Apart from the dielectric characterization of the nanodielectrics, it is fundamentally important for composite material design to precisely understand the dielectric properties of the individual components and the interactions at the nanoscale and, further, how those interactions are manifested in the macroscopic performance of the nanodielectrics.

Dielectric spectroscopy (DS), coupled with performance measurements, is crucial to quantify such properties and unveil molecular-level structure-property interdependencies and in order to develop correlations with device performance [8].

These molecular-level structure property aspects are not unique to electrical composites or dielectrics: the composition of the composites is identical depending on application, where fillers are ceramic, glassy, or clay and vary in particle size and geometry. The matrix can be coceramic, such as with grain boundaries in a sintered ceramic solid, or as particles dispersed in a polymer material, either thermoplastic or thermoset. The measured quantities are electrical in nature for all techniques presented in this chapter and strictly analogous in meaning, whether intended as an electrical or mechanical analysis technique. The analyses present identical data toward conclusions regarding charge storage, conductivity or impedance, or dipolar mobility resulting from particle surface conductivity/polarity, dispersion quality of the particles within the composite, and interfacial versus bulk matrix polymer chain mobility.

In this chapter, the dielectric characterization of ceramic nanoparticles and the use of dielectric or impedance spectroscopy for dielectric characterization of nanofillers and their nanocomposites will be reviewed. In addition, the use of thermally stimulated current (TSC) and photoacoustic emission analysis spectroscopies to study the influence of nanofillers on polymer matrix and charge trap carrier storage and mobility will be presented. In each of the following example references, the dispersion quality and interfaces of the particles inside the matrix result in charge or absence of charge structure relaxations. The range of electrical properties for different structures overlap and are not unique to any one structure; hence, the interpretation of these analytical data can be less than straightforward.

---

## 10.2 DIELECTRIC ANALYSIS OF CERAMIC NANOFILLERS

Ceramic grain size influences the effective dielectric permittivity of ceramics dramatically. Traditionally, the permittivity of ceramic powders, which can be single crystal to polygranular in structure, is measured through dielectrical characterization of pressed or sintered dense pellets using impedance spectroscopy [9–11]. The structure and the dielectric properties of solid, sintered powders can differ significantly from the original loose particulate powders.

Sintered ceramic powders can show a different dielectric behavior than the powder used to manufacture the sintered ceramic or the original bulk ceramic from which the powder materials were made. Internal stresses that may result due to the process of sintering could alter the dielectric properties of the sintered ceramic materials, whereas the unsintered ceramic particles tend to be less mechanically constrained. In addition, grains of the ceramic particles can grow irreversibly during low temperature, or even brief, high temperature sintering.

This is particularly true when measuring high surface area and surface energy per volume, nanometer-size particles. The process for assessing a nanosize effect by using a traditional solid-state pellet technique will perturb the nanopowder properties through sintering and grain growth [9–11].

Dielectric properties of sintered ceramic materials are widely studied, whereas the investigations on the dielectric properties of the ceramic particulates, especially nanosized particulates have been limited, mainly due to the lack of reliable characterization methods to determine the permittivity of particulate materials [11]. Size effects in nanostructured materials are of great importance from both fundamental considerations and practical applications points of view. Hence, either measurement or accurate prediction of the dielectric permittivity of nanosized ceramic particles is required as a prerequisite for the design of the nanodielectric component.

Recently, traditional inorganic ceramic materials have become available in different aspect ratio forms to enable the processing of devices of controlled geometry and grain orientation [12]. In the preparation of the nanodielectrics, unsintered particulate materials are usually employed, rather than sintered ceramics. Ceramic nanopowders supplied by several manufacturing companies may be obtained by different preparation methods and, therefore, have different characteristics (e.g., solid state sintering and crushing, solution precipitation, or hydrothermal syntheses). It is desirable to use an optimum powder for each application, but to individually screen all available products to find a suitable powder would usually require significant time and effort. Therefore, the evaluation method of the dielectric permittivity of ceramic nanopowder itself is demanding [13,14].

Several methods have been employed to characterize the ceramic particulates dielectric properties of various average particle size powders. Wakino et al. [15] have reported on the Monte Carlo modeling of dielectric measurements of mixed powders using pressed compact bodies. Wada et al. [16] measured barium titanate powder dielectric properties in slurry (particles suspended in a suitable liquid) as a two phase system. In this methodology, capacitance measurements at a single frequency (usually a high frequency) were obtained, followed by the application of theoretical models based on the mixing rules to determine the dielectric permittivity of the ceramic particle component of the slurry [16–19]. However, in this methodology, the dielectric constant measurement of the slurry should be obtained very precisely with an accuracy of several decimal points in order to be able to calculate the dielectric constant of the ceramic particles component of the slurry within the acceptable margins of error.

Other factors affecting the reliability of measurements using slurry methodology include size, shape, agglomeration, and sedimentation of the particles. Slurries with poor quality of dispersion could lead to significant errors in the dielectric permittivity calculations of the ceramic particles. Hence, the theoretical models that are used to calculate the dielectric constant have been modified by introducing various parameters based, for example, on particle shape, size, and orientation factors in order to minimize the deviations from ideal slurry

dispersion systems [11,17–20]. Moreover, the presence of conductivity in a powder slurry makes the use of this method even more challenging [21]. Hence, there is a need for the development of a more reliable and reproducible measurement technique for measuring the dielectric properties of the insulative ceramic particles.

---

### 10.3 DS OF CERAMIC PARTICULATES

DS, also known as *electrochemical impedance spectroscopy*, is a well-established method to investigate the dielectrical properties of materials as a function of frequency. It is based on the interaction of an electric field with the net electric dipole moment of the sample, often expressed as a material resistance to formation of the electric field or permittivity [22,23]. According to macroscopic polarization theory, dielectrics are described or modeled by electrically equivalent resistor-capacitor circuits (ERCs). The equivalency of the material under test (MUT) and its ERC are only formal analogs from a mathematical point of view. For instance, the electric response of a MUT can be modeled by more than one equivalent circuit. Thus, additional information describing the MUT must be known to best select the appropriate ERC. Formally, physical properties of dielectrics were described by complex functions like complex dielectric permittivity ( $\epsilon^*$ ), electric modulus ( $M^*$ ;  $M^* = 1/\epsilon^*$ ), as well as electric impedance ( $Z^*$ ), etc., which relate to separate storage and loss function of permittivity, modulus, or impedance, respectively. For full MUT characterization, one must vary temperature and/or frequency in order to establish  $\epsilon^*$ ,  $M^*$ , and  $Z^*$  dependences, the real (storage) and imaginary (loss) vectors for each, on these variables. Data obtained by DS may be expressed graphically in a Bode plot (phase angle versus frequency and impedance versus frequency) or a Nyquist plot ( $Z''$  versus  $Z'$ , where  $Z'$  and  $Z''$  constitute real and imaginary vector scalars of the complex impedance,  $Z^*$ ) [22,24].

In a recent study, Petrovsky et al. [11] applied the DS techniques for the first time to determine the dielectric permittivity within ceramic particles, using appropriate equivalent circuit models and employing a slurry sampling methodology. Using this slurry methodology, DS accurately measured the dielectric constant of particles that were suspended in butoxyethanol (BOE), a lossy dielectric liquid, when the slurry response was modeled as a combination of series and parallel circuits. DS techniques characterize the particles within the slurries as one of two phases in the systems, analogous to the analysis of multiphase polycrystalline ceramic materials, for example, bulk and grain boundary conductivities, using DS [11]. The dielectric property contributions of individual components of the slurries can be extracted from specific frequency sections of the spectra, which are frequency dependent. For instance, the lower-frequency region of the impedance spectra contains the dielectric property information of the dispersed particles component of the slurries.

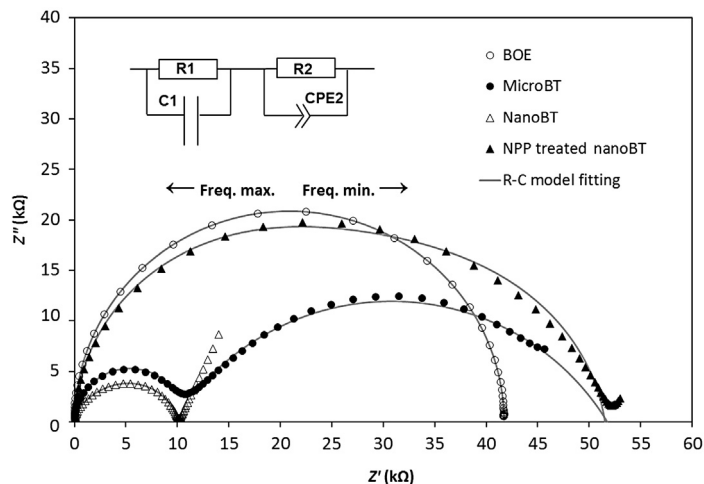


**FIGURE 10.1**

Summary of the Nyquist plots of the impedance spectra of 20 vol. % BT-based powders in BOE in comparison with the pure host liquid, BOE. The ERC model containing two RC elements in series is shown [25].

*Copyright 2013. Reprinted with permission from American Ceramic Society.*

The dielectric constants are obtained from the data by first fitting the complex impedance data obtained from DS with the appropriate ERC models (Figure 10.1) and then applying the simultaneous equivalent circuit equations to calculate the element (e.g., resistance or capacitance), parameter of the ERC models. Standard software is available for corresponding fittings and calculation of parameter for ERC elements, such as Z-View (Scribner Associates, Inc., Charlottesville, VA). It was shown that this approach allowed accurate and reliable measurement of the dielectric constant of various ceramic particles (of  $\epsilon \sim 100\text{--}7000$ , like  $\text{TiO}_2$ ,  $\text{BaTiO}_3$ ,  $\text{SrTiO}_3$ , and  $\text{CaTiO}_3$ ) suspended in different “lossy” host liquids (of  $\epsilon \sim 10\text{--}65$ , like propylene carbonate, ethylene glycol, and BOE). The results reported for powders were comparable to those of bulk ceramic materials [11,20,21,25]. Evaluating the dielectric properties of the ceramic particles using this novel technology was also confirmed by Nakao [26] in a follow-up study, which reported the dielectric permittivity of  $\text{SrTiO}_3$  and  $\text{BaTiO}_3$  particles, and the values were in good agreement with the dielectric permittivities of single-crystal  $\text{SrTiO}_3$  and  $\text{BaTiO}_3$ .

The slurry methodology utility using DS by Petrovsky et al. and Nakao has been demonstrated for a variety of different ceramic metal oxide powders; however, the methodology, when applied to micrometer-sized ceramic particles, was ineffective for nanosized ceramic particles. Nanoparticles’ surface chemistry often renders the particles inherently conductive, similar to metallic particles, though they are bulk resistive. In a recent study, Siddabattuni et al. [25] reported the applicability

**Table 10.1** Fitting Parameters of the Impedance Data and the Permittivity Values of the Samples [25]

Sample	R1 (k $\Omega$ )	C1 (F)	R2 (k $\Omega$ )	CPE2-T (F)	CPE2-P	C2 (F)	$\epsilon_r^a$	$\epsilon_r^b$
BOE	41.7	1.80E-10	—	—	—	—	9.7	—
MicroBT	9.9	4.40E-10	41.9	7.00E-07	0.66	1.10E-07	24.7	6383
NanoBT	10.1	4.50E-10	—	—	—	—	25.1	—
NPP	25.4	5.00E-10	26.1	5.90E-09	0.9	2.20E-09	28.4	133
NanoBT								

<sup>a</sup>Permittivity of liquid component of the slurry.

<sup>b</sup>Permittivity of particulate component of the slurry.

Copyright 2013. Reprinted with permission from American Ceramic Society.

of slurry methodology using DS for the first time for dielectric characterization of ceramic nanoparticles, BaTiO<sub>3</sub> (BT, nanoBT) and nanoparticulate anatase upon remediating the surface conductivity effects of nanoparticles. Slurries of microparticle BT (MicroBT) powder, nanoparticle BT, and surface-remediated nanoparticle BT were dispersed in a suitably lossy liquid, BOE, at 20 vol. % particle concentration. Their dielectric properties were studied using DS. Figure 10.1 shows the Nyquist plots of the impedance spectra of the slurries in comparison with pure BOE and Table 10.1 shows their ERC model fitting parameters and the calculated dielectric permittivities of the different components of the slurries.

Impedance spectra of the pure BOE sample ( $\epsilon \sim 10$ ) contained one semicircle (Figure 10.1) associated with a Maxwell relaxation process of a single, leaky dielectric phase, and was modeled with one RC circuit. Slurries, on the other hand, can be considered as a 0–3 mixed composite system in which the dielectric particles incorporated in the host liquid result in an additional relaxation process, separate from that of the pure host liquid, due to changes in electrical field distribution. A second semicircle resulted in the impedance spectra of 20 vol. % ceramic particle, for example, MicroBT and slurry spectra (Figure 10.1).

A low frequency semicircle corresponded to the MicroBT relaxation, whereas the high frequency semicircle corresponded to that of the lossy host liquid, BOE. Two RC elements connected in series were used for ERC modeling [25]. The shape of impedance spectra is not sensitive to the resistivity of host liquid, but is sensitive to dielectric contrast between the host liquid and dielectric particles. A higher dielectric contrast results in more distinct relaxation semicircles. The dielectric permittivity of the MicroBT sample was calculated from Figure 10.1 data to be approximately 6400 (Table 10.1) [21,25].

For a nanoBT slurry (Figure 10.1), due to a lower dielectric contrast between nanoBT and host liquid, the relaxation semicircles of the individual components are convoluted, resulting in a single but elongated semicircle. The impedance spectra of the nanoBT slurry (Figure 10.1), however, did not show distinguishable dielectric characteristics or relaxation of the nanoparticles, for example, the particles are

sufficiently lossy (i.e., conductive, metallic-like) that only a high-frequency relaxation of the “solvent” environment appeared visible. Permittivity of bare nanoBT particles could not be reliably obtained because no particle relaxation is observed. This was mainly attributed to the higher surface energy and a surface conductivity of the nanoBT particles despite possessing bulk resistivity, altering the dielectric relaxation properties. Though surface conductivity may also be present in the microBT particles, due to their lower surface area per volume the surface conductivity does not screen the bulk relaxation internal to the particle [25].

Bulk or coarse metal oxide ceramic particles are usually robust and stable systems with well-defined crystallographic structures. However, nanosized ceramic particles have higher surface energy, crystal lattice defects, and stress/strain generation at the particle surface, mainly generated due to changes in thermodynamic stability associated with reduction in particle size and surface curvature [27]. Difficulties in dispersing ceramic nanoparticles in organic matrices are direct consequences of higher surface energy [28]. Surface conductivity of nanosized ceramic particles is also higher in comparison to analogous micron-sized particles or bulk ceramics, due to size effects. Dielectric properties, as previously observed, are influenced by surface conductivity and surface energy effects. It is surface conductivity and surface energy effects, compounded by larger surface areas per volume of nanoparticles, that make it difficult to characterize the dielectric properties of ceramic nanopowders by DS reliably using the slurry methodology [25].

To control surface energy and improve the dielectric characteristics of nanosized dielectric particles, surface passivation is important and critical. One primary requisite for dielectric characterization of surface-passivated ceramic nanoparticles using the slurry approach is stability of surface passivation chemistry within the host liquid. Surfactants are useful for dispersion stability but may be less effective since they form weak surface bonds and may be displaced by the host liquid. Surface modifying agents that form stable bonds with the particle surface are preferred.

Siddabattuni et al. reported the use of organophosphate modifiers, such as nitrophenyl phosphate (NPP), which has the ability to interact strongly with the surface of metal oxide ceramics to form a stable, multidentate-complexed organic oxide layer, that effectively passivates the surface of nanoparticle barium titanate (nanoBT). Impedance spectra of the NPP treated nanoBT slurry showed significantly different dielectric characteristics of the nanoBT, as evident from higher resistivity values and significantly less loss compared to untreated nanoBT slurry impedance spectra (Figure 10.1). NPP treated nanoBT impedance spectra showed a single, elongated semicircle indicative of more than one convoluted relaxation that was successfully ERC modeled with two RC elements connected in series. The effective dielectric permittivity of the NPP treated nanoBT particles obtained was approximately 135, which appeared to be a reasonable value [25].

In a later study, Siddabattuni et al. extended the impedance analysis of the ceramic nanoparticles by DS using slurry methodology to nanoparticle anatase (nanoTiO<sub>2</sub>) particles [2]. Impedance spectra of bare nanoTiO<sub>2</sub> compared with various organophosphates-treated nanoTiO<sub>2</sub> were studied. Like nanoBT, untreated

nanoTiO<sub>2</sub>, also exhibited sufficiently high surface conductivity that resembled metallic particles and the dielectric relaxation characteristics of the nanoparticles were not distinct. NPP-treated nanoTiO<sub>2</sub> allowed equivalent circuit modeling of the impedance spectra and the calculated effective dielectric permittivity of the NPP treated nanoTiO<sub>2</sub> particles obtained was  $\epsilon_r \sim 70$ .

The accuracy and the limitations of the previously described methodology can be summarized as follows: (1) The effective dielectric constant of the powders determined using DS of slurries greater than 10 vol. % and lower than the percolation threshold are highly reproducible and reliable [20]. (2) Physical modeling confirms the validity of this novel approach, which allows reliable measurement of the dielectric constant of particulate materials by impedance spectroscopy techniques [29]. (3) Accurate or prior knowledge of the slurry component parameters, such as the permittivity and conductivity of the host liquid as well as the permittivity and volume fraction of the powder are not required. All parameters for an unknown slurry can be extracted from the impedance spectra by scaling techniques, such as resistivity scaling to normalize the impedance spectra, provided the individual slurry components have distinctly different permittivities and distinct relaxation semicircles in the impedance spectra [21,25]. (4) A specific physical model is not necessary to obtain the parameters of slurry components in the case of a well-dispersed and stable slurry containing dielectric particles with a low bulk and surface conductivities [21]. (5) Direct current (DC) conductivity of the host liquid should be adjusted to have both semicircles of the low- and high-frequency relaxations for particle and host liquid components, respectively, to be within the range of equipment used [25]. (6) Dielectric losses in the slurry are mostly connected with the conductivity of the liquid. Therefore, it can be difficult to extract information about the dielectric losses in the dielectric powder material [11]. (7) If the surface conductivity of ceramic powders (especially in nanoparticles) is large enough, they are not detectable as dielectrics in the DS studies of slurries due to conductive shielding of the internal dielectric relaxation event. Suitable surface passivation of the particles to reduce the surface conductivity is required for dielectric characterization of ceramic particles [25].

DS studies of ceramic nanoparticles employing slurry technology have shown excellent utility for the characterization of, for example, macroparticles and nanoparticles of BT and TiO<sub>2</sub> alike. Future applicability of this novel technology and the composition of suitable surface passivation chemistries for various other dielectric ceramic nanopowders, such as CaTiO<sub>3</sub>, SrTiO<sub>3</sub>, ZrO<sub>2</sub>, SiO<sub>2</sub>, etc., remain to be explored.

---

## 10.4 DS STUDIES OF NANOCOMPOSITES

Irrespective of the type of base polymer material (thermoplastic or thermoset), significant changes in the dielectric properties of the matrix polymers, like resistivity, permittivity, dielectric strength, tracking, and partial discharge resistant characteristics,

can be observed upon incorporation of ceramic nanoparticles at relatively low filler concentrations when compared with similar properties in traditional polymer-ceramic microcomposites [30–34]. The change in the bulk properties of the nanodielectrics compared to the polymer alone are mainly attributed to the unique properties of the nanoparticles and creation of polymer-particle interfacial regions.

The polymer-particle interfacial regions in turn affect the polymer mobility in the interfacial regions and change the length scale of interaction between the polymer chains as perturbed by polymer and particle interactions. Changes in the chain dynamics of the polymer, packing structure, with consequent changes in the free volume distribution, can result in property changes in the composite [3,28]. A large number of scientific methods such as DS, nuclear magnetic resonance (NMR), dynamic mechanical analysis (DMA), and quasielastic light scattering, and neutron scattering are used to probe the structural and molecular interaction between the polymer matrix and nanofiller inclusion. Among these techniques, DS is a powerful technique for investigating the structure and molecular dynamics of polymers and their composites and augments the other scientific methods [35].

In comparison to other similar techniques, DS provides the advantage of studying the molecular dynamics in a very broad frequency range. In this way, DS electrical testing is analogous to DMA testing of polymer materials. The extremely broad frequency range of analysis allows one to measure sample processes with very different characteristic (relaxation) times and, correspondingly, different characteristic length scales. These include fast secondary (local) relaxations at high frequencies with characteristic length scales of less than 1 nm size; cooperative relaxations like the glass transition of the polymer matrix at intermediate frequencies, with characteristic length scales of a few nanometers; DC conductivity and conductivity effects such as interfacial Maxwell–Wagner–Sillars relaxations at lower frequencies, with characteristic length scales that vary in the nm to  $\mu\text{m}$  scale range [34–37]. Molecular dynamics differences between the polymer and polymer-particle interface, as monitored by DS in polymer-ceramic nanodielectrics, are reviewed in this section.

The theoretical and mathematical relationships have been well-treated in other recent DS reviews, in particular see Refs. [8,38,39]. DS applies an external alternating current (AC) electric field across a dielectric medium. For permanent dipole moments, the complex dielectric function  $\varepsilon^*(\omega) = \varepsilon'(\omega) - i\varepsilon''(\omega)$  is associated with a correlation function of polarization fluctuations. Measurement of the polarization fluctuations can be performed in the frequency (AC) or time (DC) domains. A correlation function is measured for materials with dipole groups of different reorientation polarizations as they decay in multiple steps, giving rise to several relaxation processes. Heterogeneous systems, such as composites, or systems with strongly interacting dipoles, such as polar polymers and polymer composites, have broad and asymmetric distributions of relaxation times that correspond to a material's structure(s) at the molecular level.

Polizos et al. [40] used DS in wide frequency and temperature ranges to study the local and segmental dynamics of the thermoplastic polyurethane (PU) with

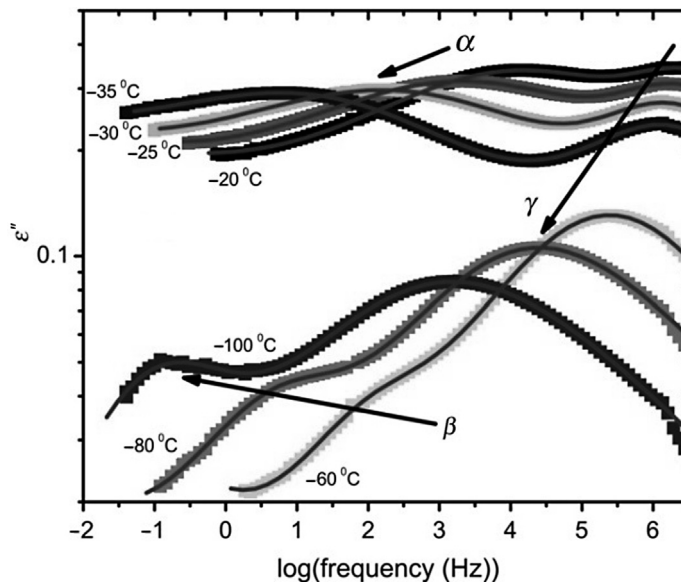


**FIGURE 10.2**

Dielectric loss curves of the unfilled PU matrix for selected temperatures, indicating the cooperative  $\alpha$  (associated with  $T_g$ ) and the local  $\gamma$ ,  $\beta$  relaxations [40].

*Copyright 2011. Reprinted with permission from Elsevier Ltd.*

polyethylene glycol (PEG) functionalized nanoTiO<sub>2</sub> dispersed in it. Three relaxations were observed (Figure 10.2) at temperatures below room temperature for the unfilled PU. In the order of increasing temperature, the first two subglass transition relaxation modes,  $\gamma$  and  $\beta$ , are associated with local motions of chain segments. The segmental,  $\alpha$ , relaxation at higher temperatures is positioned close to the calorimetric glass transition temperature ( $T_g$ ) and is attributed to dipole moment cooperative reorientations during the glass transition of soft segment microdomains. In the nanocomposites, an  $\alpha$  process overlaps with a low-frequency conductivity contribution due to variations in the surface charge density of the TiO<sub>2</sub>.

Segmental dynamics showed significant changes upon introduction of TiO<sub>2</sub> fillers (Figure 10.3). At higher temperatures, the segmental relaxation times were found to be nearly identical for composites and pristine PU (Figure 10.3a). However, as the temperature was decreased, a clear difference in the behavior of segmental dynamics was observed. The segmental relaxation mode of the composite shifted towards higher frequencies and became relatively faster compared with  $\alpha$  relaxation in the pristine PU at the same temperature (Figure 10.3b). Interestingly, the local dynamics and the activation energies calculated from the Arrhenius equation in the pristine PU and in the composites were found to be similar, indicating that the local conformations were independent of the

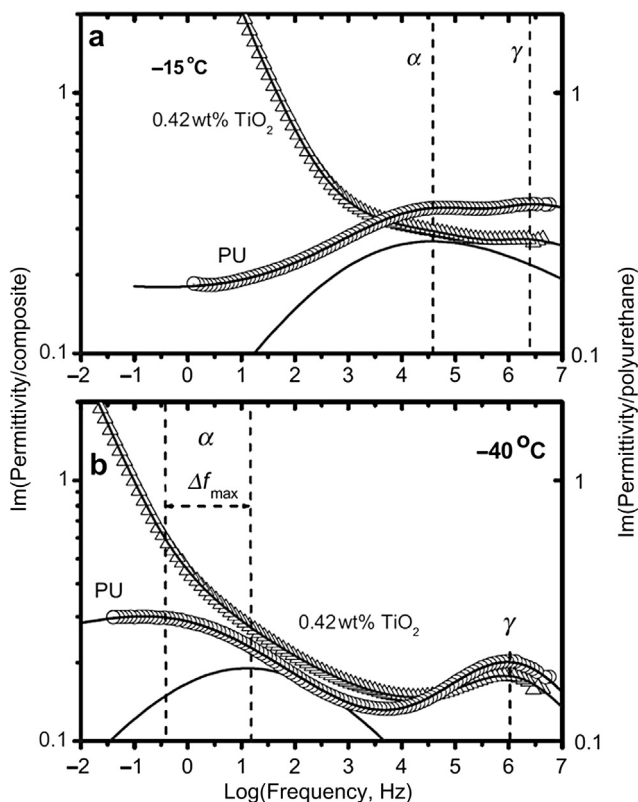


**FIGURE 10.3**

Comparison plot of the dielectric relaxations for the pristine PU and the 0.42 wt% in  $\text{TiO}_2$ . No shift is observed in the peak maximum frequencies of the local  $\gamma$  relaxations. However, when the temperature decreases toward the glass transition temperature, the segmental  $\alpha$  mode of the composite shifts toward higher frequencies [40].

Copyright 2011. Reprinted with permission from Elsevier Ltd.

PU–particle interaction strengths. Segmental relaxation exhibited a temperature dependence. The steepness of the temperature dependence for the segmental relaxation, such as the slope of the glass transition, can be quantified through the so-called fragility index ( $m$ ) [40–42].

Polymers, when filled with particles, displayed changes in fragility due to geometrical frustration and changes in the polymer-packing density [43]. Typically, the fragility index depends on the particle polymer interactions and is expected to increase or decrease for attractive and repulsive interactions, respectively. Despite hydrogen bond formation between the  $\text{TiO}_2$  particles and a PU matrix, both the  $T_g$  and the fragility were found to decrease with increasing  $\text{TiO}_2$  content in the PU. It was found that the  $\text{TiO}_2$  particles primarily associated with the hard

segments of the PU matrix due to favorable acid-base interactions with the N-H groups lead to a reduced number of interactions between hard and soft domains within the PU matrix. As a result, an increase in TiO<sub>2</sub> loading lead to increases in the amount of soft domains with higher segmental mobilities, a lower and broader  $T_g$ , and a decreased fragility index for the composites.

The effect of polymer segmental mobility on the DC conductivity of the composites at different temperatures, above and below their  $T_g$ , was also discussed. At the higher temperatures, the impedance response of the composites, characterized by conductivity values, was higher than unfilled (neat polymer) samples. At very low temperatures, composites exhibited better electrical insulation properties compared with the unfilled polymer, PU. The drastic temperature dependence of the conductivity/insulating ability of the flexible and lightweight, low- $T_g$  composites could be utilized as polymer electrolytes, as well as in the design of an electronic device operating in response to broad temperature windows [40].

Fragiadakis et al. analyzed the effect of silica nanoparticles on glass transition and molecular dynamics of a poly(dimethylsiloxane) polymer (PDMS) [44–46]. They carried out DS measurements in the frequency range from  $10^{-2}$  to  $10^6$  Hz over temperatures ranging from 140 to 310 K, and compared the results with those obtained by differential scanning calorimetry (DSC), TSC, and DMA. The DS, DSC, and TSC techniques showed, in general agreement with each other, that a fraction of polymer in an interfacial layer around the silica nanoparticles, with a thickness of 2–3 nm, presented modified dynamic behaviors.

Dielectric loss, measured isothermally in frequency scans, were replotted as a function of temperature for pure PDMS and two nanocomposites at three frequencies (Figure 10.4). They found a single loss peak in pure PDMS, while a double peak for nanocomposites was observed. The  $\alpha$  loss peak of nanocomposites was located at the same temperature as in the pure polymer matrix, with another ( $\alpha'$ ) loss peak at higher temperatures. Both relaxations became more separated and distinguished as a function of increasing frequency. The second loss peak corresponded to a fraction of the polymer in the interfacial layer of reduced mobility due to fine dispersion and strong interactions (hydrogen bonding) with the silica surface. Strong interactions slowed chain dynamics. They probed this fact by comparing with results obtained by computer simulations [47] that calculated a continuous distribution of relaxation times as the particle surface was approached. The distribution led to the presence of the double peak in nanocomposites.

Tomer et al. probed the local dynamics of the organic/inorganic composites of two and three phases. The composites were prepared by dispersing BT and/or organically modified montmorillonite (OMMT) particles in the epoxy resin and characterized the interfaces by DS over broad frequency (from  $10^{-2}$  to  $10^6$  Hz) and temperature (180–100 °C) ranges [48]. The interfacial dynamics below the glass transition temperature were found to depend on the polymer-particle interactions and particle weight fraction. In the temperature range between the  $T_g$  and 40 °C, a new relaxation mode was evident in the composites with 3 and 6 wt% OMMT, 30 vol. % BT, as well as in a three-phase system with both BT and

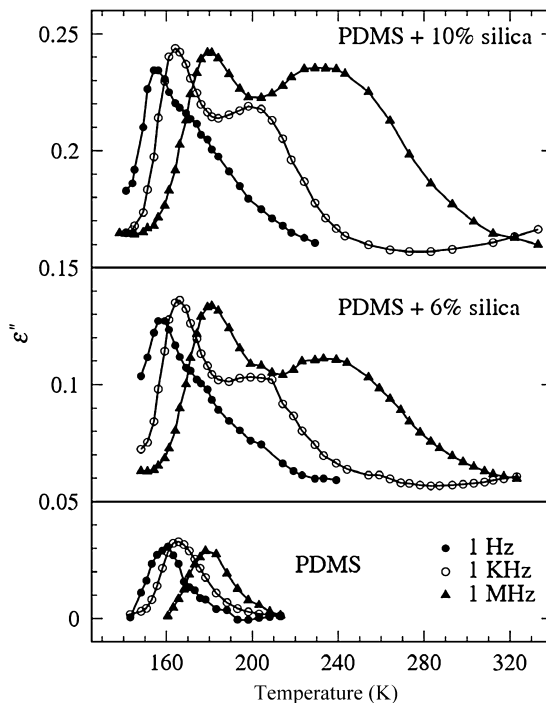


**FIGURE 10.4**

Dielectric loss ( $\epsilon''$ ) against temperature for pure PDMS and two nanocomposites at three frequencies are indicated on the plot [46].

*Copyright 2007. Reprinted with permission from Elsevier B.V.*

OMMT fillers. This relaxation mode was absent in pristine cross-linked epoxy matrix and in composites with 1 wt% OMMT and 10 vol. % BT. Figure 10.5 shows a comparison plot at 90 °C.

As the dynamics of the new relaxation mode were dependent on the particle type and weight fraction, they associated origin of the new relaxation mode to the formation of interfaces and, specifically, to unreacted and therefore mobile epoxy segments relaxing in the vicinity of the inorganic fillers. Despite large interfacial area per composite volume in the 30 vol. % BT composite, the dielectric relaxation of the interfacial process was suppressed when the BT surface was modified with organic coupling agents based on silane functional monolayers (Figure 10.5b). The proper functionality of the fillers allowed their integration with the polymer matrix and prevented formation of mobile segments at the polymer-particle interfaces, thereby enhancing the dielectric breakdown performance of these composites and thus energy storage densities.

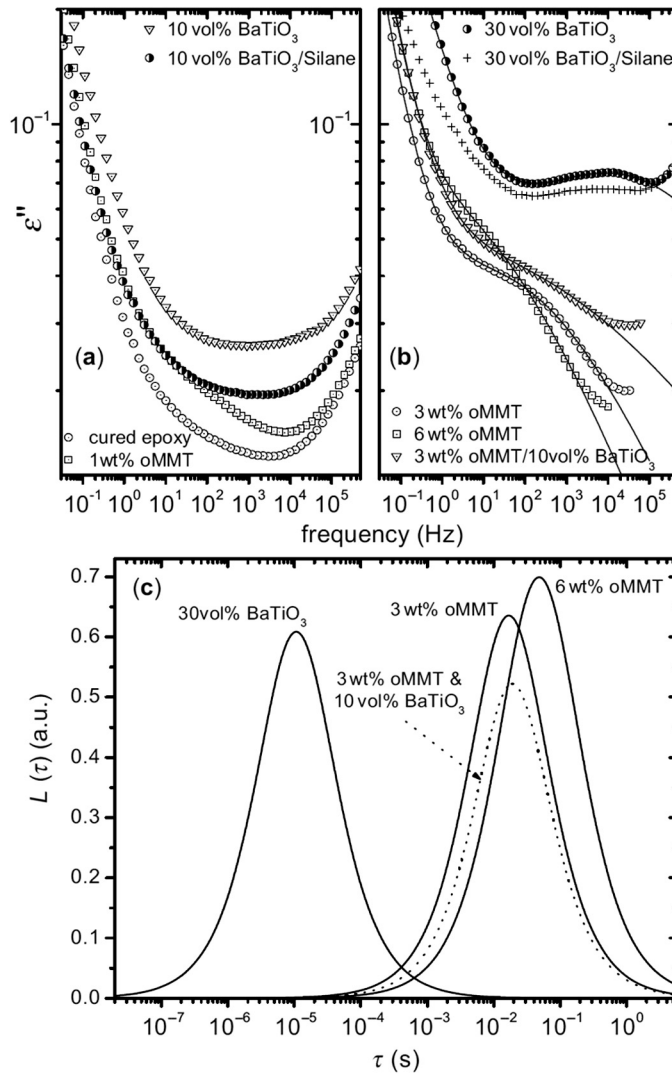


**FIGURE 10.5**

(a) Summarized dielectric loss plot at 90 °C for the pristine epoxy matrix and the two- and three-phase composites. (b) A relaxation process is evident in the composites with high filler content. The Cole–Cole dielectric function was found to yield the best fitting data. (c) The corresponding distributions of relaxation times are presented in the plot [48].

Copyright 2010. Reprinted with permission from AIP Publishing LLC.

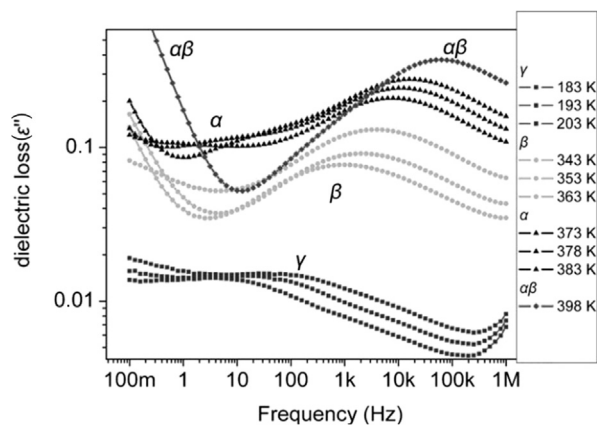


**FIGURE 10.6**

Representative dielectric relaxation spectroscopy spectra of dielectric loss as a function of frequency for sample with 3% silica for selected temperatures [49].

Copyright 2012. Reprinted with permission from Wiley Periodicals, Inc.

It was also noticed that the dynamics of the OMMT composites were about three orders of magnitude slower than those of the BT composites, as manifested by the time distribution shift toward longer relaxation times. This dynamical behavior clearly showed differences between dynamics of the physisorbed (restricted mobility) polymer on the MMT and BT surfaces, indicating a more coherent and robust interface for the epoxy/OMMT than for the epoxy/BT. The corresponding energy barriers (activation energies) associated with these motions for MMT systems were twice those of the BT systems.

To elucidate the impact of the silica nanoparticles on the molecular dynamics of poly(methyl methacrylate) (PMMA), Kyriakos et al. [49] employed DS along with other techniques, such as DSC and TSC. A significant impact of the silica nanoparticles on the segmental dynamics of the polymer matrix was observed based on the shift of the  $\alpha$  (segmental) relaxation to lower frequencies using DS. Figure 10.6 shows the dielectric loss spectra recorded for 3 wt% silica particles in PMMA at selected temperatures. The temperature dependence of dielectric loss versus frequency was presented for selected temperatures.

Three dielectric relaxations ( $\gamma$ ,  $\beta$ , and  $\alpha$ ) were observed in the order of increasing temperature, in addition to a complex  $\alpha\beta$  relaxation at high temperatures. The  $\gamma$  and  $\beta$  relaxations were characterized as secondary relaxations as they originate from local motions of two different side groups of the polymer chain. The  $\alpha$  relaxation, attributed to the dynamic glass transition, marks the dielectric fingerprint of a glass transition and originates from the cooperative, concerted motions of large fragments of the chain backbone. The  $T_g$  was observed

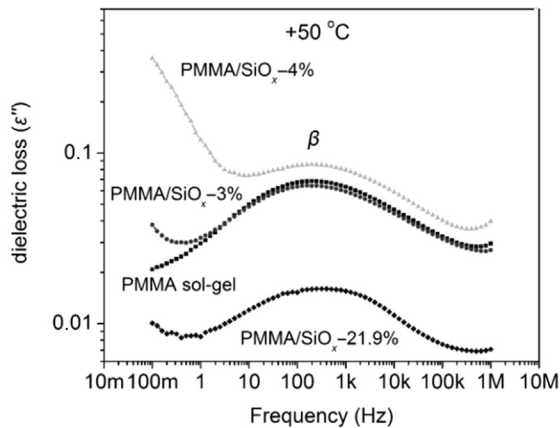


**FIGURE 10.7**

Comparative isothermal plot of the dielectric loss versus frequency at 323 K for PMMA and PMMA-silica composite samples as a function of silica mass concentration [49].

Copyright 2012. Reprinted with permission from Wiley Periodicals, Inc.

at 5 Hz and 378 K. In the region of higher temperatures and frequencies, the merging of the  $\alpha$  and  $\beta$  relaxation to a complex  $\alpha\beta$  relaxation was observed, which is a typical behavior for PMMA.

The  $\beta$  relaxation is the dominant relaxation in the DS spectrum of PMMA because the molecular group that creates it has a very strong dipole moment; therefore, PMMA displays its relaxation mainly through the  $\beta$  mode. It was stressed that the  $\alpha$  relaxation is very difficult to detect in isothermal plots for two reasons: (i) the  $\alpha$  relaxation of PMMA is very weak and broad (that is, the  $\alpha$  transition covers a very large range of frequencies as a very broad distribution of relaxation times, but was observed over only a limited temperature region); (ii) the presence of a strong conductivity contribution in the region of low frequencies at temperatures above  $T_g$ , where the  $\alpha$  relaxation is expected, is also a typical behavior for acrylates and methacrylates. The observed conductivity (Figure 10.6), usually found near or below unit frequencies region, originates either from charges trapped between the interfaces of the polymer and the filler or from trapped large molecules of solvent.

A comparative DS spectra in the region of  $\beta$  relaxation (Figure 10.7) was presented to study the effect of silica nanoparticles on the PMMA matrix. Secondary relaxations related to the motions of the side chains were not affected as a function of the weight fraction of silica. Results were in agreement with those reported by Li et al. [50]. A more general survey of the dielectric behavior of the composite samples was obtained through an Arrhenius plot (dielectric map) in Figure 10.8, where the frequency at maximum dielectric loss was plotted against reciprocal temperature. The Arrhenius depiction revealed the temperature/timescale behavior of each relaxation.

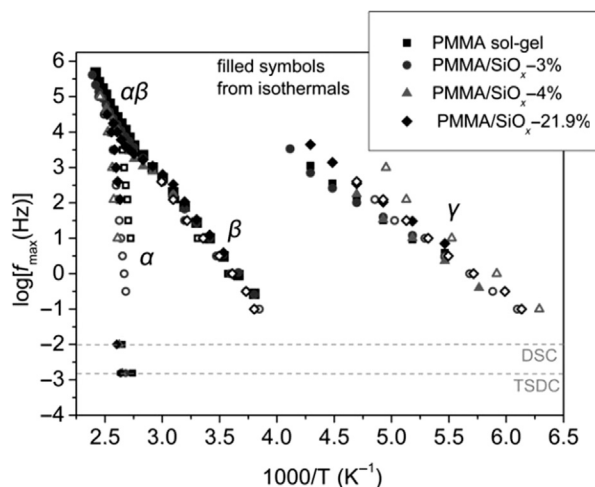


**FIGURE 10.8**

Arrhenius plot (dielectric map) for PMMA and PMMA-silica composite samples as a function of silica mass concentration. The data from DSC and TSDC have been included at the equivalent frequencies. Data obtained from isothermal (filled symbols) and isochronal (blank symbols) plots are presented [49].

Copyright 2012. Reprinted with permission from Wiley Periodicals, Inc.

In one plot, the temperature points obtained by other techniques, such as DSC and thermally stimulated depolarization current (TSDC), were included at the equivalent frequencies of  $\sim 0.01$  Hz and 1.6 mHz, respectively. In addition to the data obtained from the simple isothermal depiction, data obtained from isochronal plots were also used. In these plots, dielectric loss data obtained isothermally at various frequencies were replotted as functions of temperature. Though such plots are not presented in this review, their use enriches the Arrhenius plot, especially in the region of the  $\alpha$  relaxation.

All three relaxations were observed in a respective temperature region (Figure 10.8). An interesting point in the Arrhenius plot was the region of merged  $\alpha$  and  $\beta$  relaxations in a complex  $\alpha\beta$  relaxation. This complex process is faster than the  $\beta$  relaxation alone (smaller slope) but slower than the  $\alpha$  relaxation alone (larger slope). The  $\alpha\beta$  relaxation, despite being attributed to a rubbery state of the polymer above its  $T_g$ , originates from segmental molecular motions typically associated with the  $\alpha$  relaxation.

No systematic changes in  $\gamma$  or  $\beta$  relaxations were observed due to the added silica fillers in PMMA. In the region of the glass transition temperature ( $\sim 373$  K), the  $\alpha$  relaxation enters the measurement window, and, through its evolution, merges with the  $\beta$  relaxation into a complex  $\alpha\beta$ . Comparing samples with different silica content, a shift of the  $\alpha$  relaxation to higher temperatures—lower frequencies (as superpositioned variables for materials response) with increasing

silica content was observed. The results obtained were found to be in agreement with those obtained through the DSC and TSC data, which demonstrates the mechanical (i.e., structural) relationship to electrical DS phenomena.

The  $\alpha\beta$  relaxation maximum was also shifted to higher temperatures—lower frequencies for increasing silica content. In general, DS demonstrated that the presence of silica resulted in a slowing down of segmental dynamics of the PMMA matrix, which reflects a restriction of molecular mobility of the matrix induced by the silica. This was observed as temperature or frequency effects on  $\alpha$  or  $\alpha\beta$  relaxations. To further explain the electrical effects, one must determine the structural differences, such as measuring the formation of hydrogen-bonding interactions between silica surface hydroxyl groups and the ester side group of the polymer chain, that is, spectrally analyze the polymer-particle interface.

---

## 10.5 TSC SPECTROSCOPY STUDIES OF NANODIELECTRICS

The nonisothermal dielectric relaxation behavior of polymers may be used to study the nature of permanent dipoles and assess trapped charge in a material. Dielectric relaxation is a characterization of the amount of charge and the hindrance of motion of the charge by frictional forces. The resistance to motion by applied electrical forces is a strong function of temperature. It follows that the motion and response time to electrical stimuli (such as the frequency, of dipoles and free or bound charges) will also be temperature dependent. The basis for TSC methods seeks to fingerprint charge mobility processes through a thermal activation of bound and free charges. It is widely used and complementary to the DS technique [51]. TSC, also called TSDC, is applied to study dispersed phases, such as dispersed or porous metal oxides, polymers, liquid crystals, amorphous and crystalline solids, polymer nanocomposites, biomaterials, cells, tissues, etc. [52].

There are several reports on dielectric properties of nanodielectrics in recent years. For example, how charge trapping energy levels or strengths are related to the insulation performance of nanodielectrics, as breakdown resistance [52]. Another question is whether the addition of nanofillers or additives changes dielectric performance due to their ability to enable or impede the motion of charges in composite material [52]. Since there is increasing evidence that the internal interface regions in nanodielectrics provide sites for carrier traps, the TSC technique can be used to probe the interaction zone by examining the temperature-activated movement of stored charge in the interfacial regions surrounding the particles [51–54]. This section reviews the use of the TSC technique to analyze the influence of nanoparticles in the polymer matrix of polymer-ceramic nanodielectrics.

Gaur et al. studied the effect of low loading concentrations (i.e., 2, 4, 6, and 8 wt%) of BT on  $\beta$ -phase polyvinylidene fluoride (PVDF) [55]. Nanodielectric samples were prepared by a solution mixing-dispersion method. The film samples

were electrically poled at room temperature with different polarizing fields (i.e., 10, 20, 30, 40  $\text{kV cm}^{-1}$ ). The samples were discharged and then TSC was measured as a function of temperature with a constant heating rate of 3  $^{\circ}\text{C min}^{-1}$ .

In general, the TSC of PVDF is characterized by two emission peaks. One at  $-42^{\circ}\text{C}$  corresponds to the glass-to-rubber transition contributed by a dipolar relaxation of the amorphous phase. The second emission, obtained at 120–180  $^{\circ}\text{C}$ , was assigned as a dipolar relaxation of either the crystalline phase or of the interfacial transitional regions, intermediate between crystalline and amorphous phases. Since this higher temperature peak appeared well above the matrix glass transition temperature, the current detected was due to the mobility of charges accumulated near the amorphous–crystalline boundaries, analogous to a Maxwell–Wagner (MW) effect. Figure 10.9 shows evolution of this emission peak as a function of polarization potential as undistributed polarization.

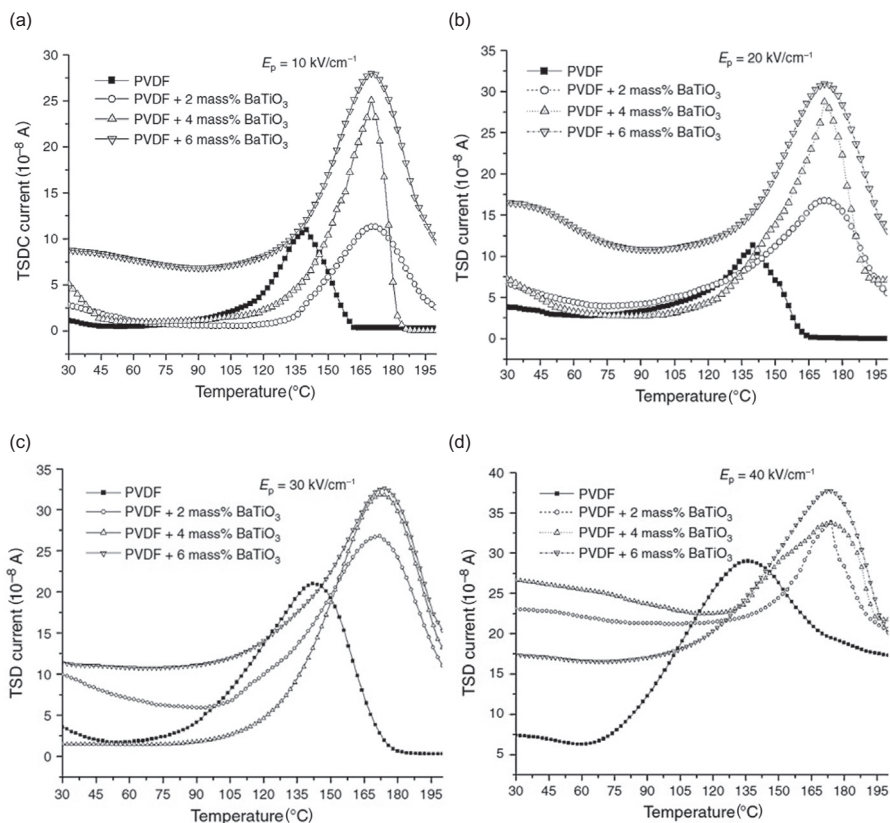


**FIGURE 10.9**

TSC spectra of  $\beta$  phase PVDF and its BT nanocomposites at polarizing fields of (a) 10, (b) 20, (c) 30, and (d) 40  $\text{kV cm}^{-1}$  [55].

During collection of the TSC spectrum, interfacial charges are displaced as local fields in dissimilar parts of the sample are reversed. Neutralizing charges of the opposite sign are conveyed to the interface, resulting in a current. A current emission resulting from discharge of interfacially located charges is known as a MW effect. This effect is only expected for semicrystalline or micro- and nanocomposite materials that have interfacial regions and are able to store charge.

The relaxation time, charge storage, and activation energies are significantly affected by the charge “friction” of induced charges for a BT in PVDF matrix nanodielectrics composite. The charge friction in the presence of nanoparticles increased with the increase in the particle concentration of the nanodielectrics, as evident from an increased emission temperature and TSC currents (Figure 10.9). The nanoparticles’ high surface area presents the capability for charge transfer between the inorganic (ionic) phase to the organic (covalent) phase, though the nanoparticle interfaces hold charge more tightly than the polymer alone. It was reported that the activation energy of the MW emission peak increased with the increase of polarizing field.

Since the structures of polymer nanocomposites can be quite complicated, it can also be very difficult to distinguish one from another of several possible charge relaxation processes. Appearance of only a single relaxation peak, as evident from Figure 10.9, might suggest the merging of dipolar and interfacial relaxations. Many TSC spectra show convoluted emissions that represent different relaxation mechanisms related to formation and activation energy to discharge of different charge storage structures.

Rathore et al. [52] studied the TSC relaxation of silica fillers in a polycarbonate (PC) matrix. Figure 10.10 shows the TSC spectrum of pure PC or PC/nanoSiO<sub>2</sub> (7 wt%), which showed a single stimulated current emission peak, while nanocomposites with intermediate 3 or 5 wt% silica concentrations in PC showed two emission peaks. The TSC parameters such as activation energy, charge released, and relaxation time are summarized in Table 10.2.

It was observed from Table 10.2 that more charge current was released for 3%, 5%, and 7% filled nanocomposite than for pristine PC. These results suggested the SiO<sub>2</sub> nanofiller enhanced the charge storage capacity of PC. The nanocomposite samples showed a nonlinear behavior of activation energy with SiO<sub>2</sub> concentration, which might be a concern with regard to the consistency of dispersion across composite samples.

The single peak in the TSC spectra of PC polymer was attributed to an  $\alpha$ -relaxation (main chain segment motion of the polymer) associated with a glass transition of the amorphous phase of the PC matrix. The depolarization current peaks in 3% and 5% SiO<sub>2</sub> nanocomposites showed two relaxation processes: dipolar and space charge relaxations. The single broad peak in 7% SiO<sub>2</sub> nanocomposites indicated that the two components’, dipolar and space charge, relaxations were merged. This was therefore provided as the reason why activation energy was unable to explain the behavior of this emission.

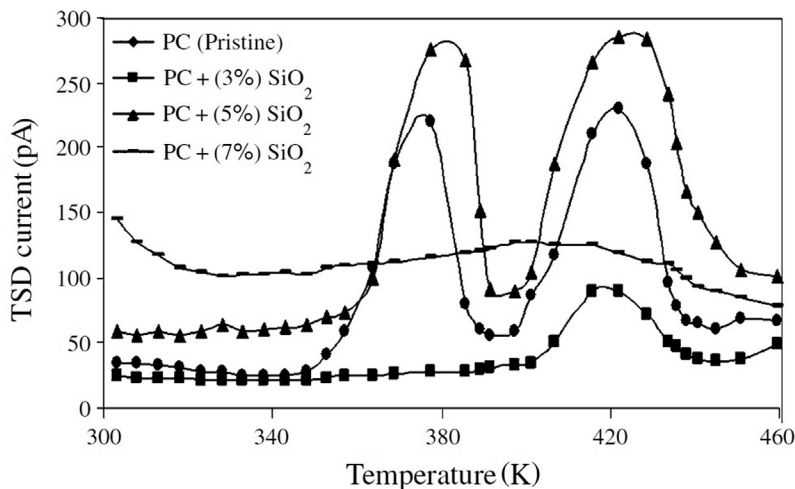


FIGURE 10.10

TSC spectra of PC and PC-Silica nanocomposites polarized at 423 K and at  $100 \text{ kV cm}^{-1}$  poling field [52].

Copyright 2011. Reprinted with permission from Springer.

Table 10.2 TSC Parameter of PC and PC/SiO<sub>2</sub> Nanocomposite Samples [52]

Sample	Peak	Peak Current (pA)	Peak Temperature (K)	Activation Energy (eV)	Charge Released $\times 10^{-12}$ (C)	Relaxation Time $\times 10^{-14}$ (s)
PC	II	91	419	0.12	273	2180
PC + SiO <sub>2</sub> (3%)	II	204	367	0.68	607	46
PC + SiO <sub>2</sub> (3%)	II	241	422	0.12	765	17
PC + SiO <sub>2</sub> (5%)	II	275	367	0.08	851	0.01
PC + SiO <sub>2</sub> (5%)	II	295	425	0.09	1276	27
PC + SiO <sub>2</sub> (7%)	II	128	403	0.01	2878	0.06

Copyright 2011. Reprinted with permission from Springer.

The appearance of single broad peak at the higher concentrations might also be due to the saturation of resultant polarization or to diffusion of a large number of oxygen atoms/ions in polymer matrix. The sharp TSC emission at higher temperature for the samples filled at 3% or 5% SiO<sub>2</sub> indicated the existence of deeper, that is, stronger, trap energies related to the charge stability. The traps for nanodielectrics are commonly formed at the interface between the inorganic silica (SiO<sub>2</sub>) nanoparticles and matrix, PC.

Generally, space charge relaxation emission is shifted with an increase of the polarizing field. The relaxation can be shifted to either higher or lower temperature. In the case of samples from [Figure 10.10](#), when the concentration of SiO<sub>2</sub> was increased from 3% to 5%, no shift of the TSDC emission was observed upon increasing the polarizing field (not shown in this figure). Instead, a second emission peak was observed that was assigned as due to an altered space charge in the polymer nanocomposites. The two sharp TSC peaks in nanocomposite samples filled with lower concentration of SiO<sub>2</sub> show a strong modification of TSC spectra compared with pristine PC.

The activation energy of the newly formed emission was largest for 3% SiO<sub>2</sub>-filled samples and lowered in activation energy as a function of increasing SiO<sub>2</sub> concentration. Here TSC is utilized to examine the modification of the composite space charge relaxation process. The addition of silica is responsible for the creation of a new charge trap structure by introducing nanofillers. The trapping of charge carriers in shallow versus deeper traps for the nanocomposite is an indication of the dispersion quality, where, in this case, better dispersion created a deeper trap site, which is a possible reason for this current emission [52].

Okhlopko et al. [56] acquired TSC spectra for nanoceramic alumina and  $\beta$ -sialon fillers incorporated into a polytetrafluoroethylene (PTFE) matrix to assess the surface charge effects of nanofiller introduction ([Figure 10.11](#)) without prior applied polarization. While nanoceramics each showed TSC emission peaks, neat PTFE did not generate TSC currents. Nanosize  $\beta$ -sialon had a broad peak in the 470–570 K range, which indicated the presence of high-temperature traps for the charge carriers and was related to the relaxation of the polarization of  $\beta$ -sialon. The TSC spectrum of Al<sub>2</sub>O<sub>3</sub> showed two peaks at 430 and 510 K, respectively. Carrier relaxation at lower temperatures indicated the presence of traps in the alumina-crystal structure.

The polarization charge of the nanoceramic particles affected PTFE polarization in polymer nanocomposites and charge adhesion to the polymer matrix. While the neat PTFE was electrically neutral (see [Figure 10.11b](#)), samples containing 2 wt% nanoceramic particles ([Figure 10.11c](#)) showed stable currents, resembling conduction currents. However, a stable current with significantly high values suggested that the TSC currents might be related to the charge relaxation on the filler particles. Since the samples did not undergo electric polarization, the most probable origins of the currents could be due to the movement of charge carriers released from the nanoceramic particles under heating. It was believed that a structuring of the polymer matrix around nanoceramics occurred under influence of the field of electric charge present on the nanoparticle surface. What is interesting is that the charges are continuously released over a range of temperatures, rather than discretely, implying a distribution of binding states rather than just one.

Roy et al. [57] used TSC measurements to investigate the nature and the origin of charge carrier traps in cross-linked polyethylene (XLPE)/silica nanocomposites. A peak in the temperature region 50–60 °C for all the microcomposites and nanocomposites ([Figure 10.12](#)) was observed that originates from the

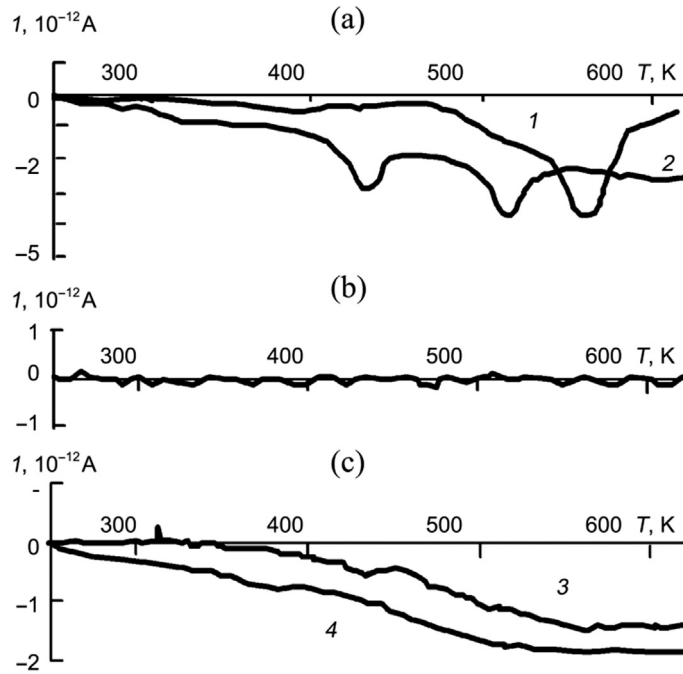


**FIGURE 10.11**

TSC currents as a function of temperature for (a-1)  $\beta$ -sialon, and (a-2)  $\text{Al}_2\text{O}_3$  nanoceramic (NC) particles; (b) neat PTFE; and (c) polymer nanocomposite samples consisting of PTFE with 2 wt%  $\beta$ -sialon (3) and PTFE with 2 wt%  $\text{Al}_2\text{O}_3$  (4) [56].

Copyright 2013. Reprinted with permission from KCS Publications.

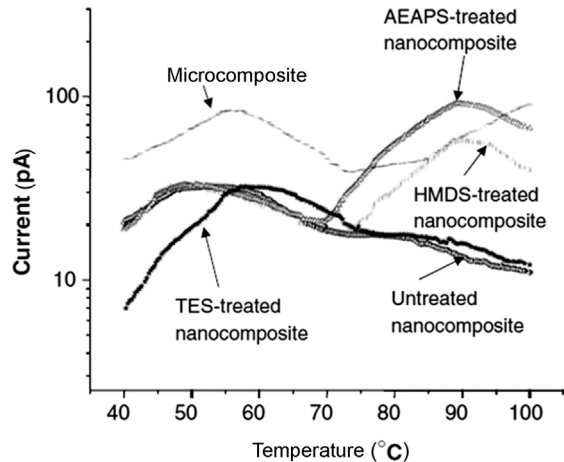


**FIGURE 10.12**

TSC spectra of silica-filled composites. Triethoxyvinylsilane (TES), *n*-(2-aminoethyl) 3-aminopropyltrimethoxysilane (AEAPS), or hexamethyldisilazane (HMDS) were the surface modifiers employed for silica nanofillers [57].

Copyright 2007. Reprinted with permission from Springer.

amorphous–crystalline interface of the polyethylene. At higher temperatures (80 °C), the TSC spectra for the microcomposite and untreated nanocomposite were different. A larger microcomposite current is attributed to a larger MW interfacial relaxation of the silica microparticles (labeled the  $\rho$ -peak). The large MW response is a result of charges trapped at the interface of the microparticle, which was not present in the nanocomposite sample [58]. The Auger-electron appearance-potential spectroscopy (AEAPS)- and HMDS-treated nanocomposites showed an emission peak at approximately 90 °C, much different from the microcomposite peak or other nanocomposites. These were ascribed to originate from charge carriers trapped at the polar surface groups of the silane surface modifiers employed. Such groups may create surface states with strong polar interactions as deeper trap sites.

Smith et al. [59] used TSC measurements to investigate the nature and origin of charge carrier traps in nanosilica/XLPE nanocomposites. An ambient temperature poling of 25 °C followed by a temperature ramp of 3 °C min<sup>-1</sup> from -160 to 90 °C resulted in TSC spectra (Figure 10.13) that indicated changes in number and perhaps energy of charge trap sites. Smith et al. observed a threefold enhancement of  $\alpha$  relaxation peaks above room temperature in their nanocomposites. Polar surface nanosilica increases the number of charge trap sites with a concurrent increase in thermally-assisted relaxation current. Upon poling, more charge carriers were captured in interfacial trap sites so that, upon heating, more charge carriers were thermally excited into the conduction band, producing TSC current.

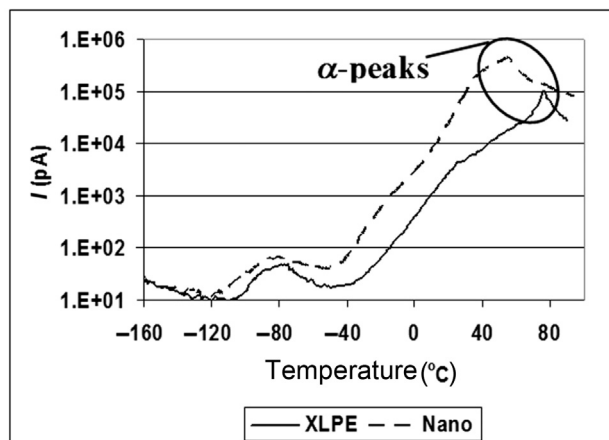


**FIGURE 10.13**

TSC plot for the base XLPE polymer and 12-1/2% untreated XLPE/nanosilica composite [59].

Copyright 2008. Reprinted with permission from IEEE.

## 10.6 PULSED ELECTRO-ACOUSTIC ANALYSIS OF NANODIELECTRICS

Knowledge of the spatial distribution and evolution of embedded charge in thin dielectric films has important applications in semiconductors, high-power electronic devices, and high-voltage DC power cable insulation, etc. [60]. It can be studied using various mechanical, thermal, or, for example, acoustical stimulation methods. This is analogous to the thermal stimulation of current observed in TSC, but with additional spatial distribution information from where the currents originate within the sample. The thermal methods consist of post-polarization and discharge, applying a thermal pulse on the surface of the dielectric film, and measuring the response of the electric signal from the sample that contains charge distribution information.

In acoustic methods, an ultrasonic pulse results in a charge signal emission. The pressure wave or acoustic pulse is thus used to excite electrical signals that will also contain charge distribution information. Alternatively, an electrical excitation pulse will induce an acoustic signal that contains such information. One of the most commonly utilized acoustic techniques is the pulsed electro-acoustic (PEA) method [61]. The density and polarity of the space charge may be obtained from the physical characteristics of the resulting acoustic signal. The difficulty lies in the ability to apply a vibration stress uniformly. Problems may also arise when the charge distribution or polarization profiles are complex [62–64]. Large excursions on the PEA curve at the electrodes are compensating for the “image charge,” that results from the applied field.

Smith et al. [59] reported the use of PEA measurements of XLPE/silica nanocomposites. The PEA results suggested that increased trap sites leads to decreased charge mobilities and lower energy (more stable) carriers. PEA measurements (refer to Figure 10.14) were performed on three different samples: XLPE, XLPE/silica microcomposites, and surface-treated XLPE/silica nanocomposites.

Neat XLPE film displayed a region of cathode-shielding homocharge (injected from the electrode, with same sign) extending nearly to the anode, where some recombination would occur with homocharges there, in effect acting as a linear resistor. Similarly, the microcomposite contained some field-strengthening heterocharge regions near both the electrodes, probably due to the electron migration from the cathode. However, the surface treated XLPE/silica nanocomposite (labeled “VS-Nano” in Figure 10.14) plot indicated the presence of a shielding homocharge at both the anode and cathode, which can be evidence of increased trap sites at the charge carriers’ paths, indicating a lack of charge mobility for injected space charges under the influence of the applied field and/or scattering due to the inclusion of the nanoparticles.

Schadler et al. [65] measured the space charge using PEA in unfilled and 7.5 wt% alumina-filled polyamideimide (PAI) subject to a DC field where the field strength was varied from 5 to 30 kV mm<sup>-1</sup>. Figure 10.15 shows the

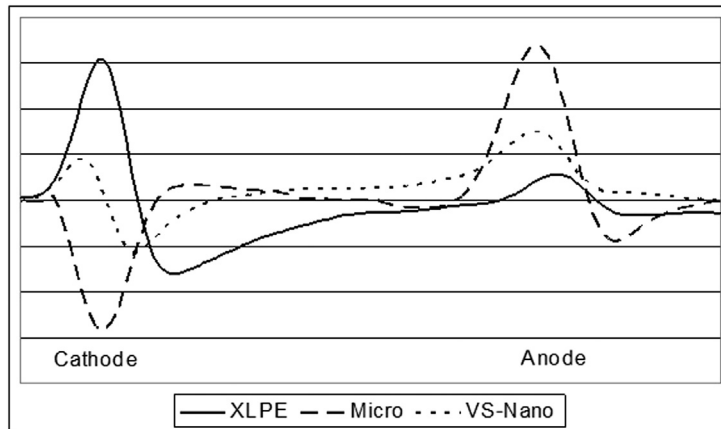


**FIGURE 10.14**

Space charge profiles from the PEA experiment 10 s after powering off. The nanocomposite shows regions of homopolar charge near both electrodes [59].

*Copyright 2008. Reprinted with permission from IEEE.*

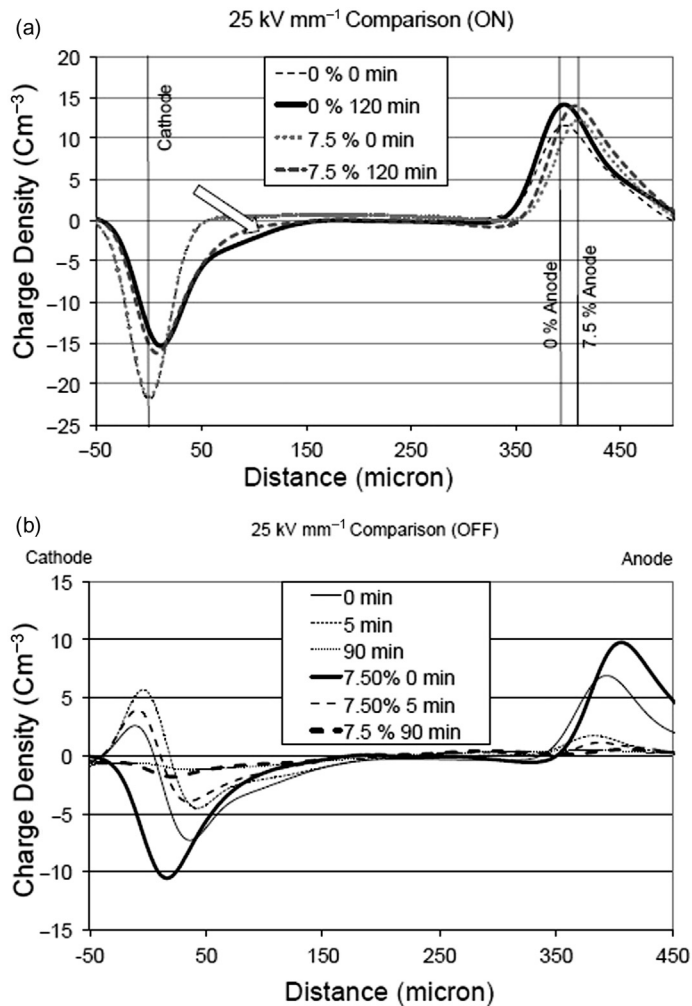
evolution of the charge profile as a function of time. With the voltage on, large “image” charges at the electrodes can mask the contribution to the PEA signal from charge buildup in the sample, though some charge injection was observed for the neat polymer at 120 min.

To visualize and measure the charge distribution in the sample, the field was removed and the sample grounded. The total charge at the cathode was quantified by integrating the charge density near the cathode after 1 min of grounding. The charge integral over the range of fields used is shown in Figure 10.16.

Where charge injection was measured, higher fields lead to more charge injection. Within the resolution of this method, no differences were measured between the composite material and the unfilled material. This is in contrast with many other cases and, as observed in the TSC studies above, where the addition of nanoparticles will alter the space charge buildup within the polymer, typically decreasing the total charge accumulation [66].

Charge distribution evolution involves the injection, transport, and trapping of the carriers. In this system, the influence of the PAI dominates the steady-state space charge accumulation and no changes are apparent in these mechanisms for the composite. For both materials, the removal of the field prior to PEA analysis revealed a homocharge present adjacent to the cathode, indicated by the negative charge density in the sample. At the anode, no charge injection was seen, only the decay in the image charge.

Nelson et al. [67] studied the PEA response of epoxy/titania composite systems. Differences in charge accumulation were observed in various composites systems depending on whether the titania filler particles had micrometer or

**FIGURE 10.15**

Pulsed electroacoustic results showing: (a) charge profile evolution in unfilled and 7.5 wt% alumina-nanofilled PAI over a period of 2 h at a field of 15 kV mm<sup>-1</sup>; and, (b) charge distribution in unfilled and 7.5 wt% alumina-filled PAI with the voltage off and sample grounded after poling at 25 kV mm<sup>-1</sup> for 2 h [65].

*Copyright 2012. Reprinted with permission from IEEE. The times listed are the time elapsed after the voltage was turned off. Homocharge injection can be seen at the cathode.*

nanometer dimensions. PEA results suggested that, for micron-sized titania/epoxy composite system, carriers were blocked at the anode yielding heterocharge, giving rise to large, anomalous field distortions (Figure 10.17). The behavior clearly has substantial implications for the subsequent migration of charges. In contrast, the decay of charge was observed (Figure 10.18) to be very rapid in the

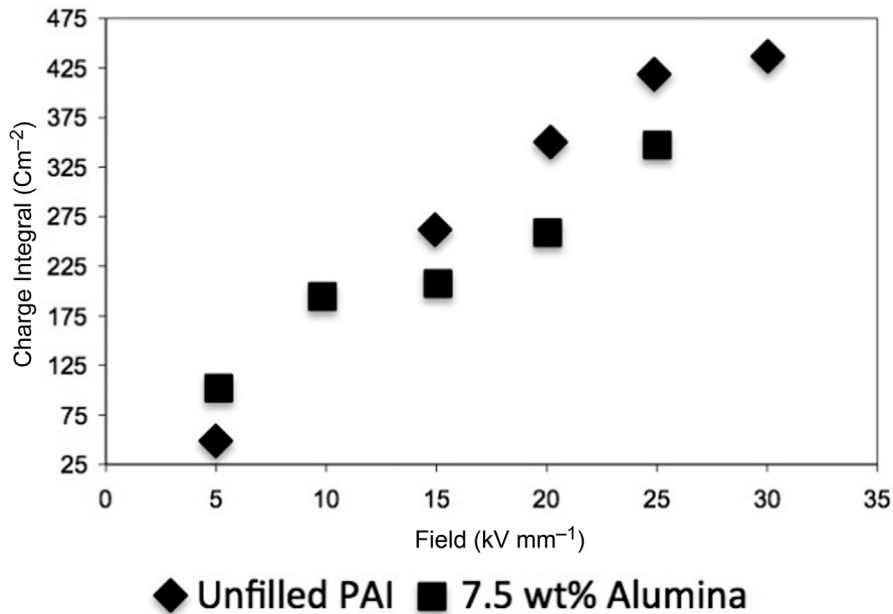


**FIGURE 10.16**

Absolute value of the charge integral at the cathode after removal of the field and grounding for 1 min [65].

Copyright 2012. Reprinted with permission from IEEE.

nanosized titania/epoxy composite system, with insignificant homocharge remaining after just 2 min. Although some injection of negative charge was observed at the cathode, the nanofilled material was characterized by much less charge transport, probably the result of the larger density of traps.

Liao et al. [68] studied the space charge profiles of low-density polyethylene/montmorillonite (LDPE/MMT) composite systems at varied filler contents of MMT, obtained using the PEA method. Less accumulations and transfer of space charge in the LDPE/MMT with MMT content of 1 wt% was observed compared with those of pure LDPE. On the other hand, when the MMT concentration was raised to 3 or 5 wt%, large amounts of heterocharges were accumulated in the sample bulk due to ionization. The difficulty with clay materials in hydrophobic polymers is the achievement of quality particle dispersion, which can lead to inorganic aggregation and inhomogeneous fields that assist in the creation or storage of charge.

Chakraborty et al. [69] investigated the space charge accumulation behavior in epoxy composites loaded with different concentrations of Al<sub>2</sub>O<sub>3</sub> fillers using the PEA method. It was reported that the presence of Al<sub>2</sub>O<sub>3</sub> particles lead to space charge accumulation inside the bulk of sample, attributed to the presence of Al<sub>2</sub>O<sub>3</sub> particles that modified the space charge trap distributions. Space charge

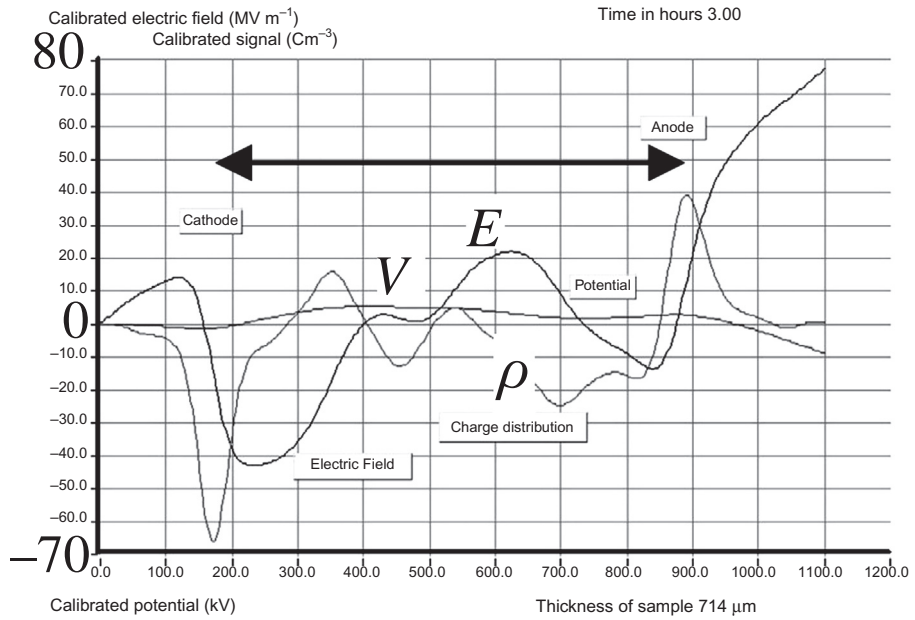


**FIGURE 10.17**

Pulsed electroacoustic study of micronized  $\text{TiO}_2/\text{epoxy}$  showing complexity of the PEA measured charge distribution [67].

Copyright 2002. Reprinted with permission from IEEE.

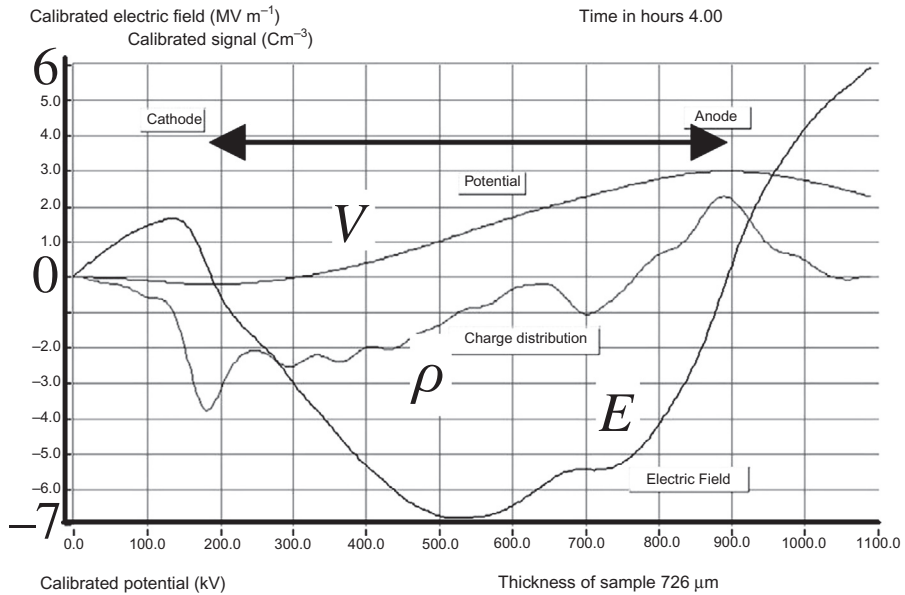


**FIGURE 10.18**

Pulsed electroacoustic study of nanosized  $\text{TiO}_2/\text{epoxy}$  showing complexity of the PEA measured charge distribution [67].

Copyright 2002. Reprinted with permission from IEEE.

accumulations were especially observed at higher particle concentrations though it was also reported that epoxy/ $\text{Al}_2\text{O}_3$  composite samples appeared to accumulate lesser amounts of charge compared with the unfilled epoxy.

Ju et al. [70] studied the PEA results of silica/LDPE nanocomposites using four different silica nanoparticles with varied surface modification. All silica nanoparticle composites suppressed the formation of space charge through injection or accumulation. Surface modification of the nanoparticles was suggested to improve its interfacial adhesion and dispersion in the matrix to provide more homogeneous internal field and suppress space charge injection. Huang et al. [71] and Ma et al. [72] also reported changes in the distribution of space charge caused by surface modification.

---

## 10.7 SUMMARY

Nanodielectrics are readily processed via solution or extrusion processing techniques and are comprised of highly insulating polymeric materials mixed with nanometer-sized ceramic fillers of unique dielectric permittivity and properties. Nanodielectrics with well-dispersed ceramic nanoparticles offer large interfacial contact zones between the high surface area per volume nanoparticulate fillers and their surrounding matrix, compared with conventional microcomposites employing microparticles. To properly engineer these composites, it is necessary to measure and well-characterize the interfacial phase dielectric properties in addition to those presented by the polymer or particles alone. Measurement of the properties of nanoparticles alone is rather difficult due to, for example, field exclusion which is caused by high surface activity and conductivity. This chapter discussed the tools of DS of polymer and nanocomposites and the special challenges of nanoparticles' measurements, TSC analyses of polymer composites, and pulsed electroacoustic analysis as one modality to measure localization of charge with respect to electrodes during polarization cycling.

The techniques presented are used only in conjunction with good material characterizations, including transmission or scanning electron microscopies, x-ray or electron diffraction, and x-ray and chemical spectroscopies, which were not presented here. The most significant aspect with regard to nanoparticles, compared with their analogous microparticle counterparts, is the surface activities and mobility of charge that are enabled with respect to the large interfacial interaction areas per volume of nanocomposite. These interaction zones vary greatly in strength and structure, from physisorbed to chemisorbed to coordinate covalent and direct covalent bonds, with distinct delocalized or localization of charge. Quality of dispersion presents potential for particle-particle and void tunneling behaviors in addition to bulk materials properties that are commonly observed in microparticle composites. The techniques reviewed measure the dielectric properties for nanodielectrics, but also permit the characterization of their nanostructure by implicating structures that are capable to produce the behaviors observed.

DS measures the applied field response of dielectric relaxation mechanisms as a function of frequency and temperature. Ceramics, polymers, and the composite interfaces, respond at unique time scales that allow measurement of ceramic and polymer behaviors and phases. The quantity of the interface per volume is unique for nanoparticle composites. The surface conductivity of nanoparticles precludes most other means to characterize nanoparticle impedances directly, though a slurry methodology was found to be well suited. Permittivity and dynamic and static conductivity losses as a function of composition and temperature are characterized.

Through TSCs, a separate means to observe the importance of the phase and phase transitions of the polymer matrix are measured. The resistance to motion by applied electrical forces is a strong function of temperature. The basis for TSC methodology is to fingerprint charge mobility processes and measure thermal activation of bound and free charge mobilities, which can be induced during sample manufacturing, after induced polarization, or polarization cycles (i.e., to assess sample lifetime performance or degradation mechanisms). TSC is widely used and complementary to the DS technique.

Pulsed electroacoustic analysis is one modality for a pressure wave propagation induction of charge relaxation, which is therefore analogous to laser-induced pressure pulse, piezo-electrically induced pressure step, thermal pulse, thermal pulse step, and laser-induced modulation techniques for measurements of space charge. PEA uses an applied electric pulse stimulus to induce charge mobility and relaxations, which results in an acoustic emission signal containing charge sign, quantity, and location within the sample. The PEA charge profiles can be quite complex and difficult to analyze effectively. While both TSC and PEA offer quantification of “trapped” charges, PEA supports analysis of charge location relative to electrodes with the capability to monitor sensitivity to charge injection, transport, and migration through the dielectric composite as a function of composition, polarization field, and temperature.

---

## ACKNOWLEDGMENT

The authors acknowledge the support for the preparation of this article through a DST-SERB start-up research grant for young scientists (No. SB/FT/CS-019/2012), Government of India.

---

## REFERENCES

- [1] Ciuprina F, Hornea A, Barbuta M-G. Influence of temperature on dielectric performance of epoxy nanocomposites with inorganic nanofillers. *UPB Sci Bull* 2013;75(3):159–68.
- [2] Siddabattuni S, Schuman TP, Dogan F. Dielectric properties of polymer–particle nanocomposites influenced by electronic nature of filler surfaces. *ACS Appl Mater Interfaces* 2013;5(6):1917–27.

- [3] Siddabattuni S, Schuman TP. Polymer–ceramic nanocomposite dielectrics for advanced energy storage. In: Li L, Wong-Ng W, Sharp J, editors. *Polymer composites for energy harvesting, conversion, and storage*. ACS symposium series, vol. 1161. Washington, DC: American Chemical Society; 2014.
- [4] Sugumaran CP. Experimental investigation on dielectric and thermal characteristics of nanosized alumina filler added polyimide enamel. *J Electr Eng Technol* 2014;9(3):978–83.
- [5] Inuzuka K, Inano H, Hayakawa N, Hirose T, Hamaguchi M, Okubo H. Partial discharge characteristics of nanocomposite enameled wire for inverter fed motor. *IEEE conference on electrical insulation and dielectric phenomena, Annual report*; 2006. pp. 594–597.
- [6] Singha S, Thomas MJ. Permittivity and tan delta characteristics of epoxy nanocomposites in the frequency range of 1 MHz-1 GHz. *IEEE Trans Dielectrics Electr Insulation* 2008;15(1):2–11.
- [7] Ramasamy S, Purniah B. Electrical properties of nanostructured materials. *Proc Indian Natl Sci Acad* 2001;67A(1):85–102.
- [8] Polizos G, Tuncer E, Tomer V, Sauers I, Randall CA, Manias E. Dielectric spectroscopy of polymer-based nanocomposite dielectrics with tailored interfaces and structured spatial distribution of fillers. In: Musa SM, editor. *Nanoscale spectroscopy with applications*. Boca Raton, FL: CRC Press; 2013.
- [9] Zhou W, Hinojosa BB, Nino JC. Applicability of the Bruggeman equation for analyzing dielectric slurries containing ceramic powders with high permittivity. *J Am Ceramic Soc* 2012;95(2):457–60.
- [10] Zhou W, Nie YM, Li SJ, Liang HY. The importance of the solids loading on confirming the dielectric nanosize dependence of BaTiO<sub>3</sub> powders by slurry method. *Sci World J* 2013 120983/1-3
- [11] Petrovsky V, Manohar A, Dogan F. Dielectric constant of particles determined by impedance spectroscopy. *J Appl Phys* 2006;100(1):014102/1–4.
- [12] Wang Z, Nelson JK, Hillborg H, Zhao S, Schadler LS. Dielectric constant and breakdown strength of polymer composites with high aspect ratio fillers studied by finite element models. *Composites Sci Technol* 2013;76:29–36.
- [13] Sekine T, Hoshina T, Nam S-M, Yasuno H, Kakemoto H, Wada S, et al. Dielectric measurement of BaTiO<sub>3</sub> powder and its statistical analysis. *Key Eng Mater* 2006;301:251–6.
- [14] Tsurumi T, Sekine T, Kakemoto H, Hoshina T, Nam S-M, Yasuno H, et al. Evaluation and statistical analysis of dielectric permittivity of BaTiO<sub>3</sub> powders. *J Am Ceramic Soc* 2006;89(4):1337–41.
- [15] Wakino K, Okada T, Yoshida N, Tomono K. A new equation for predicting the dielectric constant of a mixture. *J Am Ceramic Soc* 1993;76(10):2588–94.
- [16] Wada S, Yasuno H, Hoshina T, Nam S-M, Kakemoto H, Tsurumi T. Preparation of nm-sized barium titanate fine particles and their powder dielectric properties. *Jpn J Appl Phys* 2003;42 part 1(9B):6188–95.
- [17] Wada S, Hoshino T, Yasuno H, Ohishi M, Kakemoto H, Tsurumi T, et al. Dielectric properties of nm-sized barium titanate fine particles and their size dependence. In: Yao S, Tuttle B, Randall C, Viehland D, editors. *Advances in electronic ceramic materials: ceramic engineering and science proceedings*. Hoboken, NJ: John Wiley & Sons; 2005.

- [18] Tsurumi T, Sekine T, Kakemoto H, Hoshina T, Nam S-M, Yasuno H, et al. Evaluation of dielectric permittivity of barium titanate fine powders materials, integration and packaging issues for high-frequency devices II. *MRS Proc* 2005;833: 243–7.
- [19] Manohar A, Dogan F. Dielectric properties of suspensions containing BaTiO<sub>3</sub> particles. In: Dogan F, Kumta P, editors. *Advances in electronic and electrochemical ceramics: ceramic transactions*. Westerville, OH: American Ceramic Society; 2005.
- [20] Petrovsky V, Petrovsky T, Kamlapurkar S, Dogan F. Characterization of dielectric particles by impedance spectroscopy (part I). *J Am Ceramic Soc* 2008;91(6): 1814–16.
- [21] Petrovsky V, Dogan F. Fundamentals of impedance spectral analysis applied to determine permittivity of dielectric particles. *J Am Ceramic Soc* 2009;92(5):1054–8.
- [22] Vassilikou-Dova A, Kalogeras IM. Dielectric analysis (DEA). In: Menczel JD, Prime RB, editors. *Thermal analysis of polymers, fundamentals and applications*. New York, NY: Wiley; 2009.
- [23] Kremer F, Schönhals A. Theory of dielectric relaxations. In: Kremer F, Schönhals A, editors. *Broadband Dielectric Spectroscopy*, Verlag, Berlin: Springer; 2003.
- [24] Bak W. Characterisation of Ba<sub>1-x</sub>Na<sub>x</sub>Ti<sub>1-x</sub>Nb<sub>x</sub>O<sub>3</sub> ceramic by dielectric spectroscopy. *Arch Mater Sci Eng* 2008;34(1):5–8.
- [25] Siddabattuni S, Schuman TP, Petrovsky V, Dogan F. Impedance analysis of dielectric nanoparticles enabled via a self-assembled monolayer. *J Am Ceramic Soc* 2013;96(5):1490–6.
- [26] Nakao Y. Dielectric constant evaluation of dielectric powders by complex impedance analysis with model of RC–RC parallel circuits connected in series. *Jpn J Appl Phys* 2007;46(10B):7008–12.
- [27] Fernandez-Garcia M, Rodriguez JA. Metal oxide nanoparticles. In: Lukehart CM, Scott RA, editors. *Nanomaterials: inorganic and bioinorganic perspectives*. New York, NY: Wiley; 2009.
- [28] Siddabattuni S, Schuman TP, Dogan F. Improved polymer nanocomposite dielectric breakdown performance through barium titanate to epoxy interface control. *Mater Sci Eng B* 2011;176(18):1422–9.
- [29] Petrovsky V, Petrovsky T, Kamlapurkar S, Dogan F. Physical modeling and electrodynamic characterization of dielectric slurries by impedance spectroscopy (Part II). *J Am Ceramic Soc* 2008;91(6):1817–19.
- [30] Tanaka T. Dielectric nanocomposites with insulating properties. *IEEE Trans Dielectrics Electr Insulation* 2005;12(5):914–28.
- [31] Zhang SH, Zhang NY, Huang C, Ren KL, Zhang QM. Microstructure and electromechanical properties of carbon nanotube/poly(vinylidene fluoride—trifluoroethylene—chlorofluoroethylene) composites. *Adv Mater* 2005;17(15):1897–901.
- [32] Cao Y, Irwin PC, Younsi K. The future of nanodielectrics in the electrical power industry. *IEEE Trans Dielectrics Electr Insulation* 2004;11(5):797–801.
- [33] Kotsilkova R, Fragiadakis D, Pissis P. Reinforcement effect of carbon nanofillers in an epoxy resin system: rheology, molecular dynamics, and mechanical studies. *J Polym Sci Part B: Polym Phys* 2005;43(5):522–33.
- [34] Schuman TP, Siddabattuni S, Cox O, Dogan F. Improved dielectric breakdown strength of covalently-bonded interface polymer-particle nanocomposites. *Composite Interfaces* 2010;17(8):719–31.

- [35] Chanmal C, Jog J. Dielectric relaxation spectroscopy for polymer nanocomposites. In: Mittal V, editor. *Characterization techniques for polymer nanocomposites*. Weinheim, Germany: Wiley-VCH, Verlag; 2012.
- [36] Hedvig P, editor. *Dielectric spectroscopy of polymers*. Bristol: Adam Hilger; 1977.
- [37] Runt JP, Fitzgerald JJ, editors. *Dielectric spectroscopy of polymeric materials*. Washington, DC: American Chemical Society; 1997.
- [38] Jimeno A, Kortaberria G, Arruti P, Tercjak A, Blanco M, Mondragon I. Dynamics and dielectric properties of polymer/nanoparticle nanocomposites by dielectric spectroscopy. In: Kortaberria G, editor. *Biopolymers and nanocomposites as studied by dielectric spectroscopy*. Kerala, India: Transworld Research Network; 2009.
- [39] Pissis P, Fragiadakis D, Kanapitsas A, Delides K. Broadband dielectric relaxation spectroscopy in polymer nanocomposites. *Macromol Symp* 2008;265(1):12–20.
- [40] Polizos G, Tuncer E, Agapov AL, Stevens D, Sokolov AP, Kidder MK, et al. Effect of polymer–nanoparticle interactions on the glass transition dynamics and the conductivity mechanism in polyurethane titanium dioxide nanocomposites. *Polymer* 2012;53(2):595–603.
- [41] Richert R, Angell CA. Dynamics of glass-forming liquids. V. On the link between molecular dynamics and configurational entropy. *J Chem Phys* 1998;108(21):9016–26.
- [42] Wong HC, Sanz A, Douglas JF, Cabral JT. Glass formation and stability of polystyrene–fullerene nanocomposites. *J Mol Liquids* 2010;153(1):79–87.
- [43] Riggelman RA, Douglas JF, de Pablo JJ. Tuning polymer melt fragility with antiplasticizer additives. *J Chem Phys* 2007;126(23):234903.
- [44] Fragiadakis D, Pissis P, Bokobza L. Glass transition and molecular dynamics in poly (dimethylsiloxane)/silica nanocomposites. *Polymer* 2005;46(16):6001–8.
- [45] Fragiadakis D, Pissis P, Bokobza L. Modified chain dynamics in poly (dimethylsiloxane)/silica nanocomposites. *J Non-Crystalline Solids* 2006;352(42):4969–72.
- [46] Fragiadakis D, Pissis P. Glass transition and segmental dynamics in poly (dimethylsiloxane)/silica nanocomposites studied by various techniques. *J Non-Crystalline Solids* 2007;353(47–51):4344–52.
- [47] Scheidler P, Kob W, Binder K. The relaxation dynamics of a supercooled liquid confined by rough walls. *J Phys Chem B* 2004;108(21):6673–86.
- [48] Tomer V, Polizos G, Manias E, Randall CA. Epoxy-based nanocomposites for electrical energy storage. I: effects of montmorillonite and barium titanate nanofillers. *J Appl Phys* 2010;108(7):074116.
- [49] Kyriakos K, Raftopoulos KN, Pissis P, Kyritsis A, Näther F, Häußler L, et al. Dielectric and thermal studies of the segmental dynamics of poly(methyl methacrylate)/silica nanocomposites prepared by the sol–gel method. *J Appl Polym Sci* 2013;128(6):3771–81.
- [50] Li C, Wu J, Zhao J, Zhao D, Fan Q. Effect of inorganic phase on polymeric relaxation dynamics in PMMA/silica hybrids studied by dielectric analysis. *Eur Polym J* 2004;40(8):1807–14.
- [51] Nelson JK, editor. *Dielectric polymer nanocomposites*. New York, NY: Springer; 2010.
- [52] Rathore BS, Gaur MS, Singh KS. Investigation of thermally stimulated charge relaxation mechanism in SiO<sub>2</sub> filled polycarbonate nanocomposites. *J Therm Anal Calorimetry* 2012;107(2):675–80.

- [53] Gunko VM, Zarko VI, Goncharuk EV, Andriyko LS, Turov VV, Nychiporuk YM, et al. TSDC spectroscopy of relaxational and interfacial phenomena. *Adv Colloid Interface Sci* 2007;131(1–2):1–89.
- [54] Gaur MS, Rathore BS, Singh PK, Indolia A, Awasthi AM, Bhardwaj S. Thermally stimulated current and differential scanning calorimetry spectroscopy for the study of polymer nanocomposites. *J Therm Anal Calorimetry* 2010;101(1):315–21.
- [55] Gaur MS, Singh PK, Ali A, Singh R. Thermally stimulated discharge current (TSDC) characteristics in  $\beta$ -phase PVDF–BaTiO<sub>3</sub> nanocomposites. *J Therm Anal Calorimetry* 2014;117(3):1407–17.
- [56] Okhlopkova AA, Sleptsova SA, Alexandrov GN, Dedyukin AE, Shim EL, Jeong D-Y, et al. Nanoceramic and polytetrafluoroethylene polymer composites for mechanical seal application at low temperature. *Bull Korean Chem Soc* 2013;34(5): 1345–8.
- [57] Roy M, Nelson JK, MacCrone RK, Schadler LS. Candidate mechanisms controlling the electrical characteristics of silica/XLPE nanodielectrics. *J Mater Sci* 2007;42(11): 3789–99.
- [58] Nelson J, Fothergill JC. Internal charge behaviour of nanocomposites. *Nanotechnology* 2004;15(5):586–95.
- [59] Smith RC, Liang C, Landry M, Nelson JK, Schadler LS. The mechanisms leading to the useful electrical properties of polymer nanodielectrics. *IEEE Trans Dielectrics Electr Insulation* 2008;15(1):187–96.
- [60] Dennison JR, Pearson LH. Pulsed electro-acoustic (PEA) measurements of embedded charge distributions. *Proc SPIE* 2013;8876:887612.
- [61] Pei D, Shkel Y, Klingenberg DJ, Segal Z, Nishi Y, Shohet JL. Measuring the volume charge in dielectric films using single frequency electro-acoustic waves. *J Mater Res* 2014;29(4):501–8.
- [62] Takada T, Sakai T. Measurement of electric fields at a dielectric/electrode interface using an electric transducer technique. *IEEE Trans Electr Insulation* 1983;18 (6):619–28.
- [63] Vázquez A, Chen G, Davies AE, Bosch R. Space charge measurement using pulsed electroacoustic technique and signal recovery. *J Eur Ceramic Soc* 1999;19(6–7): 1219–22.
- [64] Takada T. Acoustic and optical methods for measuring electric charge distribution in dielectrics. *IEEE Trans Electr Insulation* 1999;6(5):519–47.
- [65] Schadler LS, Nelson JK, Calebese C, Travelpiece A, Schweickart DL. High temperature breakdown strength and voltage endurance characterization of nanofilled polyamideimide. *IEEE Trans Dielectrics Electr Insulation* 2012;19(6):2090–101.
- [66] Taima J, Inaoka K, Maezawa T, Tanaka Y, Takada T, Murata Y. Observation of space charge formation in LDPE/MgO nano-composite under DC stress at high temperature. *IEEE conference on electrical insulation and dielectric phenomena*; 2006. pp. 302–305.
- [67] Nelson J.K., Fothergill J.C., Dissado L.A., Peasgood W.. Towards an understanding of nanometric dielectrics. *IEEE conference on electrical insulation and dielectric phenomena*; 2002. pp. 295–298.
- [68] Liao R, Bai G, Yang L, Cheng H-C, Yuan Y, Guan J. Improved electric strength and space charge characterization in LDPE composites with montmorillonite fillers. *J Nanomater* 2013 712543/1-7

- [69] Chakraborty H, Sinha A. Effect of space charge density and high voltage breakdown of surface modified alumina reinforced epoxy composites. *Trans Electr Electron Mater* 2013;14(3):121–4.
- [70] Ju S, Chen M, Zhang H, Zhang Z. Dielectric properties of nanosilica/low-density polyethylene composites: the surface chemistry of nanoparticles and deep traps induced by nanoparticles. *Express Polym Lett* 2014;8(9):682–91.
- [71] Huang XY, Jiang PK, Yin Y. Nanoparticle surface modification induced space charge suppression in linear low density polyethylene. *Appl Phys Lett* 2009;95(24):242905.
- [72] Ma D, Hugener TA, Siegel RW, Christerson A, Martensson E, Onneby C, et al. Influence of nanoparticle surface modification on the electrical behavior of polyethylene nanocomposites. *Nanotechnology* 2005;16(6):724–31.

# 11 Photothermal spectroscopy of polymer nanocomposites

Mihai Chirtoc<sup>1</sup>, Nicolas Horny<sup>1</sup>, Ismail Tavman<sup>2</sup> and Alpaslan Turgut<sup>2</sup>

<sup>1</sup>*GRESPI, Multiscale Thermophysics Lab, Université de Reims Champagne Ardenne URCA, Reims, France* <sup>2</sup>*Mechanical Engineering Department, Dokuz Eylul University, Tinaztepe-Buca/Izmir, Turkey*

## 11.1 INTRODUCTION

The class of composite materials implicitly refers to a solid matrix with particulate inclusions, as distinguished from nanofluids which consist of particles suspended in a base liquid. In rare cases, the matrix or the inclusions may undergo phase changes (e.g., smart textiles [1] or phase-change composites for energy storage applications [2]). Despite this distinction, most of the models used to predict the effective thermal transport properties can be applied to both classes of multiphase compounds. Polymer nanocomposites are polymer matrices reinforced with nanoscale fillers. This new generation of composite materials has shown enhanced optical, thermal, electrical, and dielectric properties [3–5]. In the case of high aspect ratio fillers, the term “nanocomposites” is still justified because at least one dimension is typically in the nanoscale range—e.g., the thickness of expanded graphite (EG) or clay flakes, or the diameter of carbon nanotubes (CNTs).

The subject of this chapter is the thermophysical and optical characterization of polymer nanocomposites using photothermal (PT) methods [6,7]. A sample that absorbs electromagnetic radiation will relax following different deexcitation processes like radiative deexcitation and/or photochemical reactions. PT effects arise when the complementary excess energy stored in vibrational or electronic excited states is converted into heat until thermal equilibrium is achieved. If the excitation is modulated, the generated heat diffuses away from the location of the absorption, giving rise to a nonstationary temperature field which behaves mathematically like a critically damped, diffusive wave. The temperature change can be detected by direct contact with the sample, or via temperature-dependent properties of the sample and those of the neighboring media. Such PT effects consist of thermoelastic waves in the bulk of the sample, thermal expansion and optical reflectivity modulation of the surface, enhanced emission of blackbody (Planck) infrared (IR) radiation from the surface, acoustic waves launched by the surface

into the adjacent (air or liquid) medium, and modulation of the refractive index of this medium or of the sample itself (if it is transparent).

The PT effects can be measured in different ways, which form the basis of various PT methods [8]. Usually the excitation is achieved by a pump laser in the visible wavelength range. For some methods, a second laser is necessary to probe the sample-related property modulated by the temperature fluctuations due to the pump beam. This detection scheme requires a flat sample surface with various degrees of specular optical reflectivity. All-optical methods like PT reflectance, PT displacement, PT deflection or “mirage,” PT lens, PT interferometry, PT gratings, or other combinations [9,10] are not suitable for investigations of inhomogeneous materials. In contrast, single-beam methods that are presented below from the historical viewing angle are applicable to composites. Their theoretical background and specific differences will be discussed in Sections 11.3 and 11.4, respectively.

The mathematical description of heat transfer problems by J. Fourier and S. D. Poisson in the first half of eighteenth century preceded the first thermal-wave experiments. In 1861, Angström proposed a variable-temperature method to measure the thermal diffusivity of a rod-shaped sample [11]. The photoacoustic (PA) effect was discovered two decades later by Bell [12], who observed that audible sound is produced when chopped sunlight is incident on optically absorbing materials. He also invented the spectrophone, a device able “to produce sound by light.” This was the precursor of a modern (PA) cell that contains a microphone to measure the acoustic wave produced in the vicinity of a periodically heated sample surface. The first quantitative theoretical foundation (in the frequency domain) of the PA effect with solids was reported in Ref. [13]. In some experiments, the microphone is replaced by a piezoelectric transducer attached to the sample [14–16]. The PA method has been largely used for spectroscopic analysis [7,17,18].

The physical basis of the photothermal radiometry (PTR) method is the change of the blackbody IR radiation from the sample surface due to temperature modulation by the absorbed laser beam [19]. The detector is usually an IR detector, insensitive to the (visible) radiation of the pump laser. Full theories for periodically modulated PTR with solids were developed [20–23] in analogy to the ones for the PA method. Theory and experiments of pulsed PTR are outlined in Ref. [24]. PA and PTR are noncontact techniques. A remote technique that derives from PTR is the IR thermography in pulsed [25] or periodically modulated lock-in [26,27] operation modes. Instead of a single-point measurement it is able to capture an IR image. This can be achieved with a point detector and a mechanical scanner or with a solid state IR focal plane array [28].

The pyroelectric effect consists of the induction of spontaneous polarization in a noncentrosymmetric ferroelectric crystal as a result of a temperature change. The electrical charges accumulated on opposite faces of the sensor are drained by metallic electrodes and give rise to a current signal. This property allows for the direct detection of a PT effect, provided the sensor is placed in thermal

contact with the sample via a coupling fluid. Such a detection scheme is known as the photopyroelectric (PPE) method and was proposed simultaneously in Refs [29–31] and became a new, flexible spectroscopic, and thermophysical characterization method. The theory for a four- and six-layer PPE cell [32,33] contains special cases similar to those of Ref. [13]. In this experiment, a partially reflecting electrode of the sensor is accounted for. The respective technique is termed reflection-mode PPE (R-PPE) [34] and has the advantage of doubling the optical path length in semitransparent samples. In the usual PPE experiment, the temperature rise is detected by a pyroelectric sensor in thermal contact with the rear sample's surface, in a back-detection configuration, BD-PPE. Another variant is the front-detection configuration, FD-PPE (initially known as inverse IPPE), in which the sensor is irradiated directly and the sample is placed in contact with its rear surface [35].

The PPE is a contact technique, but a noncontact operation (NC), NC-PPE (via a millimeter-sized air gap) has been demonstrated as well [36]. A similar configuration is the so-called thermal wave resonator cavity [37], also known as thermal wave interferometer [38]. It is based on pseudothermal wave interference [39] and allows for accurate thermal diffusivity measurement of fluids based on a length scan of the gap at fixed frequency, instead of a frequency scan at fixed gap length [40,41].

The term *PT spectroscopy* has usually been associated with the PT investigation of an optical property of a sample, upon scanning the wavelength of the probing radiation. More scarce in the literature, the term *emission spectroscopy* designates the investigation of the optical spectrum of the radiation emitted by the sample which has been excited by various means. Optical spectra carry specific information on the composition of the sample or on the interaction between its constituents. PT spectroscopy performed as previously outlined and based on various PT detection methods is a sensitive and versatile tool. There is an abundant literature on applications ranging from trace detection in gases or liquids to the measurement of highly absorbing (opaque in transmission) solids [42]. The dynamic range of more than 10 orders of magnitude for absorbance coefficient measurement is possible due to the fact that with PT methods the absorbed fraction of radiation is being measured, as opposed to spectrophotometers which measure the transmitted radiation and yield the absorption as a difference between incident and exiting radiation [42].

In its traditional meaning, the spectroscopy of composites is addressed in other chapters of this volume. The present chapter is dedicated to the measurement of thermal transport parameters of selected polymer nanocomposites. With periodic excitation modulation, the thermal diffusion length in the material is frequency-dependent. Therefore, the spreading of the thermal wave in a sample with a given geometry can be controlled by merely scanning the modulation frequency. The resulting temperature oscillations are converted in alternating current (AC) signals generated by the PT method used. The set of amplitude and phase curves as a function of frequency will be referred to as the PT signal spectrum throughout

this chapter. The relatively scarce reports on applications of PT methods to thermophysical characterization of composites are discussed in [Section 11.2](#). The theoretical background necessary for data interpretation is outlined in [Section 11.3](#). The description of the materials used for sample preparation is given in [Section 11.4](#), together with the presentation of typical experimental setups of the main PT techniques employed. Examples of frequency- and time-domain spectra obtained in various PT configurations are compared with theoretical fits as shown in [Section 11.5](#). Results of effective values of thermal transport parameters as a function of filler fraction are synthetically presented in [Section 11.6](#). Eventually, these data are used as input values for confrontation with predictions of mean field models. [Section 11.7](#) illustrates how optical information derived from PT frequency-domain spectra can be used to characterize the fillers or the polymer matrix.

---

## 11.2 RELATED PHOTOTHERMAL STUDIES OF COMPOSITE MATERIALS

For consistency with the title of this chapter, thermo-optical characterization of composites other than by PT methods (commercial flash instruments, direct current (DC) or AC techniques with standard temperature sensors, transient or  $3\omega$  hot wire, hot guarded plate, etc.) are not discussed here.

### 11.2.1 COMPLEX COMPOSITES

For some industrial applications, the composites have scale-dependent structures. It can be a multilayer at the macro scale, a quasihomogeneous material at the millimeter scale, and a composite at the micro-/nanoscale. For a complete study of the material, each of these aspects must be taken into account. Multiscale modeling of the effective thermal conductivity tensor of a stratified composite material made from carbon fibers, phenolic resin, and carbon loads has been reported in Ref. [43]. The thermal conductivities are computed separately for the yarn (longitudinal and transverse ones), for the loaded matrix (by an effective medium model), and for the fabric (thermal conductivity tensor). Finally, analytical relations are proposed which can be used in a multiphenomenon simulation. Fiber-reinforced composites have been investigated theoretically [44,45], and experimentally using the “mirage” technique [46]. A stack of such aligned sheets can be superposed at varying alignment angles (e.g., in steps of  $60^\circ$ ) in order to mediate the anisotropy of mechanical properties. In a comparative study, three-directional carbon/carbon (3D C/C) composites were measured by front detection (FD)- and back detection (BD)-flash method and by BD-PTR to determine their properties for various thicknesses and orientations of the reinforcement in the matrix [47].

The microscopic thermoelastic properties of the matrix and fibers of composites before and after the process of preparation are often not known.

Flash thermography was applied for *in-situ* measurement of C/C-SiC tensile material [48]. The observed thermal diffusivity decrease was attributed to the increase of stress-induced transverse microcracks.

Composites with complex structures and shapes can be characterized and tested by nondestructive evaluation methods [49,50]. Among these, active IR thermography [51] can be performed with various external stimuli such as warm or cold air [52], heat pulses [25,53], periodic thermal waves [54], mechanical oscillations (ultrasounds) [54,55], X-rays [56], microwave [57] or THz radiation [58], and particle beams [59]. Such remote techniques are cost-effective solutions to such issues as assessing the integrity of large aircraft structures [60].

### 11.2.2 COMPOSITES WITH DEFINED MICROSTRUCTURE

Many composite materials used in industry and in daily life have a layered structure at the mm-scale and below. This length scale is compatible with investigations by pulsed PT methods [61]. The thermal diffusion length can be tuned in the mm to  $\mu\text{m}$  range via the change of modulation frequency between 0.1 Hz and 1 MHz. This feature can be used as the basis of PT nondestructive tomography [62] and allows the detection of subsurface defects, contact resistance, or to retrieve the depth profile of a material parameter. In the latter case, analytical solutions do not exist for the direct problem and the inversion procedure (retrieving the temperature profile from frequency- or time-domain spectra) is an ill-posed problem due to the diffusive character of thermal waves. Grosse and Depasse showed that the solutions for staircase multilayer profiles converge to the exact solutions of the continuous depth profiles when the layers are taken thinner and thinner [63].

Localized delamination spots between polymeric coatings and metallic substrates are most likely starting points for corrosion at the interface and eventually for the propagation of disbonding. Samples from metallic cans for soda drinks consisting of 30- $\mu\text{m}$ -thick polymer coating on 500- $\mu\text{m}$ -thick steel backing were imaged by a scanning PPE microscope [64]. The signal contrast between the defective area and the healthy area is sensitive both, to the thickness of the gap and to the depth where it is situated below the surface. An only 1- $\mu\text{m}$ -thick air gap produces a readily detectable phase contrast of  $5^\circ$ . Using a two-dimensional approach [65], it was possible to retrieve the subsurface defect depth, the lateral size, and the thermal resistance from the time-dependent surface temperature map obtained by a thermographic camera.

Most packaging composite materials are coated with a transparent polymer varnish atop the paper, polymeric, or Al substrate. In the packaging industry, a method capable of accurately controlling the varnish thickness in the 0.1–100- $\mu\text{m}$  range is necessary. A PT configuration was adopted which assumed a subsurface heat source. The varnish is transparent to the visible (VIS) excitation radiation and opaque in the IR range, while the backing is opaque at all wavelengths. The thermal

wave propagates from the substrate across the varnish up to the surface, where it is detected by PA and PTR methods [66].

Thin adhesive tapes are used in many types of electrical appliances for mechanical contact and acoustic damping. The achievement of thermal contact is also a topic of interest [67]. Double-sided adhesive tapes with various thicknesses were clamped between a  $\text{LiTaO}_3$  pyroelectric sensor and a 6 cm-thick Cu backing [68]. In addition to the thermal conductivity of  $0.12\text{--}0.19 \text{ W m}^{-1} \text{ K}^{-1}$  of the tapes, a specific contact resistance of  $2.2 \times 10^{-5} \text{ m}^2 \text{ K W}^{-1}$  was obtained. It was equivalent to a  $0.57\text{-}\mu\text{m}$ -thick air gap, and was due to the roughness of the metallic substrate.

More intimate contact between layer and substrate exists in Cu-coated carbon systems which are produced in the form of metal matrix composites (MMC) with carbon fibers, CNTs, or diamond crystallite fillers. PA and PTR methods were applied to characterize the thermal properties of diamond crystallites, which were coated by Cu, Cr, or Cu/Cr layers. Delgadillo-Holfort et al. found that the Cr interlayer reduces the interfacial thermal resistance (ITR) [69].

Samples consisting of  $1\text{-}\mu\text{m}$ -thick Cu films deposited by magnetron sputtering on vitreous carbon (Sigradur™) were studied using PTR [70,71]. A semiempirical formula was developed that correlates the ITR with the adhesion strength of the layer as determined by pull-off tests [72]. On average, the ITR value in the Cu/Sigradur system ( $1.7\text{--}3.4 \times 10^{-7} \text{ m}^2 \text{ K W}^{-1}$ ) is higher than that in the Cu/diamond system ( $1.5\text{--}4.5 \times 10^{-8} \text{ m}^2 \text{ K W}^{-1}$ ), which is attributable to the amorphous/crystalline structure of the two forms of C.

PT characterization of composites works best for opaque (both in the VIS and IR) samples (as required by commercial laser flash diffusivity instruments), or for samples that are opaque at least in one wavelength range (the PT theory being symmetrical with respect to the VIS and IR ranges). However, there are reports on studies where the VIS and IR optical properties of the samples were not well-defined. The key to successful results was the use of complementary investigation techniques.

A composite sample designed for heat shock shields had woven carbon fiber reinforcement layers oriented parallel to the surface. This topography was modeled by a two-layer structure. The PTR signal was approximated by a vector superposition of two signals corresponding to each layer geometry. The thermal effusivity and optical absorption coefficient can be determined independently at different frequencies (kilohertz and tens of kilohertz ranges, respectively) [73]. A more advanced characterization of the same sample was possible by a combination of PTR and PA techniques [74]. The former is sensitive to IR sample emissivity while the latter is not. This feature allowed for determining the VIS and IR absorption coefficient and the IR emissivity, in addition to the thermophysical parameters.

FD- and BD-PTR and photoacoustic Fourier transform spectroscopy (FT-IR/PAS) were used for the measurement of the thermophysical properties of specialty papers with various cotton contents, which are seen as composite materials [75].

The thermal diffusivity from PTR data was valuable for quality control while the FT-IR/PAS spectra improved the understanding of the chemical origin of depth inhomogeneities.

Thermophysical and spectroscopic studies of polymers have been reported since the early developments of PT techniques [76,77]. Depth-profile analysis was performed by PA spectroscopy on low-density polyethylene (LDPE) [78]. The ratios of near-infrared (NIR) peaks of CH<sub>3</sub>, CH<sub>2</sub>, and OH groups, relative to that of methylene groups, increase with increasing modulation frequency (or with decreasing thermal diffusion length from 56 to 11 μm). It was concluded that near-to-surface layers of solid PE are richer in these functional groups than the polymer bulk.

### 11.2.3 COMPOSITES WITH RANDOM MORPHOLOGY

In macroscopically homogeneous (nano)composites, the relevant parameter for applications is the “average” thermal conductivity,  $k$ . Unlike the specific heat  $c_p$ , the former cannot be predicted by the rule of mixtures. Despite the wealth of theories attempting to model it, none is universally valid. Therefore, the term *effective*  $k$  is more appropriate than *average*  $k$ . A straightforward method to evaluate  $k$  is by applying a constant temperature gradient in one-dimensional geometry and to measure the resulting heat flux density, with the two related by the Fourier law of heat transfer  $\varphi = -k \times \text{grad}(T)$ . Nonstationary methods are preferred because they are more sensitive and exempt from base-line drift. In this case, the response of the material can be described by the propagation of a temperature—heat flux vector through a thermal quadrupole, which incorporates the thermophysical material properties [79]. In nonstationary regime, the matrix elements of this quadrupole mixes the  $k$  and  $c_p$  parameters into the thermal diffusivity  $a = k/\rho c_p$  and thermal effusivity  $e = (\rho c_p k)^{1/2}$ , with  $\rho$  being the density. For this reason, all PT methods yield  $a$  and  $e$  in the first place, and  $k$  is determined indirectly from the other parameters. However, in well-defined, special cases one can obtain all four parameters directly and independently (see Section 11.5).

The simplest form of composites can be considered single-phase granular materials sintered by heat and/or pressure. As expected, their thermal diffusivity decreases drastically compared to the bulk because of the ITR of the grain boundaries. Some examples are nanostructured Ag studied by PA [80], and the anisotropic thermal diffusivity of silicon nitride ceramic grains measured by thermorefectance microscopy [81]. The thermal diffusivity and conductivity of compressed expanded graphite investigated by BD-PTR and FD-PT beam deflection revealed the strong anisotropy (higher in-plane values) of dynamic thermophysical parameters [82]. Local thermal conductivity inside grains of high-quality polycrystalline diamond grown by chemical vapor deposition was measured with micrometer spatial resolution and a maximum value of 2350 W m<sup>-1</sup> K<sup>-1</sup> was found [83].

The effect of interfaces is even more important in two-phase composites. It was studied, for instance, by high-resolution PT imaging of an MMC interface [84].

Composites with phenolic resins and SiC fibers/particles have remarkable thermal barrier properties and are used for turbine engine components and spacecraft reentry thermal protection shields. The flash method and space-resolved IR thermography were applied to measure simultaneously transverse and in-plane thermal diffusivities, globally and locally [53]. A contact technique which is a combination of PPE and PA used a piezoelectric sensor attached to a fiber-reinforced composite sample [16]. The thermal diffusivity was determined based on a thermoelastic theory.

The studies of Refs [85,86] illustrate the typical stepwise approach in characterizing a composite. The respective specimens were polymer/C fiber or polymer/CNT, and the measurement techniques were the PT beam deflection and BD-PPE. The experimental effective  $k$  values (as a function of filler fraction) served as inputs to mean field theory (MFT) models [87] and resulted in the fitted ITR values between the fillers and the matrix (see also Section 11.6.3). Massey et al. recently reported unconventional computing using a poly(butyl methacrylate)/CNT composite as an alternative to metal–oxide–semiconductor field-effect transistor (MOSFET) technology [88].

A complex experimental challenge was raised by an epoxy/Si particles (50  $\mu\text{m}$  in size) composite. It was studied combining PTR and PA methods to establish the thermal, optical, and electronic parameters in the simultaneous presence of the free carriers signal and the thermal signal. PA detection was used to study the variation of the thermal diffusivity as a function of Si volume fraction, and PTR was used to determine the influence of the electronic carrier contribution to the thermal transport with the optical properties taken into consideration [89].

The composite materials briefly presented in this section have a wide range of structures at different length scales, compositions, and morphologies. These examples demonstrate the ability of PT techniques to not only address the measurement of thermophysical parameters, but also to gain meaningful insight into the physics of thermo-optical properties of composites. One interesting conclusion is that such heterogeneous materials can be treated as homogeneous if PT measurements are performed over an averaging length which is larger than the distance between fillers [46]. However, this is not valid for anisotropic materials. In general, the modulation frequency range must be adapted to the sample: for low-thermal-diffusivity matrices like polymers, it is necessary to work at low frequency. In this way, an effective thermal diffusivity of the matrix and fillers is measured.

---

### 11.3 THEORETICAL BACKGROUND FOR 1D PT RESPONSE OF ADIABATIC SOLID SLABS

When nonstationary heat sources are applied to a body, its internal temperature field  $T(x,t)$  above the ambient temperature  $T_0$ , is a function of space coordinates

and time, and is given by the solution of the parabolic heat diffusion equation. In 1D geometry, this equation is

$$\frac{\partial^2 T(x, t)}{\partial x^2} - \frac{1}{a} \frac{\partial T(x, t)}{\partial t} = \frac{P_v(x, t)}{k} \quad (11.1)$$

where  $P_v(x, t)$  is the heat source per unit volume. For periodic, pulsed (dirac delta function), or step (heavyside function) heating of a homogeneous semi-infinite solid, the solutions to the above equation are given respectively by [8]

$$T(x, t) = \frac{I_0}{2e\sqrt{\omega}} \exp \left[ -(1+i) \frac{x}{\mu} - i \frac{\pi}{4} + i\omega t \right] \quad (11.2)$$

$$T(x, t) = \frac{Q_0}{e\sqrt{\pi t}} \exp \left( -\frac{x^2}{4at} \right) \quad (11.3)$$

$$T(x, t) = \frac{I_0}{k} \left[ \sqrt{\frac{at}{\pi}} \exp \left( -\frac{x^2}{4at} \right) - \frac{x}{2} \operatorname{erfc} \left( \frac{x}{2\sqrt{at}} \right) \right] \quad (11.4a)$$

$$T(x, t) = T_1 \operatorname{erfc} \left( \frac{x}{2\sqrt{at}} \right) \quad (11.4b)$$

where  $t$  is time,  $f$  is frequency,  $\omega = 2\pi f$  is angular frequency,  $\mu = [a/(i\omega)]^{1/2}$  is thermal diffusion length,  $\sigma = (i\omega/a)^{1/2} = (1+i)/\mu$  is the complex thermal wave vector, and  $i$  is the imaginary number. The heat flux  $I_0$  ( $\text{W m}^{-2}$ ) and the energy  $Q_0$  density ( $\text{J m}^{-2}$ ) result from the absorption of the excitation radiation power at the opaque sample surface. The notations  $T$ ,  $\rho$ ,  $c_p$ ,  $k$ ,  $a$ ,  $e$ , and  $\varphi$  were defined in Section 11.2.3. For the sake of generality, Eqns (11.4a) and (11.4b) apply for imposed heat flux step  $I_0$  and for imposed temperature step  $T_1$  at the sample surface, respectively.

From these simple examples, it is evident that in the case of periodic modulation (Eqn 11.2), the PT signal from the surface of the material (at  $x = 0$ ) is proportional to the inverse thermal effusivity, it decreases as  $f^{-1/2}$  and it has a phase lag of  $-45^\circ$ . In the case of pulsed excitation, it decays as  $t^{-1/2}$  from a maximum value depending on the effusivity (Eqn 11.3), while for step-function excitation it increases as  $t^{1/2}$  (Eqn 11.4a). The quantity  $F_0(t) = at/x^2$  in the transient cases is the dimensionless Fourier number that characterizes heat conduction.

PT experiments can be carried out with pulsed, periodical, or random sequence modulation, which are equivalent in principle. However, in practice there are specific advantages and drawbacks to be considered. One may simply state that pulsed measurements are faster than frequency scans, but periodic modulation allows for the necessary integration time required by the lock-in to yield the desired signal-to-noise ratio of the frequency spectrum. This chapter is mostly dedicated to PT measurements using periodical modulation. Such a scheme offers two information channels: the amplitude and the phase signals, corresponding respectively to the magnitude of the temperature response of the sample and to the delay of the response relative to the excitation.

### 11.3.1 THEORY OF FD- AND BD-PT RESPONSE WITH PERIODIC EXCITATION

As mentioned in Section 11.1, most PT techniques rely on the measurement of the surface temperature of the sample. Elaborated initially for the PPE method [32,33,90], a modular 1D analytical model was developed for the generalized thermal impedance of a multilayer sample [91,92]. By analogy with electrical networks, the thermal impedance is given by the temperature rise divided by the heat flux which results from the absorption of the excitation radiation power. It is convenient to express the PT signals in terms of thermal impedance [8] rather than of temperature  $T$ , because the former is independent of the excitation power and of the specific PT method used.

Solving the 1D heat conduction equation with uniform irradiation flux and periodic excitation allows the determining of the AC temperature field in a multilayer system. The depth-dependent temperature oscillations in each layer are described by:

$$T_j(x) = A_{1j}\exp(\sigma_j x) + A_{2j}\exp(-\sigma_j x) \quad (11.5)$$

The coefficients  $A_{ij}$  are obtained by inverting the matrix equation formed by the boundary conditions on temperature and heat flux continuity between layers. If the heat losses to the ambient are neglected, the specific thermal impedance  $z$  ( $\text{m}^2 \text{K W}^{-1}$ ) of a sample slab of finite thickness and having finite optical absorption coefficient  $\beta$  ( $\text{m}^{-1}$ ) in the VIS range, is given by:

$$z(\text{FD}) = z_0 \tau \frac{-2e^{-\beta d} \tau M^{-1} + (\tau - 1) + (\tau + 1)M^{-2}}{(\tau^2 - 1)(1 - M^{-2})} \quad (11.6)$$

Equation 11.6 refers to the FD configuration (excitation and detection at the same side). The impedance in BD configuration (excitation and detection at opposite sides) is given by

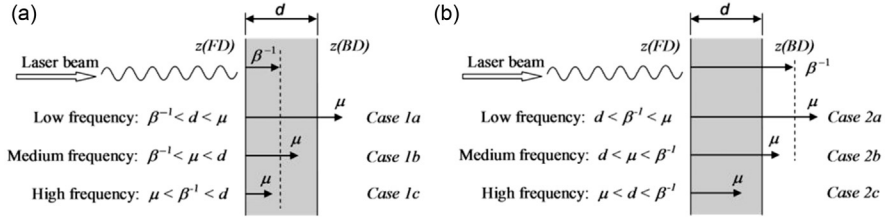
$$z(\text{BD}) = z_0 \tau \frac{2\tau M^{-1} - e^{-\beta d} [(\tau + 1) + (\tau - 1)M^{-2}]}{(\tau^2 - 1)(1 - M^{-2})} \quad (11.7)$$

The notations are  $M = \exp(\sigma d)$  and  $d$  is the sample thickness. Symbol  $\tau$  stands for the dimensionless, thermo-optical parameter:

$$\tau = \frac{\beta}{\sigma} = \frac{1 - i}{2} \beta \mu = (1 - i) \beta \left( \frac{a}{2\omega} \right)^{1/2} \quad (11.8)$$

The factor  $z_0$  represents the surface impedance of an opaque, semi-infinite material (surface absorber):

$$z_0 = \frac{1}{k\sigma} = \frac{1 - i}{\sqrt{2\omega e}} \quad (11.9)$$


**FIGURE 11.1**

Special cases generated by the interplay between three characteristic lengths:  $d$ ,  $\mu$ , and  $\beta^{-1}$  in (a) optically thick samples (Case 1) and (b) in optically thin samples (Case 2).

and  $z_0\tau$  is the surface impedance of a semitransparent, semi-infinite material (volume absorber):

$$z_0\tau = \frac{1}{k\sigma}\tau = -\frac{i\beta}{\omega C} \quad (11.10)$$

where  $C = \rho c_p$  is the volumetric heat capacity.

The Eqns (11.6) and (11.7) contain dimensionless parameters  $\beta d$ ,  $\beta\mu$ , and  $d/\mu$  which are combinations of three characteristic lengths:  $d$ ,  $\mu$ , and  $\beta^{-1}$ . Their interplay generates special cases which are depicted in Fig. 11.1. For carbon-filled composites, the optical penetration depth does not exceed the sample thickness,  $\beta^{-1} < d$  even at very low charge. Then the special Case 1 of Fig. 11.1a applies. For a pure polymer matrix or for translucent fillers like the nanoclay particles, the opposite inequality holds,  $d < \beta^{-1}$ , with the respective special Case 2 shown in Fig. 11.1b. Once the relative values of  $\beta^{-1}$  and  $d$  have been established, there are three possible further cases which are scanned by the continuous variation of the thermal diffusion length  $\mu$  via the modulation frequency. The data reduction procedure consists of identifying the Cases a, b, and c in the experimental spectra, and fitting suitable frequency ranges with the respective analytical expressions. Usually, the fits are performed with the general Eqns (11.6) and (11.7), but the derivation of analytical special cases enlightens the physics behind the general formulas. Only the cases of interest for the discussed applications are presented next.

- a. In Case 1 (Fig. 11.1a), as the frequency increases (and  $\mu$  decreases), two transitions are swept in the FD spectrum. Across the first one (Case 1a/1b), the sample switches between thermally thin/thick regimes, and since  $\beta^{-1} < d \approx \mu$ , the Eqn (11.6) reduces to:

$$z(FD) = z_0 \frac{1 + M^{-2}}{1 - M^{-2}} \quad (11.11)$$

Equation (11.11) shows that fitting the FD-PT spectrum at low frequency yields the thermal diffusivity  $a$ . In particular, when  $d = \mu$ ,  $a = \pi f_c d^2$  with  $f_c$  as the corner frequency for the 1a/1b transition.

Across the second transition (Case 1b/1c), the sample switches between thermo-optically thin/thick regimes, and since  $\beta^{-1} \approx \mu < d$ , Eqn (11.6) reduces to:

$$z(\text{FD}) = z_0 \frac{\tau}{\tau + 1} \quad (11.12)$$

At high frequency, optical and thermal parameters are mixed in Eqn (11.12), and  $\beta$  can be derived by using the previously determined diffusivity. In particular, when  $\beta^{-1} \approx \mu$ ,  $\beta = (\pi f_c / a)^{1/2}$ , with  $f_c$  being the corner frequency for the 1b/1c transition. The simple expressions for the particular cases are valid provided the respective corner frequencies  $f_c$  are more than two decades apart from each other.

In the BD configuration, the useful case for PT spectroscopy is Case 1b. Then, for  $\beta^{-1} < \mu < d$ , the Eqn (11.7) reduces to

$$z(\text{BD}) = 2z_0 \exp[-(1 + i)d/\mu] \quad (11.13)$$

According to Eqn (11.13), the logarithm of the amplitude and the phase data plotted versus  $f^{1/2}$  have the same slope:

$$\log_e(|z/z_0|) = -d\sqrt{\pi/a}\sqrt{f} + \text{Const.} \quad (11.14)$$

$$\varphi(z/z_0)(\text{rad}) = -d\sqrt{\pi/a}\sqrt{f} \quad (11.15)$$

The thermal diffusivity  $a$  can be determined with the knowledge of the sample thickness as  $a = \pi d^2 / (\text{slope})^2$ . The correct  $a$  value is obtained in the frequency range where the amplitude and phase slopes are the same. No amplitude calibration is required.

- b.** In Case 2 (Fig. 11.1b), the sample is optically thin,  $d < \beta^{-1}$ . The transition 2a/2b is situated at too low a frequency to be detected. Across the transition 2b/2c, the sample switches between thermally thin/thick regimes and since  $d \approx \mu < \beta^{-1}$ , Eqns (11.6) and (11.7) reduce to

$$z(\text{FD, BD}) = z_0 \tau \left( 1 \mp \tau \frac{1 - M^{-1}}{1 + M^{-1}} \right) \quad (11.16)$$

where  $-$  stands for FD and the  $+$  stands for BD. The second term in the parentheses behaves in a similar way to Eqn (11.11), when the frequency sweeps across the condition  $d = \mu$ . However, since  $\tau < 1$ , a larger constant term (the unity) is added to a smaller term containing the spectral features of interest. This degrades the signal-to-noise ratio in this case.

### 11.3.2 SPECIFIC TRANSFER FUNCTIONS OF PT METHODS

The complex PT signal  $V(f)$  produced by a specific setup is a convolution of the thermal impedance given by Eqn (11.6) or (11.7) and the transfer function  $F$  of

the PT method being used [91,92]. The  $F$  factor for the PTR method is frequency-independent and has 0 phase:

$$V_{\text{PTR}}(f) \propto \varepsilon_{\text{IR}} T_{\text{dc}}^3 z(f) \quad (11.17)$$

The symbol  $\varepsilon_{\text{IR}} < 1$  is the integral IR emissivity of the sample surface and  $T_{\text{dc}}$  is the absolute temperature. For the PA method,  $F$  has  $f^{-1/2}$  dependence and  $-45^\circ$  phase:

$$V_{\text{PA}}(f) \propto \frac{1-i}{\sqrt{2\omega}} \frac{p_0}{V_0 T_0} z(f) \quad (11.18)$$

with  $p_0$  and  $T_0$  the equilibrium pressure and the temperature in the cell volume  $V_0$ . The  $F$  factor for the PPE method depends on the electronics for signal processing. With a current preamplifier,  $F$  has  $f$  dependence and  $+90^\circ$  phase:

$$V_{\text{PPE}}^C(f) \propto i\omega p_{\text{PE}} z(f) \quad (11.19)$$

where  $p_{\text{PE}}$  is the pyroelectric coefficient (which has negative sign) of the transducer material.

As shown previously, the PA and PPE methods have their own frequency and phase features, while the PTR method renders a signal proportional to  $z$ . To remove from it the unwanted contribution of the quantities  $z_0$  or  $z_0\tau$  (Eqns 11.9 and 11.10), it is advantageous to plot the signal amplitude multiplied by  $f^{1/2}$  or by  $f$ , and to add  $45^\circ$  or  $90^\circ$  to the phase, respectively. The choice depends on whether the sample is opaque or semitransparent. By doing this using Eqns (11.6) and (11.7), the frequency spectrum of the last factor alone, which contains the information on the sample structure, is revealed. Alternatively, the experimental spectra can be normalized either to an opaque or to a semitransparent material to remove the  $z_0$  or  $z_0t$  factors.

### 11.3.3 THEORY OF BD-PT IMPULSE RESPONSE

The time evolution of the normalized rear temperature of an adiabatic slab of thickness  $d$  irradiated at its front side by a short pulse is given by [93]

$$\frac{T(t)}{T_{\text{max}}} = 1 + 2 \sum_{n=1}^{\infty} (-1)^n \frac{\sin[n\pi/(\beta d)]}{n\pi/(\beta d)} \exp(-n^2 \pi^2 F_0(t)) \quad (11.20)$$

where the Fourier number is  $F_0(t) = at/d^2$ , as in Eqns (11.3) and (11.4). Equation (11.20) assumes 1D heat diffusion. The material is considered to be optically thick ( $\beta^{-1} < d$ ), that is, the radiation energy is absorbed in a small depth corresponding to  $\beta^{-1}$ . The maximum temperature  $T_{\text{max}}$  is proportional to the reciprocal heat capacity of the sample,  $mc_p$ . With  $t_{1/2}$  the time to the half maximum, the diffusivity of an opaque sample is obtained from Eqn (11.20) as

$$a = 0.1388d^2/t_{1/2} \quad (11.21)$$

Contrary to Eqn (11.3) for FD, the expression of Eqn (11.20) for BD contains an infinity of terms because of thermal wave reflections in the finite thickness slab. If keeping only one term in the series, the constant factor in Eqn (11.21) is 0.1405. The simple Eqn (11.21) is known as the Parker model. The neglect of heat losses to the ambient is justified if the transient response is well below 1 s, but still much longer than the flash duration which is in the 10-ms range. More elaborate models account for finite pulse duration [94], for lateral and front heat losses [95,96], and for higher semitransparency of the sample [97].

---

## 11.4 MATERIALS AND METHODS

This section is dedicated to the description of measured samples and of typical PT methods and setups that can be applied to the measurements of nanocomposites.

### 11.4.1 MOTIVATION FOR MATERIALS CHOICE

The salient feature of nanocomposites is the drastic improvement of physical properties due to the incorporation of small amounts (less than 10 wt%) of nanosized fillers into the polymer matrix. The fillers may have their own internal structure, such as multilayered clay, EG, multiwall CNTs, or vegetal fibers. The main preparation methods are solution mixing, melt blending, and *in situ* polymerization.

Thermally conductive polymer composites offer an alternative to metal parts in several applications, as a result of the polymer light weight, corrosion resistance, and ease of processing. Among the nanofillers with high thermal conductivity, the largest variety is offered by various carbon-based reinforcing particles like carbon black, graphite, EG, carbon fibers, carbon nanofibers, and CNTs. All these forms are possible because of the element's unique hybridization ability [98]. The electrical, thermal, and mass transport properties depend not only on the nanofiller physical properties, but also on their shape, which can be nearly-spherical, flake-, or rod-like. Both deviations from sphericity are shown to enhance the respective property of the composite induced by the filler, as compared with the effect of the same fraction of spherical particles. The two extreme cases are single-wall CNTs [99] and graphene (a single, two-dimensional layer of carbon atoms bonded together in the hexagonal graphite lattice), the basic building block of graphite [100,101]. Both forms exhibit unusually high intrinsic  $k$ , but the effective  $k$  of respective composites is lower than expected due to the large ITR between these particles and the polymer matrix, which hinders the phonon heat transport in such materials.

The procedure to obtain EG in a sulfuric acid environment has been known for a century [102]. When mixing natural or synthetic graphite flakes with an intercalation agent, a graphite salt forms. Upon subjecting this compound to a

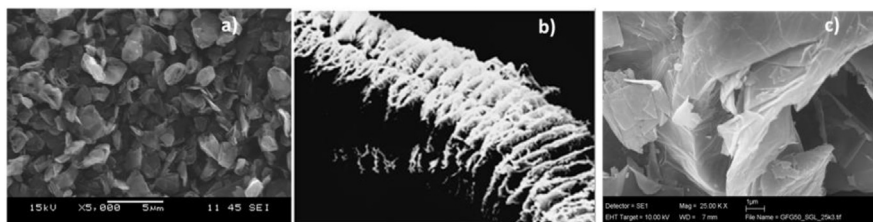


**FIGURE 11.2**

(a) As-supplied unexpanded graphite particles (UG04), (b) expanded graphite “worm”  $\approx 700 \mu\text{m}$  in diameter, and (c) exfoliated graphite (EG50).

(a) and (c) Courtesy of Chirtoc et al. [105]. Copyright 2012. Reprinted with permission from Elsevier.

Figure (b) [104], Copyright 1998–2013 SGL CARBON SE.

high temperature shock, the flakes expand by a factor of 200–400 into wormlike structures which eventually exfoliate [103]. The manufacturing process diagram can be found in Ref. [104] while SEM micrographs of the three graphite forms are shown in Fig. 11.2.

Recently, biodegradable nanocomposites based on starch [106] and biopolyesters have raised great interest [107]. Much effort has been devoted to research into the polyester/nanoclay system [4]. The clay particles have hydrophilic character while the biopolyesters are organophilic compounds. In the case of montmorillonite (MMT, layered silicate particles), the reciprocal affinity is increased by substitutions resulting in organomodified montmorillonite (OMMT).

For efficient solar energy usage, thermal energy storage (TES) is a key technology for reducing the mismatch between energy supply and demand for heating or cooling applications. Latent heat thermal energy storage (LHTES) can store a great amount of thermal energy in a narrow temperature interval [108]. The performance of LHTES depends, among other parameters, on the thermal conductivity of the phase change materials (PCM) employed.

## 11.4.2 MATERIAL PREPARATION AND PROPERTIES

The matrices used for the investigated samples were high- and low-density PE (HDPE, LDPE), ethylene vinyl acetate copolymer (EVA), a fatty acid (myristic acid, MA), and two polyesters, the poly(lactic acid) (PLA) and the poly(butylene succinate) (PBS). The fillers were expanded and unexpanded graphite (EG, UG), graphite platelets (Gr), multiwalled CNT (MWCNT), MMT, and Al particles.

For the HDPE/EG and LDPE/EG samples, HDPE type BP 5740 3 VA (British Petroleum, UK) and LDPE type RA 2–19 (Slovnaft, Slovakia) were used as the matrix materials. The EG fillers Ecophit type GFG5, GFG50, and GFG 500 (SGL Technol. GmbH, [104]) have nominal particle sizes of 5, 50, and 500  $\mu\text{m}$  in diameter (EG5, EG50, and EG500) and 60 nm in thickness. The precursor is natural

graphite. For the HDPE/UG04, EVA/UG22, EVA/EG5, and HDPE/Al samples, two matrix materials were used: HDPE-I-668 (Petkim A.S., Turkey) and an EVA copolymer containing ethylene and 14 wt% of vinyl acetate, type Miravithen D 14010 V (Leuna Polymer GmbH, Germany). The UG04 filler was UG with a nominal particle size of 0.40  $\mu\text{m}$  supplied as type D50 by Nanoamor Inc. The nonspherical particles were rather flaky, with real lateral size of  $\approx 2 \mu\text{m}$ . The UG22 filler had a larger size between 20 and 25  $\mu\text{m}$ . The Al particles (99.9% purity) type 0137HW (Nanoamor Inc.) were approximately spherical, with cubic crystallographic structure and 80 nm in diameter. The HDPE/MWCNT composites denoted HDPE/CNT12 and HDPE/CNT58 were produced using two types of particles supplied by Grafen Chemical Industries Co., Turkey: KNT-M12 (10–20 nm in diameter, 10–30  $\mu\text{m}$  in length, with 200  $\text{m}^2 \text{g}^{-1}$  surface area) and KNT-M58 (50 nm in diameter, 10–20  $\mu\text{m}$  in length, with 40  $\text{m}^2 \text{g}^{-1}$  surface area). The matrix was a semi-high molecular weight HDPE copolymer type LITEN FB 75 supplied by Unipetrol Co., Czech Republic. HDPE/Al powder samples were also produced. For MA/Gr composite PCM, the MA (Alfa Aesar Co.) with a melting temperature range of 53–56  $^\circ\text{C}$  was heated at 60  $^\circ\text{C}$ . The Gr particles (platelets) type iGP2 (Grafen Chem. Ind. Co., Turkey) with size, thickness, and specific area of 5  $\mu\text{m}$ , 5–8 nm, and 120–150  $\text{m}^2 \text{g}^{-1}$ , respectively, were added in proportion of 0.5, 1, and 2 wt% during ultrasonic homogenization [108].

Different weight percentages of polymer/carbon particle composites were prepared by melt mixing at 180/150  $^\circ\text{C}$  (for HDPE/EVA, LDPE matrix) in the 30-mL mixing chamber of a Brabender Plasticorder PLE 331 apparatus. The rotors turned at 35 rpm in a counter-rotating fashion. After 10–15 min the mixture was passed through rollers and solidified. Finally, sample sheets with 0.25–0.45 mm thickness and few square centimeters of surface area were produced by compression molding at 150/120  $^\circ\text{C}$  (for HDPE/EVA, LDPE matrix) under 40 kPa pressure for 4 min [105,109–114].

Two aliphatic polyesters, the homopolymer PLA and the copolymer PBS were also used as matrices for investigated samples. They were commercial extrusion grades supplied by NatureWorks LLC Co. as PLA 4042D and by NaturePlast Co. as PBE 003, respectively. A plasticizer was added to PLA, that is, 15% triethyl citrate (TEC) supplied by Sigma Aldrich Co. The EG5, EG50, and EG200 fillers (the latter 200  $\mu\text{m}$  in diameter) had the same origin as those for HDPE/EG samples. The same biopolyesters were used in combination with OMMT with 30% quaternary ammonium, the Cloisite 30B supplied by Southern Clay Co. was C30B. Clay nanoplatelets have length/thickness aspect ratios on the order of  $\mu\text{m}$ /tens of nm and surface area of more than 700  $\text{m}^2 \text{g}^{-1}$ . The particles were functionalized by a silanization process with (3-aminopropyl) triethoxysilane (APTS), following Refs [115–117] for EG and Refs [118–120] for C30B. No significant improvement could be observed in our case for functionalized particles.

The composites based on biopolyester matrices were prepared by melt mixing using two models of twin-screw extruders, the Haake MiniCTW and the laboratory scale Haake Rheomex CTW 100 OS from Thermo Fisher Scientific Inc., at

170–175 °C for PLA and 145 °C for PBS [121]. Samples for PTR measurement had a thickness of about 0.45 mm and those for flash measurement were about 2.5 mm. This route produced mostly amorphous PLA and semicrystalline PBS. The solvent intercalation route by stirring the mixture in chloroform at 40 °C resulted in samples having less thermal stability and inferior rheological properties. In addition, there was less degradation of molecular chains with the melting route, as evaluated by size exclusion chromatography. For both routes, X-ray diffraction analysis revealed the increase of the interlayer spacing in OMMT from the initial value of 1.85 nm as specified by the producer to about 3.0 nm. This is an indicator of exfoliation of nanoclay sheets and intercalation of polymer chains. The granulometry of polymer/EG composites was studied by optical microscopy. On the whole, the laboratory-scale extruder achieved better homogeneity than the mini extruder.

In the course of sample preparation, the filler mass fraction  $\phi_{wt}$  is used. The models predicting the effective  $k$  are based on the volumetric fraction  $\phi_{vol}$  which can be obtained from  $\phi_{wt}$  provided the densities  $\rho_f$  and  $\rho_m$  of the fillers and matrix are known:

$$\phi_{vol} = \left[ 1 + (\phi_{wt}^{-1} - 1)(\rho_f / \rho_m) \right]^{-1} \quad (11.22)$$

The densities of a sample series that has different  $\phi_{vol}$  can be determined by the gas pycnometer method or by weighing the samples in air and in water. The difference represents the Archimedes' force and allows determination of the volume of the samples. Alternatively, the densities can be calculated by the linear rule of mixtures in terms of  $\phi_{vol}$ :

$$\rho = \phi_{vol}\rho_f + (1 - \phi_{vol})\rho_m \quad (11.23)$$

or, in terms of  $\phi_{wt}$ ,

$$\rho^{-1} = \phi_{wt}\rho_f^{-1} + (1 - \phi_{wt})\rho_m^{-1} \quad (11.24)$$

The static thermophysical parameters  $C$  and  $c_p$  are also predictable by simple rules of mixtures:

$$C = \phi_{vol}C_f + (1 - \phi_{vol})C_m \quad (11.25)$$

$$c_p = \phi_{wt}c_{pf} + (1 - \phi_{wt})c_{pm} \quad (11.26)$$

Mass specific heat capacity  $c_p$  can be measured with modulated differential scanning calorimetry (DSC) instruments. Incidentally, for polymer/graphite composites the opposite variations of  $\rho$  and  $c_p$  compensate each other. Therefore,  $C$  is constant [105]. As a result, the thermal conductivity  $k$  and diffusivity  $a = k/C$  have similar evolutions as a function of filler fraction. One should note that thermophysical properties of polymers depend to some extent on their degree of crystallinity. Table 11.1 gathers the thermophysical data of the pure components of the prepared composites.

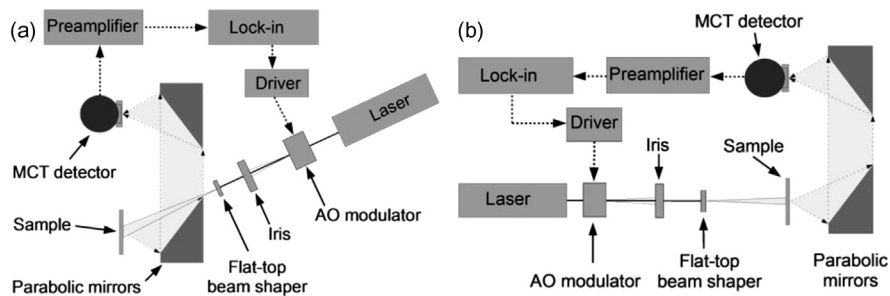
**Table 11.1** Thermophysical Properties at 25 °C of Pure Matrices and of 100% Dense Phase of Fillers Used to Prepare the Investigated Nanocomposites.

Material	Density (kg m <sup>-3</sup> )	Specific Heat Capacity (J kg <sup>-1</sup> K <sup>-1</sup> )	Thermal Conductivity (W m <sup>-1</sup> K <sup>-1</sup> )
HDPE	940–965 [122]	1800–2700 [122]	0.46–0.52 [122]
LDPE	890–920 [113,122,123]	1900–2300 [113,122,123]	0.33–0.35 [113,123]
EVA	920–935 [109]	1500–2000 [109]	0.13 [109]
PLA	1245–1285 [86]	1276 [121]	0.135 [86]
PBS	1240–1260 [124]	1622 [121]	0.25 [121]
MA	990 [125]	2164 [126]	0.45 [127]
Graphite	2250 [123]	712 [123]	(average) 80 [123] (  ) 300 [123]
MWCNT	1986–2000 [86,114]	780 [114]	(  ) 3000 [99]
MMT	2780 [128]	800–850 [129,130]	(⊥) 1.76 [128], (  ) 10.7 [128] (aggregates) 3 [128]
Al	2700 [123]	900 [123]	237 [123]

### 11.4.3 EXPERIMENTAL PHOTOTHERMAL SETUPS

In the case of a multiphase composite, the specific (mass) heat capacity and the volumetric heat capacity obey the mixture rules because they are static thermophysical parameters. In contrast, the dynamic thermophysical parameters ( $k$ , and the conductivity-dependent  $a$  and  $e$ ) are more difficult to predict because there is no unique model for heat transport in inhomogeneous media, which will be discussed in Section 11.6. This explains the importance of experimental methods and instruments for the direct or indirect measurement of thermal conductivity of polymers and composites [131]. Classical steady-state methods measure the temperature gradient across the specimens in response to an applied heating power. Nonsteady-state methods include the hot wire and hot plate methods with pulsed or periodic ( $3\omega$ ) modulation, the temperature wave method [11], and the transient or oscillatory DSC. Finally, PT methods may address all thermophysical parameters and, moreover, the optical absorption coefficient  $\beta$ . However, up to this point, their versatility has been better exploited in laboratory environments than in commercial instruments. As mentioned in Section 11.1, the discussion of nonimaging PT methods will be restricted to those compatible with composite samples. These are mainly the PA, PTR, and PPE techniques.

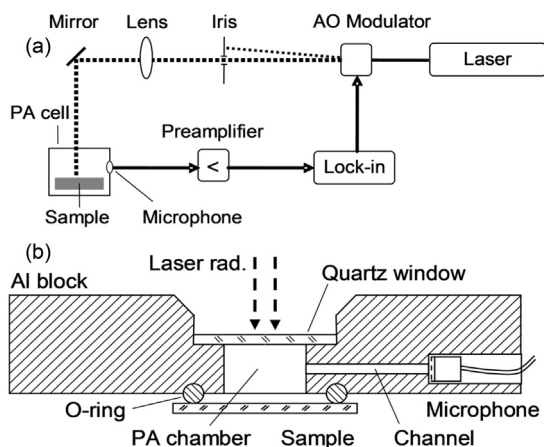
Figures 11.3–11.5 present typical setups for PTR, PA, and PPE experiments with periodic excitation. For the PTR setups (Fig. 11.3) [105,110], optical excitation was provided by a 300-mW diode-pumped solid state laser at a 532-nm



**FIGURE 11.3**

Photothermal radiometry setup (a) in front-detection configuration, and (b) in back-detection configuration.

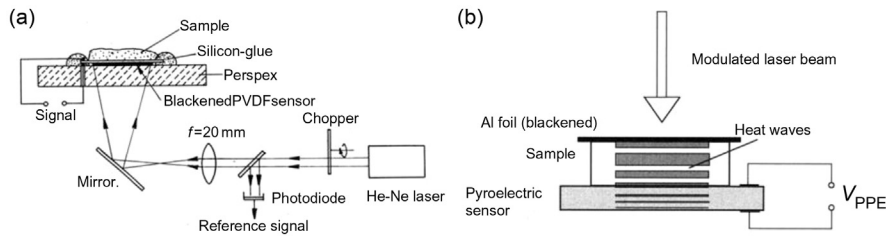
(b) After [105]. Copyright 2012. Reprinted with permission from Elsevier Ltd.



**FIGURE 11.4**

(a) Front-detection photoacoustic setup (FD-PA), and (b) design of a FD-PA cell which minimizes the PA chamber volume thus maximizing the signal amplitude.

wavelength, modulated by an acousto-optical cell. The iris selects the zero-order diffracted beam with a diameter of  $0.7 \text{ mm}$  at  $1/e^2$ . The two parabolic off-axis Au-coated mirrors collect the modulated IR radiation generated by the periodic heating of the irradiated sample spot. The liquid-nitrogen cooled HgCdTe photoresistive detector with  $1\text{-mm}^2$  active area is sensitive between  $5\text{-}$  and  $12\text{-}\mu\text{m}$  wavelength radiation. It has an antireflection-coated Ge window which is transparent in the IR range of the detector and blocks the visible radiation of the pump laser which may be scattered from the sample surface. The homemade preamplifier has a gain of 2000 in a bandwidth of  $0.1 \text{ Hz}$  to  $2 \text{ MHz}$ , and an equivalent

**FIGURE 11.5**

(a) Front-detection photopyroelectric setup, and (b) design of a back-detection photopyroelectric cell [132].

Copyright 1994. Reprinted with permission from Elsevier Ltd.

input noise of  $1.7\text{ nV Hz}^{-1/2}$ . The SR850 lock-in amplifier outputs the amplitude and phase signal. Its local oscillator modulates the 80 MHz carrier envelope of the acousto-optical driver at frequencies between 0.1 Hz and 100 kHz.

The PTR signals were normalized by the electro-optical transfer function of the setup, measured with a photodiode. Uniform irradiation over an area of 8 mm in diameter was achieved with a flat-top beam-shaper [133]. This configuration justifies the 1D heat diffusion assumption, even at low frequencies (below 10–100 Hz), where 2D (lateral) heat diffusion would alter the frequency spectra with a normal beam excitation. The pure polymer samples were translucent in the VIS and IR range, and were metalized with 60-nm-thick Au coatings on both sides and covered by 10- $\mu\text{m}$ -thick black paint layers. The main error source in the data reduction procedure is the variation of thickness  $d$  (typically  $\pm 10\text{ }\mu\text{m}$ ) over the sample surface.

The schematic layout of the PA setup of Fig. 11.4a is similar to the one for the PTR setup, except for the PA cell. Figure 11.4b depicts an FD-PA cell with minimal air volume. The pressure-tight PA chamber is sealed by the quartz window and by the sample slab. The maximum frequency response is limited by the sensitivity characteristic of the microphone used (e.g., from 10 Hz to 50 kHz). The actual high frequency limit is decreased due to the Helmholtz resonance of the acoustic system formed by the PA chamber and the tube across the chamber wall for connection with the microphone. According to Eqn (11.18), the PA signal magnitude is proportional to the inverse cell volume. The ultimate limit in reducing the latter is reached in the so-called open PA cell [134]. This BD-PA configuration requires minimal sample preparation. The (solid) slab is a few millimeters in diameter and is attached with silicone grease directly to the aperture of the microphone. The PA gas chamber is the air gap between the sample and the membrane. Compared to closed-cell design, the use of a minimal gas chamber ensures an enhanced signal-to-noise ratio.

The setups based on the PPE method require less excitation power (in the mW-range). Currently used pyroelectric sensor materials are  $\text{LiTaO}_3$  crystals,

polycrystalline ceramics with Pb-Zr-Ti oxides (PZT), and poly(vinylidene difluoride) (PVDF) polymer foils. Figure 11.5a shows a setup with a FD-PPE cell. The sensor (Solef C117, Solvay Co.) is a biaxially stretched, poled, and Al-metalized, 25- $\mu\text{m}$ -thick PVDF foil. Direct irradiation of the sensor across the transparent Perspex plate allows liquid or solid samples to be placed atop the sensor. With solids, the thermal contact is achieved with a thin layer of silicone grease. Since the expanded laser beam diameter (5 mm) is much larger than the sensor thickness, 1D heat diffusion is valid. The sensor integrates the temperature oscillations over its area and generates electrical charges at the electrodes. The signal is passed to a lock-in amplifier via a transimpedance (current-to-voltage) preamplifier. The useful frequency range of the setup is limited to 27 Hz because at higher frequencies, the sensor becomes thermally thick and the thermal wave does not penetrate the sample. In contrast, in the BD-PPE cell of Fig. 11.5b, the thermal wave has to cross the sample in order to reach the sensor, hence the upper frequency limit may be even lower.

The FD- and BD-configurations presented in Figs 11.3–11.5 give access to different thermophysical parameters, as discussed in Section 11.3.

#### 11.4.4 FLASH METHOD FOR THERMAL DIFFUSIVITY MEASUREMENT

Most PT techniques are compatible with pulsed excitation [135]. Among them, the flash thermal diffusivity measurement is widely used [136]. In this method, one side of the plane-parallel sample with mm-size thickness  $d$  is heated by the energy of a short pulse produced by a flash lamp and the temperature of the rear side produces the thermogram of the sample according to Eqn (11.20). Based on a pulsed BD-PTR configuration, modern instruments like the LFA 4  $\times$  7 series from Netzsch Co. are equipped with a pulsed laser of up to 18 J per pulse and with an IR detector for noncontact transient temperature measurement. The sample average temperature can be set between  $-120$  and  $2800$   $^{\circ}\text{C}$  under a controlled atmosphere. In addition to the thickness variations of the samples, another source of errors in composites is the local inhomogeneity of the particle charge. The flash diffusivity instruments are designed for averaging the result over a larger surface and therefore they are complementary to PT techniques.

The instrument used in this study for diffusivity measurements of biopolyester composites was developed at LEMTA Lab., University of Lorraine, Nancy, France [137]. The front side of the sample (3 cm in diameter) is made opaque (if necessary) with black paint while the rear side is made electrically conductive using silver paste. When the sample is mounted in the sample holder, the conductive side is in contact with a p- and an n-type  $\text{Bi}_2\text{Te}_3$  semiconductor. This thermoelectric system has a high Seebeck coefficient of  $360$   $\mu\text{V K}^{-1}$  at  $20$   $^{\circ}\text{C}$ . The thermocouple voltage is amplified by an AD624 instrumentation operational amplifier. The required condition is  $d^2/a > 200t_f$ , where  $t_f \approx 5$  ms is the duration of the flash irradiation. Thus, for pure polymers having  $a \approx 10^{-7}$   $\text{m}^2 \text{s}^{-1}$ , the sample thickness should be  $d > 0.3$  mm.

An advanced homemade flash thermography instrument was used for measurements of diffusivity of HDPE/EG composites [110]. The IR camera (3- to 5- $\mu\text{m}$  band) model Titanium from Cedip Infrared Systems Co. had a frame rate of 500 Hz and 1.7 ms integration time. The Tirade 5000 flash excitation system comprised four flash lamps delivering  $4 \times 1000$  J for 10 ms. The system is designed for imaging large-scale samples in FD or BD configuration, but the camera can be adjusted to capture small areas as well. The sample was placed at a distance of 0.5 m from the flash lamps and the camera averaged the back-side temperature distribution over  $\approx 1 \text{ cm}^2$  of the sample surface (compared to  $1 \text{ mm}^2$  with the PTR method).

---

## 11.5 FREQUENCY- AND TIME-DOMAIN PT SPECTRA OF NANOCOMPOSITES

The model presented in Section 11.3 assumes that the sample has a finite optical absorption coefficient  $\beta$  in the VIS range and that it is opaque in the IR range. The carbon fillers assure the opaqueness of high-charged composites, but for low charges one has to consider that most polymers are semitransparent both in the VIS range and in the IR range around  $10 \mu\text{m}$ . In that case, the  $\beta$  coefficient resulting from the fit is an average value between the VIS and IR ranges, and is an effective value of the matrix and of the sparse fillers.

### 11.5.1 PTR SPECTRA OF NANOCOMPOSITES WITH CARBON FILLERS

The nanocomposites with various forms of carbon are usually optically thick, falling into theoretical Case 1 (Section 11.3). In order to extract the  $f^{-1/2}$  constant slope of  $z_0$  prefactor (Eqn 11.9), the PTR spectra of Figs 11.6 and 11.7 were plotted against ( $\text{Amplitude} \times f^{1/2}$ ) on the  $y$ -axis, as explained in Section 11.3.2. The phases were not shifted.

Figure 11.6 shows the PTR results for a sample with a high charge of EG50 particles. The vertical dashed lines mark the transition frequencies between the special cases. In Fig. 11.6c, the parallelism of amplitude and phase curves as predicted by Case 1b (Eqns 11.14 and 11.15) is proof that the conditions  $\beta^{-1} < \mu < d$  are satisfied. As a result, in Fig. 11.6a and b, the two transitions (1a/1b and 1b/1c) are well separated, the latter being situated outside the range of the plot at 300 kHz. Thus fitting the bending of the curves at high frequency with Eqn (11.12) yields the  $\beta$  coefficient. The diffusivity  $a$  can be correctly determined at low frequency by the fit with Eqn (11.11) around the 1a/1b transition (Fig. 11.6a and b), and/or by the fit with Eqns (11.14) and (11.15) in Case 1b (Fig. 11.6c). The deviations of the experiment from the fit below 1 Hz are due to lateral (2D) heat diffusion beyond the limit of the flat-top laser beam profile and also to heat losses to the air, which were neglected in the theoretical model.

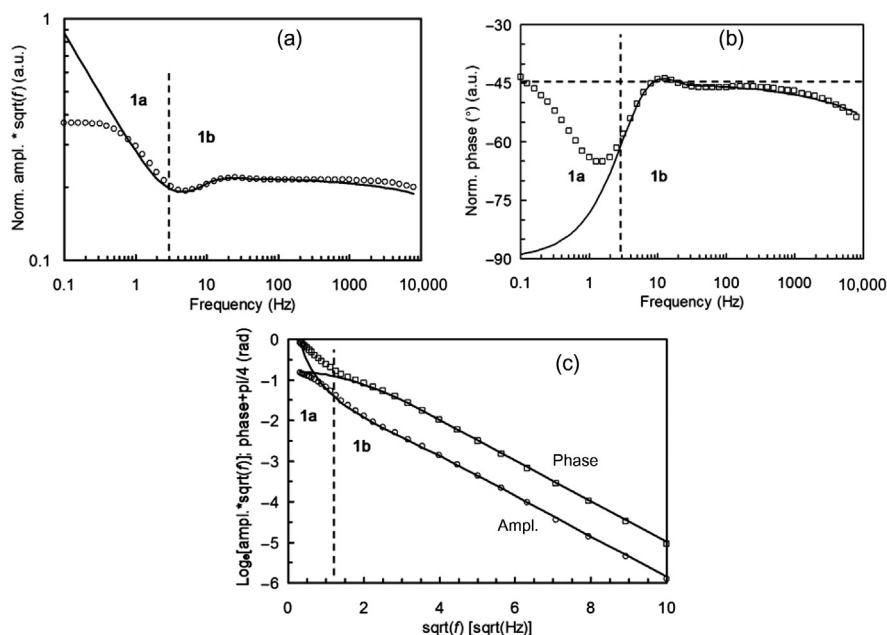


**FIGURE 11.6**

FD-PTR spectra of (a) amplitude, (b) phase signals, and (c) BD-PTR spectra of amplitude and phase signals, for HDPE/EG50 nanocomposite with 27 vol.% charge and sample thickness  $d = 325 \mu\text{m}$ ; points—experiment, solid curves—theoretical fits with  $a = 10^{-6} \text{ W m}^{-2} \text{ K}^{-1}$ , and  $\beta = 10^6 \text{ m}^{-1}$ . The markers delimit the frequency ranges for the special cases corresponding to an optically thick sample (Case 1).

Figure 11.7 illustrates a different situation. The sample had low particle charge of 1.5 vol.%. Compared with Fig. 11.6, the optical properties are changed to a much larger extent ( $\beta$  lower by a factor of 100) than the thermal ones and the sample is not optically thick enough. Therefore, the slopes in Fig. 11.7c are not parallel and in Fig. 11.7a and b the two transitions are not well separated (0.8 and 9.5 Hz, respectively). Equations (11.11) and (11.12) are not valid but nevertheless the fit with Eqns (11.6) and (11.7) is satisfactory up to 100 Hz yielding correct  $a$  and  $\beta$  values. Above 100 Hz, the deviation of the experimental points from the fit is due to the violation of the approximation of the granular two-phase (transparent/opaque) system by a homogeneous semitransparent medium (see also Section 11.7). A more advanced signal analysis may establish a link with the particle size, orientation, distribution, and clustering.

In the preceding discussion the FD-PTR spectra were exploited in view of  $a$  and  $\beta$  determination from the transition regions. Further expressions restricted to single special cases can be derived from Eqns (11.11) and (11.12). One finds that the phase is saturated to  $0^\circ$ ,  $-45^\circ$ , or  $-90^\circ$ , and that the amplitude is proportional to  $C^{-1}$ , to  $e^{-1}$ , or to  $\beta/C$  in Cases 1a, 1b, and 1c, respectively [110]. However, only

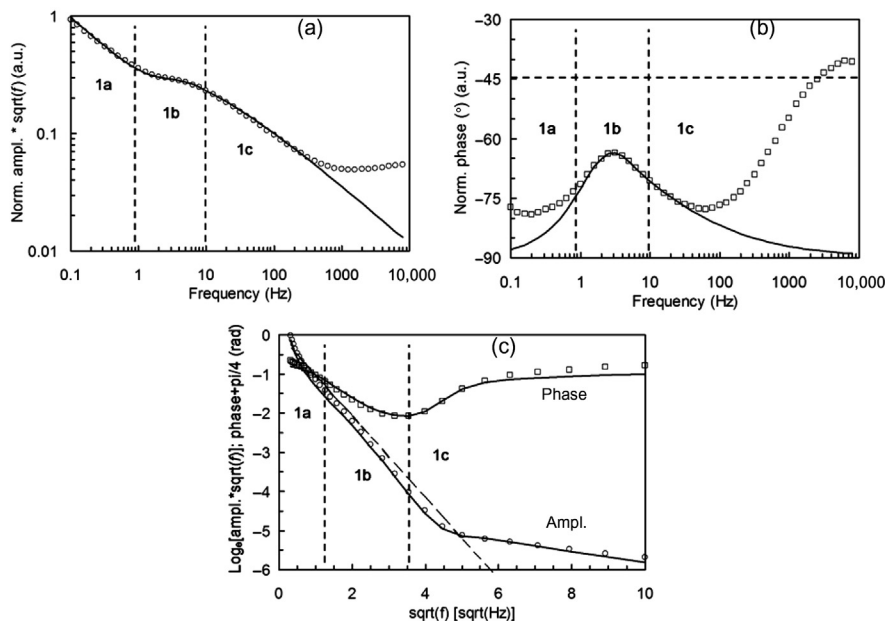


**FIGURE 11.7**

The same as in Fig. 11.6 for a nanocomposite with 1.5 vol.% charge and  $d = 345 \mu\text{m}$ ,  $a = 0.3 \times 10^{-6} \text{ W m}^{-2} \text{ K}^{-1}$ , and  $\beta = 10^4 \text{ m}^{-1}$ . The oblique dashed line is the slope of the amplitude and phase if the sample was opaque.

relative values can be derived in this way because the amplitude is usually not calibrated. It depends on the reflection coefficient of the sample surface at the laser wavelength, on  $\epsilon_{\text{IR}}$  and on  $T_{\text{dc}}$  (Eqn 11.17) among other parameters.

### 11.5.2 FLASH METHOD SPECTRA OF NANOCOMPOSITES WITH CARBON FILLERS

PT measurements with pulsed excitation produce time-domain response spectra. Figure 11.8 shows a typical thermogram of a 2.5-mm-thick sample, obtained with the flash instrument using semiconductor thermoelectric sensors [137]. The curve is normalized to its maximum value which is reached after 19 s. After that, it starts to decay due to heat loss to the ambient air. The lower curve shows the fit residues (amplified and shifted by  $-0.1$  units). The right-hand panel shows the diffusivity results obtained with the three established methods: the Parker model [93] for the adiabatic case (Eqn 11.21) or the more realistic models based on partial times and on partial time moments [96,137]. As one can see, the Parker model overestimates the diffusivity by 6%, while the difference between the other two models is only 1%. In all cases the software accounts only for opaque samples. The instrument was used for measurements on PLA/EG and PBS/EG samples [121].

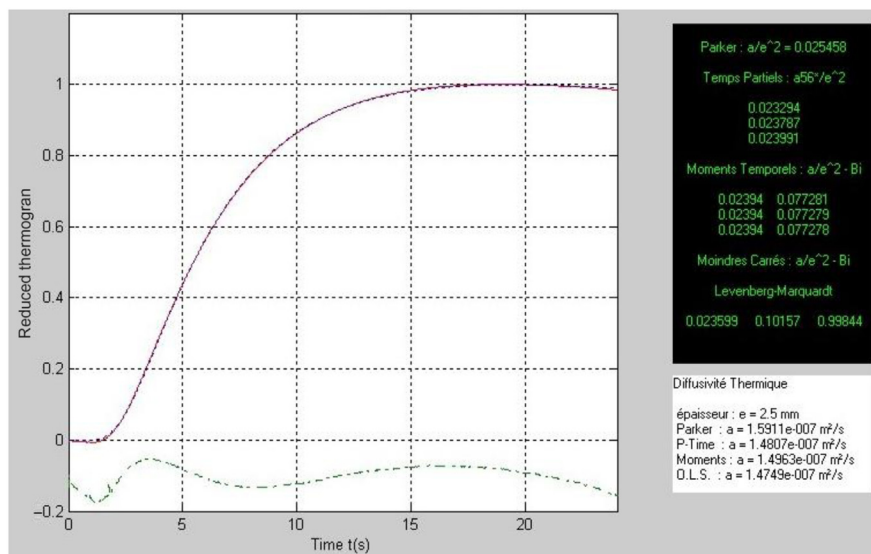


**FIGURE 11.8**

Example of a thermogram and fit results displayed by the BD-flash instrument using contact thermoelectric sensors.

The flash IR thermography system described in Section 11.4.4 is more flexible regarding the geometry of the sample. The thermograms shown in Fig. 11.9 were obtained with  $\approx 0.33$ -mm-thick HDPE/EG50 samples. The maximum temperature increase on the order of few K was reached in less than 150 ms. Up to 12 terms were used in Eqn (11.20) for the fit at short times, while beyond 50 ms, the fourth and higher terms were negligible. In Fig. 11.9, one can see the effect on the response time of two almost opaque samples having different filler charges and thermal diffusivities.

Contrary to modulated PT techniques which yield two simultaneous information channels (amplitude and phase), in the flash technique there is a single curve  $T(t)$  available for the fit, making it harder to separate the parameters  $a$  and  $\beta$ . Simulations performed with Eqn (11.20) and experimental results prove that  $a$  and  $\beta$  can still be decorrelated, provided  $\beta d > 5$  [110]. An additional problem for lower  $\beta d$  values is the optically transmitted IR radiation from the flash lamps to the IR camera which saturates the response at short times.

### 11.5.3 PTR AND PPE SPECTRA WITH OPTICALLY THIN SAMPLES

For rather transparent samples ( $d < \beta^{-1}$ ) the signal amplitude is low and rendering the sample opaque by a thin metallic coating or by black paint (which is not necessarily opaque in the IR) is preferred. Nanocomposites with very low filler

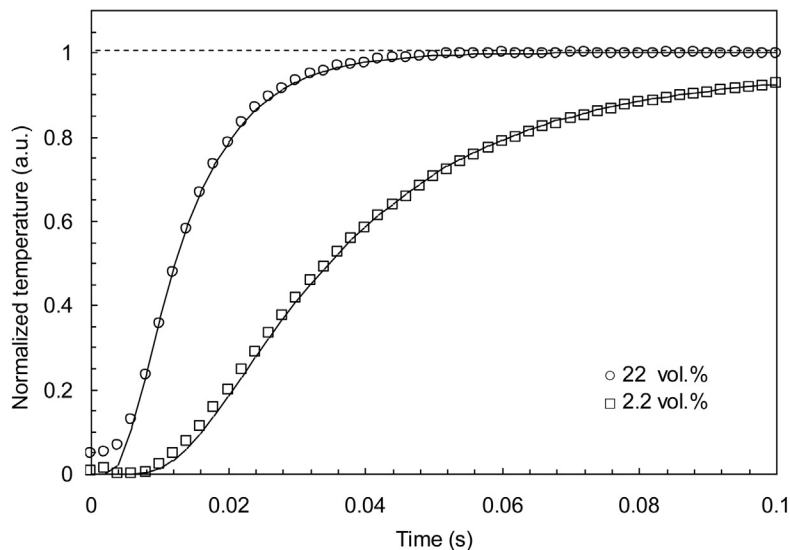


**FIGURE 11.9**

Rear-side temperature evolutions of two HDPE/EG50 samples measured with the home-built flash IR thermography system (points). Solid curves fit with Eqn (11.20), with the thermal diffusivity as fit parameter. Shorter response time is correlated with enhanced thermal diffusivity due to higher filler charge. Sample parameters are:  $\beta d = 431$ ,  $a = 1.35 \times 10^{-6} \text{ m}^2 \text{ s}^{-1}$  for  $\phi_{vol} = 22\%$ , and  $\beta d = 9.5$ ,  $a = 0.44 \times 10^{-6} \text{ m}^2 \text{ s}^{-1}$  for  $\phi_{vol} = 2.2\%$ .  $\beta$  values were determined by independent PTR measurements.

charge or with translucent filler materials may be optically thin, falling into theoretical Case 2 (Section 11.3). In this case, in order to extract the  $f^{-1}$  constant slope of the  $z_0\tau$  prefactor (Eqn 11.10), it is convenient to plot modulated PTR spectra against (Amplitude  $\times f$ ) on the  $y$ -axis (see Section 11.3.2). An example of FD-PTR measurement of an optically thin nanocomposite is shown in Fig. 11.10.

Despite its apparent transparency, the 250- $\mu\text{m}$ -thick PLA/MMT sample with 1.6-vol.% charge generates a PTR signal 14 times stronger than that of the pure PLA, which indicates that the measured signal is indeed generated by the MMT fillers. The phase close to  $-90$  degrees selects the theoretical Case 2 in the 1D regime. However, the transition between cases 2b/2c (Eqn 11.16) is hardly visible in the measurements with flat-top beam excitation (not shown here). Instead, the frequency spectra of Fig. 11.10 were obtained with normal beam (0.7 mm equivalent diameter) excitation. The vertical dashed lines at 2.5 Hz mark the transition between the 1D and 2D heat flow regimes. At this frequency, the lateral thermal diffusion length  $\mu$  in the sample sheet reaches the borders of the zone of 1 mm in diameter which is seen by the detector. At lower frequency, the heat that diffuses outside this perimeter is lost for the measurement and the signal amplitude decays, as in Fig. 11.10a. A very rough estimation of the in-plane thermal

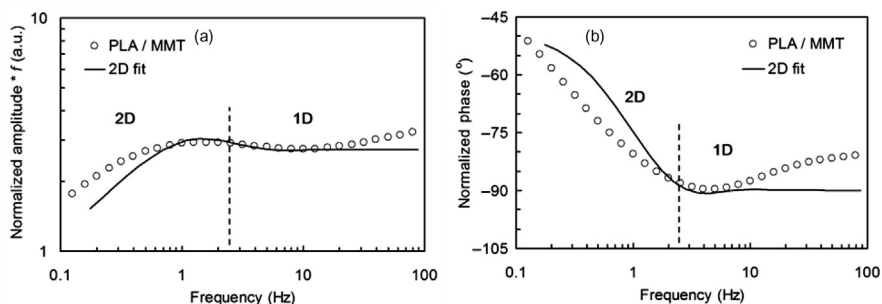


**FIGURE 11.10**

(a) Amplitude, and (b) phase spectra of PLA/MMT nanocomposite with 1.6-vol.% charge measured by FD-PTR (points). Solid lines fit with a 2D model. The markers show the transition frequency between the 1D and 2D heat diffusion regimes, which depend on the in-plane thermal diffusivity of the sample sheet.

diffusivity yields  $a \approx 1.8 \times 10^{-7} \text{ m}^2 \text{ s}^{-1}$ , which represents roughly a two-fold increase relative to that of the pure PLA matrix as calculated from Table 11.1 ( $a \approx 0.84 \times 10^{-7} \text{ m}^2 \text{ s}^{-1}$ ). The deviations of the points from the fits are caused by the fact that, in the case of semitransparent samples, the PTR signal is a combination of surface and bulk absorption.

Biodegradable composites for packaging applications can be produced using plasticized starch as the matrix material [106]. Natural starch is not soluble in water, but it is rather hygroscopic, precluding its use with foods of high water content. Water uptake affects both optical and thermal properties of the material and such evolution can readily be monitored by PT techniques. The PPE method was used for measuring the thermal parameters of starch sheets as a function of water content and temperature under quasistatic conditions. The parameters  $k$ ,  $C$ , and  $e$  increase with water content, while  $a$  remains nearly constant. No phase transition was observed at  $0^\circ \text{C}$ , which proves that water is bound in the starch matrix [138–140].

A study using PPE tomography was dedicated to the investigation of water migration in  $5 \times 5 \times 0.5 \text{ mm}^3$  starch samples as a function of depth and exposure time to liquid water at one side [141]. After the contact with a wet blotting paper for the specified time, the samples were mounted in a R-PPE cell in direct contact with the gold-coated PZT sensor, with either the wet or the dry side facing the sensor. The samples were kept in place by a 0.15-mm-thick glass plate and a retaining spring. The cell was placed at the exit slit of a monochromator tuned to a  $1.94\text{-}\mu\text{m}$  wavelength. This wavelength coincides with a strong NIR absorption band of water while dry starch is relatively transparent [139]. The value of the corresponding NIR absorption coefficient was used to calibrate the obtained PPE spectra in terms of water content  $W$  (kg/kg). The radiation source was a 50 W halogen lamp modulated by a mechanical chopper. The power reaching the sample

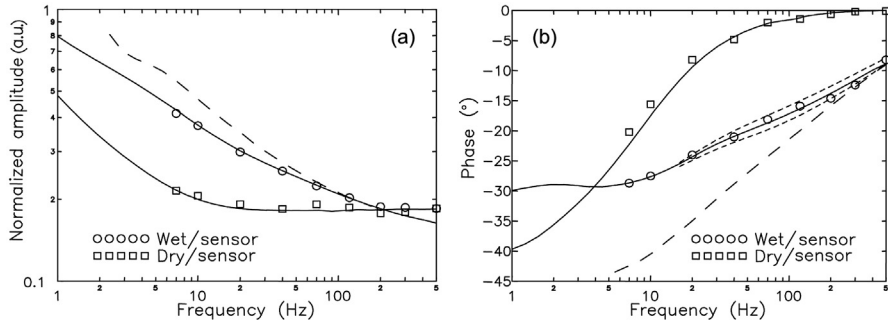


**FIGURE 11.11**

(a) Reflection-mode PPE amplitude, and (b) phase for starch sheets hydrated for 45 s on one side prior to the measurement. The curves are best fits with a three-layer sample model. The dotted curves correspond to variations of the first layer thickness of  $17 \pm 5 \mu\text{m}$ . The fit of the whole sample with the parameters of the first wet layer (dashed curves) is obviously inaccurate [141].

*Copyright 1999. Reprinted with permission from AIP Publishing LLC.*

was  $\approx 10 \mu\text{W}$ . In Fig. 11.11, the configuration “wet side on sensor” signal is mainly due to IR absorption (A) in the wet layer which is in contact with the sensor. In the reversed configuration (“dry side on sensor”), the signal is due to the fraction of IR radiation transmitted (T) across the front wet layer and passing unattenuated through the rest of the transparent sample before reaching the detector [141]. The (T) frequency spectrum served for calibration of the total moisture content in the profiles derived from the (A) spectrum. The clear difference between the (A) and (T) PPE spectra corresponding to either side of the sample in contact with the sensor is due to the nonuniform depth profile of water distribution. The details on the solution to this inverse problem are presented in Section 11.7.

## 11.6 MULTISCALE ANALYSIS OF EFFECTIVE THERMAL CONDUCTIVITY OF NANOCOMPOSITES

### 11.6.1 BACKGROUND ON EFFECTIVE THERMAL CONDUCTIVITY MODELING

Based only on parameters  $\phi_{vol}$ ,  $k_f$ , and  $k_m$ , it is possible to establish upper and lower bounds on the effective thermal conductivity  $k_e$  [142]. The parallel arrangement of the two phases with respect to the temperature gradient is equivalent to imposing parallel adiabats in the real medium. The upper bound is obtained by

$$k_e = \phi_{vol}k_f + (1 - \phi_{vol})k_m \quad (11.27)$$

For comparison among different materials, it is convenient to consider the conductivities relative to the value of the neat matrix,  $k_e/k_m$ . In the case of high conductivity contrast between the two phases ( $k_f/k_m > 1$ ), the following approximate relation is obtained from Eqn (11.27):

$$\frac{k_e}{k_m} \approx 1 + \phi_{vol} \frac{k_f}{k_m} \quad (11.28)$$

which is unrealistically sensitive to  $k_f$ . Alternatively, the lower bound limit is obtained for series arrangement of the two phases in the form of layers perpendicular to the temperature gradient. This hypothetical material implies the presence of perpendicular isotherms in the real medium and then  $k_e$  is obtained by:

$$k_e^{-1} = \phi_{vol} k_f^{-1} + (1 - \phi_{vol}) k_m^{-1} \quad (11.29)$$

In this case, the relative  $k_e$  is limited to the following approximate expression, even for large  $k_f/k_m$  contrast:

$$\frac{k_e}{k_m} \approx 1 + \phi_{vol} \quad (11.30)$$

In practice, the upper and lower bounds have little relevance because of the very broad conductivity interval between them.

Much effort has been devoted in the past to the development of more accurate models, which accounts for the large variability in the  $k_e$  of composites [143–146]. All these models necessarily yield  $k_e$  values situated between the two bounds mentioned above (in absence of the ITR). Historically, the first model stems from electrostatics and is based on the Maxwell's Mean Field Theory (MFT) [147]. It assumes spherical, noninteracting particles embedded in a continuous medium and no ITR between the two phases. The predicted relative conductivity valid for low filler charges depends only on  $\phi_{vol}$ ,  $k_f$ , and  $k_m$  as [148]

$$\frac{k_e}{k_m} = \frac{k_f + 2k_m - 2\phi_{vol}(k_m - k_f)}{k_f + 2k_m + \phi_{vol}(k_m - k_f)} \approx 1 + 3\phi_{vol} \quad (11.31)$$

Its approximate form predicts a three-times higher relative conductivity enhancement  $k_e/k_m - 1$  than the lower bound of Eqn (11.30), regardless of particle size. One of the most complete models for  $k_e$  of particulate composites is the model of Nan et al. [87] which additionally contains the effects of particle size, shape, orientation distribution, and ITR. It is based on a generalized Maxwell-Garnett type MFT and assumes low concentration of particles which are well-dispersed in a continuous matrix. In the case of randomly oriented ellipsoidal inclusions having principal radii  $a_1 = a_2 \neq a_3$ , the particular solution can be expressed as the sum of unity value plus the relative enhancement term:

$$\frac{k_e}{k_m} = 1 + \frac{\phi_{vol}(2\beta_{11} + \beta_{33})}{3 - \phi_{vol}(2\beta_{11}L_{11} + \beta_{33}L_{33})} \quad (11.32)$$

The geometrical factors  $L_{ii}$  and the dimensionless equivalent thermal conductivity components  $\beta_{ii}$  are explicitly defined by Nan et al. [87]. The  $\beta_{ii}$  quantities contain a factor which is the product of the ITR (symbol  $R_{bd}$ ) by  $k_m$ . It represents the thickness of a matrix shell around the particle that has the same thermal resistance as the ITR. This equivalent length is known as the Kapitza radius. The aspect ratio of the ellipsoid is  $p = a_3/a_1$ . The EG particles can be assimilated to oblate ellipsoids ( $p < 1$ ) with  $a_3$  as the thickness of the flakes, and then the matrix elements become

$$L_{11} = L_{22} = \frac{p^2}{2(p^2 - 1)} + \frac{p}{2(1-p^2)^{3/2}} \cos^{-1} p, \quad L_{33} = 1 - 2L_{11} \quad (11.33)$$

and

$$\beta_{ii} = \left\{ L_{ii} + \left[ \frac{1}{(k_m/k_f) + (2a_1^{-1} + a_3^{-1})R_{bd}k_m L_{ii}} - 1 \right]^{-1} \right\}^{-1} \quad (11.34)$$

The CNTs are modeled by prolate ellipsoids ( $p > 1$ ) with  $a_3$  as the length of the tubes, and the respective matrix elements are

$$L_{11} = L_{22} = \frac{p^2}{2(p^2 - 1)} - \frac{p}{2(p^2 - 1)^{3/2}} \cos h^{-1} p, \quad L_{33} = 1 - 2L_{11} \quad (11.35)$$

and

$$\beta_{ii} = \left\{ L_{ii} + \left[ \frac{1}{(k_m/k_f) + 2(2a_1^{-1} + a_3^{-1})R_{bd}k_m L_{ii}} - 1 \right]^{-1} \right\}^{-1} \quad (11.36)$$

According to this model, for large conductivity contrast ratio  $k_f/k_m$ ,  $k_e$  becomes independent of  $k_f$  and is merely controlled by the other parameters.

Xie et al. reported a comparison of the effective conductivity between composites reinforced by graphene nanosheets and CNTs [149]. It is demonstrated that the former are more effective in conductivity enhancement than the latter, and both fillers lead to substantially higher conductivity and a much reduced electrical percolation threshold in composites. The effects of conductivity anisotropy and ITR are also discussed. Im and Kim investigated the synergistic effects of graphene oxide and CNT fillers in epoxy composites [150].

Another class of models is based on the effective medium approximation (EMA) concept. Here, neither phase is continuous and  $k_e$  is obtained by the homogenization of local distortions of temperature distribution. Bruggeman [151] introduced the popular differential EMA model in which the particles are added incrementally to a homogeneous medium that has the  $k_e$  of the composite in the previous step. Thus, higher filler charge is better accounted for. Jiajun and Xiao-Su presented a unified approach to MFT and EMA models [145].

Numerical models based on finite element computation achieve better predictions at even higher filler fractions [152]. A random walk simulation was used to

model the effect of ITR on the heat flow for different orientations of single-wall CNTs (SWCNTs) dispersed in the polymers [153]. Revisions of earlier models, or new models, are based on nanoscale heat transfer theories in which the ITR is implicitly incorporated in the description of heat transfer mechanism [154,155]. The role of network percolation is discussed in Section 11.6.3.

## 11.6.2 EFFECTIVE THERMAL CONDUCTIVITY RESULTS AND DISCUSSION

The thermal diffusivities determined from the PT spectra served for the calculation of effective thermal conductivities as  $k_e = aC$ . For consistent evaluations at low and at high filler charges, and based on Eqns (11.28) and (11.30)–(11.32), it is more appropriate to use the relative conductivity enhancement parameter  $k_e/k_m - 1$ .

The results on the investigated materials are gathered in Fig. 11.12. Almost all materials are situated above the prediction of the Maxwell model because the fillers are nonspherical ( $|p| > 1$ ) to various extents. As one can see, the composites can be grouped roughly into three classes. In the lower class there is no significant difference between nearly-spherical (EU22, HA) and flaky (LE5) particle shapes, or CNT (HC58). HDPE/Al nanocomposite with 80-nm particle size

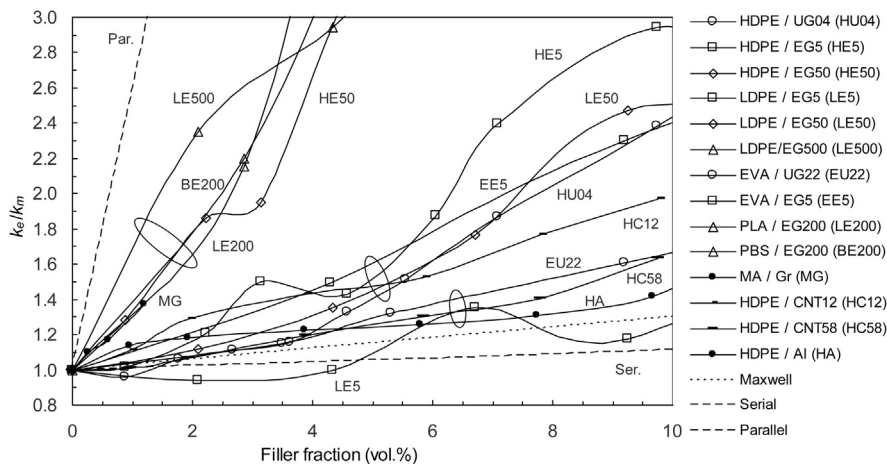


**FIGURE 11.12**

Relative effective thermal conductivity versus filler fraction for the investigated nanocomposite series. Long dashed lines are lower and upper bound limits (Eqns 11.28 and 11.30) and the short dashed line is the prediction with the Maxwell model (Eqn 11.31). Solid lines are guides for the eye. Typical errors for individual points are  $\pm 10\%$ .

Some data are adapted from: (HU04, HE5, HE50) [105], (EU22, EE5) [111], (LE200, BE200) [121], (MG) [108], and (HC12, HC58) [114].

(curve HA) has a factor 1.5 lower  $k_e/k_m - 1$  parameter than the same composite with 80- $\mu\text{m}$  particle size [156] (not shown in the figure). This is because smaller particles have larger specific areas, and the effect of the ITR between the matrix and particles is to reduce  $k_e$ . Several reports indicate that the actual sizes of MWCNTs [86] and EG [105] fillers are substantially reduced during the blending process. Thus, the low relative conductivity in this class should be attributed to the real aspect ratios of the fillers not exceeding  $|p| \approx 50$ . The average  $k_e/k_m$  is slightly higher than that predicted by the Maxwell model (Eqn 11.31). The notable exception is LE5, which initially shows a decrease of conductivity. This effect can be explained in the frame of the model of Nan et al. [87] by anomalously large ITR (Eqn 11.32) and points to a preparation problem.

The intermediate class comprises typical composites with good contact between fillers and matrix. It suggests that comparable  $k_e/k_m$  increase can be obtained with various matrices (i.e., HDPE, LDPE, and EVA) charged with fillers having rather high real aspect ratios ( $|p| > 100$ ). The curve for HU04 ( $|p| \approx 5$ ) seems to be an exception, but at low filler charge ( $\phi_{vol} < 4\%$ ) it belongs to the lower class. Despite the very high nominal aspect ratio ( $|p| \approx 1000$ ) of CNT12 fillers, the HC12 curve does not reach the highest class. In addition to the length reduction during the preparation of the composite, the high intrinsic  $k_f \approx 3000 \text{ W m}^{-1} \text{ K}^{-1}$  of MWCNTs cannot be fully exploited because of the large ITR between CNTs and the amorphous matrix [99].

The high relative  $k_e$  values in the upper class are clearly correlated to very high nominal aspect ratios of the fillers ( $|p| > 1000$ , possibly up to  $10^4$  for LE 500). Nevertheless, their real size is not known. It should be noted that the increase of HE50 is saturated at  $\phi_{vol} > 6\%$ , unlike LE200 and BE200 which have  $k_e/k_m = 14\text{--}28$  at  $\phi_{vol} = 23\%$ . With  $|p| \approx 10$ , the MG series is the exception in this class. Its very high conductivity can be explained only by a very low ITR. This assumption is supported by the similar high  $k_e$  values obtained in the liquid phase at  $60^\circ\text{C}$  [108]. In Fig. 11.12, the upper bound for relative conductivity increase calculated with the parallel model of Eqn (11.28) and with  $k_f/k_m = 160$  is still situated much higher than any experimental result.

Figure 11.13 compares selected experimental results of some of the highest reported relative conductivity increases, with simulations using the model of Nan et al. [87]. The simulations with Eqn (11.32) illustrate the effect of EG particle size, ITR, and particle orientation on  $k_e/k_m$  increase. Curve 3 is a fit to HDPE/EG50 data (curve 1), which yielded the true particle size of EG50 in the composite as  $a_1 = 13 \mu\text{m}$  and the ITR value as  $2.1 \times 10^{-7} \text{ m}^2 \text{ K W}^{-1}$  [105]. The exceptionally high  $k_e$  increase (curve 2) of an epoxy/EG composite [157] can be the consequence of the use of highly sheared EG. The theoretical curves (4–6) are simulations for materials that have a hypothetical technological improvement at each step in addition to previous formulations: about four times larger particles for curve (4), about five times lower ITR for curve (5), and finally a material with aligned particles (curve 6). Roughly each step resulted in more than doubling the  $k_e/k_m$  increase up to an extrapolated value of 40 at 10 vol.% filler fraction.

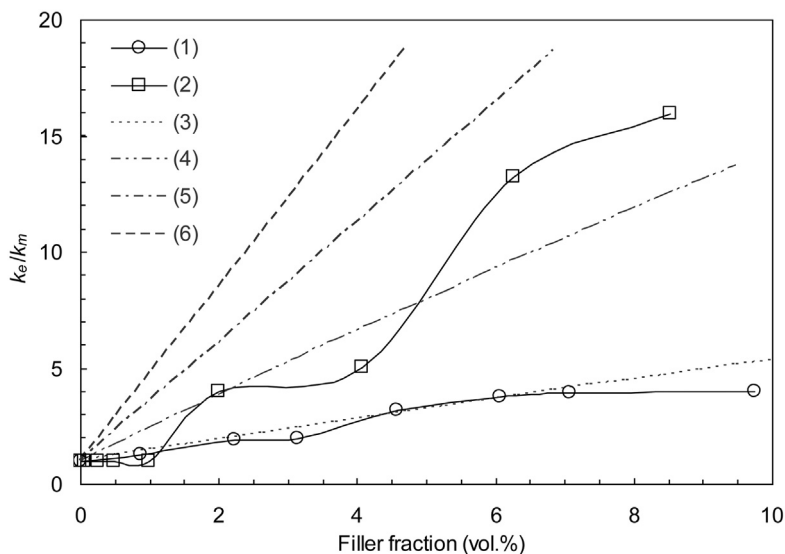


**FIGURE 11.13**

Comparison of high experimental and theoretical values of relative effective thermal conductivity as a function of EG filler fraction. Experimental points are: (1) results for HDPE/EG50 composites (adapted from [105]), and (2) for a polymer/EG composite series (adapted from [157]). Solid lines are guides for the eye. Dashed lines are theoretical predictions with Eqn (11.32), with the following lateral sizes of EG flakes and ITR values: (3)  $13\ \mu\text{m}$  and  $2.1 \times 10^{-7}\ \text{m}^2\ \text{K}\ \text{W}^{-1}$ , (4)  $50\ \mu\text{m}$  and  $2.1 \times 10^{-7}\ \text{m}^2\ \text{K}\ \text{W}^{-1}$ , (5)  $50\ \mu\text{m}$  and  $5 \times 10^{-8}\ \text{m}^2\ \text{K}\ \text{W}^{-1}$ , and (6)  $50\ \mu\text{m}$  and  $5 \times 10^{-8}\ \text{m}^2\ \text{K}\ \text{W}^{-1}$  for particles aligned to the heat flow direction.

In fact, it appears that the particle size is relevant only in relation to ITR, the increase of the two having opposite effects on  $k_e$ . Note that, at the scale of the y-axis of Fig. 11.13, the prediction of the Maxwell model (Eqn 11.31) is an almost horizontal line ( $k_e/k_m = 1.3$  at  $\phi_{vol} = 10\%$ ).

According to Fig. 11.13, technological improvements of thermally conducting composites are still possible in principle. Since, as previously mentioned, the actual sizes of the fillers are limited by the fabrication process, the efforts should be directed towards the reduction of the ITR and the alignment of the fillers along the preferential direction of the heat flow.

### 11.6.3 INDIRECT EVIDENCE OF THERMAL PERCOLATION IN COMPOSITES WITH EG AND CNT FILLERS

A subject of great interest in materials science is the nonlinear thermal and electrical transport properties in composites as a function of filler content. There

are fundamental questions related to the universal behavior of critical exponents [158], while interesting functional applications in electronics and thermal engineering have already been demonstrated. However, the clear observation of the thermal percolation effect accompanying electrical percolation is still controversial. The theories for the prediction of the  $k_e$  presented in Section 11.6.1 did not take into consideration the possible effects of the formation of a contiguous filler network throughout the matrix of the composite. This event is more likely to occur with strongly nonspherical particles, at very low filler fractions ( $<1$  vol.% for CNT) [99,150,159]. The main feature is the existence of a percolation threshold which triggers a sharp and large enhancement of the measured property. The classical, phenomenological percolation theory [158] is used to describe the discontinuous conducting behavior of heterogeneous systems around a threshold volume fraction  $\phi_c$  [160]:

$$k_e = k_m \left( \frac{\phi_c - \phi_{vol}}{\phi_c} \right)^{-s}, \quad \phi_{vol} < \phi_c \quad (11.37)$$

$$k_e = k_f \left( \frac{\phi_{vol} - \phi_c}{1 - \phi_c} \right)^t, \quad \phi_{vol} > \phi_c \quad (11.38)$$

where  $\phi_c$  depends on particle size and shape and on the composite topology [161]. For lattice percolation in three dimensions, the universal values of critical exponents are  $s = 0.87$  and  $t = 2$  [162]. Here  $k$  symbolizes a generic conductivity.

In the case of electrical conductivity, the corresponding jump in the values encompasses more than 10 orders of magnitude, as illustrated in Fig. 11.14 for HDPE/EG composites [163]. It has been argued that an analogous thermal percolation effect could not be observed because of a much lower contrast between the thermal conductivity values of fillers and matrix. Moreover, because of the weak Van der Waals forces binding CNTs, there is significant particle-to-particle ITR, which has no corresponding mechanism in the case of electrical conductivity [99,164].

The  $k_e$  values for the same HDPE/EG5 and HDPE/EG50 composites [105] are plotted in Fig. 11.14 on a log–log scale adapted to allow for visual comparison with the electrical conductivity data. While there is no clear evidence for a thermal percolation behavior, the qualitative similitude is noteworthy. It consists of apparently parallel, shifted shoulders of both curves in the range between 0.01 and 0.1 filler fraction, followed by a saturation trend at higher charge. The maximum observed  $k_e$  increase is by a factor of 5. A weak thermal percolation effect in Si-epoxy composites was observed experimentally at  $\phi_{vol} = 10\text{--}20\%$  by using PTR and PA methods [89].

The following example illustrates the fact that, in some cases, the models discussed in Section 11.6.1 fail to capture the salient features of the behavior of  $k_e(\phi_{vol})$  curves. The PLLA/CNT composites studied by Lizundia et al. [86] contain MWCNTs with similar characteristics as those used in our HDPE/CNT12 composites [114]. Unexpectedly, the (interpolated) relative conductivity increase

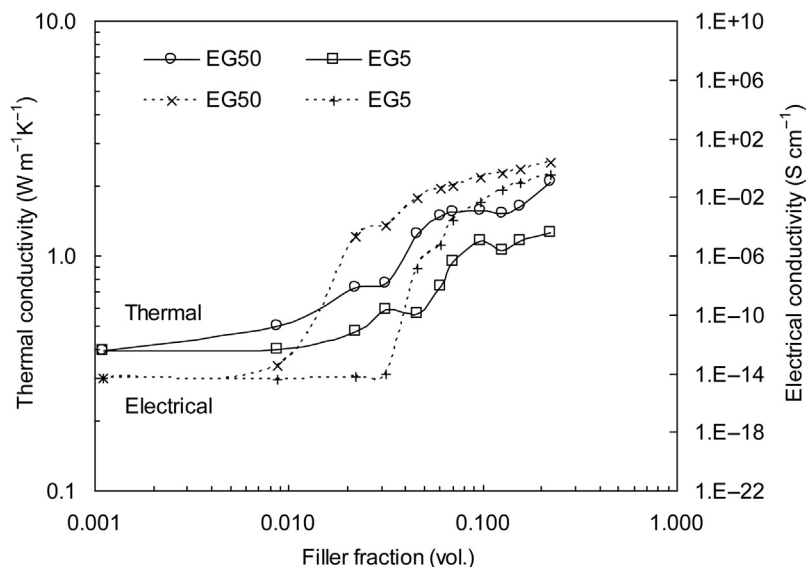


**FIGURE 11.14**

Comparison of log–log plot of thermal and electrical conductivities of two HDPE/EG composite series versus filler fraction (adapted from [105] and [163], respectively). Note the large span of electrical conductivity values and their sharp increase between 0.01 and 0.05 vol. fraction associated to the percolation phenomenon. Lines are guides for the eye.

for the two materials is very different:  $k_e/k_m = 2.05$  and  $1.35$ , respectively, for  $\phi_{vol} = 3\%$ . The relative conductivity enhancement  $k_e/k_m - 1$  also does not conciliate the two data sets. The extensive use of the effective conductivity normalized to that of the matrix in evaluating the conductivity increase is a natural choice in the frame of MFT and EMA models. In this particular case, however, it was found that a plot of the absolute conductivity enhancement  $k_e - k_m$  achieves very good agreement between the two curves, as shown in Fig. 11.15. The explanation could be related to the percolation phenomenon which is suggested by the initial nonlinearity of the dotted curve. According to Lizundia et al. [86], the negative enhancement below  $\phi_{vol} = 0.75\%$  is due to the large CNT-polymer ITR of  $1.8 \times 10^{-8} \text{ m}^2 \text{ K W}^{-1}$ , which causes strong phonon scattering at the interface. Above  $\phi_{vol} = 1\%$ , the existence of a contiguous CNT network confirmed by atomic force microscopy images and transmission electron microscopy micrographs prevails over the negative effect of the ITR. The other experiment (circles) missed the points below  $\phi_{vol} = 1\%$ . Based on these observations one may reasonably assume that, in the presence of the CNT network, the role of the matrix in the heat transport is diminished as compared with its contribution in a dispersed medium. This is equivalent to (partial) decoupling the conduction through the matrix from the conduction through the network. Eventually, the two act in

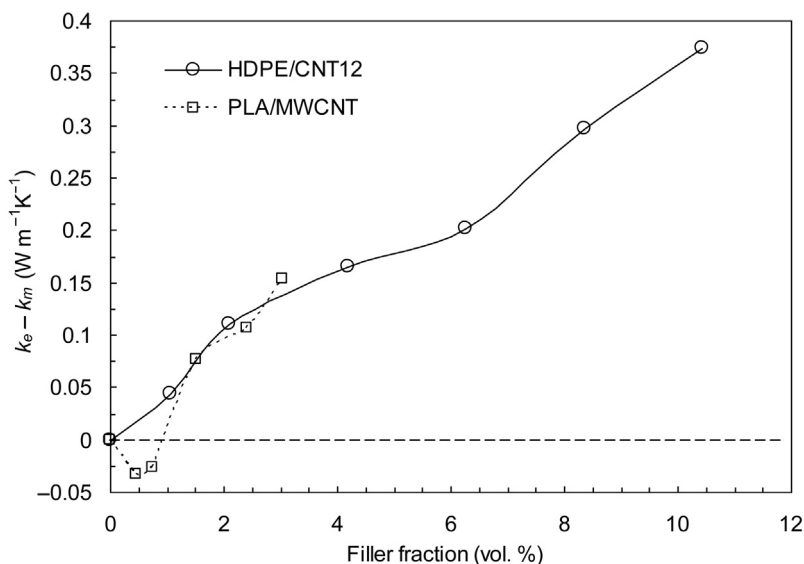


**FIGURE 11.15**

Comparison of the absolute thermal conductivity enhancement  $k_e - k_m$  of HDPE/CNT12 and PLLA/MWCNT composites versus filler fraction (adapted from Refs [114] and [86], respectively). The two composite series have different matrix materials but similar MWCNT fillers. Lines are guides for the eye.

parallel, a morphology described by Eqn (11.27). Therefore, the removal of the matrix influence by subtracting the  $k_m$  value from  $k_e$  leads to a more pertinent parameter for assessing the overall effect of CNT in different polymer-based composites than taking the ratio of the two quantities. A similar approach was used in an attempt to extract the contribution of the network alone and to retrieve the thermal percolation feature of SWCNTs in a poly(methyl methacrylate) (PMMA) matrix [165]. The discussed example illustrates the fact that the optimal approach for comparing different composite types is not unique.

## 11.7 DISCUSSION OF OTHER RESULTS OF PT SPECTROSCOPY

As discussed in Section 11.3.1 and illustrated in Section 11.5.1, the PTR spectra also contain information on optical properties of the composites. Pure graphite has high absorptivity, low reflectivity, and is practically opaque in the VIS-IR range. When graphite particles are dispersed in a transparent matrix, the effective absorption coefficient  $\beta$  of the composite depends on the particle charge, but is still much higher than the scattering coefficient. By analogy with a homogeneous

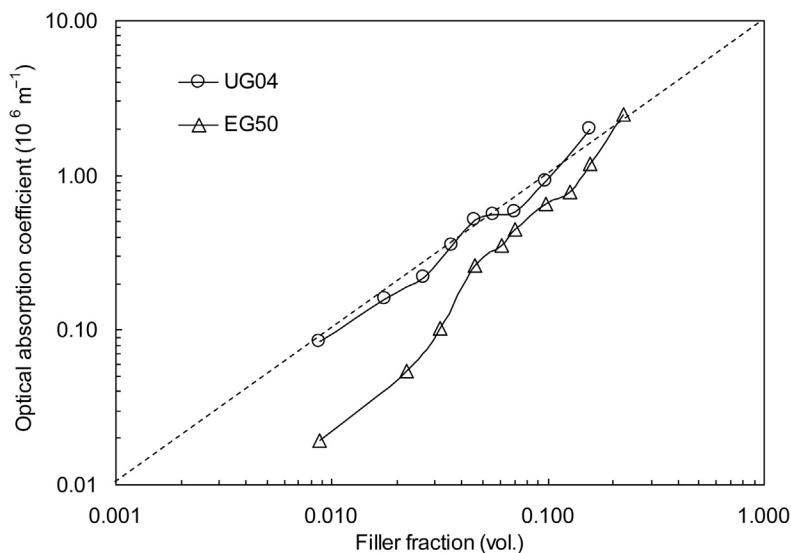


**FIGURE 11.16**

Optical absorption coefficient of HDPE/UG04 and HDPE/EG50 composites versus filler fraction, determined from FD-PTR frequency spectra. The excitation laser had a 532-nm wavelength. The slope of the dashed line represents the direct proportionality dependence. Solid lines are guides for the eye.

medium consisting of an absorbing solute having molar extinction coefficient  $\varepsilon$  dissolved in a transparent solvent, the Beer–Lambert law can be expressed as  $I = I_0 \exp(-\beta d) = I_0 \exp(-\varepsilon c_m d)$ , where  $c_m$  is the molar concentration. It follows that a linear relation between  $\beta$  and the filler charge  $\phi_{vol}$  is expected in this approximation for polymer/carbon composites. This assumption is confirmed by the results shown in Fig. 11.16. The  $\beta$  values represent averages over the sample surface seen by the detector (diameter = 1 mm), which is larger than the particle size.

In the case of HDPE/UG04 composite, the size of the nearly-spherical particles is of the same order as the wavelength of the excitation laser. The composite is optically nearly-homogeneous and one finds  $\beta \propto \phi_{vol}$ . It also proves that the calculated filler charge in the measured sample series is correct. The behavior of the HDPE/EG50 composite is different and the linear dependence of  $\beta$  with  $\phi_{vol}$  is not obeyed. At low charge, one observes up to five times lower  $\beta$  values than for the HDPE/UG04 composite. The reduced optical absorption efficiency is explained by the fact that the particle size is roughly two orders of magnitude larger than the laser light wavelength. At this scale, the granular morphology of the medium cannot be approximated by a continuous medium. At higher charge ( $\phi_{vol} > 0.05$ ), the difference between UG04 and EG50 composites is reduced, possibly because of contiguous EG50 network formation. Thus, the projection of the

carbon network in the plane of the sample slab would contain completely opaque patches. Upon closer look at Fig. 11.16, it appears that the transition between the low and high charge behavior takes place in the form of a shoulder in the interval of 0.02–0.05 filler fraction. The analogy with the features of the thermal conductivity curves of Fig. 11.14 in the same interval is striking, suggesting the same network percolation phenomenon to be at the origin of both effects observed in HDPE/EG composites. It is noteworthy that the  $\beta$  values shown in Fig. 11.16 are very high, reaching  $2 \times 10^4 \text{ cm}^{-1}$  for  $\phi_{vol} = 20\%$ , which is equivalent to  $1/\beta = 0.5\text{-}\mu\text{m}$  optical penetration depth into the sample. Such high absorption in the prepared samples cannot be measured using conventional transmission spectrophotometers.

Section 11.5.3 presented the PPE frequency spectra from an experiment designed for transient monitoring of mass transport (water) in a biopolymer (starch) (Fig. 11.11). The selectivity between the two constituents was achieved using a strong NIR absorption band of water. The inhomogeneous starch sheet was modeled by a stack of homogeneous layers with all thermo-optical parameters and layer thicknesses dependent on the water content. At the highest frequency of 500 Hz, the signal phase is determined by the water content in an 8.3- $\mu\text{m}$ -thick superficial layer. The frequency intervals situated at lower frequency were fitted with progressively thicker starch layers (because  $\mu \propto f^{-1/2}$ ) which contained less water. Modeling three layers was sufficient to smoothly fit the data shown in Fig. 11.11. The points plotted in Fig. 11.17 are the parameters of the layers (excess water content  $W_i - W_0$  and thickness  $d_i$ ). The figure shows the depth distribution of the absorbed water as a function of initial hydration time. According to the sorption isotherm of starch, the excess water content  $W_{\max} - W_0 = 0.67$  at the wet surface corresponds to a 97% relative humidity, indicating the saturation with water due to direct contact with wet paper during the specified time.

For the interpretation of the results in Fig. 11.17, it should be noted that the Eqns (11.1)–(11.4) also apply to mass diffusion processes because heat and mass diffusion are governed by similar laws [166]. In particular, the transient water diffusion into a material is formally described by Eqns (11.4a) and (11.4b), which are the solutions of Fick's second diffusion law. A diffusion process initiated by imposing a sudden constant water content at the interface corresponds to the boundary condition of Eqn (11.4b), which can be rewritten as

$$\frac{W(x,t) - W_0}{W_{\max} - W_0} = \text{erfc}\left(\frac{x}{2\sqrt{Dt}}\right) \quad (11.39)$$

where  $D$  is the mass diffusion coefficient. The solid lines in Fig. 11.17 fit with Eqn (11.39) to the three data sets, revealing the mass diffusion-like behavior of water migration. The obtained average value of the fit parameter is  $D = 2.0 \times 10^{-10} \text{ m}^2 \text{ s}^{-1}$ , with an estimated overall error of  $\pm 20\%$ . The result is within the variability interval of literature data on moisture diffusion coefficient in starch of various origins [167]. An alternative approach to the inverse problem

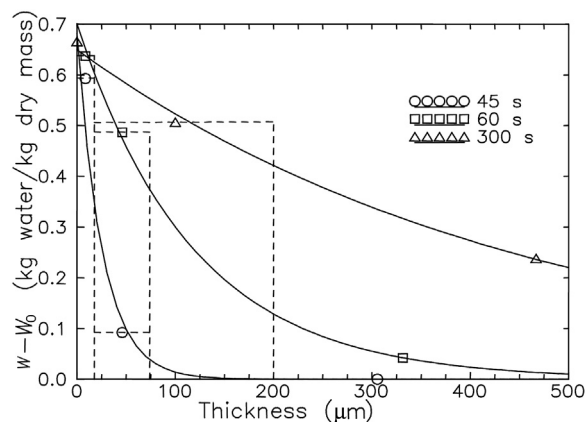


**FIGURE 11.17**

Depth profiles of excess water distribution in a  $\approx 500 \mu\text{m}$ -thick starch sheet for different initial hydration times. The points are fit results of the frequency spectra from Fig. 11.11 with a three-layer model. The first two equivalent homogeneous layers (dashed lines) for 45 and 60 s hydration times have the thicknesses  $d_1 = 17 \mu\text{m}$  and  $d_2 = 58 \mu\text{m}$ . For 300 s of hydration time,  $d_1 = 17 \mu\text{m}$  and  $d_2 = 183 \mu\text{m}$ . The third layer extends over the rest of the sample thickness (to the right in the figure). Solid lines are fits to the points using Eqn (11.39) [141].

Copyright 1999. Reprinted with permission from AIP Publishing LLC.

of moisture depth profile in starch sheets is using neural networks [168]. The knowledge of parameter  $D$  with tens of microns of depth resolution is necessary for the design of multilayer, starch-based packaging materials with controlled biodegradability or for other moisture-barrier studies in composite materials for the food industry.

## 11.8 CONCLUSIONS

PT methods use modulated laser light irradiation of a sample to excite a thermal response which contains information on its thermophysical and optical properties. The term *spectroscopy* has been used in relation to frequency- or time-domain PT spectra that can be acquired by various PT laboratory methods. The goal of this chapter is to demonstrate that PT spectroscopy is complementary to more specific and well-established spectroscopic techniques for the assessment of polymer nanocomposites. Section 11.2 presents a literature survey of applications of PT methods to various classes of composite materials which have defined functional structures at the macro-, mezo-, or micro-/nanoscale. The corresponding PT instrumentation ranges from industrial-scale, lock-in thermography

with multiple flash lamps, to PT microscopy with submicron lateral resolution. The disadvantage of PT methods being available only as laboratory setups rather than as commercial instruments is compensated for by a broader versatility, the capability to handle small sample quantities of various shapes and surface conditions, and to respond to customers' demand concerning the type and range of parameters to be measured.

Among various PT methods, the photothermal radiometry in FD-PTR or BD-PTR configurations has the advantage of being noncontact, broad band, and highly sensitive. The PTR method can handle semitransparent samples better than the commercial flash radiometry diffusivity-meters, which are variants of the BD-PTR. Frequency-modulated PTR allows for self-checking of the results obtained from simultaneous fits of signal amplitude and phase spectra, while the flash method yields a single time-dependent signal. With fitting modulated FD-PTR spectra, it is possible to independently determine the specific heat capacity, thermal diffusivity, thermal effusivity, and effective optical absorption coefficient (in this order), from 0.1 Hz to 100 kHz. From BD-PTR spectra, the thermal diffusivity can be accurately determined in the range between 1 and 100 Hz. Eventually, the thermal conductivity is derived by combining measurements of thermal diffusivity with density and specific heat capacity data.

Setting up a database with  $k_e$  of composites is important not only for practical applications, but also because it can feed input data for scaling laws which have a fundamental relevance. They can pass from effective macroscopic quantities to local properties, which are meaningful only at that scale. In other words, starting from macroscopic measurements using conventional instrumentation one can access quantities which are related to the morphology of the composite material at the micro- and nanoscale.

The difficulty in predicting the effective thermal conductivity  $k_e$  of a heterogeneous medium stems from the fact that  $k_e$  is a dynamic heat transport quantity. In contrast, the volumetric heat capacity which is a static thermal parameter quantifying the heat storage by the medium, obeys the mixture law. Several modeling approaches have been used in the literature to interpret the anomalously high and/or the nonlinear  $k_e$  dependence on the volumetric particle charge. Some of the highest reported relative conductivity increases are by factor 4.0 [157] and 1.9 [121] at 2 vol.%. Among the exact models based on MFTs or on EMAs, we focused on a model containing explicit dependence on particle size and shape, and on ITR [87,145]. Strongly nonspherical particles are more efficient than spherical ones in bridging high conductivity paths within the insulating matrix, while larger particles achieve this with less connectivity points between them. On the other hand, the ITR between particles and matrix has an adverse effect on the conductivity enhancement of the composite. We bring new indirect evidence that the geometric percolation phenomenon (attested by the existence of electrical percolation) may leave its blueprint on  $k_e$  and  $\beta$  behavior at concentrations around the threshold for the formation of an EG and CNT network in the polymer matrix.

When comparing the relative  $k_e$  increase of different composites, some contradictory results point to the importance of the sample preparation process for the final material properties. The predictions of theoretical simulations suggests that technological improvements of thermally conducting composites are, in principle, still possible and should be directed towards the reduction of the ITR and the alignment of the fillers along the preferential direction of the heat flow.

The very high optical absorption coefficient  $\beta$  of polymer/carbon composites is also accessible by the PTR method, contrary to conventional transmission spectrophotometry. The obtained values are consistent with the model neglecting light scattering and for small particles,  $\beta$  is proportional to the volumetric filler fraction over a broad range of values. Thus  $\beta$  can be used to control the filler amount and its distribution homogeneity, as well as for more intricate spectroscopic studies, such as the real-time monitoring of water migration process in biopolymer (starch) sheets.

The content of this chapter also reflects the historical development of the subject, from the early patents on EG fabrication and the elaboration of MFT and EMA models around the turn of the twentieth century, through the emergence of PT methods over the course of 70 years, the industrial development of composites over the course of 80 years, until the recent advances on graphene and CNTs composites and their theoretical approach in terms of nanoscale phonon heat transfer theories. In parallel, one assists to a regain of the interest in PT methods capable of high-frequency and short time-scale operation. Overall, one may conclude that PT methods have the unique capability of characterizing several effective thermophysical and optical properties of particulate multiphase polymer nanocomposites.

---

## ACKNOWLEDGMENTS

The LDPE/EG samples were kindly provided by Dr I. Krupa. The biopolymer/EG samples were prepared and measured by Y. Kanake. J.F. Henry performed flash IR thermography measurements.

---

## REFERENCES

- [1] Mondal S. Phase change materials for smart textiles—an overview. *Appl Therm Eng* 2008;28:1536–50.
- [2] Seki Y, Ince S, Ezan MA, Turgut A, Ereğ A. Development and evaluation of graphite nanoplate (GNP)-based phase change material for energy storage applications. *Int J Energy Res* 2015;39:696–708.
- [3] Tjong SC, Mai YW. *Physical properties and applications of polymer nanocomposites*. Cambridge, UK; Philadelphia: Woodhead Publishing; 2010.
- [4] Sinha Ray S. *Clay-containing polymer nanocomposites, from fundamentals to real applications*. Amsterdam: Elsevier; 2013.

- [5] Thomas S, Joseph K, Malhotra SK, Goda K, Sreekala MS. Polym composites, vol. 2: Nanocomposites. Weinheim, Germany: Wiley; 2013.
- [6] Tam AC. Applications of photoacoustic sensing techniques. *Rev Mod Phys* 1986;58:381–431.
- [7] Vargas H, Miranda LCM. Photoacoustic and related photothermal techniques. *Phys Rep* 1988;161:43–101.
- [8] Almond DP, Patel P. Photothermal science and techniques. London: Chapman & Hall; 1996.
- [9] Sell JA. Photothermal investigations of solids and fluids. New York, NY: Academic Press; 1989.
- [10] Mandelis A. Progress in photothermal and photoacoustic science and technology, vol. I: principles and perspectives of photothermal and photoacoustic phenomena. New York, NY: Elsevier; 1992.
- [11] Angström AJ. A new method of determining the thermal conductivity of solids. *Ann Phys* 1861;2:513–30.
- [12] Bell AG. On the production and reproduction of sound by light. *Am J Sci* 1880;118:305–24.
- [13] Rosencwaig A, Gersho A. Theory of the photoacoustic effect with solids. *J Appl Phys* 1976;47:64–9.
- [14] Helander P. A method for the analysis of optothermal and photoacoustic signals. *Meas Sci Technol* 1993;4:178–85.
- [15] Chirtoc M, Bicanic D, Chirtoc I, Lubbers M. Processing of weak photothermal signals from the optothermal window (OW) cell; application to the determination of ammonium ion in water. *Instrum Sci Technol* 1998;26:281–8.
- [16] Sun L, Zhang SY, Zhao YZ, Li ZQ, Cheng LP. Thermal diffusivity of composites determined by photoacoustic technique. *Rev Sci Instrum* 2003;74:834–6.
- [17] Rosencwaig A. Photoacoustics and photoacoustic spectroscopy, chemical analysis. In: Elving PJ, Winefordner JD, Kolthoff IM, editors. *Chemical analysis*, vol. 57. New York, NY: Wiley; 1980.
- [18] Coufal H, Lüscher E, Korpiun P, Schneider S, Tilgner R. Photoacoustics: principles and applications. Wiesbaden: Vieweg; 1981.
- [19] Nordal PE, Kanstad SO. Photothermal radiometry. *Phys Scr* 1979;20:659–62.
- [20] Santos R, Miranda LCM. Theory of the photothermal radiometry with solids. *J Appl Phys* 1981;52:4194–8.
- [21] Tom RD, O'Hara EP, Benin D. A generalized model of photothermal radiometry. *J Appl Phys* 1982;53:5392–400.
- [22] Fuente R, Apinaniz E, Mendioroz A, Salazar A. Simultaneous measurement of thermal diffusivity and optical absorption coefficient using photothermal radiometry. I. Homogeneous solids. *J Appl Phys* 2011;110:033515.
- [23] Salazar A, Fuente R, Apiñaniz E, Mendioroz A, Celorrio R. Simultaneous measurement of thermal diffusivity and optical absorption coefficient using photothermal radiometry. II. Multilayered solids. *J Appl Phys* 2011;110:033516.
- [24] Imhof RE, Zhang B, Birch DJS. Photothermal radiometry for NDE [chapter 7]. In: Mandelis A, editor. *Progress in photothermal and photoacoustic science and technology*, vol. II: Non-Destructive Evaluation (NDE). Englewood Cliffs: Prentice Hall; 1994.
- [25] Maldague X, Marinetti S. Pulse phase infrared thermography. *J Appl Phys* 1996;79:2694–8.

- [26] Breitenstein O, Langenkamp M. Lock-in thermography: basics and use for functional diagnostics of electronic components, vol. 10. Berlin/Heidelberg: Springer Sci & Business Media; 2003.
- [27] Horny N, Lannoy B. Lock-in thermography with a focal plane array. *Meas Sci Technol* 2003;14:439–43.
- [28] Maldague X. Infrared methodology and technology. Stanford: Gordon and Breach Science Publishers; 1994.
- [29] Coufal H. Photothermal spectroscopy using a pyroelectric thin-film detector. *Appl Phys Lett* 1984;44:59–61.
- [30] Dădârlat D, Chirtoc M, Căndea RM, Bratu I. Direct pyroelectric detection of optical absorption in non-transparent materials. *Infrared Phys* 1984;24:469–71.
- [31] Mandelis A. Frequency-domain photopyroelectric spectroscopy of condensed phases (PPES): a new, simple and powerful spectroscopic technique. *Chem Phys Lett* 1984;108:388–92.
- [32] Mandelis A, Zver MM. Theory of photopyroelectric spectroscopy of solids. *J Appl Phys* 1985;57:4421–30.
- [33] Chirtoc M, Mihilescu G. Theory of the photopyroelectric method for investigation of optical and thermal materials properties. *Phys Rev B* 1989;40:9606–17.
- [34] Chirtoc M, Chirtoc I, Bicanic D, Pelzl J. Photopyroelectric (PPE) spectroscopy: absorption, transmission, or reflectance? *Ferroelectrics* 1994;165:27–38.
- [35] Dădârlat D, Chirtoc M, Neamtu C, Căndea RM, Bicanic D. Inverse photopyroelectric detection method. *Phys Stat Sol (A)* 1990;121:231–4.
- [36] Antoniow JS, Chirtoc M, Egee M. A photopyroelectric method with air as the thermal coupling fluid. *J Phys D Appl Phys* 1997;30:1934–44.
- [37] Shen J, Mandelis A. Thermal wave resonator cavity. *Rev Sci Instrum* 1995;66:4999–5005.
- [38] Lima JAP, Marin E, Correa O, Da Silva MG, Cardoso SI, Gatts C, et al. Measurement of the thermal properties of liquids using a thermal wave interferometer. *Meas Sci Technol* 2000;11:1522.
- [39] Li Voti R, Liakhou GL, Paoloni S, Sibilica C, Bertolotti M. Thermal waves physics. *J Optoelectronics Adv Mat* 2001;3:779–816.
- [40] Balderas-López JA, Mandelis A, Garcia JA. Thermal-wave resonator cavity design and measurements of the thermal diffusivity of liquids. *Rev Sci Instrum* 2000;71:2933–7.
- [41] Dădârlat D, Neamtu C, Surducă E, Hadj Saharaoui A, Longuemart S, Bicanic D. Accurate photopyroelectric measurements of thermal diffusivity of (semi)liquids. *Instrum Sci Technol* 2002;30:387–96.
- [42] Proskurnin MA. Photothermal spectroscopy. In: Baudelet M, editor. *Laser spectroscopy for sensing: fundamentals, techniques and applications*. Cambridge: Woodhead Publishing; 2014.
- [43] Goyhénèche JM, Cosculluela A. A multiscale model for the effective thermal conductivity tensor of a stratified composite material. *Int J Thermophys* 2005;26:191–202.
- [44] Terrón JM, Salazar A, Sánchez-Lavega A. General solution for the thermal wave scattering in fiber composites. *J Appl Phys* 2002;91:1087–98.
- [45] Salazar A, Terrón JM, Sánchez-Lavega A, Celorrio R. On the effective thermal diffusivity of fiber-reinforced composites. *Appl Phys Lett* 2002;80:1903–5.

- [46] Salazar A, Sanchez-Lavega A, Ocariz A. Temperature dependence of the thermal diffusivity of unidirectional composites by the mirage technique. *High Temp. High Pressures* 1997;29:467–72.
- [47] Balageas DL, Pujolà RM, Rousset G, Bertrand L. Compared photothermal measurements of thermal diffusivity in composites. In: Bertrand L, Cielo P, Leblanc R, Monchalain JP, Mongeau B, editors. Proc. 4th Int. topical meeting on photoacoustic, thermal and related sciences, Quebec, Canada, August 4–8, 1985. *Can J Phys* 64.
- [48] Krapez JC, Spagnolo L, Frieß M, Maier HP, Neuer G. Measurement of in-plane diffusivity in non-homogeneous slabs by applying flash thermography. *Int J Therm Sci* 2004;43:967–77.
- [49] Busse G. Nondestructive evaluation of polymer materials. *NDT & E Int* 1994;27:253–62.
- [50] Karbhari VM. Non-destructive evaluation (NDE) of polymer matrix composites, techniques and applications. Cambridge: Woodhead Publ.; 2013.
- [51] Maldague X. Theory and practice of infrared technology for nondestructive testing. New York, NY: Wiley; 2001.
- [52] Bai W, Wong BS. Evaluation of defects in composite plates under convective environments using lock-in thermography. *Meas Sci Technol* 2001;12:142–50.
- [53] Bamford M, Florian M, Vignoles GL, Batsale JC, Cairo CAA, Maillé L. Global and local characterization of the thermal diffusivities of SiC fibers/SiC composites with infrared thermography and flash method. *Compos Sci Technol* 2009;69:1131–41.
- [54] Ibarra-Castanedo C, Genest M, Piau JM, Guibert S, Bendada A, Maldague X. Active infrared thermography techniques for the nondestructive testing of materials. In: Chen CH, editor. Ultrasonic and advanced methods for nondestructive testing and material characterization. Singapore: World Sci Publ.; 2007.
- [55] Zweschper T, Riegert G, Dillenz A, Busse G. Frequency-modulated elastic wave thermography. In: Cramer KE, Maldague XP, editors. Proc. SPIE 2003; 5073, pp. 386–91, Thermosense XXV, April 3, 2003, Orlando, FL.
- [56] Masujima T, Eyring EM. X-ray thermal-wave non-destructive evaluation [chapter 9]. In: Mandelis A, editor. Progress in photothermal and photoacoustic science and technology, vol. II: Non-Destructive Evaluation (NDE). Englewood Cliffs: Prentice Hall; 1994.
- [57] Pelzl J, Geisau O. Spatially resolved detection of microwave absorption in ferrimagnetic materials [chapter 8]. In: Mandelis A, editor. Progress in photothermal and photoacoustic science and technology, vol. II: Non-Destructive Evaluation (NDE). Englewood Cliffs: Prentice Hall; 1994.
- [58] Pradere C, Caumes JP, Balageas D, Batsale JC. New concept of room-temperature THz camera based on photon thermo-conversion, coupled to an IR camera (French). Proc. Congrès Français de Thermique, SFT2012, vol. 2. 2012. p. 763–9 [Online] Available from: <[www.sft.asso.fr/Local/sft/dir/user-3775/documents/actes/Congres\\_2012/Tome2\\_bordeaux\\_2012.pdf](http://www.sft.asso.fr/Local/sft/dir/user-3775/documents/actes/Congres_2012/Tome2_bordeaux_2012.pdf)>
- [59] Kovari M, Crowley B, Cox SJ. Thermographic measurement of the emittance plot of a single positive ion beamlet. *Rev Sci Instrum* 2008;79:046106.
- [60] Avdelidis NP, Almond DP, Dobbinson A, Hawtin BC, Ibarra-Castanedo C, Maldague X. Aircraft composites assessment by means of transient thermal NDT. *Prog Aerospace Sci* 2004;40:143–62.

- [61] Balageas DL, Krapez JC, Cielo P. Pulsed photothermal modeling of layered materials. *J Appl Phys* 1986;59:348–57.
- [62] Vavilov V, Maldague X, Dufort B, Robitaille F, Picard J. Thermal nondestructive testing of carbon epoxy composites: detailed analysis and data processing. *NDT & E Int* 1993;26:85–95.
- [63] Grosse P, Depasse F. Thermophysical continuous profiles and their discretization. *Int J Therm Sci* 2011;50:2078–83.
- [64] Van Den Brand J, Chirtoc M, Wübbenhorst MR, De Wit JHW. Photothermal imaging of localized delamination between organic coatings and metallic substrates using a scanning photopyroelectric microscope. *J Appl Phys* 2003;93:2019–27.
- [65] Krapez JC, Maldague X, Cielo P. Thermographic nondestructive evaluation: data inversion procedures. *Res Nondestr Eval* 1991;3:101–24.
- [66] Chirtoc M, Gibkes J, Walter HG, Christ A, Antoniow JS, Bicanic D, et al. Comparative study of coating thickness determination in packaging composite materials using PTR, PA and PPE methods. *Anal Sci/Suppl* 2001;17:185–8.
- [67] Tilgner R, Baumann J. Photothermal examination of an adhesive layer. *J Nondestr Eval* 1982;3:111–13.
- [68] Chirtoc M, Chirtoc I, Pittois S, Glorieux C, Thoen J. Thermal resistance of adhesive tapes measured by the photopyroelectric method. *Rev Sci Instrum* 2003;74:632–4.
- [69] Delgadillo-Holtfort I, Gibkes J, Chirtoc M, Neubauer E, Bein BK, Pelzl J. Characterization of metal coated diamond crystallites by combined photoacoustic effect and photothermal radiometry. *Acta Phys Pol A* 2008;114:57–61.
- [70] Kijamnajsuk P, Giuliani F, Chirtoc M, Horny N, Gibkes J, Chotikaprakhan S, et al. Interface resistance in copper coated carbon determined by frequency dependent photothermal radiometry. *J Phys Conf Series* 2010;214:012053.
- [71] Kijamnajsuk P, Pelzl J, Chirtoc M, Horny N, Schäfer D, Eisenmenger-Sittner C. Photothermal evidence of laterally inhomogeneous interfacial thermal resistance in copper-coated carbon samples. *Int J Thermophys* 2012;33:2132–8.
- [72] Pelzl J, Kijamnajsuk P, Chirtoc M, Horny N, Eisenmenger-Sittner C. Correlation between thermal interface conductance and mechanical adhesion strength in Cu-coated glassy carbon. *Int J Thermophys* 2015. Available from: <http://dx.doi.org/10.1007/s10765-015-1879-2>
- [73] Bolte J, Chirtoc M, Bein BK, Pelzl J. Error limits and distinction of optical and thermal properties in thermal depth profiling. *Prog Nat Sci* 1996;6:705–8.
- [74] Gibkes J, Fosting JLN, Dietzel D, Bein BK, Pelzl J. Optical properties in the visible and infrared spectrum of fiber-reinforced composites determined by combined photoacoustic and IR detection. *Rev Sci Instrum* 2003;74:651.
- [75] Garcia JA, Mandelis A, Marinova M, Michaelian KH, Afrashtehfar S. Quantitative photothermal radiometric and FT-IR photoacoustic measurements of specialty papers. *Appl Spectrosc* 1998;52:1222–9.
- [76] Busse G, Rief B, Eyerer P. Nondestructive evaluation of polymers with optically generated thermal waves. *Polym Compos* 1987;8:283–6.
- [77] Coufal H. Photothermal methods for the measurement of thermal properties of thin polymer films. *Polym Eng Sci* 1991;31:92–8.
- [78] De Oliveira MG, Pessoa O, Vargas H, Galembeck F. Low-density polyethylene depth profile analysis by photoacoustic spectroscopy. *J Appl Polym Sci* 1988;35:1791–802.

- [79] Maillet D, André S, Batsale JC, Degiovanni A, Moynes C. Thermal quadrupoles. New York, NY: Wiley; 2000.
- [80] Wu B, Du Y, Tang H, Du P, Qin X, Zhang L. Reduced thermal diffusivity of nanostructured silver. *J Phys Chem Sol* 1996;57:1211–13.
- [81] Li B, Pottier L, Roger JP, Fournier D, Watari K, Hirao K. Measuring the anisotropic thermal diffusivity of silicon nitride grains by thermoreflectance microscopy. *J Eur Ceram Soc* 1999;19:1631–9.
- [82] Bodzenta J, Mazur J, Kazmierczak-Balata A. Thermal properties of compressed expanded graphite—photothermal measurements. *Appl Phys B* 2011;105:623–30.
- [83] Reichling M, Klotzbücher T, Hartmann J. Local variation of room-temperature thermal conductivity in high-quality polycrystalline diamond. *Appl Phys Lett* 1998;73:756–8.
- [84] Chen FC, Netzelmann U, Disque M, Kröning M. High resolution photothermal imaging of metal matrix composite interface. *Mat Sci Forum* 1996;210:447–54.
- [85] Macedo F, Ferreira JA. Thermal contact resistance evaluation in polymer-based carbon fiber composites. *Rev Sci Instrum* 2003;74:828–30.
- [86] Lizundia E, Oleaga A, Salazar A, Sarasua JR. Nano- and microstructural effects on thermal properties of poly(L-lactide)/multi-wall carbon nanotube composites. *Polymer* 2012;53:2412–21.
- [87] Nan CW, Birringer R, Clarke DR, Gleiter H. Effective thermal conductivity of particulate composites with interfacial thermal resistance. *J Appl Phys* 1997;81:6692–9.
- [88] Massey MK, Kotsialos A, Qaiser F, Zeze DA, Pearson C, Volpati D, et al. Computing with carbon nanotubes: optimization of threshold logic gates using disordered nanotube/polymer composites. *J Appl Phys* 2015;117:134903.
- [89] Rodríguez ME, Mendoza PJ, Mandelis A, Nicolaidis L. Combined photothermal and photoacoustic characterization of silicon–epoxy composites and the existence of a particle thermal percolation threshold. *Nucl Instrum Methods Phys Res B* 2001;184:421–9.
- [90] Chirtoc M, Glorieux C, Thoen J. Thermophysical properties and critical phenomena studied by PPE method [chapter 5]. <[www.trnres.com](http://www.trnres.com)> In: Marín Moares E, editor. Thermal wave physics and related photothermal techniques: basic principles and recent developments. Trivandrum, Kerala: Transworld Research Network; 2009
- [91] Chirtoc M. Investigation of layered systems by photothermal methods with periodic excitation [chapter 2]. <[www.trnres.com](http://www.trnres.com)> In: Marín Moares E, editor. Thermal wave physics and related photothermal techniques: basic principles and recent developments. Trivandrum, Kerala: Transworld Research Network; 2009
- [92] Chirtoc M. Investigation of layered systems and temperature-dependent thermophysical characterization by photothermal methods with periodic excitation. *J Phys Conf Series* 2010;214:012005.
- [93] Parker WJ, Jenkins RJ, Butler CP, Abbott GL. Flash method of determining thermal diffusivity, heat capacity and thermal conductivity. *J Appl Phys* 1961;32:1679–84.
- [94] Cape JA, Lehman GW. Temperature and finite-pulse-time effects in the flash method for measuring thermal diffusivity. *J Appl Phys* 1963;34:1909–13.
- [95] Blumm J, Opfermann J. Improvement of the mathematical modeling of flash measurements. *High Temp High Pressures* 2002;34:515–21.
- [96] Maillet D, André S, Degiovanni A. Errors on thermal diffusivity measured by flash method: theory-experiment confrontation. *J Phys III France* 1993;3:883–909.

- [97] Salazar A, Mendioroz A, Apiñaniz E, Pradere C, Noël F, Batsale JC. Extending the flash method to measure the thermal diffusivity of semitransparent solids. *Meas Sci Technol* 2014;25:035604.
- [98] Sengupta R, Bhattacharya M, Bandyopadhyay S, Bhowmick AK. A review on the mechanical and electrical properties of graphite and modified graphite reinforced polymer composites. *Prog Polym Sci* 2011;36:638–70.
- [99] Han Z, Fina A. Thermal conductivity of carbon nanotubes and their polymer nanocomposites: a review. *Prog Polym Sci* 2011;36:914–44.
- [100] Mohamadi S, Sharifi-Sanjani N, Foyouhi A. Evaluation of graphene nanosheets influence on the physical properties of PVDF/PMMA blend. *J Polym Res* 2013;20:1–10.
- [101] Stankovich S, Dikin DA, Dommett GH, Kohlhaas KM, Zimney EJ, Stach EA, et al. Graphene-based composite materials. *Nature* 2006;442:282–6.
- [102] Aylsworth JW. Expanded graphite. US Patent 1191383. 1916.
- [103] Inagaki M, Kang F, Toyoda M. Exfoliation of graphite via intercalation compounds [chapter 1]. In: Radovic LR, editor. *Chemistry and physics of carbon*, vol. 29. New York: CRC Press; 2004.
- [104] SGL Group—The Carbon company. Products, *Lexicon of Materials*, Expanded natural graphite, Expansion process. [Online] Available from: <[www.sglgroup.com/cms/international/products](http://www.sglgroup.com/cms/international/products)>; [accessed 20.03.15].
- [105] Chirtoc M, Horny N, Tavman I, Turgut A, Kökey I, Omastová M. Preparation and photothermal characterization of nanocomposites based on high density polyethylene filled with expanded and unexpanded graphite: particle size and shape effects. *Int J Therm Sci* 2012;62:50–5.
- [106] Avérous L. Biodegradable Multiphase systems based on plasticized starch: a review. *J Macromol Sci Part C Polym Rev* 2004;44:231–74.
- [107] Pandey JK, Kumar AP, Misra M, Mohanty AK, Drzal LT, Palsingh R. Recent advances in biodegradable nanocomposites. *J Nanosci Nanotechnol* 2005;5:497–526.
- [108] Ince S, Seki Y, Ezan MA, Turgut A, Ereğ A. Thermal properties of myristic acid/graphite nanoplates composite phase change materials. *Renewable Energy* 2015;75:243–8.
- [109] Tlili R, Boudenne A, Cecen V, Ibos L, Krupa I, Candau Y. Thermophysical and electrical properties of nanocomposites based on ethylene–vinylacetate copolymer (EVA) filled with expanded and unexpanded graphite. *Int J Thermophys* 2010;31:936–48.
- [110] Chirtoc M, Horny N, Henry JF, Turgut A, Kökey I, Tavman I, et al. Photothermal characterization of nanocomposites based on high density polyethylene (HDPE) filled with expanded graphite. *Int J Thermophys* 2012;33:2110–17.
- [111] Tavman IH, Turgut A, Da Fonseca HM, Orlande HRB, Cotta RM, Magalhaes M. Thermal-diffusivity measurements of conductive composites based on EVA copolymer filled with expanded and unexpanded graphite. *Int J Thermophys* 2013;34:2297–306.
- [112] Tavman I, Turgut A, Horny N, Chirtoc M. Polymer matrix composites reinforced with expanded and unexpanded graphite particles for electronic packaging applications. In: *Proc. IEEE 19th Int Symp Design Technol in Electronic Packaging (SIITME)* October 24–27, 2013; Galați, Romania: IEEE No. CFP 1307I-ART. pp. 43–7.

- [113] Kratochvíla J, Boudenne A, Krupa I. Effect of filler size on thermophysical and electrical behavior of nanocomposites based on expanded graphite nanoparticles filled in low density polyethylene matrix. *Polym Compos* 2013;34:149–55.
- [114] Evgin T, Koca HD, Horny N, Turgut A, Tavman I, Chirtoc M, et al. Effect of aspect ratio on thermal conductivity of HDPE/MWCNTs nanocomposites. *Composites Part A* (in review process, 2015).
- [115] Ganguli S, Roy AK, Anderson DP. Improved thermal conductivity for chemically functionalized exfoliated graphite/epoxy composites. *Carbon* 2008;46:806–17.
- [116] Murariu M, Dechief AL, Bonnaud L, Paint Y, Gallos A, Fontaine G, et al. The production and properties of polylactide composites filled with expanded graphite. *Polym Degrad Stab* 2010;95:889–900.
- [117] Wu TC, Tsai KC, Lu MC, Kuan HC, Chen CH, Kuan CF, et al. Synthesis, characterization, and properties of silane-functionalized expandable graphite composites. *J Compos Mater* 2012;46:1483–96.
- [118] Chen GX, Yoon JS. Clay functionalization and organization for delamination of the silicate tactoids in poly(L-lactide) matrix. *Macromol Rapid Commun* 2005;26:899–904.
- [119] Chen GX, Yoon JS. Nonisothermal crystallization kinetics of poly(butylene succinate) composites with a twice functionalized organoclay. *J Polym Sci Part B Polym Phys* 2005;43:817–26.
- [120] Bertuoli PT, Piazza D, Scienza LC, Zattera AJ. Preparation and characterization of montmorillonite modified with 3-aminopropyltriethoxysilane. *Appl Clay Sci* 2014;87:46–51.
- [121] Kanake Y. Development of biopolymer-based nanocomposites; optimisation of thermal and mass transport properties [Doctoral dissertation]. Reims, France: Université de Reims Champagne Ardenne; 2016.
- [122] Matbase, natural and synthetic polymers. [Online] Available from: <[www.matbase.com](http://www.matbase.com)>.
- [123] Goodfellow Inc., Materials catalogue. [Online] Available from: <[www.goodfellow.com](http://www.goodfellow.com)>.
- [124] DuPont Co. High performance materials; plastics, polymers and resins. [Online] Available from: <[www.dupont.com](http://www.dupont.com)>.
- [125] Nouredini H, Teoh BC, Clements LD. *JAOCS* 1992;69:1184–8.
- [126] Hoover MJ, Grodzka PG, O'Neill MJ. Space thermal control development, final report. Contract NAS8-25183. Huntsville: Lockheed Missiles and Space Co; 1971.
- [127] Bayram U, Aksoz S, Marasli N. *J Therm Analysis Calorim* 2014;118:311–21.
- [128] Clauser C, Huenges E. Thermal conductivity of rocks and minerals. In: Ahrens TJ, editor. *Rock physics and phase relations. A handbook of physical constants*. American Geophysical Union Reference; 1995.
- [129] Skauge A, Fuller N, Hepler LG. *Thermochim Acta* 1983;61:139–45.
- [130] Michot A, Smith DS, Degot S, Lecomte GL. *J Eur Ceram Soc* 2011;31:1377–82.
- [131] Rides M, Morikawa J, Halldahl L, Hay B, Lobo H, Dawson A, et al. Intercomparison of thermal conductivity and thermal diffusivity methods for plastics. *Polym Testing* 2009;28:480–9.
- [132] Bicanic D, Chirtoc M, Dadarlat D, Chirtoc I, Van Loon W, Bot G. Measurement of the heat penetration coefficient ( $k_{pc}$ )<sup>1/2</sup> in margarine and cultured milk products by the inverse photopyroelectric technique. *Int Dairy J* 1994;4:555–65.

- [133] Suss Micro Tec A.G. Introduction to Beam Homogenizing. [Online] Available from: <[www.sussmicrooptics.com](http://www.sussmicrooptics.com)>; [accessed 10.11.14].
- [134] Vargas H, Miranda LCM. Photothermal techniques applied to thermophysical properties measurements. *Rev Sci Instrum* 2003;74:794–9.
- [135] Balageas DL. Thermal diffusivity measurement by pulsed methods. *High Temp High Pressures* 1989;21:85–96.
- [136] Nunes Dos Santos WN, Mummery P, Wallwork A. Thermal diffusivity of polymers by the laser flash technique. *Polym Testing* 2005;24:628–34.
- [137] Degiovanni A, Laurent M. New technique for identification of thermal diffusivity by flash method. *Rev Phys Appl* 1986;21:229–37.
- [138] Frandas A, Chirtoc M, Paris D, Egée M. Influence of humidity on thermophysical properties of starch sheets. In: Scudieri F, Bertolotti M, editors. *Proc 10th int conf photoacoustic and photothermal phenomena*. AIP conf proc, 463. Woodbury, NY: AIP; 1999. p. 640–2.
- [139] Frandas A, Paris D, Bissieux C, Chirtoc M, Antoniow JS, Egée M. Classical and photopyroelectric studies of optical and thermophysical properties of starch sheets: dependence on water content and temperature. *Appl Phys B* 2000;71:69–75.
- [140] Cruz-Orea A, Bentefour EH, Jamée P, Chirtoc M, Glorieux C, Pitsi G, et al. Thermal characterization of starch–water system by photopyroelectric technique and adiabatic scanning calorimetry. *Rev Sci Instrum* 2003;74:818–21.
- [141] Chirtoc M, Chirtoc I, Paris D, Antoniow JS, Egée M. Photopyroelectric (PPE) study of water migration in humidified laminated starch sheets. In: Scudieri F, Bertolotti M, editors. *Proc 10th int conf on photoacoustic and photothermal phenomena*. AIP conf proc, 463. Woodbury, NY: AIP; 1999. p. 646–8.
- [142] Elrod HG. Two simple theorems for establishing bounds on the total heat flow in steady-state heat-conduction problems with convective boundary conditions. *J Heat Transfer* 1974;96:65–70.
- [143] Progelhof RC, Throne JL, Ruetsch RR. Methods for predicting the thermal conductivity of composite systems: a review. *Polym Eng Sci* 1976;16:615–25.
- [144] Tavman IH. Effective thermal conductivity of isotropic polymer composites. *Int Commun Heat Mass Transfer* 1998;25:723–32.
- [145] Jiajun W, Xiao-Su Y. Effects of interfacial thermal barrier resistance and particle shape and size on the thermal conductivity of AlN/PI composites. *Compos Sci Technol* 2004;64:1623–8.
- [146] Karayacoubian P. Effective thermal conductivity of composite fluidic thermal interface materials [Doctoral dissertation]. ON, Canada: Waterloo University; 2006.
- [147] Maxwell JC. *A treatise on electricity and magnetism*. Oxford: Clarendon; 1881.
- [148] Eucken A. Thermal conductivity of ceramic refractory materials; calculation from thermal conductivity of constituents. *Ceram Abstr* 1932;11:576.
- [149] Xie SH, Liu YY, Li JY. A comparison of the effective conductivity between composites reinforced by graphene nanosheets and carbon nanotubes. *Appl Phys Lett* 2008;92:243121.
- [150] Im H, Kim J. Thermal conductivity of a graphene oxide–carbon nanotube hybrid/epoxy composite. *Carbon* 2012;50:5429–40.
- [151] Bruggeman VD. Calculation of various physical constants in heterogeneous substances. I. Dielectric constants and conductivity of composites from isotropic substances (German). *Ann Phys* 1935;416:636–64.

- [152] Karkri M, Boudenne A, Ibos L, Garnier B, Candau Y. Numerical and experimental study of thermophysical properties of spheres composite materials. *High Temp High Pressures* 2011;40:61–84.
- [153] Duong HM, Papavassiliou DV, Mullen KJ, Maruyama S. Computational modeling of the thermal conductivity of single-walled carbon nanotube–polymer composites. *Nanotechnology* 2008;19:065702.
- [154] Minnich AJ, Chen G. Modified effective medium formulation for the thermal conductivity of nanocomposites. *Appl Phys Lett* 2007;91:073105.
- [155] Behrang A, Grmela M, Dubois C, Turenne S, Lafleur PG, Lebon G. Effective heat conduction in hybrid sphere and wire nanodispersions. *Appl Phys Lett* 2014;104:233111.
- [156] Kuumlutaş D, Tavman IH, Çoban MT. Thermal conductivity of particle filled polyethylene composite materials. *Compos Sci Technol* 2003;63:113–17.
- [157] Debelak B, Lafdi K. Use of exfoliated graphite filler to enhance polymer physical properties. *Carbon* 2007;45:1727–34.
- [158] Stauffer D, Aharony A. *Introduction to percolation theory*. 2nd ed. Boca Raton, FL: CRC Press; 1994.
- [159] Gojny FH, Wichmann MHG, Fiedler B, Kinloch IA, Bauhofer W, Windle AH, et al. Evaluation and identification of electrical and thermal conduction mechanisms in carbon nanotube/epoxy composites. *Polymer* 2006;47:2036–45.
- [160] Cai WZ, Tu ST, Gong JM. A physically based percolation model of the effective electrical conductivity of particle filled composites. *J Compos Mater* 2006;40:2131–42.
- [161] Garboczi EJ, Snyder KA, Douglas JF, Thorpe MF. Geometrical percolation threshold of overlapping ellipsoids. *Phys Rev E* 1995;52:819.
- [162] Nan CW. *Physics of inhomogeneous inorganic materials*. *Prog Mater Sci* 1993;37:1–116.
- [163] Sever K, Tavman IH, Seki Y, Turgut A, Omastova M, Ozdemir I. Electrical and mechanical properties of expanded graphite/high density polyethylene nanocomposites. *Compos Part B Eng* 2013;53:226–33.
- [164] Shenogina N, Shenogin S, Xue L, Keblinski P. On the lack of thermal percolation in carbon nanotube composites. *Appl Phys Lett* 2005;87:133106.
- [165] Bonnet P, Sireude D, Garnier B, Chauvet O. Thermal properties and percolation in carbon nanotube-polymer composites. *Appl Phys Lett* 2007;91:201910.
- [166] Mandelis A. *Diffusion-wave fields: mathematical methods and green functions*. New York, NY: Springer; 2013.
- [167] Yu X, Schmidt AR, Bello-Perez LA, Schmidt SJ. Determination of the bulk moisture diffusion coefficient for corn starch using an automated water sorption instrument. *J Agric Food Chem* 2008;56:50–8.
- [168] Glorieux C, Antoniw JS, Chirtoc M, Chirtoc I, Thoen J. Neural network photothermal depth profiling of a heat source distribution. Application to water migration in starch sheets. *Anal Sci* 2001;17:S398–401.

# 12 Brillouin spectroscopy of polymer nanocomposites

**Didier Rouxel, Camille Thevenot, Van Son Nguyen and Brice Vincent**

*Institut Jean Lamour, CNRS, Université de Lorraine, Vandoeuvre-lès-Nancy, France*

## 12.1 INTRODUCTION

Brillouin spectroscopy (BS) derives its name from Leon Brillouin, who first predicted the Brillouin scattering effect in 1914. Like its cousin, Raman spectroscopy, BS is a light scattering technique. While Raman spectroscopy provides access to the optical phonons, which characterize the local structure of the material, BS provides direct information on the acoustic phonons of the material, on collective oscillations of atoms, and on the propagation of acoustic waves in the material. In applications of polymers and polymer nanocomposites, BS mainly concerns inelastic light scattering on thermally excited sound waves, which occur at hypersonic frequencies.

Therefore, BS is used primarily to explore the acoustic properties of the materials at the acoustic phonon frequencies. It offers an optical way to access the hypersonic elastic and viscoelastic properties of the polymer. This analytical technique can determine the mechanical properties of the material.

Today, various techniques are available to characterize the elastic-mechanical properties of materials [1–3] including microindentation (or microhardness), which provides the Knoop hardness  $H_k$  and the Vickers hardness  $H_v$ , and then, indirectly, the Young's modulus  $E$ ; the torsion pendulum, which provides information on the shear modulus  $G$ ; the dynamic mechanical analysis (DMA) which gives the Young's modulus  $E$ ; and finally the acoustic microscopy (ultrasounds) and the BS, both of which allow for reaching the set of elastic constant  $c_{ij}$  [4]. Of course these techniques are not directly comparable, and in particular the different frequency of the measurement has to be considered, ranging from static measurement for microhardness to some GHz for BS (i.e., the frequency of the acoustic phonons in the material), through the Hertz range for torsion pendulum and DMA, and MHz–GHz for ultrasounds. In fact, the measurement frequency of BS is intermediate between that of acoustic microscopy and neutron scattering. DMA is the one of the most used techniques for nanocomposites [5,6].

The main advantage of BS is to avoid direct contact of the sample, which may be crucial for many experiments, especially for thin films with or without

substrates, viscoelastic samples, or samples in a liquid medium. This technique is especially well adapted to study soft materials, since the optomechanical coupling between photons and acoustic phonons is much more important in such cases than for the hard materials. Therefore, it can provide noninvasive measurement of acoustic and elastic properties of oligomer [7,8], polymers [9], and polymer nanocomposites [10–13]. In recent years, BS became a powerful tool to monitor the viscoelastic properties during polymerization or network formation. However, it can also study soft or hard thin films [14] and characterize single crystals and biological tissues [15]. By combining with confocal microscopy or other focalization setup, it is then called Brillouin microscopy and is able to give local information with the spatial resolution in the submicron scale. Moreover, BS is the only technique to provide, besides  $c_{ij}$ , the optical index  $n$  of the material.

BS is not widely used because it requires optical tweaks which are sometimes difficult. In addition, as light must penetrate the sample to interact with matter, BS is suitable for transparent or at least translucent materials. However, under certain conditions that will be discussed in this chapter, the interaction at the surface can also be explored.

The basic concepts of BS and some of its first applications on polymers have been reviewed in the contribution of Krüger [16] and references therein. Therefore, only a short introduction to the theory and the scattering geometries most often used in polymer measurement are given in Section 12.2.

## 12.2 BRILLOUIN SPECTROSCOPY

### 12.2.1 BRILLOUIN SCATTERING THEORY

BS is a characterization technique that analyzes the light scattered by a material. The interaction between the photons of the incident beam and the acoustic phonons in a material at hypersonic frequencies (10 MHz–100 GHz) leads to specific frequency shifts ( $f$ ) of the scattered laser light. The cinematic approach to the principle of BS involves the energy and momentum of photons and phonons. Photons and phonons involved in the scattering process follow two conversation laws. The first law is the conservation of energy, expressed as a scalar equation in terms of the frequencies of the phonon and the incident and scattered photons:

$$\hbar\omega_s = \hbar\omega_i \pm \hbar\Omega \quad (12.1)$$

The second law is the conservation of momentum, expressed as a vector equation in terms of the wave vectors of the phonon and the incident and scattered photons:

$$\hbar k_s = \hbar k_i \pm \hbar q \quad (12.2)$$

In these equations, the  $\pm$  signs refer to the creation/annihilation of a phonon, known as Stokes/anti-Stokes scattering, as in Raman spectroscopy.

Unlike Raman scattering, the energy transfer in BS between photons and phonons is extremely small, hence the ratio between their frequencies is in the range of  $10^{-6}$ . Therefore, in a first approximation the vectors  $\vec{k}_i$  and  $\vec{k}_s$  have the same

length with the assumption generally verified by a negligible acoustic attenuation. The relation between the sound velocity  $v$ , the acoustic phonon frequency  $f$ , and its wave vector  $q$  can be calculated using Eqns (12.1) and (12.2) and geometric arguments:

$$v = \frac{2\pi f}{q} = \frac{\lambda_0 f}{2n \sin(\frac{\theta_i}{2})} \quad (12.3)$$

where  $\lambda_0$  is the laser wavelength, and  $\theta_i$  is the angle between the incident and scattered wave vectors  $\vec{k}_i$  and  $\vec{k}_s$ .

The elastic modulus is related to the sound velocity and the mass density  $\rho$  of the medium using the equation:

$$c(\vec{q}) = \rho \cdot v^2(\vec{q}) \quad (12.4)$$

A typical Brillouin spectrum will present around the elastic line, called the Rayleigh line, two sets of phonon lines, one longitudinal mode, and two transverse modes (reduced to one if the material is anisotropic). A schematic presentation of a Brillouin spectrum is given in Fig. 12.1 and an example of Brillouin

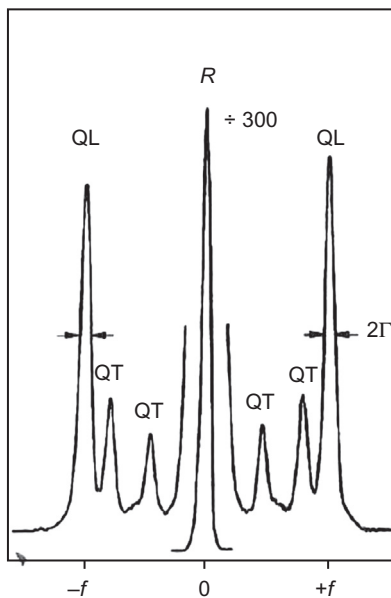


**FIGURE 12.1**

A typical Brillouin spectrum of hexatriacontane at room temperature. QT and QL are the Stokes ( $-f$ ) and anti-Stokes ( $+f$ ) quasilongitudinal and quasitransverse acoustic phonons. The width  $2\Gamma$  contains information about the acoustic losses.  $R$  is the Rayleigh line which is due to elastic light scattering. The Rayleigh line has been reduced in height by a factor of 300 compared to the phonon lines [16].

*Copyright 1989. Reprinted with permission from Elsevier Ltd.*

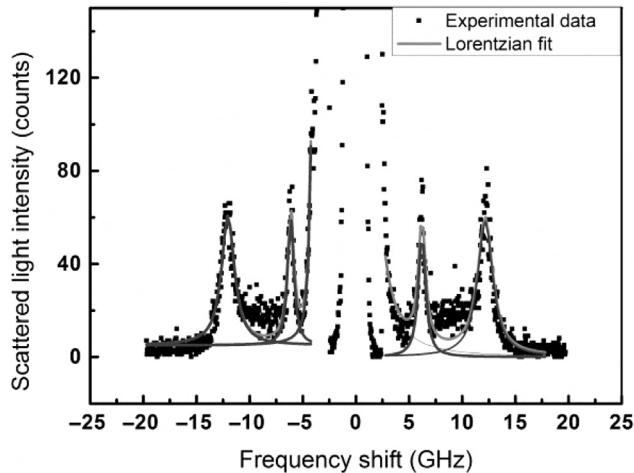


**FIGURE 12.2**

Brillouin spectrum for thin films of P(VDF-TrFE)/Al<sub>2</sub>O<sub>3</sub> 10 wt.% nanocomposite.

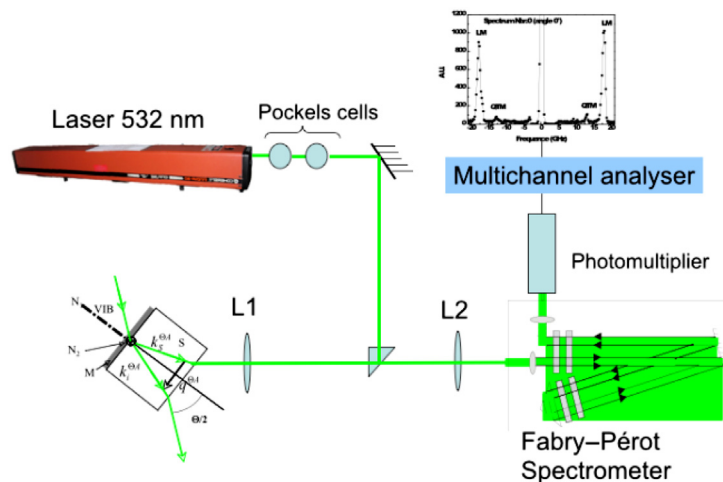
spectrum for thin films of polymer nanocomposite is shown in Fig. 12.2. Note that the longitudinal phonon mode, generally the most intense line, gives rise to the elastic constant  $c_{11}$ , related with the Young's modulus. The transverse mode gives access to the  $c_{44}$  modulus, also called shear modulus [17].

The collected scattered light intensity is proportional to the Fourier transform of the autocorrelation function. Many kinds of stimuli may contribute to this intensity, including not only thermal phonons, but also spin waves. The contribution of spin waves in the Brillouin spectrum opens the door to a specific spectroscopy on magnetic materials [18], which will not be discussed in this chapter.

### 12.2.2 EXPERIMENTAL SETUP

Figure 12.3 shows a schematic of a typical BS setup, here with a backscattering geometry.

As seen in Fig. 12.3, BS measurements are performed using a laser, for instance of power 200 mW and wavelength 532 or 514 nm, with the requirements of a narrow spectral band width and very stable power. Usually the power level received by the sample is about 100 mW. The average diameter of measurement areas on the sample is about 50  $\mu\text{m}$ . The laser light passes through the Pockels cells, whose function is to greatly attenuate the elastically scattered spectral light (Rayleigh scattering) because its intensity is several orders of magnitude higher than those of phonons, and the photomultiplier has to be protected from too much light. To achieve this, Pockels cells are synchronized with the scan rate and the frequency window of the interferometer. To reduce the size of the experimental

**FIGURE 12.3**

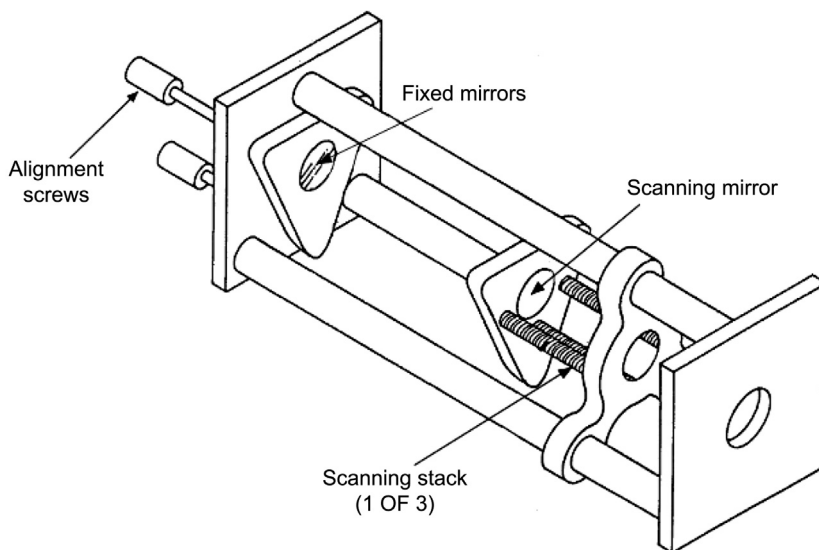
Example of Brillouin spectroscopy setup.

setup, the light is generally directed using mirrors. In Fig. 12.3, the laser light is reflected at a right angle on a small prism and focused on the sample by the lens L1. Of course, the scattered light can be collected according to different geometries (see Section 12.2.2.1). In Fig. 12.3, the light scattered by the sample is collected by L1 and refocused by the lens L2 to the input pinhole of the Fabry–Pérot (FP). This interferometer allows for the realizing of the spectrum of the scattered light by the scanning of the distance between the parallel mirrors, a given distance selecting a particular frequency. At the output of the FP, the optoelectronic conversion is carried out by means of a photon-counting photomultiplier, and the spectrum is accumulated in a multichannel analyzer.

### 12.2.2.1 FP Interferometer

Contrary to Raman spectroscopy, the BS cannot be satisfied with a single or double grating to analyze the scattered light: the lines of acoustic phonons are too close to the Rayleigh line and must be discriminated in the foot of the central line. An FP has to be used for the analysis of the spectral distribution in high-resolution spectroscopy where a resolution of MHz to GHz is required.

The FP is the main element of the Brillouin spectrometer. The other elements are from the family of classical optics, mainly lenses, laser, and photomultiplier. The FP consists of two plane mirrors mounted accurately parallel to one another, with an optical spacing  $L1$  between them [19]. For a given spacing  $L1$  between the mirrors, the interferometer transmit only certain wavelengths, satisfying  $L1 = \frac{1}{2} p \lambda$  for integral values of  $p$ . The FP is used as a spectrometer by varying the spacing  $L1$ , so as to scan the light intensity at different wavelengths [19]. The

**FIGURE 12.4**

Schematic view of a Fabry–Perot interferometer [19].

Copyright 1980. Reprinted with permission from Sandercock.

first generation of scanning FP used only one set of mirrors (Fig. 12.4) with multiple wavelengths passing through them. One mirror is fixed and the other, guided by three piezoelectric crystals, is driven in translation performed with three scanning stacks (Fig. 12.4) by keeping the parallelism between the two mirrors.

However, the interpretation of the resulting spectrum may be ambiguous because the measured intensity at a given spacing is the sum of the intensities at all wavelengths satisfying equation  $L1 = \frac{1}{2} p\lambda$  [19]. Tandem interferometry was developed to remove this ambiguity.

### 12.2.2.2 Tandem Interferometry

In tandem interferometry, the light goes through two FP in series, with spacing  $L1$  and  $L2$  between their mirrors, respectively. In this case the wavelengths which are transmitted simultaneously satisfy two conditions:  $L1 = \frac{1}{2} p\lambda$  and  $L2 = \frac{1}{2} q\lambda$ ,  $p$  and  $q$  being integers. In this case, only one peak for the given wavelength will appear in the spectrum, the neighbor peaks being almost eliminated (Fig. 12.5) [19].

For a classical FP, a five-pass FP is usually used. The “tandem FP interferometer AMT-1” of JRS Scientific Instruments (Switzerland) is a FP  $2 \times 3$  tandem pass.

Note that the operators must check some precise points given in the list below before realizing Brillouin experiments with good feasibility. These questions are

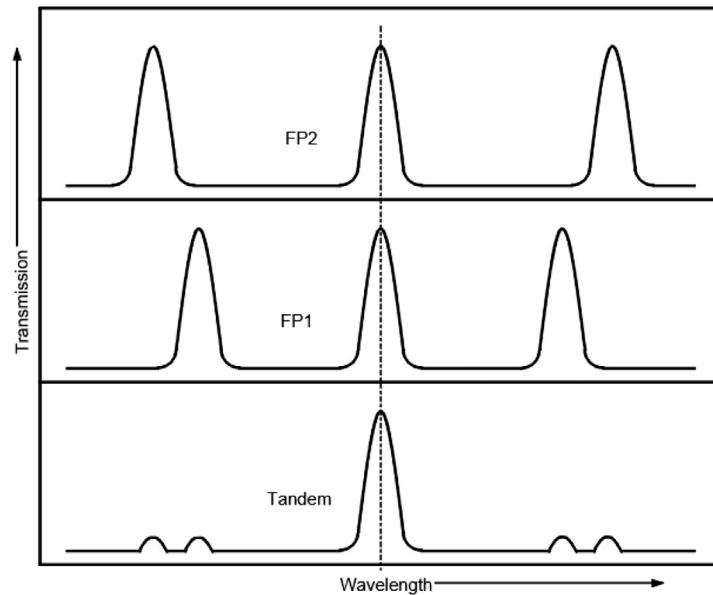


**FIGURE 12.5**

Spectra given by FP1, FP2, and tandem interferometers [19].

Copyright 1980. Reprinted with permission from Sandercock.

also useful for nonspecialists to understand which sample is well adapted for BS characterization:

- *What is the interaction volume between incident laser beam and tested material?*  
 All the matter within this volume will potentially scatter the incident light. It should be considered as homogeneous if the acquired spectrum presents conventional peaks, one longitudinal (or quasilongitudinal) and not more than two transverse (or quasitransverse) modes.
- *What is (or “are” if the material is anisotropic) the refractive index that must be taking into account for the incident and scattered photons?*  
 If the refractive index varies with the physical parameters studied, it must be measured with very high precision. If not, the variation of the acoustic wave velocity cannot be deduced from the acoustic mode frequency.
- *What is the surface roughness or homogeneity of the sample?*  
 If the surface plane of the sample is not known very precisely, it will induce an error on the incidence angle. In addition, if the roughness is not at least one order of magnitude under the laser wavelength, the signal/noise ratio will be rather bad, and a large broadening of the elastic central peaks can prevent the observation of low frequency modes.

- *What is the transparency of the material at the wavelength of the incident laser?*

If the material is not transparent, the interaction with the incident beam can produce strong heating and a local change of its physical properties. The transparency of the matter will also allow the choice of the geometrical interaction. For some nontransparent materials, like metals, only surface modes can be observed.

- *What are the dimensions of the measured sample?*

For thin films, such as piezoelectric films for passive electronic applications, with a thickness of about hundreds of nanometers, the propagating acoustic waves are not considered as bulk waves but as guided waves. For these specific modes, the acoustic velocity is much more complicated and for main structures, it must be determined by numerical simulation because no analytical solution exists.

### 12.2.2.3 Scattering Geometries

Different geometries are possible, bringing different information about the studied material (Fig. 12.6).

From Eqn (12.3) and Snell–Descartes law, these geometries give access to different acoustic velocities:

$$v^{90N} = \frac{\Omega^{90N}}{2\pi} \frac{\lambda_0}{2n \sin \frac{\theta_i}{2}} \quad (12.5)$$

$$v^{90A} = \frac{\Omega^{90A}}{2\pi} \frac{\lambda_0}{2 \sin \frac{\theta_i}{2}} \quad (12.6)$$

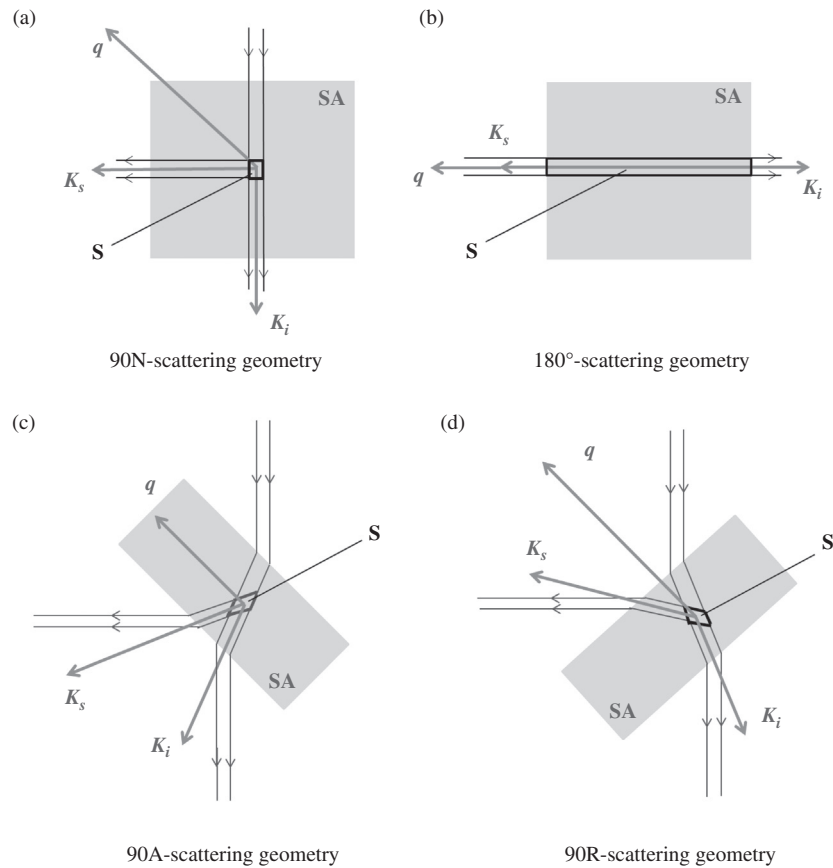
$$v^{90R} = \frac{\Omega^{90A}}{2\pi} \frac{\lambda_0}{2n \sin \frac{\theta_i}{2}} \quad (12.7)$$

$$v^{180} = \frac{\Omega^{180}}{2\pi} \frac{\lambda_0}{2n} \quad (12.8)$$

Three geometries will be discussed more extensively: 90A, 180, and RITA. This last one, which is a kind of combination of 90A and 180, is particularly interesting for studying polymers and nanocomposites.

#### 12.2.2.3.1 90A-Scattering Geometry

For this scattering geometry (Fig. 12.6c), the angle of incident laser beam on the sample surface is  $45^\circ$  [20]. The scattered light is collected perpendicularly to the incident beam. This particular geometry allows the determining of the acoustic velocity without the refractive index value [7], which is usually unknown and difficult to measure for nanocomposites.


**FIGURE 12.6**

Four scattering geometries, with S: scattering volume; SA: sample;  $k_i$  and  $k_s$ : the wave vectors of the incident and scattered light;  $q$ : the phonon wave vector.

In this geometry, for an angle  $\theta$  between the wave vector of the incident photon  $\vec{k}_i$  and the wave vector of the detected scattered photon  $\vec{k}_s$ , the momentum  $\vec{q}$  associated to the phonon is equal to:

$$\vec{q} = 2\vec{k}_i \sin \frac{\theta}{2} \quad (12.9)$$

From the Snell–Descartes law, this gives

$$n \sin \frac{\theta}{2} = \sin \frac{\theta_i}{2} \quad (12.10)$$

Where  $\theta_i$  is the angle between incident and scattered beam, here  $90^\circ$ . The acoustic velocity is obtained by the following equation, independent of the refractive index:

$$v(q) = \frac{2\pi f(q)}{q} = \frac{f \lambda^{laser}}{\sqrt{2}} \quad (12.11)$$

and the elastic constant  $c_{11}$ , the first constant of the stiffness tensor, is determined from the following equation:

$$c_{11} = \rho v^2 \quad (12.12)$$

where  $\rho$  is the mass density of the material.

Finally, it is worth noting that in the case of isotropic material,  $c_{11}$  is simply related to the Young's modulus  $E$  and the Poisson ratio  $\nu$  by the relation:

$$E = c_{11} \frac{(1 - 2\nu)(1 + \nu)}{1 - \nu} \quad (12.13)$$

### 12.2.2.3.2 180A-Scattering Geometry

In this geometry, the incident and scattered wave vectors  $\vec{k}_i$  and  $\vec{k}_s$  are antiparallel. Considering an elastically isotropic and homogeneous material, only the longitudinal phonons can be measured in this scattering geometry. Indeed, backscattering from transverse phonons is forbidden by selection rules [21].

The backscattering geometry is useful for bulk samples with badly defined or roughly polished surfaces, as well as for measurement within cells. In Fig. 12.7,

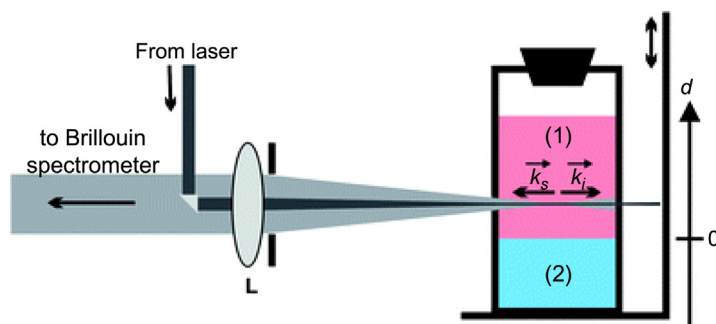


**FIGURE 12.7**

Schematic view of the backscattering geometry and the cuvette on the scanning stage. (1) Upper DETA compartment, (2) bottom compartment containing DGEBA or the freshly prepared epoxies EP(100/5) or EP(100/10);  $\vec{k}_i$  and  $\vec{k}_s$ : wave vector of the incident and scattered laser light, L: lens,  $d$ : vertical axis fixed to the cuvette coordinate system with origin at the initial phase boundary between both compartments. Cuvette dimensions:  $1 \times 1 \times 4 \text{ cm}^3$  [22].

the laser beam focused by a lens into a cuvette moves step by step along the vertical axis. This setup may be used to study the curing of epoxy resin with high precision, in particular at the interphase between the resin and the hardener [22].

### 12.2.2.3.3 RITA-Scattering Geometry

This geometry is identical to 90A if a virtual incident beam, denoted  $k'_{i,e}$  in Fig. 12.8, is considered. However, this particular geometry gives access in the same acquisition to the backscattering spectrum with the acoustic wave vector  $q^{180}$  and, simultaneously, to what is called RITA-scattering with the acoustic wave vector  $q^{2\alpha}$ .

Due to the reflection of the light beam, this scattering geometry theoretically gives access in the same spectrum to both the elastic constants within the plane of the film and in the parallel direction to the incident beam. As can be seen in Fig. 12.8, the spectra are collected in the same direction of the incident beam (the incident direction slightly inclines with respect to the surface normal) [23].

The RITA-scattering geometry allows for carrying out the measurement at the surface of nontransparent materials. The acoustic phonon wave vector is given by  $q = 2 \sin(\alpha/\lambda_0)$ , where  $2\alpha$  is the angle between the incident (and scattered) wave vector and the surface normal. The main advantage of this geometry is that there

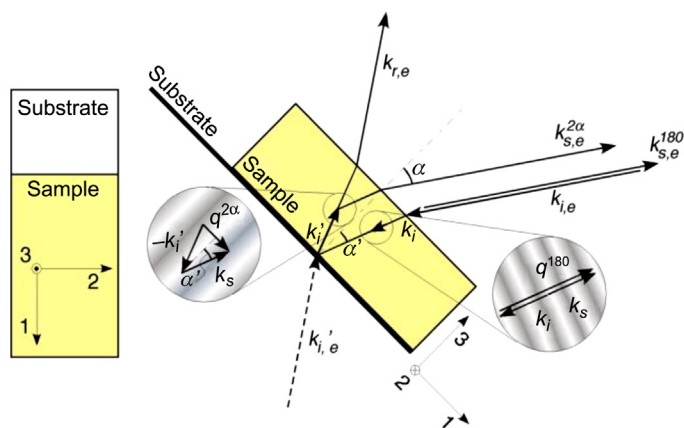


**FIGURE 12.8**

Brillouin light scattering in backscattering geometry. Here,  $k_i$ ,  $k_s$ , and  $k_r$  are the incident, scattered, and reflected beams, respectively; 1 and 2 directions are in the growth plane of the sample, and direction 3 is normal to the growth plane;  $R$  is the angle that  $k_i$  makes with the direction 3;  $q$  is the phonon wave vector, which is constructed based on the vector sum  $q = k_s - k_i$ . Accordingly, the propagation direction of the phonon probed by the direct incident beam is nearly perpendicular to that of the phonon probed by the incident beam reflected off the sample support [23].

Copyright 2010. Reprinted with permission from American Chemical Society.

is no interaction in the bulk for opaque materials. The refractive index is not necessary to calculate the acoustic wave velocity from the acoustic phonon frequency and the magnitude of the acoustic wave vector can be adjusted by varying the angle  $\alpha$ .

This geometry is also well adapted to determine the elastic properties of polymers as well as crystalline thin films. Considering that the scattering comes from the ripple propagating at the surface of the sample, knowing the thickness of the deposited thin film and the properties of the substrate, the surface acoustic wave velocity can be calculated from the elastic constant of the material constituting the thin film. The determination of the surface acoustic wave (SAW) velocity by BS gives a direct access to the mechanical properties of the thin films (but does not allow determining  $c_{11}$  and  $c_{44}$  for isotropic materials independently because SAW velocity is relied on for both these elastic constants).

It's worth noting that the 180-scattering will appear in the spectrum when the film thickness is more than two or three times the detected wavelength of the acoustic phonons in back scattering, i.e., approximately 180 nm for most common systems. The obtained spectrum involving both 180- and RITA-scattering can be used to determine the refractive index of the material (with a precision of about 1%) from the ratio of the measured acoustic frequencies (Eqns 12.6 and 12.7).

---

## 12.3 APPLICATIONS TO POLYMERS AND NANOCOMPOSITES

### 12.3.1 ACOUSTIC WAVE VELOCITY

The characterization of acoustic properties, including wave velocity and wave absorption, of polymers and nanocomposites is useful for various applications involving transducers and piezoelectronic devices, as well as to provide an insight into the molecular structure of materials [24,25]. As a molecular probe, acoustic properties are connected with the structural features such as morphology, chemical composition, cross-linking density, and glass transition [24]. Longitudinal and shear waves are the only two possible types in an unbounded, isotropic solid and propagate independently [25]. The longitudinal wave is the vibration of chain segments along the direction of propagation. The motion of the segments perpendicular to the direction of propagation is called shear or transverse wave.

As mentioned in introduction, the wave velocity can be measured by dynamic mechanical analysis (DMA) for audio or ultralow frequency (1 Hz–20 kHz), ultrasonic experiments for the frequency in the range of 1 kHz–1 GHz, and Brillouin light scattering at hypersonic frequencies (0.1–100 GHz) [25]. For applications such as passive electronic, the acoustic frequency of interest is in the range of GHz. Therefore, to measure properties of materials in this range, BS is still the most suitable technique in particular for expensive or rare samples. The data of BS measurement of some polymer composites are given in Table 12.1. Furthermore, for transparent and translucent materials, BS is able to monitor

**Table 12.1** Experimental Data of Various Polymers Measured by Brillouin Spectroscopy

Material	Thickness	$v_l$ (m s <sup>-1</sup> )	$v_t$ (m s <sup>-1</sup> )	$c_{11}$ (GPa)	$c_{44}$ (GPa)	$E$ (GPa)	$T_g$ (K)	References
Bilayer PET(12 μm)/glass oxide (variable)	0 nm	—	—	11.73	—	—	—	[33]
	200 nm	—	—	139	65.5	134	—	
Poly(methylmethacrylate)	3 mm	—	—	9.10	—	—	—	[34]
PMMA/nonsilanized nanoparticles SiO <sub>2</sub> 0.1 wt. %		—	—	9.03	—	—	—	
PMMA/nonsilanized nanoparticles SiO <sub>2</sub> 0.5 wt. %		—	—	8.96	—	—	—	
PMMA/nonsilanized nanoparticles SiO <sub>2</sub> 2 wt. %		—	—	8.99	—	—	—	
PMMA/silanized nanoparticles SiO <sub>2</sub> 0.1 wt. %		—	—	9.13	—	—	—	
PMMA/silanized nanoparticles SiO <sub>2</sub> 0.5 wt. %		—	—	9.41	—	—	—	
PMMA/silanized nanoparticles SiO <sub>2</sub> 1 wt. %		—	—	9.24	—	—	—	
PMMA/silanized nanoparticles SiO <sub>2</sub> 2 wt. %		—	—	9.30	—	—	—	
P2VP	—	2710	—	—	—	—	356	[31]
P2VP/nanoparticles SiO <sub>2</sub> 45 wt. %	—	—	—	—	—	—	361	
PMMA	50 μm	2850	1400	—	—	6.26	378	[29]
Poly(carbonate)		2430	1070	—	—	4.11	413	
Multilayers PC/PMMA (total: 50 μm)	Periodicity: 12 nm	2625	1270	—	—	—	395	
	Periodicity: 25 nm	2625	—	—	—	—	—	
	Periodicity: 390 nm	2625	1130	—	—	—	—	
	25 μm	2400	—	11	—	—	—	[9]

$v_l$ , longitudinal velocity;  $v_t$ , transversal velocity;  $c_{11}, c_{44}$ , elastic constant;  $E$ , Young's modulus;  $T_g$ , glass temperature; PET, poly(ethylene terephthalate); PMMA, poly(methyl methacrylate); P2VP, poly(2-vinyl pyridine); PC, polycarbonate; P(VDF-TrFE), poly(vinylidene difluoride-trifluoroethylene).

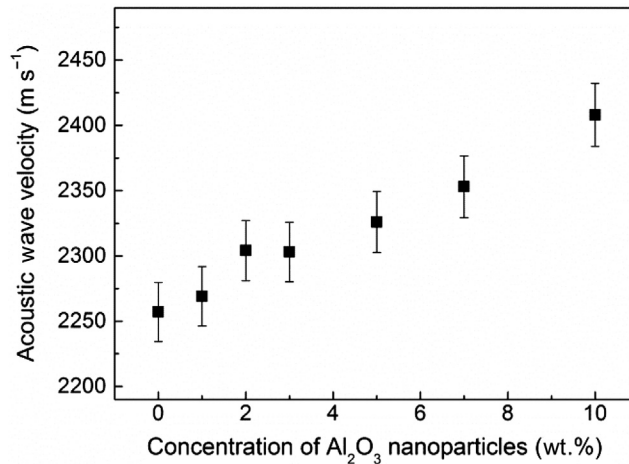


**FIGURE 12.9**

The variation of the velocity of the longitudinal wave of P(VDF-TrFE)/Al<sub>2</sub>O<sub>3</sub> films as a function of alumina concentration.

changes of acoustic properties as a function of time, temperature, pressure [26,27], and deformation [28].

One of the purposes of adding nanofillers in polymers consists in modulating mechanical and acoustic properties. Different techniques can be applied to measure the elastic constants and acoustic wave velocity in the obtained composite. However, such materials are usually expensive and/or very difficult to produce in large quantity, and BS is very useful to characterize samples with submillimeter dimensions. The acoustic velocity of the longitudinal mode as a function of the percentage of alumina nanoparticles in thin films is given in Fig. 12.9. The obtained high precision, less than 1%, allows concluding an increase of about 10% of the wave velocity with 10% of alumina nanoparticles [4].

As a result of the high sensitivity of the phonon dispersion, the longitudinal and transversal acoustic velocities in nanostructured materials can be measured down to a single-layer level, which allows the study of the evolution of the phonon dispersion in relation to composition and periodicity in polymeric 1D periodic structure. The different dependence of the longitudinal and transversal velocity, and hence moduli, on confinement effects in the polymer nanolayers is observed for a series of layer-multiplying, coextruded, free-standing films composed of alternating poly(carbonate) (PC) and poly(methylmethacrylate) (PMMA) nanolayers [29] (Fig. 12.10). Despite the negligible impact on the longitudinal velocity, the shear velocity increases with decreasing layer thickness, which may be linked to the confinement-induced stronger shearing force on polymer chains during processing [29].

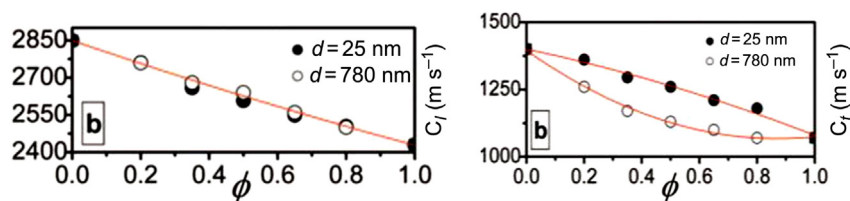


**FIGURE 12.10**

Longitudinal sound velocity  $c_l$  and shear sound velocity  $c_t$  plotted as a function of PC composition in the PC/PMMA multilayer films with bilayer spacing [29].

Copyright 2008. Reprinted with permission from American Chemical Society.

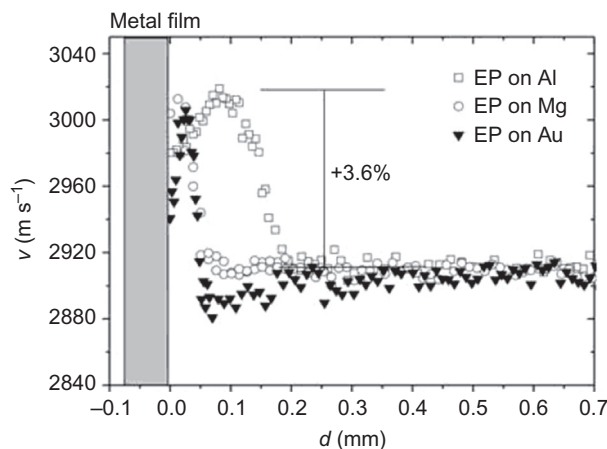


**FIGURE 12.11**

Profiles of sound velocity ( $v$ ) as function of distance ( $d$ ) from the metal of epoxy (EP) adhesive on different metal films [7].

Copyright 2005. Reprinted with permission from John Wiley & Sons.

In addition, the acoustic anisotropy [30] and the behavior of the acoustic phonon [31] can provide information on the interfacial region of a nanocomposite. Different phonon modes in BS correspond to different metastable microscopic phases in the material which depend on the interfacial structure of nanoparticles and polymers. This structure can be controlled by the processing conditions, such as casting solvent [31].

The local characterization by BS can indicate different morphologies of polymer-substrate interface that may result from different mechanisms. Figure 12.11 illustrates that the sound velocity increases near to the substrate surface, showing the formation of a large interphase up to several hundred micrometers [7], depending on the metal substrate. Moreover, the analysis of the

hypersonic velocity profile reveals that the hardener, e.g., diethylene triamine, can penetrate into epoxy resin through small convective channels. Thus, the curing process may occur not only at the interface, but also at the end of the channels [22]. However, the matter transport and polymerization are modified by the presence of alumina nanoparticles in the resin. On one hand, the nanoparticles may act as barriers, preventing the formation of convective transport channels. On other hand, they can catalyze the self-healing procedures [32].

### 12.3.2 ELASTIC CONSTANTS

The elastic constants of viscoelastic materials such as polymers depend on frequency and can be determined by Eqn (12.12). The produced deformation depends on the time that the stress is applied on the sample. In high frequency measurements, the moving portion of the material is small in comparison with the strain induced in static and low frequency measurements. Therefore, the elastic constants measured by BS are higher than those determined by DMA or static method [25]. In other respects, BS considers the short-scale segment motions in materials, while DMA examines the motions of large-length scale.

The elastic constants of free-standing films and films on substrates can be determined without difficulties by BS, which is very sophisticated for other techniques like DMA or tensile test. The mechanical properties are affected by various parameters including film thickness, shaping methods (e.g., spin-coating, casting methods), preparation conditions (i.e., ultrasonication, thermal history), and composition [4,9,17,33,35,36]. As can be seen from Figs 12.12 and 12.13, the

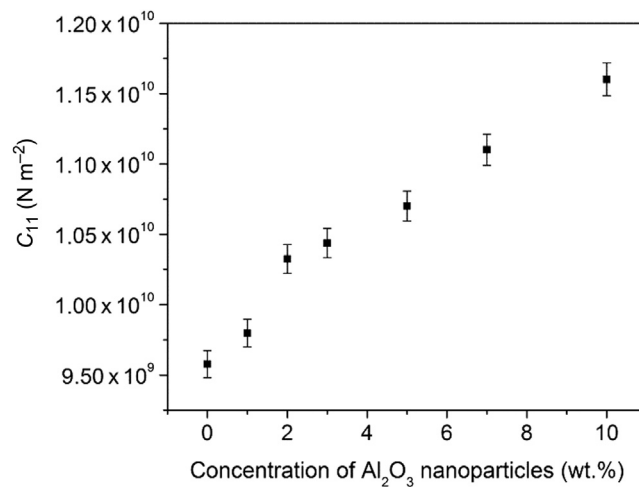


**FIGURE 12.12**

The variation of elastic constant  $c_{11}$  of P(VDF-TrFE)/Al<sub>2</sub>O<sub>3</sub>-casted films as a function of alumina concentration.

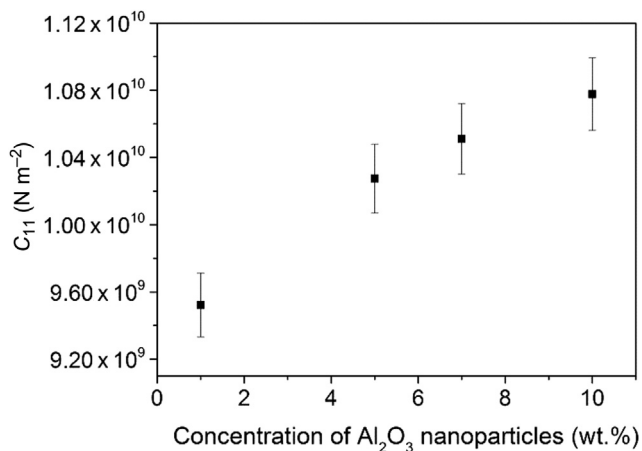


**FIGURE 12.13**

The variation of elastic constant  $c_{11}$  of P(VDF-TrFE)/Al<sub>2</sub>O<sub>3</sub> thin films on silicon substrate as a function of alumina concentration.

free-standing films and films on substrates show the same increase in elastic constants as a function of alumina concentration. The enhancement was confirmed by the numerical model using homogenization techniques [13]. It seems that the film thickness higher than critical value of crystallization, for example about 100 nm for P(VDF-TrFE), does not have a significant effect on the mechanical properties of the films [9].

It is possible to study the effect of film thickness on the elastic constants and elastic anisotropy of thin film less than 100 nm by BS [33]. Figure 12.14 shows the evolution of the elastic constant parallel and perpendicular to the growth direction of a multilayer film prepared by layer-by-layer (LBL) deposition method. The films of chitosan are elastically isotropic. The addition of cellulose nanocrystal (cellN) increases the elastic constants of polymer films more significantly in the parallel direction than in the perpendicular direction [23], resulting in elastic anisotropy. In the parallel direction, the elastic constant can be described by the traditional rules of mixture for elastic elements in parallel, i.e., it increases linearly with the volume fraction of fibers. The modulus in the perpendicular direction likely involves elastic elements in series and reaches a maximum at around 50% volume fraction of fiber before starting to decrease. It can be explained by the lack of polymer layers serving to transmit load between fibers.

The monitoring of resin during polymerization (Fig. 12.15) [36–38] reveals that the elastic constants of epoxy resin result from the network of covalent bonds, and van der Waals and hydrogen bonding between network segments. The latter arises during the reorganization process of the polymer segment into an optimal configuration [38].

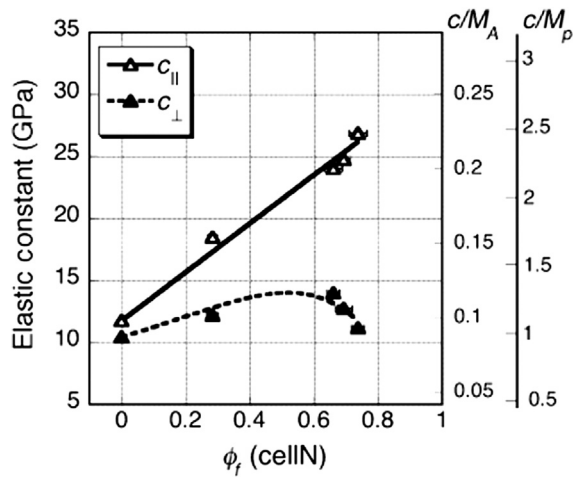


**FIGURE 12.14**

Elastic constants of [(chitosan/cellulose nanocrystal)<sub>x</sub>/(chitosan/poly(sodium styrenesulfonate))<sub>y</sub>] films as a function of cellN volume fraction [23].

Copyright 2010. Reprinted with permission from American Chemical Society.

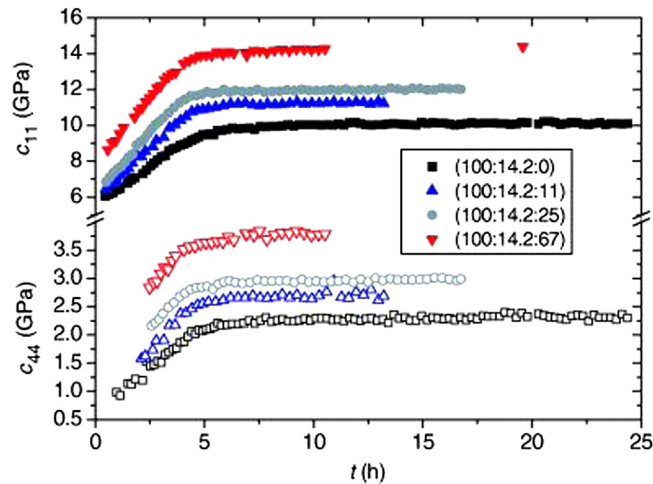


**FIGURE 12.15**

Longitudinal moduli  $c_{11}$  (filled symbols) and shear moduli  $c_{44}$  (open symbols) versus time during polymerization at 298 K for the DGEBA/DETA/silica [36].

Copyright 2009. Reprinted with permission from IOP Science.

### 12.3.3 GLASS TRANSITION TEMPERATURE

The elastic constants and velocity vary linearly with the temperature when the material is in the same phase. By studying the evolution of the longitudinal frequency with the temperature, the glass temperature ( $T_g$ ) can be determined where a change of slope occurs between the glassy and rubbery phases. The addition of nanoparticles increases the  $T_g$  (Fig. 12.16), which is often explained by the interaction between the nanofillers and polymer matrix [31,39].

The BS offers advantages to determine the  $T_g$  compared with the traditional methods like differential scanning calorimetry (DSC) and DMA. Indeed, DMA imposes external shearing forces, causing a possible change in the network structure whereas the Brillouin measurement is noninvasive and noncontact.

BS gives values of  $T_g$  lower (from 3 to 12 K) than that of DSC, nanocalorimetry, and broadband dielectric spectroscopy (Table 12.2). BS offers a high sensibility for detecting  $T_g$  of very thin layer (tens of nanometer). The results reveal the decrease of  $T_g$  with film thickness, while no variation is observed by nanocalorimetry [40]. The decrease of  $T_g$  (Fig. 12.17) is also observed by other techniques like ellipsometry and dielectric spectroscopy [41–43]. The origin of the thickness dependence of  $T_g$  is still an open question, despite two decades of intense research in this area [42,44–54]. Several factors can significantly affect the  $T_g$  of supported thin film such as polymer microstructure, conformation of the polymer

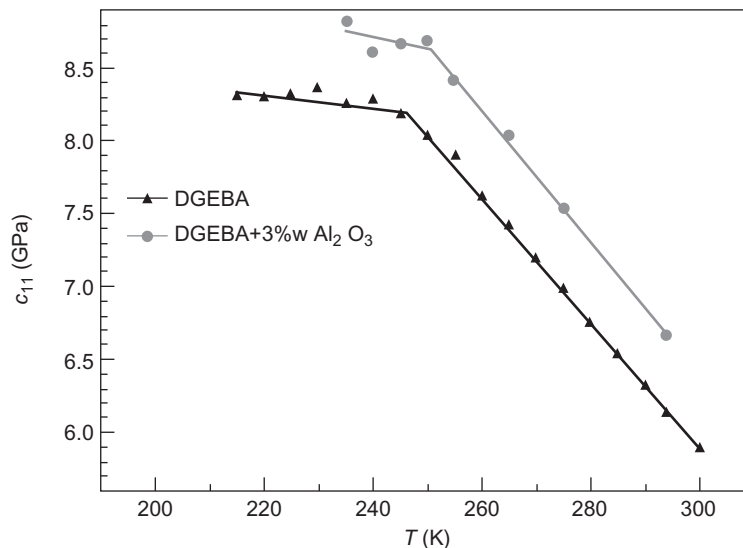


**FIGURE 12.16**

Evolution of the elastic constant  $c_{11}$  (Young's modulus) versus temperature for pure DGEBA (triangles) and nanocomposites (circles) [39].

Copyright 2007. Reprinted with permission from Elsevier Ltd.

**Table 12.2** Glass Temperatures of Various Polymers and Polymer Nanocomposites Determined for Different Techniques

<b>Materials</b>	<b>BS</b>	<b>DSC</b>	<b>Nanocalorimetry<sup>a</sup></b>	<b>Broadband Dielectric Spectroscopy</b>	<b>References</b>
Poly(2-vinyl pyridine)	356 K	367 K	363 K (film thickness of 3–400 nm)	–	[31,40]
Poly(2-vinyl pyridine)/45 wt.% SiO <sub>2</sub> nanoparticles	361 K	373 K	–	368 K	[31,57]
Polystyrene	368 K (film thickness of 514 nm) 378 K (film thickness of 39 nm)	–	367 K (film thickness of 3–400 nm)	–	[40,56]
Poly(methyl methacrylate)	387 K (film thickness of 492 nm) 372 K (film thickness of 41 nm)	–	405 K (film thickness of 3–400 nm)	–	[40]
Salol confined to pore glasses (2.5 nm)	203 K	200 K	–	–	[58]

<sup>a</sup>Calculated from the limiting fictive temperature [40].

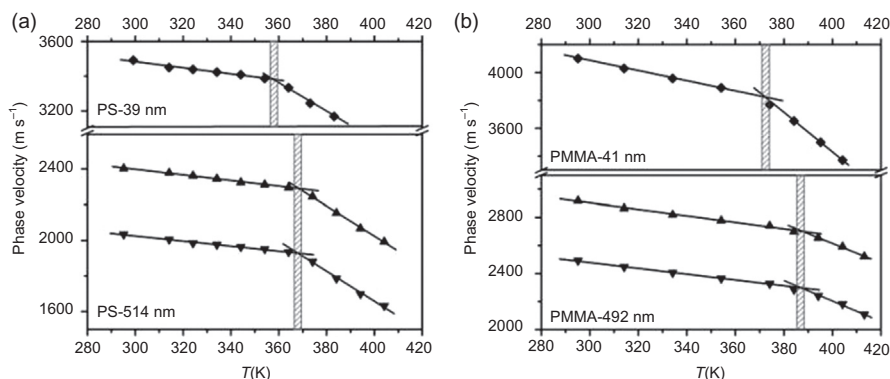


**FIGURE 12.17**

Phase velocities of a few general Lamb modes (at constant  $q$ ) propagating in the PS (a) and PMMA (b) films with two thicknesses as a function of temperature. For the thicker films, the two strongest general Lamb modes are presented [56].

Copyright 2007. Reprinted with permission from American Chemical Society.

chains, interfacial interactions between film and substrate, and experimental parameters including surface roughness, oxidative degradation, film preparation artifacts, moisture adsorption, dewetting, solvent purity for spin-coating solutions, etc., which are discussed in [41,43,55] and the references therein.

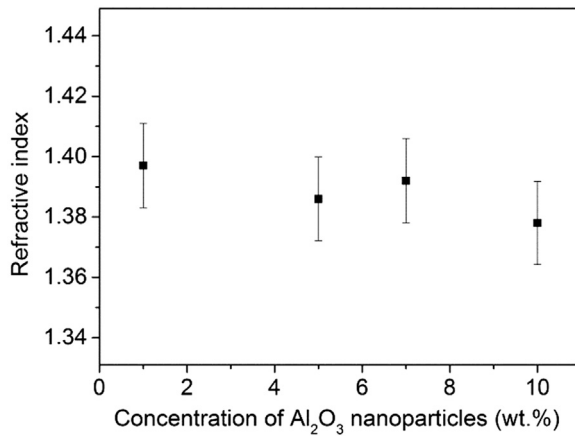
### 12.3.4 REFRACTIVE INDEX

Interestingly, BS offers the optic and elastic properties from the same scattering volume. As mentioned in Section 12.2, by combining two different scattering geometries 90A and backscattering, the refractive index ( $n$ ) of polymer and nanocomposite can be determined [35,59,60]. Furthermore, the anisotropy of refractive index can be determined by changing the polarization of the incident light [61]. For poly(vinylidene fluoride) (PVDF), the refractive index of extraordinary lay ( $n_s$ ) (the axial direction) and ordinary lay ( $n_p$ ) (perpendicular to the axial direction) are determined respectively by the s-polarized and p-polarized incident laser beam [60]. The accuracy of the refractive index determined by BS is comparable with those measured by the Abbé refractometer (Table 12.3). The small difference between these two methods may be associated with the measured area, whose diameter is 50  $\mu\text{m}$  for BS. In addition, the BS measures mainly bulk properties, which is in contrast to refractometer-based on total refraction that gives optical properties close to the sample surface [16]. Another advantage of BS results from the fact that the measurement can be taken on thin films with or without substrate (Fig. 12.18), at extreme temperature, for example, above the Curie temperature of PVDF (Fig. 12.19) [60].

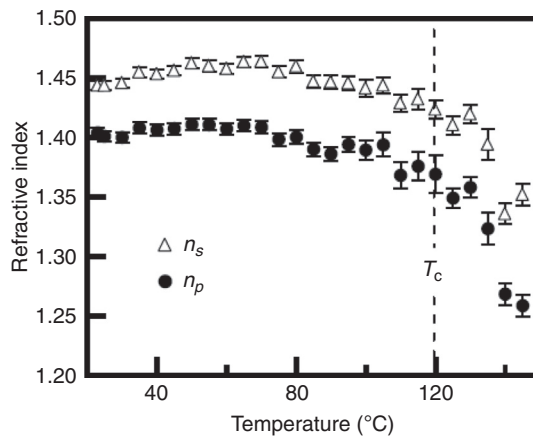
**Table 12.3** Refractive Index of PVDF at Room Temperature [60]

Method	Refractive Index	
	$n_s$	$n_p$
BS	$1.444 \pm 0.004$	$1.404 \pm 0.004$
Abbé refractometer	$1.445 \pm 0.004$	$1.416 \pm 0.005$

Copyright Reprinted with permission from Elsevier Ltd.

**FIGURE 12.18**

The variation of refractive index of P(VDF-TrFE)/Al<sub>2</sub>O<sub>3</sub> thin films on silicon substrate as a function of alumina concentration.

**FIGURE 12.19**

Effects of temperature on the refractive indices of the PVDF film [60].

Copyright 2006. Reprinted with permission from Elsevier Ltd.

### 12.3.5 COUPLING OF BRILLOUIN AND OTHER TECHNIQUES

Both Brillouin and Raman light scattering are based on inelastic light scattering which measures the change in energy of scattered light from its incident light. The main difference is that for Raman spectroscopy an optical phonon interacts with the incident photon to give rise to a scattered photon, and for BS an acoustic phonon is implied. The frequency shift for Raman spectroscopy is usually in the order of the THz and of the GHz for BS. That is why for Raman spectroscopy, a conventional optical grating is used to separate the elastic and the inelastic scattered light. However, this device is not convenient for BS because of a rather low resolution. In addition, the oscillators characterized in each case are different.

Raman spectrum is used to observe the molecular structure and concentration of a substance. Therefore it can be used to monitor *in situ* polymerization and cross-linking processes under network formation. The combination of Brillouin and Raman spectroscopy allows simultaneous characterization of the cure kinetics and the evolution of viscoelastic properties during thermoset curing (Fig. 12.20). In addition, the coupling results are able to associate the obtained elastic properties to the microstructure of the materials, e.g., to structural reorganization in the interface region [37] or to the state of functionalization of the filler within the polymer matrix [62].

In tribology, wear and friction properties are investigated as a function of various parameters including composition, surface treatments, roughness, microstructure, or environment of the sample. The analysis of the surface topography allows for determining the stick-slip and the depth wear by applying a constant force with a fixed pin on a rotating sample. The combination of Brillouin and tribological results enables the correlation between the stick-slip and the stiffness, probing the homogeneous behavior of the material [12].

### 12.3.6 BIOLOGICAL SYSTEMS

For biological tissues and biomaterials, the viscoelastic properties are closely connected with their functional abilities, and thus play significant roles in many areas of medicine [63]. The disturbance in the mechanical properties and the constituent biopolymers of tissue is widely implicated in disease. Therefore, the noninvasive *in vivo* characterization of viscoelastic properties at the microscopic (cellular) scale would have a broad variety of applications in biology and medicine.

BS has been used successfully to characterize *ex vivo* and *in vivo* biological systems, including proteins [64–71], bone [72–75], cornea and crystalline lens [76–83], scaffold [84], viruses [85], and spider silks [86]. It offers the possibility to characterize living tissues with spatial resolutions of a few tens of micrometers, therefore shedding light on structure–function relationships under normal and pathological conditions. In addition, the capacity of mapping the elastic modulus of a cornea using BS (Fig. 12.21) suggests several potential applications, such as early detection of keratoconus and corneal ectasia as well as monitoring of corneal cross-linking procedures [78,83].

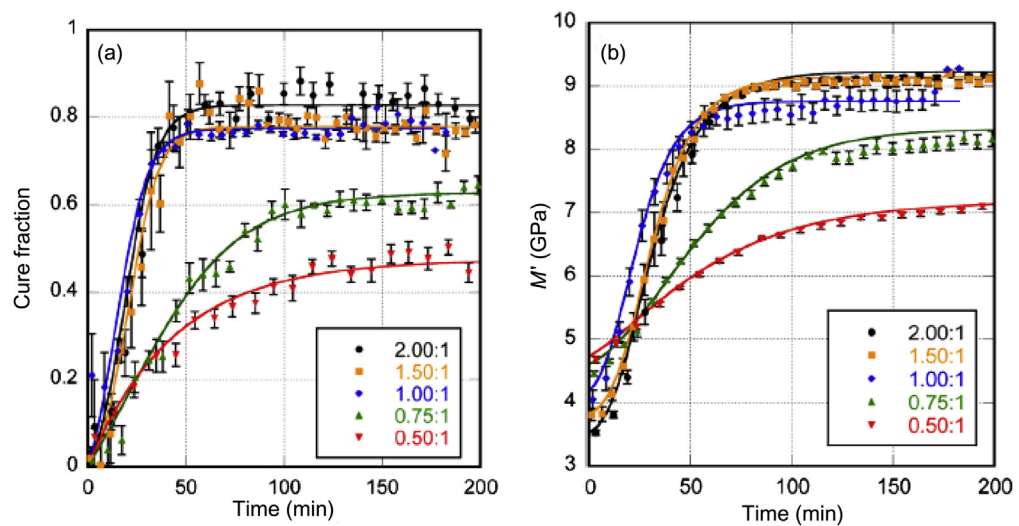


**FIGURE 12.20**

Degree of (a) cure and (b) longitudinal elastic modulus as a function of time for different epoxy resin-hardener stoichiometries [38].

Copyright 2014. Reprinted with permission from American Chemical Society.

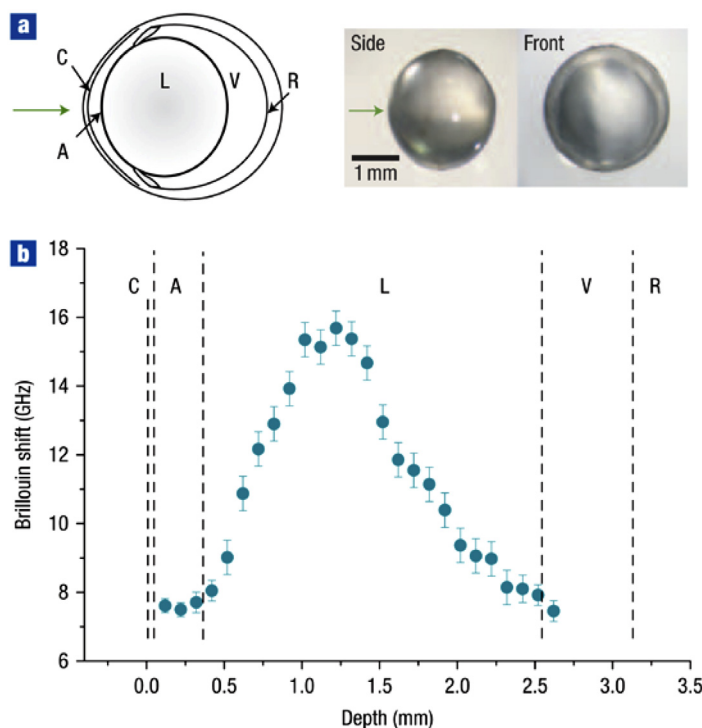


**FIGURE 12.21**

*In situ* characterization of the crystalline lens in a mouse eye (a) Left: schematic of the murine eye. Right: images of the crystalline lens extracted after measurement. The arrow indicates the beam entrance direction. (b) Brillouin frequency shifts measured at various depths along the central optic axis (blue circles), showing a two-fold increase from the outer layers (cortices) towards the lens center (nucleus). Error bars represent the measurement uncertainty [83]. C, cornea; A, aqueous humour; L, lens; V, vitreous humour; and R, retina.

Copyright 2007. Reprinted with permission from Nature Publishing Group.

## 12.4 CONCLUDING REMARKS

BS is a versatile and nondestructive method to determine the frequency of the acoustic phonons for the nanocomposites, in bulk form as well as in thin films, and study their elastic properties. Indeed, provided the refractive index is known (or calculated via the RITA-scattering geometry) the acoustic wave velocity is deduced from the phonon frequency. Knowing the density, the whole elastic constant tensor can be obtained.

The BS requires few conditions for the sample. First, only a small size is required: a few mm<sup>2</sup> of surface exposed to the laser beam, which may be a great

advantage of BS versus other mechanical characterization techniques. Then, only some knowledge is needed about the sample, mostly the density. A variety of forms is possible, even if a low diffusing surface is preferable: transparent or translucent materials are more easily studied, but opaque materials can also be characterized.

BS is particularly powerful for studying glass transitions, *in situ* polymerization, and various transitions phase of polymers and oligomers. The use of multiple geometries allows access to the optical index of the material with good accuracy, and the evolution of this index as a function of temperature.

This chapter gives indications about the important parameters for the sample which should be considered by the reader aiming to perform a BS experiment—such as opacity, dimension, homogeneity, etc. It summarizes all the parameters that the BS gives access to and demonstrates that many nanocomposite materials can be characterized, as well as biological samples. Finally, it shows that this technique can be interestingly coupled with others, for instance Raman spectroscopy, so as to relate macroscopic elastic properties and chemical bindings.

---

## REFERENCES

- [1] Mittal V. *Characterization techniques for polymer nanocomposites*. Weinheim: John Wiley & Sons; 2012.
- [2] Thomas S, Grohens Y, Jyotishkumar P. *Characterization of polymer blends: miscibility, morphology and interfaces*. Weinheim: John Wiley & Sons; 2014.
- [3] Thomas S, Zaikov GE. *Polymer nanocomposite research advances*. New York: Nova Publishers; 2008.
- [4] Hadji R, Nguyen VS, Vincent B, Rouxel D, Bauer F. Preparation and characterization of P(VDF-TrFE)/Al<sub>2</sub>O<sub>3</sub> nanocomposite. *IEEE Trans Ultrason Ferroelectr Freq Control* 2012;59:163–7.
- [5] Nguyen VS, Rouxel D, Vincent B, Badie L, Santos FDD, Lamouroux E, et al. Influence of cluster size and surface functionalization of ZnO nanoparticles on the morphology, thermomechanical and piezoelectric properties of P(VDF-TrFE) nanocomposite films. *Appl Surf Sci* 2013;279:204–11.
- [6] Nguyen VS, Badie L, Lamouroux E, Vincent B, Santos FDD, Aufray M, et al. Nanocomposite piezoelectric films of P(VDF-TrFE)/LiNbO<sub>3</sub>. *J Appl Polym Sci* 2013;129:391–6.
- [7] Krüger JK, Müller U, Bactavatchalou R, Liebschner D, Sander M, Possart W, et al. Mechanical interphases in epoxies as seen by nondestructive high-performance Brillouin microscopy. In: Possart W, editor. *Adhesion*. Weinheim: Wiley-VCH Verlag GmbH & Co. KGaA; 2005. p. 125–42.
- [8] Bactavatchalou R, Alnot P, Bailer J, Kolle M, Müller U, Philipp M, et al. The generalized Cauchy relation: a probe for local structure in materials with isotropic symmetry. *J Phys: Conf Ser* 2006;40:111–17.

- [9] Nguyen VS, Rouxel D, Meier M, Vincent B, Dahoun A, Thomas S, et al. Effect of ultrasonication and other processing conditions on the morphology, thermomechanical, and piezoelectric properties of poly(vinylidene difluoride-trifluoroethylene) copolymer films. *Polym Eng Sci* 2014;54:1280–8.
- [10] Sato A, Knoll W, Pennec Y, Djafari-Rouhani B, Fytas G, Steinhart M. Anisotropic propagation and confinement of high frequency phonons in nanocomposites. *J Chem Phys* 2009;130:111102.
- [11] Sato A, Pennec Y, Shingne N, Thurn-Albrecht T, Knoll W, Steinhart M, et al. Tuning and switching the hypersonic phononic properties of elastic impedance contrast nanocomposites. *ACS Nano* 2010;4:3471–81.
- [12] Rouxel D, Eschbach J, Vincent B. Nanocomposite PMMA/SiO<sub>2</sub>: Brillouin scattering and tribological study. *Int J Surf Sci Eng* 2010;4:322–36.
- [13] Maurice G, Rouxel D, Vincent B, Hadji R, Schmitt J-F, Taghite MB, et al. Investigation of elastic constants of polymer/nanoparticles composites using the Brillouin spectroscopy and the mechanical homogenization modeling. *Polym Eng Sci* 2013;53:1502–11.
- [14] Beghi MG, Fonzo FD, Pietralunga S, Ubaldi C, Bottani CE. Precision and accuracy in film stiffness measurement by Brillouin spectroscopy. *Rev Sci Instrum* 2011;82:053107.
- [15] Maznev AA, Manke KJ, Klieber C, Nelson KA, Baek SH, Eom CB. Coherent Brillouin spectroscopy in a strongly scattering liquid by picosecond ultrasonics. *Opt Lett* 2011;36:2925–7.
- [16] Krüger JK. Brillouin spectroscopy and its application to polymers. In: Heinz B, editor. *Optical techniques to characterize polymer systems*. Amsterdam: Elsevier; 1989. p. 429–534.
- [17] Houf L, Mugnier Y, Rouxel D, Le Dantec R, Badie L, Vincent B, et al. Preparation of transparent PMMA/Fe(IO<sub>3</sub>)<sub>3</sub> nanocomposite films from microemulsion polymerization. *J Appl Polym Sci* 2013;130:1203–11.
- [18] Liu HJJ. Brillouin light scattering study of linear and nonlinear spin waves in continuous and patterned magnetic thin films. Colorado State University; 2014. p. 139.
- [19] Sandercock JR, Fabry-Perot interferometer; 1980. [http://tablestale.com/en/products/view/1/Manual\\_TFP\\_1.pdf](http://tablestale.com/en/products/view/1/Manual_TFP_1.pdf).
- [20] Hakiki ME, Eschbach J, Rouxel D, Vincent B, Vialle S, Krüger JK, et al. Elastic and piezoelectric constants of potassium niobate studied by Brillouin spectroscopy. *Ferroelectrics* 2007;351:96–104.
- [21] Vacher R, Boyer L. Brillouin scattering: a tool for the measurement of elastic and photoelastic constants. *Phys Rev B* 1972;6:639–73.
- [22] Philipp M, Mueller U, Sanctuary R, Kieffer J, Possart W, Krueger JK. On the interplay between matter transport and structure formation at epoxy-hardener interfaces visualized by scanning Brillouin microscopy. *Soft Matter* 2011;7:118–24.
- [23] Sui L, Huang L, Podsiadlo P, Kotov NA, Kieffer J. Brillouin light scattering investigation of the mechanical properties of layer-by-layer assembled cellulose nanocrystal films. *Macromolecules* 2010;43:9541–8.
- [24] Jarzynski J, Balizer E, Fedderly JJ, Lee G. Acoustic properties. *Encyclopedia of polymer science and technology*. John Wiley & Sons, Inc.; 2002. Online ISBN: 9780471440260. DOI: <http://dx.doi.org/10.1002/0471440264>.
- [25] Sinha M, Buckley DJ. Acoustic properties of polymers. In: Mark JE, editor. *Physical properties of polymers handbook*. New York, NY: Springer; 2007. p. 1021–31.

- [26] Ko J-H, Ko YH, Kim KJ. Acoustic behaviour and equation of state of amorphous ethylene–vinyl acetate copolymer studied by means of high-pressure Brillouin scattering spectroscopy. *Phase Transit* 2014;87:582–91.
- [27] Shin S, Ko J-H, Park J, Ko YH, Kim KJ. Pressure dependence of acoustic anomalies of polydimethylsiloxane studied by Brillouin spectroscopy. *Phys B Condens Matter* 2015;466–467:50–3.
- [28] Tomohiro S-I, Matsukawa M, Otani T, Ohtori N. Brillouin scattering study on the opto-acoustic properties of thin piezoelectric polymer films. *Jpn J Appl Phys* 2004;43:2916.
- [29] Cheng W, Gomopoulos N, Fytas G, Gorishnyy T, Walish J, Thomas EL, et al. Phonon dispersion and nanomechanical properties of periodic 1D multilayer polymer films. *Nano Lett* 2008;8:1423–8.
- [30] Voudouris P, Choi J, Gomopoulos N, Sainidou R, Dong H, Matyjaszewski K, et al. Anisotropic elasticity of quasi-one-component polymer nanocomposites. *ACS Nano* 2011;5:5746–54.
- [31] Zhao D, Schneider D, Fytas G, Kumar SK. Controlling the thermomechanical behavior of nanoparticle/polymer films. *ACS Nano* 2014;8:8163–73.
- [32] Sanctuary R, Philipp M, Kieffer J, Mueller U, Possart W, Krueger JK. Trans-interface polymerization and matter transport processes in epoxy-alumina nanocomposites visualized by scanning Brillouin microscopy. *J Phys Chem B* 2010;114:8396–404.
- [33] Lefeuvre O, Kolosov OV, Every AG, Briggs GA, Tsukahara Y. Elastic measurements of layered nanocomposite materials by Brillouin spectroscopy. *Ultrasonics* 2000;38:459–65.
- [34] Rouxel D, Eschbach J, Vincent B, Baret G. Brillouin scattering and tribological study of PMMA/SiO(2) nanocomposite. In: Postnikov A, editor. 3rd France-Russia Seminar. Metz, France: EDP Sciences; 2008.
- [35] Nguyen VS, Hadji R, Vincent B, Rouxel D, Sarry F, Bauer F, P(VDF-TrFE)/Al<sub>2</sub>O<sub>3</sub> piezoelectric nanocomposite thin films. In: European conference on the applications of polar dielectrics (ECAPD); 2010. pp. 1–4.
- [36] Philipp M, Mueller U, Jimenez Rioboo RJ, Baller J, Sanctuary R, Possart W, et al. Interphases, gelation, vitrification, porous glasses and the generalized Cauchy relation: epoxy/silica nanocomposites. *New J Phys* 2009;11:023015.
- [37] Aldridge M, Waas A, Kieffer J. Spatially resolved, in situ elastic modulus of thermoset polymer amidst carbon fibers in a polymer matrix composite. *Compos Sci Technol* 2014;98:22–7.
- [38] Aldridge M, Wineman A, Waas A, Kieffer J. In situ analysis of the relationship between cure kinetics and the mechanical modulus of an epoxy resin. *Macromolecules* 2014;47:8368–76.
- [39] Eschbach J, Rouxel D, Vincent B, Mugnier Y, Galez C, Dantec RL, et al. Development and characterization of nanocomposite materials. *Mater Sci Eng C-Biomim Supramol Syst* 2007;27:1260–4.
- [40] Efremov MY, Olson EA, Zhang M, Zhang Z, Allen LH. Probing glass transition of ultrathin polymer films at a time scale of seconds using fast differential scanning calorimetry. *Macromolecules* 2004;37:4607–16.

- [41] Grohens Y, Hamon L, Reiter G, Soldera A, Holl Y. Some relevant parameters affecting the glass transition of supported ultra-thin polymer films. *Eur Phys J E* 2002;8:217–24.
- [42] Kawana S, Jones RAL. Character of the glass transition in thin supported polymer films. *Phys Rev E* 2001;63:021501.
- [43] Efremov MY. Effect of free surface roughness on the apparent glass transition temperature in thin polymer films measured by ellipsometry. *Rev Sci Instrum* 2014;85:123901.
- [44] Chung PC, Glynos E, Green PF. The elastic mechanical response of supported thin polymer films. *Langmuir* 2014;30:15200–5.
- [45] Dalnoki-Veress K, Forrest JA, Murray C, Gigault C, Dutcher JR. Molecular weight dependence of reductions in the glass transition temperature of thin, freely standing polymer films. *Phys Rev E* 2001;63:031801.
- [46] Forrest JA, Dalnoki-Veress K, Stevens JR, Dutcher JR. Effect of free surfaces on the glass transition temperature of thin polymer films. *Phys Rev Lett* 1996;77:2002–5.
- [47] Gennes PGD. Glass transitions in thin polymer films. *Eur Phys J E* 2000;2:201–5.
- [48] Herminghaus S, Jacobs K, Seemann R. The glass transition of thin polymer films: some questions, and a possible answer. *Eur Phys J E* 2001;5:531–8.
- [49] Liu Y-X, Chen E-Q. Polymer crystallization of ultrathin films on solid substrates. *Coord Chem Rev* 2010;254:1011–37.
- [50] Ogieglo W, Wessling M, Benes NE. Polymer relaxations in thin films in the vicinity of a penetrant- or temperature-induced glass transition. *Macromolecules* 2014;47:3654–60.
- [51] VanHorn RM. Crystallization in polymer thin films: morphology and growth. *Ser Soft Condens Matter* 2008;1:163–93.
- [52] Xia W, Keten S. Coupled effects of substrate adhesion and intermolecular forces on polymer thin film glass-transition behavior. *Langmuir* 2013;29:12730–6.
- [53] Xia W, Mishra S, Keten S. Substrate vs. free surface: competing effects on the glass transition of polymer thin films. *Polymer* 2013;54:5942–51.
- [54] Xie S-J, Qian H-J, Lu Z-Y. The glass transition of polymers with different side-chain stiffness confined in free-standing thin films. *J Chem Phys* 2015;142:074902.
- [55] Forrest JA, Dalnoki-Veress K. The glass transition in thin polymer films. *Adv Colloid Interface Sci* 2001;94:167–95.
- [56] Cheng W, Sainidou R, Burgardt P, Stefanou N, Kiyanova A, Efremov M, et al. Elastic properties and glass transition of supported polymer thin films. *Macromolecules* 2007;40:7283–90.
- [57] Holt AP, Griffin PJ, Bocharova V, Agapov AL, Imel AE, Dadmun MD, et al. Dynamics at the polymer/nanoparticle interface in poly(2-vinylpyridine)/silica nanocomposites. *Macromolecules* 2014;47:1837–43.
- [58] Kruger JK, Holtwick R, le Coutre A, Baller J. On the influence of nano-scaling on the glass transition of molecular liquids. *Nanostruct Mater* 1999;12:519–22.
- [59] Jimenez Rioboo RJ, De Andres A, Kubacka A, Fernandez-Garcia M, Cerrada ML, Serrano C, et al. Influence of nanoparticles on elastic and optical properties of a polymeric matrix: hypersonic studies on ethylene-vinyl alcohol copolymer-titania nanocomposites. *Eur Polym J* 2010;46:397–403.

- [60] Matsukawa M, Shintani K, Tomohiro S-I, Ohtori N. Application of Brillouin scattering to the local anisotropy and birefringence measurements of thin layers. *Ultrasonics* 2006;44(Suppl. 1):e1555–9.
- [61] Hisa K, Matsukawa M, Ohtori N. “Two-Pass” Brillouin scattering geometry for the investigation of opto-acoustic properties of thin films. *Jpn J Appl Phys* 2003;42: 5865.
- [62] Vigolo B, Vincent B, Eschbach J, Bourson P, Mareche J-F, McRae E, et al. Multiscale characterization of single-walled carbon nanotube/polymer composites by coupling Raman and Brillouin spectroscopy. *J Phys Chem C* 2009;113:17648–54.
- [63] Fung Y-C. *Biomechanics: mechanical properties of living tissues*. New York, NY: Springer; 1993.
- [64] Harley R, James D, Miller A, White JW. Phonons and the elastic moduli of collagen and muscle. *Nature* 1977;267:285–7.
- [65] Randall J, Vaughan JM, Cusak S. Brillouin scattering in systems of biological significance [and discussion]. *Philos Trans R Soc Lond A* 1979;293:341–8.
- [66] Palombo F, Winlove CP, Edginton RS, Green E, Stone N, Caponi S, et al. Biomechanics of fibrous proteins of the extracellular matrix studied by Brillouin scattering. *J R Soc Interface* 2014;11:20140739.
- [67] Svanidze AV, Huth H, Lushnikov SG, Kojima S, Schick C. Phase transition in tetragonal hen egg-white lysozyme crystals. *Appl Phys Lett* 2009;95:263702.
- [68] Svanidze AV, Romanov VP, Lushnikov SG. Anomalous behavior of Brillouin light scattering at thermal denaturation of lysozyme. *JETP Lett* 2011;93:409–14.
- [69] Troitzsch RZ, Vass H, Hossack WJ, Martyna GJ, Crain J. Molecular mechanisms of cryoprotection in aqueous proline: light scattering and molecular dynamics simulations. *J Phys Chem B* 2008;112:4290–7.
- [70] Asenbaum A, Pruner C, Schroerer HW, Plaetzer K, Bieler L, Brandstetter H, et al. Rayleigh and Brillouin scattering in a lysozyme-water mixture: an unusual behavior around 343 K. *J Mol Liq* 2011;158:7–12.
- [71] Yoshihara A, Miyazaki A, Maeda T, Fukushima M, Abe T. Brillouin light scattering from thin albumen of chicken egg. *J Phys Soc Jpn* 2010;79:125001.
- [72] Lees S, Tao NJ, Lindsay SM. Studies of compact hard tissues and collagen by means of Brillouin light scattering. *Connect Tissue Res* 1990;24:187–205.
- [73] Mathieu V, Fukui K, Matsukawa M, Kawabe M, Vayron R, Soffer E, et al. Micro-Brillouin scattering measurements in mature and newly formed bone tissue surrounding an implant. *J Biomech Eng* 2011;133:021006.
- [74] Kawabe M, Matsukawa M, Ohtori N. Measurement of wave velocity distribution in a trabecula by micro-Brillouin scattering technique. *Jpn J Appl Phys* 2010;49:07HB05.
- [75] Mathieu V, Fukui K, Mastukawa M, Kawabe M, Anagnostou F, Soffer E, et al. Assessment of the biomechanical properties of newly formed bone tissue using micro-Brillouin scattering. In: 2010 IEEE Ultrasonics Symposium (IUS); 2010. pp. 2231–2234.
- [76] Randall J, Vaughan JM. The measurement and interpretation of Brillouin scattering in the lens of the eye. *Proc R Soc Lond B Biol Sci* 1982;214:449–70.
- [77] Vaughan JM, Randall JT. Brillouin scattering, density and elastic properties of the lens and cornea of the eye. *Nature* 1980;284:489–91.
- [78] Scarcelli G, Pineda R, Yun SH. Brillouin optical microscopy for corneal biomechanics. *Invest Ophthalmol Vis Sci* 2012;53:185–90.

- [79] Reiss S, Burau G, Stachs O, Guthoff R, Stolz H. Spatially resolved Brillouin spectroscopy to determine the rheological properties of the eye lens. *Biomed Opt Express* 2011;2:2144–59.
- [80] Reiss S, Stachs O, Guthoff R, Stolz H. Non-invasive, spatially resolved determination of tissue properties of the crystalline lens with regard to rheology, refractive index, density and protein concentration by using Brillouin spectroscopy. *Klin Monbl Augenheilkd* 2011;228:1079–85.
- [81] Pinero DP, Alcon N. *In vivo* characterization of corneal biomechanics. *J Cataract Refract Surg* 2014;40:870–87.
- [82] Piñero DP, Alcón N. Corneal biomechanics: a review. *Clin Exp Optom* 2015;98:107–16.
- [83] Scarcelli G, Yun SH. Confocal Brillouin microscopy for three-dimensional mechanical imaging. *Nat Photonics* 2007;2:39–43.
- [84] Beroud J, Vincent B, Paternotte E, Nguyen VS, Kerdjoudj H, Velot E, et al. Brillouin spectroscopy: a new tool to decipher viscoelastic properties of biological scaffold functionalized with nanoscale films. *Bio-Med Mater Eng* 2013;23:251–61.
- [85] Stephanidis B, Adichtchev S, Gouet P, McPherson A, Mermet A. Elastic properties of viruses. *Biophys J* 2007;93:1354–9.
- [86] Koski KJ, Akhenblit P, McKiernan K, Yarger JL. Non-invasive determination of the complete elastic moduli of spider silks. *Nat Mater* 2013;12:262–7.

# Mössbauer spectroscopy of polymer nanocomposites

# 13

Abdulsalam Abdulkadir<sup>1</sup>, Tanusree Sarker<sup>1</sup>, Qingliang He<sup>2</sup>,  
Zhanhu Guo<sup>3</sup> and Suying Wei<sup>1,2</sup>

<sup>1</sup>Department of Chemistry and Biochemistry, Lamar University, Beaumont, TX, United States

<sup>2</sup>Dan F. Smith Department of Chemical Engineering, Lamar University,

Beaumont, TX, United States <sup>3</sup>Department of Chemical and Biomolecular Engineering,

University of Tennessee, Knoxville, TN, United States

## 13.1 INTRODUCTION

Polymer nanocomposites (PNCs) are a group of hybrid materials that uses polymers as the matrix and nanomaterial as the filler (also called *nanofiller*). Due to the unique synergistic multifunctions through the incorporation of multiple components/structures into one compatible entity, multifunctional PNCs have been extensively studied [1–18]. PNCs have found wide technological applications including microwave absorption/electromagnetic interference shielding [19,20], high-density information storage [21], bimodal imaging agent [22], environmental remediation [23–26], drug delivery [27], and energy storage [28–30]. When incorporating magnetic nanostructures into a polymer matrix, unique physicochemical properties can be achieved in the form of magnetic polymer nanocomposites (mPNCs). Usually, their magnetic properties are strongly associated with the nanostructure morphology (size and shape) and crystalline structure [13,17]. For the aforementioned cutting-edge materials science and nanotechnology development, mPNCs have been of special interest for research efforts during the past decades. For example, the development of highly efficient electrochemical energy storage material and highly kinetic, recyclable nanoadsorbents for waste water remediation requires detailed insight on the chemical structures of these magnetic nanostructures. In order to understand the remediation mechanisms and the chemical stability of the mPNCs during the interactions with the waste species and the charge–discharge process, the chemical environments of the magnetic components, such as iron species, is of critical importance.

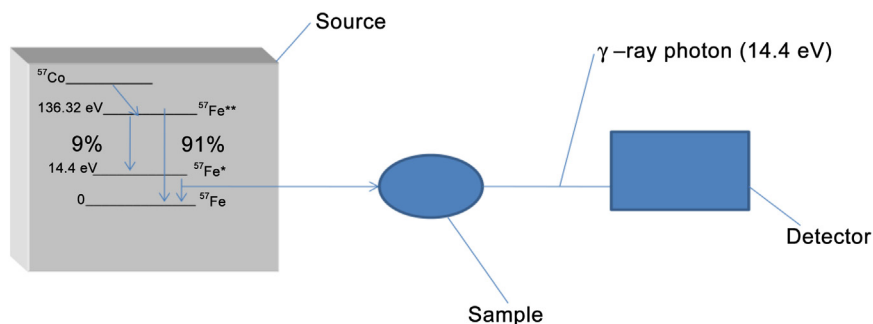
Characterization techniques including x-ray diffraction (XRD), x-ray photoelectron spectroscopy (XPS), and Fourier transform infrared spectroscopy (FT-IR) have been extensively applied to study the chemical structure of nanostructures within the polymer matrix. However, obtaining the detailed fingerprints, such as

the valence states, the oxygen environments, and chemical structures of magnetic iron-groups is still challenging, and cannot be achieved by techniques such as XRD, XPS, or FT-IR. Specifically, for PNCs filled with magnetic nanoparticles (NPs), FT-IR can only give limited information on the bond vibrations, which cannot determine the specific valence state of certain magnetic materials. XRD can provide the crystalline structures of magnetic NPs in the polymer matrix, and the information becomes less useful if amorphous structured fillers are formed in polymer matrices. In addition, due to the similarity in crystalline structures of magnetic materials (i.e.,  $\text{Fe}_2\text{O}_3$  and  $\text{Fe}_3\text{O}_4$ ), it is difficult for XRD to determine such chemical environments. While XPS is powerful for determining the surface chemistry, it is still impossible for it to determine the oxygen environment on magnetic NPs embedded in a polymer matrix on its own. Mössbauer spectroscopy is a unique, motion-based, highly sensitive spectroscopic technique that has helped to elucidate the fate of iron fillers in the PNCs by differentiating among the various iron species, because each of them has a unique Mössbauer spectroscopic fingerprint. For example, it is difficult to distinguish between magnetite and maghemite NPs by XRD because their diffraction patterns are quite similar. Nonetheless, Mössbauer spectroscopy will be more powerful and suitable for such studies. Magnetite ( $\text{Fe}_3\text{O}_4$ ) has the spinel structure  $(\text{Fe}^{3+})_A[\text{Fe}^{3+}\text{Fe}^{2+}]_B\text{O}_4$ , where the coordination symmetry in the A and B sites is tetrahedral and octahedral, respectively [31]. Above the Verwey transition temperature (at about 120 K), rapid electron exchange occurs between  $\text{Fe}^{2+}$  and  $\text{Fe}^{3+}$  on B sites and leads to an anomalous change in both the specific heat and the electrical conductivity at this temperature [31]. On the other hand, pure maghemite consists of two sextets due to  $\text{Fe}_A^{3+}$  and  $\text{Fe}_B^{3+}$  in the tetrahedral and octahedral sites, respectively. The magnetic hyperfine fields and the isomer shifts (IS) differ very little, and it is therefore not possible to distinguish the two components in spectra obtained without applied magnetic fields. These detailed fingerprints indisputably proved that Mössbauer spectroscopy is of great importance to study the chemical environments of iron species and further understand the interactions/changes of the magnetic nanostructures after their usages.

---

## 13.2 BASIC OPERATIONAL PRINCIPLES OF MÖSSBAUER SPECTROSCOPY

The Mössbauer spectroscopic technique operates on the principle of the use of recoil-less emission and absorption (so called resonance fluorescence) of the  $\gamma$ -radiation by nuclei [32]. The method is mostly studied on a sample that contains iron and other elements that have a suitable nuclear energy level and  $\gamma$ -emission half-lives, in order to get a meaningful spectrum. For example,  $^{57}\text{Co}$  nucleus decays by an electron capture to produce an excited state of  $^{57}\text{Fe}$ , and this nucleus further decays to another excited state that lies 14.4 keV above the ground state [33]. However,  $\gamma$ -ray is emitted by the nuclei during the process, and

**FIGURE 13.1**

A typical Mössbauer spectrometer.

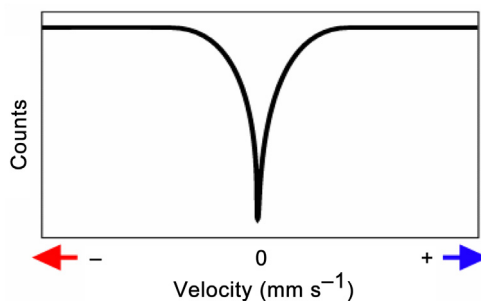
this corresponds to the energy value of 14.4 keV. Moreover, if this radiation is focused into a sample matrix so that the sample nucleus does not recoil, a highly monochromatic radiation is generated [34]. When this highly monochromatic  $\gamma$ -ray emitted radiation is directed to a sample containing Fe, the sample absorbs the radiation resonantly, which then results in a change in the sample's exact electronic and magnetic environment [35,36]. Resonance absorption occurs only if the sample is chemically identical to that of the emitting  $^{57}\text{Fe}$ . More importantly, the energy of  $\gamma$ -ray is minuscule, in an order of billionths of an electron volt [37]. Therefore, it is necessary to use a Doppler effect; this is often obtained from a radioactive source with a velocity of a few mm/s and recording the spectrum in stepwise order of velocity. The velocity is then compared with the speed of light due to the small shift in energy needed to observe the interactions. Fig. 13.1 shows the typical block diagram of a Mössbauer spectrometer.

When the modulated  $\gamma$ -energy from the oscillating source produces an increment in the  $\gamma$ -energy that matches the energy of the nuclear transition, the  $\gamma$ -energy is absorbed and then a peak can be observed. The resonance absorption that occurs as the velocity changes results in the Mössbauer spectrum; therefore, in Mössbauer spectroscopy the energy scale is usually in terms of velocity. Fig. 13.2 shows a simple Mössbauer spectrum. In Fig. 13.2, the absorption peak occurs at  $0 \text{ mm s}^{-1}$ ; this is the point at which the source and absorber are identical. Energy level in absorbing nuclei can be influenced by IS, quadrupole splitting (QS), and magnetic splitting [38].

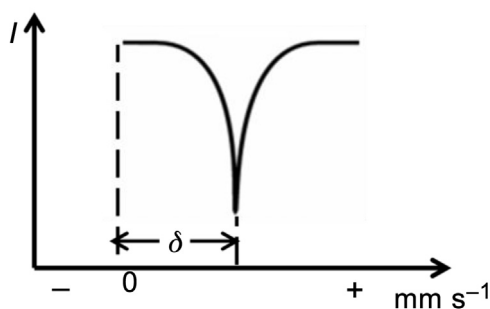
## 13.3 HYPERFINE INTERACTIONS OF THE NUCLEUS WITH ITS SURROUNDING ENVIRONMENT

### 13.3.1 IS DUE TO ELECTRON DENSITY AT THE NUCLEUS

IS ( $\delta$ ) can be used to determine the surface structure of samples and is also helpful for the determination of valence states of elements. Moreover, coordination

**FIGURE 13.2**

Simple spectrum showing the velocity scale and motion of source relative to the absorber.

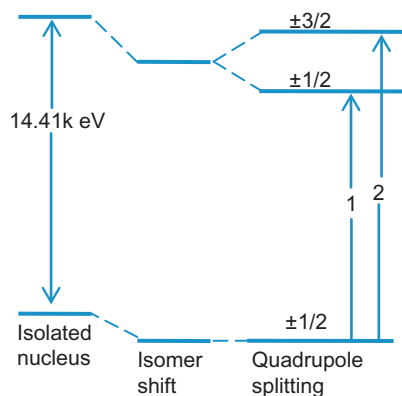
**FIGURE 13.3**

Isomer shift ( $\delta$ ) due to the s-electron density difference of source and absorber nuclei.

chemistry IS can be used to examine the bonding state of some ligands, as well as for the determination of the electron shielding and electron-drawing capacity of electronegative groups [37]. It arises as a result of the nonzero volume of the nucleus and the s-electron density or bonding electrons with s character. The shift in resonance energy of the transition produced, as a result of the change in the s-electron environment between the source and the absorber, will lead to the shift of the whole spectrum positively or negatively depending on the s-electron density [35] (Fig. 13.3).

### 13.3.2 QS AS A RESULT OF ELECTRIC FIELD GRADIENT

When nuclei in state possess a nonspherical charge distribution, it results in a quadrupole moment [39]. The presence of an asymmetrical electrical field produced by the asymmetric electronic charge distribution or ligand arrangement causes the split of this nuclear energy level. Fig. 13.4 shows that the splitting of the first excited state of  $^{57}\text{Fe}$  has led to two substates,  $m_I = \pm 1/2$  and  $m_I = \pm 3/2$ , therefore

**FIGURE 13.4**

Energy-level diagram showing the isomer shift and quadrupole splitting due to the electric field gradient for the transitions in  $^{57}\text{Fe}$  [41].

Copyright 2011. Reprinted with permission from John Wiley & Sons.

producing a two-line spectrum, a so-called doublet in Mössbauer spectroscopy. This splitting is due to the electric field gradient around the nucleus [40,41].

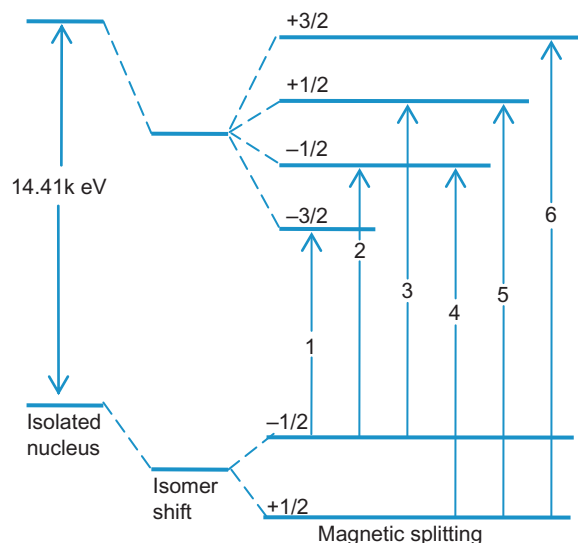
### 13.3.3 SURROUNDING MAGNETIC FIELD CAUSED HYPERFINE SPLITTING

The effect of the magnetic field on the magnetic dipole moment of the nucleus causes a dipolar interaction within the atoms [40,41]. This interaction provides information about magnetic properties of the materials. The splitting of atomic nuclear level with a spin of  $I$  into  $(2I + 1)$  will cause the transitions between the excited state and ground state only where  $m_I$  changes by 0 or  $\pm 1$ . This splitting is the so-called nuclear Zeeman effect. The hyperfine magnetic splitting will usually give six possible transitions, thus six lines in the Mössbauer spectra (sextet); such as those shown in Fig. 13.5 for  $^{57}\text{Fe}$  [41].

The splitting energy level is related to the line positions, and the intensities are a function of the angle between Mössbauer  $\gamma$ -ray and the nuclear spin moment. The Mössbauer spectrum is a characteristic of the combination of all these interactions including IS, QS, and magnetic splitting.

## 13.4 GENERAL APPLICATIONS OF MÖSSBAUER SPECTROSCOPY

A number of articles on the use of the Mössbauer spectroscopy for the analysis of the polymeric materials have been reported to achieve great success, especially

**FIGURE 13.5**

Energy-level diagram illustrating magnetic splitting in  $^{57}\text{Fe}$  [41].

Copyright 2011. Reprinted with permission from John Wiley & Sons.

for the characterization of some ferrogel samples. Kuzmanna et al. [42] reported the use of Mössbauer spectroscopy for the investigation of magnetite-loaded polyvinyl alcohol and polystyrol hydrogels. However,  $^{57}\text{Fe}$  Mössbauer spectra were taken at temperatures of 78, 150, and 290 K; it was discovered that at 78 K, the spectra can be decomposed to three sextets, and at 150 K, the spectra decomposed to two sextets. The spectra at 290 K gave a broad envelope collapse with magnetic splitting. In another development, this technique has provided a nondestructive measurement on atomic scale of the iron in biological function such as hemoglobin, myoglobin, and cytochrome [43]. Moreover, only an element of iron and iodine gives considerable possibility in the Mössbauer experiment of a biological nature. More importantly, the extreme dilution of the most available Mössbauer isotopes in the biological compound, poses some difficulty that may be encountered while using Mössbauer spectroscopy. Although this is an experimental problem that can be resolved [44].

The influence of the polymeric ligand nature on the structure of the polymer–metal complexes of poly(2-vinylpyridine), poly(2-methyl-5-vinylpyridine), poly(4-vinylpyridine), copolymers of vinyl imidazole, and vinylpyrrolidone with  $\text{Fe}^{3+}$  were studied with Mössbauer spectroscopy by Bekturov et al. [45]. However, the spectra revealed asymmetric doublets in all the metal complexes except in poly(2-vinylpyridine)- $\text{Fe}^{3+}$ , which contains one doublet. Furthermore, the IS and the QS for all poly(pyridine) indicates a coordination surrounding the

iron. In another experiment conducted by Ahmed et al., Mössbauer spectroscopy was used to study the structure of the nanoconfined metal oxide, and confirmed the synthesis of  $\text{CoFe}_2\text{O}_4$  nanoclusters exhibiting an inverse spinel structure [46]. The polymer complex shows a quadrupolar component at the center of the spectrum and a magnetically split component at the outer parts of the spectrum. At 4.2 K, the spectrum is completely magnetic and can be used to study the hyperfine structure of the nanoclusters.

As for the typical Mössbauer spectroscopy measurement: from the chemical formula of the substance under investigation one calculates the atomic density of iron. Then, having measured the size of the sample holder, one calculates the amount of substance to be packed in the sample holder, so that the surface density of iron is about  $10 \text{ mg cm}^{-2}$ , the optimal thickness of the  $^{57}\text{Fe}$  absorption experiment. The sample is powdered (if necessary), weighed, distributed evenly in the sample holder, sealed, and placed between the source and a detector. Then the spectrometer is set to produce a high-precision Doppler velocity modulation of the source  $\gamma$ -radiation. The effects of the Doppler velocity modulation on the absorption of  $\gamma$ -radiation are recorded synchronously in the 1024 channels of the multichannel analyzer. The result is 1024 numbers representing registered  $\gamma$ -quanta passing through the absorber under the condition of different Doppler velocities. A separate calibration procedure establishes the exact correspondence of channel velocity. Finally, the shape of the absorption spectrum is fitted to a theoretical model line shape, which is a superposition of singlets, doublets, and sextets ( $^{57}\text{Fe}$  case) in a Lorentzian shape using specialized computer programs. The result is tested by chi 2 criterion and the parameters of the fit—IS, QS, hyperfine magnetic field (HMF), and corresponding intensities are to be a subject of further analysis.

QS on Mössbauer spectra is a measure of the charge distribution asymmetry around the Fe nucleus. The nearest environment of an Fe nucleus is its own electron shells. A fully occupied shell has spherical symmetry and does not produce electric field gradient [47]. An HMF is induced in Fe nuclei when atomic spins are ordered and do not fluctuate. One observes a sextet in the Mössbauer spectrum with splitting proportional to the value of the hyperfine field on the nucleus [47]. The value of a hyperfine field is correlated to the atomic magnetic moment. The highest magnitude is observed in iron oxides about 500 kOe at room temperature. Metallic iron in  $\alpha$ -form shows a characteristic value of 330 kOe and in cementite about 210 kOe [47]. Spectral lines are pretty narrow (about  $0.25 \text{ mm s}^{-1}$ ) when all iron atoms are in the same condition. In composites, on the contrary, the local environment of iron atoms can vary. A typical example is the case of alloys. Iron atoms can have 6Fe, 5Fe1Ni, 4Fe2Ni, 3Fe3Ni, 2Fe4Ni, 1Fe5Ni, and 6Ni environments in the Fe–Ni alloy, so the magnetic condition is different and this contributes to sextets with different values of the hyperfine field. As a result, one observes a broad pattern built by multiple overlapping sextets in the Mössbauer spectrum.

## 13.5 ANALYSIS OF PNCs WITH MÖSSBAUER SPECTROSCOPY

This section uses several typical examples to demonstrate the powerful application of Mossbauer spectroscopy in semiquantitative analysis of PNCs, especially mPNCs.

### 13.5.1 STUDY OF mPNCs BY COMBINING TEM-SAED AND MÖSSBAUER SPECTROSCOPY

Usually, the study of Mössbauer spectra is necessary when XRD and XPS are not enough to precisely identify and determine the species of magnetic components in one polymer matrix. For example, in our previous work regarding the *in situ* synthesized polypropylene (PP)/iron oxide mPNCs [12], XRD can only show the characteristic peaks of the PP matrix without providing any useful information regarding the magnetic NPs in the mPNCs. The crystalline structure of the NPs was further identified from the comparison between the experimental and simulated transmission electron microscopy (TEM)–selected area electron diffraction (SAED) patterns. Mössbauer analysis was also used to justify the valence of iron in the NPs. The particle composition is examined by the consistence between the experimental and simulation results based on the SAED data. However, there are still differences between the experimental curve and the standard simulated  $\text{Fe}_2\text{O}_3$  pattern (Fig. 13.6a). To further confirm the particle composition, room-temperature Mössbauer spectrum analysis was conducted on the mPNCs with a particle loading of 20 wt% (Fig. 13.6b). The paramagnetic doublet observed in the center of the Mössbauer spectra, Fig. 13.6b (I), confirms the existence of

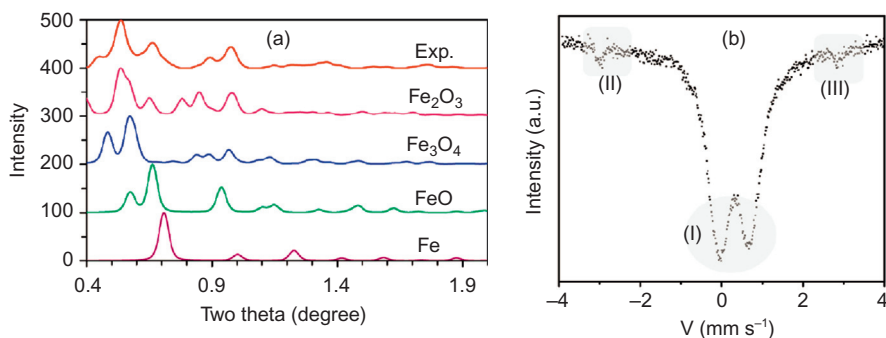


**FIGURE 13.6**

(a) Experimental and simulation results of the nanoparticles from transmission electron microscopy selected area electron diffraction patterns and (b) Mössbauer spectra of the polymer nanocomposites with particle loading of 20 wt% [12].

Copyright 2011. Reprinted with permission from American Chemical Society.

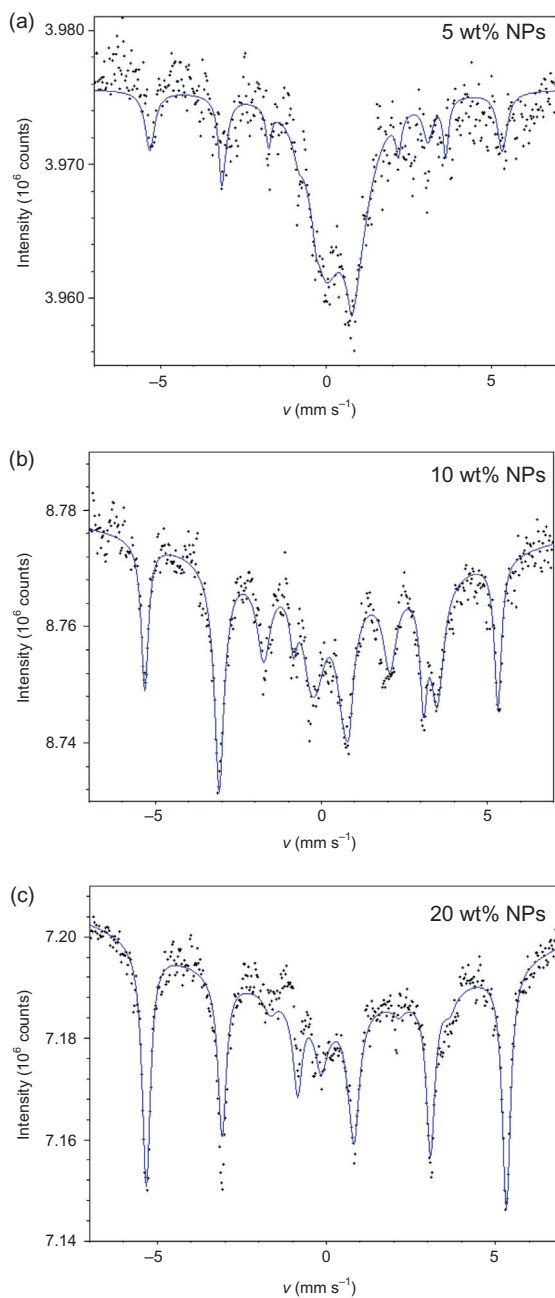
$\text{Fe}^{3+}$ , which corresponds to the superparamagnetic behavior of  $\text{Fe}_2\text{O}_3$ . The fitting results show a main component at  $\text{IS} = 0.35 \text{ mm s}^{-1}$  and  $\text{QS} = 0.80 \text{ mm s}^{-1}$ , which is  $\text{Fe}^{3+}$  in a paramagnetic state in the distorted oxygen octahedral site. Fig. 13.6b (II, III) depicts the secondary component with  $\text{IS} = 0$  and correspondent  $\text{H} = 335 \text{ kOe}$ , which represents a spectral contribution of 5%  $\alpha$ -Fe metallic magnetically ordered state. The aforementioned analysis justifies that the formed NPs have a chemical structure composed of an Fe core and  $\text{Fe}_2\text{O}_3$  shell.

### 13.5.2 QUANTITATIVE ANALYSIS OF IRON SPECIATION WITH MÖSSBAUER SPECTROSCOPY

As for the magnetic iron oxide core-shell NPs reinforced magnetic polyethylene (PE) PNCs, the composition identification of these magnetic NPs is difficult using XRD. After studying the Mössbauer spectrum of the as-synthesized PE mPNCs, it is clear that increased metallic iron percentage and changed iron chemical environments resulted upon increasing the magnetic component loadings (Fig. 13.7) [48]. Meanwhile, the chemical environment for each loading of mPNCs can also be identified in detail: at low iron loading, i.e., 5.0 wt%, the Mössbauer spectrum demonstrates a main component of 72% at IS of  $0.41 \text{ mm s}^{-1}$  and QS of  $0.88 \text{ mm s}^{-1}$ , which correspond to  $\text{Fe}^{3+}$  in a paramagnetic state in the distorted oxygen octahedral site. The second component is metallic iron (18%), as indicated by the other two symmetric peaks ( $\text{IS} = 0 \text{ mm s}^{-1}$  and  $\text{H} = 330 \text{ kOe}$ ). In addition, the final 10% iron is in the  $\text{Fe}^{2+}$  state at low spin magnetic state ( $\text{IS} = 0.23 \text{ mm s}^{-1}$  with  $\text{H} = 210 \text{ kOe}$ ) [48]. When particle loading increased from 5.0 to 10.0 wt%, Fig. 13.7b, the metallic iron percentage increased from 18% to 32% ( $\text{IS1} = 0 \text{ mm s}^{-1}$ ,  $\text{H1} = 330 \text{ kOe}$ ); and  $\text{Fe}^{3+}$  decreased to 21% ( $\text{IS2} = 0.28 \text{ mm s}^{-1}$ ,  $\text{QS2} = 0.86 \text{ mm s}^{-1}$ ); meanwhile,  $\text{Fe}^{2+}$  in the low-spin magnetic state increased to 47% ( $\text{IS3} = 0.19 \text{ mm s}^{-1}$ ,  $\text{H3} = 204 \text{ kOe}$ ). Similarly, the metallic iron further increased to 76% ( $\text{IS1} = 0 \text{ mm s}^{-1}$ ,  $\text{H1} = 330 \text{ kOe}$ ) with particle loading increased to 20.0 wt%, Fig. 13.7c; and  $\text{Fe}^{3+}$  decreased to 13% ( $\text{IS2} = 0.28 \text{ mm s}^{-1}$ ,  $\text{QS2} = 0.86 \text{ mm s}^{-1}$ ); and  $\text{Fe}^{2+}$  decreased to 11% ( $\text{IS3} = 0.18 \text{ mm s}^{-1}$ ,  $\text{H3} = 204 \text{ kOe}$ ) [48].

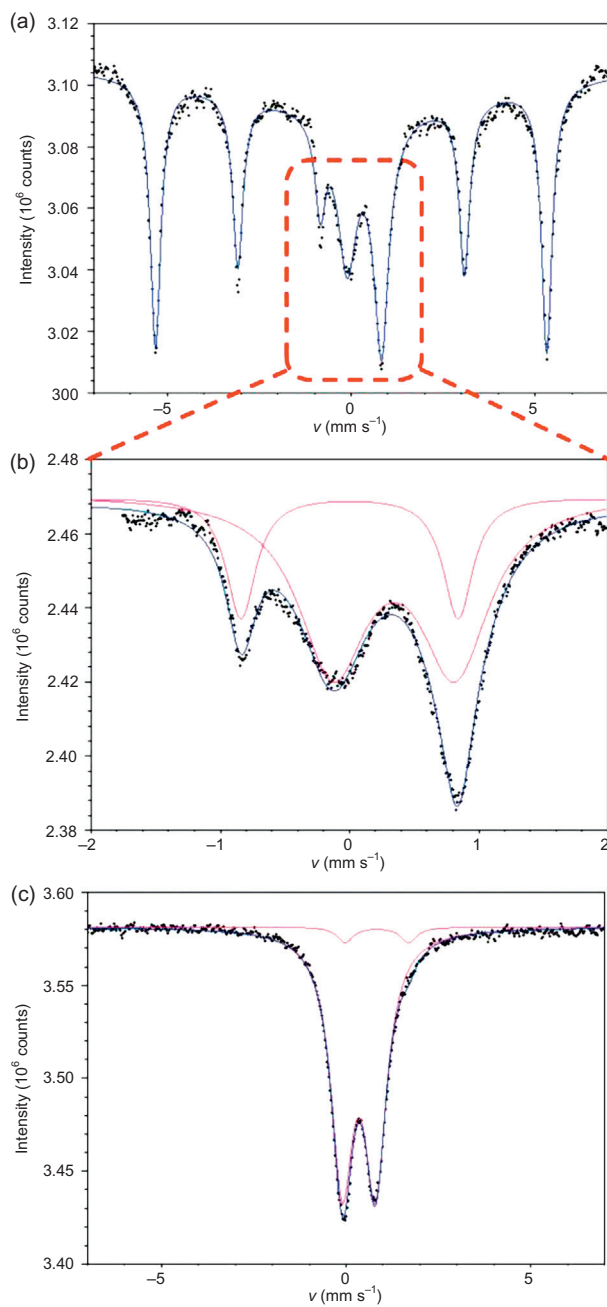
### 13.5.3 CHARACTERIZATION OF THE SURFACE LAYER OF IRON SPECIES WITH MÖSSBAUER SPECTROSCOPY

The Mössbauer spectra study can also be used to identify the surface protection of unstable iron NPs under air condition by different molecular weight surfactants. For example, the room-temperature Mössbauer spectrum of PP mPNCs-1 (with 20.0 wt% iron NPs protected by LM-PP, low molecular weight surfactant) shows a combination of one paramagnetic doublet in the center and one magnetically split sextet pattern (Fig. 13.8a and b). The curve-fitting results show the main component at IS of  $0 \text{ mm s}^{-1}$  and the corresponding HI of 330 kOe, which represents a 67% metallic iron in the magnetically ordered state [49]. Fig. 13.8b

**FIGURE 13.7**

Room-temperature Mössbauer spectra of high-density polyethylene nanocomposites with a particle loading of (a) 5.0, (b) 10.0, and (c) 20.0 wt%, respectively [48].

Copyright 2012. Reprinted with permission from Elsevier Ltd.

**FIGURE 13.8**

Room-temperature Mössbauer spectra of (a) nanoparticles (LM-PP)-PP, (b) enlarged spectrum of nanoparticles (LM-PP)-PP, and (c) nanoparticles (HMPP)-PP PNCs [49].

Copyright 2012. Reprinted with permission from Royal Society of Chemistry.

depicts the secondary component (33%) with IS of  $0.35 \text{ mm s}^{-1}$ , QS of  $0.91 \text{ mm s}^{-1}$ , which is  $\text{Fe}^{3+}$  in a paramagnetic state in the distorted oxygen octahedral site. On the other hand, the Mössbauer spectrum of PP mPNCs-2 (with 20.0 wt% iron NPs protected by HM-PP, high molecular weight surfactant), Fig. 13.8c, shows two paramagnetic doublet patterns consisting of a major component of  $\text{Fe}^{3+}$  (96%) with IS of  $0.34 \text{ mm s}^{-1}$ , QS of  $0.90 \text{ mm s}^{-1}$ , and  $\text{Fe}^{2+}$  (4%) as the secondary component with IS of  $0.83 \text{ mm s}^{-1}$ , QS of  $1.72 \text{ mm s}^{-1}$ . This observation indicates that iron was completely oxidized in the case of HM-PP stabilized mPNCs. The comparison demonstrates that the molecular weight of the maleic anhydride PP plays a significant role in determining the chemical composition of the synthesized magnetic NPs. The maleic anhydride functional groups have been covalently bonded to the particle surface leaving the PP tails behind along the radial direction of the NPs. The larger PP tail of HM-PP introduces significant steric hindrance on the NP surface and thus a lower packing density would be expected, which leaves more free volume at the PP–NPs interface facilitating the oxygen penetration. With a compact LM-PP grafting layer, less uncovered area of the NPs is exhibited at the interfacial area and thus the NPs would be better protected from oxidation, which is consistent with the observed less fraction of iron oxide in the NPs revealed by the Mössbauer spectrum (Fig. 13.8).

### 13.5.4 ANALYSIS OF MAGNETIC CARBON NANOSTRUCTURES WITH MÖSSBAUER SPECTROSCOPY

Mössbauer spectroscopy here is focused to characterize magnetic materials, thus carbon nanomaterials are not suitable candidates for this technique when used solely in polymer matrix. However, hierarchical nanostructures such as carbon nanotubes (CNTs) or graphene coated with magnetic NPs are widely reported for many applications. Here, CNTs surface coated with magnetic nanomaterials were used to further demonstrate the powerful usage of Mössbauer spectra for determining the chemical environments of the magnetic component when *in situ* grown on the CNTs with/without the aids of surfactant [50]. The spectra curves are shown in Fig. 13.9. When thermodecomposing  $\text{Fe}(\text{CO})_5$  is introduced directly into a PP matrix with the aid of surfactant polypropylene grafted with maleic anhydride, PP-g-MA (S), four components are observed (Fig. 13.9a), indicating the complexity of the magnetic NPs formed in the PP matrix: the majority of the iron is found to be in metallic Fe state (44%), as evidenced by IS of  $0 \text{ mm s}^{-1}$  and the hyperfine field (HI) of 329 kOe (29%), and IS of  $0.05 \text{ mm s}^{-1}$  with the HI of 320 kOe (15%). The surfactant and PP matrix can function as oxygen shielding for preventing the *in situ* formed iron against oxidization, however, the polymer chain cannot form a solid shell so that the iron NPs were further oxidized during the synthesis of the PP PNCs. Therefore, the  $\text{Fe}^{3+}$  in a distorted octahedral oxygen environment was observed as indicative of an IS of  $0.38 \text{ mm s}^{-1}$  and QS of  $1.20 \text{ mm s}^{-1}$  (Fig. 13.8a). Cementite was also found with IS of  $0.2 \text{ mm s}^{-1}$

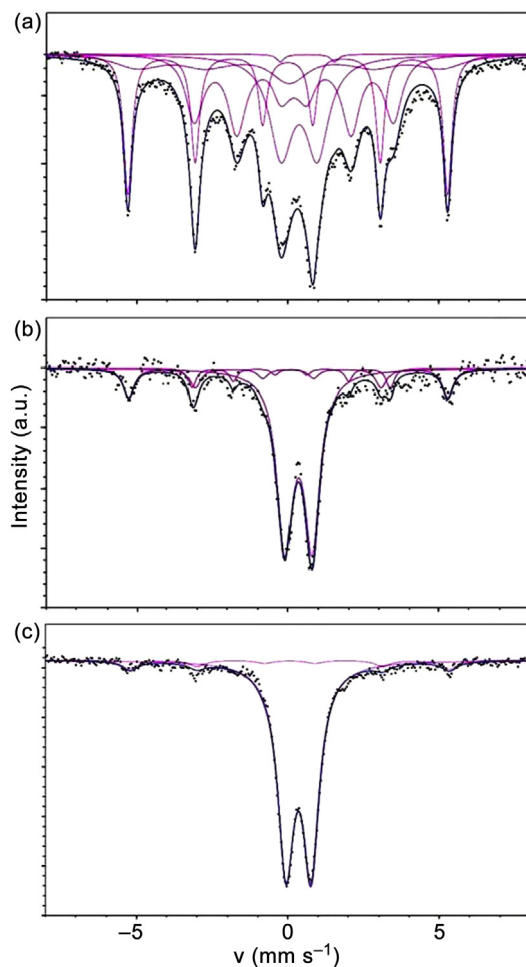


**FIGURE 13.9**

Mössbauer spectra of PP magnetic polymer nanocomposites with: (a) 5.0% PP-g-MA(S)/20.0% Fe, (b) 5.0% PP-g-A(S)/1.0 MWNTs/20.0% Fe, (c) PP/5.0% PP-g-MA (L)/1.0 MWNTs/20.0% Fe [50].

*Copyright 2014. Reprinted with permission from American Chemical Society.*

and its HI of 205 kOe. The last component (1%) located at an IS of  $0.65 \text{ mm s}^{-1}$  and QS of  $1.80 \text{ mm s}^{-1}$  (Fig. 13.9a) indicates the presence of  $\text{Fe}^{2.5+}$  in a distorted octahedral oxygen environment.

When the  $\text{Fe}(\text{CO})_5$  was thermally decomposed in the presence of multiwall CNTs (MWCNTs), the magnetic NPs decorated the MWCNTs and were formed in the PP matrix: Mössbauer spectrum in Fig. 13.9b further identifies three Fe chemical environments on the surface of MWCNTs: 74%  $\text{Fe}^{3+}$  in the distorted

octahedral oxygen environment (IS of  $0.35 \text{ mm s}^{-1}$  and QS of  $0.90 \text{ mm s}^{-1}$ ), 18% metallic Fe (IS of  $0 \text{ mm s}^{-1}$  with the corresponding HI of 329 kOe), followed by 8% cementite (IS of  $0.10 \text{ mm s}^{-1}$  and HI of 202 kOe). It thus suggests that more iron was oxidized from metallic state to  $\text{Fe}^{3+}$  after adding 1.0 wt% MWCNTs in the PP matrix.

Different Fe chemical environments are observed when the molecular weight of surfactant PP-g-MA was used in the PP matrix. Here, the Mössbauer spectrum in Fig. 13.9c indicates more oxidization took place when high molecular weight surfactant PP-g-MA (L) was used in the PP matrix when thermodecomposing 20 wt%  $\text{Fe}(\text{CO})_5$  in the presence of 1.0 wt% MWCNTs: 92%  $\text{Fe}^{3+}$  in the distorted octahedral oxygen environment (IS of  $0.35 \text{ mm s}^{-1}$  and QS of  $0.83 \text{ mm s}^{-1}$ ) and only 8% metallic Fe at IS of  $0.06 \text{ mm s}^{-1}$  with the HI of 327 kOe were observed. Hence, the molecular weight of PP-g-MA plays an important role on the oxidization of Fe NPs in the synthesized mPNCs. Other similar determinations of the surfactant molecular weight-affected iron composition in the PP/iron mPNCs were also reported [20]. With the aid of other characterization techniques, such as the combination of vibrating sample magnetometry and Mössbauer spectra, this technique can further be used to identify the crystalline structure of iron oxides [15]. Hence, it is clear that the Mössbauer spectra can provide the chemical environments quantitatively and qualitatively. It determines the specific type of magnetic species by providing its characteristic fingerprints in detail. However, the crystalline structures of magnetic iron-group materials may not able to be determined only by Mössbauer spectra, but in combination with other techniques, such as XPS and XRD, exact conclusions can be drawn for certain *in situ* formed magnetic nanostructures in a polymer matrix.

---

## 13.6 SUMMARY

In summary, the Mössbauer spectra are powerful tools to identify, determine, and quantify the chemical environments of iron-group species among different surrounding materials. The Mössbauer spectra is capable of showing the spin structure of iron species, which can be used to determine the chemical stability of iron-group nanostructures. The identification of iron-group species and the quantification of their composition allows researchers to better understand the formation pathway/evolution of the magnetic component in polymer matrix nanocomposites and their function mechanism in different applications.

---

## REFERENCES

- [1] Kommareddi NS, Tata M, John VT, McPherson GL, Herman MF, Lee YS, et al. Synthesis of superparamagnetic polymer–ferrite composites using surfactant microstructures. *Chem Mater* 1996;8:801–9.

- [2] Tang BZ, Geng Y, Lam JWY, Li B, Jing X, Wang X, et al. Processible nanostructured materials with electrical conductivity and magnetic susceptibility: preparation and properties of maghemite/polyaniline nanocomposite films. *Chem Mater* 1999;11:1581–9.
- [3] Tannenbaum R, Zubris M, Goldberg EP, Reich S, Dan N. Polymer-directed nanocluster synthesis: control of particle size and morphology. *Macromolecules* 2005;38:4254–9.
- [4] Guo Z, Henry LL, Palshin V, Podlaha EJ. Synthesis of poly(methyl methacrylate) stabilized colloidal zero-valence metallic nanoparticles. *J Mater Chem* 2006;16:1772–7.
- [5] Guo Z, Park S, Hahn HT, Wei S, Moldovan M, Karki AB, et al. Giant magnetoresistance behavior of an iron/carbonized polyurethane nanocomposite. *Appl Phys Lett* 2007;90:053111.
- [6] Guo Z, Lin H, Karki AB, Wei S, Young DP, Park S, et al. Facile monomer stabilization approach to fabricate iron/vinyl ester resin nanocomposites. *Composites Sci Technol* 2008;68:2551–6.
- [7] Guo Z, Lei K, Li Y, Ng HW, Prikhodko S, Hahn HT. Fabrication and characterization of iron oxide nanoparticles reinforced vinyl-ester resin nanocomposites. *Composites Sci Technol* 2008;68:1513–20.
- [8] Biswas S, Belfield KD, Das RK, Ghosh S, Hebard AF. Block copolymer-mediated formation of superparamagnetic nanocomposites. *Chem Mater* 2009;21:5644–53.
- [9] Zhu J, Wei S, Ryu J, Sun L, Luo Z, Guo Z. Magnetic epoxy resin nanocomposites reinforced with core-shell structured Fe@ FeO nanoparticles: fabrication and property analysis. *ACS Appl Mater Interfaces* 2010;2:2100–7.
- [10] Hickey RJ, Haynes AS, Kikkawa JM, Park SJ. Controlling the self-assembly structure of magnetic nanoparticles and amphiphilic block-copolymers: from micelles to vesicles. *J Am Chem Soc* 2011;133:1517–25.
- [11] Zhu J, Wei S, Li Y, Pallavkar S, Lin H, Haldolaarachchige N, et al. Comprehensive and sustainable recycling of polymer nanocomposites. *J Mater Chem* 2011;21:16239–46.
- [12] Zhu J, Wei S, Li Y, Sun L, Haldolaarachchige N, Young DP, et al. Surfactant-free synthesized magnetic polypropylene nanocomposites: rheological, electrical, magnetic, and thermal properties. *Macromolecules* 2011;44:4382–91.
- [13] Wei S, Wang Q, Zhu J, Sun L, Lin H, Guo Z. Multifunctional composite core-shell nanoparticles. *Nanoscale* 2011;3:4474–502.
- [14] Zhu J, Wei S, Lee IY, Park S, Willis J, Haldolaarachchige N, et al. Silica stabilized iron particles toward anti-corrosion magnetic polyurethane nanocomposites. *RSC Adv* 2012;2:1136–43.
- [15] He Q, Yuan T, Wei S, Haldolaarachchige N, Luo Z, Young DP, et al. Morphology and phase controlled iron oxide nanoparticles stabilized with maleic anhydride grafted polypropylene. *Angew Chem Int Ed* 2012;51:8842–5.
- [16] He Q, Yuan T, Yan X, Luo Z, Haldolaarachchige N, Young DP, et al. One-pot synthesis of size- and morphology-controlled 1-D iron oxide nanochains with manipulated magnetic properties. *Chem Commun* 2014;50:201–3.
- [17] He Q, Yuan T, Zhang X, Luo Z, Haldolaarachchige N, Sun L, et al. Magnetically soft and hard polypropylene/cobalt nanocomposites: role of maleic anhydride grafted polypropylene. *Macromolecules* 2013;46:2357–68.

- [18] He Q, Yuan T, Luo Z, Haldolaarachchige N, Young DP, Wei S, et al. Morphology and phase controlled cobalt nanostructures in magnetic polypropylene nanocomposites: the role of alkyl chain-length in maleic anhydride grafted polypropylene. *Chem Commun* 2013;49:2679–81.
- [19] Guo Z, Park S, Hahn HT, Wei S, Moldovan M, Karki AB, et al. Magnetic and electromagnetic evaluation of the magnetic nanoparticle filled polyurethane nanocomposites. *J Appl Phys* 2007;101:09M511.
- [20] He Q, Yuan T, Zhang X, Yan X, Guo J, Ding D, et al. Electromagnetic field absorbing polypropylene nanocomposites with tuned permittivity and permeability by nanoiron and carbon nanotubes. *J Phys Chem C* 2014;118:24784–96.
- [21] Goesmann H, Feldmann C. Nanoparticulate functional materials. *Angew Chem Int Ed* 2010;49:1362–95.
- [22] Howes P, Green M, Bowers A, Parker D, Varma G, Kallumadil M, et al. Magnetic conjugated polymer nanoparticles as bimodal imaging agents. *J Am Chem Soc* 2010;132:9833–42.
- [23] Zhu J, Gu H, Rapole SB, Luo Z, Pallavkar S, Haldolaarachchige N, et al. Looped carbon capturing and environmental remediation: case study of magnetic polypropylene nanocomposites. *RSC Adv* 2012;2:4844–56.
- [24] Qiu B, Guo J, Zhang X, Sun D, Gu H, Wang Q, et al. Polyethylenimine facilitated ethyl cellulose for hexavalent chromium removal with a wide pH range. *ACS Appl Mater Interfaces* 2014;6:19816–24.
- [25] Qiu B, Gu H, Yan X, Guo J, Wang Y, Sun D, et al. Cellulose derived magnetic mesoporous carbon nanocomposites with enhanced hexavalent chromium removal. *J Mater Chem A* 2014;2:17454–62.
- [26] Liu Z, Chen L, Zhang L, Poyraz S, Guo Z, Zhang X, et al. Ultrafast Cr (VI) removal from polluted water by microwave synthesized iron oxide submicron wires. *Chem Commun* 2014;50:8036–9.
- [27] Hoare T, Timko BP, Santamaria J, Goya GF, Irusta S, Lau S, et al. Magnetically triggered nanocomposite membranes: a versatile platform for triggered drug release. *Nano Lett* 2011;11:1395–400.
- [28] Zhu J, Chen M, Wei H, Yerra N, Haldolaarachchige N, Luo Z, et al. Magnetocapacitance in magnetic microtubular carbon nanocomposites under external magnetic field. *Nano Energy* 2014;6:180–92.
- [29] Zhao Y, Wei H, Arowo M, Yan X, Wu W, Chen J, et al. Electrochemical energy storage by polyaniline nanofibers: high gravity assisted oxidative polymerization vs. rapid mixing chemical oxidative polymerization. *Phys Chem Chem Phys* 2015;17:1498–502.
- [30] Wei H, Wang Y, Guo J, Yan X, O'Connor R, Zhang X, et al. Electropolymerized polypyrrole nanocoatings on carbon paper for electrochemical energy storage. *ChemElectroChem* 2015;12:119–26.
- [31] Chen W, Mørup S, Hansen MF, Banert T, Peuker UA. A Mössbauer study of the chemical stability of iron oxide nanoparticles in PMMA and PVB beads. *J Magn Mater* 2008;320:2099–105.
- [32] Morup S, Dumesic JA, Topsoe H. In: Cohen RL, editor. *Applications of Mössbauer spectroscopy*, vol. II. New York: Academic Press; 1980. p. 1.
- [33] Vandenberghe RE, De Grave E. In: Long GJ, Grandjean F, editors. *Mössbauer spectroscopy applied to inorganic chemistry*, vol. I. New York: Plenum Press; 1989. p. 59.

- [34] Murad E, Johnston JH. In: Long GJ, editor. Mössbauer spectroscopy applied to inorganic chemistry, vol. II. New York: Plenum Press; 1987. p. 533.
- [35] Czjzek G, Long GJ, Grandjean F. Mössbauer spectroscopy applied to magnetism and materials science, vol. 1. New York: Plenum Press; 1993. p. 373.
- [36] Borges JFM, Da Costa MI, Locatelli F, Molossi FA, Feldmann G, Toukhvatoulline R, et al. Mössbauer spectroscopic investigation of corrosion in commercial steel scrubbing and cleaning tools. *Hyperfine Interact* 1997;2:149–53.
- [37] Borge JFM, Tosin G, Schelp LF, Teixeira SR, Mosca DH, Schreiner WH. Structure and magnetoresistance of Fe/Cu superlattices grown on Si(111). *J Magn Magn Mater* 1993;121:53–6.
- [38] Diamant A, Pasternak M, Banin A. Characterization of adsorbed iron in montmorillonite by Mössbauer spectroscopy. *Clays Clay Miner* 1982;30:63–6.
- [39] Harrison PG, Phillips RC, Thornton EW. Temperature dependence of the Mössbauer recoil-free fraction as a probe of the lattice structure of Tin compound. *J Chem Soc Chem Commun* 1977:603–4.
- [40] Helsen JA, Goodman BA. Characterization of iron II and iron III, exchange montmorillonite and hectorite using the Mossbauer effect. *Clay Miner* 1983;18:117–25.
- [41] Fultz B. Mössbauer spectrometry. In: Kaufmann E, editor. *Characterization of materials*. New York: John Wiley & Sons; 2011.
- [42] Kuzmanna E, Homonnaya Z, Németha Z, Vértesa A, Gargb VK, Zrinyic M. A magnetite colloid system studied by Mössbauer spectroscopy. *American institute of physics conference proceedings* 2005;765:223.
- [43] Hoy GR, Cook DC, Berger RL, Friedman FK. Mössbauer spectroscopy studies of hemoglobin and its isolated subunits. *J Biophys* 1986;49:1009–15.
- [44] Akkara JA, Wang J, Yang DP, Gonsalves KE. Hematin-catalyzed polymerization of phenol compounds. *Macromolecules* 2000;33:2377–82.
- [45] Bekturov EA, Kudaibergenov SE, Kanapyanova GS, Saltbaeva S, Skushnikova AI, Pavlova AL, et al. Mössbauer spectroscopic studies of complexes of Fe<sup>3+</sup> with nitrogen containing polymer. *J Polym* 1991;23(4):339–42.
- [46] Ahmed SR, Kofinas P. Synthesis and magnetic properties of block CoFe<sub>2</sub>O<sub>4</sub> nanoclusters. *Materials research society symposium proceedings* 2001;661.
- [47] Goldanskii VI, Herber RH. *Chemical applications of Mössbauer spectroscopy*, vol. 66. New York: Academic Press; 1968.
- [48] He Q, Yuan T, Zhu J, Luo Z, Haldolaarachchige N, Sun L, et al. Magnetic high density polyethylene nanocomposites reinforced with *in-situ* synthesized Fe@ FeO core-shell nanoparticles. *Polymer* 2012;53:3642–52.
- [49] Zhu J, He Q, Luo Z, Khasanov A, Li Y, Sun L, et al. Property manipulated polypropylene–iron nanocomposites with maleic anhydride polypropylene. *J Mater Chem* 2012;22:15928–38.
- [50] He Q, Yuan T, Zhang X, Yan X, Guo J, Ding D, et al. Electromagnetic field absorbing polypropylene nanocomposites with tuned permittivity and permeability by nanoiron and carbon nanotubes. *J Phys Chem C* 2014;118(42):24784–96.

## 14

X-ray diffraction  
spectroscopy of polymer  
nanocomposites

**Abhilash Venkateshaiah, Rajender Nutenki and Suresh Kattimuttathu I**

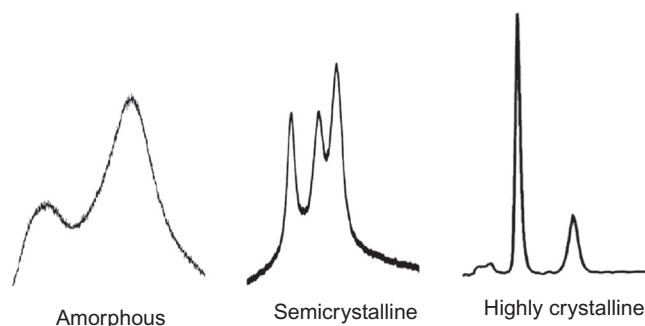
*Polymers & Functional Materials Division, CSIR-Indian Institute of Chemical Technology,  
Hyderabad, India*

## 14.1 INTRODUCTION

Polymer nanocomposites (PNCs) are hybrid materials of polymers combined with nanoparticles (NPs) or nanofillers dispersed in the polymer matrix. The nanocomposites exhibit substantial property improvements at small filler loadings due to the enormous surface area per unit volume that characterizes the nanofillers. The improvement has been observed in mechanical, electrical, optical, thermal, rheological, and the barrier properties. This is in contrast to the behavior of the traditional composite materials, where a much higher concentration of the fillers is typically employed. NPs of various shape, such as platelets, fibers, and spheroids, have been employed as filler in PNCs: the list includes nanoclays (primarily layered silicates), silica NPs, carbon nanomaterials, nanotubes, nanofibers, and many others. The performance of the nanocomposites is often controlled by further optimization of the NP surface chemistry to facilitate better dispersion of the NPs, stronger polymer–particle interactions, and better polymer adhesion on the NP. X-ray diffraction spectroscopy (XRDS) commands an important position in characterizing and optimizing these interactions. The versatile properties and applications exhibited by the polymeric nanocomposites, which are used in the form of plastics, films, coatings, and fibers, originate from their complex structural characteristics and filler polymer interactions.

X-ray diffraction (XRD) is a fundamental tool for material characterization and has been traditionally used to study the crystallographic materials including polymers, as shown in [Figure 14.1 \[1–10\]](#). The crystalline and amorphous structure of polymers, composites, and fillers has been conventionally studied with XRD.

The technique has gained popularity because of its simplicity, reliability, the quantitative information it provides, and its nondestructive nature. The technique has been used to explore the structure of bulk and thin film crystalline or polycrystalline materials on the atomic scale. Semiconductor industries use XRD to

**FIGURE 14.1**

Characteristic peaks for different polymer phases.

determine crystallite size, lattice strain, chemical composition, and crystal orientation. Biological samples such as DNA, vitamins, protein, and drug synthesis, use XRD to identify the elemental composition and their crystal structure. X-ray scattering provides structural information at three different length scales, such as 1, 10, and 100 nm, by performing scattering experiments at wide, small, and ultra-small angles, respectively.

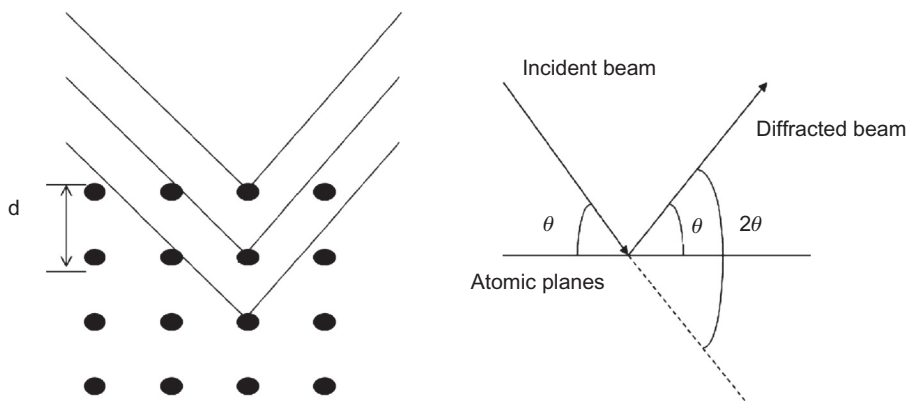
## 14.2 BASIC PRINCIPLES OF XRDS

Crystalline materials are characterized by a periodic arrangement of atoms. When irradiated with X-rays of fixed wavelengths, the electrons interact with the radiation and undergo an elastic collision to make them oscillate. The electron cloud acts as a secondary source to generate a coherent source of electromagnetic radiation at the same frequency and phase as that of the incoming X-ray. The radiation emitted from different atoms will undergo constructive or destructive interference. For constructive interference, the diffraction peaks are measured, recorded, and analyzed to calculate the desired set of crystal properties.

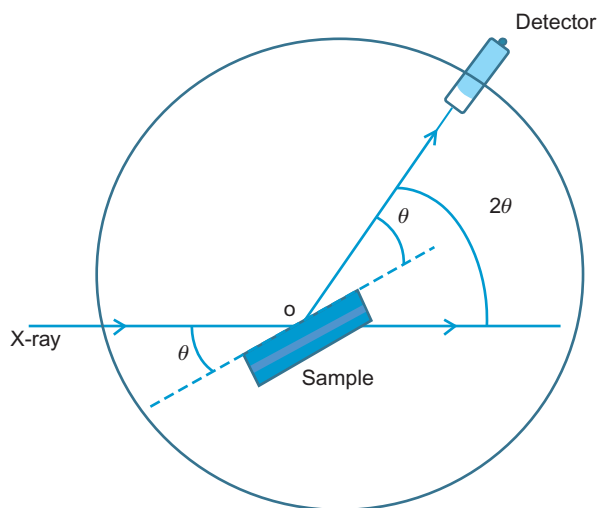
Constructive interference follows Bragg's law, while destructive interference disobeys the same. The process is schematically shown in Fig. 14.2, where the sample is exposed to an X-ray beam of wavelength ( $\lambda$ ) at an angle  $\theta$  with the tangential surface, which undergoes diffraction and is detected at an angle of  $2\theta$  represented as Eqn (14.1) here:

$$n\lambda = 2d \sin\theta \quad (14.1)$$

In Eqn (14.1),  $n$  is an integer,  $\lambda$  is the wavelength of the X-ray,  $d$  is the distance between the atomic planes, and  $\theta$  is the angle of scattering. Bragg's law is used to characterize the spacing between two consecutive crystallographic planes parallel to the surface of a film. A typical experimental setup used for XRD spectroscopy measurements is shown in Fig. 14.3.

**FIGURE 14.2**

X-ray diffraction principle.

**FIGURE 14.3**

Essential features of X-ray diffraction spectroscopy.

Experimentally, there are two methods of XRD, the Laue method, where  $\theta$  is kept constant and  $\lambda$  varied, and the powder diffraction method, where  $\lambda$  remains constant and  $\theta$  is varied. In both cases, intensity of the diffracted X-ray beam against diffraction angle  $2\theta$  is measured, which gives the diffraction pattern of the material. The pattern obtained in crystalline materials shows sharp maxima, called peaks, at their respective diffraction angle and in amorphous solids the orderly structure is absent, which gives rise to broad maxima called a hump, as shown in

**Fig. 14.1.** The different crystallographic planes in a crystal are characterized by the Miller indices (hkl), three integral numbers related to the reciprocal values of the intersection of a given plane with the crystallographic unit cell axes. When the investigated sample is a single crystal, the diffraction pattern consists of a series of spots, which are related to a particular plane in the crystal lattice. However, most materials do not appear as single crystals, but instead in a polycrystalline state, and therefore the diffraction spots transform into circles due to different orientation of the crystallites in the sample.

Since polymers are neither fully crystalline nor fully amorphous, the crystallinity is expressed in terms of a degree of crystallinity, which is a measure of the extent to which the material is crystalline. The widely used technique, wide-angle XRD (WAXD), is used to study the degree of crystallinity. The intensity of an X-ray scattered from the sample is the total area under the diffraction curve or pattern. The total intensity is divided into intensity of the diffracted beam from the crystalline part ( $I_c$ ) and intensity of the diffracted beam from the amorphous part ( $I_a$ ). The area under the sharply resolved peaks is the remaining area under the curve above the background. Then, the degree of crystallinity ( $Q$ ) is determined using the expression:

$$Q = \frac{I_c}{(I_c + I_a)} \quad (14.2)$$

The knowledge and understanding of the degree of crystallinity in polymers is vital to predict the properties and determine the application potential in various fields.

---

## 14.3 VARIANTS OF XRD SPECTROSCOPY

Wide-angle X-ray scattering (WAXS) or WAXD is the most widely used method to provide information on the crystallographic structure, atomic positions, and sizes in a unit cell, and, to some extent, chemical composition as well as chemical stoichiometry. The method specifically relies on the analysis of Bragg peaks scattered to wide angles, which implies that they are caused by nanosized structures. The diffraction pattern generated allows for the determination of chemical composition or phase composition of the film, and the crystallite size. The crystallite size is determined from XRD data with the help of the Debye–Scherrer equation:

$$L = \frac{K\lambda}{\beta(2\theta)\cos\theta} \quad (14.3)$$

In Eqn (14.3),  $\beta(2\theta)$  is the full width at half maximum,  $K$  is the shape factor depending on the Miller index of the reflecting plane and the shape of the crystal, and  $\lambda$  is the wavelength of the X-ray used. If the shape is unknown,  $K$  is often assigned a value of 0.9.

The technique is extended to smaller angles, typically from  $0.1^\circ$  to  $10^\circ$ , using the small-angle X-ray scattering (SAXS) method, where the elastic scattering of X-rays caused by nanoscale structures in the polymer is recorded. Using this method, information on structural units in the size range of 0.5–100 nm and possibly 1000 nm are obtained with a finely tuned instrument. From the angular distribution of scattered light intensity, information on the size, shape, pore sizes, and other characteristic distances of partially ordered materials are collected.

Since X-ray radiation has a large penetration depth, the technique is not surface sensitive. It becomes difficult to analyze thin films due to their small diffracting volumes, which result in low diffracted intensities compared with the substrate and background. In such cases, the glancing angle XRD or grazing incidence XRD (GIXRD) technique is used. GIXRD measurements are performed at very low angles to maximize the signal from thin layers. For the GIXRD, the incident and diffracted beams are made nearly parallel by means of a narrow slit. The stationary incident beam makes a very small angle with the sample surface, typically  $0.3\text{--}3^\circ$ , which increases the path length of the X-ray beam through the film and thereby increases the diffracted intensity from the sample, while reducing that from the substrate.

The XRD technique has been widely used for material identification, texture analysis, crystallinity determination, and several other miscellaneous applications [1–10]. However, in this chapter, our discussion is limited to the analysis of PNCs only, since it would be impossible to cover the entire usage of the technique in one chapter. Any discussion of PNCs is also invariably linked to the XRD data of the NPs, because a discussion of the pristine nanomaterial characteristics is essential to understand the XRD features of the PNC. Thus, in the following sections, our discussion of PNCs is classified on the basis of the filler type beginning with a brief introduction to the NPs. The application of newer techniques like SAXS and GIXRD will be discussed at the end of the chapter.

---

## 14.4 WIDE-ANGLE XRD

### 14.4.1 XRDS OF NPs

NPs are materials with structural features in the size range of 1–100 nm. They occupy an important place in the development of PNCs [11–14]. The most common examples are ZnO, TiO<sub>2</sub>, Ag, magnetite (Fe<sub>3</sub>O<sub>4</sub>), and silica NPs, and their XRD features are widely reported [15–23]. As a typical example, the XRD spectra of a ZnO NP and its nanocomposite are discussed here. The XRD spectra of ZnO NPs show highly crystalline peaks at  $2\theta$  values for  $36.61^\circ$ ,  $39.55^\circ$ ,  $41.45^\circ$ ,  $52.70^\circ$ ,  $61.56^\circ$ ,  $67.98^\circ$ , and  $73.13^\circ$ , corresponding to hkl planes 100, 002, 101, 102, 110, 103, and 112, respectively, as shown in Fig. 14.4. The appearance of these peaks in the nanocomposites indicates that there was no change in the crystalline structure of ZnO when it was incorporated into the polymer matrix [15].

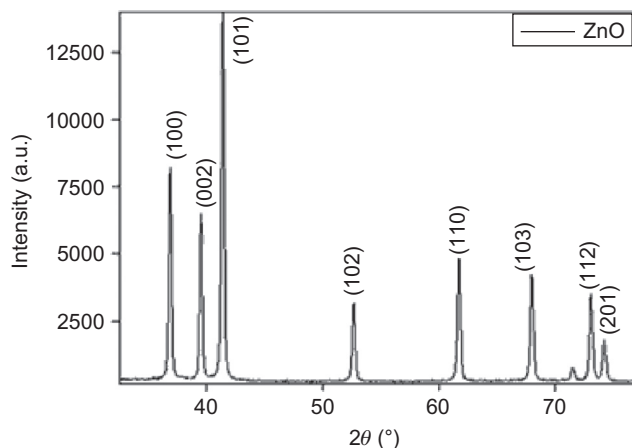


**FIGURE 14.4**

X-ray diffraction diffractogram of ZnO nanoparticles [15].

Copyright 2013. Reprinted with permission from Elsevier Ltd.

The improved properties of PNCs often result from the structure modification of the polymer by the nanosized particles. The nanomaterials have a characteristic microstructure dimension comparable to the critical length scales of physical phenomena that gives rise to the unique mechanical, optical, and electronic properties. Since the wavelength of X-rays is on the atomic scale, XRD is useful as a primary tool for probing nanomaterial structure. The NP structural characteristics and whether it possesses a crystalline, amorphous, or layered structure can be determined from XRD spectra. Layered NPs, like clay or graphite, are studied with XRD to determine the spacing between the orderly stacked layers. These two fillers are commonly subjected to surface modification to improve the interfacial interactions with the polymers, resulting in a change of the interlayer distance which can be monitored using XRDS. The NP exhibits some prominent peaks characteristic to their structure, which are generally used to confirm their existence in the composite. The peak position and intensity is monitored to determine the extent of dispersion or agglomeration of the NP in the composite. The general rule is that the higher the interlayer distance, the better the polymer penetration and associated properties.

### 14.4.2 XRDS OF PNCs

The PNCs offer an efficient and powerful strategy to upgrade the structural and functional properties of synthetic polymers. A large amount of literature is available using different combination of polymers and NPs to develop nanocomposites and study their properties and applications. The XRDS has been one of the major techniques employed to understand the effect of NPs in the modification of the

polymer structure. The application of XRDS for characterization of PNCs relies on how the basic characteristics of the polymer or the filler particles are affected and which can be conveniently probed by the technique. The NPs in a polymer matrix can act as nucleating agents, which increases the crystallinity of the composite, or act as an impurity that hinders the formation of the ordered structure. The crystal phase transformations brought about by the presence of the NPs can also be studied with XRD analysis. In the following sections, the application of the XRD technique to the structure–property correlation study of PNCs, based on the nanofiller type, are classified.

#### 14.4.2.1 Polymer clay nanocomposites

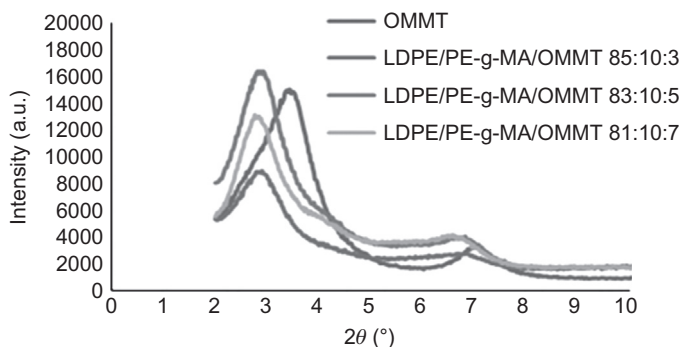
Polymer clay nanocomposites have attracted immense academic and industrial interest, beginning in the 1990s, due to their exceptional properties. The clays impart efficient reinforcement and improve properties, such as thermal stability, flame resistance, barrier properties, abrasion resistance, and also unique electrical, electronic, and optical properties [24–27]. Clay is a natural material available in various compositions and is widely used in nanocomposites [28–30]. The most commonly used are the smectite class of aluminum silicate clays, with montmorillonite (MMT) being a typical example. The crystal structure of MMT consists of a layer of octahedral aluminum hydroxide sheet sandwiched between two layers of tetrahedral silicon oxide sheets, represented by the general composition  $\text{Na}_{1/3}(\text{Al}_{5/3}\text{Mg}_{1/3})\text{Si}_4\text{O}_{10}(\text{OH})_2$ . The layer thickness of each platelet is of the order of 1 nm, and the lateral dimension is approximately 200 nm [30–31]. The clay platelets stacked over each other are held together through van der Waals forces and the interlayer regions are called galleries. These galleries are usually occupied by alkali and alkaline-earth cations such as  $\text{Na}^+$  and  $\text{K}^+$ . The intrinsic incompatibility between the hydrophilic clay particles and the hydrophobic polymer chains prevents good dispersion of clay NPs in the polymer matrix. For successful development of clay-based nanocomposites, it is necessary to chemically modify the naturally hydrophilic silicate surface to an organophilic one, so that the compatibility with the polymer matrix is improved. Normally, this is done through ion exchange reactions by replacing the interlayer cations with quaternary alkylammonium or alkylphosphonium cations. The modified clays are generally termed organoclays. The organoclays are much more compatible with the polymer chains and show a relative ease of dispersion and intercalation in the polymer matrix [32–34]. The XRD spectra of clays and organoclays exhibit a characteristic diffraction peak attributed to their unique layered structure. Changes in peak position, d-spacing, or peak intensity show the structural changes brought about by surface modification or with polymer intercalation. From the peak width at half height and peak position ( $2\theta$ ) of the XRD spectra, the interlayer spacing is calculated using Bragg's law. According to the Bragg law (Eqn (14.1)), increase of d-spacing results in broadening and shifting of the related XRD peak toward lower diffraction angles ( $2\theta$ ).

The XRD peaks of immiscible materials show no increase in the interlayer distance, indicating that the polymer molecules have not entered the galleries of the clay, while intercalated nanocomposites show an increase of the interlayer distance. The d-spacing increases with an increase in the amount of polymer chains entering the galleries. Sometimes, the exfoliated nanocomposites show no XRD peak at all, suggesting that a large amount of polymer molecules have entered the gallery resulting in large expansion of the clay layers so that no diffraction can be observed. The clay particles lose their orderly, layered structure and no XRD signal is observed. Other factors, such as concentration and order of the clay, also influence the XRD pattern of layered silicates. Many times the absence of a peak is misinterpreted as the exfoliated nanocomposite, but the reality is that the clay does not have any ordered structure for the diffraction to take place [35]. These observations are discussed in detail in the following literature.

Perez et al. [36] studied low-density polyethylene (LDPE) and organically modified MMT (OMMT) nanocomposites films. The X-ray diffractogram of the OMMT (Fig. 14.5) revealed an intense peak (001) at  $2\theta = 3.42^\circ$ , which is a characteristic peak of MMT modified with an alkyl group and gives a d-spacing of 25.8 Å. Samples with varied composition of LDPE, OMMT, and the compatibilizer PE-g-MA (maleic anhydride grafted PE) were prepared and analyzed by XRD.

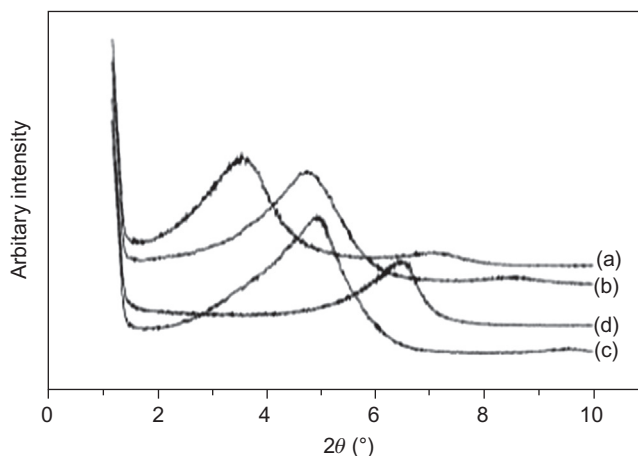
The nanocomposites showed a shift of the 001 peak to lower angle, and the d-spacing was accordingly increased from 25.8 to 30.7 Å. The peak shift was common in all studied systems, but in some cases, the peak intensity decreased. It was inferred that this reduction in peak intensity corresponds to the intercalated/exfoliated morphology of the obtained nanocomposites.

Wang et al. [37] also studied linear LDPE (LLDPE) using PE-g-MA to prepare the nanocomposites with clay. The clay (MMT) was modified using molecules of different alkylammonium chain lengths including octadecylamine (C18),



**FIGURE 14.5**

Typical X-ray diffraction patterns for organically modified montmorillonite (OMMT) and nanocomposites low-density polyethylene/maleic anhydride grafted polyethylene/OMMT prepared using the melt mixing technique [36].

**FIGURE 14.6**

X-ray diffraction patterns of organoclay modified by (a) C20, (b) C18, (c) C16, and (d) C12 [37].

Copyright 2001. Reprinted with permission from Elsevier Ltd.

hexadecylamine (C16), dodecylamine (C12), and a modifier with two long alkyl chains; dimethyl dehydrogenated tallow ammonium salt (C20). The XRD studies clearly revealed that the d-spacing of the clay increased with an increase in the chain length of the modifier. The d-spacing of the clay varied from 1.36 to 1.79 nm and then to 1.85 and 2.47 nm for C12, C16, C18, and C20 chain lengths, respectively, as shown in Fig. 14.6.

The modified clay was used in combination with maleated PEs of different maleic anhydride contents. The nanocomposites were analyzed by means of XRD. The effect of amount of maleated LLDPE and molecular weight of LLDPE in the LLDPE nanocomposites was also studied using XRD, as shown in Fig. 14.7.

The MA-g-LLDPE was used to enhance the compatibility of OMMT–LLDPE composites. For C20 and C18 composites the prominent clay diffraction peak completely disappeared with >0.1 wt% MA grafting. But for C16 (c.f. Fig. 14.7) a weak peak was observed at the same position as that of the clay regardless of the amount of grafted MA, indicating poor dispersion of clay in the polymer matrix. They observed that the MMT modified by C20 and C18 gives good intercalation with LLDPE, even in the absence of the compatibilizer MA but C16 fails to do so; this was confirmed as the XRD peaks in C20- and C18-modified clays shifted to lower angles compared to that of pure clays, but in the case of C16 no peak shift was observed. The X-ray diffractogram of nanocomposites having LLDPE with varying molecular weights were analyzed and it was observed that there was no significant change in the diffraction peaks indicating that the molecular weight of LLDPE does not play any role in the intercalation of clay [37].

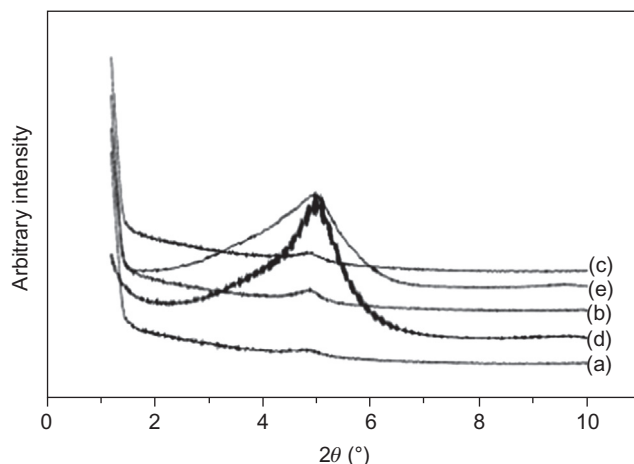


**FIGURE 14.7**

X-ray diffraction patterns of hybrids of C16 and React-maleic anhydride (MA) grafted polyethylene with various MA grafting levels prepared by reactive extrusion with MA contents (a) 0.33%, (b) 0.29%, (c) 0.22%, (d) pure linear low-density polyethylene, and (e) C16 only [37].

*Copyright 2001. Reprinted with permission from Elsevier Ltd.*

Polypropylene (PP)–clay nanocomposites with 4% and 8% loading was studied by Singala et al. [38]. The clay was modified with two organic modifiers: octadecylamine (OA) and methyl dihydroxyethyl hydrogenated tallow ammonium (TA). The extent of nanoclay distribution in the prepared nanocomposites was analyzed by XRD, as shown in Fig. 14.8.

The X-ray diffractograms showed that clay modified with OA has lower d-spacing than clay modified with TA, but in the nanocomposites the OA-modified clay has higher d-spacing than nanocomposites with TA. This confirmed that the modifying agent used in clay plays an important role during intercalation of the clay in the polymer matrix. The modifier TA has longer chain length, which might hinder the free movement of polymer chains in the interlayer region of clay and intercalate it. They also observed that the ethylene propylene copolymer was more effective than PP alone, and the d-spacing decreased marginally from 4.4 to 4 nm with increase of clay loading from 4% to 8%, for both isotactic PP and atactic PP [38].

The crystal transformation and thermomechanical properties of polyvinylidene fluoride (PVDF)/clay nanocomposites were reported by Pramoda et al. [39]. The XRD spectra of the nanocomposite revealed a diffraction peak at  $2\theta = 3.9^\circ$  that disappeared in the nanocomposites with 1% and 2% clay loading but reappeared with 5% clay loading. The peak disappearance corresponds to the good dispersion of clay within the polymer matrix. The nanocomposites also showed a new diffraction peak at  $2\theta = 20.7^\circ$ , whose intensity increased with the increase of the

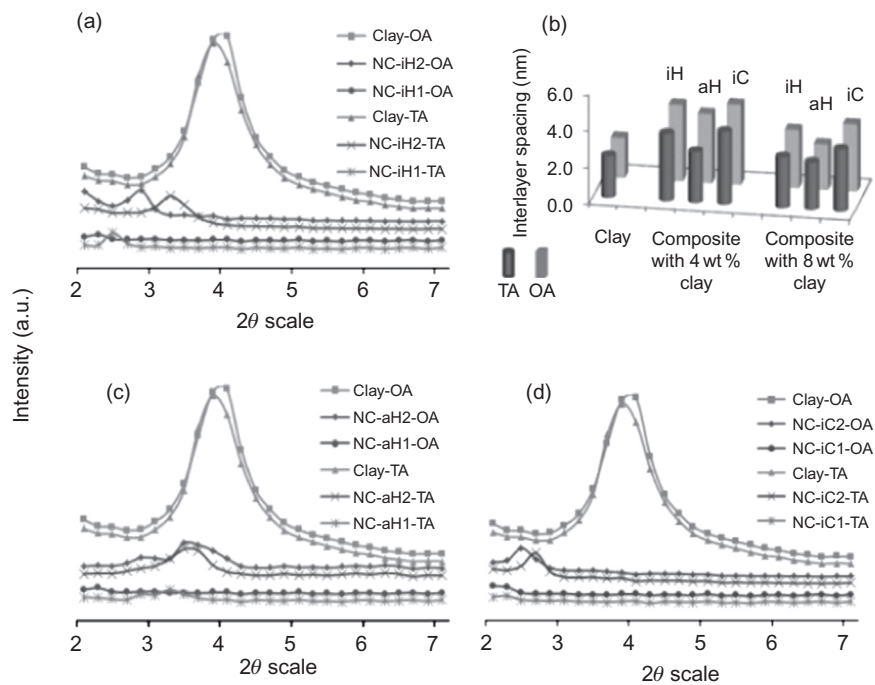


**FIGURE 14.8**

X-ray diffraction pattern of polypropylene (PP)—clay nanocomposites prepared from different organic modifications and clay loadings: (a) with isotactic homo PP, (b) interlayer spacing of clay in nanocomposites, (c) with atactic homo PP, and (d) with ethylene propylene copolymer [38].

Copyright 2012. Reprinted with permission from American Chemical Society.

clay loadings. This is attributed to the PVDF crystal transformation taking place due to the addition of clay in the polymer matrix. At clay loading of 1%, a peak at  $2\theta = 20.7^\circ$  corresponding to the  $\beta$  crystal form of PVDF was observed, which became prominent with an increase in the clay loadings to 2–5%. At the same time, the peak intensity corresponding to the  $\alpha$  form of PVDF decreased. The clay added to the polymer matrix acts as a nucleation site for the crystal transition, which leads to the crystal transformation of PVDF from  $\alpha$  to the  $\beta$  form.

The effect stretching on the crystal structure of PVDF—clay nanocomposite was also studied using XRD. The diffractogram (Fig. 14.9b) showed only one significant peak at  $2\theta = 20.4^\circ$ , corresponding to the  $\beta$  crystal form of PVDF, whereas the peaks corresponding to the  $\alpha$  form were absent or negligible. The stretched nanocomposites showed that the intensity of the prominent clay peak at  $2\theta = 3.5^\circ$  increased due to the formation of an ordered structure in the clay. The XRD observations thus confirmed that inclusion of clay, as well as stretching, has a significant effect on the crystal transformation [39]. The effects of hybrid fillers

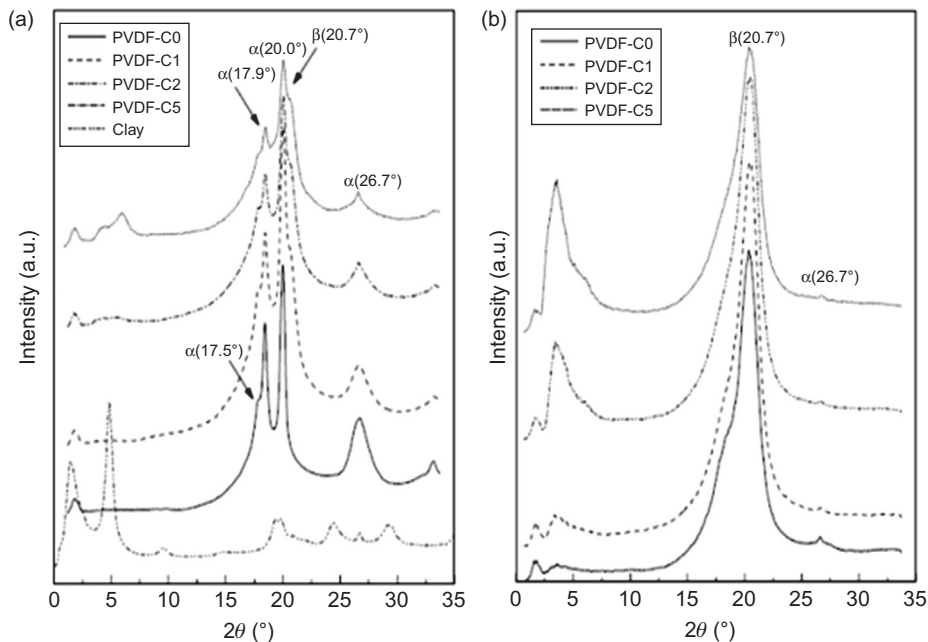


**FIGURE 14.9**

X-ray diffraction pattern of polyvinylidene fluoride and its nanocomposites: (a) unstretched and (b) stretched [39].

Copyright 2004. Reprinted with permission from John Wiley & Sons.

in PNCs have also been studied by XRDS. For example, Spoljaric et al. [40] studied MMT in combination with nanofibrillated cellulose (NFC), to prepare a hybrid nanocomposite of poly(vinyl alcohol) (PVA), which exhibited superior barrier and thermomechanical properties.

The XRD spectra of OMMT showed a strong narrow peak at  $2\theta = 7.64^\circ$  with an interlayer spacing of  $11.56 \text{ \AA}$ , which was absent in PVA–NFC–clay 0 and PVA–PAA–NFC–clay 0 nanocomposites, indicating the absence of the ordered structure of clay NPs in these nanocomposites. The nanocomposites displayed a prominent MMT peak at lower  $2\theta$  values with increased interlayer d-spacing (Fig. 14.10). This is due to the exfoliation of clay NPs by the polymer chains via ionic interactions between the hydroxyl groups present in PVA and NFC with the surface ions on the nanoclay. These results were also in agreement with the work reported by Cyras et al. [41]. The nanocomposite with 5% clay loading showed the least interlayer distance of  $15.62 \text{ \AA}$  in PVA–NFC and  $16.59 \text{ \AA}$  for PVA–NFC–PAA. The XRD peak shifted toward higher  $2\theta$  values with increase of clay loading, indicating that clay is not readily intercalated by the polymer chains because of the higher availability of clay per unit volume. The d-spacing in polyacrylic acid PAA crosslinked nanocomposites was found to be higher when

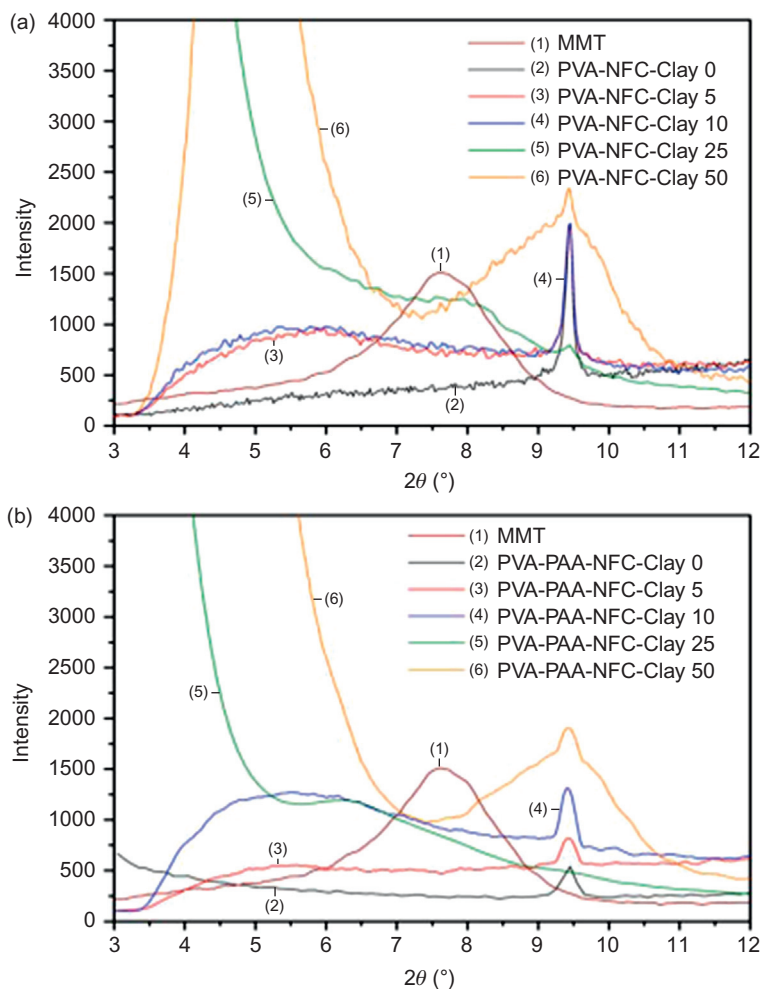


**FIGURE 14.10**

X-ray diffraction patterns of (a) poly(vinyl alcohol)–nanofibrillated cellulose–clay nanocomposites, (b) poly(vinyl alcohol)–polyacrylicacid–nanofibrillated cellulose–clay nanocomposites [40].

*Copyright 2013. Reprinted with permission from John Wiley & Sons.*

compared with the non-crosslinked one. This was attributed to the ability of PAA to exfoliate nanoclay through hydrogen bonding between the carbonyl groups of PAA and hydroxyl groups in clay, reducing the van der Waals forces of attraction between clay layers and helping in the dispersion of the clay [40]. Polyacrylate (PAC)–nanoclay composites were studied by Malin et al. [42] for anticorrosion applications, where the MMT was modified with quaternary ammonium salt.

The X-ray diffractogram of MMT clay (Fig. 14.11) showed a peak at  $2\theta = 4.72^\circ$ , with an interlayer distance of 1.87 nm but in the case of nanocomposites with PAC, the peak shifts to  $2\theta = 2.44^\circ$ , corresponding to an interlayer distance of 3.61 nm and suggesting that the polymer chains have entered the interlayer region of the clay. From XRD studies it was also confirmed that the concentration of clay did not affect the interlayer distances of the nanocomposite. Malin et al. observed that with 1% clay loading, the d-spacing was 3.61, 3.66 nm with 2% clay loading, and 3.76 nm ( $37.6^\circ\text{A}$ ) at 4% clay loading. However, these results are in contrast to the previous study which reported that the clay loading influenced the intercalation of the clay [42].

Unnikrishnan et al. [43] studied polysulfone (PSU)–clay nanocomposites by XRD. In this study, MMT modified with methyl dehydrogenated tallow quaternary ammonium salt (Cloisite 93A) and methyl tallow bis-2-hydroxyethyl quaternary ammonium salt (Cloisite 30B) was used as clay modifier. The prepared membranes were analyzed using WAXD, shown in Fig. 14.12, to study the d-spacing of the clay.

XRD studies showed that the Cloisite 30B showed a diffraction peak at  $2\theta = 5.8^\circ$  with a d-spacing of 18.5 Å, whereas Cloisite 93A showed a diffraction peak at  $2\theta = 3.62^\circ$  with an interlayer spacing of 24.4 Å. These results again confirmed that the chemical compound used to modify the MMT also affects the

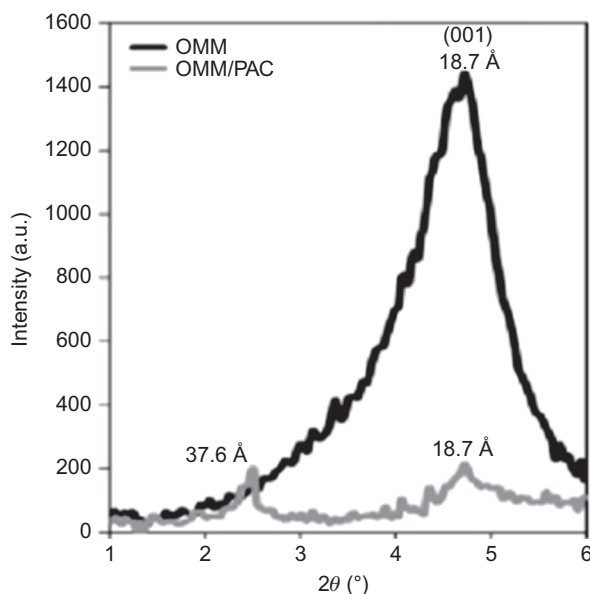


**FIGURE 14.11**

X-ray diffraction diffractograms of pure organically modified montmorillonite (OMMT) and 4% OMMT in polyacrylate [42].

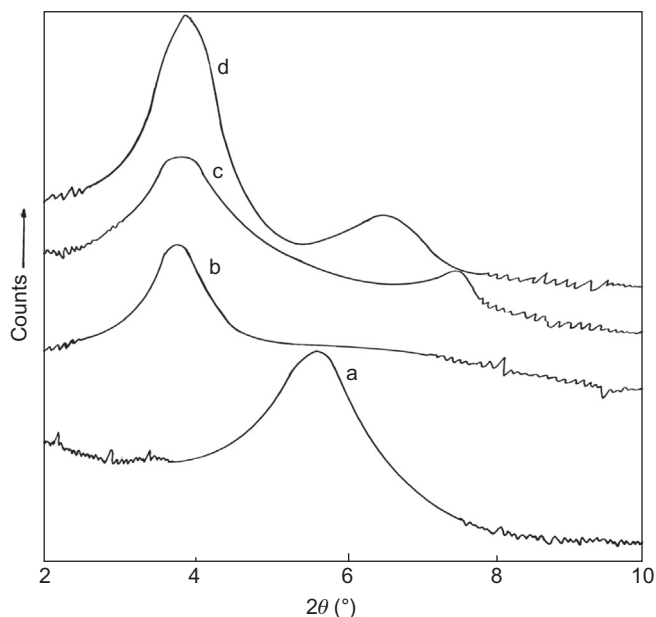


**FIGURE 14.12**

X-ray diffraction patterns of (a) Cloisite 30B, (b) Cloisite 93A, (c) polysulfone (PSU) + 1% Cloisite 30, and (d) PSU + 1% Cloisite 93A [43].

Copyright 2012. Reprinted with permission from John Wiley & Sons.

d-spacing of the clay. The nanocomposite with 1% Cloisite 30B shows a diffraction peak at  $2\theta = 2.63^\circ$ , with a d-spacing of  $24.3 \text{ \AA}$ . The shift of the XRD peak from  $5.8^\circ$  to  $2.63^\circ$  is due to intercalation of clay by the polysulfone chains and results in an increase of the d-spacing from  $18.5$  to  $24.3 \text{ \AA}$  (Fig. 14.12). In case of Cloisite 93A there is not much change in the diffraction peaks, indicating that morphology of the clay particle does not change much. The intercalation of Cloisite 30B with PSU can be due to the interaction between the hydroxyl groups present in the Cloisite 30B and the polymer matrix [43].

Thus, the literature reviewed previously on the XRD study of polymer–clay nanocomposites reveals the filler distribution in the clay–PNCs. With increase in the interlayer distance of the clays in the polymer matrix, the intercalation of clay by polymer chains also increases. The characteristic clay peak shifting to lower  $2\theta$  values and a decrease in intensity of the peak might also mean that the polymer chains have successfully intercalated the clay NPs. The XRD studies further confirm that the effect of different modifiers used in the clay plays a very important role in the intercalation of the polymer, apart from the type of polymer matrix used.

However, there are also contradicting results reported on the effect of clay loadings on the extent of clay intercalation. The work carried out by Singala et al. [38] as well as by Spoljaric et al. [40] reported that an increase of clay loading

reduces the intercalation because of the increased availability of clay NPs per unit volume. This phenomenon has also been observed in other polymer clay nanocomposites [44–45]. However, studies by Malin et al. support the theory that the clay loading has no effect on the intercalation of the clay. This theory was also supported by other research groups [46–47]. Thus, more studies are necessary to get conclusive results on the contradictory observations. However, the general agreement is that the addition of clay NPs produces nanocomposites with increased barrier, thermal stability, and mechanical properties through other thermomechanical property measurements.

#### 14.4.2.2 Silica–PNCs

Silica/PNCs are an important class of organic/inorganic hybrid nanocomposites with several potential applications ranging from aerospace materials, structural materials, electronics, sensors, and in other areas [48–54]. Silica nanocomposites usually contain dense silica particles dispersed within a polymer matrix. The addition of rigid silica particles to a polymer matrix results in an increase of strength, modulus, and thermal stability of the composite.

The effect of silica on the polymer matrix was extensively studied by XRD spectroscopy. Xu et al. [55] studied the polyamide 6 (PA6)–silica nanocomposites and observed that the X-ray diffractogram of the nanocomposite showed signal at  $2\theta = 19^\circ$  and  $23^\circ$ , assigned to the  $\alpha$  crystalline form, and at  $2\theta = 21^\circ$ , corresponding to the  $\gamma$  crystalline form of PA6 (Fig. 14.13). The nanocomposite showed a weaker  $\alpha$  crystalline form and a stronger  $\gamma$  crystalline form than pure PA6.

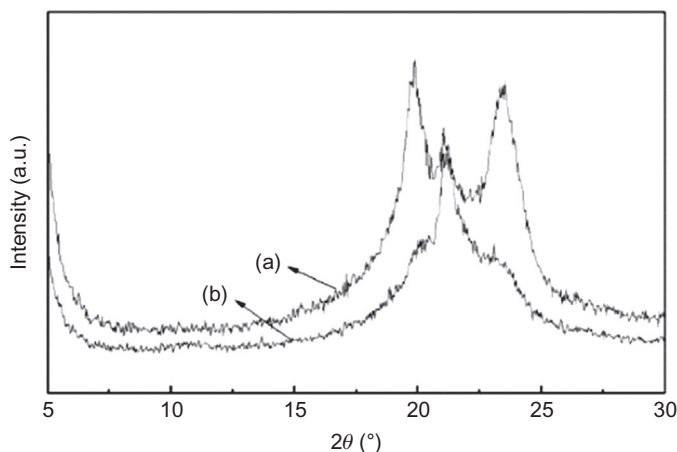


**FIGURE 14.13**

X-ray diffraction patterns of (a) polyamide 6 (PA6) and (b) PA6–silica (0.5%) nanocomposite [55].

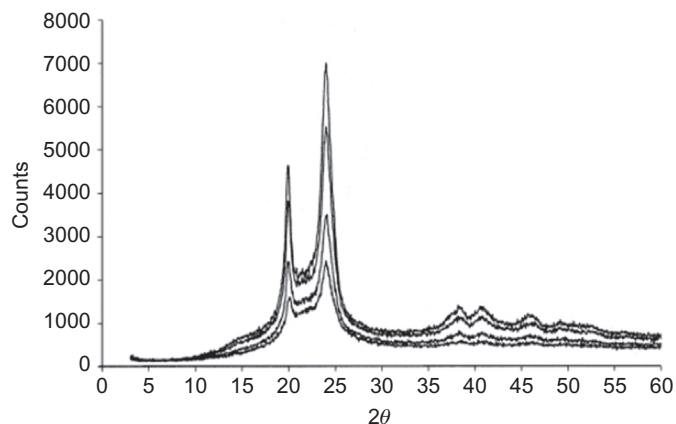


**FIGURE 14.14**

X-ray diffraction patterns of pure polyamide 6 (PA6) having a spectrum of highest intensity and PA6–silica nanocomposites in decreasing order of intensity with the addition of 3, 15, 30 wt% silica [56].

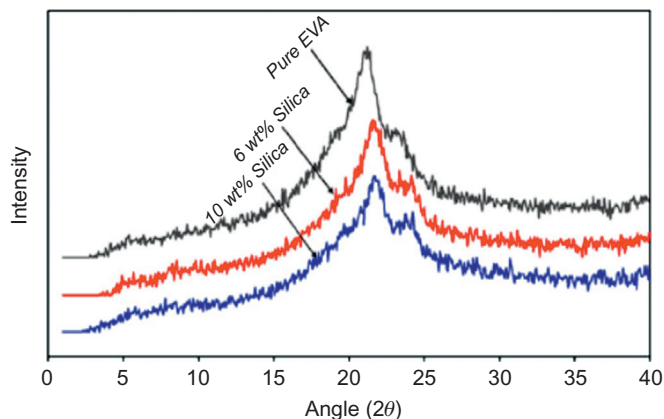
*Copyright 2002. Reprinted with permission from John Wiley & Sons.*

The results were attributed to the increase in viscosity of the reaction system with the addition of silica that reduces the molecular movement of the polymer chains. The  $\gamma$  crystalline form is helpful to improve the toughness of the nanocomposite [55]. Another study on PA6 and silica nanocomposites was reported by van Zyl et al. [56]. The nanocomposites' crystallinity as a function of wt% of silica added was studied with the help of XRD as shown in Fig. 14.14.

They observed that PA6 was semicrystalline whereas the silica was amorphous with no distinct peaks. The diffractogram also showed that, even with the lowest amount of silica addition (3 wt%), the crystallinity of the PA6 reduced and continued to decrease further with increase of the silica concentration as indicated by the reduced peak heights (Fig. 14.14) [56].

Sadeghi et al. [57] studied the ethylene vinyl acetate (EVA)–silica nanocomposites using XRD because the polymer was crystalline. The XRD pattern of the nanocomposite shown in Fig. 14.15 shows a sharp narrow peak at  $2\theta = 21.2^\circ$ , corresponding to its crystalline form of EVA.

The addition of silica to EVA produced no significant shift of the peak position for 6 and 10 wt% silica, but the peak intensity was comparatively lower than that of pure EVA, suggesting a decrease in the crystallinity. The crystallinity of the nanocomposite was measured by calculating the area under the curve and normalized based on the peak area of pure polymer. This decrease in crystallinity and increase of the amorphous nature was found to be directly proportional to the silica content in the nanocomposite (Fig. 14.15). The crystallinity dropped by 17% with 6 wt% silica and 19% with 10 wt% silica, when compared to pure EVA [57]. Similar results were also reported by Chen et al. [58] in silica–PVA nanocomposites.

**FIGURE 14.15**

X-ray diffraction patterns of pure ethylene vinyl acetate (EVA) and EVA–silica nanocomposites [57].

Copyright 2008. Reprinted with permission from Elsevier Ltd.

In a related study on PVA–silica nanocomposites carried out by Peng et al. [59], negatively charged silica NPs were used as templates to adsorb positively charged polyallylamine hydrochloride chains via electrostatic interactions onto which the PVA molecular chains were assembled through hydrogen bonding between the hydroxyl groups of PVA and amino groups of polyallylamine hydrochloride.

The XRD diffractograms of PVA nanocomposites and that of pure PVA were analyzed. The PVA showed a peak corresponding to the main crystalline peak at  $2\theta = 18.8^\circ$  (Fig. 14.16). The addition of silica NPs caused the crystalline peak of PVA to become broader and the intensity also reduced, indicating a decrease in the crystallinity of the nanocomposite. The crystallinity of PVA is basically attributed to the presence of hydrogen bonding between its hydroxyl groups. The addition of silica to the PVA matrix caused a decrease of the intermolecular interaction. Another peculiar feature observed was that, at very low silica particle loading, there was an increase in the crystallinity of the PVA, attributed to the fact that the NPs might be acting as a heterogeneous nucleating agent during crystallization [58,59]. These studies show that XRD studies of silica PNCs basically rely on following the crystallinity variation of the polymer matrix, which increases or decreases as a function of the silica content.

### 14.4.2.3 Carbon nanotube PNCs

Nanostructured carbon materials of various size and shape have been studied as important reinforcements in the development of PNCs. The earliest of these, fullerenes, were developed in 1985. The CNTs, which are covalently bonded carbon

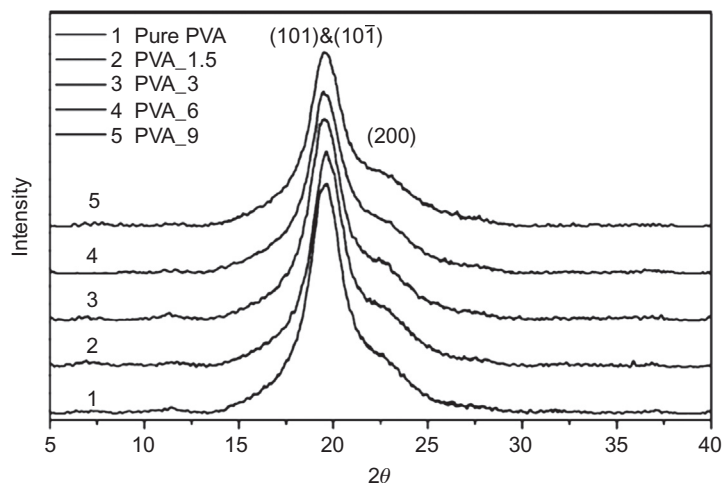


**FIGURE 14.16**

X-ray diffraction patterns of pure silica, pure poly(vinyl alcohol) (PVA), and PVA/silica nanocomposites with 0.5%, 5%, and 10% silica [58].

*Copyright 2010. Reprinted with permission from American Chemical Society.*

atoms organized in the form of a cylinder, are another important NP from the carbon family. CNTs were first reported by Iijima [60] in 1991 and caught the attention of many researchers because of their high flexibility [61], low mass density [62], high tensile modulus [63], high tensile strength [64], and unique combination of mechanical, electrical, and thermal properties. Basically, there are two types of CNTs: single-walled CNTs (SWCNTs) which are considered as a single sheet of  $sp^2$  hybridized carbons rolled into a seamless cylinder and multi-walled CNTs (MWCNTs), which are considered as cylinders coaxially arranged around a hollow core with interlayer separations. These nanotubes are ideal fillers in the preparation of multifunctional PNCs [65–66]. The properties of PNCs containing CNTs depends on several factors, such as the polymer type, synthetic process used to produce nanotubes, nanotube purification process, amount and type of impurities in the nanotubes, diameter, length, and aspect ratio of the nanotube objects in the composite (isolated, ropes, and/or bundles), and nanotube orientation in the polymer matrix. Two critical issues associated with translating or transferring the unique properties of CNTs to a polymer matrix are that nanotubes must be uniformly distributed and dispersed throughout the polymer matrix, and that there must be an enhanced interfacial interaction/wetting between the polymer and the nanotubes. Thus, there have been several reports on the surface modifications of the nanotubes [67–68].

XRD methods offer structural information on different length scales in going from SWCNT to MWCNT. The SWCNT–PNCs are hierarchically organized materials. Understanding the macroscopic properties in terms of microscopic models

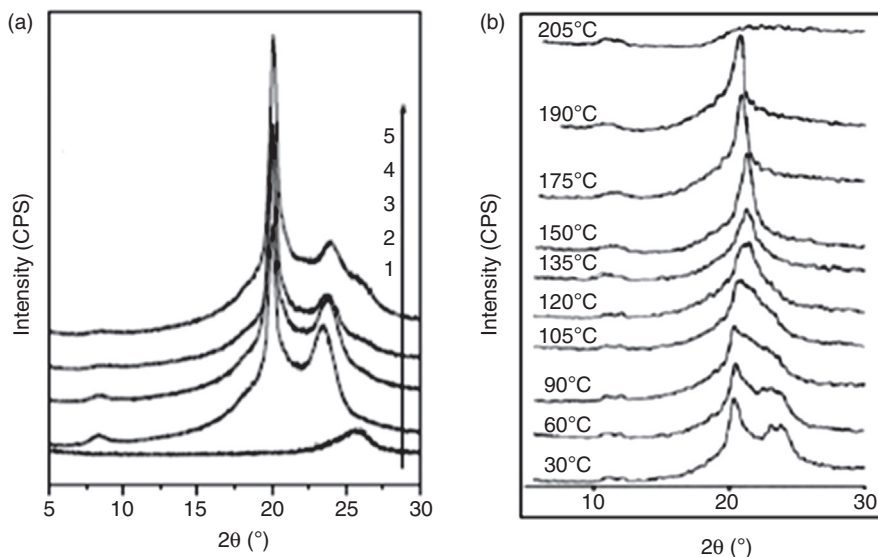


**FIGURE 14.17**

(a) Wide-angle X-ray diffraction (WAXD) patterns of (1) multiwalled carbon nanotube (MWCNT)-COOH, (2) polyamide (PA) + 1% MWCNT, (3) PA + 5% MWCNT, (4) PA + 10% MWCNT, (5) PA + 20% MWCNT at room temperature. (b) WAXD patterns at different temperatures of neat PA1010 [69].

Copyright 2006. Reprinted with permission from Elsevier Ltd.

requires an analysis of the characteristic order appearing on different length scales. Here, X-ray scattering methods offer crucial information about the level CNT dispersion as detailed in the following paragraphs.

Zeng et al. [69] prepared polyamide (PA) 1010 and MWCNT nanocomposites to study the crystallization behavior using XRD. The crystalline transitions observed in the nanocomposites were analyzed via XRD. The PA exhibits two crystal forms, the  $\alpha$  and  $\gamma$  forms. The  $\alpha$  form of the crystal has diffraction peaks at  $2\theta = 20^\circ$  and  $24^\circ$  (corresponding to 100,010/110 reflections), and the  $\gamma$  form was represented by the peak at  $2\theta = 22^\circ$  in the WAXD pattern. The nanocomposites showed peaks at  $2\theta = 20^\circ$  and  $24^\circ$ , suggesting that all the composites only exhibit the  $\alpha$  form (Fig. 14.17). This is attributed to the presence of one-dimensional (1D) CNTs, which act as the nucleation site for the crystal formation and encourage the formation of  $\alpha$  phase.

The effect of temperature on the structure evolution in these nanocomposites was also studied by XRD. The nanocomposites were heated from room temperature to their melting temperature and the XRD (Fig. 14.17) was recorded. At room temperature, only two peaks at  $2\theta = 20^\circ$  and  $24^\circ$  were observed, corresponding to the  $\alpha$  form. With an increase in temperature, these two peaks move toward each other but do not merge with each other. At 182–190°C, only one

broad peak was observed. However, in the case of pure PA1010 (Fig. 14.17b), the two peaks at  $2\theta = 20^\circ$  and  $24^\circ$  gradually move toward each other and at  $150^\circ\text{C}$  merge into a single diffraction peak appearing at  $2\theta = 22^\circ$ . This indicated a crystal to crystal transition from  $\alpha$  form to  $\gamma$  form taking place with an increase in temperature, which is termed Brill transition, named after the scientist who observed it in 1942 for nylon 66. It was later observed for many even–even nylons during heating and was attributed to the local melting of methylene sequences between amido groups and the hydrogen bonds that remain intact during this transition.

Mahmood et al. [70] studied PA6–MWCNT nanocomposites by XRDS and observed that addition of amine-functionalized CNT facilitates the growth of the  $\alpha$  form of crystal alone. This was confirmed by the appearance of two peaks at  $2\theta = 19.8^\circ$  and  $23.7^\circ$  with d-spacing values of 4.43 and  $3.7 \text{ \AA}$  for (200) and [(002), (220)] planes, respectively, in the XRD spectra. The  $\alpha$  phase is a thermodynamically stable phase consisting of hydrogen-bonded polymer chains packed in an antiparallel fashion, whereas the  $\gamma$  form is comparatively less stable, with hydrogen-bonded chains between parallel chains.

The increased crystallinity of the nanocomposites was inferred from the increase in the intensity of the peaks (Fig. 14.18). The CNTs were found to act as a nucleation site for the polymer chains for the  $\alpha$  form of crystals. The crystallite size calculated from the XRD data using the Debye–Scherrer equation (Eqn (14.2)) was found to be approximately 8.4 nm for neat PA6 and 10.5 nm for the amine-functionalized CNT nanocomposite, but with the incorporation of pristine CNTs, the crystallite size

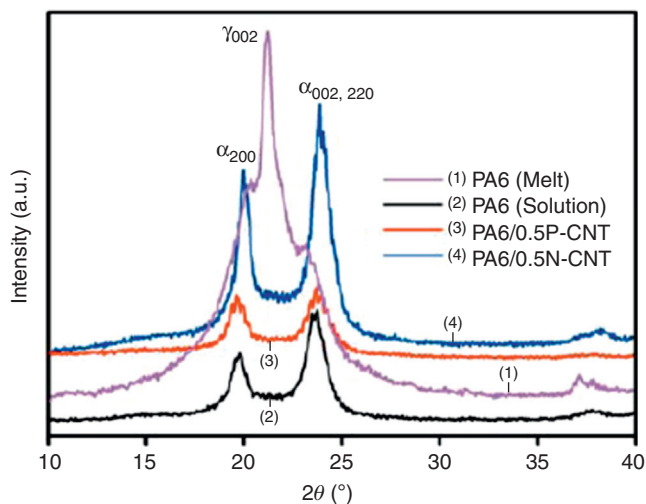


**FIGURE 14.18**

X-ray diffraction patterns of neat polyamide 6 (PA6) (both from solution mixing and melt extrusion) and PA6/carbon nanotube nanocomposites [70].

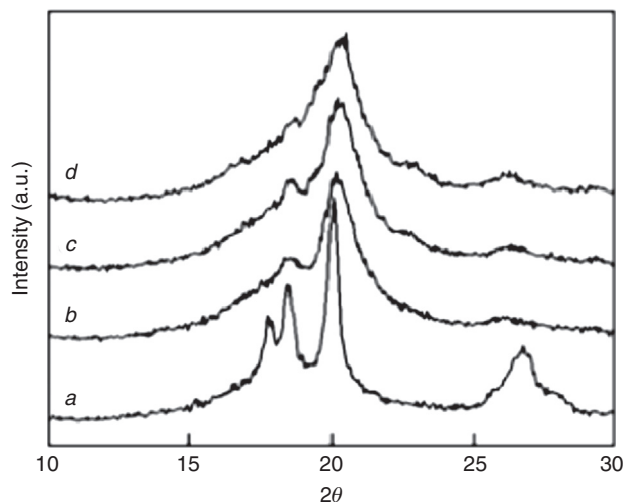


**FIGURE 14.19**

X-ray diffraction patterns of (a) polyvinylidene fluoride (PVDF) and PVDF/multiwalled carbon nanotube (MWCNT) composites with (b) 0.5% MWCNT, (c) 1% MWCNT, and (d) 1.5% MWCNTs [71].

decreased to 8 nm [70]. The crystallization behavior of PVDF–MWCNT nanocomposites were studied by Yue et al. [71] using XRD, and correlated the crystallization to the mechanical behavior of the nanocomposites (Fig. 14.19).

In this case, the diffractogram showed signals at  $2\theta = 17.8^\circ$ ,  $18.6^\circ$ , and  $19.8^\circ$  corresponding to reflections from (100), (110), and (020) planes, respectively, belonging to the  $\alpha$  form of crystals, whereas the signal at  $2\theta = 20.6^\circ$  corresponds to the reflections of unresolved (110)/(200) planes belonging to the  $\beta$  phase. The addition of MWCNTs to the PVDF matrix increased the intensity of the peaks corresponding to the  $\alpha$  phase decreases and a broad peak was observed at  $2\theta = 20.3^\circ$ , which may be due to the merging of (020) of  $\alpha$  phase and the (110)/(200)  $\beta$  phase peaks. The reflection from 021 plane of the  $\gamma$  phase is seen at  $2\theta = 20.6^\circ$ , which overlaps the reflection location of the unresolved (110)/(200) of  $\beta$  phase, and no other reflections of  $\gamma$  phase were observed. All these observations suggested that the peak at  $2\theta = 20.6^\circ$  was attributed to the unresolved (110)/(200) planes of  $\beta$  phase. So it was confirmed that the addition of MWCNTs to the matrix resulted in the formation of  $\beta$  phase of crystals. It was also observed that the MWCNTs' addition will result in the shifting of the peak at  $2\theta = 26.5^\circ$  of  $\alpha$  phase to the lower angles, indicating a restricting effect in the  $\alpha$  crystals which is known to produce tensile stress in the crystals [71].

Polystyrene (PS)–MWCNT nanocomposites were studied by Sun et al. [72] using XRDS. To study the crystalline behavior of syndiotactic PS with the addition of MWCNTs, the temperature-dependent X-ray diffractograms were recorded at a heating rate of  $10^\circ\text{C}/\text{min}$  and the results obtained are shown in Fig. 14.20.

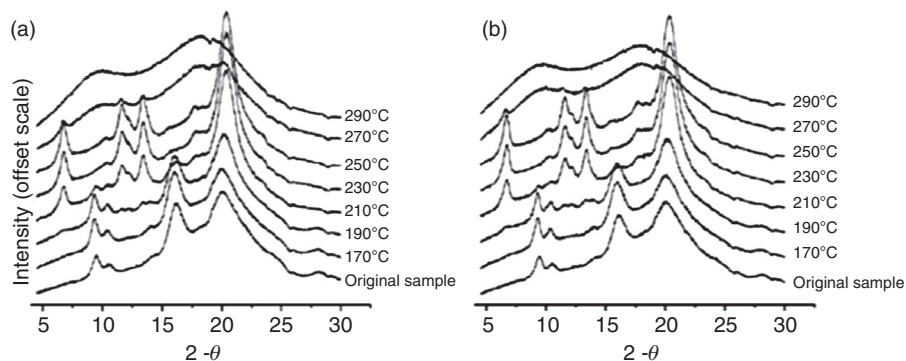


**FIGURE 14.20**

Temperature-dependent X-ray diffraction patterns of (a) polystyrene (PS) and (b) PS/multiwalled carbon nanotube nanocomposite [72].

Copyright 2010. Reprinted with permission from Elsevier Ltd.

The diffraction peaks at  $2\theta = 9.4^\circ$ ,  $10.5^\circ$ ,  $16.0^\circ$ ,  $20.0^\circ$ , and  $28.1^\circ$  were observed in both pure polymers (Fig. 14.20) and the nanocomposites (Fig. 14.20b), which corresponds to the  $\gamma$  form. As the temperature increased, the solvent was removed and resulted in the crystalline phase transition from  $\gamma$  to  $\alpha$  form, in both cases. The peak intensity corresponding to the  $\gamma$  phase decreased while the  $\alpha$  phase peaks at  $2\theta = 6.8^\circ$ ,  $11.6^\circ$ ,  $13.4^\circ$ ,  $17.8^\circ$ , and  $20.4^\circ$  increased in intensity to  $250^\circ\text{C}$ . Above  $270^\circ\text{C}$ , the syndiotactic PS and its MWCNT nanocomposites melted and broad peaks were observed, and when the temperature was beyond  $290^\circ\text{C}$ , no peak was observed. It was reported that the MWCNTs played a very minor role in the crystalline transition during heating in this system [72].

Thus, the literature cited previously clearly demonstrates that the presence of CNTs results in an increase in the crystallinity of the composites and most importantly, undergoes crystal transition from one form to another by acting as a nucleation site for crystal growth. The MWCNTs improve the crystal quality, but also bring certain stresses into the composites. The XRDS has proved to be a valuable technique to study the structural transition taking place in these nanocomposites, which can be correlated to the improvement in properties occurring in these composites.

#### 14.4.2.4 Graphene PNCs

The field of PNCs changed with the arrival of graphene, the newest member of the carbon family, discovered by Geim et al. in 2004 [73]. Currently, a great deal of research is ongoing in the development of PNCs with graphene and its derivatives because of its multifunctional properties and the relative ease of modifying the functional groups on the graphene surface. Graphene is one-atom-thick; 2D

layers of  $sp^2$ -bonded carbon sheets with certain unique set of electrical, mechanical, and thermal properties [74–75]. One of the ways to harness these properties of graphene is to incorporate it into a composite material. Graphene nanocomposite materials and ultrathin membrane materials hold great potential in various applications [76–82].

Oxidized graphite termed as graphite oxide or graphene oxide (GO), bears oxygen-containing functional groups on its basal plane and edges [83–84]. These functional groups render it hydrophilic and the water molecules can easily intercalate the galleries, which can be confirmed from XRD experiments. Stankovich et al. studied the synthesis of graphene-based nanosheets via chemical reduction of exfoliated GO, where they measured the interlayer distance of dry GO and hydrated GO and observed that the interlayer distance for GO varies with the amount of absorbed water, with values such as 0.63 and 0.61 nm reported for dry GO samples to 1.2 nm for hydrated GO [85]. GO still retains a layered structure and XRD spectroscopy has proved to be a valuable technique for structural elucidation of graphene and its derivatives.

Fu et al. synthesized GO and reduced GO (rGO), and studied them with XRD. The characteristic peak (002) of graphite at  $26.58^\circ$  disappeared after the oxidation, while an additional peak at  $11.42^\circ$  was observed corresponding to the characteristic (001) plane of GO. The interlayer spacing of GO was also higher than in graphite, which indicated the introduction of oxygen functionalities at the galleries in the form of hydroxyl, epoxy, and carboxyl groups [85–90]. The exfoliation of rGO from GO can also be confirmed with XRD. Yang et al. [91] analyzed the prepared rGO with XRD and observed that only a weak and broad diffraction peak is found at  $26.5^\circ$  in rGO powder. This suggested that a small number of graphene sheets slightly stack due to the strong van der Waals forces between them after reduction, but most of the graphene sheets are exfoliated into monolayered or few-layered sheets. It was also observed that the interlayer distance of rGO decreases from 0.86 to 0.34 nm, suggesting that the oxygen functionalities of the GO were removed thus reducing the interplanar distance in rGO [91].

Morimune et al. [92] studied GO–poly(vinyl alcohol) nanocomposites. The XRD (Fig. 14.21) analysis revealed that the prominent diffraction peak of GO at  $2\theta = 11.1^\circ$  disappeared in the PVA–GO nanocomposites, indicating that the GO was well exfoliated and homogeneously dispersed in the PVA matrix.

The crystallinity of the nanocomposites was determined using XRD and was found to increase with the GO loading from 28% for the neat PVA to 30%, 33%, 35%, and 39% for 0.1%, 0.5%, 1%, and 5% GO loading, respectively. Thus, it was observed that GO enhances the crystallization of PVA and affects the microstructure of the PVA. With the incorporation of GO into the PVA matrix, the mechanical and thermal properties of the nanocomposite also increased, compared with the neat PVA films. The barrier properties of the PVA–GO nanocomposites were also improved with the incorporation of the GO, which was attributed to the rigid sheetlike structure of GO [92].

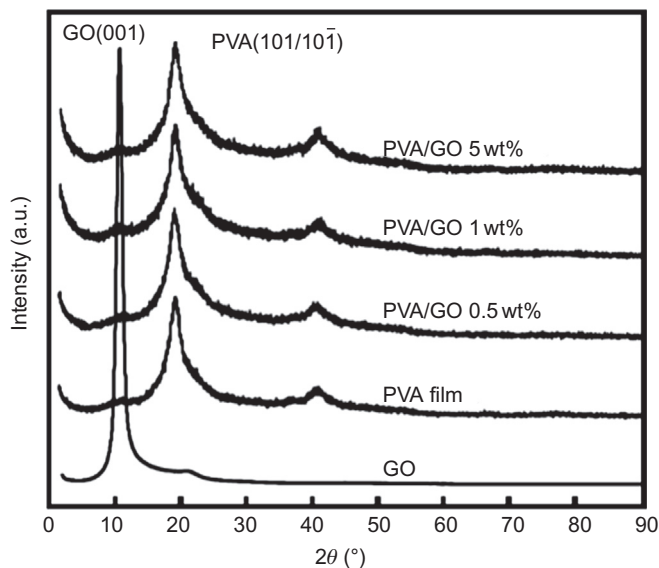


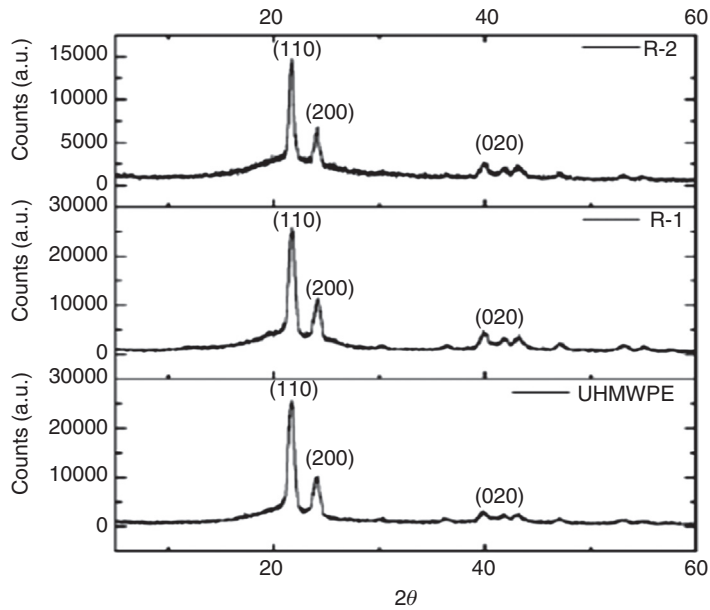
**FIGURE 14.21**

X-ray diffraction patterns of poly(vinyl alcohol) (PVA), graphene oxide (GO), and PVA/GO nanocomposites [92].

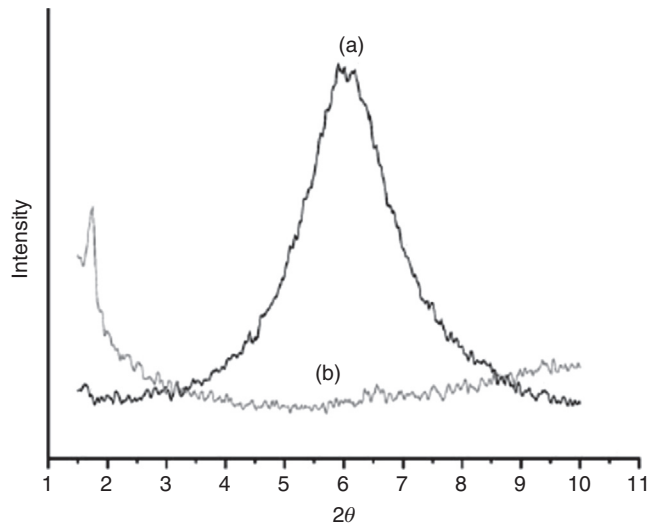
Bhattacharyya et al. [93] studied the graphene-reinforced ultrahigh molecular weight polyethylene (UHMWPE) and found by XRD that nanocomposites prepared using a different route possessed different degrees of crystallinity, ranging from 39% to 32%, as illustrated in Fig. 14.22.

This reduction in crystallinity was attributed to the exfoliated graphene sheets, which restrict the free movement of polymer chains to arrange themselves in an orderly fashion, thus reducing its crystallinity. This was also supported by the differential scanning calorimetry data obtained, but is contrary to the assumption that the graphene sheets act as nucleating agents, resulting in the increase of crystallinity [93]. The aqueous emulsion route has been used by several groups to study the preparation of PS/GO nanocomposites and the degree of intercalation of GO by PS has been widely studied using XRD.

The diffraction peak of the pristine GO shifted to a lower angle at  $2\theta = 1.78^\circ$  indicating the intercalation of PS (Fig. 14.23). The increase in the interplanar distance of the GO from 15.3 to 34.7 Å also indicates that the GO layers are intercalated by monolayer and/or multilayer of PS chains, resulting in the increase of the interplanar distance [94]. In a recent study, we have also observed (Fig. 14.24) that, as compared to neat PS, the major diffraction peak of the GO/PS nanocomposite arises due to the 100 plane, with a d-spacing of 0.46 nm and a grain size of 1.28 nm as compared to the 8 nm grain size in the PS homopolymer for the 220

**FIGURE 14.22**

Wide-angle X-ray curves for ultrahigh molecular weight polyethylene film and nanocomposites prepared by route 1 (R-1) and route 2 (R-2) [93].

**FIGURE 14.23**

X-ray diffraction patterns of (a) graphene oxide (GO) and (b) polystyrene-intercalated GO [94].

Copyright 2003. Reprinted with permission from Elsevier Ltd.

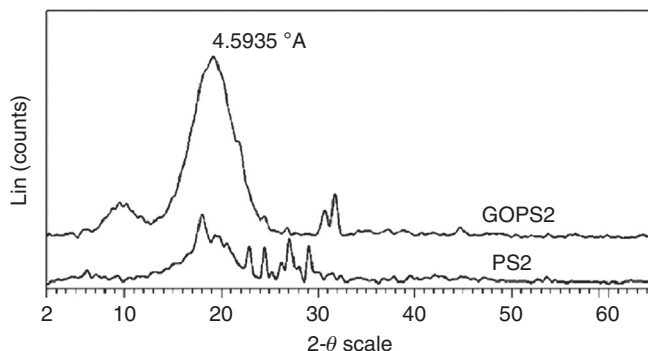


**FIGURE 14.24**

Powder X-ray diffraction spectra of a graphene oxide (GO)–polystyrene (PS) 2 nanocomposite with 0.5 wt% GO and PS2 without any GO [95].

Copyright 2014. Reprinted with permission from John Wiley & Sons.

plane. The small grain size of the nanocomposite was indicative of a higher order and the interlayer spacing of 0.46 nm observed was different from that of graphite (0.34 nm) and GO (0.87 nm), suggesting a polymer-intercalated structure.

The effect of graphene nanoplatelets and rGO on poly(lactic acid) (PLA) and plasticized PLA was studied by Chieng et al. [96]. The XRD pattern of the nanocomposites (Fig. 14.25) showed a broad diffraction peak from 10° to 25° of the PLA polymer matrix and another sharp diffraction peak at 26.6°, with an interlayer spacing of 0.34 nm of the graphitic plane. These peaks were common for all the GO–PLA nanocomposites. In case of rGO–PLA nanocomposites, the peak at 26.6° was absent indicating the complete exfoliation of the graphitic layers of rGO [96].

Upadhyay et al. [97] studied the polymethyl methacrylate (PMMA)–GO nanocomposite prepared via electrospinning. The XRD curves obtained for GO, PMMA pellets, and PMMA–GO nanofibers indicated that, in GO, the sharp peak at  $2\theta = 10^\circ$  confirms the effective oxidation of graphite and the interlayer distance also increased between the graphene planes. The results observed for PMMA pellets and PMMA–GO nanofibers do not show any sharp peaks. The smooth curve for PMMA–GO nanofibers and the disappearance of the GO sharp peaks indicates a high level of exfoliation and dispersion of individual GO sheets in the polymer matrix [97].

The *in situ* synthesis of PMMA–graphene nanocomposites was studied by Aldosari et al. [98]. The X-ray diffractogram of graphite showed a strong signal at  $2\theta = 26.54^\circ$  with an interlayer spacing of 0.34 nm, while the GO diffractogram showed its characteristic peak at  $2\theta = 9.34^\circ$  with d-spacing of 0.94 nm. The increase of the interlayer distance is due to the introduction of oxygen functionalities in the form of carboxyl, epoxy, or hydroxyl groups. In rGO the peak was shifted to  $2\theta = 12.42^\circ$ , corresponding to an interlayer distance of 0.71 nm. The reduction of the interlayer spacing was attributed to the reduction and removal of

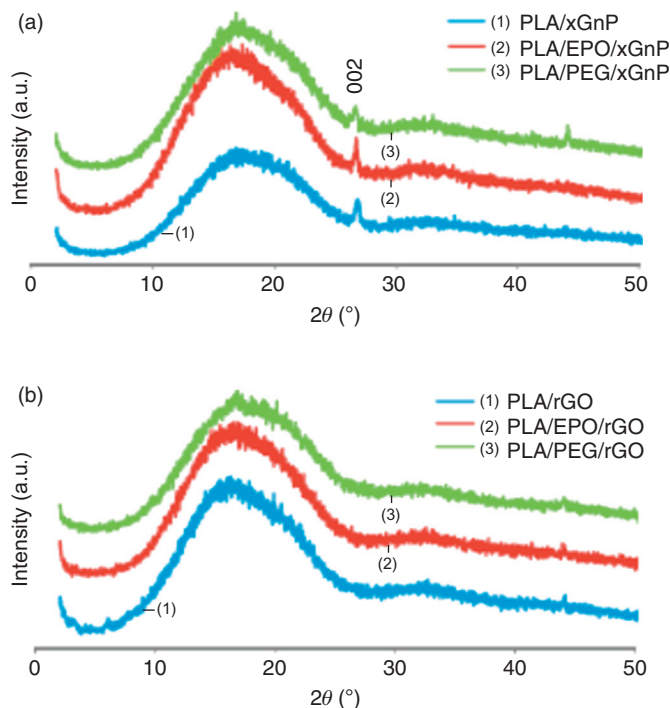


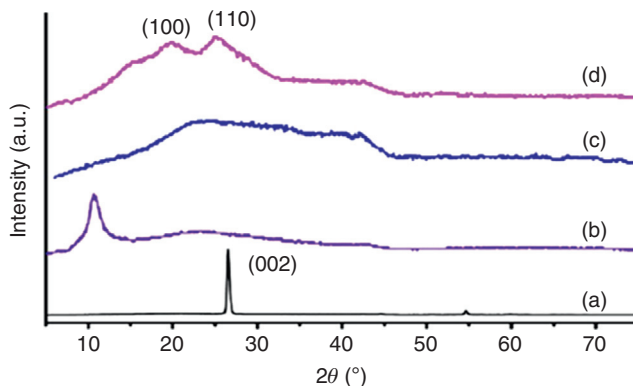
**FIGURE 14.25**

(a) X-ray diffraction patterns of poly(lactic acid), poly(lactic acid) with epoxidized palm oil, and poly(lactic acid) loaded with polyethylene glycol and 0.3% graphene nanoplatelets. (b) The same samples with 0.3% reduced graphene oxide [96].

oxygen functionalities using hydrazine hydrate resulting in the exfoliated rGO sheets. The broad peaks near  $19^\circ$  in the (rGO–PMMA) spectrum showed less broadening compared with the rGO–PMMA nanocomposite, indicating agglomeration in these nanocomposites, which might be due to the strong van der Waals forces of attraction between the GO sheets. In the nanocomposites, no characteristic peaks of GO and rGO were found, which suggests that the NP was completely exfoliated in the polymer matrix [98].

Graphene and its derivatives have also been used in the development of multifunctional materials with conjugated polymers. The development of interfacially polymerized polyaniline/GO nanocomposites was carried out by Zhu et al. [99]. The average grain size of the GO particles was calculated from XRD analysis. XRD analysis of graphite, GO, and the prepared nanocomposite with and without GO was done.

They observed that the prominent graphite peak at  $2\theta = 26.5^\circ$ , with interlayer distance of  $3.4 \text{ \AA}$ , disappeared in GO with the introduction of a peak at

**FIGURE 14.26**

X-ray diffraction patterns of (a) graphite, (b) graphene oxide (GO), (c) polyaniline (PANI)–GO nanocomposite, and (d) PANI nanofibers [99].

Copyright 2012. Reprinted with permission from Elsevier Ltd.

$2\theta = 10.7^\circ$  with an interlayer distance of  $8.3 \text{ \AA}$  (Fig. 14.26). This suggested the graphite expansion on oxidation. The average grain size of graphite and GO was estimated by the Debye–Scherrer equation. The average grain size of graphite and GO was found to be 24.2 and 5.1 nm, respectively. It can be observed that the particle size was reduced with the oxidation of graphite. This was also confirmed from our studies with the GO/PS system [95]. In the PANI/GO nanocomposite, the prominent peak of GO disappeared indicating the complete exfoliation of GO in the polymer matrix. The peak of PANI/GO was found to be a broad peak, as compared with the narrow peaks of PANI crystal planes, attributed to the loss of crystallinity of PANI with the introduction of GO due to its surface tension [99]. The XRD results of nanocomposites of GO were also reported with other conjugated polymers like P3HT [100,101].

Thus, all the literature cited previously clearly shows that XRD is an indispensable tool in the development of graphene, graphene derivatives, and its PNCs. The graphene nanocomposites are important materials projected to be useful in several future applications. Crucial information about the nanofiller dispersion, grain size, sample morphology, and confirmation of the presence of the nanofiller can be obtained by XRD. The structural changes taking place during conversion of graphite to GO or rGO was confirmed by the XRD spectra. The distribution and exfoliation of GO in the polymer matrix was confirmed by an increase of the interlayer distance (d), indicating that the polymer chains are intercalated in the galleries of GO. In certain cases the GO particles favored an increase in crystallinity by acting as the crystallization nucleus whereas in certain cases, it inhibited the crystalline growth by acting as an impurity which obstructed the orderly arrangement of the molecules.

### 14.4.2.5 Cellulose nanocrystal PNCs

In recent years, a concern for the environment and the depleting fossil reserves is driving the development of sustainable approaches to nanocomposite development. Cellulose is one of the world's most abundant renewable and biodegradable polymers and is a very promising material available at low cost for the preparation of various functional materials. Synthesis of cellulose-based NPs, nanowhiskers, or nanocrystals from bioresources, like plants and agricultural residues from corn grain, sugarcane bagasse, wheat stems, and seed coats using top-down technologies has been reported [102–105]. Cellulose nanocrystals (cellNs) were first introduced as reinforcing nanofiller in poly(styrene-co-butyl acrylate)-based nanocomposites by Favier et al. [106]. The dispersion of cellNs in polymers is hindered by its hydrophilic nature and the strong hydrogen bonding interactions, resulting in aggregation leading to the inferior property of the nanocomposites. XRD spectroscopy has been used in cases of cellNs to determine the crystal orientation, effect of filler on the polymer matrix, degree of crystallinity, crystal size, etc. The XRD spectrum of PVA–cellN nanocomposites studied by Kumar et al. [107] is shown in Fig. 14.27.

The X-ray diffractogram showed peaks at  $2\theta = 16.5^\circ$ ,  $22.5^\circ$ , and  $33^\circ$  corresponding to the (110), (200), and (004) planes, which represent the cellulose structure, whereas the diffractogram of PVA revealed peaks at  $19.4^\circ$ ,  $22.5^\circ$ , and  $40.3^\circ$ , corresponding to the crystallinity of the polymer (Fig. 14.27). The nanocomposites revealed both the PVA and the cellN peaks. The crystallinity of all the nanocomposites was calculated by amorphous subtraction method. The cellN exhibited a crystallinity of 68.3% and the PVA exhibited a crystallinity of 49.2% while the nanocomposite had a crystallinity of 59%. The reduction in nanocomposite crystallinity is attributed to the strong interaction of the cellN with the

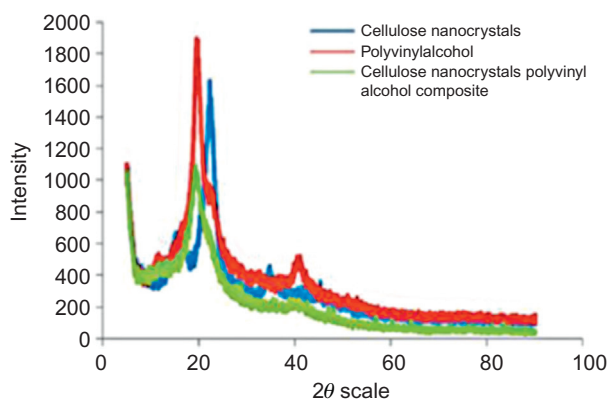


**FIGURE 14.27**

X-ray diffraction patterns of cellulose nanocrystals (cellNs), polyvinyl alcohol, and cellNs/poly(vinyl alcohol) porous composite [107].

hydroxyl groups of the PVA forming a twisted mass, which caused a steric effect and resulted in the destruction of the PVA-ordered structure. The high crystallinity of the cellN is indicative of effective hydrolysis which removed the amorphous cellulose part [107]. The composites of cellN with other polymers like waterborne polyurethanes [108], polyethylene oxide [109], and starch [110] have also been reported.

From the literature cited previously on application of XRD spectroscopy to characterization of cellN–PNCs, we can infer that the application of renewable based NPs and its nanocomposites are scarcely reported and most of the literature is very recent. Considering the importance of sustainable materials development, this may be topic for future detailed studies with other nanocrystals. In addition, some of the other widely used fibrous natural reinforcements need to be studied in detail to assess their crystalline characteristics and that of the nanocomposites produced.

---

## 14.5 SMALL-ANGLE X-RAY SCATTERING

SAXS is another widely used XRD technique utilized in the characterization of PNCs. In contrast to WAXD that mainly deals with the atomic structure of crystals, SAXS probes relatively large-scale structures [111]. The state of the NP distribution can be characterized by synchrotron SAXS in a straightforward fashion. As mentioned in the previous sections of this chapter, WAXD is mostly useful for measurement of the d-spacing in ordered, immiscible, and intercalated PNCs and the technique is insufficient for measurement of disordered and exfoliated materials that give no peak. For example, in nanocomposites where the clay is not well ordered and fails to produce a Bragg diffraction peak. The absence of a peak obtained during XRD analysis merely states that no peak was observed; however, it does not prove, or disprove, the existence of exfoliated clay platelets in the nanocomposite.

SAXS combined with electron microscopy was used by Bandyopadhyay and Ray [112] for quantitative study of the degree of clay dispersion in the polymer matrix. Nanocomposites of poly[(butylene succinate)-co-adipate] (PBSA) copolymer with OMMT clay was studied. The SAXS pattern revealed that the clay (Cloisite 30B), showed a peak at  $q = 3.4 \text{ nm}^{-1}$  with a d-spacing of 1.85 nm. The pattern also revealed some crystalline arrangement of the polymer at  $q = 0.5 \text{ nm}^{-1}$ , which was observed in all the nanocomposites. However, the disappearance of the characteristic clay peak in the nanocomposites suggested that the ordered structure of the clay had been completely destroyed [112] (Fig. 14.28).

The orientation of layered nanoclays dispersed in the polymer matrix is one parameter controlling the nanocomposite properties. Wilson et al. [113] used multidirectional 2D SAXS to study the orientation distribution of organoclays (e.g., Cloisite C20A) in the nanocomposite films of EVA copolymer as the polymer

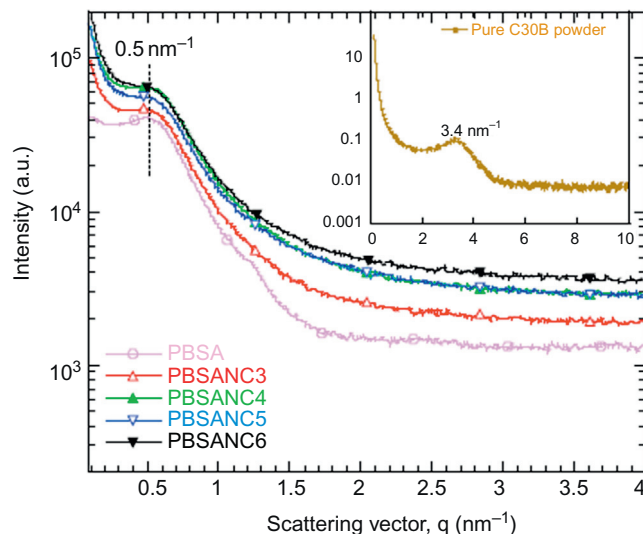


**FIGURE 14.28**

Small-angle X-ray scattering pattern of pure C30B (inset), pure polymer (poly[(butylene succinate)-co-adipate], PBSA), and the nanocomposites. The PBSA nanocomposites (PBSANCs) with four different C30B loadings of 3, 4, 5, and 6 wt%, were abbreviated as PBSANC3, PBSANC4, PBSANC5, and PBSANC6, respectively [112].

Copyright 2012. Reprinted with permission from Elsevier Ltd.

matrix. The nanocomposites exhibited a mixed intercalation/exfoliation clay morphology, where the intercalated structure possessed partial orientation parallel to the in-plane direction of the film. The higher content of the clay loading showed a higher clay orientation. The authors determined an orientation parameter (P2), the results of which were correlated to the gas permeation properties of the nanocomposite films [113,114].

Nanocomposites of clay with SEBS (PS-*b*-poly(ethylene-co-butylene)-*b*-PS) block copolymers having cylindrical domains were studied by Carastan et al. [115]. Samples were also studied with the middle block functionalized using maleic anhydride (SEBS-MA). Two types of organoclays were added, namely Cloisite 20A and Cloisite 30B. SAXS scattering results showed that the addition of Cloisite 20A to SEBS and SEBS-MA resulted in nanocomposites with intercalated and partially exfoliated structures, respectively. The addition of Cloisite 30B to SEBS and SEBS-MA promoted the formation of composites containing relatively large micron-sized and partially exfoliated clay particles, respectively. The extrusion processing promoted alignment of the axes of the PS cylinders along the extrusion direction in all samples, and the basal planes of the clay particles were mostly parallel to the main external surfaces of the extruded tapes. These results were further confirmed with TEM studies.

Wang et al. [116] studied epoxy–clay nanocomposites prepared using epoxy resins derived from soybean oils and OMMT. The quality of dispersion of soybean oil epoxy with the organomodified clay particle was studied by SAXS and TEM. The nanocomposites' morphologies were a mix of intercalated and exfoliated structures, dependent on the dispersion technique (Fig. 14.29).

Apart from these SAXS studies, SEBS, EVA copolymers, siloxane–PEG, and siloxane–PPG, with different type of organoclays, and PU–silica nanocomposites have also been reported [113,117–120].

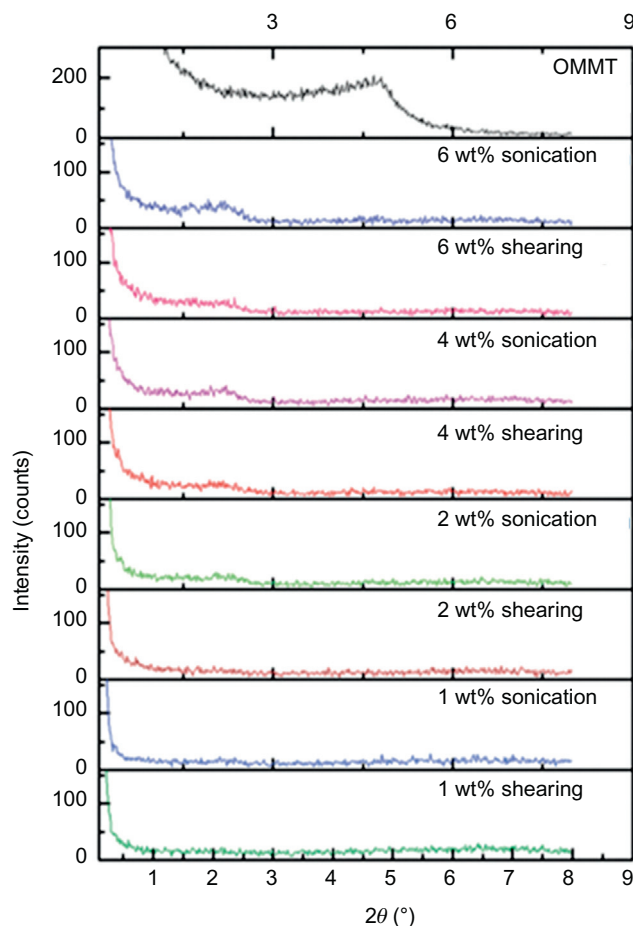


**FIGURE 14.29**

Small-angle X-ray scattering of nanocomposites with different organically modified montmorillonite content and dispersion methodology [116].

Copyright 2013. Reprinted with permission from Royal Society of Chemistry.

XRD studies of CNTs–PS nanocomposites have also been reported [121], using small angle scattering. The effect of the CNT modification on the agglomeration behavior in dilute toluene dispersions was studied. Chen et al. studied the toughening mechanism of nanocomposite films comprising UHMWPE and modified carbon nanofiber (MCNF) using *in situ* synchrotron SAXS and WAXD techniques during uniaxial stretching. Surface modification of carbon nanofibers included oxidation and subsequent chemical reaction with OA [122]. WAXD and SAXS results indicated that MCNF acted as a solvent carrier in the stiff UHMWPE matrix, whereby the grafted short hydrocarbon chains ( $n = 18$ ) plasticized the surrounding UHMWPE chains in the nanoscale vicinity (10–20 nm) and induced interfacial flow under stretching, resulting in a large elongation-to-break ratio ( $> 500\%$ ). At high temperature (118 °C), the toughness of the MCNF/UHMWPE composite films was still about two times more than that of pure UHMWPE. The mobile hydrocarbon layers at the UHMWPE/MCNF interface appeared to be the key to overcoming the barrier of high chain entanglements in the solid UHMWPE matrix and to induce the significantly toughened performance [122].

---

## 14.6 NEW DEVELOPMENTS IN XRD

New developments in XRD spectroscopy like GISAXS have also been used for characterization of the structure formation in new materials required in energy research or in nanoporous materials. Two-dimensional grazing incidence SAXS (2D GISAXS) was used to study the evolution of nanopores from composite films by Lee et al. [123]. The structural characteristics such as size, size distribution, shape, electron density, and porosity, were studied as a function of temperature and time. The formation of imprinted nanopores in the dielectric films by sacrificial thermal degradation of the porogen was determined by *in situ* GISAXS analysis. For example, solution-processed zinc oxide/polyethylenimine nanocomposites were studied as tunable electron transport layers for highly efficient bulk heterojunction polymer solar cells by Chen et al. [124] using synchrotron GISAXS.

---

## 14.7 SUMMARY

In this chapter, we reviewed some of the important literature on PNCs, with special reference to the application of XRDS for structure–property correlation studies. The basic principles of XRD and its application in the characterization of clay polymer, silica polymer, various types of carbon nanofiller –polymer composites have been reviewed. More recent developments in XRD spectroscopy like SAXS and GISAXS have also been reviewed. The review underlines that the XRD technique is an indispensable tool to study the microstructural and morphological changes taking place in the PNCs and can also be correlated to the various

property profiles exhibited by these nanocomposites. The diffractogram obtained by analyzing a compound is like a fingerprint of the crystal structure of the compound. In the formation of the nanocomposite, often these structures are affected and thus information on the interaction between the two components in the nanocomposite can be extracted. By carefully examining the character of the scattering, secondary information, like the crystallite size, lattice distortion, and occupancy can also be extracted. This information comes with advantages such as minimal sample preparation and the relatively straightforward interpretation of the results. However, at times, the XRD might provide ambiguous results which have to be further analyzed by other techniques, like TEM. In spite of this drawback XRD is the preferred method to obtain information on the structure and morphology of all sorts of nanocomposite materials. The significance of XRD spectroscopy in PNC research is expected to grow in the coming years as the societal demand for new materials grows.

---

## ABBREVIATIONS

<b>XRDS</b>	X-ray diffraction spectroscopy
<b>SAXS</b>	small-angle X-ray scattering
<b>WAXS</b>	wide-angle X-ray scattering
<b>PNC</b>	polymer nanocomposites
<b>NP</b>	nanoparticle
<b>XRD</b>	X-ray diffraction
<b>WAXD</b>	wide-angle X-ray diffraction
<b>GIXRD</b>	glancing angle X-ray diffraction/grazing incidence X-ray diffraction
<b>MMT</b>	montmorillonite
<b>OMMT</b>	organically modified montmorillonite
<b>LDPE</b>	low density polyethylene
<b>PE-g-MA</b>	maleic anhydride grafted polyethylene
<b>LLDPE</b>	linear low density polyethylene
<b>OA</b>	octadecylamine
<b>TA</b>	methyl dihydroxyethyl hydrogenated tallow ammonium
<b>PP</b>	polypropylene
<b>PVDF</b>	polyvinylidene fluoride
<b>PVA</b>	poly vinylalcohol
<b>NFC</b>	nanofibrillated cellulose
<b>PAA</b>	polyacrylicacid
<b>PAC</b>	polyacrylates
<b>PSU</b>	polysulfones
<b>PA 6</b>	polyamide 6
<b>EVA</b>	ethylene vinyl acetate
<b>CNT</b>	carbon nanotubes
<b>SWCNT</b>	single-walled carbon nanotubes
<b>MWCNT</b>	multiwalled carbon nanotubes
<b>PA 1010</b>	polyamide 1010

<b>GO</b>	graphite oxide/graphene oxide
<b>rGO</b>	reduced graphene oxide
<b>UHMWPE</b>	ultrahigh molecular weight polyethylene
<b>PS</b>	polystyrene
<b>PLA</b>	poly(lactic acid)
<b>PMMA</b>	polymethylmethacrylate
<b>PANI</b>	polyaniline
<b>CNC</b>	cellulose nanocrystals
<b>PBSA</b>	poly[(butylene succinate)-co-adipate]
<b>PBSANC</b>	poly [(butylene succinate)-co-adipate] nanocomposites
<b>SEBS</b>	polystyrene-b-poly(ethylene-co-butylene)-b-polystyrene
<b>TEM</b>	transmission electron microscope
<b>PEG</b>	polyethylene glycol
<b>PPG</b>	polypropylene glycol
<b>MCNF</b>	modified carbon nanofiber

---

## REFERENCES

- [1] Kittel C. *Introduction to solid state physics*. 7th ed. New York, NY: John Wiley & Sons; 1996.
- [2] Cullity BD. *Elements of X-ray diffraction*. Reading, MA: Addison-Wesley Publishing Company, Inc; 1956.
- [3] Klug HP, Alexander LE. *X-ray diffraction procedures*. New York: John Wiley & Sons; 1973.
- [4] Roe RJ. *Methods of X-ray and neutron scattering in polymer science*. New York: Oxford University Press; 1999.
- [5] Sharma R, Bisen DP, Shukla U, Sharma BG. X-ray diffraction: a powerful method of characterizing nanomaterials. *Recent Res Sci Technol* 2012;4(8):77–9.
- [6] Murthy NS. Recent developments in polymer characterization using x-ray diffraction. *Rigaku J* 2004;21:15–24.
- [7] Van Brussel BA, De Hosson JTM. Glancing angle x-ray diffraction: a different approach. *Appl Phys Lett* 1994;64(12):1585–7.
- [8] Tarey RD, Rastogi RS, Chopra KL. Characterization of thin films by glancing incidence x-ray diffraction. *Rigaku J* 1987;4:11–15.
- [9] Glatter O, Kratky O. *Small angle X-ray scattering*. London: Academic Press; 1982.
- [10] Balta-Calleja FJ, Vonk CG. *X-ray scattering of synthetic polymers*. New York: Elsevier; 1989 [chapter 7].
- [11] Laus M, Francescangeli D, Sandrolini F. New hybrid nanocomposites based on an organophilic clay and poly(styrene-b-butadiene) copolymers. *J Mater Res* 1997;12: 3134–9.
- [12] Couvreur P, Vauthier C. Polyalkylcyanoacrylate nanoparticles as drug carrier: present state and perspectives. *J Control Release* 1991;17:187–98.
- [13] Lewis LN. Chemical catalysis by colloids and clusters. *Chem Rev* 1993;93:2693–730.
- [14] Golden H, Deng H, Disalvo FJ, Frecht JMJ, Thompson PM. Monodisperse metal clusters 10-angstroms in diameter in a polymeric host the monomer-as-solvent approach. *Science* 1995;268:1463–6.

- [15] Roy AS, Gupta S, Sindhu S, Parveen A, Ramamurthy PC. Dielectric properties of novel PVA/ZnO hybrid nanocomposite films. *Composites Part B* 2013;47:314–19.
- [16] Gaur MS, Singh PK, Suruchi, Chauhan RS. Structural and thermal properties of polysulfone–ZnO nanocomposites. *J Therm Anal Calorim* 2013;111:743–51.
- [17] Min M, Shi Y, Ma H, Huang H, Shi J, Chen X, et al. Polymer–nanoparticle composites composed of poly(3-hydroxybutyrate-co-3-hydroxyvalerate) and coated silver nanoparticles. *J Macromol Sci Part B Phys* 2015;54:411–23.
- [18] Li Z, Li Y, Lu J, Zheng F, Laven J, Foyet A. Polyaniline/Ag nanocomposite synthesized by using aniline as dispersant and stabilizer of nanosilver sol. *J Appl Polym Sci* 2013;128:3933–8.
- [19] Safarpour M, Khataee A, Vatanpour V. Preparation of a novel polyvinylidene fluoride (PVDF) ultrafiltration membrane modified with reduced graphene oxide/titanium dioxide (TiO<sub>2</sub>) nanocomposite with enhanced hydrophilicity and antifouling properties. *Ind Eng Chem Res* 2014;53:13370–82.
- [20] Zohrevand A, Ajji A, Mighri F. Morphology and properties of highly filled iPP/TiO<sub>2</sub> nanocomposites. *Polym Eng Sci* 2014;54:874–86.
- [21] Yin HR, Jiang JS. Synthesis and characterization of  $\gamma$ -Fe<sub>2</sub>O<sub>3</sub>–polythiophene nanocomposites. *J Mater Sci* 2005;40:3013–15.
- [22] Bajpai AK, Gupta R. Synthesis and characterization of magnetite (Fe<sub>3</sub>O<sub>4</sub>)–polyvinyl alcohol-based nanocomposites and study of superparamagnetism. *Polym Composites* 2010;31:245–55.
- [23] Reddy KR, Lee K-P, Gopalan AI, Showkat AM. Synthesis and properties of magnetite/poly (aniline-co-8-amino-2-naphthalenesulfonic acid) (SPAN) nanocomposites. *Polym Adv Technol* 2007;18:38–43.
- [24] Giannelis EP. Polymer layered silicate nanocomposites. *Adv Mater* 1996;8:29–35.
- [25] Burnside SD, Giannelis EP. Synthesis and properties of new poly (dimethylsiloxane) nanocomposites. *Chem Mater* 1995;7:1597–600.
- [26] Silvestre C, Duraccio D, Cimmino S. Food packaging based on polymer nanomaterials. *Prog Polym Sci* 2011;36:1766–82.
- [27] Okada A, Usuki A. Twenty years of polymer–clay nanocomposites. *Macromol Mater Eng* 2006;291:1449–76.
- [28] Huskic M, Zigon M. PMMA/MMT nanocomposites prepared by one-step *in situ* intercalative solution polymerization. *Eur Polym J* 2007;43:4891–7.
- [29] Priolo MA, Gamboa D, Holder KM, Grunlan JC. Superior gas barrier of transparent polymer–clay multilayer ultrathin films. *Nano Lett* 2010;10:4970–4.
- [30] Yalcin B, Cakmak M. The role of plasticizer on the exfoliation and dispersion and fracture behaviour of clay particles in PVC matrix: a comprehensive morphological study. *Polymer* 2004;45:6623–38.
- [31] Pinnavaia T, Beall G. *Polymer–clay nanocomposites*. New York: Wiley; 2000.
- [32] Blumstein A. Polymerization of adsorbed monolayers, II. Thermal degradation of the inserted polymer. *J Polym Sci A* 1965;3:2665–72.
- [33] Theng BKG. *Formation and properties of clay–polymer complexes*. Amsterdam: Elsevier; 1979.
- [34] Krishnamoorthi R, Vaia RA, Giannelis EP. Structure and dynamics of polymer-layered silicate nanocomposites. *Chem Mater* 1996;8:1728–34.
- [35] Morgan AB, Gilman JW. Characterization of polymer-layered silicate (clay) nanocomposites by transmission electron microscopy and x-ray diffraction: a comparative study. *J Appl Polym Sci* 2003;87:1329–38.

- [36] Perez MA, Rivas L, Garrido-Miranda KA, Campos-Requena VH, Martinez M, Castano J, et al. Low density polyethylene (LDPE) nanocomposites with passive and active barrier properties. *J Chilean Chem Soc* 2014;59:2442–6.
- [37] Wang KH, Choi MH, Koo CM, Choi YS, Chung IJ. Synthesis and characterization of maleated polyethylene/clay nanocomposites. *Polymer* 2001;42:9819–26.
- [38] Singala, Mungray AA, Mungray AK. Degradation behavior of polypropylene–organically modified clay nanocomposites. *Ind Eng Chem Res* 2012;51:10557–64.
- [39] Pramoda KP, Mohammed A, Phang IY, Liu T. Crystal transformation and thermomechanical properties of poly(vinylidene fluoride)/clay nanocomposites. *Polym Int* 2005;54:226–32.
- [40] Spoljaric S, Salminen A, Luong ND, Lahtinen P, Vartiainen J, Tammelin T, et al. Nanofibrillated cellulose, poly(vinyl alcohol), montmorillonite clay hybrid nanocomposites with superior barrier and thermomechanical properties. *Polym Composites* 2014;35:1117–31.
- [41] Cyrus VP, Manfredi LB, Ton-That M, Vazquez A. Physical and mechanical properties of thermoplastic starch/montmorillonite nanocomposite films. *Carbohydr Polym* 2008;73:55–63.
- [42] Malin F, Znoj B, Segedin U, Skale S, Golob J, Venturini P. Polyacryl–nanoclay composite for anticorrosion application. *Prog Org Coat* 2013;76:1471–6.
- [43] Unnikrishnan L, Mohanty S, Nayak SK, Singh N. Synthesis and characterization of polysulfone/clay nanocomposite membranes for fuel cell application. *J Appl Polym Sci* 2012;124:E309–18.
- [44] De Moraes JO, Muller CMO, Laurindo JB. Influence of the simultaneous addition of bentonite and cellulose fibers on the mechanical and barrier properties of starch composite-films. *Food Sci Technol Int* 2012;18(1):35–45.
- [45] Wilhelm H, Sierakowski M, Souza GP, Wypych F. Starch films reinforced with mineral clay. *Carbohydr Polym* 2003;52:101–10.
- [46] Ceccia S, Turcato EA, Maffettone PL, Bongiovanni R. Nanocomposite UV-cured coatings: organoclay intercalation by an epoxy resin. *Prog Org Coat* 2008;63:110–15.
- [47] Strankowski M, Strankowska J, Gazda M, Piszczyk Ł, Nowaczyk G, Jurga S. Thermoplastic polyurethane/(organically modified montmorillonite) nanocomposites produced by *in situ* polymerization. *Express Polym Lett* 2012;6(8):610–19.
- [48] Percy MJ, Barthet C, Lobb JC, Khan MA, Lascelles SF, Vamvakaki M, et al. Synthesis and characterization of vinyl polymer–silica colloidal nanocomposites. *Langmuir* 2000;16(17):6913–20.
- [49] Luna-Xavier J-L, Bourgeat-Lami E, Guyot A. The role of initiation in the synthesis of silica/poly (methyl methacrylate) nanocomposite latex particles through emulsion polymerization. *Colloid Polym Sci* 2001;279(10):947–58.
- [50] Amalvy JJ, Percy MJ, Armes SP, Wiese H. Synthesis and characterization of novel film-forming vinyl polymer/silica colloidal nanocomposites. *Langmuir* 2001;17(16):4770–8.
- [51] Percy MJ, Armes SP. Surfactant-free synthesis of colloidal poly(methyl-methacrylate)/silica nanocomposites in absence of auxiliary comonomers. *Langmuir* 2002;18:4562–5.
- [52] Luna-Xavier J-L, Guyot A, Bourgeat-Lami E. Synthesis and characterization of silica/poly (methyl methacrylate) nanocomposite latex particles through emulsion polymerization using a cationic azo initiator. *J Colloid Interface Sci* 2002;250(1):82–92.

- [53] Kawashima D, Aihara T, Kobayashi Y, Kyotani T, Tomita A. Preparation of mesoporous carbon from organic polymer/silica nanocomposite. *Chem Mater* 2000;12:3397–401.
- [54] Hsiue GH, Kuo WJ, Huang Y-P, Jeng RJ. Microstructural and morphological characteristics of PS–SiO<sub>2</sub> nanocomposites. *Polymer* 2000;41:2813–25.
- [55] Xu Q, Li X, Chen F, Zhang Z. Improving the mechanical properties of polyamide 6-nanosilica nanocomposites by combining masterbatch technique with *in situ* polymerization. *J Braz Chem Soc* 2014;25(7):1218–25.
- [56] Werner E, van Zyl{single author group}, Garcia M, Schrauwen BAG, Kooi BJ, De Hosson J Th M{single author group}, et al. Hybrid polyamide/silica nanocomposites: synthesis and mechanical testing. *Macromol Mater Eng* 2002;287:106–10.
- [57] Sadeghi M, Khanbabaei G, Dehaghani AHS, Sadeghi M, Aravand MA, Akbarzade M, et al. Gas permeation properties of ethylene vinyl acetate–silica nanocomposite membranes. *J Membr Sci* 2008;322:423–8.
- [58] Chen L, Zheng K, Tian X, Hu K, Wang R, Liu C, et al. Double glass transitions and interfacial immobilized layer in *in situ* synthesized poly(vinyl alcohol)/silica nanocomposites. *Macromolecules* 2010;43:1076–82.
- [59] Peng Z, Kong LX, Li S, Spiridonov P. Poly(vinyl alcohol)/silica nanocomposites: morphology and thermal degradation kinetics. *J Nanosci Nanotechnol* 2006;6:3934–8.
- [60] Iijima S. Helical microtubules of graphitic carbon. *Nature* 1991;354:56–8.
- [61] Cooper CA, Young RJ, Halsall M. Investigation into the deformation of carbon nanotubes and their composites through the use of Raman spectroscopy. *Composites Part A* 2001;32A:401–11.
- [62] Gao G, Cagin T, Goddard WA. Energetics, structure, mechanical and vibrational properties of single-walled carbon nanotubes. *Nanotechnology* 1998;9:184–91.
- [63] Uchida T, Kumar S. Single walled carbon nanotube dispersion and exfoliation in polymers. *J Appl Polym Sci* 2005;98:985–9.
- [64] De Heer WA. Nanotubes and the pursuit of applications. *MRS Bull* 2004;29(4):281–5.
- [65] Ajayan P. *Handbook of nanostructured materials and nanotechnology*, vol. 5. New York: Academic Press; 2000. p. 501–75.
- [66] Wang C, Guo Z, Fu S, Wu W, Zhu D. Polymers containing fullerene or carbon nanotube structures. *Prog Polym Sci* 2004;29(11):1079–141.
- [67] Velasco SC, Martinez HAL, Lozada CM, Alvarez CA, Castano VM. Chemical functionalization of carbon nanotubes through an organosilane. *Nanotechnology* 2002;13(4):495–8.
- [68] Bubert H, Haiber S, Brandl W, Marginean G, Heintze M, Bruser V. Characterization of the uppermost layer of plasma-treated carbon nanotubes. *Diamond Related Materials* 2003;12:811–15.
- [69] Zeng H, Gao C, Wang Y, Watts PCP, Kong H, Cui X, et al. *In situ* polymerization approach to multiwalled carbon nanotubes-reinforced nylon 1010 composites: mechanical properties and crystallization behaviour. *Polymer* 2006;47:113–22.
- [70] Mahmood N, Islam M, Hameed A, Saeed S. Polyamide 6/multiwalled carbon nanotube nanocomposites with modified morphology and thermal properties. *Polymers* 2013;5:1380–91.
- [71] Yue X, Wei TZ, Wen XY, Li GH, Yu JZ, Zhu DZ. Crystallization behavior and mechanical properties of poly(vinylidene fluoride)/multi-walled carbon nanotube nanocomposites. *Chem Res Chin Univ* 2010;26(3):491–5.

- [72] Sun G, Chen G, Liu Z, Chen M. Preparation, crystallization, electrical conductivity and thermal stability of syndiotactic polystyrene/carbon nanotube composites. *Carbon* 2010;48:1434–40.
- [73] Novoselov KS, Geim AK, Morozov SV, Jiang D, Zhang Y, Dubonos SV, et al. Electric field effect in atomically thin carbon films. *Science* 2004;306(5696):666–9.
- [74] Geim AK, Novoselov KS. The rise of graphene. *Nat Mater* 2007;6:183–91.
- [75] Park S, Ruoff RS. Chemical methods for the production of graphenes. *Nat Nanotechnol* 2009;4:217–24.
- [76] Xu C, Wang X, Zhu JW. Graphene–metal particle nanocomposites. *J Phys Chem C* 2008;112(50):19841–5.
- [77] Wang F, Zhang YB, Tian CS, Girit C, Zettl A. Gate-variable optical transitions in graphene. *Science* 2008;320:206–9.
- [78] Eda G, Chhowalla M. Graphene-based composite thin films for electronics. *Nano Lett* 2009;9(2):814–18.
- [79] Yang XY, Zhang XY, Ma YF, Huang YS. Super paramagnetic graphene oxide–Fe<sub>3</sub>O<sub>4</sub> nanoparticles hybrid for controlled targeted drug carriers. *J Mater Chem* 2009;19:2710–14.
- [80] Varghese N, Mogera U, Govindaraj A, Das A, Maiti PK, Sood AK. Binding of DNA nucleobases and nucleosides with graphene. *ChemPhysChem* 2009;10:206–10.
- [81] Wu ZS, Pei SF, Ren WC, Tang D, Gao LB, Liu BL, et al. Field emission of single-layer graphene films prepared by electrophoretic deposition. *Adv Mater* 2009;21(17):1756–60.
- [82] Balandin AA, Ghosh S, Bao WZ, Calizo I, Teweldebrhan D, Miao F, et al. Superior thermal conductivity of single-layer graphene. *Nano Lett* 2008;8:902–7.
- [83] He H, Klinowski J, Forster M, Lerf A. A new structural model for graphite oxide. *Chem Phys Lett* 1998;287:53–6.
- [84] Lerf A, He H, Forster M, Klinowski J. Structure of graphite oxide revisited. *J Phys Chem B* 1998;102:4477–82.
- [85] Stankovich S, Dikin DA, Piner RD, Kohlhaas KA, Kleinhammes A, Jia Y, et al. Synthesis of graphene-based nanosheets via chemical reduction of exfoliated graphite oxide. *Carbon* 2007;45:1558–65.
- [86] Hummers Jr WS, Offeman RE. Preparation of graphitic oxide. *J Am Chem Soc* 1958;80:1339.
- [87] Fu C, Zhao G, Zhang H, Li S. Evaluation and characterization of reduced graphene oxide nanosheets as anode materials for lithium-ion batteries. *Int J Electrochem Sci* 2013;8:6269–80.
- [88] Zhu Y, Murali S, Cai W, Li X, Suk JW, Potts JR, et al. Graphene and graphene oxide: synthesis, properties, and applications. *Adv Mater* 2010;22(35):3906–24.
- [89] Park S, An J, Potts JR, Velamakanni A, Murali S, Ruoff RS. Hydrazine-reduction of graphite- and graphene oxide. *Carbon* 2011;49:3019–23.
- [90] Chen W, Yan L. Preparation of graphene by a low-temperature thermal reduction at atmosphere pressure. *Nanoscale* 2010;2:559–63.
- [91] Yang J, Huang Y, Lv Y, Zhao P, Yang Q, Li G. Intrinsically thermal-oxidative stabilization effect of chemically reduced graphene oxide on polypropylene. *J Mater Chem A* 2013;1(37):11184–91.
- [92] Morimune S., Nishin, Goto T., Graphene oxide reinforced poly(vinyl alcohol) nanocomposites (21 Aug 2011–26 Aug 2011) 18th international conference on composite materials, Jeju International Convention Center, Jeju Island, South Korea, <<http://www.iccm-central.org/Proceedings/ICCM18proceedings/iccm.htm>>.

- [93] Bhattacharyya A, Chen S, Zhu M. Graphene reinforced ultra high molecular weight polyethylene with improved tensile strength and creep resistance properties. *Express Polym Lett* 2014;8(2):74–84.
- [94] Ding R, Hu Y, Gui Z, Zong R, Chen Z, Fan W. Preparation and characterization of polystyrene/graphite oxide nanocomposite by emulsion polymerization. *Polym Degradation Stability* 2003;81:473–6.
- [95] Suresh KI, Chithambaram K, Vinod VTP, Rajender N, Venkateshwara Reddy M, Černík M. *Polym Adv Technol* 2015;26:214–22.
- [96] Chieng BW, Ibrahim NA, Yunus WM, Hussein MZ, Then YY, Loo YY. Effects of graphene nanoplatelets and reduced graphene oxide on poly(lactic acid) and plasticized poly(lactic acid): a comparative study. *Polymers* 2014;6(8):2232–46.
- [97] Upadhyay J, Das R, Rao S, Liu D, Bhattacharyya D. Manufacturing and characterization of PMMA–graphene oxide (GO) nanocomposite sandwich films with electrospun nano-fibre core. *J Achiev Mater Manuf Eng* 2012;55(2):835–40.
- [98] Aldosari MA, Othman AA, Alsharaeh EH. Synthesis and characterization of the *in situ* bulk polymerization of PMMA containing graphene sheets using microwave irradiation. *Molecules* 2013;18:3152–67.
- [99] Zhu J, Chen M, Qu H, Zhang X, Wei H, Luo Z, et al. Interfacial polymerized poly-aniline/graphite oxide nanocomposites toward electrochemical energy storage. *Polymer* 2012;53(25):5953–64.
- [100] Pavithra S, Rajender N, Venkateswara Reddy M, Murugan K, Suresh KI. Effect of graphene oxide (GO) size and structure on synthesis and optoelectronic properties of hybrid GO–poly (3-hexylthiophene) nanocomposites. *Polym Compos* 2015. Available from: <http://dx.doi.org/10.1002/pc.23646>.
- [101] Saini V, Abdulrazzaq O, Bourdo S, Dervishi E, Petre A, Bairi VG, et al. Structural and optoelectronic properties of P3HT–graphene composites prepared by *in-situ* oxidative polymerization. *J Appl Phys* 2012;112:054327–054327-9.
- [102] Kumar S, Negi YS, Upadhyaya JS. Studies on characterization of corn-cob based nanoparticles. *Adv Mater Lett* 2010;1(3):246–53.
- [103] Wegner TH, Jones PE. Advancing cellulose-based nanotechnology. *Cellulose* 2006;13(2):115–18.
- [104] Lima MMD, Borsali R. Rodlike cellulose microcrystals: structure, properties, and applications. *Macromol Rapid Commun* 2004;25(7):771–87.
- [105] Frone A, Panaitescu NDM, Donescu D, Spataru CI, Radovici C, Trusca R, et al. Preparation and characterization of PVA composites with cellulose nanofibers obtained by ultrasonication. *Bioresources* 2011;6(1):487–512.
- [106] Favier V, Canova GR, Cavaille JY, Chanzy H, Dufresne A, Gauthier C. Nanocomposite materials from latex and cellulose whiskers. *Polym Adv Technol* 1995;6:351–5.
- [107] Kumar A, Negi YS, Bhardwaj NK, Choudhary V. Synthesis and characterization of cellulose nanocrystals/PVA based bionanocomposite. *Adv Mater Lett* 2013;4(8):626–31.
- [108] Cao X, Dong H, Li CM. New nanocomposite materials reinforced with flax cellulose nanocrystals in waterborne polyurethane. *Biomacromolecules* 2007;8:899–904.
- [109] Zhou C, Chu R, Wu R, Wu Q. Electrospun polyethylene oxide/cellulose nanocrystal composite nanofibrous mats with homogeneous and heterogeneous microstructures. *Biomacromolecules* 2011;12(7):2617–25.

- [110] Cao X, Chen Y, Chang PR, Muir AD, Falk G. Starch-based nanocomposites reinforced with flax cellulose nanocrystals. *Express Polym Lett* 2008;2(7):502–10.
- [111] Chu B, Hsiao BS. Small-angle X-ray scattering of polymers. *Chem Rev* 2001;101(6):1727–62.
- [112] Bandyopadhyay J, Ray SS. The quantitative analysis of nano-clay dispersion in polymer nanocomposites by small angle X-ray scattering combined with electron microscopy. *Polymer* 2010;51(6):1437–49.
- [113] Wilson R, George SM, Maria HJ, Plivelic TS, Kumar A, Thomas S. Clay intercalation and its influence on the morphology and transport properties of EVA/clay nanocomposites. *J Phys Chem C* 2012;116(37):20002–14.
- [114] Nawani P, Burger C, Rong L, Chu B, Hsiao BS, Tsou AH, et al. Characterization of nanoclay orientation in polymer nanocomposite film by small-angle X-ray scattering. *Polymer* 2010;51(22):5255–66.
- [115] Carastan DJ, Amurin LG, Craievich AF, Gonçalves MC, Demarquette NR. Clay-containing block copolymer nanocomposites with aligned morphology prepared by extrusion. *Polym Int* 2014;63(2):184–94.
- [116] Wang R, Schuman T, Vuppalapati RR, Chandrashekhara K. Fabrication of bio-based epoxy–clay nanocomposites. *Green Chem* 2014;16(4):1871–82.
- [117] Carastan DJ, Amurin LG, Craievich AF, Goncalves MD, Demarquette NR. Morphological evolution of oriented clay-containing block copolymer nanocomposites under elongational flow. *Eur Polym J* 2013;49(6):1391–405.
- [118] Wang D, Das A, Leuteritz A, Mahaling RN, Jehnichen D, Wagenknecht U, et al. Structural characteristics and flammability of fire retarding EPDM/layered double hydroxide (LDH) nanocomposites. *RSC Adv* 2012;2:3927–33.
- [119] Dahmouche K, Santilli CV, Pulcinelli SH, Craievich AF. Small-angle X-ray scattering study of sol-gel-derived siloxane–PEG and siloxane–PPG hybrid materials. *J Phys Chem B* 1999;103(24):4937–42.
- [120] Hood MA, Gold CS, Beyer FL, Sands JM, Li CY. Extraordinarily high plastic deformation in polyurethane/silica nanoparticle nanocomposites with low filler concentrations. *Polymer* 2013;54(24):6510–15.
- [121] Golosova AA, Adelsberger J, Sepe A, Niedermeier MA, Lindner P, Funari SS, et al. Dispersions of polymer-modified carbon nanotubes: a small-angle scattering investigation. *J Phys Chem C* 2012;116(29):15765–74.
- [122] Chen X, Yoon K, Burger C, Sics I, Fang D, Hsiao BS, et al. *In-situ* X-ray scattering studies of a unique toughening mechanism in surface-modified carbon nanofiber/UHMWPE nanocomposite films. *Macromolecules* 2005;38(9):3883–93.
- [123] Lee B, Yoon J, Oh W, Hwang Y, Heo K, Jin KS, et al. *In-situ* grazing incidence small-angle X-ray scattering studies on nanopore evolution in low-k organosilicate dielectric thin films. *Macromolecules* 2005;38(8):3395–405.
- [124] Chen H, Lin S, Jiang J, Su Y, Wei K. Solution-processed zinc oxide/polyethylenimine nanocomposites as tunable electron transport layers for highly efficient bulk heterojunction polymer solar cells. *ACS Appl Mater Interfaces* 2015;7:6273–81.

# 15

## X-ray photoelectron spectroscopy of nanofillers and their polymer nanocomposites

**A.T. Mane and V.B. Patil**

*Functional Materials Research Laboratory, School of Physical Sciences, Solapur University, Solapur, Maharashtra, India*

---

### 15.1 INTRODUCTION

Over the past decade, semiconductor metal oxide-conducting polymer composites have been a rising area of research in different fields of science and technology. Composites are a special class of materials formed by the intermixing of two or more nanosized materials, resulting in materials having more premier properties than the single counterpart. Polypyrrole (PPy) is a p-type material and has fascinated many because of its chemical stability against atmospheric conditions, low cost, room temperature operation, easy processability, excellent conductivity, convenient processing, tunable electronic properties, and potential for semiconducting and even metallic behavior.  $\text{WO}_3$  is a n-type metal oxide consisting of useful properties as catalytic behavior, high structural flexibility, switchable optical properties, etc. A PPy–tungsten oxide ( $\text{WO}_3$ ) nanocomposite is a new class of materials with superior properties which can overcome the insufficiency of a single counterpart [1]. The PPy– $\text{WO}_3$  nanocomposite is a sophisticated system with strong electronic relations between organic and inorganic materials, and thus shows better chemical and physical properties [2,3].

Moreover, among various conducting polymers, PPy has attracted much curiosity due to its ease of synthesis by electrochemical and chemical methods, and disadvantages such as insolubility, poor stability, and long response time [3]. Among the semiconducting metal oxides,  $\text{WO}_3$  is one of the best materials and has attracted much interest due to its excellent physical and chemical properties. It possesses a high operating temperature of about 300–500 °C, which increases power consumption, reduces sensor life, heat loss, and poisoning [4].

As per the literature survey, Salaneck [5] utilized X-ray photoelectron spectroscopy (XPS) to characterize the conducting polymer  $\text{BF}_4^-$  doped PPy, and found that the pyrrole units were preserved in the polymer. The dopent occurs as  $\text{BF}_4^-$  ions, there are four pyrrole units per each  $\text{BF}_4^-$  ion, and that electronic charge is extracted uniformly from all pyrrole units by the dopent ion.

Lim et al. [6] studied the XPS investigation of physicochemical interactions that occurred during the deposition of copper atoms on the as-synthesized PPy–dodecylbenzene sulfonic acid (DBSA) salt film. The *in-situ* XPS studies allowed for the elucidation of the changes in the intrinsic oxidation state of the polymer, metal, and dopent under the high vacuum environment during metallization. Gautier et al. [7] uses XPS characterization of the GC/PPy/PPy ( $\text{Ni}_{0.3}\text{Co}_{22.7}\text{O}_4$ )/PPy composite electrode. The results indicate that the electronic structure of PPy is independent of the thickness of the PPy used to prepare the electrodes. Slimane et al. [8] utilizes poly(vinyl chloride) powder particles which were suspended in aqueous solutions and served as the substrate for the *in-situ* polymerization of chloride-doped PPy. The main objective was to improve the processability of PPy.

Herein, PPy is prepared by a chemical oxidative polymerization method with the use of ammonium per sulfate as an oxidizing agent [9].  $\text{WO}_3$  is prepared by sol-gel method using anhydrous tungsten hexachloride ( $\text{WCl}_6$ ) as a source of “W” [4]. PPy– $\text{WO}_3$  nanocomposites were prepared by a mechanical mixing method. Nanocrystalline  $\text{WO}_3$  was added to PPy in the ratio 1:0.5 wt.% to obtain a homogeneous mixture of the PPy– $\text{WO}_3$  nanocomposite [10]. The prepared powder was characterized by XPS, and confirms the formation of the PPy– $\text{WO}_3$  nanocomposite that improves the physical and chemical properties and the oxidation state of PPy, which leads to improvement of the processability of PPy.

---

## 15.2 XPS: TOOL FOR CHARACTERIZATION OF POLYMER AND ITS COMPOSITE

### 15.2.1 BASIC PRINCIPLE

The foundation to electron spectroscopy was laid in 1887, when Heinrich Hertz discovered the photoelectric effect. However, it took more than half a century more to establish photoelectron spectroscopy as a technique. In 1950, Kai Siegbahn reported the first successful study in photoelectron spectroscopy for which he received the 1981 Nobel Prize for Physics [11,12]. The researchers coined the term electron spectroscopy for chemical analysis. However, since other methods also give chemical information, it is more commonly known as XPS today.

The term electron spectroscopy is generic and covers a large number of techniques such as XPS, ultraviolet photoelectron spectroscopy, Auger electron spectroscopy, electron energy lens spectroscopy, etc. The techniques wherein monochromatic photons are used as the probing signal and the characteristics of

the electrons emitted from the surface are studied, falls under the umbrella of photoelectron spectroscopy [13]. Electrons with low energies do not have the penetrability in the specimen and thus, only those electrons from atoms on the first few atomic layers of the specimen (surface) leave the surface without losing part of their energy. Those electrons arising from deep inside the specimen will lose part of their energy and form the background in the energy spectrum of the emitted electrons. The inelastic mean free path of the electrons in a specimen depends on the energy of the electrons and the nature of the specimen. It is given by

$$\lambda = \frac{538a_A}{E_A^2} + 0.41a_A(a_A E_A)^{1/2} \quad (15.1)$$

where “ $E_A$ ” is energy of the electron in eV, “ $a_A$ ” is the volume of the atom, and “ $\lambda$ ” is expressed in nm. The intensity of electrons emitted from the depth of the specimen is reduced following Beer-Lamberts law, and the angular distribution follows cosine law. Hence, almost 95% of electrons emitted from the surface are from atoms within a depth of  $3\lambda$ . In photoelectron spectroscopy, the depth of penetration of a probing signal is larger than that of the emitted electrons and hence, the limitation on the layers analyzed is not restricted by the penetrability of the probing signal. Any species that has electrons exists in certain states with corresponding binding energies. A measure of the binding energies leads to the identification of the species and the number of electrons associated with the energy leads to the quantification of the states and in turn, of the number of electrons as a function of the binding energy in a given sample. Measurement of the kinetic energy (KE) of the electrons that are emitted from a solid will lead to the measurement of the bound electron spectrum in that solid. When a monochromatic beam of photons of energy “ $h\nu$ ” is launched on an isolated atom, the photons may get scattered elastically or inelastically. When the energy of the photons is more than the binding energy BE of the electron in the atom, the electron is ejected from an atomic energy level by an X-ray photon, mostly from an Al- $K_\alpha$  or Mg- $K_\alpha$  primary source, and energy of the emitted photoelectron is analyzed by detectors. The XPS process is schematically represented in Fig. 15.1 for the emission of an electron from the 1s shell of an atom.

As the recoil energy of the atom due to the emission of an electron is negligible, due to the heavy mass differences between the two particles, KE is given by Eqn (15.2)

$$\text{KE} = h\nu - \text{BE} - e\phi \quad (15.2)$$

where KE = kinetic energy of the ejected photoelectron,  $h\nu$  = characteristic energy of the X-ray photon, BE = binding energy of the atomic orbital from which the electron originates, and  $e\phi$  = spectrometer work function.

The work function is the minimum amount of energy an individual electron needs to escape from the surface. Each element produces a unique set of electrons with specific energies. By measuring the number of these electrons as a function of kinetic (or binding) energy, an XPS spectrum is obtained. All elements can be detected, except H and He.

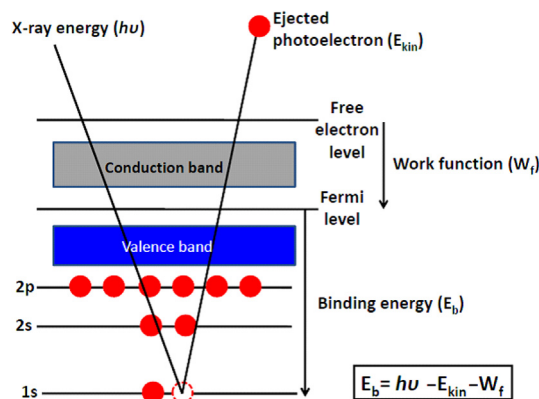


**FIGURE 15.1**

Schematic representation of the XPS process.

The same experiment may be extended to a solid specimen with appropriate correction for the work function of the spectrometer.

$$KE = h\nu - BE \quad (15.3)$$

This correction is necessary as the solid specimen is in electrical contact with the spectrometer. It is clear that only binding energies lower than the exciting radiation (1486.6 eV for Al- $K_\alpha$  and 1253.6 eV for Mg- $K_\alpha$ ) are probed.

### 15.2.2 BASIC COMPONENTS OF XPS MEASUREMENTS

Photoelectron spectrometers consist of a source of EM radiation, either an X-ray source or an ultraviolet source, an electron kinetic energy analyzer, and an electron counter, all housed in an ultra-high vacuum system. A schematic illustration is given in Fig. 15.2. The line width of the X-ray source should be as narrow as possible. The X-ray source could be an X-ray tube, or radiations from a synchrotron. A synchrotron is an excellent source of high fluxes of X-rays, whose wavelength can be tuned but are not readily available. An X-ray tube with a metallic target, such as aluminum, operated at voltages needed to excite the K-electron will give the characteristic family of X-rays. The characteristic lines are almost a hundred times the intensity of the Bremsstrahlung radiation that forms the background. Thus, X-ray tubes are directly used as photon sources in X-ray photoelectron spectrometers. An appropriate filter can be used to cut off other lines such as  $K_\beta$ . Normally aluminum, magnesium, and zirconium are used as targets in the source of radiation with energies 1486.6, 1253.6, and 2042.4 eV, respectively [14]. Different types of electron spectrometers analyze the spectrum of electrons from the specimen.

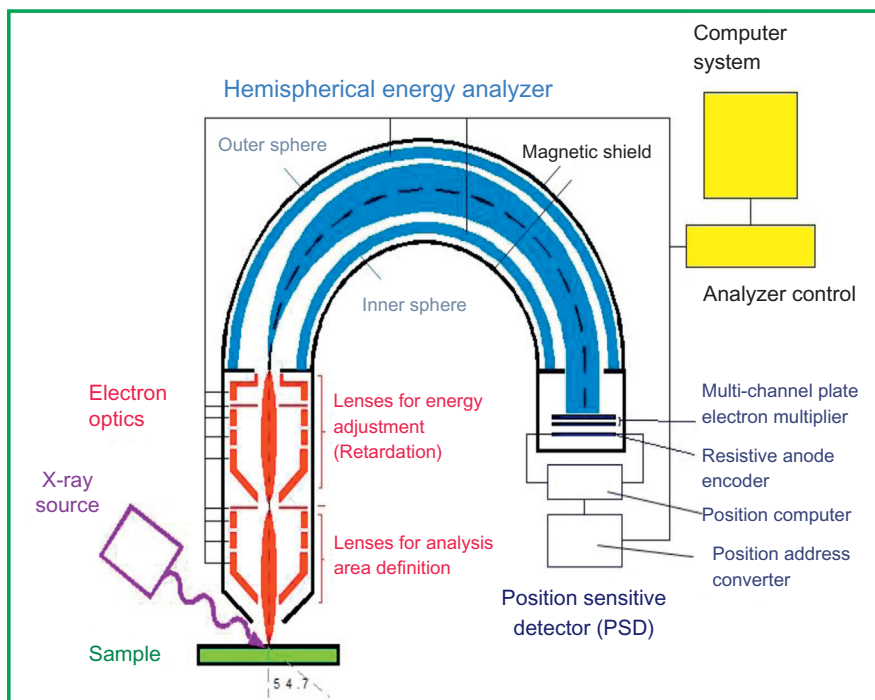


**FIGURE 15.2**

A schematic illustration of XPS.

### 15.2.3 APPLICATIONS

The major use of XPS is for the identification of compounds using energy shifts due to changes in the chemical structure of the sample atoms. For example, an oxide exhibits a different spectrum than a pure element ( $\text{SiO}_2$  on Si for example). Chemical compounds or elements are identified by the location of energy peaks on the undifferentiated XPS spectrum. Concentration determination is more difficult. Peak heights and peak areas can be used with appropriate correction factors to obtain concentrations, but this method is primarily used for identifications.

## 15.3 XPS STUDY OF PPy

XPS analysis was used to confirm the formation of PPy. A representative survey spectrum of PPy is shown in Fig. 15.3a. The survey spectrum consists of C 1s, N 1s, and O 1s, a peak which represents elemental compositions present in PPy. The start binding energy, peak binding energy, end binding energy, full width at half maximum (FWHM), and atomic % of corresponding elements are

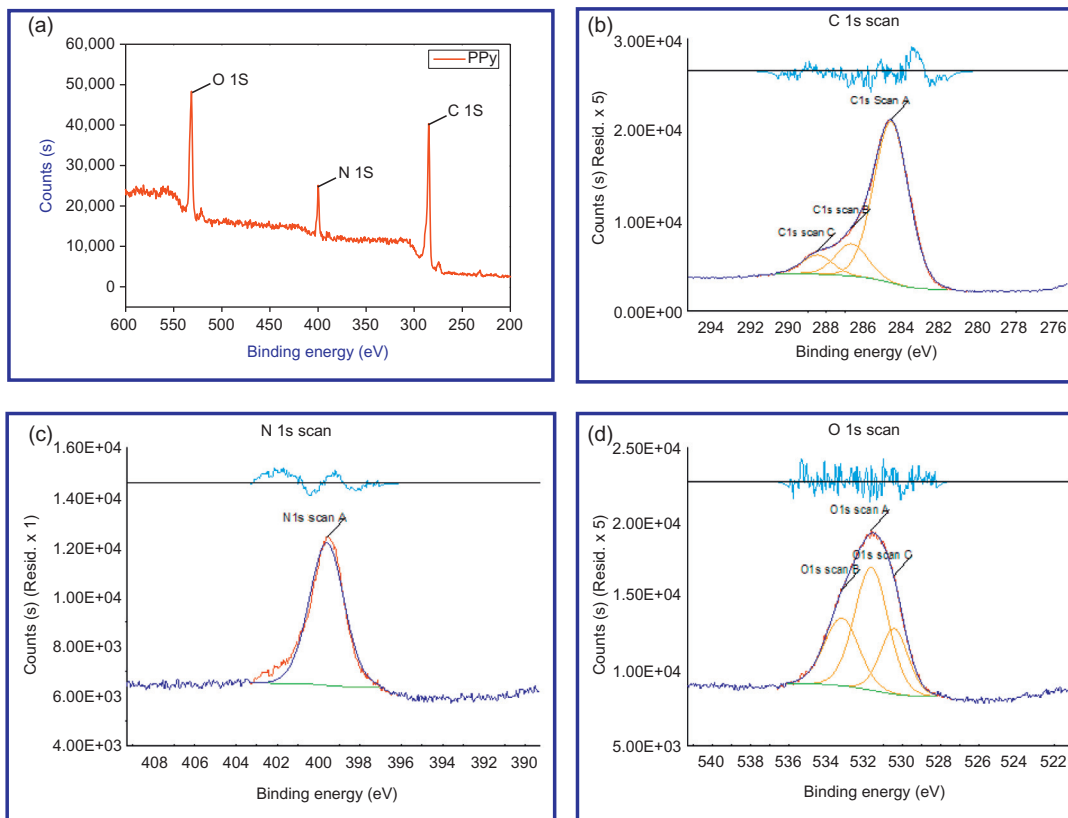


**FIGURE 15.3**

(a) Survey spectra of PPy, (b) C 1s, (c) N 1s, and (d) O 1s. Core-level XPS spectra of PPy.

Table 15.1 Survey Table of PPy

Name	Start BE	Peak BE	End BE	Height Counts	FWHM (eV)	Area (P) CPS (eV)	at. (%)
C 1s	294.3	284.86	280.13	34,457.08	2.63	122,725.72	68.91
O 1s	537.57	531.79	527.45	29,416.04	3.39	106,869.23	20.96
N 1s	402.96	399.8	395.5	12,126.62	2.13	32,161.55	10.13

summarized in Table 15.1. The core-level XPS spectrum of C 1s, N 1s, and O 1s are shown in Fig. 15.3b–d. The core-level spectrum C 1s (Fig. 15.3b) verified that the towering value of number of counts (s) at the binding energy 284.60 eV (C–C) contains a large FWHM value followed by a high binding energy tail [15]. The core-level spectrum of C 1s has been deconvoluted into two neutral carbons peaks at about 286.68 eV which is due to the –COH and 288.48 eV and the –COOH, respectively [16]. The N 1s core-level spectrum of PPy is shown in Fig. 15.3c. The core nitrogen peak is attributed to the neutral nitrogen (–NH–) in the pyrrole ring centered at about 399.6 eV [15,16]. The oxygen peak O 1s in the XPS spectrum of PPy is shown in Fig. 15.3d. The core-level spectrum of O 1s is deconvoluted into three peaks at binding energies of 530.44, 531.64, and 533.44 eV. The binding energy peak at 531.64 eV is due to the O = C, and binding energy peak at 533.44 eV relates to the C–O [17]. All of the binding energy peaks agree well with those reported, and indicate that the formation of PPy is achieved [18,19].

## 15.4 XPS STUDY OF WO<sub>3</sub>

The formation of WO<sub>3</sub> was confirmed by XPS analysis. The wide region XPS spectra (survey spectra) WO<sub>3</sub> is shown in Fig. 15.4a, and the survey table of WO<sub>3</sub> is shown in Table 15.2. This overview spectrum demonstrates that W, C, and O atoms were present in the sample. The survey spectrum shows that the two peaks W4f5 and W4f7 are located at 38.2 and 35.62 eV, respectively, with a difference in energy of 2.12 eV, which is characteristic of the W<sup>6+</sup> state and confirms the existence of WO<sub>3</sub> [20]. The peak O 1s at 530.94 eV indicates the presence of oxygen and matches well with the reported value [21].

Figure 15.4b shows the core-level spectra of W4f. The two peaks observed at the binding energies of 35.62 and 38.2 eV, correspond to spin–orbit splitting of the W4f7/2 and W4f5/2 components respectively in tungsten oxide [22]. Figure 15.4c shows four peaks in the core-level spectra of O 1s. The peak with a binding energy of 530.5 eV is due to the W, the peak at 529.8 eV is due to OH-groups, the peak located at 531.8 eV illustrates the C contamination and is attributed to C–O bonds. The highest energy peak at 533.2 eV is attributed to water bound at the surface of the samples [21].

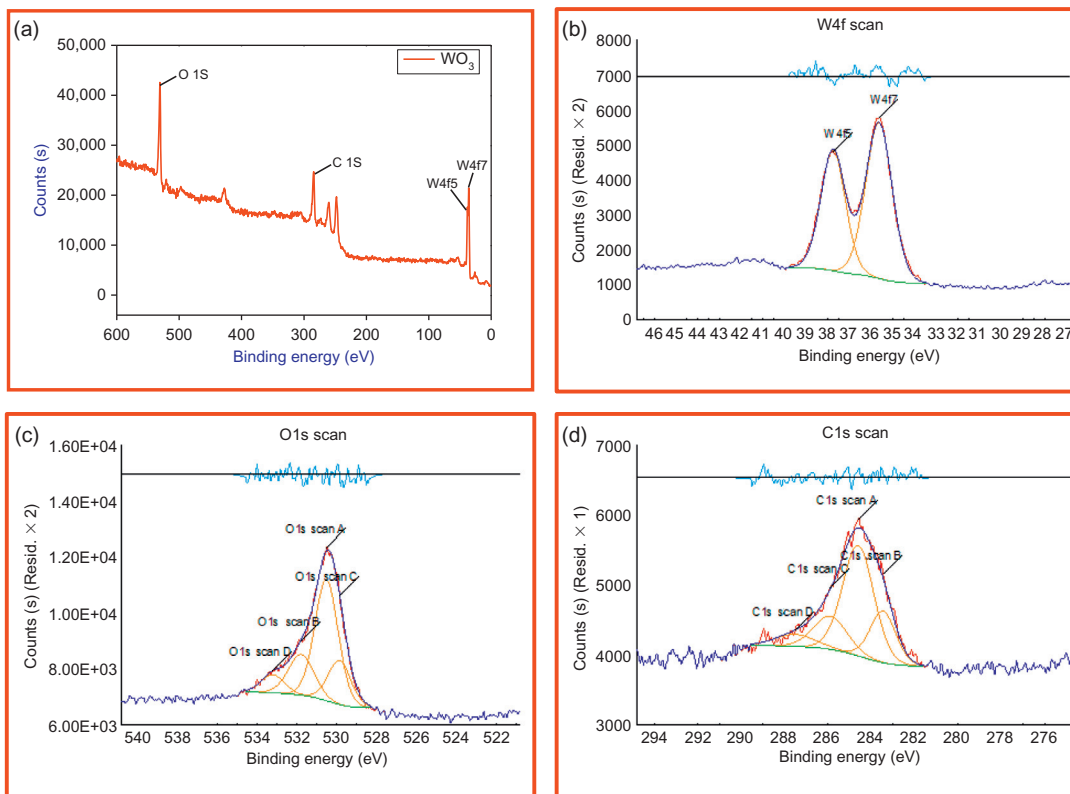


**FIGURE 15.4**

(a) Survey spectra of  $\text{WO}_3$ , (b) C 1s, (c) N 1s, and (d) O 1s. Core-level XPS spectra of  $\text{WO}_3$  at  $700\text{ }^\circ\text{C}$ .

Table 15.2 Survey Table of WO<sub>3</sub>

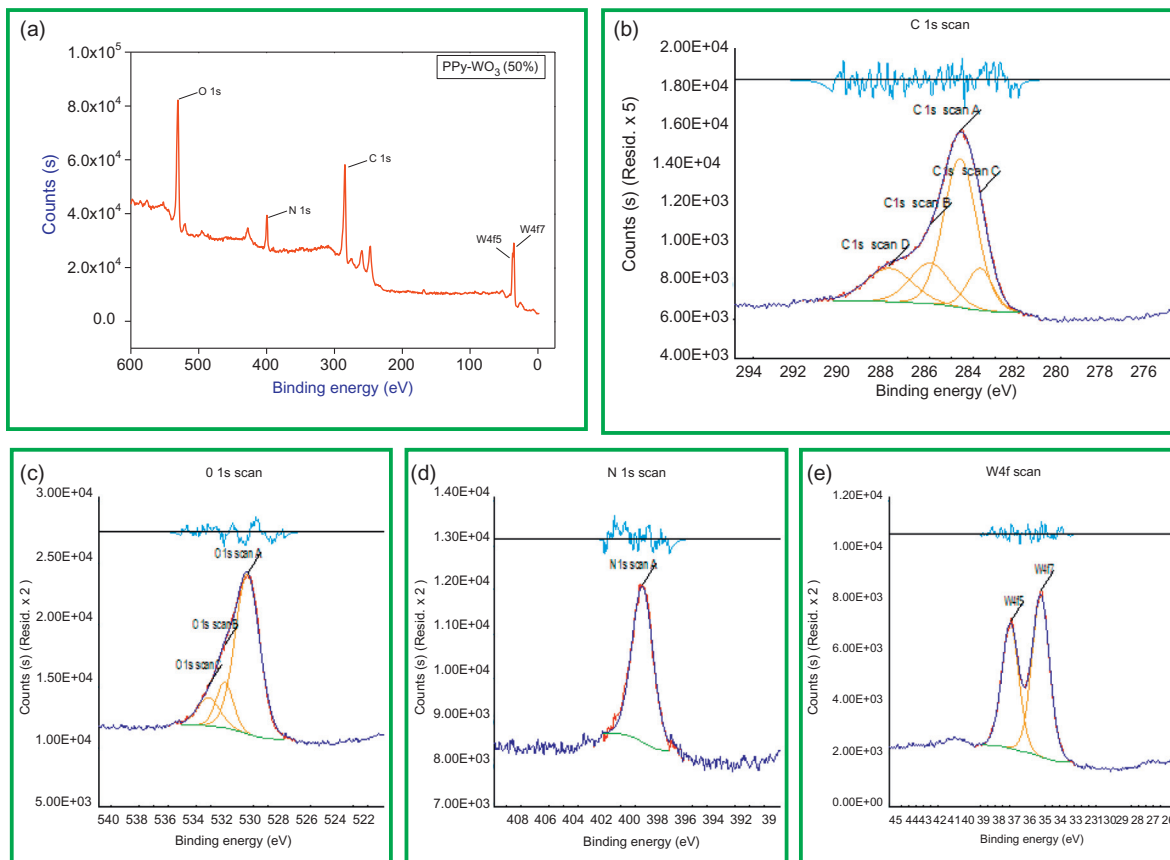
Name	Start BE	Peak BE	End BE	Height Counts	FWHM (eV)	Area (P) CPS (eV)	at. (%)
C 1s	293.55	284.6	280.5	10,054.95	3.31	41,008.01	62.76
O 1s	537.34	530.94	527.54	19,116.6	2.72	60,313.36	32.23
W4f7	37.05	35.62	32.96	7611.36	1.5	12,447.62	3.41
W4f5	40.42	38.2	37.05	4660.31	0.59	4594.32	1.6

Figure 15.4d shows the high-resolution XPS spectrum of the C 1s region at approximately 285 eV. The binding energy with a peak at 285.89 eV was ascribed to sp<sup>2</sup>-hybridization bonding structures of C atoms [23]. The peaks at 283.45 and 287.49 eV were characteristic of the oxygen-bound species C=O and C–O, respectively [24,25]. Thus, XPS results prove the formation WO<sub>3</sub>.

## 15.5 XPS STUDY OF PPy–WO<sub>3</sub> NANOCOMPOSITE

The surface composition and the chemical states of PPy–WO<sub>3</sub> hybrid nanocomposites were investigated by XPS. The wide region XPS spectrum for the PPy–WO<sub>3</sub> (50%) nanocomposite is shown in Fig. 15.5a with the referenced binding energy scale. The binding energy peaks C 1s and N 1s are located at the binding energy of 284.6 eV (C–C) and 399.56 eV (N–C), respectively, which agree well with reported values of PPy [15]. The peak O 1s at 530.7 eV indicates the presence of oxygen and most likely corresponds to O<sub>2</sub> in the PPy–WO<sub>3</sub> lattice [18]. The W4f5 peak is found at 37.63 eV and the W4f7 peak is located at 35.07 eV. The splitting of the 4f doublet of W was found to be 2.1 eV, which indicates that the energy position of this doublet corresponds to the W<sup>6+</sup> oxidation state [26]. The overview of the spectrum demonstrates that W, C, O, and N atoms were present in the sample and their details are summarized in Table 15.3.

In order to confirm the core-sheath structure of PPy–WO<sub>3</sub> nanocomposites, XPS analysis was used. Figure 15.5b–e shows high-resolution XPS spectra of PPy–WO<sub>3</sub> nanocomposites with carbon, oxygen, nitrogen, and tungsten, respectively, with the referenced binding energy scale. The main characteristic carbon 1s peak corresponds to binding energy of 284 eV (Fig. 15.5b). The carbon peak is asymmetric and can be decomposed into four lines by shape analysis with Gaussian–Lorentzian fitting functions. The lowest binding energy line is located at 283.6 eV, whereas the second peak is at 284.3 eV. These lines are recognized as a and b carbons in the PPy ring, respectively. The energy splitting between the peaks is 0.7 eV and is slightly less than that of a and b carbons in the pyrrole monomer, which are reported as 0.9 eV [27,28]. The third Gaussian–Lorentzian component is located at 286 eV and may be associated with the presence of doped hydrocarbons and contaminants. The fourth peak is due to the photoemission



**FIGURE 15.5**

(a) Survey spectra of PPy-WO<sub>3</sub> nanocomposite, (b) C 1s, (c) O 1s, (d) N 1s, and (e) W4f. Core-level XPS of PPy-WO<sub>3</sub> nanocomposite.

**Table 15.3** Survey Table of PPy–WO<sub>3</sub> Nanocomposite

Name	Start BE	Peak BE	End BE	Height Counts	FWHM (eV)	Area (P) CPS (eV)	at. (%)
C 1s	293.27	284.6	280.24	35,014.07	3.1	133,570.3	61.79
O 1s	537.77	530.7	527.22	46,384.43	3.37	168,992.3	27.3
W4f7	36.8	35.07	32.69	8353.07	1.57	14,076	1.17
W4f5	40.17	37.63	36.68	5495.82	1.02	5556.07	0.58
N 1s	403.28	399.56	395.27	12,431.1	2.42	35,258.58	9.15

peak observed at 288 eV. The presence of oxygen in the sample is shown in Fig. 15.5c. The peak at 529.8 eV most likely corresponds to O<sub>2</sub><sup>-</sup> in the PPy–WO<sub>3</sub> lattice. The wide peak of the O 1s spectrum can be fitted with three Gaussian functions at 530.1, 531.9, and 533.2 eV, and it represents the existence of crystal lattice oxygen (OW–O), hydroxyl groups (OOH), and absorbed water. The deconvolution of the N 1s region indicates the presence of two nitrogen heteroatoms (Fig. 15.5d). The main N peak located at 399.7 eV is attributed to neutral N in the pyrrole ring. The second peak is located at 401.6 eV, and is due to NH<sup>+</sup>, a bipolaron charge carrier species. The shift of 1.9 eV to the higher binding energy is attributed to the electrostatic interaction with doped anions and confirms the interaction between WO<sub>3</sub> nanoparticles and PPy. In Fig. 15.5e, the peaks located at 37.3 and 35.2 eV are due to W4f5 and W4f7, respectively. The energy difference of 2.1 eV indicates that the energy position of this doublet corresponds to the W<sup>6+</sup> oxidation state [26].

## 15.6 XPS STUDY OF DBSA-DOPED PPy–WO<sub>3</sub> NANOCOMPOSITE

The survey spectra between BE V/S counts (s) of DBSA-doped PPy–WO<sub>3</sub> nanocomposites are shown in Fig. 15.6a. The binding energy peak for O 1s positioned at binding energy 531.96 eV represents the oxygen and most corresponds to O<sup>2-</sup> [18]. The binding energy peaks of N 1s and C 1s are located at 400.18 eV (N–C) and 285.09 eV (C–C), respectively, which agree well with reported values of PPy [15]. The presence of S2p peak is due to dopant DBSA and located at 168.72 eV. The W peaks 4f5 and 4f7 are found at 37.84 and 35.46 eV, respectively. The splitting of the 4f doublet of W was found to be 2.38 eV, indicating that the energy position of this doublet is equivalent to the W<sup>6+</sup> oxidation state [26]. Furthermore, the start binding energy, end binding energy, height counts, FWHM, area, and atomic percent of present elements are summarized in Table 15.4.

Thus, electronic environment as well as surface composition can nondestructively be determined by XPS [29]. Figure 15.6b–f shows core-level XPS spectra of the DBSA-doped PPy–WO<sub>3</sub> nanocomposite. The entire core-level spectra are

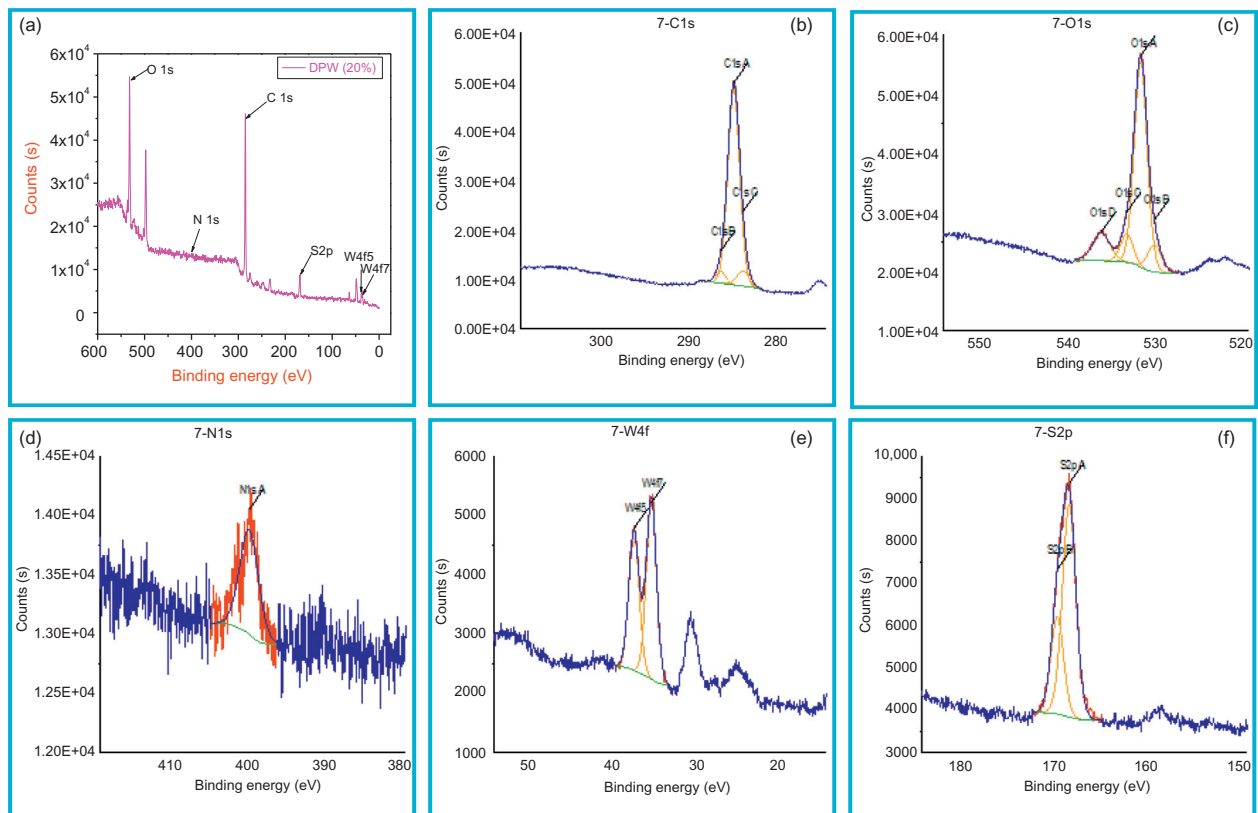


**FIGURE 15.6**

(a) Survey spectra of DBSA-doped PPY–WO<sub>3</sub> nanocomposite, (b) C 1s, (c) O 1s, (d) N 1s, and (e) W4f (f) S 2p. Core-level XPS of DBSA-doped PPY–WO<sub>3</sub> nanocomposite.

**Table 15.4** Survey Table of DBSA-Doped PPy–WO<sub>3</sub> Nanocomposite

Name	Start BE	Peak BE	End BE	Height Counts	FWHM (eV)	Area (P) CPS (eV)	at. (%)
C 1s	290.44	285.09	281.3	37,494.39	1.85	80,277.66	62.50
O 1s	538.58	531.96	529	33,802.32	2.15	97,158.3	26.26
N 1s	405.69	400.18	398.79	964.87	2.01	3542.63	1.6
S2p	172.05	168.72	166.47	5119.1	2.53	13,123.93	5.25
W4f5	39.32	37.84	36.87	1501.7	0.61	1467.57	2.00
W4f7	36.83	35.46	33.95	2269.06	1.19	2797.26	2.39

fitted along with the deconvoluted peaks using a Lorentzian fitting procedure. Figure 15.6b shows carbon C 1s core-level spectra. The observed peaks at binding energy 285.01, 286.5, and 283.91 eV are called C 1s A, C 1s B, and C 1s C, respectively. The first component at 285.01 eV can be attributed to the C–C bond [15]. The second contribution at 286.5 eV can be assigned to the carbon bonded due to C–N and the third peak at 283.91 eV corresponds to the  $\beta$ -carbons of PPy ring [19,30]. Figure 15.6c shows the XPS core-level spectra of O 1s. The four deconvoluted peaks are at 531.81, 530.21, 533.39, and 536.3 eV. The peak at 531.81 eV is due to the O=S of the dopant [31], while the peak located at 530.21 eV represents the existence of crystal lattice oxygen (O<sub>W-O</sub>) hydroxyl groups (O<sub>OH</sub>) [18], and the peak at 533.39 eV corresponds to the oxygen contribution of bound water and polymer-oxidized moieties [31]. The N 1s core-level spectrum of the DBSA-doped PPy–WO<sub>3</sub> nanocomposite is shown in Fig. 15.6d. The main nitrogen peak is centered at approximately 399.88 eV and is attributed to the nitrogen (N–C) in the pyrrole ring [30]. Figure 15.6e shows the XPS core-level evolution of the W4f doublet peak of WO<sub>3</sub>. The deconvoluted peak at binding energy 35.43 eV corresponds to W4f7 and 37.53 eV for the W4f5. W4f7 corresponds to tungsten in the +6 oxidation state (W6<sup>+</sup>) of WO<sub>3</sub>, and W4f5 corresponds to tungsten in the +2 oxidation state (W2<sup>+</sup>) of WO<sub>3</sub> [26]. The core-level spectrum of S 2p is shown in Fig. 15.6f. The existence of sulfur is due to dopant DBSA. The S 2p core-level spectrum is deconvoluted into two binding energies at 168.53 and 169.81 eV. XPS studies indicate that doping of DBSA into the PPy–WO<sub>3</sub> nanocomposite matrix is achieved.

## 15.7 CONCLUSIONS

XPS spectra are obtained by irradiating a material with a beam of X-rays while simultaneously measuring the KE and number of electrons that escape from the top 0–10 nm of the material being analyzed. The aim of this chapter has been to understand the atomic level behavior of materials with the help of XPS measurements. We have discussed the XPS survey spectra and core-level spectra of PPy,

WO<sub>3</sub>, the PPy–WO<sub>3</sub> nanocomposite, and the DBSA-doped PPy–WO<sub>3</sub> nanocomposite. Hybrid nanocomposite materials are a new class of materials with improved properties which can overcome the lacunas of their distinct counterparts. This makes hybrid nanocomposites an excellent material for large-scale applications. The results obtained through XPS are promising and give solid proof of the formation of the desired material.

XPS is used to measure the following:

- The elemental composition of the top 0–10 nm surface.
- To calculate the empirical formula of a material.
- To detect elements that contaminate a surface.
- To give the information regarding the local bonding of atom.
- The identification of chemical states for the elements in the sample.
- Uniformity of elemental composition.
- The binding energy of electronic states.
- The thickness of one or more thin layers (1–8 nm).
- The density of electronic states.

The advantages of XPS are as follows:

- XPS readily yields excellent quantitative accuracy from homogeneous solid-state materials and is used to generate an empirical formula.
- Absolute quantification requires the use of certified or independently-verified standard samples, and is generally more challenging, and thus, is generally less common.
- Relative quantification involves comparisons between several samples in a set, for which one or more analytes are varied while all other components are held constant.
- Quantitative accuracy depends on peak intensity, signal-to-noise ratio, accuracy of relative sensitivity factors, correction for electron transmission function, correction for energy dependence of electron mean free path, surface volume homogeneity, and degree of sample degradation due to analysis.
- The quantitative accuracy of the atomic percent (at.%) values are 90–95% for each major peak. If a high level quality control protocol is used, the accuracy can be further improved.
- Quantitative precision.

---

## REFERENCES

- [1] Navale ST, Khuspe GD, Chougule MA, Patil VB. Room temperature NO<sub>2</sub> gas sensor based on PPy/a-Fe<sub>2</sub>O<sub>3</sub> hybrid nanocomposites. *Ceram Int* 2014;40:8013.
- [2] Gangopadhyay R, De A. Conducting polymer nanocomposites: a brief overview. *Chem Mater* 2000;12:608.
- [3] Mane AT, Navale ST, Patil VB. Room temperature NO<sub>2</sub> gas sensing properties of DBSA doped PPy–WO<sub>3</sub> hybrid nanocomposite sensor. *Org Elect* 2015;1915:25.

- [4] Mane AT, Kulkarni SB, Navale ST, Ghanwat AA, Shinde NM, Kim JH, et al. NO<sub>2</sub> sensing properties of nanostructured tungsten oxide thin films. *Ceram Int* 2014;40:16495.
- [5] Salaneck WR. X-ray photoelectron spectroscopy of boron fluoride doped polypyrrole. *Synth Metals* 1983;5:125.
- [6] Lim VWL, Kang ET, Neoh KG. Physicochemical interactions of deposited copper atoms with chemically synthesized polypyrrole films—an *in-situ* x-ray photoelectron spectroscopy study. *Macromol Chem Phys* 2001;202:2824.
- [7] Gautier JL, Marco JF, Gracia M, Gancedo JR, Garza Guadarrama V, de la, Nguyen-Cong H, et al. Ni<sub>0.3</sub>Co<sub>2.7</sub>O<sub>4</sub> spinel particles/polypyrrole composite electrode: study by X-ray photoelectron spectroscopy. *Electrochim Acta* 2002;48:119.
- [8] Slimane AB, Chehimi MM, Vaulay Marie J. Polypyrrole-coated poly(vinyl chloride) powder particles: surface chemical and morphological characterization by means of X-ray photoelectron spectroscopy and scanning electron microscopy. *Colloid Polym Sci* 2004;282:314.
- [9] Navale ST, Mane AT, Chougule MA, Sakhare RD, Nalage SR, Patil VB. Highly selective and sensitive room temperature NO<sub>2</sub> gas sensor based on polypyrrole thin films. *Synth Metals* 2014;189:94.
- [10] Mane AT, Navale ST, Sen S, Aswal DK, Gupta SK, Patil VB. Nitrogen dioxide (NO<sub>2</sub>) sensing performance of p-polypyrrole/n-tungsten oxide hybrid nanocomposites at room temperature. *Org Elect* 2015;16:195.
- [11] Nordling C, Hagstrom S, Siegbahn K. Application of electron spectroscopy to chemical analysis. *Z Physik* 1964;178:433.
- [12] Hagstrom S, Nordling C, Siegbahn K. Electron spectroscopic determination of the chemical valence state. *Z Physik* 1964;178:439.
- [13] Brundle CR, Baker AD. Chapter I, 2: 6 Electron spectroscopy, theory, techniques and applications. Oxford: Pergamon Press; 1978.
- [14] Hufner S. Photoelectron spectroscopy, principles and applications. IInd ed. Berlin Heidelberg New York: Springer-Verlag; 1995.
- [15] Ge H, Qi G, Kang ET, Neoh KG. Study of overoxidized polypyrrole using X-ray photoelectron spectroscopy. *Polymer* 1994;35:504.
- [16] Joshi A, Gangal SA, Gupta SK. Ammonia sensing properties of polypyrrole thin films at room temperature. *Sens Actua B* 2011;156:938.
- [17] Dall'Ollio A, Dascola G, Varacca V, Bocchi V. Comptes rendus hebdomadaires Des Seances. De L Academie des Sciences Serie C 1968;267:433.
- [18] Brinen JS, Greenhouse S, Pinatti L. ESCA and SIMS studies of plasma treatments of intraocular lenses. *Surf Interface Anal* 1991;17:63.
- [19] Su N, Li HB, Yuan SJ, Yi SP, Yin EQ. Synthesis and characterization of polypyrrole doped with anionic spherical polyelectrolyte brushes. *Express Polym Lett* 2012;6:697.
- [20] Wagner CD, Riggs WM, Davis LE, Moulder JF. p. 146 Handbook of X-ray photoelectron spectroscopy. Eden Prairie, MN: Perkin-Elmer Corporation; 1979.
- [21] Bertus LM, Faure C, Danine A, Labrugere C, Campetb G, Rougier A, et al. Synthesis and characterization of WO<sub>3</sub> thin films by surfactant assisted spray pyrolysis for electrochromic applications. *Mater Chem Phys* 2013;140:49.
- [22] Brundle CR, Baker AD. Electron spectroscopy: theory, techniques and applications, vol. 2. New York, NY: Academic Press; 1978.

- [23] Shalini J, Sankaran KJ, Dong CL, Lee CY, Tai NH, Lin IN. *In situ* detection of dopamine using nitrogen incorporated diamond nanowire electrode. *Nanoscale* 2013;5:1159.
- [24] Xia F, Hu X, Sun Y, Luo W, Huang Y. Layer-by-layer assembled MoO<sub>2</sub>/graphene thin film as a high-capacity and binder-free anode for lithium-ion batteries. *Nanoscale* 2012:44707.
- [25] Jankovský O, Šimek P, Sedmidubský D, Matějková S, Janoušek Z, Šembera F, et al. Water-soluble highly fluorinated graphite oxide. *RSC Adv* 2014:41378.
- [26] Penza M, Tagliente MA, Mirengi L, Gerardi C, Martucci C, Cassano G. Tungsten trioxide (WO<sub>3</sub>) sputtered thin films for a NO<sub>x</sub> gas sensor. *Sens Actu B* 1998;50:9.
- [27] Pfluger P, Street GB. Chemical, electronic, and structural properties of conducting heterocyclic polymers: a view by XPS. *J Chem Phys* 1984;80:544.
- [28] Atanasoska L, Naoi K, Smyrl WH. XPS studies on conducting polymers: polypyrrole films doped with perchlorate and polymeric anions. *Chem Mater* 1992;4:988.
- [29] Chusuei CC, Goodman DW. X-ray photoelectron spectroscopy. *Encyclopedia of physical science and technology*, 17. New York, NY: Academic Press; 2002. p. 922.
- [30] Chougule MA, Pawar SG, Patil SL, Raut BT, Godse PR, Sen S, et al. Polypyrrole thin film: room temperature ammonia gas sensor. *Sensors J IEEE* 2011;11:2137.
- [31] Andreoli E, Rooney A, Redington W, Gunning R, Breslin CB. Electrochemical deposition of hierarchical micro/nanostructures of copper hydroxysulfates on polypyrrole–polystyrene sulfonate films. *J Phys Chem C* 2011;115:8725.

# Index

*Note:* Page numbers followed by “*f*” and “*t*” refer to figures and tables, respectively.

## A

Absorbance, 125–126  
Acoustic phonon frequencies, 362  
Acoustic wave velocity, 373–377  
Acrylamide monomer (AM), 134–135  
Adiabatic solid slabs, 1D PT response of, 319–325  
    specific transfer functions of PT methods, 323–324  
    theory of BD-PT impulse response, 324–325  
    theory of FD- and BD-PT response with periodic excitation, 321–323  
Aerosol process, 20–21  
Aliphatic polyesters, 327  
Alkoxides, 23–24  
Alkyl chain structures, 33*f*  
(3-Aminopropyl) triethoxysilane (APTS), 327  
Applications of polymer nanocomposites, 1–5  
Arc discharge, 28–29, 28*f*  
Aryldiazonium salts, 49  
Atom transfer radical polymerization (ATRP), 38  
Atomic absorption spectroscopy, 6  
Atomic emission spectroscopy, 6  
Atomic fluorescence spectroscopy, 6  
Atomic force microscopy (AFM), 75  
Auger effect, 6  
Auger electron spectroscopy, 453–454  
Auger-electron appearance-potential spectroscopy (AEAPS), 297–299  
Avogadro’s number, 71  
2,2’-Azo-bis(2-amidinopropane) dihydrochloride (AIBA), 39

## B

Back detection (BD)-flash method, 315  
Beer–Lambert law, 125  
Biological systems, 384–385  
Biopolymer matrices, 139–141  
Biopolymer nanocomposites, 193–197  
Boron nitride nanotubes (BNNTs), 66  
Brillouin and other techniques, coupling, 384  
Brillouin spectroscopy (BS), 362  
    Brillouin scattering theory, 363–365  
    experimental setup, 365–373  
    FP interferometer, 366–367  
    scattering geometries, 369–373  
    tandem interferometry, 367–369

    polymers and nanocomposites, 373–385  
    acoustic wave velocity, 373–377  
    biological systems, 384–385  
    coupling of Brillouin and other techniques, 384  
    elastic constants, 377–379  
    glass transition temperature, 380–382  
    refractive index, 382–383  
Bucky-balls *see* Fullerenes  
Bulk heterojunctions (BHJ), 202–204, 247  
Butoxyethanol (BOE), 279

## C

<sup>13</sup>C cross-polarization (CP) magic-angle spinning, 181–182  
<sup>13</sup>C spin-lattice relaxation times, 8–9  
Calcium silicate hydrate (CSH)/PVA nanocomposite, 195  
Carbon dots (C-dots), 9, 171–172, 171*f*  
Carbon nanotubes (CNTs), 8, 25–26, 119, 312  
    chemical methods of dispersion, 41–45  
    chemical functionalization/surface modification, 42  
    defect functionalization, 42–44  
    other methods of sidewall and terminus functionalization, 44–45  
    as fillers in nanocomposites, 40–46  
    physical functionalization/physical blending, 45–46  
    physical methods of dispersion, 41  
    polymer nanocomposites (PNCs), 427–432  
Carbonaceous nanofiller, 119–120  
Carbon-based nanomaterials as nanofillers, 152–154  
Carbon-based nano-objects, 24–30  
    preparation methods, 27–30  
    fullerene and CNTs, 27–30  
    graphene, 30  
    properties of carbon-based nanomaterials, 27  
    structural considerations, 24–27  
Carboranes, 67–68  
Carboxyl-terminated polybutadiene (CTPB), 186–187  
Catalyzed chemical vapor deposition, 29  
Catalyzed CVD (C-CVD) process, 29  
Cationic initiators, 39

- C-CVD setup, 29f  
 Cellulose nanocrystal CNCs, 439–440  
 Ceramic matrix nanocomposites (CMCs), 131  
 Ceramic nanofillers, dielectric analysis, 277–279  
 Ceramic particulates, dielectric spectroscopy, 279–283  
 Cetyl trimethylammonium bromide (CTAB), 19  
 Charge recombination, 206–207, 211–212  
 Charge transport mechanism in polymers, 219–220  
 Chemical elements, dissemination, 3–4  
 Chemical enhancement effect, 89  
 Chemical methods of dispersion of CNTs, 41–45  
 Chemically functionalized CNTs, 43–44  
 Clay, 30–34, 118, 125  
   modifications, 32–34  
   structures, 31–32  
 Complex composites, 315–316  
 Composite materials, 2  
   hybrid, 464–465  
   photothermal studies, 315–319  
     complex composites, 315–316  
     composites with defined microstructure, 316–318  
     composites with random morphology, 318–319  
 Conducting polymers, 35, 254  
 Conduction band, 164  
 Conjugated polymers, 252  
 Continuous wave (CW) EPR spectrometer, 208  
 Controlled-morphology of nanoparticles, 21  
 Core/shell nanofiller-incorporated polymer composite, 169–171  
 Coulomb field, 211  
 Coulomb interactions, 225  
 Coulomb potential, 211  
 Covalent functionalization  
   of graphene and graphene oxide sheets, 48–49  
   of nanotubes, 45  
 Cross-linked polyethylene (XLPE), 300  
 Crystalline materials, 411  
 Cuboctahedron, 17  
 Cyclopentanone, 70–71
- D**  
 D band, 88  
 Deuterated PS (dPS), 78  
 Dielectric relaxation, 290–291, 293  
 Dielectric spectroscopy (DS), 276  
   of ceramic nanofillers, 277–279  
   of ceramic particulates, 279–283  
   of nanocomposites, 283–293  
   nanodielectrics  
     pulsed electro-acoustic analysis, 300–305  
     TSC spectroscopy studies, 293–299  
 Differential scanning calorimetry (DSC), 287, 292, 328, 380  
 Diffuse reflectance FT-IR spectroscopy, 8  
 Dimethylformamide (DMF), 66  
 Dispersion of nanoparticles, 4–5  
 Dispersive IR spectrometers, 113  
 Dispersive spectrometers, 113  
 Dodecylbenzene sulfonic acid (DBSA)-doped PPy-WO<sub>3</sub> nanocomposite, study, 462–464, 464t  
 Double-walled carbon nanotubes (DWCNTs), 26–27  
 Dynamic light scattering (DLS), 174–175  
 Dynamic mechanical analysis (DMA), 362
- E**  
 Effective medium approximation (EMA) concept, 341  
 Elastic constant, 364–365, 372, 377–379  
 Elastomer nanocomposites, 185–188  
 Electrochemical impedance spectroscopy  
   *see* Dielectric spectroscopy (DS)  
 Electromagnetic (EM) enhancement effect, 89  
 Electromagnetic (EM) radiation, 160, 312, 455  
 Electron energy lens spectroscopy, 453–454  
 Electron paramagnetic resonance (EPR) spectroscopy, 9, 208–220  
   Dysonian spectral contribution, 217–218  
   electron relaxation and spin dynamics, 218–219  
   Landé factor, 209–210  
   line shape and width, 214–217  
   mechanism of charge transport in polymers, 219–220  
   spin charge carriers  
     electron relaxation and dynamics, 247–252  
     LEPR line width, 244–247  
     line shape and g-factor, 221–237  
     magnetic resonance parameters, 220–252  
     photoinitiation and recombination, 238–244  
     spin susceptibility, 210–214  
 Electrospinning, 4  
 Electropray ionization, 10  
 Electrostatic repulsion stabilization, 19  
 Elliot model, 219–220  
 Emission spectroscopy, 314  
 Emulsion polymerization, 37  
 Equivalent resistor-capacitor circuits (ERCs), 279–280  
 Ethylene glycol (EG), 134–135  
 Ethylene vinyl acetate (EVA), 326, 426

- Exchange-coupled pairs (ECP) model, 210–211  
 Exfoliated nanocomposites, 191  
 Expanded graphite (EG), 312, 326
- F**
- Fabrication and challenges existing in the field, 4–5  
 Fabry–Perot (FP) interferometer, 366–367, 367*f*  
<sup>57</sup>Fe isotope, 396–397  
 Fermi energy, 258  
 Field emission scanning electron microscopy (FESEM), 131  
 Flash method spectra of nanocomposites with carbon fillers, 335–336  
 Flash thermography, 315–316  
 Flory Huggins Solution Theory, 69–70  
 Fluorescence correlation spectroscopy (FCS), 174–175, 174*f*  
 Fluorescence resonance energy transfer (FRET), 172–173  
 Fluorescence spectroscopy, 5, 158  
   advances, 173–176  
   fluorescence correlation spectroscopy (FCS), 174–175  
   multiphoton fluorescence microscopy, 173  
   single molecule detection, 175–176  
 fluorescence measurement types, 163–164  
   steady-state fluorescence, 163  
   time-resolved fluorescence, 163–164  
 instrumentation, 161–163, 161*f*  
   detector, 162–163  
   light source, 162  
   sample holder, 162  
 material characteristics, 164–166  
 mechanism of fluorescence, 160–161  
 nanofiller and polymer nanocomposites, studies, 167–172  
   core/shell nanofiller-incorporated polymer composite, 169–171  
   polymer composite with fluorescent semiconducting nanofiller, 167–169  
   properties of polymer nanocomposites, 172–173  
 Fluorophores, 164–165, 173  
 Förster distances, 166  
 Fourier transform infrared (FTIR) spectroscopy, 8, 113–114, 393–394  
   versus dispersive IR, 114  
 nanofillers and their nanocomposites, 115–127  
   qualitative analysis, 115–125  
   nanofiller identification, 116–122  
   polymer nanocomposite identification, 123–125  
   quantitative analysis, 125–127
- Fourier transform spectroscopy (FT-IR/PAS), 317–318  
 Fragility index, 285–287  
 Free-induction decay (FID), 185  
 Freeze drying, 4  
 Frequency- and time-domain PT spectra of nanocomposites, 333–339  
   flash method spectra of nanocomposites with carbon fillers, 335–336  
   PTR and PPE spectra with optically thin samples, 336–339  
   PTR spectra of nanocomposites with carbon fillers, 333–335
- Front detection (FD)-flash method, 315  
 Fullerenes, 25, 25*f*  
   arc discharge, 28–29  
   catalyzed chemical vapor deposition, 29  
   laser ablation, 27  
   miscellaneous preparation techniques, 30
- Functionalized CNTs, 43
- G**
- G band of SWCNTs, 92  
 Galleries, 416  
 Gaussian distribution function, 215  
 G-band region of the SWCNT/PS composites, 99  
 G-factor anisotropy, 209–210  
 Glass transition temperature, 172, 380–382  
 Gold nanoparticles (AuNPs), 188  
 Grafting-to or grafting-from methods of inclusion, 37–39, 38*f*  
 Granular activated carbon (GAC), 122  
 Graphene, 25, 30, 437  
   as filler in nanocomposites, 46–50  
   covalent functionalization of graphene and graphene oxide sheets, 48–49  
    $\pi$ - $\pi$  interactions, individualization, 49  
   polymer/graphene nanocomposites, preparation methods, 49–50  
   surface modification, 47–48  
 Graphene nanocomposites, Raman study of interfacial load transfer, 95–98  
 Graphene oxide (GO), 47, 119–120, 433, 438*f*  
 Graphene platelets (GPLs), 95  
 Graphene polymer nanocomposites, 432–438  
 Graphite, 119–120, 438*f*  
 Graphite oxide, 433  
 Grazing incidence XRD (GIXRD) technique, 414
- H**
- Hahn echo pulse sequence, 185  
 Helicity vector, 26

- Hexamethyldisilazane (HMDS) -treated nanocomposites, 297–299
- High pressure liquid chromatography (HPLC), 70–71
- High-density PE (HDPE), 326–327
- Highest occupied molecular orbital level of the donor (HOMOD), 203–205
- High-resolution Brillouin spectroscopy (HRBS), 9–10
- High-resolution transmission electron microscopy (HRTEM), 131
- Hildebrand solubility parameter, 67–71
- Hildebrand–Scatchard solution theory, 70
- Hoesterey-Letson formalism, 220
- Hump, 412–413
- Hybrid Plastics Inc., 24
- Hydrazine hydrate (HH), 135–137
- Hyperfine polaron interaction, 233
- I**
- Icosahedra, 17
- In situ* nanoparticle and/or polymer formation for nanocomposite synthesis, 39–40
- In situ* polymerization with pre-formed nanoparticles, 37
- Infrared (IR) spectroscopy, 112–115
- basics, 112–113
- IR instruments, 113–114
- dispersive IR spectrometers, 113
- FTIR versus dispersive IR, 114
- interferometric IR spectrometers, 113–114
- sample preparation, 114–115
- Inorganic nanoparticles, 16–24, 34–40
- grafting-to or grafting-from methods of inclusion, 37–39
- in situ* nanoparticle and/or polymer formation for nanocomposite synthesis, 39–40
- in situ* polymerization with pre-formed nanoparticles, 37
- nanoparticle preparation, 20–24
- metallic nanoparticles, 21–23
- metal oxide nanoparticles, 23–24
- nanoparticle structures, 16–17
- nucleation and growth, 17–19
- physical methods of inclusion, 36–37
- physicochemical properties, 19–20
- Interchain spin dynamics, 252
- Interfacial thermal resistance (ITR), 317
- Interferometric IR spectrometers, 113–114
- Intrachain polaron dynamics, 249, 251–252
- Inverse IPPE, 313–314
- Iron and gallium (Fe Ga)-filled polyurethane, 10
- Iron speciation with Mössbauer spectroscopy, 401
- Isomer shifts (IS), 393–394
- J**
- Jahn-Teller effect, 223–226
- Jalbonaski diagram, 160–161, 160f
- K**
- Kaolinite, 31–32
- KBr, 114–115
- Kinetic energy (KE), 453–454
- L**
- Landé factor, 209–210
- Larmor frequency, 183
- Laser ablation, 27, 28f
- Laser-induced plasma spectrometry, 6
- Latent heat thermal energy storage (LHTES), 326
- Latex compounding, 4
- Layer by layer (LbL) deposition, 39
- Lead dimethacrylate polymer films (PLDMA), 38
- Lead sulfide, 147
- Light-induced electron paramagnetic resonance (LEPR) spectroscopy, 207, 218, 223–226, 229–230, 244–247
- Load, 2
- Lorentzian distribution function, 215
- Low-density polyethylene (LDPE), 318, 326, 417
- Low-density polyethylene/montmorillonite (LDPE/MMT) composite systems, 303
- Lowest unoccupied molecular orbital level of the electron acceptor (LUMO), 203–205
- Luminescent polymer nanocomposites, 132
- M**
- M3EH-PPV macromolecules, 226–228
- Magic-sandwich echo (MSE), 185
- Magnetic carbon nanostructures, analysis, 404–406
- Magnetic polymer nanocomposites (mPNCs), 393, 400–401
- Magnetic splitting, 395, 398f
- Market growth of nanocomposites, 3–4
- Material under test (MUT), 279
- Matrix assisted laser desorption ionization, 10
- Mean field theory (MFT) models, 319, 340
- Mechanical reinforcement, improving, 3
- Melt processing and film casting techniques, 36f
- Metal matrix nanocomposites (MMCs), 131, 317
- Metal nanoparticles as nanofillers, 132–144
- Metal oxide nanoparticles, 23–24
- Metal oxides nanofiller, 116–118
- MnO<sub>2</sub> nanocrystals, 117–118
- TiO<sub>2</sub> nanoparticle, 118
- ZnO nanoparticle, 117

- Metal salt reduction, 21
- Metallic nanoparticles, 21–23  
 metal salt reduction, 21  
 organometallic complex reduction/  
 decomposition, 22–23
- Metal–oxide–semiconductor field-effect transistor  
 (MOSFET) technology, 319
- Methanofullerene anion radicals, 233–235
- Michelson interferometer, 113–114
- MicroBT relaxation, 281
- Micro-Raman spectroscopy, polarized, 8
- Microwave-induced plasma techniques, 6
- Mill mixing, 4
- Miller indices, 16–17
- MnO<sub>2</sub> nanocrystals, 117–118
- Modified carbon nanofiber (MCNF), 443
- Monte Carlo simulations, 78–79
- Montmorillonite (MMT), 191, 416  
 organomodified, 326  
 structure, 32f
- Mössbauer spectroscopy, 10, 393, 395f  
 basic operational principles, 394–395  
 general applications, 397–399  
 hyperfine interactions of nucleus, 395–397  
 hyperfine splitting, 397  
 IS due to electron density at nucleus,  
 395–396  
 QS as result of electric field gradient, 396–397  
 iron speciation, 401  
 magnetic carbon nanostructures with, analysis,  
 404–406  
 polymer nanocomposites (PNCs) analysis,  
 400–406  
 surface layer of iron species, characterization,  
 401–404  
 TEM-SAED, 400–401
- Multiphoton fluorescence microscopy, 173
- Multiple quantum (MQ) measurements, 185
- Multiwalled carbon nanotubes (MWCNTs),  
 26–27, 152–154, 326, 427–428
- Myristic acid (MA), 326
- N**
- Nano oxides as nanofillers, 148–152
- Nanodielectrics, 276  
 dielectric analysis, 276–277  
 pulsed electro-acoustic analysis, 300–305  
 TSC spectroscopy studies, 293–299
- Nanofiller, 16–34, 116–122, 132–154, 393  
 carbonaceous nanofiller, 119–120  
 carbon nanotube (CNT), 119  
 graphite, graphene oxide (GO), reduced  
 graphene oxide(rGO), 119–120  
 carbon-based nanomaterials, 152–154  
 carbon-based nano-objects, 24–30  
 preparation methods, 27–30  
 properties of carbon-based nanomaterials, 27  
 structural considerations, 24–27
- carbon nanotubes as fillers in nanocomposites,  
 40–46  
 chemical methods of dispersion of CNTs,  
 41–45  
 physical functionalization/physical blending  
 of CNTs, 45–46  
 physical methods of dispersion of CNTs, 41  
 clay, 30–34, 118  
 modifications, 32–34  
 structures, 31–32
- fluorescence studies, 167–172  
 core/shell nanofiller-incorporated polymer  
 composite, 169–171  
 polymer composite with fluorescent  
 semiconducting nanofiller, 167–169
- graphene as filler in nanocomposites, 46–50  
 covalent functionalization of graphene and  
 graphene oxide sheets, 48–49  
 individualization by  $\pi$ - $\pi$  interactions, 49  
 preparation methods of polymer/graphene  
 nanocomposites, 49–50  
 surface modification of graphene, 47–48
- inorganic nanoparticles, 16–24  
 nanoparticle preparation, 20–24  
 nanoparticle structures, 16–17  
 nucleation and growth, 17–19  
 physicochemical properties, 19–20
- inorganic nanoparticles including clays, 34–40  
 grafting-to or grafting-from methods of  
 inclusion, 37–39  
*in situ* nanoparticle and/or polymer formation  
 for nanocomposite synthesis, 39–40  
*in situ* polymerization with pre-formed  
 nanoparticles, 37  
 physical methods of inclusion, 36–37
- metal nanoparticles, 132–144
- metal oxides nanofiller, 116–118  
 MnO<sub>2</sub> nanocrystals, 117–118  
 TiO<sub>2</sub> nanoparticle, 118  
 ZnO nanoparticle, 117
- nanofiller synergy, 120–122  
 GO/Fe<sub>3</sub>O<sub>4</sub>, 122  
 GO/ZnO nanoparticle, 120–122  
 TiO<sub>2</sub>/Granular activated carbon (GAC/TiO<sub>2</sub>),  
 122
- nano oxides, 148–152
- semiconductor nanocrystals, 144–148
- synergy, 120–122  
 GO/Fe<sub>3</sub>O<sub>4</sub>, 122

- Nanofiller (*Continued*)  
 GO/ZnO nanoparticle, 120–122  
 TiO<sub>2</sub>/Granular activated carbon (GAC/TiO<sub>2</sub>), 122
- Nanoinclusions, 35
- Nanoparticle preparation, 20–24  
 metallic nanoparticles, 21–23  
 metal salt reduction, 21  
 organometallic complex reduction/  
 decomposition, 22–23  
 metal oxide nanoparticles, 23–24
- Nanoparticle structures, 16–17
- Neutron reflectivity (NR), 78–80  
 in interphase and phase segregation studies, 78–79
- Neutron reflectivity studies, 79–82
- 90A-scattering geometry, 369–371
- Nitrophenyl phosphate (NPP), 282
- N*-methyl pyrrolidone (NMP), 74–75
- Nuclear magnetic resonance (NMR) spectroscopy, 7–9, 181  
 NMR analysis of polymer composites, 184–197  
 biopolymer nanocomposites, 193–197  
 elastomer nanocomposites, 185–188  
 thermoplastic nanocomposites, 188–192  
 theoretical backgrounds, 182–184
- Nucleation and growth, 17–19
- O**
- Octahedral aluminum hydroxide, 416
- Octaisobutyl POSS (Oib-POSS), 75–76
- 180A-scattering geometry, 371–372
- Organic dyes, fluorescence studies, 158–159
- Organic polymers, 217–218
- Organic/ inorganic PLLA/ZnO nanocomposites, 195
- Organically modified montmorillonite (OMMT), 287–288, 290, 326, 417
- Organometallic complex reduction/decomposition, 22–23
- Oxidized graphite, 433
- P**
- P3DDT:AFNP composite, 246–247
- P3DDT:PC61BM composite, 229–230, 233–235, 238–239, 242–244, 246–247, 249, 255–256
- P3HT:*bis*-PC61BM composites, 229–230, 233–235, 244, 248–250  
 LEPR spectra, 239
- P3HT:PC61BM composite, 229–230, 233, 239–241, 244, 247, 249–250  
 LEPR spectra, 223–225, 223*f*, 229–230, 239  
 line width of charge carriers photoinduced, 245*f*
- Parker model, 325, 335
- PCDTBT:PC61BM, 230–231, 233, 241–242, 246, 250–252  
 LEPR spectra, 223–225, 223*f*  
 line width of stabilized and mobile charge carriers photoinduced, 246, 246*f*
- PCDTBT:PC61BM BHJ, 231–233  
 intrachain polaron dynamics, 251–252
- Peak width at half of maxima (PWHM), 135–137
- Phase change materials (PCM), 326
- Phase segregation and interphases of polymer nanocomposites, 76–82  
 neutron reflectivity, in interphase and phase segregation studies, 78–79  
 neutron reflectivity studies, 79–82  
 segregation and diffusion of polymer chains, 77–78
- [6,6]-Phenyl-C61-butanoic acid methyl ester (PC61BM), 203–205
- Phosphorescence, 160–161
- Photo bleaching, 158, 175–176
- Photothermal (PT) spectroscopy of polymer nanocomposites, 312  
 adiabatic solid slabs, 1D PT response, 319–325  
 specific transfer functions of PT methods, 323–324  
 theory of BD-PT impulse response, 324–325  
 theory of FD- and BD-PT response with periodic excitation, 321–323  
 composite materials, photothermal studies  
 complex composites, 315–316  
 composites with defined microstructure, 316–318  
 composites with random morphology, 318–319  
 frequency- and time-domain PT spectra of nanocomposites, 333–339  
 flash method spectra of nanocomposites with carbon fillers, 335–336  
 PTR and PPE spectra with optically thin samples, 336–339  
 PTR spectra of nanocomposites with carbon fillers, 333–335  
 materials and methods, 325–333  
 experimental photothermal setups, 329–332  
 flash method for thermal diffusivity measurement, 332–333  
 motivation for materials choice, 325–326  
 preparation and properties, 326–328  
 multiscale analysis of effective thermal conductivity, 339–347  
 background on effective thermal conductivity modeling, 339–342

- effective thermal conductivity results and discussion, 342–344
  - indirect evidence of thermal percolation in composites with EG and CNT fillers, 344–347
  - results of, 347–350
- Physical methods of dispersion of CNTs, 41
- Physical vapor deposition (PVD) process, 17–18
- $\pi$ - $\pi$  interactions, individualization, 49
- Plasma emission spectroscopy, 6
- Plastics, applications of nanocomposites, 3–4
- Polarized micro-Raman spectroscopy, 8
- Polaron dynamics, 219, 250–252
- Polarons, 204–205, 211–213, 238–239, 244–245, 255–256
- Poly(3-alkylthiophene) (P3AT), 152–154, 203–204, 218–219
- Poly(3-hexylthiophene)-b-polystyrene (P3HT-b-PS), 152–154
- Polyacrylate (PAC), 421–422
- Polyamide 6 (PA6), 430f
- Polyamidoamine (PAMAM), 169–170
- Polyaniline (PANI), 149–151, 253, 437–438
  - PANI:TSA, 255–256
  - PANI-ES, 255
  - PANI-GO nanocomposite, 438f
  - PANI/tin oxide (SnO<sub>2</sub>) hybrid nanocomposite, 149–151
- Poly(butylene succinate) (PBS), 326
- Poly[(butylene succinate)-co-adipate] (PBSA), 440
- Polycarbonate (PC), 375
  - PC matrix, 295
- Polycarbonate/TiO<sub>2</sub> (PC/TiO<sub>2</sub>), 124–125
- Poly(dimethylsiloxane) polymer (PDMS), 95, 287
- Polyethylene (PE)/montmorillonite (MMT) nanocomposites, 191
- Polyhedral oligomeric silsesquioxane (POSS), 24, 75–76
- Poly(HEMA-co-MMA)-g-POSS, 188–190, 190f
- Polyisoprene, 169–170
- Poly(lactic acid) (PLA), 326, 436
- Polymer clay nanocomposites, 416–425
- Polymer composite with fluorescent semiconducting nanofiller, 167–169
- Polymer matrix nanocomposites (PMCs), 131–154
  - carbon-based nanomaterials as nanofillers, 152–154
  - metal nanoparticles as nanofillers, 132–144
  - nano oxides as nanofillers, 148–152
  - optical properties, 131–132
  - semiconductor nanocrystals as nanofillers, 144–148
- Polymer nanocomposite identification, 123–125
  - polycarbonate/TiO<sub>2</sub> (PC/TiO<sub>2</sub>), 124–125
  - polypropylene/clay, 125
  - polystyrene/TiO<sub>2</sub> (PS/TiO<sub>2</sub>), 123–124
  - quantitative analysis, 125–127
- Polymer/graphene nanocomposites, preparation methods, 49–50
- Polymer/inorganic nanocomposites (PINC)s, 34–35
- Polymer:fullerene nanocomposites, EPR spectroscopy, 202, 208–220
  - Dysonian spectral contribution, 217–218
  - electron relaxation and spin dynamics, 218–219
  - Landé factor, 209–210
  - line shape and width, 214–217
  - mechanism of charge transport in polymers, 219–220
  - spin-assisted molecular electronics, utilization of polymer composites, 252–261
  - spin charge carriers, magnetic resonance parameters, 220–252
    - electron relaxation and dynamics, 247–252
    - LEPR line width, 244–247
    - line shape and g-factor, 221–237
    - photoinitiation and recombination of charge carriers, 238–244
  - spin susceptibility, 210–214
- Polymers and nanocomposites, 373–385
  - acoustic wave velocity, 373–377
  - biological systems, 384–385
  - Brillouin and other techniques, coupling, 384
  - elastic constants, 377–379
  - glass transition temperature, 380–382
  - refractive index, 382–383
- Poly(methyl methacrylate) (PMMA), 66, 77, 146–147, 290–291, 345–347, 375, 436
- Poly[*N*-9'-hepta-decanyl-2,7-carbazole-alt-5,5-(4',7'-di-2-thienyl-2',1',3'-benzothiadiazole)] (PCDTBT), 204–205, 230–231
- Polyol one, 21
- Polypropylene (PP), 125, 191, 419
- Polypyrrole (PPy), 452, 458t
- Polystyrene (PS), 66, 146–147, 159, 431
  - PS/TiO<sub>2</sub>, 123–124
  - Raman spectroscopy study on, 90–95
- Poly(styrene sulfonate), 67, 139–141
- Polysulfone (PSU), 423
- Polytetrafluoroethylene (PTFE) matrix, 297
- Polyurethane (PU), 168–169, 284–287
- Polyvinyl alcohol (PVA), 39, 135–139, 167, 194–195, 427
- Poly(vinyl pyrrolidone), 67

- Polyvinylidene fluoride (PVDF), 77, 126, 293–294, 382, 419–420, 431f  
thermally stimulated current, 294
- Polyvinylidenedifluoride (PVDF)–ZnO nanocomposite, 149
- PPy–WO<sub>3</sub> nanocomposite, 462t  
XPS study, 460–462
- Pre-formed nanoparticles, *in situ* polymerization, 37
- Pristine graphene, 46–47
- PS-*b*-ethylene propylene (PS-PEP) diblock copolymers, 76–77
- Pulsed electro-acoustic (PEA) method, 300–305
- Q**
- Quadrupole splitting (QS), 395
- Quantum dots (QDs), 144–146, 159, 173  
core-shell, 170f
- Quantum efficiency, 73–74, 204–205
- Quasi-one-dimensional (Q1D) charge transfer, 207
- Quasi-three-dimensional (Q3D) hopping, 207
- R**
- Radial breathing mode (RBM), 88
- Raman and TERS spectroscopy studies, 98–108  
interaction of SWCNT and PS at the interface in SWCNT/PS nanocomposites, 98–101  
TERS spectroscopy study of local interactions at the interface of SBR/MWCNT nanocomposites, 101–108
- Raman spectroscopy, 8, 41, 88–89, 99, 120–122, 362, 384  
study of interfacial load transfer in graphene nanocomposites, 95–98  
study on SWCNT/polystyrene nanocomposites, 90–95
- Rayleigh line, 364–365, 364f
- Reduced graphene oxide (rGO), 119–120, 433
- Reflection-mode PPE (R-PPE), 313–314
- Refractive index, 9, 132, 144, 382–383
- Refractometry, 74–76
- Reptation model, 80
- Resonance energy transfer, 166
- Resonance Raman (RR) spectrum, 120–122
- Reversible addition fragmentation chain transfer polymerization (RAFT), 188–190
- RITA-scattering geometry, 372–373
- S**
- Scanning electron microscopy (SEM), 75, 95
- Scattering geometries, 369–373  
90A-scattering geometry, 369–371
- Scotch® tape method, 30
- Selected area electron diffraction (SAED), 400–401
- Semiclassical Marcus theory, 216
- Semiconductor nanocrystals as nanofillers, 144–148
- Shear/transverse wave, 373
- Silica/PNCs, 425–427
- Silica-filled composites, TSC spectra, 298f
- Single molecule detection, 175–176
- Single-walled carbon nanotubes (SWCNTs), 25–26, 26f, 44, 65–68, 80–81, 152–154, 427–428  
and polystyrene at the interface studied by Raman and TERS spectroscopy, 98–101  
Raman spectroscopy study, 90–95
- Sintered ceramic materials, dielectric properties, 277–278
- Slurry methodology, 280–281
- Small-angle X-ray scattering (SAXS) method, 440–443, 441f, 442f
- Sodium dodecyl sulfate (SDS), 46
- Sodium formaldehyde (SFS), 135–137
- Sol–gel process, 23–24, 131
- Solid state NMR, 8–9, 182, 193–194
- Solid-echo pulse sequence, 185
- Solubility parameters, 67–68, 70
- Spark/arc (emission) spectroscopy, 6–7
- Spectral applications in polymers and its nanocomposites, 8–10
- Spectral techniques and advantages, 5–7
- Spin angular momentum, 182–183
- Spin charge carriers  
electron relaxation and dynamics, 247–252  
LEPR line width, 244–247  
line shape and g-factor, 221–237  
magnetic resonance parameters, 220–252  
photoinitiation and recombination, 238–244
- Spin flip-flop probability, 214
- Spin susceptibility, 217–218, 258–259
- Spin-assisted molecular electronics, utilization of polymer composites, 252–261
- Spins, 208
- SP-N5.0 system, 194–195
- Stabilization by surfactant use, 19
- Starch–clay nanocomposites, clay dispersion, 193–194
- Static light scattering, 69, 71  
theory, 71–74  
thermodynamic solution behavior of nanoparticle systems, 74–76
- Static paramagnetic susceptibility, 210–211
- Steady-state fluorescence, 163
- Step-growth polymerization, 165–166

Steric hindrance stabilization, 19  
 Stober process, 23–24  
 Stokes shift, 159, 164  
 Stokes/anti-Stokes scattering, 363  
 Styrene-butadiene rubber (SBR), 186  
 Surface modification of graphene, 47–48  
 Surface plasmon resonance (SPR) absorption, 132–134

## T

T<sub>2</sub> relaxometry, 184–185  
 Tandem interferometry, 367–369  
 TEM-SAED and Mössbauer spectroscopy, 400–401  
 Tetraethyl orthosilicate (TEOS), 23–24  
 Thermal barrier effects, 3–4  
 Thermal conductivity of nanocomposites, 339–347  
   effective thermal conductivity modeling, 339–342  
   effective thermal conductivity results and discussion, 342–344  
   indirect evidence of thermal percolation in composites with EG and CNT fillers, 344–347  
 Thermal diffusivity measurement, flash method, 332–333  
 Thermal energy storage (TES), 326  
 Thermally stimulated current (TSC), 293–299  
 Thermally stimulated depolarization current (TSDC) *see* Thermally stimulated current (TSC)  
 Thermodynamic solution behavior of nanoparticle systems, 67–76  
   as defined with static light scattering and refractometry, 74–76  
   static light scattering, 71  
   theory, 71–74  
 Thermoplastic nanocomposites, 188–192  
 Time-resolved fluorescence, 163–164  
 Tip-enhanced Raman scattering (TERS) spectroscopy, 89, 101–108  
 Titanium dioxide (TiO<sub>2</sub>) nanoparticle, 118, 151–152  
 Transient absorption techniques, 206–207  
 Transmission electron microscopy (TEM), 400–401  
 Transmittance, 126  
 Transparent polymer matrices, 132  
 Trisilanophenyl POSS (Tsp-POSS), 75–76  
 Tungsten hexachloride (WCl<sub>6</sub>), 453  
 Tungsten oxide (WO<sub>3</sub>), 453, 458–460  
   survey table, 460r  
   XPS study, 458–460

Turkevich synthesis, 21  
 Twinned cuboctahedra, 17

## U

Ultrahigh molecular weight polyethylene (UHMWPE), 434, 435f  
 Ultraviolet and visible spectroscopy studies, 130  
   characterization techniques, 131  
   polymer matrix nanocomposites (PMCs), 131–154  
     carbon-based nanomaterials as nanofillers, 152–154  
     metal nanoparticles as nanofillers, 132–144  
     nano oxides as nanofillers, 148–152  
     optical properties, 131–132  
     semiconductor nanocrystals as nanofillers, 144–148  
   types of nanocomposites, 130–132  
 Ultraviolet photoelectron spectroscopy, 453–454  
 Unexpanded graphite (UG), 326  
 UV absorption, 132, 149, 167–168  
 UV-Vis spectroscopy, 7, 70–71, 131–139, 141–146, 149–155  
 UV-visible absorption spectrum, 9

## V

Valence band, 164  
 Van der Waals interactions, 47, 93  
 Vibrational spectroscopy, 7

## W

Wallace's approach, 47–48  
 Wide-angle X-ray scattering (WAXS), 413  
 Wide-angle XRD, 414–440  
   carbon nanotube PNCs, 427–432  
   cellulose nanocrystal PNCs, 439–440  
   graphene PNCs, 432–438  
   of nanoparticles (NPs), 414–415  
   polymer clay nanocomposites, 416–425  
   of polymer nanocomposites, 415–440  
   silica/PNCs, 425–427  
 Wulff polyhedra, 16–17

## X

Xenon bulbs, 162  
 X-ray diffraction (XRD), 393–394  
 X-ray diffraction spectroscopy (XRDS), 410  
   basic principles, 411–413  
   new developments, 443  
   of polymer nanocomposites, 410  
   small-angle x-ray scattering, 440–443

- X-ray diffraction spectroscopy (XRDS)  
(*Continued*)  
variants, 413–414  
wide-angle XRD, 414–440  
  carbon nanotube PNCs, 427–432  
  cellulose nanocrystal PNCs, 439–440  
  graphene PNCs, 432–438  
  of NPs, 414–415  
  of PNCs, 415–440  
  polymer clay nanocomposites, 416–425  
  silica/PNCs, 425–427  
  of ZnO nanoparticles, 415*f*
- X-ray photoelectron spectroscopy (XPS), 393–394  
  applications, 456  
  basic principle, 453–455  
  DBSA-doped PPy–WO<sub>3</sub> nanocomposite,  
    462–464  
  measurements, basic components, 455  
  of nanofillers and polymer nanocomposites, 452  
  PPy, 456–458  
  PPy–WO<sub>3</sub> nanocomposite, 460–462  
  tool for characterization of polymer and its  
    composite, 453–456  
  WO<sub>3</sub>, 458–460
- X-ray spectroscopy, 6
- Y**  
Young's moduli, 27, 89
- Z**  
Zimm plots, 72–73  
ZnO nanoparticle, 117, 149, 167–168  
  FTIR spectrum, 411*f*  
  X-ray diffraction diffractogram, 415*f*  
ZnO-based polymer nanocomposite, 167